Forests are expanding—which could be bad news for climate p. 788

Problematic internet use parallels drug addiction p. 798

Policy implications of research on biological sex p. 802

Science

$15
20 MAY 2022
science.org

AAAS

LASTING IMPRESSIONS

Fossil imprints show the resilience of nannoplankton pp. 795 & 853

AAAS

AMERICAN ASSOCIATION FOR
THE ADVANCEMENT OF SCIENCE

Thank you to the 2021 members of the AAAS Corporate Circle

AAAS is thankful to last year's members whose philanthropic contributions provide critical support to AAAS and its programs.

3M

Johnson & Johnson

SANOFI
Empowering Life

Stories that captivated youth in 2021 included AI-driven approaches to predicting protein structure.

2021 Tencent–*Science* Breakthroughs: Continuous Curiosity and Innovation

Despite challenges spurred by the ongoing pandemic, last year was a wellspring for scientific discovery, exploration, and innovation. From the launch of a massive new space station and "microflyers" inspired by maple seeds to new methods for predicting protein structure and manufacturing starch from carbon dioxide, and from enlightening discoveries about the obesity gene to revelations about the muon's magnetism that could upend the Standard Model of particle physics, 2021 gave us gift upon gift of scientific delights. We marveled at the identification of a skull belonging to a previously unknown species that could be an even closer ancestor to modern humans than we've ever seen before, and we got closer to potentially harnessing fusion energy. It's fitting that we pause a moment and honor those whose tireless yearning for discovery contributed to our knowledge about nature's systems and structures in spectacular ways.

For more than 30 years, *Science* magazine has been recognizing the intersection of human curiosity and the gusto of people who want to give back through innovation. The 2021 breakthroughs described below were collected by the News team at *Science* with suggestions from the next generation of science's movers and shakers: kids. Tencent—a world-leading internet company and artificial intelligence (AI) leader—leveraged its social, data, and analysis services, and collected votes from over 3.4 million young users via Tencent Docs, QQ Browser, and Sogou Wenwen. After fully gauging the interests of these teens, Tencent and editorial and news teams of *Science* chose the final 10 breakthrough topics.

This year, the breakthroughs have two especially interesting themes: Each showcases humanity's ever-increasing capacity to tackle tough problems, while it also takes a significant step in shaping how we will explore the next frontier of the unknown. For example, when scientists utilized two AI-driven approaches to predict protein structure—an amazing discovery given the high complexity and large quantity of these twisty, geometric shapes—they ticked multiple boxes. By demonstrating that AI could help solve this knotty problem, they further opened the door to AI's expanding power as a tool for pursuing other scientific investigations.

Another 2021 breakthrough involved Chinese scientists discovering a de novo route for artificial starch synthesis from carbon dioxide (CO_2). Starch is the major component of grain as well as an important industrial feedstock. In nature, it is mainly produced by green plants fixing CO_2 through photosynthesis, and for crops the theoretical energy conversion efficiency of this process is no more than 2%. Since it does not rely on plant photosynthesis, this new technology requires only carbon dioxide, hydrogen, and electricity as raw materials, saving extensive farming, fertilizing, and processing of large quantities of crops. The novel artificial route designed by researchers consists of only 11 core reactions to convert CO_2 into starch, with an efficiency 8.5-fold higher than starch biosynthesis in maize. Synthesizing starch will be a significant disruptive technology in today's world. It allows us to see more possibilities: A shift in the agricultural mode from traditional planting to industrial manufacturing, which helps address the pressing issues of food production, arable land, ecology, and climate. And even further into the future, this technology will prove to be indispensable for space colonization.

Expanded capacity and innovative methodology has emboldened us, engendering a renewal of the human spirit to take on the most formidable challenges. As scientists and engineers collaborate in harmony, prompted only by a dedication to excellence and a commitment to serve, we witness breakthroughs that help us to see the world differently. But perhaps more importantly, these breakthroughs enable us to see ourselves differently—as better, stronger, more agile, and more committed to excellence than ever before. This selection of annual breakthroughs is more than just a review of achievements in the past year. More importantly, it carries forward the spirit of science from generation to generation. We hope that by passing the torch of science, more talented young minds will be inspired to devote themselves to scientific careers and press ahead with a passion for seeking the truth and the audacity to overcome the greatest hardships.

Sponsored by

Tencent 腾讯

PHOTO: © PRODUCTION PERIG/SHUTTERSTOCK.COM

MICHELSON PHILANTHROPIES & Science PRIZE FOR IMMUNOLOGY

REWARDING HIGH-RISK RESEARCH. SUPPORTING EARLY-CAREER SCIENTISTS. HELPING TO FIND CURES FASTER. **APPLY TODAY**

Now accepting applications for the Michelson Philanthropies & *Science* Prize for Immunology.

The Michelson Philanthropies and Science Prize for Immunology focuses on transformative research in human immunology, with trans-disease applications to accelerate vaccine and immunotherapeutic discovery. This international prize supports investigators 35 and younger, who apply their expertise to research that has a lasting impact on vaccine development and immunotherapy. It is open to researchers from a wide range of disciplines including computer science, artificial intelligence/machine learning, protein engineering, nanotechnology, genomics, parasitology and tropical medicine, neurodegenerative diseases, and gene editing.

Application deadline: Oct. 1, 2022.

For more information visit:
www.michelsonmedicalresearch.org

#MichelsonPrizes

"The Michelson Philanthropies & Science Prize for Immunology will greatly impact my future work. As I am just starting my scientific career, it will illuminate my work, spark interest and support me to continue my research in this field."

Paul Bastard, MD, PhD,
Laboratory of Human Genetics of Infectious Diseases, Imagine Institute (INSERM, University of Paris), Paris, France; and The Rockefeller University, New York.

Dr. Bastard received the inaugural Grand Prize for his essay: "Why do people die from COVID-19: Autoantibodies neutralizing type I interferons increase with age."

GRAND PRIZE:
$30,000

FINALIST PRIZE:
$10,000

CONTENTS

20 MAY 2022 • VOLUME 376 • ISSUE 6595

788

Forests produce water vapor and other compounds that promote cloud formation, helping to cool the planet.

NEWS

IN BRIEF

780 News at a glance

IN DEPTH

782 'COVID-ization' of research levels off
Researchers who pivoted from distant disciplines produced lower impact work, study finds *By J. Brainard*

783 Do you hate your face mask? There's hope
A U.S. government contest has 10 companies competing to make better face coverings
By J. Cohen

785 Shadow of Milky Way's giant black hole revealed
Scene resembles earlier image from a distant galaxy, as Einstein's theory predicts
By D. Clery
PODCAST

786 Soils' coating helps keep dust storms at bay
Breakdown of "biocrusts" allows wind to attack dryland soils *By E. Pennisi*

787 NIH rolls out stricter disclosure rules for sexual harrassment
Institutions now legally required to inform agency if grantees are "disciplined" for workplace misbehavior *By J. Kaiser*

FEATURES

788 The forest forecast
Climate change could lead to a net expansion of global forests. But will a more forested world actually be cooler?
By F. Pearce

INSIGHTS

PERSPECTIVES

792 Managing forests for competing goals
Tree plantations face difficult trade-offs between production and ecological goals
By J. Gurevitch
RESEARCH ARTICLE p. 839; REPORT p. 865

794 Mitochondrial complex complexification
Variation in complex composition provides clues about the function of individual subunits *By M. A. Huynen and D. M. Elurbe*
RESEARCH ARTICLE p. 831

795 Fossil imprints from oceans of the past
Marine phytoplankton show notable resilience during extreme ocean states
By J. Henderiks
REPORT p. 853

796 T cell immune responses deciphered
A machine-learning approach reveals antigen encoding that predicts T cell responses
By A. Nourmohammad
REPORT p. 880

798 Can internet use become addictive?
Problematic internet use parallels drug addiction, but the mechanisms are not yet clear *By M. Brand*

800 Electric buzz in a glass of pure water
Hydrogen bond charge transfer in water may have far-reaching chemical implications
By D. Ben-Amotz

POLICY FORUM

802 Law, policy, biology, and sex: Critical issues for researchers
Researchers should be aware of how sex-difference science is (mis)applied in legal and policy contexts
By M. Sudai et al.

BOOKS *ET AL.*

805 Shaping Earth in our image
An interdisciplinary interrogation of the Anthropocene misses the chance to probe broader and deeper
By E. C. Ellis and M. Maslin

806 The fastest R&D lab on the planet
From car safety to road design, motorsport innovation has spilled over into other arenas *By L. Vinsel*

LETTERS

809 Good science requires better animal welfare
By V. Neville et al.

810 Indigenous lands protect Brazil's agribusiness
By L. Ferrante and P. M. Fearnside

PHOTO: PHILIPPE HENRY/BIOSPHOTO/MINDEN PICTURES

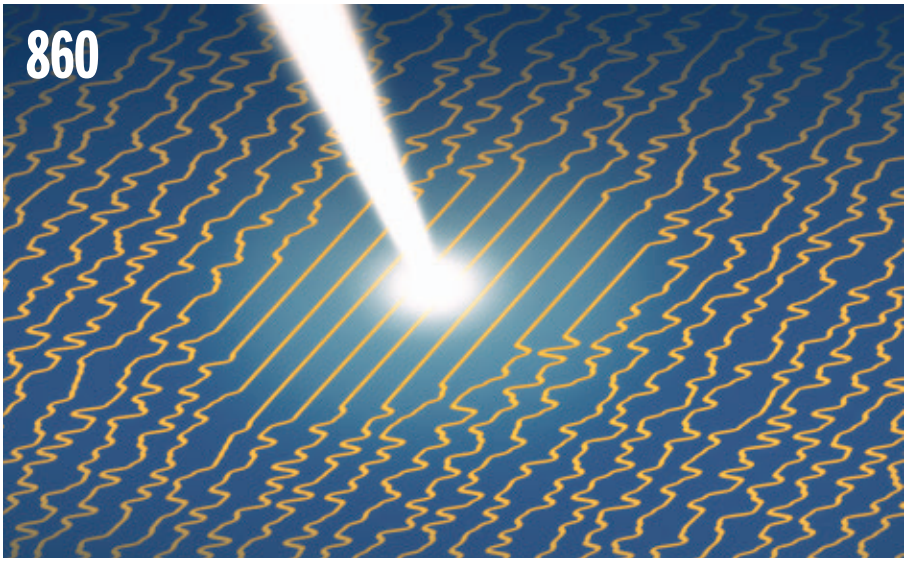

A pulse of light enhances the coherence of charge density waves in a high-temperature superconductor.

810 Irrawaddy dolphins continue to decline
By C. Sonne et al.

RESEARCH

IN BRIEF

812 From *Science* and other journals

RESEARCH ARTICLES

815 Microtubules
Posttranslational modification of microtubules by the MATCAP detyrosinase *L. Landskron* et al.
RESEARCH ARTICLE SUMMARY; FOR FULL TEXT: DOI.ORG/10.1126/SCIENCE.ABN6020

816 Topological matter
All topological bands of all nonmagnetic stoichiometric materials *M. G. Vergniory* et al.
RESEARCH ARTICLE SUMMARY; FOR FULL TEXT: DOI.ORG/10.1126/SCIENCE.ABG9094

817 Neurodevelopment
Oligodendrocyte precursors guide interneuron migration by unidirectional contact repulsion *F. Lepiemme* et al.
RESEARCH ARTICLE SUMMARY; FOR FULL TEXT: DOI.ORG/10.1126/SCIENCE.ABN6204

818 Cell biology
The deubiquitinase USP8 targets ESCRT-III to promote incomplete cell division *J. Mathieu* et al.

823 Molecular evolution
Epistatic drift causes gradual decay of predictability in protein evolution *Y. Park* et al.

831 Structural biology
Structures of *Tetrahymena*'s respiratory chain reveal the diversity of eukaryotic core metabolism *L. Zhou* et al.
PERSPECTIVE p. 794

839 Forest ecology
The biodiversity and ecosystem service contributions and trade-offs of forest restoration approaches *F. Hua* et al.
PERSPECTIVE p. 792

844 Kinetochore
Structure of the human inner kinetochore bound to a centromeric CENP-A nucleosome *S. Yatskevich* et al.

REPORTS

853 Fossil record
Global record of "ghost" nannofossils reveals plankton resilience to high CO_2 and warming *S. M. Slater* et al.
PERSPECTIVE p. 795

857 Plant science
Recognition of pathogen-derived sphingolipids in *Arabidopsis* *H. Kato* et al.

860 Superconductivity
Enhanced charge density wave coherence in a light-quenched, high-temperature superconductor *S. Wandel* et al.

865 Forestry
Multispecies forest plantations outyield monocultures across a broad range of conditions *Y. Feng* et al.
PERSPECTIVE p. 792

869 Biocatalysis
Directed evolution of nonheme iron enzymes to access abiological radical-relay C(sp^3)–H azidation *J. Rui* et al.

874 Geophysics
Optical interferometry–based array of seafloor environmental sensors using a transoceanic submarine cable *G. Marra* et al.

880 Immunology
Universal antigen encoding of T cell activation from high-dimensional cytokine dynamics *S. R. Achar* et al.
PERSPECTIVE p. 796

DEPARTMENTS

779 Editorial
The Court is ignoring science
By D. G. Foster

886 Working Life
Don't panic *By S. Holzer*

ON THE COVER

Scanning electron micrograph of minuscule coccolithophorid plankton cell wall coverings preserved as exquisite fossil impressions on the surface of 183-million-year-old Jurassic organic matter. Coccolithophores are a type of microscopic marine phytoplankton, and their hard calcareous plates, called coccoliths (~5 micrometers long), are normally abundant in the fossil record. Here they have dissolved from these ancient rocks deposited during a global warming interval, leaving only their imprint "ghosts" behind. See pages 795 and 853. *Credit: Sam M. Slater, Paul Bown, Richard J. Twitchett, Silvia Danise, Vivi Vajda*

ILLUSTRATION: GREG STEWART, SLAC NATIONAL ACCELERATOR LABORATORY

Science Careers 885

SCIENCE (ISSN 0036-8075) is published weekly on Friday, except last week in December, by the American Association for the Advancement of Science, 1200 New York Avenue, NW, Washington, DC 20005. Periodicals mail postage (publication No. 484460) paid at Washington, DC, and additional mailing offices.

Copyright © 2022 by the American Association for the Advancement of Science. The title SCIENCE is a registered trademark of the AAAS.

Domestic individual membership, including subscription (12 months): $165 ($74 allocated to subscription). Domestic institutional subscription (51 issues): $2212; Foreign postage extra: Air assist delivery: $98. First class, airmail, student, and emeritus rates on request. Canadian rates with GST available upon request, GST #125488122. Publications Mail Agreement Number 1069624. **Printed in the U.S.A.**
Change of address: Allow 4 weeks, giving old and new addresses and 8-digit account number. **Postmaster:** Send change of address to AAAS, P.O. Box 96178, Washington, DC 20090–6178. **Single-copy sales:** $15 each plus shipping and handling available from backissues.science.org; bulk rate on request. **Authorization to reproduce** material for internal or personal use under circumstances not falling within the fair use provisions of the Copyright Act can be obtained through the Copyright Clearance Center (CCC), www.copyright.com. The identification code for *Science* is 0036-8075. *Science* is indexed in the *Reader's Guide to Periodical Literature* and in several specialized indexes.

EDITORIAL

The Court is ignoring science

A recently leaked draft opinion indicated that the US Supreme Court is prepared to overturn *Roe v. Wade* as early as next month in the matter of *Dobbs v. Jackson Women's Health Organization*. In doing so, the Justices won't just be disregarding decades of precedent. They'll also be disregarding ample evidence of abortion's positive impact on patients' health and well-being.

In *Roe v. Wade* (1973), the Court struck down a Texas law criminalizing abortion and held that the Constitution protects the right to decide whether to end a pregnancy. Justice Samuel Alito's leaked opinion in *Dobbs* stems from the idea that abortion rights are not mentioned in the Constitution or rooted in US history. But we, as a society, are equipped with more factual information today than the framers of the Constitution were. There is a long history of Supreme Court abortion decisions drawing on evidence. In *Whole Woman's Health v. Hellerstedt* (2016), the Court emphasized the importance of considering data when reviewing abortion restrictions. It is critical now that the Court adhere to precedent and insist that constitutional rights be guided by evidence, not by ideology.

> **"It is critical now that the Court... be guided by evidence, not by ideology."**

The Turnaway Study, which I led, was designed to contribute to that body of evidence. Launched in 2007, more than 40 scientists from nine universities and four research institutes worked on the study. We were inspired to do so by Justice Anthony Kennedy, who raised the question of an abortion's effect on a pregnant woman in *Gonzalez v. Carhart* (2006), a case that considered the constitutionality of a federal ban on one abortion procedure. In his majority opinion, Justice Kennedy argued that there were "no reliable data to measure the phenomenon" of potential abortion regret, and the Court thus upheld the law.

My colleagues and I resolved to find that data—so that Supreme Court Justices and policy-makers could base their decisions not on conjecture, but on hard science. To that end, the Turnaway Study followed almost 1000 women across the country for 5 years to see how having an abortion, or being denied one, affected their physical health, mental health, finances, relationships, and children.

What we found was staggering.

The research revealed that patients who were able to receive an abortion were more than six times more likely to report aspirational 1-year plans than those who were denied one. They are more likely to have a wanted child later and better able to take care of the children they already have. Because the majority of abortion patients are already parents, this means that being able to obtain an abortion has powerful, multigenerational impacts.

By contrast, if people are forced to carry a pregnancy to term, they are more likely to experience lasting financial hardships. After being denied an abortion, women had three times greater odds of being unemployed than those who obtained abortions and had four times higher odds of being below the federal poverty level.

Their physical and mental health are also at risk: Women unable to obtain an abortion said they had more symptoms of anxiety, lower self-esteem, and lower life satisfaction. They were more likely to report "fair or poor" health than those who had received abortions. And, again, their families feel the effects: Patients report more difficulty bonding with their baby, and their older children have worse developmental outcomes and are more likely to live in poverty.

The clearest finding from the Turnaway Study is that people know what is best for themselves and their families. The results are not theories or guesses. They are not anecdotes to be trotted out at politically expedient moments. They are based on a large set of data in which statistically significant patterns emerged across many people. And they are the basis for more than 50 articles that have been published in high-quality, peer-reviewed scientific journals*.

As a researcher, I believe that science should not be merely an ivory-tower pursuit, divorced from the world around it. Understanding the nature, causes, and solutions to human problems is one of the primary goals and great gifts of science. Science is clearly relevant to the controversial issues of our time, including abortion access in the United States—in fact, science is especially critical in these moments. The highest court in the United States should not ignore it.

–Diana Greene Foster

PHOTO: SIDRA GREENE

Diana Greene Foster is a professor in the Department of Obstetrics, Gynecology, and Reproductive Sciences and director of research at Advancing New Standards in Reproductive Health, University of California San Francisco, CA, USA. diana.foster@ucsf.edu

* https://www.ansirh.org/sites/default/files/publications/files/turnawaystudyannotatedbibliography.pdf

Published online 16 May 2022; 10.1126/science.adc9968

> “We don’t think that [China’s zero COVID-19 policy] is sustainable, considering the behavior of the virus.”
>
> **Tedros Adhanom Ghebreyesus,** head of the World Health Organization, referring to strict lockdowns to prevent spread. China called the remark “irresponsible” and censored it.

IN BRIEF

Edited by **Jeffrey Brainard**

A worker disinfects a store in Pyongyang, North Korea, as an illness believed to be COVID-19 spreads.

COVID-19

A ‘fever’ hits unprotected North Korea

Aid agencies are gearing up for a robust response against what North Korea calls a “malignant fever” sweeping the country that is almost certainly COVID-19. As *Science* went to press, new cases of the illness appeared to be doubling every 2 days in the world’s last large population, some 25 million people, lacking immunity to the disease from vaccination or infection. “We’re looking at a major, major catastrophe,” says Kee Park, a global health specialist at Harvard Medical School. Early in the pandemic, North Korea closed itself off from the world in a bid to keep the virus at bay. That strategy largely succeeded for 2 years, despite occasional reports of possible outbreaks. Until last month, North Korea had tested just 66,000 people for COVID-19 and reported zero cases. It also ignored offers of COVID-19 vaccines. But the “great upheaval,” as North Korea’s leader Kim Jong Un calls the outbreak, may persuade the reclusive nation to accept such assistance as vaccines, antivirals, and rapid diagnostic tests. “We need to fast-track the aid,” Park says.

Shots cut risks of Long Covid

PUBLIC HEALTH | A study of more than 1 million Americans has found vaccination is linked to substantially lower risk of lingering symptoms after COVID-19 infections, often called Long Covid. The result, published on 7 May in *Open Forum Infectious Diseases*, confirms similar findings from smaller studies. Researchers at Case Western Reserve University used electronic medical records to compare symptoms in vaccinated and unvaccinated people before and 3 months after an infection, both before and after vaccines became available. The data include about 1.5 million unvaccinated U.S. residents and 25,000 who had been vaccinated. All participants had infections confirmed by polymerase chain reaction testing. The researchers looked for a range of new health concerns after infection, such as diabetes, heart disease, and hypertension. They also examined the persistence of symptoms associated with COVID-19, such as fatigue and body aches. For each symptom or diagnosis studied, rates were lower in the vaccinated cohort. For example, rates of persistent headaches and body aches in the vaccinated group were roughly half.

Antidepressant nixed as COVID Rx

DRUG DEVELOPMENT | The U.S. Food and Drug Administration (FDA) decided this week not to approve the antidepressant fluvoxamine to treat COVID-19. Fluvoxamine is a selective serotonin reuptake inhibitor typically prescribed for depression or obsessive-compulsive disorder. In October 2021, a randomized, controlled trial in Brazil showed unvaccinated people with preexisting conditions who took the drug were 32% less likely than those who took a placebo to be hospitalized or need prolonged medical care. But FDA said proof of the drug’s effectiveness was “not persuasive.” Other treatments for COVID-19, including the oral antiviral pills Paxlovid and molnupiravir, have been available since October 2021 and have proved to be more effective than fluvoxamine.

PHOTO: KYODO NEWS/GETTY IMAGES

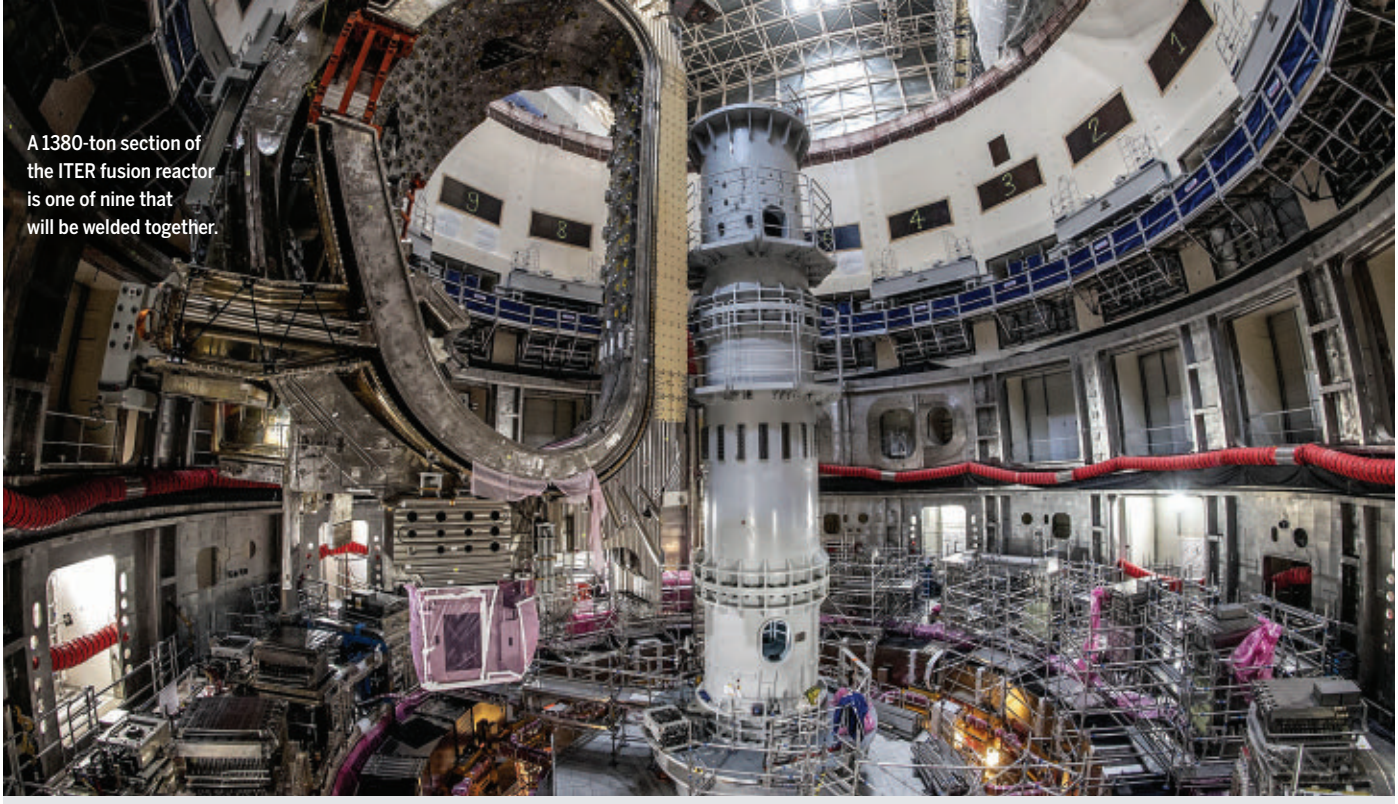

A 1380-ton section of the ITER fusion reactor is one of nine that will be welded together.

PHOTO: © ITER ORGANIZATION/ HTTP://WWW.ITER.ORG/

ENERGY RESEARCH

Leader who revamped fusion project dies

Bernard Bigot, who as director-general of the giant ITER fusion test reactor under construction in France was credited with turning around the behind-schedule and overbudget project, died last week at age 72 after an illness. A theoretical chemist, Bigot took control of the world's biggest science project in 2015, as some politicians in the United States were pushing to withdraw from the seven-member partnership. Bigot transformed ITER from an industrial stimulus program to a bona fide scientific experiment, observers say. In fact, the parts for the ITER reactor are now more than 75% complete. Last week, ITER announced the installation of the first of nine segments of its 11-meter-tall, doughnut-shaped vacuum chamber—although further work is paused as regulators look into certain safety issues. When it starts up in 2025, the facility, costing more than €17 billion, aims to fuse hydrogen nuclei to form helium, ultimately yielding 10 times more energy than is needed to produce the plasma. Bigot will be succeeded on an interim basis by Deputy Director-General Eisuke Tada.

Tooth puts Denisovans in Laos

ARCHAEOLOGY | A molar recovered from a cave in northeastern Laos in 2018 closely resembles the few known examples of molars of the mysterious extinct human species known as Denisovans, close cousins of the Neanderthals. Previous Denisovan fossils have been found in Siberia and Tibet. The new finding, from Southeast Asia, greatly expands Denisovans' known range and suggests they occupied several ecologically diverse landscapes. The research team dated the single, human-looking molar to approximately 130,000 to 160,000 years ago. Although they couldn't extract DNA, they managed to identify strands of ancient proteins within the enamel that confirmed it was from a member of our genus, *Homo*, and was most likely female, the team reports this week in *Nature Communications*. Some Denisovan DNA persists in modern human populations, particularly in people from Southeast Asia.

China probes academic database

PUBLISHING | China's market regulation agency last week announced it is investigating whether the country's largest academic database engages in monopolistic behavior. China National Knowledge Infrastructure (CNKI), launched in 1996 by Tsinghua University and a state-owned software firm, provides access to the full text of 280 million papers and dissertations in both Chinese and English collected from more than 90% of the country's academic journals. Little of this material is found in other databases. In recent years, CNKI's aggressive accumulation of papers has led to copyright disputes, and the database has faced complaints about fees. Last month, the Chinese Academy of Sciences refused to pay the reported 10 million yuan ($1.5 million) annual charge and dropped the service, preventing access to the database by its more than 100 research institutes.

Energy science office head OK'd

LEADERSHIP | The U.S. Senate last week confirmed a soil scientist as chief of the U.S. Department of Energy's Office of Science, the nation's single largest funder of the physical sciences. Asmeret Asefaw Berhe of the University of California (UC), Merced, studies how soil absorbs atmospheric carbon dioxide. Some physicists complained that Berhe, who served as interim associate dean of UC Merced's graduate division, lacks leadership experience and relevant scientific background to lead an office that spends the large majority of its $7.48 billion budget on physics research. But some previous directors of the office argued the criticism was off base, and many climate researchers cheered her selection. The Senate confirmed her by a 54-45 vote, with just four Republicans voting for her. Berhe becomes the first Black person to lead the office.

IN DEPTH

PANDEMIC SCIENCE

‘COVID-ization’ of research levels off

Researchers who pivoted from distant disciplines produced lower impact work, study finds

By **Jeffrey Brainard**

In early 2020, as the COVID-19 pandemic took hold, a lab run by virologist John Schoggins at the University of Texas (UT) Southwestern Medical Center became one of many around the world to shift its full attention to the crisis. He and his seven-person lab offered help to other scientists and physicians—by testing human saliva for the SARS-CoV-2 virus, for example—and also produced a handful of pandemic-related research papers.

But in recent months, as vaccines and treatments helped reduce the pandemic’s severity, members of the lab have turned away from working on COVID-19. With so many researchers piling into the field, Schoggins says, “there was a sense of saturation.” As a result, his Ph.D. candidates began looking elsewhere for promising dissertation topics.

Schoggins’s lab is part of a wider pivot away from COVID-19 research, recent analyses of publishing trends suggest. Overall, the number of pandemic-related papers appears set to decline this year, after explosive and unprecedented growth in 2020 and 2021 (see graph, p. 783). In key disciplines such as infectious diseases and public health, the proportion of new papers devoted to COVID-19 appears to be flattening out (see table, below). And in fields more distant from pandemic science, the share of COVID-19 papers is declining, suggesting researchers are returning to their core interests.

Those developments are not surprising, observers say. “Now that many of the clinical and epidemiological knowledge gaps have been [filled], the research focus of most clinicians and epidemiologists is rightfully moving back towards their own specialist interests,” says Alimuddin Zumla, an infectious diseases researcher at University College London, who was not involved in the analyses. That’s not necessarily a bad thing, he adds: “There are many other priority killer [infectious] diseases which have been neglected during the COVID-19 era that need attention.” Other evidence suggests that in some fields, researchers who plunged into COVID-19 studies didn’t always produce their best work.

The pandemic prompted a massive influx of scientists into related research. As of April, more than 500,000 pandemic-related journal articles and preprints had appeared, according to an analysis of the Dimensions bibliographic database by Philip Shapira of the University of Manchester, who studies industrial innovation. Although those publications make up just 4% or so of all scientific papers published from 2019 through early this year, the surge of papers on a new topic was unmatched in the history of science. In certain disciplines the shift was especially dramatic. Shapira’s analysis—presented in an April bioRxiv preprint—shows that in virology, the share of papers focused on coronaviruses and the diseases they cause went from roughly 3% in 2019 to 28% in 2021, and in infectious diseases the share rose from less than 1% to 23%.

Such numbers have raised concerns about what some scientists call the COVID-ization of research.

Growth chart

The rise in COVID-19 papers has slowed in some fields and peaked in others. Data for this year are through mid-April only. Percentages are rounded.

	% OF PAPERS ABOUT COVID-19 OR RELATED DISEASE				CHANGE IN PERCENTAGE POINTS, 2021–22
	2019	2020	2021	2022	
Virology	3.1%	17.4%	28.4%	37.1%	8.8
Infectious diseases	0.8%	13.2%	23%	23.8%	0.9
Public environmental occupational health	0.2%	7.8%	17.0%	17.5%	0.5
Emergency medicine	0.0%	7.8%	11.4%	8.0%	−3.3
Medical informatics	0.0%	6.3%	13.8%	11.5%	−2.3
Respiratory system	0.1%	6.3%	10.1%	9.5%	−0.6
All science fields	0.0%	1.7%	3.7%	3.9%	0.3

CREDITS: (ILLUSTRATION) KATTY HUERTAS; (DATA) WEB OF SCIENCE DATA USED BY R. HILL, *ET AL.*, ARXIV:2107.06476

They fear too many researchers rushed into work outside of their expertise, resulting in poor-quality studies.

One recent analysis suggests such fears are not unfounded. Two-thirds of authors who had at least one publication on COVID-19 in 2020 had no previous papers on a related topic, Dashun Wang of Northwestern University and colleagues reported in an arXiv preprint in July 2021.

In addition, by using a metric it developed, the team found that papers published on COVID-19 in 2020 had lower impact on average than non–COVID-19 papers published during the same year. Using a different metric that measured a paper's novelty, the group found that the further a researcher had pivoted from their usual area of expertise, the lower the impact of their COVID-19 publications.

The lower impact of COVID-19 publications—and the corresponding lower professional rewards—could be one reason some researchers are retreating. Overall, Shapira's analysis found that, in most of the roughly 230 scientific fields he studied, the share of papers focused on COVID-19 continued to increase through early this year, but at slower rates compared with 2021. But in about 70 fields—including emergency medicine, pharmacology, and the study of the respiratory system—the share is dropping.

Another likely cause of the shifts: Journal editors have become more choosey, says Jasper Fuk-Woo Chan, a virologist at the University of Hong Kong. He helps edit several journals and receives a steady flow of requests to review COVID-19 papers for others. "It's getting more difficult to publish [COVID-19 articles] in good journals," he says, with editors "expecting more details, more robust data, than in the first 1 to 2 years" of the pandemic. At that time, he says, journals published many duplicative "me too" papers.

The easing of the COVID-19 publishing frenzy doesn't diminish the value of the work done by scientists who jumped into COVID-19 research—and of the experience they gained. "Not everything paid off," Shapira says. But the influx "probably trained a whole set of researchers to think about pandemics from medical, public health, and other aspects. There's been a human capital investment."

For early-career researchers, however, the consequences of the massive pivot could be mixed. For some, the surge provided funding and publishing opportunities that could help their careers. But it may not be easy for them to adapt and prosper as funding and enthusiasm for COVID-19 research wane.

For example, when the UT Southwestern Medical Center recently hired a number of assistant professors, close to half of the applicants had shifted into COVID-19 research and some had co-authored high-profile studies, says microbiologist Julie Pfeiffer, a member of the search panel. That raised some red flags, says Schoggins, who also served on the panel. "We were concerned about their future fundability and ability to make an impact," he says. "When they leave that incubator of high-profile [COVID-19] work, can they start their own lab and be independent?"

Future fundability might be of less concern for senior researchers who have studied COVID-19. In 2020 these older scientists were more likely than their younger peers to pivot into such work, Wang's literature analysis found. And the papers often reported no grant support, Wang notes, leading him to speculate that senior scientists had the financial wherewithal to jump into new lines of research.

Discerning how many of the researchers who rushed into pandemic research ultimately remain could take several more years. But Seema Lakdawala, a virologist at the University of Pittsburgh, is one scientist who plans to stay the course. Before the pandemic, she studied influenza viruses and their airborne transmission, so investigating that aspect of SARS-CoV-2 became a natural fit for her group, she says, and she expects to continue studies on both types of viruses.

She is less concerned about the pivot away from COVID-19 by some researchers than about whether funding for such work, crucial to coping with future pandemics, will be sustained. "What I worry about is [whether] after this pandemic and its fatigue are over … we'll have the investment that we need in all aspects of virology," Lakdawala says. "We really need to be prepared for another eventual threat. It's not hard to believe that this is going to happen again." ■

Topping out?

The number of publications on COVID-19 is forecast to decrease this year, although data lags might affect totals. (The total in all fields is also set to drop.)

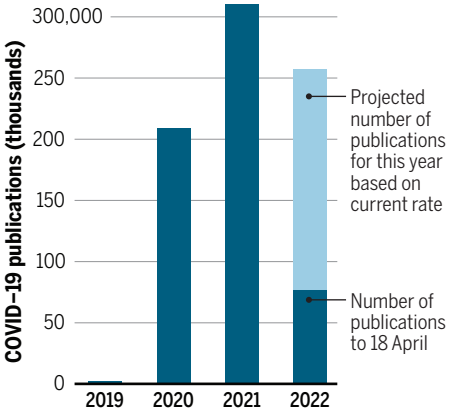

CREDITS: (GRAPHIC) K. FRANKLIN/*SCIENCE*; (DATA) DIMENSIONS DATA USED BY PHILIP SHAPIRA, BIORXIV, 2020.12.06.413682

COVID-19

Do you hate your face mask? There's hope

A U.S. government contest has 10 companies competing to make better face coverings

By **Jon Cohen**, *in Boulder, Colorado*

In the shipping room of his factory here, Richard Gordon pulls open the drawer of a restaurant-style convection oven to show off a tray filled with his company's new, freshly sterilized product: multicolored face masks that feature an origami design.

"I thought masks were a total horror," Gordon says. "They looked awful, felt awful, were hard to breathe in, were hot, and leaked." So he and Min Xiao, his wife, started a company named Air99 in 2016 to produce something much better.

Now, their mask, named the Airgami, is vying for part of the half-million dollar purse in the final phase of the Mask Innovation Challenge, run by the U.S. Biomedical Advanced Research and Development Authority (BARDA). The contest aims to promote masks that have a better fit, function, and look than existing designs and to nurture the "rather underfunded and a little stagnant" ecosystem of mask development, says Kumiko Lippold, a BARDA pharmacologist and toxicologist who organizes the challenge.

Lippold acknowledges the contest may seem "a little bit behind the curve," given that the pandemic has abated and many countries have dropped masking requirements. Still, there's "a significant appetite for mask innovation," she says. SARS-CoV-2 may have surprises in store that will require people to mask up again—and there will likely be other pandemics. "We're building tomorrow's mask," Lippold says.

The 10 finalists, selected from 1448 entrants, include mom-and-pop innovators like Air99, a team at Georgetown University, and industrial giants Amazon and Levi Strauss & Co. To evaluate the masks, BARDA has teamed up with the National Institute for Occupational Safety and Health (NIOSH)—

which tests and approves N95 "respirators," the type that snugly fit the face and have a high filtration efficiency—and the National Institute of Standards and Technology (NIST). BARDA plans to announce a winner in October.

With billions of people donning face masks for the first time in 2020—and complaining about their shortcomings—the pandemic has triggered a surge in mask research. In a study published in June 2021, for example, NIOSH engineer and aerosol researcher William Lindsley and colleagues compared 19 widely used face coverings by attaching them to a respiratory aerosol simulator, a mannequin headform that breathes and coughs.

All masks help, Lindsley stresses: "The two biggest misconceptions are that they don't work and that they're magic and you're protected, no matter what." But bandanas are "terrible" at both filtering inhaled air and capturing aerosols when people exhale and cough, the study found. Cloths, neck gaiters, and medical masks are much better, but still pale in comparison to NIOSH-approved N95 masks. (In Europe, the equivalent of N95s are known as FFP2 masks.)

The Airgami is one of 10 finalists in a competition for next-generation masks. "I thought masks were a total horror," says Richard Gordon, its developer.

The finalists in the BARDA challenge each offer unique improvements. In Airgami's case, beauty is important, says Gordon, an electrical and computer engineer—but that's not why he and Xiao entered the field. Their quest began well before the pandemic, when they moved to Suzhou, China, in 2011 for Xiao's new job. Pollution there was horrible, and the N95 masks they had brought, made by 3M for construction workers, didn't fit their young son. "I immediately started cutting out 3M masks and gluing them and stapling them just to shrink them down to fit him," Gordon says. "Gotta give [the] kid clean air. Very, very simple," he says.

His son's problem, coupled with the discomfort and fit issues he had with his own face coverings, led Gordon to devote himself to designing a better mask after the family moved back to the United States in 2015. He stumbled onto an origami show, *Above the Fold*, that had a "mind-blowing" piece by physicist Robert Lang, a world-renowned origami mathematician and artist. The Airgami is a twist on a popular origami design, the magic ball—also known as the dragon's egg—sliced in half, which creates a large breathing space and fits tightly on the face. The inner of three polypropylene layers has an electrostatic charge to trap particles—the heart of N95 technology. The mask is reusable, can be rinsed or disinfected with heat, and comes in four different sizes and various colorful prints, including rainbows and camouflage. Lang, who is now on the Air99 board, helped Gordon create a computer program to automate the creasing.

Even so, each mask must be hand-assembled and sells for $29.99. But Gordon says supply can't meet demand. "The world is flooded with $1.50 masks, and there's no way we're going to compete, but they're all ugly and they don't necessarily fit great," says Gordon, who hopes to lower the price with more automation.

Another finalist, Amazon's PerfectFit Mask, also uses an origami design and comes in various fashion patterns and sizes. A company named 4C Air, co-founded by physicist and Nobel laureate Steven Chu, makes the BreSafe Transparent Mask, which aims to improve masked conversations by allowing a listener to see the speaker's lips. The hard-shell AtmoBlue mask, made by Blue Sky Labs, has built-in fans that blow incoming air across high-efficiency particulate absorbing filters and a sensor that monitors air quality for pollution. The Georgetown group developed nanoporous metal foams that are extraordinarily efficient filters, ultralightweight, and also reusable.

Levi Strauss took a different tack: Its mask, the Veil, offers N95-level protection with a simple design that any garment manufacturer can produce with scissors and a sewing machine—and sports the brand's world-famous logo for added coolness. There is even a face covering especially for toddlers made by PaciMask that allows parents to attach a pacifier and features cartoon characters, animals, and spaceships. (Its slogan: "It's just a mask, baby!")

NIOSH's standard N95 test assesses masks' filtration efficiency by exposing them to aerosolized sodium chloride and measuring the amount that passes through. An N95 rating means a mask filters at least 95% of "nonoily" (hence the N) particles. But for the BARDA challenge, NIOSH devised additional tests. "We got to really think about the testing innovation," says physical chemist Sandeep Patel, who heads the BARDA division overseeing the challenge. Recognizing that mask fit depends on face shape, for example, researchers designed five different-size mannequin headforms, based on the faces of nearly 4000 people. The mask challenge encourages entrants to supply analyses of how their masks fit digital versions of all five.

NIST fluid dynamicist Matthew Staymates will also test the finalists for leakage with schlieren imaging, which uses lenses and mirrors to visualize changes in air temperature. Staymates couples this with high-speed video cameras, which allows him to capture air escaping from the edges of masks when people breathe. The major challenge confronting maskmakers isn't new materials, but design, Staymates says. "We can make fabrics that have amazing filtration efficiency, and the N95 is a great example," he says, but "how can we get smart about designing shapes that can really seal well so my glasses don't fog up?"

Gordon and Xiao see a bright future for their company even after the pandemic ends. "We started out as an antipollution mask, and I think it is still the core business," Xiao says. Still, COVID-19—and becoming a BARDA finalist—has given the company a boost they never imagined, Gordon says: "The pandemic was the greatest marketing awareness campaign of all history." ■

PHOTO: RICHARD GORDON/AIR99 LLC

ASTRONOMY

Shadow of Milky Way's giant black hole revealed

Scene resembles earlier image from a distant galaxy, as Einstein's theory predicts

By **Daniel Clery**

The first image of the supermassive black hole at the center of the Milky Way Galaxy—or at least of its shadow—transfixed astronomers last week. Eight radio observatories around the globe and more than 300 scientists joined forces to image the object known as Sagittarius A* (Sgr A*), a feat thought impossible until just a few years ago. "It's a truly impressive accomplishment," black hole expert Roger Blandford of Stanford University says of the work, presented at press conferences on 12 May.

The same team, known as the Event Horizon Telescope (EHT), in 2019 produced the first ever image of a black hole, at the center of the nearby giant galaxy M87. The M87 black hole is 1600 times the mass of Sgr A*. Yet the similarity of the two images—bright rings of gas trapped in death spirals around these ultimate sinkholes—shows how Albert Einstein's theory of gravity, general relativity, works the same at all scales. "In both cases, what we see is the heart of the black hole, the point of no return," team member Feryal Özel of the University of Arizona said.

Compared with M87, which converts swirling gas into a powerful jet thousands of light-years long, Sgr A* is quiet. "M87 was exciting because it was extraordinary," says CfA's Michael Johnson. "Sgr A* is exciting because it's common." Initial analysis of the new image suggests only a trickle of gas makes it to the black hole, and only one part in 1000 is being converted to light, Johnson says. Comparing the image with computer simulations points to another feature of Sgr A*, Özel says. "We may be seeing the first hints" that the black hole is spinning.

Although the black holes in the centers of galaxies have enormous masses—millions or billions of times that of the Sun—their intense gravity means their outer edge, the event horizon, is tiny in galactic terms. Sgr A*, which has a mass of 4 million Suns, has an event horizon that is just four times the Sun's diameter. Imaging something so small from 27,000 light-years away presents a huge challenge for astronomers.

Only radio telescopes can peer through the clouds of dust around the galactic center, but their long wavelengths offer poor resolution. The shortest radio wavelengths, of about 1 millimeter, can do better, and combining multiple telescopes can further sharpen the image. EHT observes the galactic center simultaneously with dishes spread across Earth's face, then processes the data with banks of computers as if each dish was a small patch of an Earth-wide telescope—a technique known as very long baseline interferometry (VLBI). "Each pair [of telescopes] contributes a little bit of information to the entire image," says EHT team member Katie Bouman of the California Institute of Technology.

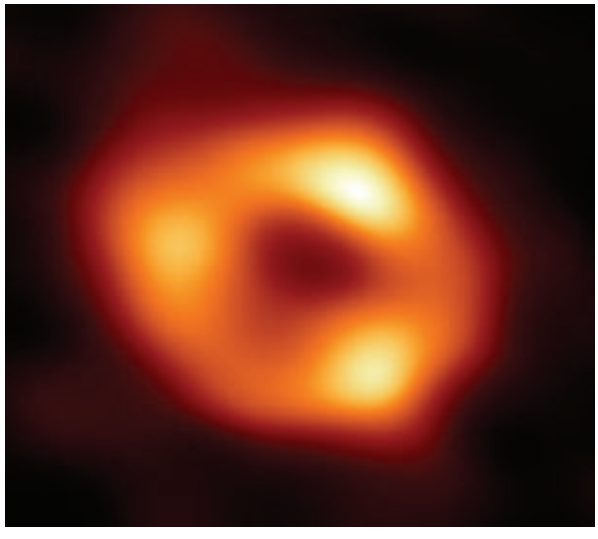

A ring of glowing gas surrounds a void that encloses the Milky Way's 4-million-solar-mass black hole. Astronomers don't know whether the bright knots are real or artifacts.

By 2017, the team was ready to take a shot at Sgr A* and the nearby giant galaxy M87. Data came from eight observatories, from Hawaii to Spain and from Arizona to the South Pole. A key addition was the Atacama Large Millimeter/submillimeter Array in Chile, a group of 64 dishes with the combined area of an 84-meter-wide telescope.

In April 2019, the team released its now famous image of M87, a result chosen as *Science*'s 2019 Breakthrough of the Year (*Science*, 20 December 2019, p. 1434). It shows the event horizon's silhouette, magnified 2.5 times by gravitational effects. Some of the light in the surrounding ring was actually emitted behind the black hole, its path bent by the intense gravity so that it appears to come from the edge.

Getting an image for Sgr A* proved to be much harder. One reason was that the telescopes were viewing it through the crowded central plane of the Milky Way, where electrons from ionized gases scatter the radio waves. Johnson describes it as peering through "frosted glass." Another challenge was motion. Gas moves slowly around M87's giant black hole, taking days to orbit the event horizon. But around the much smaller Sgr A*, an orbit takes minutes. "If an object changes in a crazy way, you can't image it with VLBI," says EHT team member Heino Falcke of Radboud University. But he says that after 2 years scrutinizing the results, the team is confident it has been able to extract the steady part of the signal. "On top of the chaotic structure you have a stable structure," he says.

Unlike for M87, the mass of Sgr A* is known very precisely from studies of star orbits close to the black hole, so the EHT researchers had a firm idea of how big of a ring they should see. The ring they found was "bang on," says EHT team member Dom Pesce of CfA. But the three "knots" visible in the image might be artifacts of the observation process, Özel says.

The EHT team carried out further observing campaigns of M87 and Sgr A* in 2018, 2021, and 2022. "All data are in various stages of calibration and processing," Pesce says. The accumulating data could help researchers understand how matter moves around a black hole and is sometimes funneled into jets. The EHT array has also expanded since 2017, adding new dishes in Greenland, France, and the United States, with plans for another in Namibia.

In the future, the researchers plan to observe at a shorter wavelength—0.86 millimeters, compared with the 1.3 millimeters used so far—which will allow them to see even closer to the event horizon. They will also attempt time-lapse movies of the gas swirling around the black holes. Observing M87 every 2 weeks is the first goal. Later, they will try for Sgr A*-The Movie. "We're still in the infancy of this field," Pesce says. "The first baby steps." ■

PHOTO: EVENT HORIZON TELESCOPE COLLABORATION

Dust storms like the one that engulfed cities in southeastern Brazil in 2021 could become more frequent as dryland soils retain less moisture.

ECOLOGY

Soils' coating helps keep dust storms at bay

Breakdown of "biocrusts" allows wind to attack dryland soils

By **Elizabeth Pennisi**

Two years ago, 24 million tons of dust lifted high above Africa to create a plume that swirled across the Atlantic Ocean and covered Puerto Rico in a pink patina. An unusually meandering jet stream helped launch the monster dust cloud. But this week, ecologists fingered another factor in such storms: the disappearance of biocrust, a microbial mat that coats dryland soil and helps keep dust in place. "It glues the sand together," says Bettina Weber, an ecologist at the University of Graz and coauthor on the new study.

Trampled by livestock and scorched by climate change, that glue is likely to become weaker in the future, researchers say, leaving the soil prey to wind. The dust study "demonstrates that the loss of biocrust in one area of the world can have wide-ranging and far-flung impacts," says Rebecca Finger-Higgens, an ecologist at the U.S. Geological Survey.

A biocrust is a hard surface coating or "skin," typically a few millimeters thick, containing a thriving community of fungi, lichen, moss, cyanobacteria, and other microbes. Historically ecologists have paid little mind to biocrusts, which cover soils in arid, semiarid, and extremely cold places all over the world. But researchers have realized these coatings produce and process nutrients that nearby organisms need to thrive, especially in arid environments. They also help a dryland soil retain its little moisture.

Biocrusts form from communities of lichen, bacteria, and other microbes.

In 2018, Weber, postdoc Emilio Rodriguez-Caballero, and their colleagues mapped all of Earth's biocrusts, concluding they cover 12% of the land surface. They then teamed up with climate modelers and dust experts to figure out how much dust formation the biocrust glue currently averts. First, the researchers compiled data about how much wind it takes to destroy the biocrust and blow the soil away. They calculated dust emissions at 31 different sites, then fed the results into a model that predicted worldwide dust emission—and how much it would rise without the biocrusts. "[They] used a very elegant combination of field data and modeling," says Fernando Maestre, a dryland ecologist at the University of Alicante.

Biocrusts reduce dust in the air by 700 million tons per year, Weber and her team report this week in *Nature Geoscience*. That amount would bury all of New York City under 35 centimeters of dust. The study "places biocrusts as key players in preventing dust emissions globally," Maestre says.

PHOTOS: (TOP TO BOTTOM) ANDREY LUZ/AFP/GETTY IMAGES; BETTINA WEBER

Over the next 65 years, between 25% and 40% of these crusts will vanish, says Rodriguez-Caballero, now at the University of Almeria. Climate change that threatens soil organisms will account for about half the destruction; other damage will come from trampling by humans, livestock, and farm machinery.

Finger-Higgens and colleagues have documented the impact of climate. In a long-term biannual survey of plots in Utah's Canyonlands National Park, they found that biocrust lichens in particular suffer when temperatures increase. As Canyonlands temperatures rose by 0.27°C per decade, lichens, especially those that help convert nitrogen in the air to a form that other organisms can use, have almost disappeared, the team reported on 11 April in the *Proceedings of the National Academy of Sciences*. With less nitrogen, fewer plants can survive, leaving ever more bare ground and more dust emission, Finger-Higgens says.

Some implications of a dustier climate are unclear, researchers say. The impact of airborne dust on temperatures depends in part on the size of the particles. Dust particles provide nuclei for cloud formation and can cause snow to melt faster. Although dust helps transport important nutrients for plant life, it can make respiratory problems and other health issues worse for people.

Up to now, dusty places like the Sahel were expected to get greener and less dusty as higher carbon dioxide levels have a fertilizing effect, but biocrust loss will likely counteract this process to some degree, Weber and her colleagues note. "Biocrust, dust, [and] climate all exert feedback on each other," says Diana Francis, an atmospheric scientist at Khalifa University who is not part of the work.

Climate modelers have often overlooked how dust affects temperature and rainfall, says Michael Mann, an atmospheric scientist at Pennsylvania State University, University Park. The effects of diminishing biocrusts shouldn't be dramatic enough to make much difference in global climate models, he says. But Joseph Prospero, an atmospheric chemist at the University of Miami, cautions that "there are large areas of the Earth for which we have essentially no information" about biocrusts. That may change. Weber, Maestre, Finger-Higgens, and other biocrust experts are seeking funding for standardized measurements of biocrusts around the world.

But researchers say the need to protect these fragile communities is already clear. Reducing emissions and changing farming and other land use practices can help reverse their decline, Maestre says. "The findings provide strong arguments for preserving biocrust communities worldwide." ■

U.S. RESEARCH POLICY

NIH rolls out stricter disclosure rules for sexual harrassment

Institutions now legally required to inform agency if grantees are "disciplined" for workplace misbehavior

By **Jocelyn Kaiser**

The National Institutes of Health announced last week that—at the direction of Congress—it is tightening rules for reporting sexual and workplace harassment by NIH-funded investigators. Institutions will now be required to tell NIH if a grantee has been disciplined because of harassment findings.

NIH calls the policy a "major step" to close loopholes that have allowed institutions to hide harassment cases. "There's no question that we're going to be hearing about cases that we either would not have heard about at all, or only after a substantial delay," says NIH Deputy Director for Extramural Research Michael Lauer.

Observers welcome the law, but they note that NIH's reporting requirements still fall short of those at the National Science Foundation (NSF). That could leave NIH unaware of some ongoing investigations.

> **The new policy "is a good, helpful, and clear step."**
> **Heather Pierce**, Association of American Medical Colleges

In recent years, NIH has beefed up its sexual harassment rules. In 2020, it asked institutions to tell them if a requested change in a grant's principal investigator (PI), other key personnel, or institutional manager was related to harassment concerns. In the past 4 years, in response to 112 harassment findings, NIH has worked with institutions to remove 92 individuals from grants.

But that reporting rule lacked teeth, NIH says. Institutions were told they "should" report harassment, but NIH couldn't require disclosure, NIH acting Director Lawrence Tabak explained in a statement. "This limited NIH's awareness" of harassment and its "ability to take necessary action," Tabak wrote.

Now, thanks to a provision Congress added to NIH's 2022 budget, disclosure will be mandatory. As of 9 July, institutions must inform NIH within 30 days if key grant personnel "are removed from their position or are otherwise disciplined due to concerns about harassment, bullying, retaliation, or hostile working conditions," the agency announced on 10 May.

Institutions must use an online form to detail the case and how it responded. NIH can then take additional steps, such as replacing personnel. If institutions ignore the rule, NIH can even suspend further awards.

NIH's new policy still falls short of NSF's because the foundation requires reporting of any "administrative action" related to a harassment finding or probe. That could include nondisciplinary actions, such as barring a PI from teaching while an investigation is underway.

Lauer, however, says he believes NIH's policy will not allow misbehavior to be swept under the rug. "When the concerns are so serious that a person is put on leave, then we do know about that," he says. Allegations result in formal findings just 25% to 30% of the time, he adds. In "a number of cases," investigators find "no wrongdoing."

NIH also hears about investigations from victims and others who contact the agency, notes Heather Pierce, a senior policy specialist at the Association of American Medical Colleges. Pierce says although the phrase "otherwise disciplined" needs clarification, overall the new reporting policy "is a good, helpful, and clear step."

Some observers, however, want NIH to go further by requiring institutions to disclose when a harassment investigation begins, before any determination of guilt—as federal rules now require for research misconduct. A 2019 report from an NIH working group recommended that the agency follow a "parallel process."

Virologist Angela Rasmussen of the University of Saskatchewan, who served on that committee, notes that institutions are sometimes reluctant to produce findings or take disciplinary action. She worries that by requiring disclosure only when there is a disciplinary action, the new policy might encourage administrators to "shield those who have committed misconduct." For that reason, she says, "It's important they [NIH officials] know about investigations." ■

FEATURES

Forests are expanding in many cooler regions, replacing snowy landscapes that reflect solar radiation with darker canopies that absorb it.

THE FOREST FORECAST

Climate change could lead to a net expansion of global forests. But will a more forested world actually be cooler?

By **Fred Pearce**

These are strange times for the Indigenous Nenets reindeer herders of northern Siberia. In their lands on the shores of the Arctic Ocean, bare tundra is thawing, bushes are sprouting, and willows that a generation ago struggled to reach knee height now grow 3 meters tall, hiding the reindeer. Surveys show the Nenets autonomous district, an area the size of Florida, now has four times as many trees as official inventories recorded in the 1980s.

In some places the trees are advancing along a wide front, but in other places the gains are patchier, says forest ecologist Dmitry Schepaschenko of the International Institute for Applied Systems Analysis in Austria, who has mapped the greening of the Siberian tundra. "A few trees appear here and there, and some shrublike trees become higher."

All around the Arctic Circle, trees are invading as the climate warms. In Norway, birch and pine are marching poleward, eclipsing the tundra. In Alaska, spruce are taking over from moss and lichen. Globally, recent research indicates forests are expanding along two-thirds of Earth's 12,000-kilometer-long northern tree line—the point where forests give way to tundra—while receding along just 1% (see map, p. 790).

Forest gains are not confined to the far north. At lower latitudes, some warmer, arid regions are also seeing an uptick in trees, in part because increasing concentrations of carbon dioxide (CO_2)—the main planet-warming gas—are enabling plants to use water more efficiently and thrive in drier soils. And the fertilizing effects of CO_2 are enabling existing forests to add more leaves and wood, increasing their biomass.

It's a startlingly different picture from what is unfolding in the tropics, where hundreds of thousands of hectares of forest are lost each year to chainsaws and fire, and climate change is stressing the remaining trees. But those tropical losses could be more than offset by gains elsewhere, some studies predict, leading in the coming decades to a world with more and faster growing trees.

That might seem like surprisingly good news for curbing global warming. Forests often have a cooling effect, releasing organic compounds and water vapor that promote the formation of clouds. And more, faster growing trees would absorb more atmospheric carbon and lock it away in wood.

But the calculus of forests' climate effects is far from straightforward, and emerging research suggests a more forested world won't necessarily be a cooler world. New forests could enhance warming in some areas, for example, by reducing the amount of sunlight that is reflected into space. Over time, that could offset any gains in carbon absorption.

"Forests are not just carbon sponges," says environmental scientist Deborah Lawrence of the University of Virginia. But that complexity, she adds, "is not adequately captured by current carbon-centric metrics."

Wildfire can destroy forests, but in some it can clear the way for faster growing trees that help curb climate change by absorbing carbon.

TO ACCOUNT for how forests will affect future climate, researchers must not only tally current trends, such as development-driven deforestation, but also forecast how powerful forces such as surges in wildfire and warmer temperatures might affect forests, sometimes helping and sometimes harming their ability to soak up atmospheric carbon.

Historically, researchers have focused much of their attention on the losses side of the balance sheet, for example by quantifying the steady erosion of tropical forests, one of the planet's major carbon sinks. In the Amazon, the world's most expansive tropical forest, the news has been almost unremittingly bad. Overall, it has shrunk by about 18% since the 1970s because of deforestation.

In 2007, meteorologist Carlos Nobre of Brazil's National Institute for Space Research (INPE) warned the ongoing losses could flip the Amazon from acting as a global carbon sink to a significant new source. Simulations of the Amazon's hydrological cycle, he found, showed deforestation would make rainforests drier, reduce tree growth, and promote tree losses, resulting in a net release of carbon to the atmosphere.

That prediction now appears to have been realized, says INPE climate researcher Luciana Gatti. Drawing on measurements of atmospheric carbon collected during 590 research flights over the Amazon between 2010 and 2018, she reported in a July 2021 *Nature* study that the southeastern Amazon—a region often called the "arc of deforestation," where agriculture has gobbled vast swaths of trees—had flipped from sink to source. So, in consequence, had the Amazon as a whole. "We have hit a tipping point," she says.

The years since 2018 have been "even worse" for the Amazon's carbon storage capacity, Gatti says, as warming temperatures have compounded the effects of deforestation. Longer dry seasons are stressing trees and increasing fire risks, accelerating the conversion of forest to more open savannas. Overall, the Amazon's total carbon storage could drop by one-third in coming decades if regional temperatures rise by 4°C, modeling studies conducted by climate scientist Chris Jones and colleagues at the United Kingdom's Met Office conclude.

In the meantime, however, some tropical forests are continuing to sequester large amounts of carbon. For example, one long-term field study in the lowland forests on the

PHOTOS: JUAN CARLOS MUNOZ/NPL/MINDEN PICTURES; (OPPOSITE PAGE) PAL HERMANSEN/NPL/MINDEN PICTURES

island of Borneo recently reported that intact 1-hectare plots, where tree deaths remain infrequent, hold an average of 20 tons more carbon today than they did in 1958, primarily because of CO_2 fertilization.

But ongoing warming is working against tropical forests, even those that are still intact. An international study that has tracked 300,000 trees in more than 500 plots of intact tropical forests over 30 years finds that even without deforestation, their ability to capture CO_2 peaked in the 1990s and has since declined by one-third. The decline began in the Amazon, and since 2010 has extended to tropical Africa, says co-author Simon Lewis, a plant ecologist at University College London. Remote-sensing techniques that assess changes in the total leaf area produced by trees and other plants also suggest many tropical forests are slowing their carbon intake.

THIS BLEAK PICTURE brightens outside the tropics. In cooler regions, research suggests climate trends are driving gains in both forest extent and productivity that could more than compensate for losses in the tropics—"presuming," Lawrence says, "that the world can meet its goals for limiting deforestation." (So far, it's not clear it will.)

One source of optimism are studies showing higher CO_2 levels are already helping forests add biomass. For example, a widely cited 2016 study headed by remote sensing researcher Zhu Zaichun of Peking University found that between one-quarter and one-half of the planet's vegetated places showed an increase in leaf area since 1982, whereas just 4% showed a decline. Simulations by Zhu's team suggest CO_2 fertilization accounts for 70% of the increase in global forest biomass.

In the future, more CO_2 will also prompt forests to expand into new areas, other planet-scale simulations indicate. These digital models allow researchers to explore how forests might respond to a wide array of factors, including changes in global temperatures and atmospheric carbon concentrations. One such study, published in December 2021 in *JGR Atmospheres* by climatologist Jennifer Kowalczyk of Brown University, found warming alone caused vegetation to decrease globally, with tropical losses from overheating exceeding nontropical gains from longer growing seasons. But that finding flipped when she added the fertilizing effects of increased atmospheric CO_2. Overall, boosting CO_2 levels to about 560 parts per million—or double preindustrial levels—increased global forest cover by 15% above preindustrial extent.

Much of the simulated increase occurred in boreal forests of the north, where longer growing seasons and thawing permafrost help trees gain ground. But forests also expanded in arid continental interiors in the subtropics.

That was somewhat surprising, Kowalczyk says, because the greening in arid zones "occurs even without significant increases in precipitation." Instead, she says, the extra atmospheric CO_2 allows trees to reduce water loss, because they don't need to open their stomata so wide to take in CO_2. That enables seedlings to take root where none grow today.

SOME RESEARCHERS question optimistic predictions of future forest expansion. One issue, they say, is that other factors could intervene. Deforestation, for example, could accelerate to satisfy growing global demand for food and resources, wiping out any global gains. And a shortage of key soil nutrients such as phosphorus could neutralize CO_2 fertilization, especially in tropical forests, says Chris Huntingford of the UK Centre for Ecology & Hydrology. In the Amazon, for example, a 2019 study published in *Nature Geoscience*, led by ecosystem modeler Katrin Fleischer of the Technical University of Munich, found that a lack of adequate phosphorus could cut forest gains from CO_2 fertilization in half.

Another big question is how a warmer, drier climate will influence wildfires. Modeling studies have long warned that climate change will increase fire risks in tropical and temperate forests. Boreal forests could also see losses. In an early portent, Global Forest Watch reported earlier this year that boreal forests lost more than 8 million hectares in 2021, 30% more than in 2020, with wildfires mostly to blame.

But fire could also enable some boreal forests to store more carbon, not less, plant ecologists say. That's because regenerating forests can produce stands that are denser or comprise more vigorous species better adapted to fire.

Michelle Mack, a forest ecologist at Northern Arizona University, has seen this arboreal phoenix in action. After fires devastated evergreen spruce forests in Alaska in 2004, their charred remains were replaced by faster growing and less flammable aspen and birch—deciduous trees that could ultimately store up to five times more carbon than their evergreen predecessors. "I thought there was no way these forests could recover the carbon they lost in the fire," Mack says. "But these deciduous trees did so rapidly."

This phenomenon appears to be widespread across western North America and in the Russian Far East, she says. Schepaschenko concurs. In Siberia, he says, fires have helped fuel the northward spread of forests into the tundra. "The flames remove moss and lichen cover, allowing [tree] seeds to reach mineral soil."

EVEN IF models suggesting a more forested future are right, however, it's not yet clear just how beneficial those trees might be for curbing global warming.

On the plus side, there's little doubt that forests can help cool the lower atmosphere. One way they do this is by moving large amounts of moisture from soils into the air. A typical tree may "sweat" up to 100 liters of water every day, and the planet's estimated 3 trillion trees release some 60,000 cubic kilometers each year,

Greening trend

Around the Arctic, trees and shrubs are encroaching on tundra thanks to warmer temperatures and longer growing seasons. From 2000 to 2020, increases in tundra greening (top) outstripped vegetation decreases (bottom), according a recent analysis of satellite data.

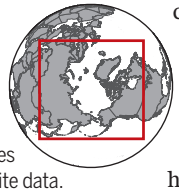

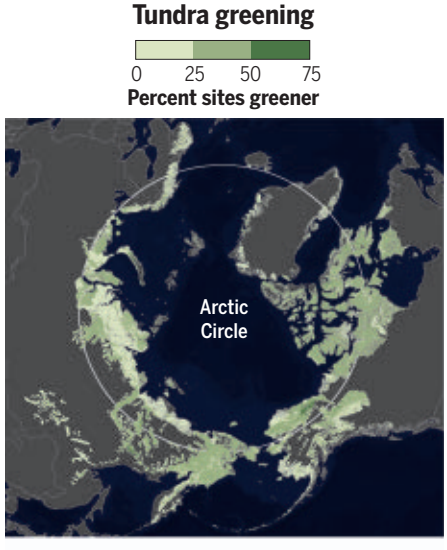

CREDITS: (GRAPHIC) K. FRANKLIN/*SCIENCE*; (DATA) LOGAN BERNER AND SCOTT GOETZ/NORTHERN ARIZONA UNIVERSITY; NASA'S ARCTIC BOREAL VULNERABILITY EXPERIMENT

the equivalent of flooding the entire U.S. land area with about 6 meters of water.

This transpiration cools the air, as energy is required to convert the liquid water to vapor. And the released vapor, together with other organic compounds produced by trees, helps create clouds that can bring down temperatures. (CO_2 fertilization could reduce transpiration by allowing trees to use water more efficiently, but researchers say it will remain a potent cooling force.)

The relative roughness of a forest canopy also helps reduce temperatures. The leaves and branches cause air currents to swirl and mix, helping dissipate heat higher into the atmosphere.

Together, these two processes currently help cool Earth's surface by 0.4°C to 0.6°C, Lawrence says, with each contributing about half of the reduction.

But it turns out forests can warm the planet, too, primarily by changing the reflectivity, or albedo, of land surfaces. Gleaming surfaces such as fresh snow have an albedo of 0.8 to 0.9 (on a scale from zero to one), meaning they bounce a lot of solar energy back into space. In contrast, a continuous canopy of broadleaf trees can have an albedo of just 0.15, meaning the trees absorb solar energy and radiate it in the form of heat. A canopy of conifers can have an even lower albedo: 0.08.

In boreal and high-altitude regions that get a lot of snow, the expansion of forests is expected to have a major impact on albedo, as dark canopies replace snow-covered surfaces. In arid regions, the shift can also be dramatic, as trees shade highly reflective sandy or rocky soils. But whether the warming caused by albedo changes will ultimately outstrip a forest's cooling contribution is likely to depend on several factors, including latitude, altitude, how fast the trees grow, and the age of the forest.

Overall, new forests are likely to have their greatest warming impact at high latitudes and high altitudes, where snow cover is extensive and long-lasting and cold temperatures mean trees grow more slowly, reducing their ability to capture carbon. In the contiguous United States, for example, a study by geographer Chris Williams of Clark University found that over a 100-year span, forests growing in the Rocky Mountains will cause net warming, whereas those growing in lower, less snowy areas east of the Mississippi River and on the Pacific Coast will cause net cooling.

But the impact depends, in part, on when during the forest's life cycle it is measured. A young forest, for example, might warm the atmosphere because of its albedo effect. But it could become net cooler as the trees age and store more carbon.

In Israel, earth system scientist Dan Yakir of the Weizmann Institute of Science has been watching this balancing act play out in the Yatir Forest, a 2-hour drive from Tel Aviv. Workers created the forest in the 1960s, planting some 4 million Aleppo pines in the yellow sands of the Negev Desert on the slopes of Mount Hebron. Today, the forest is often promoted as a valuable carbon sink.

So far, however, any climate gains are not clear-cut, Yakir says. His measurements of biomass and albedo have shown that, so far, the warming caused by the dark canopy of the pines now exceeds the cooling from their carbon capture. As the trees grow, however, he expects the cooling influence to catch up. But the crossover might not occur until the 2040s, he says—and that assumes the trees live that long.

The findings were unexpected, Yakir says. And he cautions that the Yatir forest is, in some ways, unusual. For example, "The forest is almost black and the desert almost white. … Everything makes our case extreme."

THE UNCERTAINTY surrounding how new forests will affect climate poses not just a scientific challenge: It has policy implications, too. Few large-scale tree planting projects, for example, assess the potential climate downsides from a changing albedo. As a result, such greening initiatives "could really backfire" if they "end up placing trees in locations that are counterproductive for cooling the climate," Williams says.

Then there is the question of how governments should account for new forests when they tally up their contributions to complying with global climate agreements such as the Paris accord. Typically, nations are given credit for protecting or expanding their forests. Russia, for example, calculates that roughly one-quarter of its fossil fuel emissions are offset by its huge, carbon-absorbing forests. And Schepaschenko's discovery that Russia's boreal forests are expanding and storing even more carbon suggests the nation could go much further. "We have the potential to turn [new forests] into a massive carbon capture hub," the nation's minister of development of the Far East and Arctic, Aleksey Chekunkov, told Bloomberg last year.

But what if new forests turn out to accelerate warming over the long term, not slow it? Should nations still get credit?

Such questions, scientists say, highlight the importance of gaining an even more sophisticated understanding of how forests and Earth's climate interact. Without a clearer picture, Williams says, "I really worry that we could be placing too much emphasis on forests as a climate solution, when what we really need is deep decarbonization of society." ■

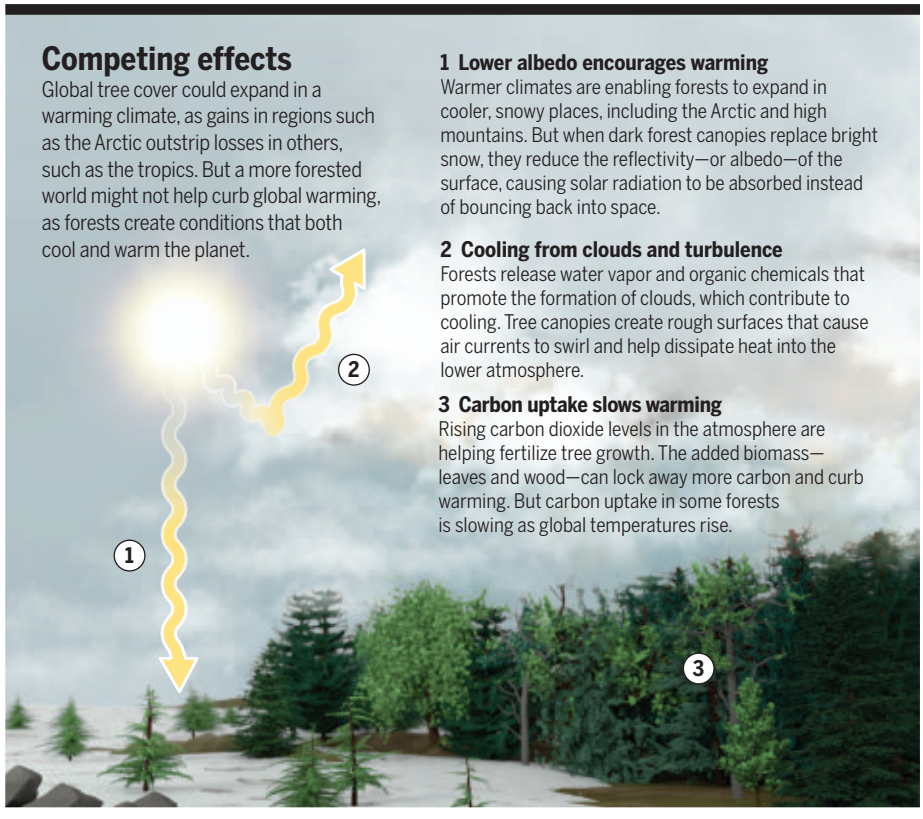

GRAPHIC: V. ALTOUNIAN/*SCIENCE*

Fred Pearce is a journalist based in London.

INSIGHTS

PERSPECTIVES

FORESTRY

Managing forests for competing goals

Tree plantations face difficult trade-offs between production and ecological goals

By **Jessica Gurevitch**[1,2]

Trees provide beauty, shade, food, and lumber. Forests of trees are reservoirs of biodiversity, sustaining a web of life while sequestering carbon, modulating regional climates, conserving soil, retaining water from rainfall, and moderating runoff. Concerns about forest losses and climate change have motivated forest replanting to support ecosystem services, such as carbon storage, soil conservation, recapture of water from rainfall, and lumber production (*1*). So, how well can tree plantations achieve the different goals they are billed as providing compared with native forests? On pages 839 and 865 of this issue, Hua *et al.* (*2*) and Feng *et al.* (*3*), respectively, provide insight into the answers to this problem. Hua *et al.* examine whether plantations purposed for lumber production can also provide a refuge for biodiversity and achieve other ecological goals, and Feng *et al.* consider whether productivity in such plantations can benefit from multispecies designs rather than the typical monoculture stands.

There has been long-standing uncertainty about how the human use of trees compromises the value of forests for biodiversity conservation and ecosystem services. Can a scenario exist in which one can plant trees profitably for lumber production while simultaneously promoting biodiversity and supporting ecosystem services? Reforestation often replaces previous native forests with non-native, low-diversity tree plantations (*4*). Hua *et al.* compared plantations with native and restored forests

[1]Department of Ecology and Evolution, Stony Brook University, Stony Brook, NY, USA. [2]Department of Forestry and Natural Resources, Purdue University, West Lafayette, IN, USA. Email: jessica.gurevitch@stonybrook.edu

PHOTO: FERNANDOPODOLSKI/GETTY IMAGES

Single-species tree farms, such as this *Eucalyptus* plantation in São Paulo, Brazil, negatively affect biodiversity and the ecosystem benefits provided by native forests (seen in the top left).

to quantify the trade-offs between wood production and biodiversity, the ecosystem services of carbon storage, soil conservation, and water provisioning. They paired site data on plantations and native forests using 25,950 matched data pairs from 53 countries, encompassing presence and abundance data on a wide range of organisms, from bats and terrestrial mammals to reptiles and amphibians, birds, arthropods and other invertebrates, and many different growth forms of plants.

Unfortunately, according to their analyses, achieving the competing goals of forest production and support for biodiversity and ecosystem services appears to be elusive. Hua *et al.* report that tree plantations produced more than twice the lumber produced by native forests and secondary forests. Plantations of single species of trees, known as monocultures, had far less biodiversity of animals and plants, much poorer erosion control, worse water yield, and lower biomass and carbon storage. Globally, tree plantations often all use the same small number of tree species, sometimes growing millions of genetically identical clonal individuals. The data of Hua *et al.* reveal that monoculture and low-diversity tree plantations may be good at providing lumber, but they do not achieve goals for biodiversity and ecosystem services. There is a marked trade-off between those goals and profitable lumber production—low-diversity forest plantations do not preserve biodiversity or provide carbon storage sufficient to combat climate change effectively.

And yet, there may be a way out, if only partially. Feng *et al.* synthesized a dataset from several hundred publications across six continents to determine whether multispecies planting had advantages over monocultures in productivity. They found that growth and productivity were substantially greater when multiple tree species were grown together compared with monocultures, echoing findings in natural systems of positive relationships between productivity and plant biodiversity. They attribute their results to niche complementarity when different plant forms—such as deciduous and needle-leafed trees—are grown together. Collectively, the studies by Hua *et al.* and Feng *et al.* suggest that more-complex, multispecies plantations may offer the promise of higher productivity while at least in part supporting biodiversity and providing ecosystem services. Replacing native forests with plantations, even multispecies plantations, cannot fully restore biodiversity, but well-designed forest restorations may support important ecological and conservation goals while providing economic value.

Lumber plantations have replaced natural forests at an almost unimaginable scale worldwide. Almost 1.4 billion trees have been planted in 74 countries since 1961 (*4*). The most commonly planted species are the most commercially profitable—cacao, teak, moringa, mango, and coffee. Although, in total, hundreds of tree species are planted in commercial plantations, this pales in comparison to the tens of thousands of native tree species—more than 15,000 of which face extinction (*5*). Plantations of single *Eucalyptus* species native to Australia in Africa, Asia, and South America for timber, paper, fuel, and sometimes carbon storage can decimate native biodiversity. The same is true for the extensive plantations of pines native to North America in Australia, New Zealand, and parts of South America and South Africa. The non-native pines disperse from plantations into native forest communities and can become dominant, displacing native species. The North American Douglas fir is planted over large expanses in the Netherlands and other parts of Europe. Non-native *Acacia* and *Syzygium* species have been widely planted in continental Africa and Madagascar, where they can be highly invasive and use excessive amounts of soil water to the disadvantage of native species.

Looking beyond lumber plantations, the picture for forest losses may be even bleaker, from the vast plantations of oil palms that have replaced high-diversity tropical forests in Southeast Asia to the deforestation and fragmentation of native forests for cattle pasture. These replacements of native forests pose grave threats to biodiversity and ecosystem services (*6*, *7*).

Loss of the complexity of tree species diversity in native forests threatens other species that live in and depend on those forests, from birds and invertebrates to fish, mammals, and even humans. Other analyses are in agreement with the general findings that economic productivity trades off against biodiversity preservation and ecosystem services (*6, 7*), although perhaps the works by Feng *et al.* and Hua *et al.*, taken together, suggest that there are strategies that might better achieve both economic and ecological goals. The growth in both commercial and nonprofit organizations planting trees has been accelerating worldwide (*4*). Although planting trees sounds like a good thing, whether the goals are providing livelihoods for local communities, profit for corporations, or carbon offsets, the results may not be as positive as anticipated. How well those efforts will effectively combat climate change, biodiversity loss, and the loss of other ecosystem services remains to be seen, but the prognosis—at least for monocultures and low-diversity plantations—is not encouraging. ■

REFERENCES AND NOTES

1. C. Einhorn, "Tree planting is booming. Here's how that could help, or harm, the planet," *New York Times*, 14 March 2022.
2. F. Hua *et al.*, *Science* **376**, 839 (2022).
3. Y. Feng *et al.*, *Science* **376**, 865 (2022).
4. M. P. Martin *et al.*, *Biol. Conserv.* **261**, 109224 (2021).
5. Botanic Gardens Conservation International, "State of the world's trees" (2021); www.bgci.org/wp/wp-content/uploads/2021/08/FINAL-GTAReportMedRes-1.pdf.
6. R. Seppelt *et al.*, in *Atlas of Ecosystem Services*, M. Schröter *et al.*, Eds. (Springer, 2019), pp. 251–256.
7. C. S. O'Connell *et al.*, *Environ. Res. Lett.* **13**, 064008 (2018).

ACKNOWLEDGMENTS

Financial support from National Science Foundation award NSF DEB 1909233 is acknowledged with appreciation.

10.1126/science.abp8463

BIOCHEMISTRY

Mitochondrial complex complexification

Variation in complex composition provides clues about the function of individual subunits

By **Martijn A. Huynen** *and* **Dei M. Elurbe**

Life's universal energy currency, adenosine triphosphate (ATP), is mainly produced in mitochondria by a series of distinct protein complexes that catalyze oxidative phosphorylation (OXPHOS). These complexes also exist in α-proteobacteria, the ancestors of mitochondria, but somehow their size and subunit count (complexity) has increased substantially since the endosymbiosis of a bacterium with a host cell at the origin of the eukaryotes. For example, complex I, which catalyzes the first step of OXPHOS, has increased from 17 subunits in the bacterial ancestors of mitochondria to 45 subunits in mammals (*1*). Why do the eukaryotic complexes contain these extra, supernumerary subunits when their primary function can be performed in bacteria with less subunits? On page 831 of this issue, Zhou *et al.* (*2*) report the structures of the OXPHOS complexes I, III, and IV in the single-celled eukaryote *Tetrahymena thermophila*. Comparing these structures with previously known ones suggests new hypotheses about the adaptive value of supernumerary subunits.

T. thermophila has all five OXPHOS complexes; is evolutionarily very distant from model eukaryotic species for which there are already OXPHOS structures (see the figure); and has inner mitochondrial membranes in which these structures reside that are quite different from the membranes in those model species, making it a relevant model species itself. Zhou *et al.* show that complexes I and IV in *T. thermophila* stand out: by their much larger numbers of extra subunits than have been observed in other eukaryotes, because most of these subunits have been added later in evolution than in other eukaryotes, and because some of the supernumerary subunits are encoded in the mitochondrial DNA (mtDNA) rather than the nuclear genome. These increases in complexity are consistent with what has been observed for complex V in this species (*3*), as well as from other species in the alveolate branch of the eukaryotic tree, such as the malaria parasite *Plasmodium falciparum* and the toxoplasmosis parasite *Toxoplasma gondii* (*4*–*6*).

One hypothesis about the function of the extra subunits is that they do not adapt the function of the complex itself, but instead allow the transfer of OXPHOS genes from the mtDNA to the nuclear genome, where, at least in animals, the mutation rate is lower than in the mitochondrion. The most concrete evidence for this exists for complex V of *T. gondii* (*4*), in which subunit-*a* that is encoded on mtDNA in other species is encoded in the nuclear genome. Parts of the gene encoding subunit-*a* that have been lost in the process of nuclear genome transfer have been replaced by the addition of subunits in the complex. However, in *T. thermophila*, the mtDNA is relatively rich in genes and encodes three of the supernumerary OXPHOS subunits, arguing against such a compensatory mitonuclear evolution process in this species.

A second hypothesis for complexification is that the extra subunits serve to assemble the large protein complexes into the inner mitochondrial membranes. Evidence supporting this idea is that human complex I fails to assemble in the absence of the additional subunits (*7*). The *T. thermophila* structure of complex IV reported by Zhou *et al.* provides more specific support for this hypothesis because it includes subunits that serve as assembly factors in other species, where they only temporarily associate with complex IV. These include proteins that are homologous to the proteins surfeit locus protein 1 (SURF1) and cytochrome c oxidase assembly protein 20 (COX20) that function in the assembly of complex IV in humans and yeast. A quite revealing example of this incorporation of assembly factors into the complex are proteins that insert so-called mitochondrial carrier proteins into the mitochondrial membrane. Zhou *et al.* show that in *T. thermophila*, three mitochondrial carrier proteins have become part of complex IV, as well as six proteins that are involved in their insertion into the membrane. It is as if those former subunits took along their own assembly factors when they became part of complex IV. Nevertheless, although there are now specific hypotheses for the function of these extra subunits, the adaptive value of making them permanent members of the complexes, instead of only using them during complex assembly, is unknown. After all, such assembly factor subunits can now only be used once per complex in *T. thermophila*.

However, there is one class of additional subunits for which an adaptive function is apparent from the structural analysis of Zhou *et al.* In mammals, fungi, and plants, the inner mitochondrial membranes are

Evolving supernumerary subunits

The evolution of the number of subunits (shown in parentheses) in oxidative phosphorylation complexes I and IV in three branches of eukaryotes from the last eukaryotic common ancestor (LECA) is shown. Data are based on protein structures (*1*, *2*, *10*), results from complexome profiling (*5*), and evolutionary reconstructions (*2*, *5*).

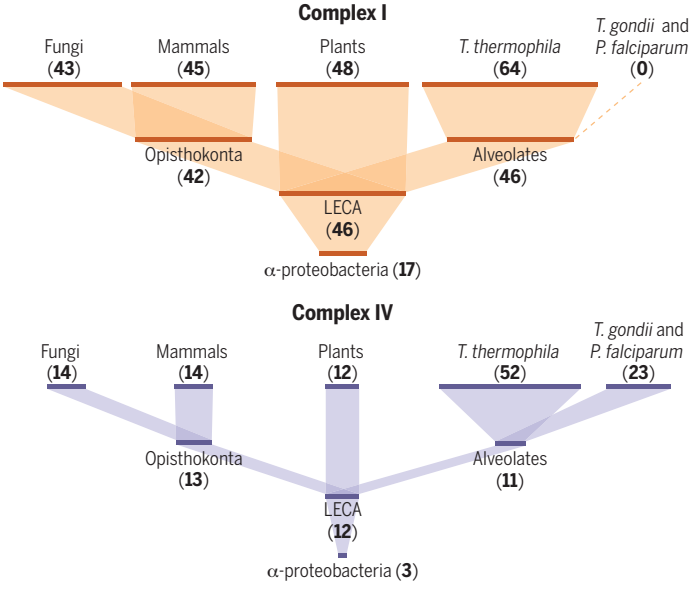

GRAPHIC: N. CARY/*SCIENCE*

Radboud University Medical Center, Nijmegen, Netherlands. Email: martijn.huijnen@radboudumc.nl

relatively flat, disk-like structures, but in *T. thermophila*, they form tubular structures. The structure of the supercomplex that contains complex I and complex III appears curved, fitting well on the tubular membranes of mitochondria in *T. thermophila* and potentially causing their curvature. Two of the supernumerary subunits appear to form a wedge between complexes I and III, such that the parts of the supercomplex within the membrane follow its curve. Bending the mitochondrial membrane is a common theme in complex V of OXPHOS (*8*), including in *T. thermophila* (*3*) and in *T. gondii* (*4*), but the findings of Zhou *et al.* now also reveal a curved shape for complexes I and III. Nevertheless, what remains puzzling is the large variation in the composition of the OXPHOS complexes between *T. thermophila*, and *P. falciparum* and *T. gondii*, because their inner mitochondrial membranes have all been classified as tubular (*9*). The variations between these membranes are, however, quite large, because the *T. gondii* membranes have knob-like structures that have not been observed in *T. thermophila* and that are caused by a distinct subunit of *T. gondii* complex V (*3*).

The view of mitochondrial OXPHOS complex evolution has, until recently, mainly been determined by that of the fungi, animals, and plants—which together represent only two of the six main branches in the eukaryotic tree of life—with relatively similar inner mitochondrial membranes and complex compositions. Elucidation of the composition and structure of these complexes in other branches of the tree of life, as in Zhou *et al.*, including those with different inner mitochondrial membrane shapes (*9*), variation in the shape of mitochondrial membranes during their life cycle (*5*), and varying mtDNA gene content, as well as elucidating covariation of these proteins with membrane shape and mtDNA gene content will provide more specific hypotheses to experimentally test and explain the enigmatic complexification of mitochondrial OXPHOS complexes. ■

REFERENCES AND NOTES

1. K. Fiedorczuk *et al.*, *Nature* **538**, 406 (2016).
2. L. Zhou *et al.*, *Science* **376**, 831 (2022).
3. R. K. Flygaard, A. Mühleip, V. Tobiasson, A. Amunts, *Nat. Commun.* **11**, 5342 (2020).
4. A. Mühleip *et al.*, *Nat. Commun.* **12**, 120 (2021).
5. F. Evers *et al.*, *Nat. Commun.* **12**, 3820 (2021).
6. A. E. Maclean *et al.*, *PLOS Pathog.* **17**, e1009301 (2021).
7. D. A. Stroud *et al.*, *Nature* **538**, 123 (2016).
8. W. Kühlbrandt, *Annu. Rev. Biochem.* **88**, 515 (2019).
9. T. Pánek *et al.*, *Curr. Biol.* **30**, R575 (2020).
10. V. Zickermann *et al.*, *Science* **347**, 44 (2015).

ACKNOWLEDGMENTS

M.A.H. thanks F. Evers for helpful comments. M.A.H. is supported by ZonMw TOP grant no. 91217009.

10.1126/science.abq0368

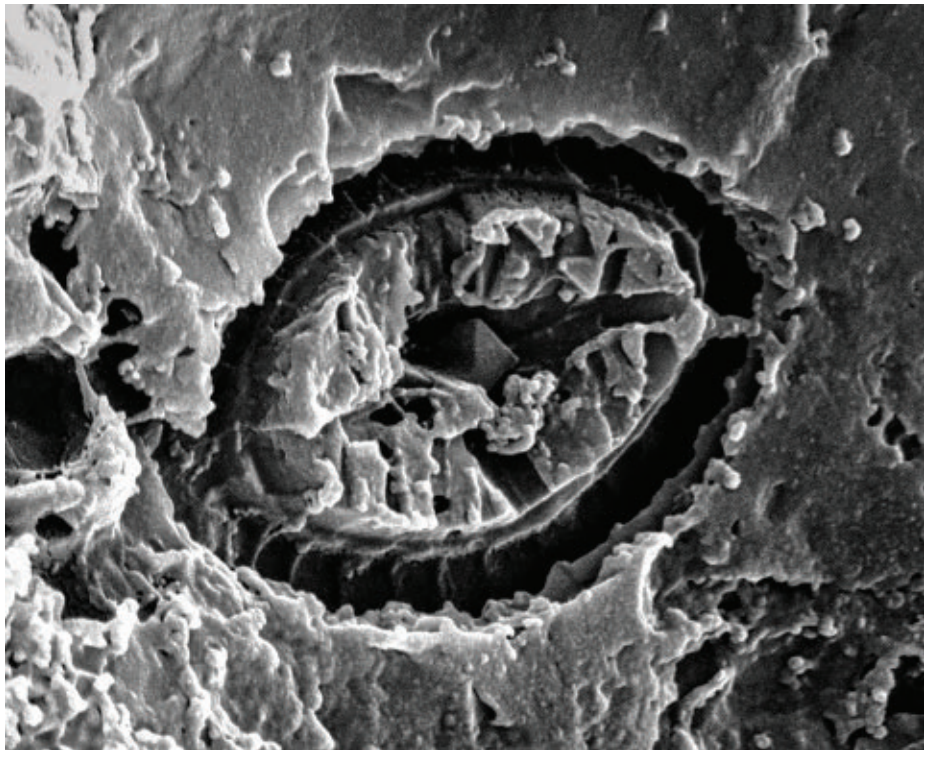

IMAGE: SAM SLATER/SWEDISH MUSEUM OF NATURAL HISTORY

Imprints of fossil coccoliths discovered in black shales reveal that calcifying microalgae remained prominent producers during previous extreme ocean conditions.

CLIMATE CHANGE

Fossil imprints from oceans of the past

Marine phytoplankton show notable resilience during extreme ocean states

By **Jorijntje Henderiks**

Throughout the long opera of Earth's oceans, algal blooms have dotted across the seascape like a cacophony of pop-up solos. Phytoplankton—the microalgae at the bottom of marine food webs—compete with each other for sunlight and nutrients to sustain photosynthesis and turn inorganic carbon into organic matter. The occasional blooms of these microalgae, often at scales visible from space, are followed by a chain of life and decay, as different species begin and end their life cycles, following each other in close succession. Phytoplankton play a pivotal role in global biogeochemical cycles and feedbacks on climate and ocean chemistry. On page 853 of this issue, Slater *et al.* (*1*) provide evidence that coccolithophores, a group of calcifying haptophyte algae, remained prominent producers throughout prolonged periods of ocean warming and oxygen depletion in the past, challenging the assumption (*2*) that they had suffered "calcification crises" under previous extreme ocean conditions.

Although far from being fully understood, it is known that Jurassic and Cretaceous oceanic anoxic events (OAEs) lasted for a few hundred thousand years and are all linked to global warming, increased atmospheric carbon dioxide (CO_2), and perturbations of the carbon cycle at the time (*3*). Increased marine production, fueled by higher nutrient supply to the oceans known as eutrophication, was a key control (*4*) in maintaining poorly oxygenated waters and enhanced burial of organic matter. The decay of excess organic matter consumed nearly all dissolved oxygen in the deep

Department of Earth Sciences, Uppsala University, Uppsala, Sweden. Email: jorijntje.henderiks@geo.uu.se

ocean, whereas the resulting anoxic conditions at the seafloor promoted the recycling of phosphate, an important nutrient. Such reinforcing feedback loops kept primary production at an increased level for a long time, before the increased burial of organic matter into the sediments was able to balance and, eventually, decrease excess atmospheric CO_2.

The black shales—dark, organic-rich shale deposits—that first drew attention to the OAEs and their abundant fish fossils (*5*) have now given up yet another of their long-kept secrets. As confirmed by Slater *et al.*, black shales have a low carbonate content and thus render very low numbers of fossil coccoliths, which are the calcite scales of coccolithophores. However, the authors prepared their rock samples with another purpose in mind—namely, to investigate different types of organic matter, including pollen and organic-walled plankton, which requires dissolving rocks in acids. Because calcite readily dissolves, researchers usually stay clear from acids when studying coccoliths, which are quantified from untreated rocks. Herein lies a beautiful example of scientific serendipity: Instead of the coccoliths themselves, the exquisitely illustrated results reveal their micrometer-scale imprints pressed into the surfaces of organic matter.

It is no surprise that because of the destructiveness of this method, this mode of coccolith preservation has been largely hidden from researchers. Slater *et al.* have shown this to be a common feature in Mesozoic black shales, including carbonate-free samples, from widely separated locations and across OAEs of different ages. Most of the coccoliths that arrived at the seafloor were thus dissolved after they were buried within organic-rich sediments, which served as a mold for their remaining imprints. The findings of Slater *et al.* contradict the assumptions that lower numbers of coccolith fossils across OAEs reflect a primary signal of decreased coccolithophore calcite export production and what some have called "abundance crises" in the photic zone (*2*). The fossil imprints confirm undoubtedly that surface water conditions did not impair intracellular calcification by coccolithophores during OAEs, at least not during their blooms.

The resilience of coccolithophores and other algae may be related to the periodicity of these short-lived blooms. Most microalgae have evolved successful ways to survive suboptimal or extreme conditions, usually by producing resting stages or switching between life phases with distinct ecophysiological traits. Still, global algal biomass may have shifted from coccolithophore-dominated, and therefore chalk-forming, producers to other noncalcifying producers. For example, nitrogen-fixing cyanobacteria and green algae also contributed to primary production during OAEs (*2*, *3*), but the actual proportions are difficult to quantify, given the selective preservation biases of fossil groups and between different sediment types.

The precise mechanisms and timing for the postburial coccolith disappearance act will need further exploration. For instance, the much younger organic-rich sediments called sapropels in the Mediterranean typically contain abundant coccoliths (*6*, *7*) and may provide some clues. If treated to an acid bath, such sediments may or may not reveal similar imprints and be a test for the idea that a certain degree of overburden pressure and lithification was required for their formation.

Even with its inherent preservation biases and "noise-canceling" properties, the sedimentary record is still the only way to gauge the long-term consequences of climate change on marine ecosystems. Organisms higher up the food web, such as the nekton and benthos, saw their habitats substantially diminished during OAEs (*2*, *3*) and sapropel formation (*6*) for thousands of years, which may be related to phytoplankton biomass resilience and stability (*8*). The Baltic Sea, a modern analog for marine anoxia, is experiencing severe eutrophication (*9*), creating conditions that support large cyanobacteria blooms in the surface waters but suffocating marine life below. In reality, the web of feedback loops around primary production is much more complex, but a key point is that the reinforcing and balancing feedbacks operate on very different time scales, which determines the outcomes. Even though phytoplankton prove resilient to climate extremes, a full recovery after marine ecosystem disturbance may be a long wait. ■

REFERENCES AND NOTES

1. S. M. Slater, P. Bown, R. J. Twitchett, S. Danise, V. Vajda, *Science* **376**, 853 (2022).
2. E. Erba, C. Bottini, G. Faucher, G. Gambacorta, S. Visentin, *Boll. Soc. Paleontol. Ital.* **58**, 51 (2019).
3. H. C. Jenkyns, *Geochem. Geophys. Geosyst.* **11**, Q03004 (2010).
4. F. M. Monteiro, R. D. Pancost, A. J. Ridgwell, Y. Donnadieu, *Paleoceanography* **27**, PA4209 (2012).
5. S. O. Schlanger, H. C. Jenkyns, *Neth. J. Geosci.* **55**, 179 (1976).
6. E. J. Rohling, G. Marino, K. M. Grant, *Earth Sci. Rev.* **143**, 62 (2015).
7. A. Incarbona, R. H. Abu-Zied, E. J. Rohling, P. Ziveri, *Paleoceanogr. Paleoclimatol.* **34**, 1597 (2019).
8. Z. Kovač, T. Platt, S. Sathyendranath, *ICES J. Mar. Sci.* **77**, 1556 (2020).
9. E. Almroth-Rosell *et al.*, *Front. Mar. Sci.* **8**, 799936 (2021).

10.1126/science.abp9754

IMMUNOLOGY

T cell immune responses deciphered

A machine-learning approach reveals antigen encoding that predicts T cell responses

By **Armita Nourmohammad**[1,2,3]

An immune response involves a coordinated orchestra of antigen-recognizing cells (*e.g.*, T cells) and signaling molecules to mount a specific response against a pathogen. Although systems immunology offers a growing list of molecular interactions that are involved in antigen-specific immune responses, an understanding of how a response is mediated by different antigen characteristics is still lacking. On page 880 of this issue, Achar *et al.* (*1*) address this question by using a robotic platform to survey a broad range of functional T cell responses to different antigen stimulations. Using machine learning, they construct a simplified map that separates six different stereotypical classes of antigen-dependent immune responses. Understanding this antigen-encoding could help guide immunotherapy, including engineering chimeric antigen receptor (CAR)–T cells and identifying vaccine antigens.

Discriminating between an organism's self-molecules and foreign (nonself) antigens is the hallmark of adaptive immunity. To achieve such specificity, the current model of T cell development in the thymus proposes that cells with very high reactivity to self-molecules (strong agonists) should be negatively selected, those with no reactivity (nonagonists) should die from neglect, and those with moderate reactivity (weak agonists) should be positively selected and enter peripheral tissues (*2*). This classification has led to the concept of antigen quality as a predictor for the efficacy of adaptive immune responses.

Antigen-specific immune responses are highly sensitive to even a small amount

[1]Department of Physics, University of Washington, Seattle, WA, USA. [2]Fred Hutchinson Cancer Research Center, Seattle, WA, USA. [3]Max Planck Institute for Dynamics and Self-Organization, Göttingen, Germany. Email: armita@uw.edu

of foreign antigens. To achieve such a degree of sensitivity and specificity, T cells sense the level of immune activity in their environments (quorum sensing) through interactions with signaling molecules and use this collective information to gauge the severity of a threat associated with an antigen (*3*). As a result, a mechanistic model of antigen-specific immune responses could involve a large number of cellular and molecular interactions with feedback, which are at least partially unknown.

However, complexity at the interaction level does not necessarily imply a lack of simplicity at a higher (coarse-grained) level. Indeed, simplicity is an emergent property of many biological systems with strongly interacting parts. This is reflected in the predictability of coarse-grained molecular characteristics in rapidly evolving populations (*4*, *5*) or reproducibility in the structure of complex ecological communities (*6*). Achar *et al*. took a similar point of view to generate a predictive coarse-grained model of antigen-specific immune responses to pathogens. Their top-down approach is data-driven and enabled by the robotic platform with which they trace many immune response profiles (i.e., dynamics of different cytokine signaling molecules) in mouse and human T cell cultures upon exposures to different antigens (see the figure). The key to generating such a model is to find an effective representation of an immune response. A powerful technique in machine learning is to produce reduced (latent) representations from models trained on large amounts of data and relate these high-level representations to identifiable features (*7*). For example, in deep-learning models of facial recognition, latent representations correspond to the eyes and nose in an image.

Achar *et al*. found a latent representation that separates immune response profiles based on the quality of the presented antigens, independent of their quantity. This observation implies that equilibrium binding association and dissociation of a T cell receptor (TCR) and an antigen cannot be a good proxy for antigenicity—in equilibrium, a high binding probability of a TCR to an antigen can be achieved even for low-affinity antigens if they are available at large quantities. Indeed, antigen recognition by T cells goes beyond equilibrium binding and involves kinetic proofreading mechanisms, whereby two or more antigen recognition events are combined to assure the fidelity of a response (*i.e.*, the interactions are kinetically proofread) (*8*–*10*). This mechanism is particularly crucial because self-antigens are present at much higher concentrations than nonself antigens, and their dissociation time from TCRs is only a few seconds shorter than that of nonself antigens (i.e., they have comparable binding constants).

The structure of the inferred latent representation reflects the amount of information encoded by biologically plausible immune profiles. Achar *et al*. found that the inferred latent representation can associate immune response profiles to six different classes of antigens, which goes beyond the three conventional antigen classes of strong agonists, weak agonists, and nonagonists. It remains to be seen how these six classes are related to the biologically meaningful molecular features of antigens.

Learning a latent representation from high-dimensional data can also be used to identify relevant parameters for a system, allowing predictability (*11*). The artificial intelligence (AI)–guided approach used by Achar *et al*. has likely identified the appropriate representation in which the profile of an immune response can be predicted by a simple model with few parameters. The remaining step is to find a biological interpretation for these parameters, which would enable experimental manipulation of the system, whereby a molecular environment (*e.g.*, availability of different cytokines) could be designed to elicit a desired immune response from a given antigen.

The importance of AI-guided design of immune and antigen environments for biomedical interventions cannot be overstated. A controlled manipulation of an immune environment could enhance the success of an anticancer CAR-T cell immunotherapy by enabling a neoantigen derived from a patient's tumor to elicit a desired immune response. The model can also inform antigen design protocols for immunotherapies and vaccine development. In addition, such a top-down data-driven approach to modeling the immune system provides a framework for constructing tractable theories for complex biological puzzles, from cracking the code of cell-fate differentiation during development to community assembly and resource allocation in ecological settings. ■

Antigen quality predicts T cell response

T cells can detect small amounts of pathogen-derived antigens and respond by proliferating and secreting different signaling molecules. A neural network trained on the complex profiles of signaling molecules over time reveals a simplified map that separates immune responses into six different classes, dependent on the quality of the presented antigens.

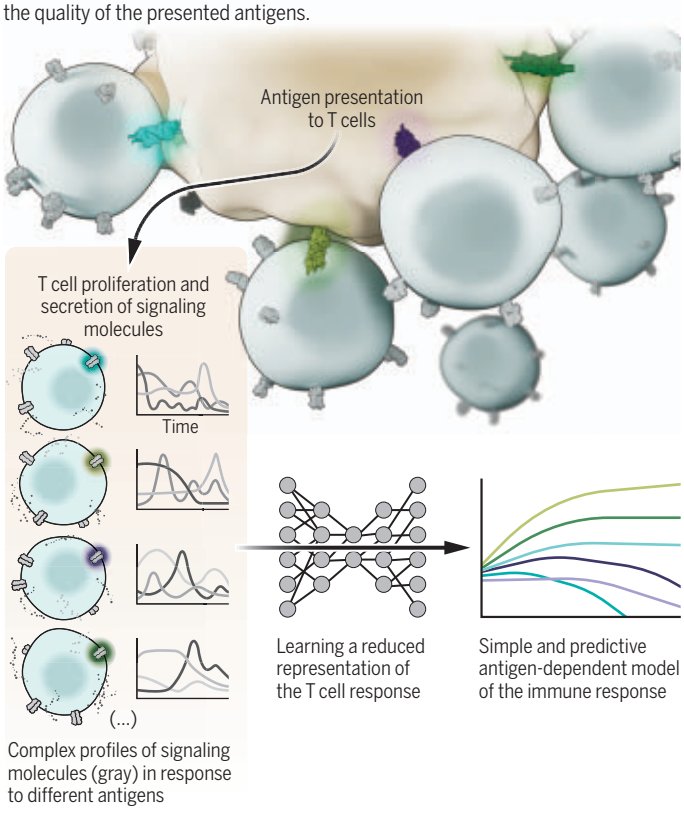

GRAPHIC: V. ALTOUNIAN/*SCIENCE*

REFERENCES AND NOTES

1. S. R. Achar *et al*., *Science* **376**, 880 (2022).
2. M. A. Daniels *et al*., *Nature* **444**, 724 (2006).
3. T. C. Butler, M. Kardar, A. K. Chakraborty, *Proc. Natl. Acad. Sci. U.S.A.* **110**, 11833 (2013).
4. A. Nourmohammad, T. Held, M. Lässig, *Curr. Opin. Genet. Dev.* **23**, 684 (2013).
5. M. Lässig, V. Mustonen, A. M. Walczak, *Nat. Ecol. Evol.* **1**, 77 (2017).
6. J. E. Goldford *et al*., *Science* **361**, 469 (2018).
7. D. P. Kingma, M. Welling, *An Introduction to Variational Autoencoders* (Now Publishers, 2019).
8. T. W. McKeithan, *Proc. Natl. Acad. Sci. U.S.A.* **92**, 5042 (1995).
9. P. François *et al*., *Proc. Natl. Acad. Sci. U.S.A.* **110**, E888 (2013).
10. J. Pettmann *et al*., *eLife* **10**, e67092 (2021).
11. R. Iten *et al*., *Phys. Rev. Lett.* **124**, 010508 (2020).

ACKNOWLEDGMENTS

A.N. is supported by a grant from the National Institutes of Health (R35 GM142795) and a CAREER award from the National Science Foundation (grant no. 2045054).

10.1126/science.abq1679

NEUROSCIENCE

Can internet use become addictive?

Problematic internet use parallels drug addiction, but the mechanisms are not yet clear

By **Matthias Brand**[1,2]

Although the internet provides many opportunities, there is a downside, which is that some people suffer from diminished control over their use of certain internet applications. There are reports of young people gaming for days without rest, adequate hydration and nutrition, or social contact outside of gaming. This has raised concerns about problematic internet use that results in functional impairment and distress in daily life. The internet applications that are often used problematically deliver pleasure and enable the reduction of negative mood. These responses show parallels with the effects of addictive drugs on the brain's reward system. Additionally, compulsive usage patterns may develop. Self-control is an important factor in whether pleasure and compulsion to use certain internet applications can drive problematic use. Given the increased use of the internet in this era of social distancing and remote working, it is important to assess harm caused by online addictive behaviors.

In the 11th revision of the International Classification of Diseases (ICD-11) by the World Health Organization, effective from January 2022, two disorders due to predominantly online addictive behaviors can be diagnosed: gambling and gaming disorders. Other potentially problematic online behaviors are being debated: problematic pornography use may be considered a subtype of compulsive sexual behavior disorder in the ICD-11, whereas problematic social-networks use and problematic buying-shopping can be diagnosed as "other specified disorders due to addictive behaviors" (*1*). Globally, up to 3% of adolescents and young adults suffer from gaming disorder (*2*), and ~7% of general populations have unspecified internet-use disorders (*3*). For gaming disorder, being younger and male increases the risk, but the choice of diagnostic instruments causes substantial variation in estimating prevalence (*2*), making it necessary to establish a standard diagnostic assessment. Negative consequences of online addictive behaviors include, for example, neglect of school or professional duties, abandonment of hobbies or leisure activities, and jeopardizing social relationships. Given increased internet use, it is important to better understand resilience and risk factors that may distinguish between a functional-enriching and a problematic-addictive usage of the internet. Moreover, although the clinical relevance of gaming disorder has been established, there are still many unanswered questions regarding etiology and neurobiological mechanisms.

There are parallels among the internet applications that are used addictively. They probably target evolutionary preconditioned reward mechanisms (related to behaviors that affect survival, such as sex, acquisition of goods, social connectedness, and discovery) and therefore deliver pleasure, resulting in positive reinforcement of the behavior (*4*). In addition, application usage can also cause negative reinforcement, such as avoidance of negative moods, which is also known from substance use (e.g., using alcohol to cope with stress). The reward and relief mechanisms may explain why specific internet applications are more likely to be used addictively than others, but they do not explain why some individuals develop addictive use, whereas most users do not and are able to use these applications in an enriching manner.

Current theoretical considerations of the development and maintenance of online addictive behaviors (*5*) are mainly based on theories and findings from substance-use research, including those related to diminished self-control (*6*), as well as hypotheses on the potential shift from reward-oriented to compulsive behaviors (*7*). There are two driving paths to online addictive behaviors that may increase the engagement in online activities: the "feels better" and the "must do" paths (see the figure). The feels better path includes both positive (pleasure, reward) and negative (reduction of stress and negative mood) reinforcement experiences and related cravings and desires. The "must do" path (which probably occurs later in the course of becoming addicted) includes habitual behaviors (automatic responses to stimuli), and especially compulsive behaviors (*7*). Compulsive behaviors describe the maladaptive persistence of a behavior despite being aware of its negative consequences. A "stop now" process, constituted by the exertion of self-control (including inhibitory control and other executive functions), may regulate the two driving paths to addiction. The main hypothesis expressed in this simplified model is that individuals with online addictive behaviors have an imbalance between the driving paths and self-control.

Neural pathways in addiction

The hypothesized main neural circuits in human addictive behaviors are shown. The "feels better" path includes positive and negative reinforcement experiences and involves the ventral striatum (nucleus accumbens), and the dorsal striatum in later stages. The "must do" path includes primarily compulsive behaviors, involving the dorsal striatum (putamen and caudate nucleus). The "stop now" self-control process mainly involves the dorsolateral prefrontal cortex.

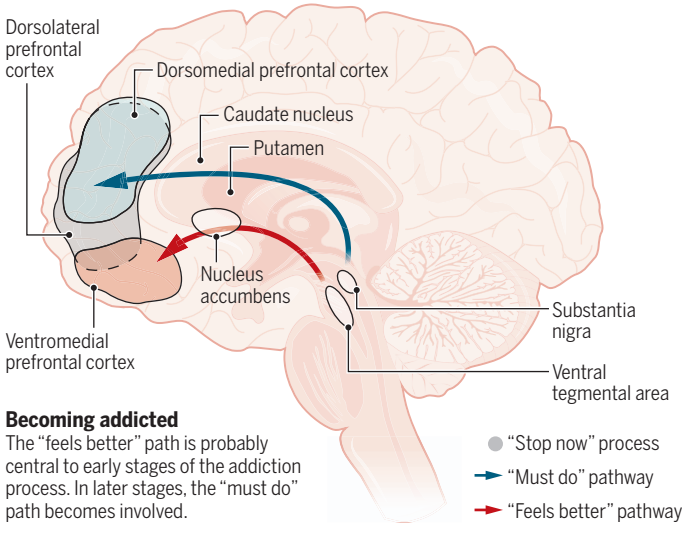

Becoming addicted
The "feels better" path is probably central to early stages of the addiction process. In later stages, the "must do" path becomes involved.

GRAPHIC: A. MASTIN/*SCIENCE*

[1]General Psychology: Cognition and Center for Behavioral Addiction Research (CeBAR), University of Duisburg-Essen, Duisburg, Germany. [2]Erwin L. Hahn Institute for Magnetic Resonance Imaging, Essen, Germany.
Email: matthias.brand@uni-due.de

Recent neuroimaging and neurocognitive studies have intensively investigated potential behavioral and neural correlates of cue reactivity and craving in online addictive behaviors and have demonstrated the involvement of both the ventral and dorsal striatum [for gaming disorder (*8*), problematic pornography use, social-networks use, and buying-shopping (*1*)]. Furthermore, meta-analyses of cognitive functions in individuals with unspecified internet-use disorders have found evidence for diminished decision-making and other executive functions related to the prefrontal cortex (*9*). This is consistent with a meta-analysis of structural brain changes in unspecified internet-use disorders showing gray matter volume reductions in the dorsolateral prefrontal cortex, anterior cingulate gyrus, and supplementary motor area (*10*). Meta-analyses on resting-state functional connectivity (*11*) for adolescents with gaming disorder have demonstrated hypoconnectivities related to limbic-frontal and fronto-parietal networks (among others), which may indicate blunted self-control in combination with increased reward sensitivity. The available findings, which are not exhaustive and not always consistent, give preliminary support for parallels between online addictive behaviors and substance-use disorders.

However, there are still many challenges in understanding the psychological and neurobiological mechanisms involved in online addictive behaviors. In particular, vulnerability, causality, and specificity are considered important. Regarding potential vulnerability, a genetic predisposition for online addictive behaviors has been reported, and polymorphisms (in most cases single-nucleotide polymorphisms) in candidate genes related to, for example, dopamine receptors, serotonin transporters, and nicotinic acetylcholine receptors have been identified (*12*). These neurotransmitters, most prominently dopamine, are involved in prefrontal-striatal loops, including the ventral and dorsal striatum. Further potential risk factors include negative early childhood experiences and insecure attachment style, personality traits (e.g., impulsivity), dysfunctional emotion regulation, stress vulnerability, low social support, and problematic family background. Self-control, assessed through questionnaire, has been found to be the most reliable protective factor for gaming disorder in a recent meta-analysis (*13*). These potential risk and resilience factors, however, are not specific for online addictive behaviors. They are also involved in drug addictions (*14*) and in other mental disorders [e.g., depression, anxiety, and attention deficit and hyperactivity disorder (ADHD)], which frequently co-occur with online addictive behaviors. Identifying more specific vulnerability factors and defining how risk and resilience factors may determine reward and relief experiences related to the use of specific internet applications may help to differentiate between enriching and problematic usage patterns.

Another major challenge is answering the question of causality related to brain mechanisms involved in online addictive behaviors, specifically the proposed imbalance between driving paths and self-control. The structural and functional brain abnormalities reported to be associated with gaming disorder and other online addictive behaviors may arise from neural plasticity and adaptations that occur while addiction is forming, but they may also be present earlier. Reduced prefrontal functioning may be a vulnerability, but may decrease further when limbic circuits become stronger in the course of the addiction process. Because most studies compare individuals with and without online addictive behaviors or are correlational, the current knowledge about causality is limited. Studies with prospective designs and with, for example, siblings (with and without gaming disorder or other online addictive behaviors), as has been done in the context of stimulant-use disorder (*15*), are needed to discover the neurobiological and psychosocial vulnerabilities and causality of online addictive behaviors.

Regarding specificity, many studies used paradigms from research on substance-use disorders and investigated potential parallels, which was theoretically most appropriate and also necessary to justify the inclusion of gaming disorder into the ICD-11 as a disorder due to addictive behaviors. A challenge for future studies is to identify the neurobiological and psychological mechanisms that are specific to online addictive behaviors. Systematic comparisons with impulse-control disorders and obsessive-compulsive disorders are needed to evaluate the involvement of impulsivity and compulsivity as potential transdiagnostic features. Internet-application–specific features and how they affect behavior should also be investigated more systematically, such as "winning elements" when finding a product on shopping sites, a pornographic video that fits best with individual preferences, or receiving likes on social networks, and should be compared with mechanisms involved in gambling disorder. Internet applications that are used addictively are designed to keep users using them. Notably, and unlike addictive substances, the applications are adaptive to usage patterns, provoking individual reinforcement experiences. This may further contribute to strengthening the "feels better" and "must do" driving paths, potentially overriding self-control while developing online addictive behaviors.

A deeper analysis of application-specific features and how these influence the user's motives (e.g., discovery, need to belong, materialistic values) may improve understanding of vulnerabilities and causalities. It is unclear whether online addictive behaviors are developed because of a general tendency to be addicted or whether the online environments are specifically addictive. Assessing general risk and resilience factors in combination with symptoms of several addiction disorders and application-specific features may help disentangle general from specific addiction mechanisms. This may then also answer the question of whether different types of online addictive behaviors should be considered independent entities (like gaming disorder), one group of problematic internet use, or the online type of a specific disorder (e.g., problematic pornography use as an online variant of compulsive sexual behavior disorder).

Online addictive behaviors are not an individual choice but may be a consequence of difficulties in making advantageous choices and regulating rewarding behaviors. To optimize prevention and treatment of these emerging mental health conditions, more global collaboration networks among research institutes are needed to realize large-scale multi-methodological longitudinal studies. Of particular interest should be if and how societal changes (e.g., increased internet use since the pandemic) will stably affect prevalence rates of online addictive behaviors. ■

REFERENCES AND NOTES

1. M. Brand *et al.*, *J. Behav. Addict.* (2020).
2. M. W. Stevens, D. Dorstyn, P. H. Delfabbro, D. L. King, *Aust. N. Z. J. Psychiatry* **55**, 553 (2021).
3. Y.-C. Pan, Y.-C. Chiu, Y.-H. Lin, *Neurosci. Biobehav. Rev.* **118**, 612 (2020).
4. R. Durrant, S. Adamson, F. Todd, D. Sellman, *Aust. N. Z. J. Psychiatry* **43**, 1049 (2009).
5. M. Brand *et al.*, *Neurosci. Biobehav. Rev.* **104**, 1 (2019).
6. R. Z. Goldstein, N. D. Volkow, *Nat. Rev. Neurosci.* **12**, 652 (2011).
7. B. J. Everitt, T. W. Robbins, *Annu. Rev. Psychol.* **67**, 23 (2016).
8. G. H. Dong *et al.*, *Commun. Biol.* **4**, 866 (2021).
9. K. Ioannidis *et al.*, *Br. J. Psychiatry* **215**, 639 (2019).
10. J. E. Solly, R. W. Hook, J. E. Grant, S. Cortese, S. R. Chamberlain, *Mol. Psychiatry* **27**, 1000 (2022).
11. H. Yan, Q. Li, K. Yu, G. Zhao, *Prog. Neuropsychopharmacol. Biol. Psychiatry* **109**, 110242 (2021).
12. S. Tereshchenko, E. Kasparov, *Behav. Sci.* **9**, 62 (2019).
13. Y. Ji, M. X. C. Yin, A. Y. Zhang, D. F. K. Wong, *Aust. N. Z. J. Psychiatry* **56**, 332 (2022).
14. N. D. Volkow, M. Michaelides, R. Baler, *Physiol. Rev.* **99**, 2115 (2019).
15. K. D. Ersche *et al.*, *Proc. Natl. Acad. Sci. U.S.A.* **117**, 15253 (2020).

ACKNOWLEDGMENTS

Thanks to A. Brandtner for help with the figure. M. B. is supported by the Deutsche Forschungsgemeinschaft (DFG, 411232260).

10.1126/science.abn4189

CHEMISTRY

Electric buzz in a glass of pure water

Hydrogen bond charge transfer in water may have far-reaching chemical implications

By **Dor Ben-Amotz**

Water is far more than a collection of neutral H_2O molecules, linked by hydrogen bonds, with a trace of hydrogen (H^+) and hydroxide (OH^-) ions. Indeed, recent work has revealed that pure water has an additional shimmering buzz arising from electron transfer between neighboring water molecules, in which the hydrogen atom on one water molecule forms a hydrogen bond with a neighbor's oxygen atom (*1*–*4*). This charge transfer, and the resulting attraction between the pair of oppositely charged water molecules, contributes to the strength of the hydrogen bonds among water molecules (*4*). Hydrogen-bonding defects in liquid water lead to the accumulation of negative or positive charge on water molecules with an odd number of hydrogen bonds (*2*–*4*). These charged waters may play an overlooked role in chemical reactions at the air–water and oil–water interfaces that are ubiquitous in biological, geological, and environmental chemistry.

The importance of hydrogen bonds in dictating the structure of water, as well as the presence of H^+ and OH^-, has been well understood since the early half of the 20th century. This understanding includes the propensity for each water molecule to donate two and accept two hydrogen bonds, and it is precisely these four hydrogen bonds that give ice its tetrahedral geometry. However, a partial breakdown of this geometry is what makes ice float on water, whose slightly denser structure includes water molecules that form an odd number of hydrogen bonds.

It has recently become clear that there is something big missing in this long-standing view of the structure of water. Specifically, recent work implies that water must also be teeming with additional, previously unrecognized, charged water molecules (*1*–*4*). The formation of these charged waters is a consequence of the quantum mechanical delocalization of electrons, which allows an electron on one water molecule to stray onto its neighbor. The resulting transfer of charge between hydrogen-bonded water molecules is supported by both theoretical predictions (*2*–*4*) and experimental evidence of charge buildup at an oil–water interface resulting from water charge transfer (*1*). This transfer of electrons between H_2O molecules is akin to the phenomenon known as quantum superposition (see the figure). Like Schrödinger's cat, which is both dead and alive, a pair of hydrogen-bonded water molecules can be either charged (i.e., as $H_2O^+\cdots H_2O^-$) or uncharged (i.e., as $H_2O\cdots H_2O$). The charged waters are formed when the hydrogen bond acceptor transfers an electron to the hydrogen bond donor. This charge transfer has a predicted probability of at least 2% (*2*, *3*), which corresponds to an average charge exchange of ±0.02 *e* for every hydrogen bond in liquid water. The resulting attraction between the positively and negatively charged waters increases the strength of all the hydrogen bonds in liquid water (*4*).

These charge transfers can also influence the average charge of individual water molecules. For most water molecules, which have an equal number of hydrogen bond donors and acceptors, the average charge is zero. However, 30% of the molecules in liquid water have an odd number of hydrogen bonds, with either two donors and one acceptor, or two acceptors and one donor. This hydrogen bond imbalance leads to a persistent average charge of ±0.02 *e* on the water molecules with an odd number of hydrogen bonds (*4*). Because water has a concentration of 55.5 moles per liter (M), this implies that these partially charged water molecules have a tremendously high concentration of ~17 M (from 55.5 M × 30%) (*4*). As electron charges are indivisible, a partial charge of ±0.02 *e* on a water molecule, in reality, means that this water molecule has a 2% chance of carrying a full charge of ±*e*. Thus, the 17 M concentration of partially charged water molecules implies that, at any instant, pure water contains 0.3 M of fully charged water molecules (from 17 M × 2%).

This instantaneous concentration of H_2O^+ and H_2O^- is about a million times higher than the 10^{-7} M equilibrium concentration of H^+ and OH^- in pure water. This implies that the trace amount of H^+ and OH^- is in equilibrium with a million times higher concentration of charged water molecules. This further suggests that there is a probability of roughly one in a million (0.0001%) of converting these charged waters to H^+ and OH^-. Converting $H_2O^+\cdots H_2O^-$ to $H_3O^+\cdots OH^-$ requires only a slight displacement of a hydrogen atom from the hydrogen bond donor toward the acceptor (note that the hydronium ion, H_3O^+, is formed by attaching a H^+ ion to a neutral H_2O molecule). Thus, hydrogen atom transfer provides a possible mechanism that converts charged water molecules to the trace amount of H^+ and OH^- in pure water (*5*). Moreover, the experimentally observed increase in the concentrations of H^+ and OH^- in water with in-

Fleeting charge transfer and longer-lived ions in water

Hydrogen bond charge transfer generates a fleeting positive (+) or negative (−) charge on water molecules. This may give rise to longer-lived partially charged water molecules ($H_2O^{+\delta}$ and $H_2O^{-\delta}$ with $\delta \approx 0.02$) in equilibrium with hydrogen (H^+) and hydroxide (OH^-) ions, and perhaps also hydrated electrons (H_2Oe^-) and water radical cations ($H_2O^{\cdot+}$).

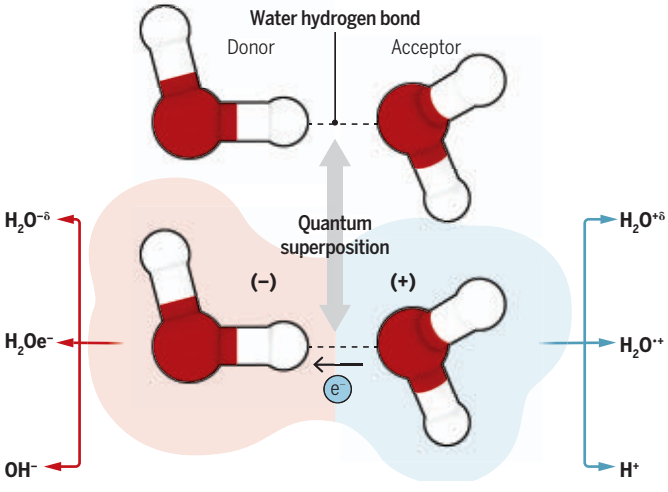

GRAPHIC: A. MASTIN/*SCIENCE*

Department of Chemistry, Purdue University, West Lafayette, IN 47907, USA. Email: bendor@purdue.edu

creasing pressure and temperature implies that the hydrogen atom transfer probability increases with increasing water density and thermal energy. In other words, although the presence of H^+ and OH^- in pure water has long been known, the possibility that these ions may be generated by the much higher concentration of charged water molecules has not been considered.

The quantum superposition of $H_2O\cdots H_2O$ and $H_2O^+\cdots H_2O^-$ also implies a rapid charge fluctuation with an on-off blinking rate on the order of a thousand terahertz—estimated by assuming the round-trip time of an electron bouncing between two neighboring water molecules. Although these fleetingly charged waters are very short-lived, they bear a striking resemblance to much longer-lived H_2O^+ and H_2O^- ions. Long-lived H_2O^+ has recently been discovered in charged water droplets and found to be chemically reactive (*6*). Long-lived H_2O^- is closely related to a "hydrated electron," whose structure has long been debated, with the current consensus being that it can best be described as an extra electron partially bound to a water molecule. However, the fleetingly charged waters, which constantly blink in and out of existence, must be structurally and chemically distinct from their longer-lived relatives. This is because long-lived ions contribute to electrical conductivity and hydrated electrons have a blue color. Thus, the experimental conductivity and optical transparency of water imply that these long-lived H_2O^+ ions and hydrated electrons have lower concentrations than H^+ and OH^-.

Water charge transfer has additional implications for interfacial water chemistry, including that occurring at macroscopic air–water or oil–water interfaces and at the surfaces of molecules such as alcohols and some amino acids dissolved in water. At all of these interfaces, there is an increase in the number of water molecules with an odd number of hydrogen bonds, and thus a buildup of charged layers near the water surface, as well as charge transfer from water to oil (*1*, *2*). The resulting layer of excess negative charge near the surface is consistent with the observed negative charge of air bubbles and oil droplets (*1*, *2*). Although the interpretation of such experimental evidence remains a subject of debate, there is no escaping the intimate link between hydrogen bonding, charge transfer, and the building up of charge layers at air–water and oil–water interfaces (*2*, *4*), as well as the following broader chemical implications.

Chemical reactivity at the surface of water is a subject of intense current interest, fueled by the discovery of up to a million-fold increase in the rates of some reactions at the surface of water compared with the rates in water (*7*). The buildup of charges near the surface, resulting from the greater number of charged water molecules with an odd number of hydrogen bonds, has been proposed as a mechanism for the observed reactivity changes (*8*).

The buildup of charge near the surface of water may also affect chemical equilibria involving H^+, OH^-, and other ions, and influence the solubilities of oily molecules in water. Although the affinities of H^+ and OH^- for air–water and oil–water interfaces remain controversial (*5*), surface tension and solubility experiments imply that such interfaces tend to expel OH^- and attract H^+. Specifically, adding OH^- ions to water increases its surface tension and decreases the solubility of oily molecules, such as benzene, whereas adding H^+ ions has the opposite effect. These observations indicate that the interfacial concentration of OH^- is lower than that in bulk water, while the opposite is true for H^+, which implies that H^+ has a slightly higher concentration near air–water and oil–water surfaces. The affinity of H^+ for such surfaces is apparently consistent with the attraction between H^+ and the negative surface charge layer induced by charge transfer. However, there may be other contributing factors, as simulations that did not consider charge transfer have also predicted that an oily methane molecule repels small positive ions less than small negative ions (*9*).

All interfacial reactivity changes, including changes in reaction rates and product yields, are linked to the propensity of the reactants, intermediates, and products to adsorb onto the surface. Such adsorption differences may depend on various chemically specific mechanisms (*10*), including stabilization of reaction intermediates resulting from the same interfacial imbalance of hydrogen bond donors and acceptors that is responsible for interfacial charge layering (*11*). More general arguments indicate that adsorption should be more favorable for neutral than charged molecules, and for larger molecules or ions than smaller ones (*12*). The resulting high interfacial concentrations of neutral molecules or large molecular ions may greatly increase reaction rates, even if the associated activation energies required for the reaction to occur are unchanged. Additionally, the activation energy may decrease, and thus rate constants increase, at surfaces—particularly for reactions involving intermediates that are physically larger than the corresponding reactant species. This expectation is consistent with recent observations of the interfacial acceleration of bimolecular, but not unimolecular, reactions (*13*), as bimolecular reactions necessarily have intermediates that are larger than the corresponding reactants.

A detailed understanding of the chemical implications of water's electrical buzz is only now beginning to emerge. There is no doubt that this buzz strengthens hydrogen bonds and produces a high concentration of partially charged water molecules. However, the precise concentrations of charged waters and the resulting interfacial charge layering have yet to be determined. The influence of water's electric buzz on interfacial chemistry is an even newer subject whose details and implications remain to be explored. This is particularly true of the similarities between chemical reactivity at both macroscopic interfaces and the molecular surfaces of solutes dissolved in water. Such similarities imply that the recently discovered acceleration of the rates of some reactions at macroscopic air–water interfaces (*7*) may also occur inside of water that contains oily molecules, as is the case in biological systems. Additionally, observations of the effect of oil chain-length on ion–oil interactions (*14*) and the effect of the concentration of oily molecules on water structure (*15*) raise questions regarding the influence of interfacial curvature and crowding on water charge transfer and chemical reactivity. Although the answers to many of these questions, as well as their practical implications, remain to be discovered, the ubiquity of water and aqueous interfaces leaves little doubt that there is much to be gained from such pursuits. ■

REFERENCES AND NOTES

1. S. Pullanchery *et al.*, *Science* **374**, 1366 (2021).
2. E. Poli, K. H. Jong, A. Hassanali, *Nat. Commun.* **11**, 901 (2020).
3. C. Schran, O. Marsalek, T. E. Markland, *Chem. Phys. Lett.* **678**, 289 (2017).
4. A. J. Lee, S. W. Rick, *J. Chem. Phys.* **134**, 184507 (2011).
5. N. Agmon *et al.*, *Chem. Rev.* **116**, 7642 (2016).
6. M. Wang *et al.*, *CCS Chem.* **4**, 1224 (2022).
7. Z. Wei, Y. Li, R. G. Cooks, X. Yan, *Annu. Rev. Phys. Chem.* **71**, 31 (2020).
8. H. Hao, I. Leven, T. Head-Gordon, *Nat. Commun.* **13**, 280 (2022).
9. H. Katsuto *et al.*, *J. Phys. Chem. B* **125**, 6296 (2021).
10. A. Chanda, V. V. Fokin, *Chem. Rev.* **109**, 725 (2009).
11. Y. Jung, R. A. Marcus, *J. Am. Chem. Soc.* **129**, 5492 (2007).
12. P. K. Wise, D. Ben-Amotz, *J. Phys. Chem. B* **122**, 3447 (2018).
13. L. Qiu *et al.*, *ChemPlusChem* **86**, 1362 (2021).
14. B. A. Rogers *et al.*, *Nat. Chem.* **14**, 40 (2022).
15. A. J. Bredt, D. Ben-Amotz, *Phys. Chem. Chem. Phys.* **22**, 11724 (2020).

ACKNOWLEDGMENTS

This work was supported by a grant from the National Science Foundation (CHE-1763581).

10.1126/science.abo3398

POLICY FORUM

SCIENCE AND LAW

Law, policy, biology, and sex: Critical issues for researchers

Researchers should be aware of how sex-difference science is (mis)applied in legal and policy contexts

By **Maayan Sudai[1], Alexander Borsa[2], Kelsey Ichikawa[3], Heather Shattuck-Heidorn[4], Helen Zhao[5], Sarah S. Richardson[6]**

The interplay between legal and bioscientific understandings of sex is prolific and complex. Biological evidence and reasoning circulate in lawmaking and policy-making across an array of politically contested issues, including health care, education, and LGBTQI+ rights and protections. There is often a substantial disjoint, however, between how scientists define and operationalize sex differences in their research and how lawmakers and policy-makers make sense of these definitions and concepts as they strategically seek to bolster or challenge legal governance. Medical and life scientists who routinely incorporate sex-related variables in their research cannot eliminate superficial or malicious misuse of research by lawmakers and policy-makers, but awareness of the legal and policy landscape can clarify the possible downstream consequences of researchers' choices about how to operationalize sex-related variables in their studies.

When lawmakers and policy-makers are required to define "sex" in rules and policies, they often rely on definitions found in professional literature from the life and health sciences. As an example, the US Department of Health and Human Services (HHS) proposed a rule in 2019 to amend the anti-discrimination section in the Affordable Care Act (ACA) to allow discrimination on the basis of gender identity or sexual orientation. The proposed rule referenced biomedical research articles on brain, liver, and cardiovascular diseases that presented sex differences as strictly biological and binary. In other cases, lawmakers and policy-makers build on the authority of scientists and on assertions about "proven science" more generally. A proposed bill in 2019 to prohibit gender-affirming care under the age of 18 in the state of Illinois stated that "Scientists and other medical professionals have recognized that biological sex is a neutral, objective, and immutable fact of human nature." Many states have proposed or passed laws that restrict the definition of sex to specific biological criteria such as "anatomy" and "genetics" at the time of birth. Policy-makers and legislators have heavily relied on biological definitions of sex when making laws that seek to limit access to public bathrooms on the basis of sex assigned at birth. These laws define sex as determined by "genetics," a "person's chromosomes," "anatomy," or "as biologically defined" (*1*).

Social movement leaders and public advocates who participate in legal and public debates also rely on medical and scientific statements when writing court amicus briefs, submitting comments on a rule, and advocating in other policy arenas. Such groups often use statements made by medical associations and scientific studies about sex, gender, and sexuality to convey their agenda. For example, in the high-profile court case of Gavin Grimm, a trans boy who was barred from using the boys' common bathroom at school, advocates for Grimm argued for an understanding of gender identity as innate and biological, citing medical and scientific literature about gender dysphoria (a term referring to persistent distress or discomfort about one's gender, often in relation to one's sex assigned at birth or bodily characteristics) and studies or theories connecting gender and the brain (such as the concepts of "brain sex" or "biological gender") (*1, 2*).

Using biological definitions in the law may sound like responsible governance, but it can result in harmful or illogical outcomes. This can occur through a variety of means, including taking biological sex categories out of context and applying them to cases of human legal rights where they are not relevant; uncritical use of binary sex categories in science; and ignoring bioscientific evidence about the complexity, mutability, context specificity, and plurality of sex and gender. In light of such concerns, we outline here central debates over conceptualizing sex in relation to biology in the law. Although we focus on US law and advocacy, reference to biomedical research on sex differences to limit or expand legal recognition of gender and sexual minorities is an emergent global strategy employed by international governing bodies, religious institutions, and national legislators, reflected, for instance, in Hungary's anti-transgender legislation passed in 2020.

Understanding how their work may be interpreted by others can help scientists identify areas where they can be more explicit about what assumptions or positions their work can, or cannot, support. These considerations are relevant for biomedical researchers and clinicians not only at the level of conducting and communicating basic and applied science, but also for ethically reflecting on the impact of scientific research on peoples' opportunities to lead full, flourishing, healthy lives.

CONTESTED AND COMPLEX

In both the science and in law, sex is a contested and complex category. Sex is a ubiquitous category across the life and health sciences, with data routinely tagged as male or female. But increasingly it is recognized in the biomedical sciences that a strict sex binary fails to describe the variation present in human biology across domains long assumed to be strongly sexed (*3*). From neuroscience (*4*) to endocrinology (*5*) to preclinical research (*6*), scientists are exploring the limitations of the sex binary as a categorical system to describe and explain the variation present in humans. For example, in contrast to widespread beliefs that humans have "sexed" brains, recent work within neuroscience reveals that human brains do not exhibit binary sex. Even in brain regions that show slight differences between females and males in aggregate, individual brains are not "male" or "female" but rather mosaic, exhibiting mixtures of "female" and "male" characteristics (*7*). Some "sex differences" in disease or health outcomes have been revealed to be accounted for by factors like age or body size (*8, 9*). This is not to say that studying sex differences does not retain usefulness in certain areas of inquiry. Biologists routinely use "sex" as a concept, and in some narrowly defined research areas, such as scientific studies of the reproductive tract, a binary works relatively well to describe the variation in humans. However, in many areas, the premise that

[1]Faculty of Law, Faculty of Humanities, Women and Gender Studies Program, University of Haifa, Haifa, Israel. [2]Department of Sociomedical Sciences, Columbia University, New York, NY, USA. [3]Harvard University, Cambridge, MA, USA. [4]Women and Gender Studies Program, University of Southern Maine, Portland, ME, USA. [5]Department of Philosophy, Columbia University, New York, NY, USA. [6]Studies of Women, Gender and Sexuality, Harvard University, Cambridge, MA, USA. Department of the History of Science, Harvard University, Cambridge, MA, USA. Email: srichard@fas.harvard.edu; smaayan@univ.haifa.ac.il

ILLUSTRATION: SARA GIRONI CARNEVALE

sex deeply pervades most aspects of human biology and cleaves humans into two essential types is being deeply challenged within scientific research.

When US law categorizes people according to sex, it usually classifies them as either male or female. Sex classifications referencing biological criteria are codified throughout state and federal laws, and regulations are sometimes found in surprising places. For example, in its 2014 regulation "Standards To Prevent, Detect, and Respond to Sexual Abuse and Sexual Harassment Involving Unaccompanied Children," the federal Office of Refugee Resettlement (ORR) defines "sex" using strictly binary groupings of "sex chromosomes, gonads, internal reproductive organs, and external genitalia."

US laws and policies vary across time, jurisdiction, and context, and so do definitions of sex in the law. For example, a recent landmark Supreme Court decision in *Bostock* v. *Clayton* held that protection from discrimination "on the basis of sex" in Title VII of the Civil Rights Act includes sexual orientation and transgender status. The HHS subsequently announced that they will apply the same interpretation to the ACA. Despite this, much legal policy continues to reductively conceptualize "sex" as binary and to source biological science as the basis for this determination.

SEX IN LAW: THREE APPROACHES

In the face of these complexities and contestations, legal actors must make situated and often value-laden choices about the use of sex classifications. Here, we characterize three broad-stroke approaches to sex classification in the law employed by lawmakers and policy-makers, which we call essentialist, abolitionist, and pluralist. Appreciating the distinctions between these approaches can inform scientists' considerations in offering constructive guidance when their expertise is invited in a law or policy setting and can clarify decisions about how to include, operationalize, interpret, and translate findings regarding sex-related variables.

An essentialist approach to sex assumes that sex is a strictly binary and essential property of people defined by biological science. Administrative classifications of sex, such as the examples of the ORR given above, exemplify the sex essentialist approach. Essentialist conceptions of sex are often used in US state anti-LGBTQI+ legal initiatives aimed at determining who is permitted to use which bathrooms or to play which youth sports, and to generally enforce and justify segregation in sexed spaces, such as prisons, locker rooms, and homeless shelters. Binary sex essentialist approaches frequently rely on selective biological claims about sex and invoke the authority of science. For example, a 2021 law passed in West Virginia requires classification of sports competitions according to "biological sex," defined as "an individual's physical form as a male or female based solely on the individual's reproductive biology and genetics at birth."

In strong juxtaposition to essentialism is abolitionism, which considers sex classifications to be an unremitting harm and aims to remove them from law and policy. Prominent examples of this stance in action include recent efforts to remove sex from official identification documents such as drivers' licenses or birth certificates, to convert sex-based bathrooms into gender-neutral or all-gender ones, and to endorse mixed-sex sport competitions. Another form of abolitionism can be found in laws that aim to replace sex classifications with different, perhaps more relevant, criteria: Instead of giving parenting-related benefits or special health

care to "mothers," it gives them to the "primary family caregiver," "pregnant person," or based on lactation status (*10*, *11*).

Such initiatives are often endorsed by medical experts and associations that attest to the complexity of gender and sex or to biological sex's lack of necessity in the specific context. For example, in June 2021 the American Medical Association resolved to "advocate for the removal of sex as a legal designation on the public portion of the birth certificate," arguing that this removal will not harm the collection of vital statistics needed for public health purposes and will help protect the privacy of and prevent discrimination against intersex, trans, and nonbinary people.

In contrast to both essentialism and abolitionism is a pluralist approach. This approach accepts that different contexts call for different definitions of sex. Pluralism is not essentialism, because it rejects that sex is a universally binary and biological property of individuals. Instead, definitions and conformations of sex-related categories are expected to vary according to the pragmatic needs of the policy or social context. But pluralism is also not abolitionism, because it recognizes that the need for and characterization of sex classifications vary with context, and that in situated cases, sex classifications may be relevant and necessary—for example, to help extend rights and protections to vulnerable groups.

Such policies create sex classifications that may change over time, perhaps retaining male and female but adding further categories to accommodate those who do not fit the binary, or expanding the definition of males and females beyond biologically essentialist ones. Examples include policies that add a third gender/sex category, as seen in some identification documents. Dana Zzyym, an intersex nonbinary individual, recently became the first US citizen to receive a passport with an "X" gender/sex marker, designated for nonbinary, intersex, and gender-nonconforming people. Similarly, a pluralist approach may support sex classifications for particular protected classes, such as in same-sex education or in sex-discrimination statutes designed to protect vulnerable populations in the workplace. In this sense, some who may endorse abolitionism in the long run may choose a pluralist course in the short run. A pluralist approach means that in any particular case of gender or sex categorization in law and policy, it is necessary to build an empirically grounded definition of sex specific to the context.

RESPONSIBLE SCIENCE

How might scientists who study sex-related variables incorporate within their own research practice an awareness and sensitivity to how their work may be taken up in these debates? The first step is to recognize that scientific claims about sex are frequently and variously mobilized in a wider policy, regulatory, and administrative space, and that "sex" has different meanings across these realms and over time. For this reason, it is important to contextualize and appropriately qualify uses of sex categories in research claims, including in publications, pedagogy, and engagement with the media, public, or policy-makers (*12*).

Where possible, biomedical researchers should consider reducing unnecessary use of sex categories in the design, conduct, and interpretation of scientific studies. Often, sex categories are retained in data merely because they come tagged with sex, even if sex is not a central or relevant category of analysis. Frequently, researchers use sex as a proxy for other variables, either because other variables are more challenging to collect or because sex is readily available in the data as a category of analysis. Rather than using crude sex categories as a proxy, scientists should use variables that are hypothesized as part of the direct mechanistic explanation for the condition of interest. This could mean, for example, reporting on hormone levels, weight, anatomy, presence or absence of gonads, or pregnancy status, instead of relying on male-female sex categories as a coarse means of capturing variability.

Although it may seem self-evident that such practices are simply good science, they are actually rarely observed in studies investigating and reporting sex differences. For example, aiming to improve women's health outcomes by correcting the historical record of androcentrism in biomedical research, in 2016 the US National Institutes of Health (NIH) introduced a Sex as a Biological Variable (SABV) funding mandate requiring preclinical biomedical researchers working with cells, tissues, and model organisms to include male and female materials and to disaggregate data by sex. As analyses of the pronounced increase in studies of sex differences since the implementation of the mandate have shown, disaggregation by sex without proper statistical power and without an a priori reason in the study design contributes to a muddle of contradictory results and false positives (*13*, *14*). Given this, and the likelihood that a proliferation of scientific reports of sex-disaggregated findings may fuel sex essentialist law and policy, research funders and publishers should work to better align the imperative of conducting carefully contextualized studies of well-defined sex-related variables with SABV policies, including in journal publication guidelines such as Sex and Gender Equity in Research (SAGER) (*12*).

Finally, investigators of sex-related variables should strive to incorporate discussion of, and where possible, variables related to gender (norms, beliefs, behaviors, and structures related to masculine and feminine gender roles and identities) and other social factors. For example, when studying sex disparities in disease, it is prudent to consider gendered behaviors and structural variables that contribute to risk of disease exposure, health care access, and likelihood of reporting certain symptoms. Understanding sex and gender in a biosocial framework (*5*) can help prevent unwarranted essentialist interpretations that pose sex and gender as simple binaries, immutable and hardwired by biology.

REFLECTIVE, ETHICAL, ACCOUNTABLE

As the broad and dynamic field of legal and policy activity reviewed here demonstrates, practices in the science of sex differences matter because conceptions of binary sex as an uncontested, simple biological fact are presently playing a central role in antidiscrimination policy and human rights law critical to protections for women and sexual and gender minorities. When scientific uses of biological sex concepts lack clarity, precision, and rigor, this increases the risk that legal advocates will misunderstand and misrepresent scientific research on biological sex. Reflective, ethical, and accountable practices surrounding how sex differences are discussed, contextualized, and applied in scientific studies are vital when science may be used to justify harmful and discriminatory policy. ■

REFERENCES AND NOTES

1. M. Sudai, Toward a Functional Analysis of "Sex" in Federal Antidiscrimination Law. Harvard J. Law Gender 42 (2018); https://ssrn.com/abstract=3207728.
2. I. Katri, Transitions in Sex Reclassification Law. *UCLA Law Rev.* **70** (forthcoming); https://papers.ssrn.com/sol3/papers.cfm?abstract_id=4042055.
3. L. Z. DuBois, H. Shattuck-Heidorn, *Am. J. Hum. Biol*. **33**, e23623 (2021).
4. L. Eliot, A. Ahmed, H. Khan, J. Patel, *Neurosci. Biobehav. Rev*. **125**, 667 (2021).
5. S. M. van Anders, *Front. Neuroendocrinol*. **34**, 198 (2013).
6. S. A. Ritz *et al*., *FASEB J*. **28**, 4 (2014).
7. D. Joel *et al*., *Front. Hum. Neurosci*. **12**, 399 (2018).
8. D. J. Greenblatt, J. S. Harmatz, T. Roth, *J. Clin. Psychopharmacol*. **39**, 189 (2019).
9. M. M. Mielke, *Psychiatr. Times* **35**, 14 (2018).
10. J. A. Clarke, *Harv. Law Rev*. **132**, 894 (2019).
11. D. Fontana, N. Schoenbaum, *Columbia Law Rev*. **119**, 309 (2019).
12. S. S. Richardson, *Pract. Biol* **14**, (2022).
13. J. W. Rich-Edwards, U. B. Kaiser, G. L. Chen, J. E. Manson, J. M. Goldstein, *Endocr. Rev*. **39**, 424 (2018).
14. Y. Garcia-Sifuentes, D. L. Maney, *eLife* **10**, e70817 (2021).

ACKNOWLEDGMENTS

We thank the participants in the April 2021 Harvard GenderSci Lab workshop "Biological Binary Sex Essentialism in the Law and Public Policy," funded by the Open Gate Foundation.

10.1126/science.abo1102

Having voted to exclude other evidence prior to the 1950s, a working group may define the Anthropocene using radionuclide signatures from Crawford Lake.

PHOTO: ANDREA ARROGANTE

ANTHROPOCENE

Shaping Earth in our image

An interdisciplinary interrogation of the Anthropocene misses the chance to probe broader and deeper

By **Erle C. Ellis**[1] *and* **Mark Maslin**[2,3]

In 12 essays by 19 scholars, *Altered Earth* seeks to set out the scientific evidence and the "human terms"' that define the Anthropocene—the unofficial era of Earth's history defined by human activities. With a foreword by esteemed historian Dipesh Chakrabarty, chapters by geologist Jan Zalasiewicz and Earth system scientist Will Steffen, and essays by various scholars across the humanities, this would seem the ideal text for those seeking to connect Anthropocene science with the humanities. If only it were so.

The book employs a personal essay format designed to engage readers beyond the sciences. There are some positive visions of Anthropocene futures here, and editor Julia Adeney Thomas's proposition that "stories…mold the real world" is an inspiring jumping-off point for a book in which "narratives can emerge from conversations across disciplines—geologists and Earth scientists, on one hand, humanists and social scientists on the other." Chapters explore topics as varied as disease (including COVID-19), the colonial politics of wind power, humans as political agents, the Chernobyl disaster, an expedition to Mars, and a vision of cities that "restabilize the Earth System."

Altered Earth: Getting the Anthropocene Right
Julia Adeney Thomas, Ed.
Cambridge University Press, 2022. 300 pp.

Despite a final chapter proposing that "the Anthropocene calls for opening up perspectives," the book consistently defers to a "growing consensus that our planet entered a dangerous new state in the mid-twentieth century." There is no doubt that a "Great Acceleration" in environmental and social trends occurred after World War II or that many of these—including greenhouse gas emissions—demand serious attention and action. But there is more to the Anthropocene than the events that have transpired since the 1950s.

Earth scientists have variously proposed Anthropocenes beginning 5000, 2000, 500, 200, and 70 years ago, defined by land clearing for agriculture, soil tillage, the European colonization of the Americas, the start of the Industrial Revolution, and nuclear fallout, respectively. Related terminologies, including "Plantationocene," "Capitalocene," "Technocene," and even "Chthulucene," have emerged in the social sciences and humanities, as scholars seek to articulate the myriad factors and behaviors that are changing the planet.

All this scholarly ferment should surprise no one. At stake is no less than what it means to change the planet—and even what it means to be human. Yet these varied proposals are treated here as diversions from a single, "correct" scientific definition.

Perhaps the most remarkable thing about this book is what is left out. There are no archaeologists among the authors, and some of the most important works ever published on the subject are not cited. The early Anthropocene hypothesis, which posits that intense farming activities triggered considerable anthropogenic changes in Earth's climate as long as 8000 years ago, goes unmentioned. Nor do any of the essays challenge how the Anthropocene might eventually be defined by scientists as an epoch of geologic time, despite ongoing efforts to do so by several of the authors.

One chapter explains the entangling of Indigenous history and sedimentary processes in Crawford Lake in southern Ontario and how a "golden spike" in those sediments due to radionuclide fallout from nuclear tests might come to mark the start of the Anthropocene in the year 1952. Less clear, however, is the fact that the working group responsible for epoch definition had already voted not to consider any earlier human evidence in these or any other sediments (*1*).

More concerning is the book's failure to explain why leading stratigraphers and environmental scientists are increasingly convinced that defining the Anthropocene as an epoch of geologic time—1950s or otherwise—is neither useful nor scientifically accurate (*2*). Dividing Earth's history into two parts at a single point in time seems arbitrary to them, when it is so clear that human transformations of this planet represent an ongoing and evolving geological event that has been spreading and scaling up for millennia.

Where is the essay on defining the Anthropocene in relation to the wealthiest people on Earth—those most responsible for climate change? Where are the billion black Anthropocenes (*3*) and the communities who suffered as a result of European colonialism? What of the Indigenous peoples who have sustained Earth's biodiversity for millennia? In *Altered Earth*, this fertile and important ground for discussion is left to others. ■

The reviewers are at the [1]Department of Geography and Environmental Systems, University of Maryland, Baltimore County, Baltimore, MD, USA; [2]Department of Geography, University College London, London, UK; and [3]Natural History Museum of Denmark, University of Copenhagen, Copenhagen, Denmark. Email: ece@umbc.edu

REFERENCES AND NOTES

1. P. Voosen, *Science* 10.1126/science.abq8466 (2022).
2. P. Gibbard *et al.*, *J. Quat. Sci.* **37**, 395 (2022).
3. K. Yusoff, *A Billion Black Anthropocenes or None* (Univ. of Minnesota Press, 2018), pp. 130.

10.1126/science.abq1474

INNOVATION

The fastest R&D lab on the planet

From car safety to road design, motorsport innovation has spilled over into other arenas

By **Lee Vinsel**

Although long ago established as a serious and popular sport, automobile racing, or motorsport, is not everyone's cup of tea. But in his new book, *Racing Green*, journalist Kit Chapman argues that we should all be thinking about how racing has contributed to society at large.

The book's title is something of a misnomer, as only about a third of the volume is dedicated to environmental topics, with the remainder focusing on safety and speed. The main question that the book confronts—what are the sources of innovation?—has been a constant locus of attention in capitalist nations since at least the 1950s.

The vectors of new ideas are various. There are independent inventors, of course, and some corporations have research and development (R&D) labs. Universities also play a part, although not as big a part as they like to imagine. But in mature industries, such as the automobile industry, innovation is typically slow and incremental, focused on slightly improving established ideas, for instance, to better reach different consumer markets.

Chapman argues that things are different in motorsport, which he dubs "the world's fastest R&D lab." His story is one of what people in technology studies call "knowledge spillover"—how new ideas spread from one industry or sector to another.

Unlike big automakers, Chapman contends, racing teams are constantly looking for technological breakthroughs that will give them advantages on the track. Motorsport has also contributed to safety in vehicles, in road design, and in the operations of ambulances and emergency rooms. Perhaps more contentiously, Chapman argues that the sport could have big impacts on environmental improvements, including through battery technologies and artificial intelligence systems that maximize fuel efficiency.

Although Chapman is prone to overstatement—"This is a book about how racing cars will save your life"—the book is full of well-told, often humorous, surprising, and interesting stories of how innovations moved from the racetrack to other domains of human life. Readers learn how famous crashes, such as the one that resulted in the tragic death of Dale Earnhardt, led to changes in safety technology both on and off the track; the state of battery research and how racing teams have pursued electric power to gain split-second advantages over competitors; and how the sport has expermented and is currently experimenting with previously unexplored materials such as carbon, wood, and flax. Chapman also does an excellent job conveying just how far motorsport has come environmentally, although he could have done more to highlight how much energy these cars are using for what some would no doubt consider frivolous ends.

At times, I wished Chapman had looked at motorsport in the larger context of technological change. Knowledge spillover is normal, and new ideas are constantly moving from one area of society to another. Chapman demonstrates that auto racing has spun out ideas that have had impacts elsewhere, but the spillover from motorsport pales in comparison with the innovation seeded by the US Department of Defense, which has created so many things, including GPS and the internet.

The state is missing in other areas of Chapman's picture, too. Although motorsport may generate new ideas, the mainstream auto industry has adopted many safety and environmental technologies only by being forced to do so through regulation (see airbags and catalytic converters) or by being offered subsidies (see electric vehicles). Put another way, one is sometimes left wondering exactly how Chapman thinks innovations in motorsport will travel elsewhere to do the important work he hopes they will do.

Still and all, the book is an entertaining and often insightful read that will be enjoyed by both racing fans and people generally interested in processes of innovation. Its tales of spillover from motorsport to other domains are useful for further contemplation, and *Racing Green* would be an excellent resource to engage students in deeper discussions about technological change. ■

The reviewer is at the Department of Science, Technology and Society, Virginia Polytechnic Institute and State University, Blacksburg, VA 24061, USA. Email: leev@vt.edu

Racing Green: How Motorsport Science Can Save the World
Kit Chapman
Bloomsbury Sigma, 2022. 320 pp.

NASCAR driver Kyle Larson stands next to his wrecked vehicle after a crash in 2013.

PHOTO: REUTERS/PIERRE DUCHARME

10.1126/science.abq0111

You're only an essay away!

Check out our Awards and Prizes that are currently seeking submissions.

Neurobiology
Submissions Opened: February 1
Submissions Close: June 15

Cell and Molecular Biology
Genomics, Proteomics, and Systems Biology
Ecology and Environment
Molecular Medicine
Submissions Opened: March 1
Submissions Close: July 15

Immunology
Submissions Open: May 1
Submissions Close: October 1

Scientific Innovation & Entrepreneurship
Submissions Open: June 1
Submissions Close: November 1

Science Awards and Prizes seeks to find the next generation of early-career researchers on the cusp of changing the scientific landscape. Start your journey by finding the Award or Prize that fits you and find out how to apply today!

Science
AAAS

bit.ly/3qKxMN0

Scan the code to start your application process!

Pushing the Boundaries of Knowledge

As AAAS's first multidisciplinary, open access journal, *Science Advances* publishes research that reflects the selectivity of high impact, innovative research you expect from the *Science* family of journals, published in an open access format to serve a vast and growing global audience. Check out the latest findings or learn how to submit your research: **science.org/journal/sciadv**

Science Advances
AAAS

GOLD OPEN ACCESS, DIGITAL, AND FREE TO ALL READERS

LETTERS

Standard housing for research animals does not provide enough space for healthy behaviors.

PHOTO: PASCAL GOETGHELUCK/SCIENCE SOURCE

Edited by **Jennifer Sills**

Good science requires better animal welfare

Biomedical research suffers from a crisis of reproducibility and translatability (*1*), with some studies estimating that more than 50% of preclinical studies are irreproducible (*2*). The lack of reproducible results has led to annual economic losses of about US$28 billion in the United States alone, delays to new treatments, and unnecessary use of animals (*2*). To improve reproducibility and generate findings that are more generalizable to both sexes, the US National Institutes of Health (NIH) and the UK Medical Research Council (MRC) have each recently announced that they will only fund research that includes both male and female animals as default (*3*, *4*). It is important that funders drive for better science, and inclusion of both sexes is to be welcomed given the heavy skew of biomedical research toward male subjects, which restricts diversity of research findings (*1*). However, the new rules conflict with efforts to minimize the use of animals in research and overlook the role of animal welfare in facilitating good science.

The United Kingdom, the United States, and other countries have introduced plans for replacing, reducing, and refining the use of animals in research (known as the 3Rs) (*5*–*7*), based on long-established principles (*8*). The reduction goal refers to reducing sample sizes wherever possible. If both male and female animals are used, as required by the new rule, sample sizes will likely need to be increased to prevent underpowered studies that fail to detect effects of treatments, sex, and their interactions. The MRC and NIH will have to provide clear guidance on how to accommodate both objectives.

Especially given the need for larger sample sizes, it is crucial to ensure good animal welfare (consistent with 3Rs refinement goals) so as not to compromise results. It is widely argued that good animal welfare equals good science, but most funders have stalled in implementing better animal welfare standards. The standard housing used by most labs for animals, which is in line with guidelines and codes of practice (*9*, *10*), includes confined spaces that don't allow enough space to move normally, a lack of shelter from bright lights, and insufficient stimulation. These conditions lead to stress and poor health, which can affect both behavior and physiology (*11*). Animals in confined spaces are unable to perform highly motivated behaviors such as rearing and exploring, exhibit behavioral signs of depression such as anhedonia, show exacerbated severity of induced diseases such as cancer, and have increased mortality rates (*11*). To improve reproducibility (and live up to the aspirations of the 3Rs), the requirement to include both male and female animals must be accompanied by a requirement for substantial and long-awaited improvements to the housing of laboratory animals (*12*), including increased space, increased environmental complexity, and increased opportunities to engage in normal behaviors such as digging and nesting.

V. Neville*, B. Lecorps, M. Mendl
Bristol Veterinary School, University of Bristol, Langford BS40 5DU, UK.
*Corresponding author.
Email: vikki.neville@bristol.ac.uk

REFERENCES AND NOTES

1. "Working Group on Sex in Experimental Design of Animal Research: Meeting report" [MRC, National Centre for the Replacement, Refinement, and Reduction of Animals in Research (NC3Rs), 2021]; www.ukri.org/wp-content/uploads/2022/03/MRC-090322-SexInExperimentalDesign-SummaryReport.pdf.
2. L. P. Freedman, I. M. Cockburn, T. S. Simcoe, *PLOS Biol*. **13**, 1 (2015).
3. National Institutes of Health, "NIH policy on sex as a biological variable" (2017); https://orwh.od.nih.gov/sex-gender/nih-policy-sex-biological-variable.
4. UK Research and Innovation, "Use of both sexes to be default in laboratory experimental design" (2022); www.ukri.org/news/use-of-both-sexes-to-be-default-in-laboratory-experimental-design/.
5. NC3Rs, "The 3Rs" (2017); https://nc3rs.org.uk/who-we-are/3rs#anchor_0.
6. NA3RCs, "Annual report" (2021); www.na3rsc.org/wp-content/uploads/2022/05/NA3RC_2021-Annual-Report_FINAL.pdf.
7. Norecopa, "Annual report for 2021" (2021); https://norecopa.no/media/zybhfucd/annual-report-2021.pdf.
8. W. M. S. Russell, R. L Burch, *The Principles of Humane Experimental Technique* (Methuen, London, 1959).
9. United Kingdom Home Office, Code of Practice for the Housing and Care of Animals Bred, Supplied or Used for Scientific Purposes. (2014); https://assets.publishing.service.gov.uk/government/uploads/system/uploads/attachment_data/file/388535/CoPanimalsWeb.pdf.
10. National Research Council of the National Academies, *Guide for the Care and Use of Laboratory Animals* (The National Academies Press, ed. 8, Washington, 2011).
11. J. Cait, A. Cait, R. W. Scott, C. B. Winder, G. J. Mason, *BMC Biol.* **20**, 1 (2022).
12. I. J. Makowska, D. M. Weary, *ILAR* **60**, 3 (2019).

10.1126/science.abq7198

Indigenous lands protect Brazil's agribusiness

Since taking office as Brazil's president in 2019, Jair Bolsonaro has greatly weakened the protection of the Amazon and its Indigenous peoples (*1*). Bolsonaro's hate speech against Indigenous peoples and policies dismantling the protection of Indigenous lands have led to an increase in invasions and attacks on Indigenous, public, and conservation lands (*2*), which his administration has rewarded rather than deterred (*2*, *3*). Proposed bill PL 490/2007 (*4*) would continue this trend by blocking or reversing the recognition of the rights of many Indigenous peoples to their traditional lands.

Brazilian law guarantees that Indigenous residents have exclusive rights to their Indigenous lands, protecting them from non-Indigenous individuals and companies (*5*). However, the protected status requires approval through a bureaucratic process that can take decades. There are currently 303 Indigenous lands that are in the process of obtaining protection.

PL 490/2007 would impede the final approval of the Indigenous lands currently working toward protection and allow revocation of the protected status enjoyed by many lands that were approved after 5 October 1988, the date of Brazil's current constitution (*6*). Those that reached the final approval stage before 1988 will not be affected by PL 490/2007, although they continue to face threats from illegal invasions.

The bill, which has been stalled in the National Congress since 2007, is now racing toward final approval. It has passed the lower house of Congress and is being given priority in the Senate. A case before the Supreme Federal Court will decide on its constitutionality in the coming weeks. On 25 April, President Bolsonaro stated that if the court rejects the policies outlined in the bill, he will likely refuse to comply with the decision (*7*).

Agribusiness representatives justify their support for the bill with the misleading argument that the preservation of Indigenous lands would negatively affect Brazil's agricultural production (*7*). However, the amount of idle deforested land in Brazil is more than sufficient to ensure the projected growth of Brazilian agribusiness (*8*). Indigenous lands protect 25% of Brazil's Amazon biome, where deforestation is now close to the limit that the forest can tolerate (*9*). Brazil is already facing a severe water crisis that has affected both agribusiness and the water supply for domestic use (*10*). Further deforestation in the Amazon would worsen this crisis (*11*, *12*), jeopardizing the country's agribusiness.

It is crucial that the Supreme Federal Court reject the policies proposed by PL 490/2007. If the protection of Indigenous lands is withheld or revoked, countries that import soy and beef from Brazil must boycott these commodities to prevent increased deforestation in the Amazon and violation of Indigenous rights.

L. Ferrante[1]* and P. M. Fearnside[2]
[1]Ecology Graduate Program, National Institute for Research in the Amazon (INPA), 69060-001 Manaus, AM, Brazil. [2]INPA, 69067-375 Manaus, AM, Brazil.
*Corresponding author.
Email: lucasferrante@hotmail.com

REFERENCES AND NOTES

1. L. Ferrante, P. M. Fearnside, *Die Erde* **152**, 200 (2021).
2. L. Ferrante *et al.*, *Land Use Pol.* **108**, 105559 (2021).
3. L. Fuhrmann, B. S. Bassi, T. Merlino, "Titula Brasil beneficia madeireiros na nova fronteira do desmatamento," *De Olho nos Ruralistas* (2022) [in Portuguese].
4. Câmara dos Deputados, PL 490/2007 (2007); www.camara.leg.br/propostas-legislativas/345311.
5. I. Almeida, "Estatuto do Índio: o que diz? qual sua importância?" *Politize* (2021); www.politize.com.br/estatuto-do-indio/ [in Portuguese]
6. "Marco temporal: Entenda por que julgamento no STF pode definir o futuro das terras indígenas," *Conectas Direitos Humanos* (2021) [in Portuguese].
7. "Militares contestam afirmação de Barroso sobre processo eleitoral," Band Jornalismo (2022); www.youtube.com/watch?v=FEYR8NZm9HQ [in Portuguese].
8. B. B. N. Strassburg *et al.*, *Glob. Environ. Chang.* **28**, 84 (2014).
9. T. E. Lovejoy, C. Nobre, *Sci. Adv.* **4**, eaat2340 (2018).
10. A. J. Getirana, R. Libonati, M. Cataldi, *Nature* **600**, 218 (2021).
11. D. V. Spracklen, L. Garcia-Carreras, *Geophys. Res. Lett.* **42**, 9546 (2015).
12. J. A. Marengo *et al.*, *Front. Earth Sci.* **6**, 228 (2015).

10.1126/science.abq7243

Irrawaddy dolphins continue to decline

The Indo-West Pacific Irrawaddy dolphin (*Orcaella brevirostris*) inhabits coastal areas and rivers in South and Southeast Asia. The global population, listed as Critically Endangered by the International Union for Conservation of Nature, has declined by 50% over the past two decades (*1*) and recently became locally extinct in Vietnam's Sekong, Sesan, and Srepok Rivers (*1*). In February, the last Irrawaddy dolphin in the Mekong River in Laos was found dead, entangled in gillnets (*2*, *3*). The remaining Mekong River population—about 90 individuals—spans only 180 km in Cambodia (*1*). Irrawaddy dolphins in the Mekong, along with those in Indonesia's Mahakam River and Myanmar's Ayeyarwady River, are threatened by anthropogenic activities that put the species at risk of imminent regional extinction (*1*, *4*). Cambodia, Indonesia, and Myanmar must therefore act quickly to conserve the species.

Gillnet fishing and dam building are among the main threats to these river dolphin subpopulations. Gillnets, which are difficult to avoid, can trap and drown the dolphins. The dams divide the remaining individuals into smaller, isolated populations (*5*). This habitat fragmentation is stressful to the species and reduces genetic variation, threatening the Mekong River subpopulation with a demographic collapse that could lead to extinction (*6*).

The extinction of local freshwater populations limits the conservation strategies available to protect the remaining populations (*7*, *8*). Therefore, the governments of Cambodia, Indonesia, and Myanmar must act immediately to implement the UN Environment Programme's Convention on Migratory Species Action Plan for the Conservation of Freshwater Populations of Irrawaddy Dolphins to designate protected areas where gillnet fishing is banned (*9*). Assessments of the species' status should use satellite telemetry to map its home range. Local fishermen outside designated refuges in all three river subpopulations should use acoustical deterrents and reflective nets to reduce dolphin bycatch (*10*, *11*).

Christian Sonne[1,2]*, Changlei Xia[3], Su Shiung Lam[4,5]
[1]Faculty of Technological Sciences, Department of Ecoscience, Aarhus University, DK-4000 Roskilde, Denmark. [2]Sustainability Cluster, School of Engineering, University of Petroleum & Energy Studies, Dehradun, Uttarakhand 248007, India. [3]Jiangsu Co-Innovation Center of Efficient Processing and Utilization of Forest Resources, International Innovation Center for Forest Chemicals and Materials, College of Materials Science and Engineering, Nanjing Forestry University, Nanjing, Jiangsu 210037, China. [4]Higher Institution Centre of Excellence, Institute of Tropical Aquaculture and Fisheries, Universiti Malaysia Terengganu, 21030 Kuala Nerus, Terengganu, Malaysia. [5]Young Scientists Network, Top Research Scientists Malaysia, Academy of Sciences, Malaysia, 50480 Kuala Lumpur, Malaysia.
*Corresponding author. Email: cs@ecos.au.dk

REFERENCES AND NOTES

1. IUCN–SSC Cetacean Specialist Group, "Mekong River Irrawaddy dolphins" (2021); https://iucn-csg.org/mekong-dolphins/.
2. C. Cowan, "Death of last river dolphin in Laos rings alarm bells for Mekong population," Mongabay (2022).
3. World Wildlife Fund, "Irrawaddy dolphins functionally extinct in Laos: WWF" (2016).
4. G. Minton *et al.*, "*Orcaella brevirostris* (errata version published in 2018)," IUCN Red List of Threatened Species (2017); www.iucnredlist.org/species/15419/123790805.
5. R. L. Brownell Jr. *et al.*, *Science* **355**, 805 (2017).
6. N. Krützen *et al.*, *PLOS One* **13**, e0189200 (2018).
7. I. Beasley *et al.*, *Mar. Mamm. Sci.* **29**, E226 (2013).
8. S. Caballero *et al.*, *Mar. Mamm. Sci.* **35**, 300 (2019).
9. Convention on the Conservation of Migratory Species of Wild Animals, "Proposal for a concerted action for the Irrawaddy dolphin (*Orcaella brevirostris*)" (2019); www.cms.int/en/document/proposal-concerted-action-irrawaddy-dolphin-orcaella-brevirostris.
10. R. A. Castelein *et al.*, *Aquat. Mamm.* **43**, 233 (2017).
11. S. Sveegaard *et al.*, *Mar. Mamm. Sci.* **27**, 230 (2011).

10.1126/science.abq5774

NEWS FROM Science | AAAS

Subscribe to **News from Science** for unlimited access to authoritative, up-to-the-minute news on research and science policy.

bit.ly/NewsFromScience

TRAVELS FOR AAAS MEMBERS AND FRIENDS
We invite you to join us!

Mt. Rushmore & the Black Hills!
Sept 24-Oct 1, 2022

Discover the historic and natural heritage of this remarkable outlier of the Rocky Mountains with an excellent local naturalist, including Mt. Rushmore and the Buffalo Roundup in Custer State Park!
$3,895 pp + air.

Hawaiian Islands
November 6 - 14, 2022

Lunar Eclipse
Nov. 8, 2022

Explore Hawaii Volcano National Park, including the Total Lunar Eclipse Nov. 8th, and see astronomical facilities which generate an enormous amount of information about our solar system.
$5,495 pp + air.

For a detailed brochure, please call (800) 252-4910
All prices are per person twin share + air

BETCHART EXPEDITIONS Inc.
17050 Montebello Rd
Cupertino, California 95014
Email: AAASInfo@betchartexpeditions.com
www.betchartexpeditions.com

RESEARCH

IN *SCIENCE* JOURNALS

Edited by Michael Funk

MOLECULAR EVOLUTION

Proteins adrift in a sea of mutations

In two related proteins, one might expect the same mutation to have the same effect, but whether this is true greatly depends on context. Looking at nine ancestral reconstructions of a DNA-binding domain, Park *et al*. evaluated the effects of 275 substitutions at predicted evolutionary steps. The effects of mutations were highly contingent on a dense network of epistatic interactions. There were mutations with both short and long memory length, but the average rate of epistatic change was generally constant. The landscape of potential and actual interactions is thus constantly shifting at a rate that can be known, but the direction of the change is contingent on evolutionary history and becomes unpredictable after a time. —MAF *Science*, abn6895, this issue p. 823

Artist's representation of the changing effects of mutations during long-term protein evolution

SUPERCONDUCTIVITY

Changing the balance of orders with light

Charge-density wave (CDW) order, the spatial modulation of electronic density, is known to compete with superconductivity in copper oxide superconductors. This understanding comes largely from equilibrium experiments, and the dynamics of the interplay of these orders are less explored. Wandel *et al*. used ultrafast laser pulses to quickly quench superconductivity in samples of the $YBa_2Cu_3O_{6+x}$ superconductor, which temporarily enhanced the CDW order. The process increased the correlation length of the CDW order, suggesting that superconductivity stabilizes CDW defects that are removed by suppressing superconductivity. —JS

Science, abd7213, this issue p. 860

PLANT SCIENCE

Extracellular processing raises alarm

Plants that lack defensive responses to given microbial pathogens can fail miserably, as the potato plant did when faced with the oomycete pathogen *Phytophthora infestans*, the cause of the potato blight that contributed to famines in the mid-19th century. Kato *et al*. show how the small mustard plant *Arabidopsis* defends against this same oomycete. A sphingolipid from the oomycete's cell membrane is cleaved by a ceramidase that the plant puts out into the apoplast. One of the cleavage products is a branched sphingoid base that is then recognized by a lectin receptor–like kinase on the plant cell surface, kicking off the plant's immune responses. Without the apoplastic ceramidase or the cell surface lectin, the plant's ability to defend against this oomycete pathogen is compromised. —PJH

Science, abn0650, this issue p. 857

WOUND HEALING

Modifying mechanotransduction

Split thickness skin grafting (STSG) is used to treat deep burns and other traumatic skin injuries, but the method is complicated by hypertrophic scar formation, contractures, and potential loss of biomechanical function. Chen *et al.* developed a porcine model of STSG and, through single-cell RNA sequencing, identified up-regulation of mechanotransduction signaling pathways in the healing grafts. Applying a hydrogel containing a focal adhesion kinase (FAK) inhibitor to the grafts to disrupt mechanotransduction improved healing and reduced contracture and scar formation, with anti-inflammatory effects in the acute setting and pro-regenerative effects at later time points. These findings suggest that FAK inhibition could be beneficial for the treatment of injuries requiring STSG. —MN

Sci. Transl. Med. **14**, eabj9152 (2022).

IMAGE: YOUNGDAE PARK

CELL DEATH

A basic way to activate necroptosis

Cell death by necroptosis canonically involves activation of the kinase RIPK3 by the upstream kinase RIPK1, leading to plasma membrane rupture by the RIPK3 effector MLKL. Zhang *et al.* found that osmotic stress directly activated RIPK3 and stimulated necroptosis in a manner that required MLKL but not RIPK1. Osmotic stress increased intracellular pH through the Na^+/H^+ exchanger SLC9A1, and RIPK3 was activated in cells with intracellular pH set at basic, nonphysiological values. Thus, induction of necroptosis by osmotic stress bypasses the activation of RIPK3 by RIPK1. —WW

Sci. Signal. **15**, eabn5881 (2022).

KINETOCHORE

A tight grip

Kinetochores are large, multiprotein complexes responsible for the attachment of chromosomes to the mitotic spindle, helping cells to segregate their DNA into two daughter cells. However, how kinetochores establish a robust attachment between chromosomes and the mitotic spindle has been unclear. Yatskevich *et al.* determined a cryo–electron microscopy structure of the human inner kinetochore bound to centromeric chromatin, revealing that these large macromolecular machines tightly grip and encircle the linker DNA emerging from the specialized centromeric CENP-A nucleosome. This study provides molecular details of how kinetochores can form robust, load-bearing attachments that can withstand chromosome congression and segregation forces. —DJ

Science, abn3810, this issue p. 844

Cryo–electron microscopy structure revealing how kinetochores interact with DNA and nucleosomes in the centromere

CREDITS (LEFT TO RIGHT): IMAGE: YATSKEVICH *ET AL.*; NUCLEUS MEDICAL MEDIA INC./ALAMY STOCK PHOTO

GEOPHYSICS

Relying on repeaters

Underwater optical cables can be used to monitor seismic disturbances and ocean currents, but the signal tends to be integrated over the entire length of the cable, which can be thousands of kilometers long. Marra *et al*. were able to isolate individual segments of a 5800-kilometer-long cable for seafloor monitoring. Because undersea cables have repeaters every 90 kilometers, these segments could each be used as vibrational sensors when coupled with a laser source. This approach allowed the authors to better constrain the location of an earthquake through triangulation, thus offering a method for much better spatial resolution for undersea monitoring. —BG

Science, abo1939, this issue p. 874

CELL BIOLOGY

Splitting cell sisters

During cell division, sister cells generally break apart so that they can function as separate entities. However, some specialized cells avoid the abscission step and remain intimately connected through cytoplasmic bridges, as seen with germline cysts. Mathieu *et al*. found that mutating the *Usp8* gene was sufficient to transform incomplete divisions into complete divisions, and, conversely, overexpressing USP8 in *Drosophila* germline stem cells was sufficient to create ectopic cytoplasmic bridges with their daughter cells. USP8 participated by deubiquitinating target ESCRT-III proteins to switch between incomplete and complete cell divisions. —BAP

Science, abg2653, this issue p. 818

IN OTHER JOURNALS

Edited by **Caroline Ash** *and* **Jesse Smith**

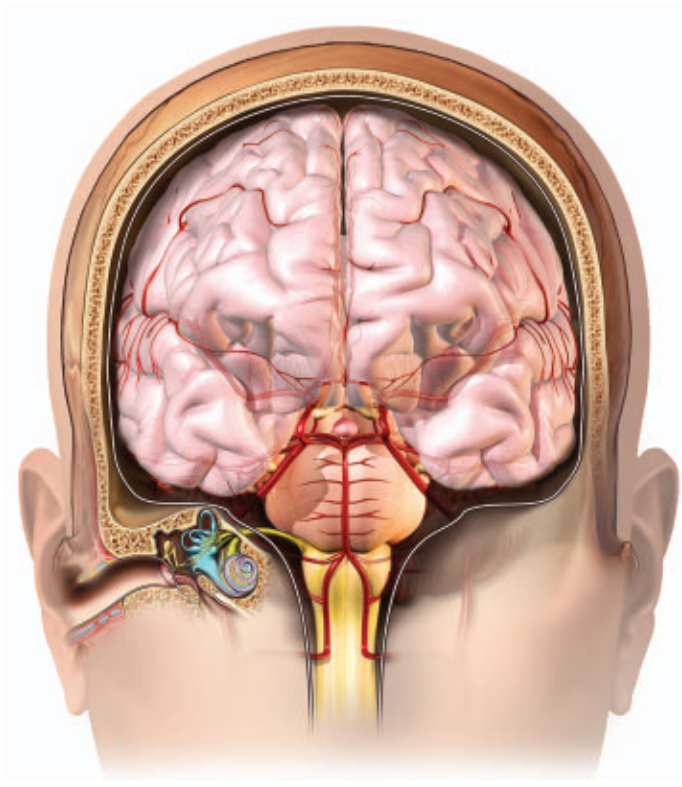

NEUROSCIENCE

Feedback shapes cochlear activity

The dorsal cochlear nucleus (DCN) of the brainstem is a crucial point in the auditory pathway where sensory sharpening, modulation, and gating take place. Descending inputs from higher-order areas of the auditory system project back to auditory pathway nodes, potentially providing attentional and contextual information. The inferior colliculus (IC) in particular sends signals back to the DCN. Balmer and Trussell identified the cell types across the entire DCN that receive input from IC and tested their postsynaptic responses. Granule cells, unipolar brush cells, and Golgi cells received direct, glutamatergic input. Numerous other cell types also processed this input, suggesting that the IC is a strong source of top-down control of the first auditory processing region in the brain that may sharpen tuning and improve auditory feature detection. —PRS *J. Neurosci.* **42**, 3381 (2022).

The inferior colliculus region in the brain contains cell types involved in feedback for fine-tuning hearing.

CELL BIOLOGY

Lipid-driven lysosome repair

Damaged lysosomes threaten cell viability if their contents leak into the cytosol. ESCRT machinery can repair damaged lysosomes, which are particularly vulnerable to injuries. Niekamp *et al.* uncovered an ESCRT-independent, sphingomyelin (SM)–based lysosomal repair pathway. Perturbations in lysosomal or plasma membrane integrity were tightly coupled to a rapid, calcium-activated scrambling of SM across the bilayer. Live-cell imaging revealed a critical role for SM in the recovery of lysosomes from acute, potentially lethal damage. SM was not required for ESCRT recruitment to damaged lysosomes. Instead, conversion of SM by neutral SMases on

PLANT ECOLOGY

Letting the needle drop

As environmental stresses such as drought become more frequent, physiological and morphological traits can provide clues as to how different species will respond. Song *et al*. examined variation in leaf and stem traits among 28 conifer species (grown in a common garden experiment) to identify how they relate to trees' drought resilience. The authors found a trade-off in stem traits between hydraulic efficiency and wood cavitation resistance (a "hydraulics spectrum") and a continuum in leaf traits from tough and long-lived to acquisitive (a leaf economics spectrum). Species from warmer climates had more acquisitive traits and greater resilience to drought. Long-lived leaves (needles or scales) signaled lower drought recovery because these species were less able to grow new leaves and adjust to changing conditions. —BEL

New Phytol. 10.1111/nph.18177 (2022).

Drought is particularly harmful to trees with long-lived leaves, such as these spruce trees, because these species have poor capacity for leaf regrowth.

PHOTO: INA FASSBENDER/AFP/GETTY IMAGES

the cytosolic surface of injured lysosomes promoted their repair. Thus, calcium-activated SM scrambling and turnover can clear minor lesions from the lysosome-limiting membrane and prevent lysosome damage–induced cell death. —SMH

Nat. Commun. **13**, 1875 (2022).

HUMAN GENETICS

Cleaning up mitochondria

Although most genetic diseases in humans are caused by alterations in nuclear DNA, some are caused by mutations in mitochondrial DNA. Because the maternal genome is inherited directly from the mother, assisted reproductive technology to help patients with mitochondrial genetic disorders involves transferring the nucleus from the mother's oocyte into a donor oocyte with healthy mitochondria. Unfortunately, the nucleus transferred through this procedure generally includes some of the patient's mitochondria, which carry the disease mutation and can gradually proliferate and cause disease recurrence in subsequent generations. A method developed by Fan *et al*. involves tagging the patient's mitochondria with an autophagy receptor before nuclear transfer, forcing the resulting oocytes to selectively destroy the mitochondria carrying the disease-causing mutation. —YN

Nat. Biomed. Eng. **6**, 339 (2022).

STRUCTURAL BIOLOGY

Snapshots of cofactor chemistry

One of the key functions of enzymes and their associated cofactors is controlling how electrons and protons are delivered during oxidation-reduction reactions. Maestre-Reyna *et al.* used serial x-ray crystallography to investigate light-driven electron- and proton-transfer steps in a flavoenzyme involved in DNA repair and observed structural changes in the flavin cofactor after light-induced electron transfer. A redox-sensitive triad of residues facilitated proton transfer from a proximal arginine residue to the single-electron reduced flavin. These snapshots reveal an uncommon mechanism of photoreduction and set the stage for understanding the photolyase chemistry that these enzymes perform. —MAF

Nat. Chem. 10.1038/s41557-022-00922-3 (2022).

STAR FORMATION

Searching for more Herbig stars

Herbig stars are objects between two and eight solar masses that are in the final stages of formation by accreting material shortly before reaching the stellar main sequence. Vioque *et al.* used optical spectroscopy to identify 128 new Herbig stars, increasing the total number known by more than 50%. By studying the emission lines in this expanded sample, they identified a change in the accretion properties at around four solar masses. This might be due to a change in the accretion mechanism, but other explanations are possible. The expanded sample of spectroscopically observed Herbig stars will aid studies of this short-lived and poorly understood phase of stellar evolution. —KTS

Astrophys. J. 10.3847/1538-4357/ac5c46 (2022).

MECHANOCHEMISTRY

Pull-apart clusters

Icosahedral carboranes are molecular polyhedra containing two carbon atoms and 10 boron atoms, each capped by hydrogen. For the most part, their rigid stability has taken center stage in applications. Sha *et al.* report that the *ortho* isomer of this class of clusters is a mechanophore: Embedded in a methylacrylate polymer and exposed to shear forces during sonication, the cage breaks apart. Nuclear magnetic resonance and trapping studies are consistent with homolytic bond cleavage. By contrast, the *meta* isomer remains stable in similar circumstances. —JSY

Angew. Chem. Int. Ed. 10.1002/anie.202203169 (2022).

ALSO IN *SCIENCE* JOURNALS

Edited by **Michael Funk**

MICROTUBULES

Trimming the cell's skeleton

An essential part of a cell's backbone is a dynamic network of microtubules that helps them move, keep their shape, and transport cargo between different compartments. To achieve different cellular functions, microtubules are flagged by posttranslational modifications. Detyrosination of α-tubulin is such an alteration, during which α-tubulin's terminal tyrosine is cleaved off. Abnormal detyrosination levels are linked to pathological conditions. Landskron *et al*. describe the enzyme MATCAP as a microtubule-binding protease that can detyrosinate α-tubulin. MATCAP, together with the previously identified detyrosinating vasohibins, is important for normal brain development and function. —SMH

Science, abn6020, this issue p. 815

TOPOLOGICAL MATTER

Ubiquitous topology

Topologically nontrivial materials were once thought to be the exception rather than the rule. More recently, high-throughput computations have shown that many more materials are topological than was initially thought. Vergniory *et al*. expanded this approach to include all processable entries in the Inorganic Crystal Structure Database and studied the materials' band structure both at and away from Fermi energy. The researchers found that almost 88% of these materials had at least one topological band. —JS

Science, abg9094, this issue p. 816

NEURODEVELOPMENT

Competitive migration steers interneurons

During brain development, both interneurons and oligodendrocyte precursor cells travel tangentially from their birthplace to the location where they will function. Lepiemme *et al*. looked for interactions during the migratory phase of mouse brain development. Although born in the same regions and destined to be intertwined in the cortex, nterneurons and oligodendrocyte precursor cells differed in how they got there. Oligodendrocyte precursor cells tended to track along blood vessels, whereas interneurons migrated in collectively organized streams. Imaging showed that oligodendrocyte precursor cells drove migrating interneurons away from the blood vessels. Left to fend for themselves, the interneurons organized in migratory streams. —PJH

Science, abn6204, this issue p. 817

NEUROSCIENCE

Is the internet addictive?

There is increasing awareness that certain applications on the internet can elicit addictive behaviors in some people. Problematic gaming and gambling are now recognized as disorders, but the same may also apply to shopping, social network usage, and pornography. In a Perspective, Brand discusses whether there are parallels between addictive internet usage and the path to substance addiction. By examining the neurobiological and psychological mechanisms that lead to addiction to internet applications, it may be possible to understand what makes some people vulnerable to addiction, what the causes are, and whether there are specific mechanisms involved in internet addiction that are different from other addictions. Given the current climate of social distancing and the attendant increased internet usage, it is important to understand how problematic internet addiction can be prevented. —GKA

Science, abn4189, this issue p. 798

STRUCTURAL BIOLOGY

Big complexes from single-celled eukaryote

Mitochondria use a series of membrane-embedded enzymes to transform chemical energy first into an electrochemical gradient and then into ATP. The series of chemical steps that take place are conserved in aerobic organisms, but there is considerable structural divergence in different lineages. Working with extracted mitochondrial membranes, Zhou *et al*. determined structures of mitochondrial electron transfer chain complexes from a model ciliate (see the Perspective by Huynen and Elurbe). Complex I and a dimer of complex III form a supercomplex as in many other eukaryotes, but both have important fundamental differences in architecture and functional apparatus. Complex IV is massive relative to previously known structures, with more than half of the mass composed of components not seen in homologous structures, including mitochondrial carrier proteins and a translocase that may be involved in assembly or may be a relic of such components. —MAF

Science, abn7747, this issue p. 831; see also abq0368, p. 794

FOREST ECOLOGY

Benefits of forest restoration

Reforestation is promoted globally as one way to mitigate climate change through the storage of carbon in woody growth and ecosystem services such as control of soil erosion and management of water supplies. Hua *et al*. assessed the relative performance of plantation and native forest in achieving these goals (see the Perspective by Gurevitch). Synthesizing data from the world's major forest biomes, the authors found that native forests consistently delivered better performance than plantations in the provision of the three major ecosystem services, with additional benefits for biodiversity. The discrepancy was particularly evident in warmer and drier regions. These findings show that the benefits of reforestation will be best achieved through the restoration of native forests rather than extensive plantation programs. —AMS

Science, abl4649, this issue p. 839; see also abp8463, p. 792

BIOCATALYSIS

Adapting iron enzymes for azidation

Nonheme iron enzymes typically activate molecular oxygen to initiate oxidation of a substrate or atom transfer through radical mechanisms. Rui *et al*. used directed evolution to encourage a nonheme iron oxidase to perform enantioselective azide transfer using an aryl *N*-fluoroamide as both substrate and radical initiator. The resulting azides, installed on an ortho alkyl group, may be useful starting points for synthesis or handles for bioorthogonal coupling. —MAF

Science, abj2830, this issue p. 869

FOSSIL RECORD

Ghosts of the past

The marine geological records of some past global warming events contain relatively few nannoplankton fossils, the lack which some interpret as being evidence of the impact of ocean acidification and/or related environmental factors on biocalcification. Slater *et al*. present a global record of imprint, or "ghost," nannofossils throughout several of those intervals during the Jurassic and Cretaceous periods (see the Perspective by Henderiks). This finding implies that a literal interpretation of the fossil record can be misleading, and demonstrates

that nannoplankton were more resilient to past warming events than traditional fossil evidence would suggest. —HJS

Science, abm7330, this issue p. 853; see also abp9754, p. 795

IMMUNOLOGY

How T cells respond to antigens

Although they are important tools in immunotherapy, we still have an incomplete understanding of how T cells respond to antigens in different temporal and molecular contexts. Achar *et al*. combined robotic sampling of mouse and human T cell responses over time with machine learning and modeling to gain insights into how T cells process information derived from the particular antigens to which they are exposed (see the Perspective by Nourmohammad). The analysis showed that patterns of cytokine release carried information about the type of antigen encountered and distinguished six distinct cellular responses rather than the three types usually recognized. Such understanding is likely to enhance strategies for immunotherapies that rely on altered and designed T cell responses. —LBR

Science, abl5311, this issue p. 880; see also abq1679, p. 796

FORESTRY

Diversity boosts plantation biomass

Across experimental and natural systems, more diverse plant communities often have higher primary productivity. This effect can be caused by complementarity between different species, which can more effectively use resources together, or by a higher likelihood of more productive species being present. Feng *et al*. used data from 255 sites to test whether forest plantations with multiple species have greater productivity than monocultures (see the Perspective by Gurevitch). They found that multispecies plantings, on average, had taller and thicker trees and greater aboveground biomass accumulation than monocultures. Complementary between species was the primary driver of this effect, with greatest benefits from pairing species with different traits. —BEL

Science, abm6363, this issue p. 865 see also abp8463, p. 792

MUCOSAL IMMUNOLOGY

BMP puts the brakes on tuft cells

Intestinal parasite infections or allergic reactions promote interleukin-13 (IL-13)–induced differentiation of tuft cells as one manifestation of type 2 immunity in the gut. Using organoid cultures of intestinal epithelial cells, Lindholm *et al.* investigated how the lymphocyte cytokines IL-13, IL-22, and interferon-γ regulate the signaling pathways that influence epithelial differentiation. Although tuft cell IL-25 promoted the expansion of IL-13–producing type 2 innate lymphoid cells in a feedforward loop, the resulting IL-13 also induced ligands of the bone morphogenetic protein (BMP) signaling pathway. BMP agonists acted on stem cells to prevent runaway tuft cell expansion by limiting the expression of Sox4, a transcription factor required for tuft cell differentiation. These findings provide new molecular insights into how intestinal epithelial differentiation is carefully choreographed in response to a diverse array of cytokine signals. —IRW

Sci. Immunol. **7**, eabl6543 (2022).

LIFE SCIENCES

Nano-cocoons for targeted RNA editing

Within the collection of CRISPR-Cas enzymes, Cas13a is an RNA-guided, RNA-targeting CRISPR effector that is able to recognize and cleave target RNA to regulate gene expression at the transcriptional level. However, Cas13a can induce collateral cleavage of nontargeted RNAs, suggesting the need for systems to target activity of Cas13a for use in therapeutic applications. Fan *et al*. designed targeted, multifunctional "nano-cocoons" that delivered Cas13a and its guide sequence within pH-responsive nanocapsules. Upon release and activation, Cas13a cleaved RNA nanosponges that were also contained within the nano-cocoons to release chemotherapy entrapped within the nanosponges. These hierarchical nano-cocoons sequentially released an RNA-editing system and chemotherapy, which together inhibited glioblastoma cell proliferation in vitro and in vivo. —AKP

Sci. Adv. 10.1126/sciadv.abn7382 (2022).

RESEARCH ARTICLE SUMMARY

MICROTUBULES

Posttranslational modification of microtubules by the MATCAP detyrosinase

Lisa Landskron, Jitske Bak, Athanassios Adamopoulos, Konstantina Kaplani, Maria Moraiti, Lisa G. van den Hengel, Ji-Ying Song, Onno B. Bleijerveld, Joppe Nieuwenhuis, Tatjana Heidebrecht, Linda Henneman, Marie-Jo Moutin, Marin Barisic, Stavros Taraviras, Anastassis Perrakis*, Thijn R. Brummelkamp*

INTRODUCTION: Microtubules are an essential multifunctional component of the eukaryotic cytoskeleton and control cell division, shape, and migration by generating force and regulating trafficking of cellular cargo. Although all microtubules are built of α- and β-tubulin dimers, they differ in their chemical composition owing to the existence of multiple tubulin isotypes and posttranslational modifications. An abundant modification is the removal of the C-terminal tyrosine of α-tubulin, called detyrosination. This occurs mostly on stable microtubules and can be reversed by the tubulin tyrosine ligase (TTL), which acts on disassembled tubulin dimers. Aberrant detyrosination is linked to mitotic errors, cardiac failure, and neurological defects, whereas retyrosination is essential for life. Although described decades ago, our understanding of the mechanism and relevance of tubulin detyrosination remains incomplete.

RATIONALE: Recently, vasohibins (VASH1 and VASH2), in complex with their cofactor small vasohibin-binding protein (SVBP), have been identified as detyrosinating enzymes. However, inactivation of vasohibins does not eliminate detyrosination in most cell types, suggesting the presence of one or more additional detyrosinating enzymes. Whereas other tubulin modifications are carried out by large protein families of multiple related enzymes, there are no proteases that closely resemble vasohibins. To identify the remaining detyrosinating enzyme(s), we ablated VASH1 and VASH2 in haploid human HAP1 cells and used genome-wide mutagenesis using tubulin tyrosination and detyrosination as readouts. The sensitivity of these genetic screens was enhanced by treatment with paclitaxel or removal of TTL, either to boost tubulin detyrosination or to make tyrosine cleavage irreversible.

RESULTS: The genetic screens identified KIAA0895L, an unstudied protein without apparent protease features, as a remaining detyrosinase. Removal of KIAA0895L in combination with VASH1 and VASH2 resulted in undetectable levels of tubulin detyrosination in cultured cells. A crystal structure of KIAA0895L revealed an atypical metalloprotease fold that belongs to the gluzincins clan [including, for example, the severe acute respiratory syndrome coronavirus 2 (SARS-CoV-2) receptor angiotensin-converting enzyme 2 (ACE2)]. KIAA0895L had escaped annotation as a protease owing to a degenerate signature motif (HExxxH instead of HExxH) that interrupts the active site–containing helix without substantially affecting the integrity of the catalytic site arrangement. We renamed the protein MATCAP (for microtubule-associated tyrosine carboxypeptidase). MATCAP and the vasohibins have adopted fundamentally different catalytic strategies (metalloprotease versus cysteine protease) to target the α-tubulin tail. In addition, whereas vasohibins cleavage relies on the second-last glutamate of the EEY terminal motif and only tolerates the chemically related phenylalanine in place of the α-tubulin terminal tyrosine, MATCAP is promiscuous as to the nature of the terminal residue and shows a dependence on α-tubulin tail residues also located further upstream for substrate recognition. A cryo-EM structure of catalytically inactive MATCAP bound to fully tyrosinated microtubules indicated that MATCAP recognizes tubulin dimers in the same protofilament, whereas the VASH1-SVBP complex sits in between neighboring microtubule protofilaments. Unexpectedly, genetic ablation of MATCAP together with SVBP in mice led to viable offspring with undetectable levels of detyrosination. Despite their viability, these mice displayed morphological brain defects accompanied by proliferation defects during neurogenesis and displayed abnormal behavior.

CONCLUSION: Our work shows that tubulin detyrosination in mammals involves two evolutionary distinct enzyme families: the vasohibin cysteine proteases in combination with their peptide cofactor SVBP and the atypical metalloprotease MATCAP identified here. The distinct evolutionary origin and structural architectures of the vasohibins and MATCAP raise the intriguing possibility that certain microtubule subpopulations could be differentially targeted by each detyrosinase. In mice, detyrosination by these enzymes was indispensable for correct brain development, which implies that defects in this posttranslational tubulin modification could contribute to cognitive abnormalities. ■

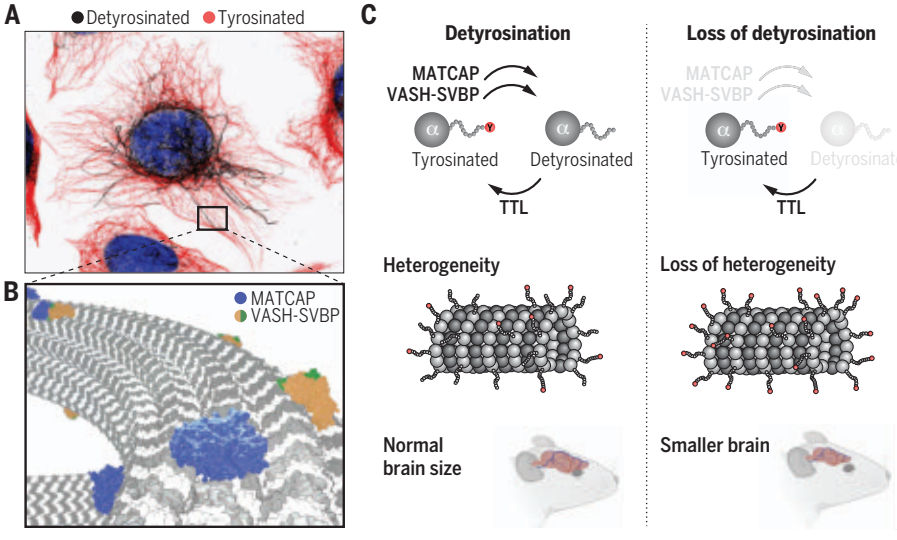

Tubulin detyrosination is carried out by the distinct MATCAP and vasohibin detyrosinases. (**A**) The cytoskeleton of (U2OS) cells consists of detyrosinated and tyrosinated microtubules. (**B**) MATCAP (blue) and VASH1-SVBP (orange and green) detyrosinate microtubules. [Drawn in Blender using the macro Geometry Nodes Microtubule] (**C**) Impaired detyrosination leads to tyrosinated microtubules and a reduction in brain volume. Illustration was created with BioRender.com.

The list of author affiliations is available in the full article online.
*Corresponding author. Email: a.perrakis@nki.nl (A.P.); t.brummelkamp@nki.nl (T.R.B.)
Cite this artice as L. Landskron *et al.*, *Science* **376**, eabn6020 (2022). DOI: 10.1126/science.abn6020

READ THE FULL ARTICLE AT
https://doi.org/10.1126/science.abn6020

RESEARCH ARTICLE

MICROTUBULES

Posttranslational modification of microtubules by the MATCAP detyrosinase

Lisa Landskron[1], Jitske Bak[1], Athanassios Adamopoulos[1], Konstantina Kaplani[2], Maria Moraiti[1], Lisa G. van den Hengel[1], Ji-Ying Song[3], Onno B. Bleijerveld[4], Joppe Nieuwenhuis[5], Tatjana Heidebrecht[1], Linda Henneman[6], Marie-Jo Moutin[7], Marin Barisic[8,9], Stavros Taraviras[2], Anastassis Perrakis[1]*, Thijn R. Brummelkamp[1]*

The detyrosination-tyrosination cycle involves the removal and religation of the C-terminal tyrosine of α-tubulin and is implicated in cognitive, cardiac, and mitotic defects. The vasohibin–small vasohibin-binding protein (SVBP) complex underlies much, but not all, detyrosination. We used haploid genetic screens to identify an unannotated protein, microtubule associated tyrosine carboxypeptidase (MATCAP), as a remaining detyrosinating enzyme. X-ray crystallography and cryo–electron microscopy structures established MATCAP's cleaving mechanism, substrate specificity, and microtubule recognition. Paradoxically, whereas abrogation of tyrosine religation is lethal in mice, codeletion of MATCAP and SVBP is not. Although viable, defective detyrosination caused microcephaly, associated with proliferative defects during neurogenesis, and abnormal behavior. Thus, MATCAP is a missing component of the detyrosination-tyrosination cycle, revealing the importance of this modification in brain formation.

Microtubules are composed of polymerized α- and β-tubulin heterodimers and are core components of the cytoskeleton that are essential for cargo trafficking, cellular organization, and force generation. Microtubule heterogeneity is created by multiple α/β tubulin genes (isotypes) in combination with an array of posttranslational modifications that particularly affect the disordered C-terminal tail of α-tubulin (*1*, *2*). Most α-tubulin isotypes are translated with a C-terminal tyrosine, which can be enzymatically removed and religated (*3*, *4*). This dynamic modification cycle has been implicated in cell division (*5*–*8*), neurogenesis (*9*–*11*), and heart failure (*12*–*15*). Detyrosinated tubulin also serves as the sole precursor for the irreversible generation of Δ2-tubulin, which when stimulated through chemotherapeutic agents leads to peripheral neuropathy (*16*). The removal of tyrosine can be catalyzed by the vasohibins (two paralogs, VASH1 and VASH2) in complex with the essential cofactor small vasohibin-binding protein (SVBP) (*10*, *17*) and reversed by the tubulin tyrosine ligase (TTL) (Fig. 1A) (*18*). Loss of VASH-SVBP in cell lines (Fig. 1, B and C) (*17*) or mice (*11*) only partially impairs tubulin detyrosination, indicating the existence of yet-to be discovered enzyme(s), which complicates functional studies on the role of detyrosination.

[1]Oncode Institute, Division of Biochemistry, Netherlands Cancer Institute, 1066CX Amsterdam, Netherlands. [2]Department of Physiology, School of Medicine, University of Patras, 26504 Patras, Greece. [3]Experimental Animal Pathology, Netherlands Cancer Institute, Amsterdam, Netherlands. [4]Proteomics Facility, Netherlands Cancer Institute, 1066CX Amsterdam, Netherlands. [5]Division of Biochemistry, Netherlands Cancer Institute, Plesmanlaan 121, 1066CX Amsterdam, Netherlands. [6]Transgenic Core Facility, Mouse Clinic for Cancer and Aging (MCCA), Netherlands Cancer Institute, 1066CX Amsterdam, Netherlands. [7]Université Grenoble Alpes, INSERM, U1216, CNRS, Grenoble Institut Neurosciences, 38000 Grenoble, France. [8]Cell Division and Cytoskeleton, Danish Cancer Society Research Center (DCRC), 2100 Copenhagen, Denmark. [9]Department of Cellular and Molecular Medicine, Faculty of Health Sciences, University of Copenhagen, Copenhagen, Denmark.
*Corresponding author. Email: a.perrakis@nki.nl (A.P.); t.brummelkamp@nki.nl (T.R.B.)

The tubulin detyrosination-tyrosination cycle is regulated by MATCAP

To identify remaining tubulin carboxypeptidases, we carried out genome-wide mutagenesis screens in human haploid HAP1 cells lacking both vasohibins (Fig. 1D). For the first genetic screen, we treated the cells with the microtubule-stabilizing agent paclitaxel (which increases detyrosination), and we searched for factors that upon gene-trap inactivation reduced tubulin detyrosination (Fig. 1E). In a second genetic screen, we removed TTL using CRISPR/Cas9 in the vasohibin-deficient cells (to make detyrosination irreversible) and used the amount of tyrosinated α-tubulin as readout (Fig. 1F). Combined analysis revealed the unstudied gene *KIAA0895L* as the strongest regulator that diminished detyrosination upon genetrap inactivation in the first screen and stimulated tubulin tyrosination upon inactivation in the second screen (Fig. 1G and fig. S1, A and B). In addition, *KIAA0895L* was also distinguished from most other hits by having no significant effect on 22 phenotypes unrelated to tubulin biology that were previously examined by use of haploid genetic screens (fig. S1C). Because *KIAA0895L* also scored in ΔTTL cells (Fig. 1F), it likely participates in tyrosine removal rather than religation. Thus, KIAA0895L affects tubulin detyrosination, and for reasons described below, we renamed it MATCAP (microtubule-associated tyrosine carboxypeptidase).

As expected, tubulin detyrosination is only moderately decreased upon the loss of both vasohibins (Fig. 1H). Combined ablation of MATCAP and vasohibins resulted in undetectable levels of detyrosination in different cell lines, even in the presence of paclitaxel (Fig. 1H). Furthermore, overexpression of MATCAP in HeLa cells, which normally have low levels of tubulin detyrosination, efficiently stimulated tubulin detyrosination (Fig. 1I). Moreover, expression of MATCAP reestablished tubulin detyrosination in cells in which ΔVASH1 ΔVASH2 ΔMATCAP had been deleted (Fig. 1J). Next, we asked whether the C termini of different α-tubulin isotypes are differentially affected by MATCAP. For that, we fused different tubulin tails to the C terminus of green fluorescent protein (GFP). Coexpression with MATCAP removes the terminal residue of all GFP-fused α-tubulin tails, including those corresponding to tubulin alpha-8 chain (TUBA8) (which possesses a phenylalanine as terminal amino acid) and to TUBA4A (which is encoded without C-terminal tyrosine but can be retyrosinated by TTL) (fig. S2A). Thus, MATCAP acts on the C terminus of α-tubulin and affects detyrosination independently of the known tyrosination and detyrosination enzymes.

MATCAP is a metalloprotease with an atypical zinc-binding motif

Because MATCAP was not annotated as a protease, we expressed and purified both full-length MATCAP and MATCAP without its disordered N-terminal region (MATCAP$^{137\text{-}471}$) (Fig. 2A). Next, we determined a crystal structure of MATCAP$^{137\text{-}471}$ using experimental phasing (Fig. 2B and table S1). The structure reveals that MATCAP belongs to the gluzincin metallopeptidase clan (*19*), which is characterized by a Zinc ion (Zn^{2+}). Consistent with this, EDTA abolished enzymatic activity (Fig. 2C). The metal ion is coordinated by a HExxH motif incorporated in an α-helix and resembles the active site and the fold of the severe acute respiratory syndrome coronavirus 2 (SARS-CoV-2) spike-protein receptor angiotensin-converting enzyme 2 (ACE2) and the anthrax lethal factor (Fig. 2D). The HExxH motif is degenerate in MATCAP (^{280}HExxxH^{285}), which has also been observed in other rare metallo-exopeptidases (*20*, *21*). The extra residue destroys the canonical N_i–O_{i+4} hydrogen bonding helical pattern (formally breaking the α6 helix in two) but forms an active site similar to that of its structural homologs, positioning the

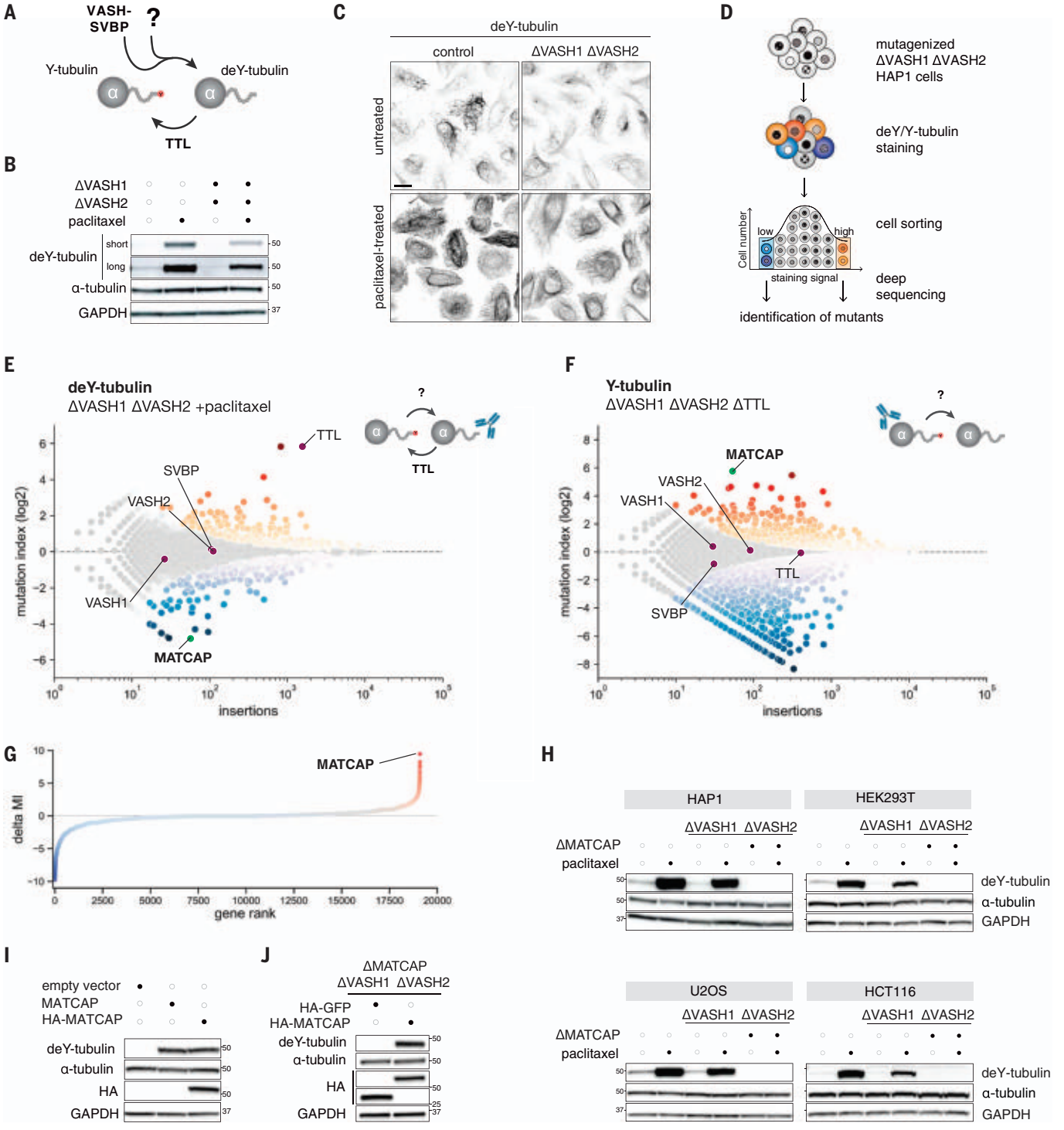

Fig. 1. Haploid genetics identify MATCAP as a regulator of α-tubulin detyrosination. (**A**) Illustration of the tubulin detyrosination cycle. Vasohibins and a yet-unknown enzyme remove the C-terminal residue (tyrosine) from α-tubulin. (**B** and **C**) U2OS cells proficient and deficient for VASH1 and VASH2, with and without paclitaxel treatment, were subjected to (B) immunoblot analysis (short and long exposures are indicated) and (C) immunostaining for detyrosinated α-tubulin. Scale bar, 20 μm. (**D**) Schematic representation of a haploid genetic screen. (**E** and **F**) Haploid genetic screens for (E) detyrosinated α-tubulin in HAP1 ΔVASH1 ΔVASH2–deleted cells and (F) tyrosinated α-tubulin in HAP1 ΔVASH1 ΔVASH2 ΔTTL–deleted cells were performed. (The schemes were created with BioRender.com.) The antibody symbol indicates which α-tubulin state was detected as readout for the genetic screen. In the fishtail plot, genes enriched for gene-trap mutations in the population with "high" or "low" antibody staining are colored with orange or blue, respectively [for both, two-sided Fisher's exact test, false discovery rate (FDR) corrected $P \leq 0.05$]. (**G**) For each gene, the difference in mutation index (MI) between the two screens is depicted as delta MI, which is calculated as $MI_{deY\text{-}tubulin\ screen} - MI_{Y\text{-}tubulin\ screen}$. (**H**) Lysates of indicated mutant cell lines analyzed for detyrosinated α-tubulin by immunoblotting. (**I**) Lysates of HeLa H1 cells upon ectopic expression of hemagglutinin (HA)–tagged and untagged MATCAP were subjected to immunoblot analysis. (**J**) Immunoblot analysis of lysates from triple-mutant HAP1 cells (ΔVASH1 ΔVASH2 ΔMATCAP) expressing HA-tagged MATCAP or GFP as control.

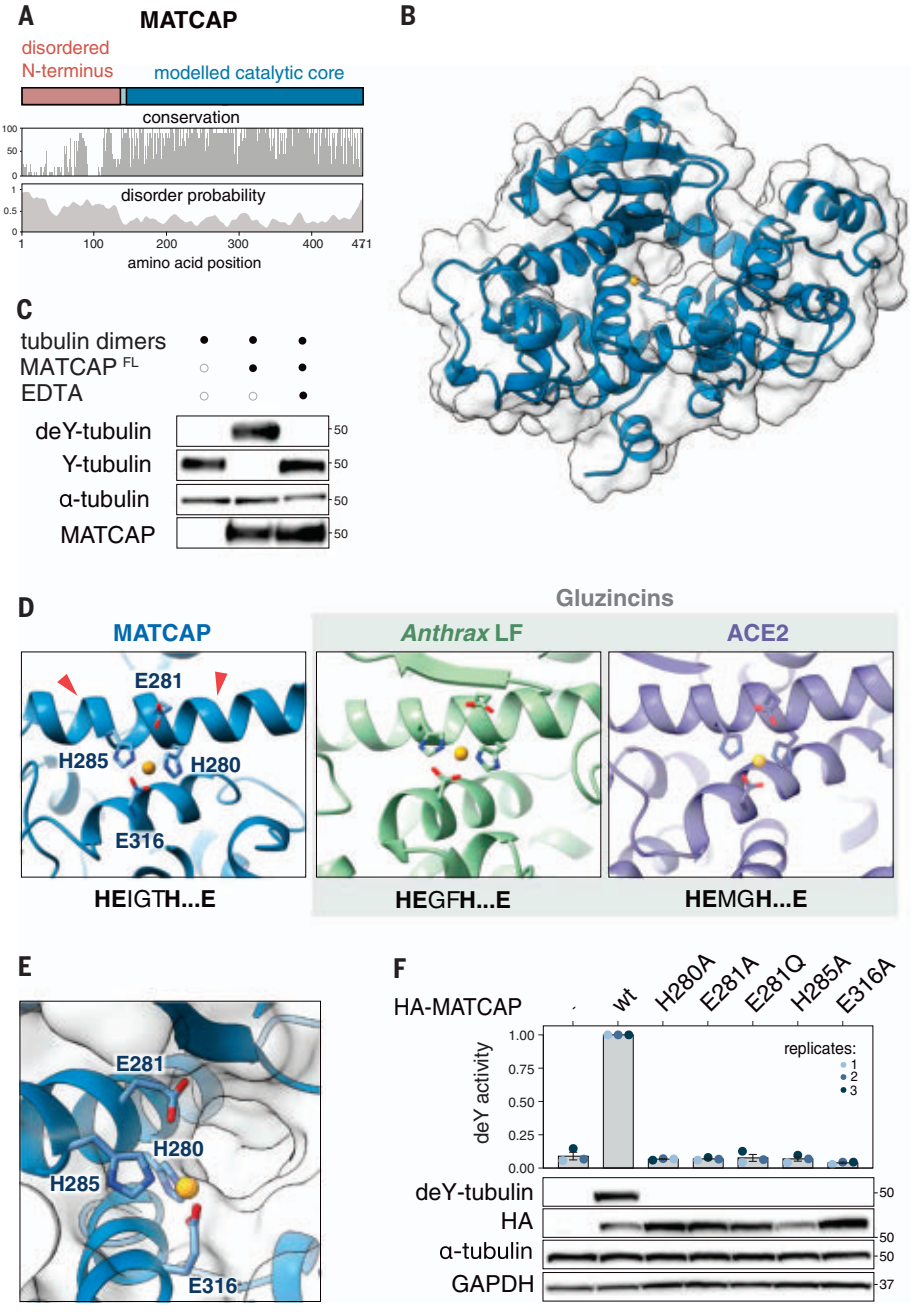

Fig. 2. The metallo-carboxypeptidase MATCAP detyrosinates α-tubulin. (**A**) Schematic representation of MATCAP and its conservation across vertebrates. Amino acid conservation of MATCAP across 39 vertebrate orthologous is shown as analysis of multiply aligned sequences (AMAS) conservation score (calculated in Jalview). The probability of disordered regions as predicted with PrDOS is shown at bottom. (**B**) Ribbon representation of MATCAP (blue) with the overlayed surface (gray). (**C**) Recombinant MATCAP protein was incubated with tubulin heterodimers in the presence or absence of EDTA. Tubulin modifications were analyzed by means of immunoblotting. (**D**) Comparison of MATCAP and two of the related members of the gluzincin clan, highlighting the zinc ion (yellow) and the binding residues. Arrows indicate the two separate α-helices. (**E**) Close-up of the MATCAP active site pocket (**F**) Quantification of immunoblots of lysates from HeLa cells expressing single-point mutants of the active site residues. The detyrosination activity (detyrosinated α-tubulin normalized to α-tubulin) was quantified in three independent experiments (top). Data are shown as mean ± SD. An example immunoblot is shown (bottom).

presumed nucleophile Glu^{281} for catalysis. Because the original crystallization conditions contained EDTA, Zinc ions were not visible. We thus determined a structure of MATCAP in the presence of Zn^{2+} and refined both the apo and the Zn^{2+}-bound structures to 2.1 and 2.5 Å, respectively. The Zinc ion is coordinated by His^{280}, His^{285}, and Glu^{316} (Fig. 2E). The structure of the zinc binding site is well maintained in the apo structure, with the exception of Glu^{316}, which is further away from the zinc ion. As expected, MATCAP activity was metal dependent in vitro (Fig. 2B), and mutating the Glu^{281} nucleophile to glutamine (E281Q) or the zinc-binding residues to alanine abolished activity in cells (Fig. 2F) and in vitro (fig. S2, B and C). The structure predicted with AlphaFold (fig. S2D) (*22*) is similar to both experimental structures. Thus, MATCAP is a peptidase that relies on an atypical catalytic domain for its optimal enzymatic efficiency.

Substrate recognition by MATCAP and VASH1-SVBP

To elucidate how MATCAP recognizes its substrate, the negatively charged glutamate-rich C-terminal α-tubulin tail, we first visualized the electrostatic potential of MATCAP's protein surface (Fig. 3A). Mutation of residues in the positively charged patch close to the catalytic site decreased or abolished the activity of MATCAP (Fig. 3B). Further experimental mutant analysis combined with in silico docking by using HADDOCK (*23*) yielded two plausible models of the α-tubulin tail bound to MATCAP (Fig. 3C and fig. S3, A and B). Further mutagenesis experiments were equally supportive for both docking models (fig. S3, C to F). The C-terminal part of the tail is firmly positioned in a pocket for catalysis by two lysine (389 and 417) and four arginine (334, 373, 376, and 393) residues in both models. According to these models, the tubulin tail could enter the pocket through two routes. In contrast with the MATCAP tail-binding pocket, VASH1-SVBP

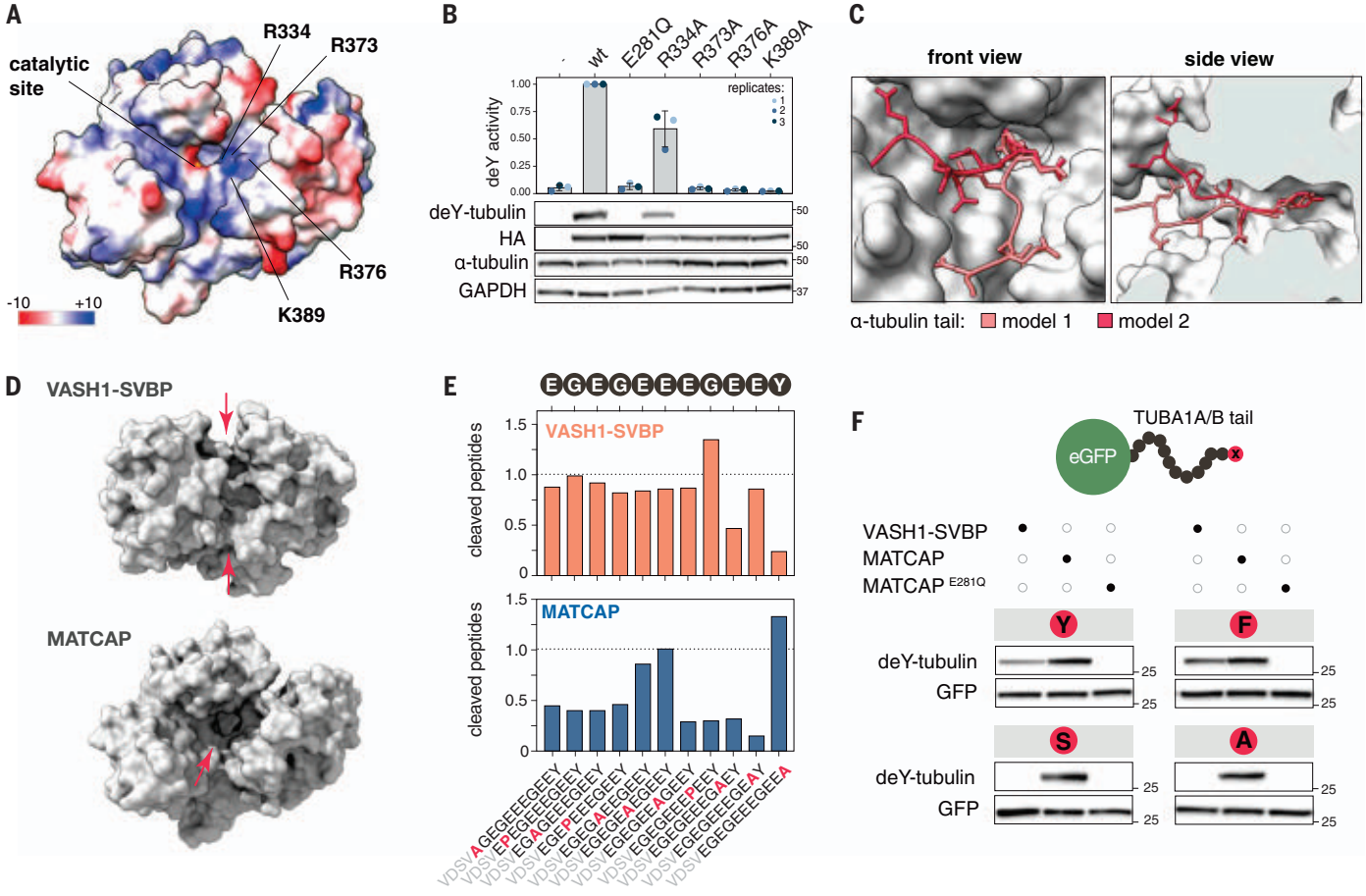

Fig. 3. The substrate binding mode of MATCAP. (**A**) Electrostatic surface potential of MATCAP. Scale bar, −10 to +10 φ. Locations of positively charged residues selected for mutagenesis are indicated. (**B**) Quantification of the activity of indicated MATCAP mutants in Hela cells. Data are shown as mean ± SD; *n* = 3 independent experiments. (**C**) Docking models of the α-tubulin tail (pink and magenta ribbon with side chains) binding to MATCAP (gray) from two different views. (**D**) MATCAP binds α-tubulin in a pocket, while the VASH-SVBP contains an open groove, both indicated with red arrows. (**E**) C-terminal α-tubulin peptides were incubated with either recombinant VASH1-SVBP or MATCAP and analyzed by means of nano–liquid chromatography–mass spectrometry (nanoLC-MS)/MS. Peptide counts were normalized to the wild-type peptide. (**F**) GFP fused to α-tubulin tails with varying terminal amino acids were coexpressed together with the indicated detyrosinating enzymes in HeLa cells.

binds its substrate in an open groove (Fig. 3D and fig. S4A) (*5*, *24*–*28*). Furthermore, VASH1-SVBP engages with the second-last glutamate of the α-tubulin tail, whereas MATCAP forms an extensive network of interactions with many glutamates, and in particular with the last one, positioned before the scissile bond (fig. S4, B and C). Consequently, the two enzymes have different dependencies on the amino acids of the tubulin tail: In contrast to VASH1, MATCAP's activity is affected by most amino acid alterations along the tubulin tail except the terminal residue, in vitro (Fig. 3E and fig. S4, D and E) and in cells (Fig. 3F). Thus, MATCAP removes the terminal residue independently of its amino acid identity and strongly relies on the penultimate residue to be a glutamate for proper substrate cleavage. By contrast, VASH1 largely tolerates amino acid changes in the α-tubulin tail as long as the terminal residue is aromatic and the second-last glutamate is intact (fig. S4, D to F). Thus, the distinct structural architectures of MATCAP and vasohibins represent two convergent solutions for tubulin detyrosination, with different substrate recognition and catalytic modes.

A cryo–electron microscopy structure of MATCAP on microtubules reveals multiple binding interfaces

Consistent with the reported preferential activity of brain detyrosinases on microtubules (*29*–*31*), recombinant MATCAP was more efficient in processing α-tubulin tails on microtubules than on free tubulin dimers (Fig. 4A). Recombinant MATCAP copelletted with microtubules in an ultracentrifugation sedimentation assay in vitro (Fig. 4B). Consistent with this, MATCAP preferentially localized to microtubules in cells, especially when the catalytic nucleophile was mutated (E281Q) (Fig. 4C).

To understand how MATCAP engages with microtubules, we prepared fully tyrosinated microtubules from triple-mutant (ΔVASH1 ΔVASH2 ΔMATCAP) cells and incubated these with recombinant catalytically inactive (E281Q) MATCAP to form a complex on cryo–electron microscopy (cryo-EM) grids. Electron micrographs showed MATCAP-decorated microtubules, further confirmed in two-dimensional (2D) and 3D class averages (Fig. 4, D and E, and fig. S5, A and B). The cryo-EM reconstruction based on particles extracted from microtubules with 14 protofilaments has a nominal resolution of 2.9 Å, with the binding interface being resolved to ~4.5 Å (Fig. 4F and fig. S6). The cryo-EM density allows a clear and distinct placement of atomic models of the tubulin dimer, and of MATCAP (Fig. 4G and fig. S5, C to E), and shows low-resolution density that can be attributed to the α-tubulin tail (Fig. 4F, inset), supporting only one of the computational

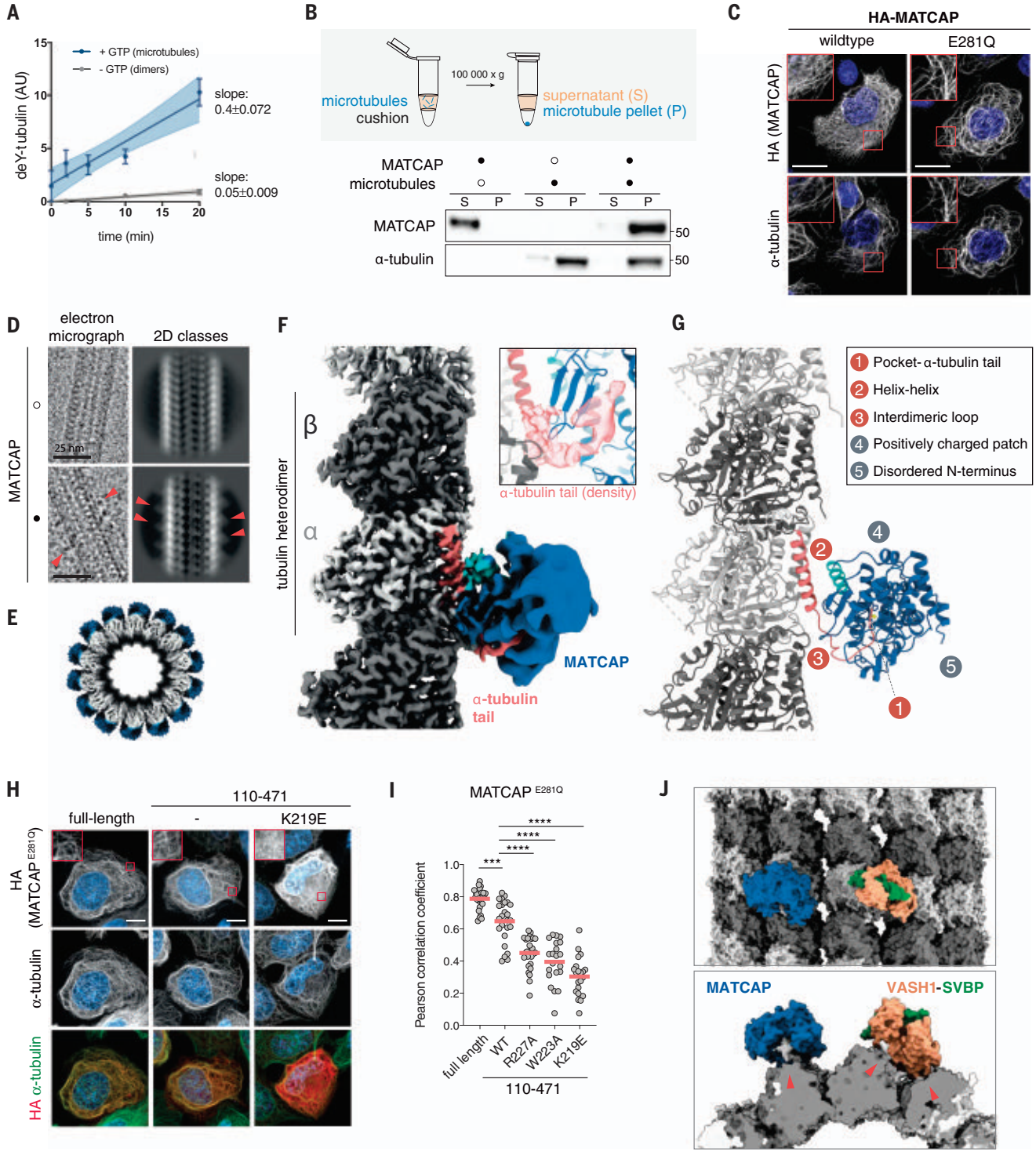

Fig. 4. Binding of MATCAP to microtubules. (**A**) In vitro incubation of wild-type purified MATCAP with HeLa tubulin heterodimers or microtubules for the indicated times. *n* = 5 independent experiments. Data are shown as mean ± SEM, and the 95% confidence interval is shown as blue and gray shades. The levels of deY-tubulin were normalized to α-tubulin levels. (**B**) Cosedimentation assay of full-length MATCAP and paclitaxel-stabilized microtubules by using a glycerol cushion. Pellet (sedimented microtubules) and supernatant (nonsedimented proteins) were subjected to immunoblot analysis. (**C**) Immunostaining of U2OS cells transfected with HA-tagged MATCAP constructs. Scale bar, 20 μm. (**D**) Representative cut-outs of electron micrographs showing microtubules (fig. S5, A and B) and 2D classes of data, with and without MATCAP. Arrows indicate bound MATCAP. (**E**) Cryo-EM density of a microtubule (gray) decorated with MATCAP (blue). (**F**) Cryo-EM map of MATCAP (blue) bound to the α-β-tubulin heterodimer (gray). Density corresponding to the C-terminal end of α-tubulin is in salmon pink; MATCAP density interacting with tubulin is in cyan. The displayed map is shown at isocontour 0.5 and 0.05 for the density belonging to tubulin and MATCAP, respectively, to better visualize the map features at each region. (Inset) Highlight of density that is attributed to the α-tubulin tail. (**G**) Pseudo-atomic model from rigid-body fitting of the MATCAP crystal structure and tubulin (PDB: 7SJ7). The docking

model of the α-tubulin tail (ribbon with the C-terminal tyrosine as ball and stick) is highlighted in the inset and connected to the last residue of the crystal structure with a dashed line. Five interfaces are indicated: interfaces observed from the structure (pink) and contact sites suggested by mutations (gray). (**H**) Immunofluorescent staining of U2OS cells expressing the indicated MATCAP mutants. Scale bar, 10 μm. (**I**) Quantification of the colocalization of MATCAP mutants from immunofluorescent stainings. Data are shown as mean. Significance was calculated as one-way analysis of variance (ANOVA) and Tukey's multiple comparisons test. ****$P < 0.0001$, ***$P < 0.001$. (**J**) Composite molecular model of MATCAP and VASH1-SVBP (PDB: 6WSL) bound to a microtubule. Arrows indicate interactions with the protofilaments.

models for the α-tubulin tail entering the catalytic MATCAP pocket (Fig. 3C).

The cryo-EM structure shows that the binding interface between α-tubulin and MATCAP has three principal constituents: [Fig. 4G, (1)] the α-tubulin tail binding pocket; [Fig. 4G, (2)] an interface between the last helix of α-tubulin and the α-helix$^{218\text{-}232}$ of MATCAP; and [Fig. 4G, (3)] the loop$^{257\text{-}259}$ that contacts an adjacent tubulin dimer along the microtubule protofilament. The structure also points out two "regions of interest": [Fig. 4G, (4)] a positively charged patch at the "backside" of MATCAP, covered by density which could possibly be attributed to binding of the negatively charged β-tubulin tail; and [Fig. 4G, (5)] the positively charged (pI 11.3), proline-rich N terminus of MATCAP, for which there is no clear experimental density.

To study the interfaces, we designed mutations in each of them and monitored their effect on microtubule localization of MATCAP in cells. All five interfaces individually contributed to microtubule localization (fig. S7). Mutations in the helix-helix interface [Fig. 4G, (2)] combined with removal of the N-terminal region [Fig. 4G, (5)] decreased the binding of MATCAP to microtubules (Fig. 4, H and I). This effect was stronger than the effect of the separate mutants (Fig. 4, G and H, and fig. S7C). This combinatorial effect further demonstrates that multiple binding interfaces are involved in recruitment of MATCAP to the polymer. Because the N-terminal disordered region contributes to microtubule binding (fig. S7L), but its positioning in the context of protofilaments is unclear, it could influence MATCAP's enzymatic activity on microtubules. To study this, we incubated ΔN-MATCAP with either tubulin dimers or assembled microtubules. In this assay, ΔN-MATCAP displayed greater enhanced activity on microtubules than on tubulin dimers (fig. S7M) compared with that of wild type (Fig. 4A). Thus, whereas the disordered region of MATCAP enhances its anchoring on microtubules, it dampens processivity on the polymerized substrate.

Multiple specific interactions between MATCAP and microtubules ensure efficient binding to particularly the microtubule polymer and regulate detyrosination activity. Whereas MATCAP recognizes adjacent tubulin dimers along the same protofilament with the interdimeric loop interface, vasohibins recognize tubulin dimers in juxtaposed protofilaments (Fig. 4J) (*32*), further illustrating the differences between these two tyrosine carboxypeptidases.

Combined loss of MATCAP and SVBP perturbs detyrosination in vivo

To address the physiological role of detyrosination, we disrupted MATCAP in mice. Homozygous mice were viable and fertile and displayed no gross alterations. We subsequently crossed these mice with a mouse strain deficient for SVBP, which is required for vasohibin's enzymatic activity. The resulting double-mutant mice were viable, born at a Mendelian ratio, and showed body weights comparable with those of wild-type mice (fig. S8, A and B). Immunohistochemical analysis of brain tissue indicated a strong decrease of detyrosinated tubulin (Fig. 5A). Similarly, immunoblot analysis on brain tissue showed a reduction of detyrosinated tubulin and a concomitant increase in tyrosinated tubulin (Fig. 5B). Whereas Δ2 tubulin was undetectable, a faint signal was detected with detyrosination-specific antibodies, which could either be unspecific background signal, detection of TUBA4A (the tubulin isotype that is translated without C-terminal tyrosine), or remaining detyrosination. Quantitative proteomics on brain tissue from double-mutant mice detected exclusively tyrosinated but not detyrosinated TUBA1A/B (Fig. 5C). This finding was in agreement with our observations in human cell lines (Fig. 1H) and in line with the undetectable levels of Δ2-tubulin in mice, whose production relies on detyrosinated tubulin as precursor. Thus, combined inactivation of SVBP and MATCAP enables the generation of viable adult mice with impaired tubulin detyrosination.

Impaired detyrosination affects brain volume

Mice in which SVBP was removed (*11*), albeit having substantial amounts of detyrosinated tubulin, have smaller brains that resemble human patients with cognitive impairments and microcephaly. Mice that lack MATCAP showed a moderate but significant reduction of total brain volume, cerebellum, and olfactory bulb (Fig. 5, D and E) as quantified by use of magnetic resonance imaging (MRI) brain scans. The combined removal of MATCAP and SVBP led to a more significant decrease in brain size compared with that of single mutants (Fig. 5E) and a reduction in total brain weight and total cell number compared with those of wild-type mice (Fig. 5, F and G). To address the origin of the small brain phenotype, we first measured apoptotic cells. Only very infrequent and similar amounts of apoptotic cells were detected in adult or embryonic brains of either genotype (fig. S8, C to E). Next, we examined cell proliferation during neurogenesis in embryos at embryonic day 14.5 (E14.5). Immunostainings showed a significant decrease in mitotic phospho-histone H3-positive cells (Fig. 5, H and I). This decrease was observed in the ventricular and subventricular zone (Fig. 5J)—the proliferative zones of the embryonic brain (Fig. 5J)—which suggests a defect in proliferation of the progenitor cells. To examine whether this brain phenotype led to behavioral phenotypes, we examined nest building, a behavior that is sensitive to brain lesions in mice. When housed with nesting material overnight, double-mutant mice completely failed to construct nests, whereas MATCAP or SVBP single-mutant mice were largely able to build nests (Fig. 5K). Thus, these distinct detyrosinating enzymes have important and overlapping roles in brain development and behavior.

Conclusion

Whereas most posttranslational modifications of the α-tubulin tail are generated by large families of related enzymes (*2*), VASH-SVBP and MATCAP constitute isofunctional yet evolutionary unrelated enzymes. Their identification now enables functional studies of detyrosination, which is further facilitated by the survival of detyrosination-impaired mice. Because detyrosination precedes retyrosination in this biochemical cascade, their viability is in unexpected contrast with the postnatal lethality of TTL-deficient mice (*33*). As such, the absence of SVBP/MATCAP interferes with the generation of (i) detyrosinated tubulin, (ii) subsequent tubulin modifications preceded by detyrosination (Δ2-tubulin formation), (iii) microtubule heterogeneity through gradients of tyrosination levels, and (iv) the presence of a modification cycle affected by tubulin polymerization. Thus, the lethality of TTL mice may not be caused by disturbance of these processes but rather by the low levels of tyrosinated tubulin owing to nonreversable detyrosination. Taken together, our findings show similar activities for these two distinct classes of tubulin detyrosinases but at the same time highlight mechanistic differences between them. These differences lay a foundation to understand how distinct enzymatic properties

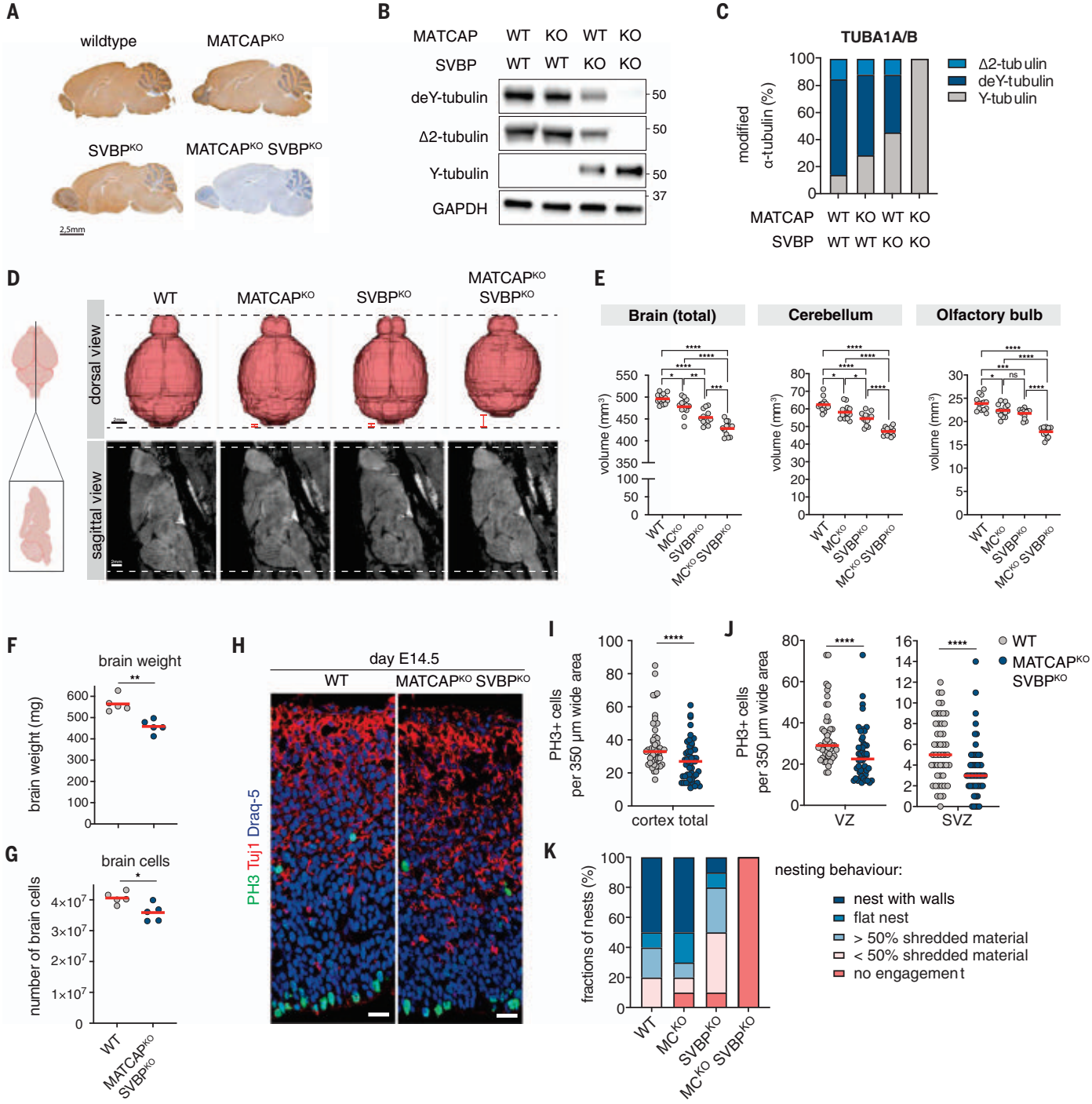

Fig. 5. Characterization of detyrosination-impaired mice. (**A**) Immunohistochemical staining of detyrosinated tubulin in adult mouse brains. (**B**) Immunoblot analysis of adult mouse brain lysates. (**C**) Microtubules isolated from adult mouse brains were subjected to nanoLC-MS/MS. Percentage of microtubules with different C-terminal modifications are shown. (**D**) MRI analysis of brain size of mice with indicated genotypes. 3D reconstructions (top) and an exemplary raw data MRI slices (bottom) are shown. Scale bar, 2 mm. (Anatomical scheme was created with BioRender.com.) (**E**) Volume quantifications of indicated regions. Wild type (WT), $n = 14$ mice; for all other genotypes, $n = 13$ mice. Significance was calculated as one-way ANOVA and Tukey's multiple comparisons test. (**F**) Weights of five adult mouse brains per genotype. (**G**) Total number of brain cells counted by means of flow cytometry using the isotropic fractionator method; $n = 5$ mouse brains per genotype. Unpaired two-tailed t test was performed for (F) and (G). (**H**) Immunofluorescence for DNA (Draq-5, blue), phospho-histone H3 (PH3; proliferation marker, green) and Tuj1 (neuron marker, red) on coronal brain sections from E14.5 mouse embryos. Scale bar, 20 µm. (**I**) Quantification of mitotic PH3$^+$ cells in the dorsal cortex at E14.5. Wilcoxon signed-rank test. (**J**) Quantification of mitotic PH3$^+$ cells in subregions of the dorsal cortex at E14.5. VZ, ventricular zone; SVZ, subventricular zone. Wilcoxon signed-rank test. In (I) and (J), $n = 6$ mouse embryos per genotype. For each animal, eight sections throughout the rostro-caudal axis of the embryonic brain were analyzed. (**K**) Nest building tests of mice with the indicated genotypes. Per genotype, $n = 10$ mice. In (E) to (G), (I), and (J), significance is depicted as $^{****}P < 0.0001$, $^{***}P < 0.001$, $^{**}P < 0.01$, $^{*}P < 0.05$, and nonsignificant (n.s.) > 0.05. Data are shown as mean in (E) to (G) and as median in (I) and (J).

may facilitate a more nuanced impact on the pool of heterogeneous microtubules.

Materials and methods

Reagents, constructs and treatments

To enhance detyrosination cells were incubated with 2 μM Paclitaxel (Santa Cruz Biotechnology) for 3 hours. MATCAP (UniProt identifier Q68EN5-1) was cloned with or without 2xHA-tag into the pcDNA3.1(-) vector and also into the pLEX_305. VASH1, SVBP and GFP-tubulin tail constructs were generated in a previous study (*17*). Mutant variants of MATCAP were derived through site-directed mutagenesis. All generated constructs were confirmed by sanger sequencing. A rabbit anti-MATCAP antibody was generated by immunizing rabbits with full-length recombinant human MATCAP protein and obtained sera were affinity purified (David Biotechnologie Gmbh).

Cell culture

Cell lines used include HAP1 (*34*), HCT116 (RRID:CVCL_0291), U2OS (RRID:CVCL_0042), HEK293T (RRID:CVCL_0063) and HeLa H1 (RRID:CVCL_3334). Cells were cultured in IMDM (HAP1) and DMEM (HCT116, U2OS, HEK293T, HeLa H1) supplemented with 10% fetal bovine serum (FBS), L-glutamine, penicillin and streptomycin at 37°C in 5% CO_2. Cell lines were monitored for mycoplasma contamination.

Generation of cell lines

Cell lines with gene mutations were generated either by lentiviral transduction of Cas9/gRNA cloned into the pLentiCrispr vector (including a blasticidin or puromycin resistance cassette) or by co-transfection of a vector with a blasticidin-resistance cassette and the pX330 vector (Addgene 42230) including the Cas9/gRNA. gRNA sequences were

TTL (5′- GTTCTCATCGCGTACCACGA-3′),

VASH1 (5′-ACGGCTTCCAGGCATTTGAT-3′),

VASH2 (5′-TTTGATAGGCAAGGACTCTC-3′), and

MATCAP (5′-TGCGCACAATCGACCATATC-3′).

After selection with antibiotics, individual clones for each cell line were derived. Genome-editing was monitored by amplifying genomic loci and subsequent sanger sequencing of PCR products. Primers used were

VASH1 (5′-GTGGGAGGTGGAAGTGAAA-GAAGG-3′, 5′-GCCAAGCAGATGACTGCA-TATGG-3′),

VASH2 (5′-TGCTATGGAGTACTGGCAC-TAACTCC-3′, 5-GTCCAAGAAGCCAAGCATT-GATTTGG-3′),

MATCAP (5′-GAGTACAGGGCCTGCTGGTCG-TTTG-3′, 5′-CGCCCACAAGACACCCTGATTTG-3′).

Compound heterozygote clones were identified with the TIDE web tool (*35*) and further confirmed by subcloning of the PCR amplicons and sequencing. TTL deletion was confirmed by immunoblotting using the rabbit anti-TTL (Proteintech, 13618-1-AP, RRID:AB_2256858).

FACS-based phenotypic screens in HAP1 cells

Screens were carried out as described previously (*17*, *36*). Retrovirus was produced by transfection of HEK293T cells with gene-trap vector, packaging plasmids Gag-pol, VSVg, and pAdv. After 48 hours the viral supernatant was harvested and filtered using Amicon filters and applied together with protamine sulfate (8 μg/ml) to 40 × 10^6 HAP1 cells. This procedure was repeated the next day. After expansion mutagenized HAP1 cells were dissociated using Trypsin-EDTA and washed with phosphate-buffered saline (PBS). Cells were fixed with ice-cold methanol for 10 min on ice, resuspended in FACS buffer (PBS with 10% FBS) and single cells were ensured by applying cells to a 40 μm strainer. After incubation with the primary antibody [rabbit anti-detyrosinated tubulin (*5*), rat anti-tyrosinated α-tubulin clone YL1/2 (Thermo Fisher Scientific, MA1-80017, RRID: AB_2210201)] for 1.5 hours at room temperature, cells were washed three times with PBS and then incubated for 1 hour with the secondary antibody (Alexa 488, Invitrogen) and DAPI for 1 hour at room temperature. After three washes with FACS buffer, G1 cells (identified by DAPI) within the highest or lowest 1% of staining signal were isolated using FACS. DNA was isolated and sequencing libraries were generated as described before (*36*). Deep sequencing reads from each sample (low and high) were aligned to HG38 allowing a single mismatch and assigned to non-overlapping protein-coding gene regions (Refseq). Unique disruptive integrations per gene body (intron and exon) of a gene were normalized to the total number of sense integrations of each sorted cell population. In this analysis the 5′UTR region was excluded in contrast to previous analysis (*36*). Then the mutation index (MI) was calculated by comparing normalized sense integrations of the high and low cell population using a two-sided Fisher's exact test. Fishtail blots were visualized using Python. Data used to plot the uniqueness across published haploid screens is available on Phenosaurus (https://phenosaurus.nki.nl).

Immunofluorescence

Cells were seeded on cover slips and fixed with ice-cold methanol for 4 min at −20°C. After 1 hour in blocking buffer (5% bovine albumin serum in PBS) at room temperature, cells were incubated with primary antibodies in blocking buffer overnight. After three washes with PBS cells were incubated for 1 hour with secondary antibodies (Alexa Invitrogen) in blocking buffer. Cell nuclei were counterstained with DAPI (1 μg/ml) for 10 min. Cells were mounted with Aqua-Poly Mount (Fisher Scientific) and imaged on a confocal microscope (Leica SP5 or Zeiss LSM 980 with Airyscan). Primary antibodies used were mouse anti-HA (BioLegend, #901503, RRID_AB:2565005), rabbit anti-detyrosinated α-tubulin (by Marin Barisic) (*5*), rabbit anti-α-tubulin (Abcam, ab18251, RRID:AB_2210057). Images were processed in Fiji (*37*) or Zen Blue Software. Colocalization was measured as Pearson correlation coefficient with the Fiji plugin EzColocalization (*38*). Colocalization was determined for cells within the same range of MATCAP intensity.

Immunoblotting

Cells were lysed directly in sample buffer containing 100 mM DTT. Proteins were separated on 4 to 12% Bis-Tris gels and transferred to nitrocellulose membranes. After blocking in TBS with 5% milk and 0.1% Tween20, membranes were incubated with primary and corresponding HRP-conjugated secondary antibodies (Thermo Fisher Scientific). Primary antibodies were anti-α-tubulin (Santa Cruz Biotechnology, sc-32293, RRID:AB_628412), rabbit anti-MATCAP (this study), rabbit anti-detyrosinated α-tubulin (Merck Millipore, AB3201, RRID:AB_177350), rabbit anti-Δ2 α-tubulin (Merck Millipore, AB3203, RRID: AB_177351), rat anti-tyrosinated α-tubulin clone YL1/2 (Thermo Fisher Scientific, MA1-80017, RRID:AB_2210201), HRP-conjugated mouse anti-GAPDH (GeneTex, GTX627408, RRID: AB_2888014).

MATCAP expression and purification

Sequence analysis based on the Protein-CCD[2] application (*39*) was used to identify the catalytic domain of MATCAP. Synthetic sequences of the catalytic domain of MATCAP (137-471) and full-length MATCAP (1-471) were used for cloning. The wildtype constructs were used to introduce the nucleophilic E281Q mutation. All proteins were expressed in *Spodoptera frugiperda* (Sf9) insect cells. In brief, a pFastBac1 plasmid with a his10-twinstrepII-3C-MATCAP genetic construct was created through ligation independent cloning (LIC) to custom expression vectors (*40*). Bacmid virus was produced with the Invitrogen Bac-to-Bac method and expressed in Sf9 insect cells using Insect-Xpress medium (LONZA). The cells were cultured in a shaker incubator at 28°C at 80 rpm and infected with the bacmid virus 8 hours after seeding a culture at 1 × 10^6 cells ml^{-1}. The insect cells were harvested 72 hours after the infection, snap-frozen in liquid nitrogen and kept at −20°C until usage.

The cell pellet was thawed on ice, and lysed with 4 min sonication (10s on/30s off) in ice cold lysis buffer [40 mM HEPES/HCl, pH 7.5, 500 mM NaCl, 1 mM Tris(2-carboxyethyl) phosphine (TCEP), 1 tablet Ethylenediaminetetraacetic acid (EDTA) free protease inhibitor (Thermo Fisher Scientific)]. To clear the lysate,

it was centrifuged (30 min, 54.000 g using a JA 25.50 rotor, Beckman Coulter). The supernatant was incubated with 500 µL pre-equilibrated Chelating Sepharose Fast Flow beads (GE healthcare) to capture the his-tagged MATCAP. After 1 hour the beads were washed with an excess of washing buffer (20 mM HEPES/HCl, pH 7.5, 500 mM NaCl, 1 mM TCEP) and MATCAP was eluted using an imidazole step-gradient (30-500 mM imidazole). The elution fractions that contained MATCAP were supplemented with 3C protease during a 4-hour-dialysis (20 mM HEPES/HCl, pH 7.5, 150 mM NaCl, 1 mM TCEP). Finally, cleaved MATCAP was gel-filtered using a s200 10/300 column (GE Healthcare) on a FPLC system (Bio-Rad) into 20 mM HEPES, pH 7.5, 140 mM NaCl (protein used for cryo-EM contained 100mM NaCl), 1 mM TCEP, 1 µM $ZnCl_2$ to remove remaining impurities. The purity of the fractions was assessed with an 8% Coomassie SDS page gel (Invitrogen) and the protein was concentrated with a 0.5 ml 10.000 MW Amicon-Ultra concentrator (Amicon) to a concentration above 5 mg ml^{-1}. The concentrated protein was snap-frozen in liquid nitrogen and kept at -80°C until usage.

Crystallization and data collection

Purified MATCAP (137-471) was concentrated at about 15-20 mg ml^{-1} for crystallization. Initial hits were obtained in a sitting drop format using 96-well two-drop MRC plates and the commercial screens PACT, JCSG+, Classics-I and II, ProComplex, ComPAS, pH-Clear and Morpheus. The drops consisted of 100 nL protein with 100 nL reservoir solution. After a period of one week, initial hits were identified in the Classics-I screen and further optimized using hanging drops in Limbro plates. Diffracting crystals of MATCAP were obtained in 4.3 M NaCl and 0.1M HEPES/NaOH pH 7. Crystals appeared as clusters, which were further optimized by using the additive screen from Hampton. Crystals grew to maximum dimensions over a period of two weeks and the most promising additive agent for growing single crystals was EDTA. We were unable to grow single crystals by varying the concentration of EDTA, but we succeeded in reducing the number of needles that grew in each cluster. Crystals were harvested and cryo-protected in a solution containing 30% ethylene glycol and vitrified in liquid nitrogen.

All data collection and refinement statistics are shown in table S1. A native crystal diffracted to 2.1 Å resolution at PSI X06DA (PXIII, Villingen Switzerland) at the Swiss Light Source (SLS) synchrotron, using a PILATUS 2M-F detector. Crystal content analysis has indicated four molecules in the asymmetric unit, with a solvent content 52.6%. As there was no structure of a close homolog of MATCAP and a reliable homology model could not be constructed at the time, the structure had to be determined by experimental phasing. We therefore soaked crystals in mother liquor containing methylmercury chloride solution (10 mM) for ~3 min, prior to cryo-protection and vitrification. A highly-redundant Hg derivative dataset was collected also in PSI X06DA at 1.00 Å wavelength at the Hg L-III edge. Crystals belong to the same space group with very similar unit cell dimensions as the native. Following structure determination, after we confirmed that MATCAP is a zinc-dependent metalloprotease, we removed EDTA from the crystallization conditions and managed to grow reasonably sized (but smaller and weaker diffracting) crystals of MATCAP (137-471) in the presence of Zn^{2+} ions; these crystals diffracted to 2.5 Å resolution. All data were also collected at PSI X06DA. All diffraction data were integrated automatically by XDS (18). Final scaling was performed in AIMLESS (*41*) within the CCP4 suite (*42*). Structures were visualized for figure panels with ChimeraX (*43*).

Crystallographic structure determination and refinement

The MATCAP structure was determined using the SIRAS phasing method, with the EDTA structure as native and the mercury soak as a derivative with anomalous scattering. Solvent content analysis identified that this crystal form had four molecules in the asymmetric unit, related by non-crystallographic symmetry. The HKL2MAP interface (*44*) was used to determine that the anomalous signal extended to about 4.0Å, and that dataset was used to run SHELXD (*45*) using all low-resolution reflections. Most solutions from the different semi-random trials of the direct methods were considered reasonable based on internal software statistics (CC versus CCweak). The best solution identified 11 mercury atoms, four with occupancy between 0.85 and 1.0. These sites were virtually identical to those detected by the same software in the context of the CRANK2 pipeline (*46*). Phasing within CRANK2 resulted to phases with a reasonable overall figure of merit (FOM) of 0.328. Following density modification, the correct hand was determined and the overall FOM improved to 0.67. Automated model building using PARROT (*47*) within the CRANK2 pipeline, resulted in a model containing 1,369 residues in ten fragments; 90% of the residues were docked in sequence.

The structure was manually completed and refined with a few iterations of REFMAC (*48*) and rebuilding in COOT (*49*). The molecules are arranged by a rotation operator as a dimer, and that dimer is related to another dimer by pure translation, making up the four molecules in the asymmetric unit. At that point, we identified that MATCAP is a metalloprotease, but that dataset clearly did not show zinc in the active site, owing to the presence of EDTA in the crystallization buffer. We thus focused our attention to the lower-resolution dataset that we collected with crystals grown with Zn^{+2} in the absence of EDTA. We determined that crystal structure by simply refining the model built for the apo form against this new dataset. The electron density map (both the 2mFo-DFc and the phased anomalous difference Fourier synthesis) confirmed the presence of a single zinc ion at the active site. Remarkably, the zinc-bound structure had minor differences with the apo structure, even at the vicinity of the active site. Following several iterations of REFMAC, COOT and using PDB-REDO (*50*) the structure refined to an Rfree of 25.5%. It has no Ramachandran plot outliers, the RamaZ score is –1.50 (*51*), and the Molprobity score of 1.11 ranking in the 100th percentile (*52*), and has been deposited to the PDB (PDBID: 7Z5H). The apo structure, has subsequently also been refined to an Rfree of 25.1%, with no Ramachandran plot outliers, RamaZ score of –0.91 (*51*), and a Molprobity score of 1.17 ranking in the 100th percentile (*52*), and has been deposited to the PDB (PDBID: 7Z5G). We note that the AlphaFold model from the EBI database (*22*) shows an ordered structure only for this MATCAP region, and rms difference of 0.89 Å from the crystallographic model.

HADDOCK modeling

A work-in progress model of MATCAP was used to predict the binding site of the C-terminal peptide into the active site of MATCAP using high ambiguity driven docking (HADDOCK) (*23*, *53*). As a substrate we used a peptide with sequence GEEEGEEY. Before docking, the crystal structure of MATCAP (137-471) was truncated digitally to 147-471, as the conformation of residues 137-147 looked like a crystallographic artefact and could be blocking the entrance of the catalytic pocket. In our initial docking model, we used three types of restraints. First, we defined active residues of the positive patch directly opposed of the active site in MATCAP (residues 334, 373, 376, and 389). Second, we defined active residues in the peptide $^{-1}EY^{0}$ as confirmed by mass spectrometry. Thirdly, analogous to the DPPIII crystal structure (PDB: 3T6J) (*54*) we restrained the distance of the zinc catalytic ion to the attacked carbonyl to 1.7 to 3.7 Å. Furthermore, we specified that the C terminus of the 8-meric peptide should be negatively charged. HADDOCK grouped 197 structures in three clusters (table S2). This initial docking model was confirmed by mutation studies of the active residues, and also suggested additional residues that could interact with the peptide. In a follow-up docking experiment, we used the original active residues $^{-1}EY^{0}$, 334, 373,

376, and 389, and additionally also 179, 312, 249, 393, and 417. As in the first model, the scissile bond was placed very close to the zinc ion, we decided to redefine the distance restraints between the zinc and the scissile bond to 1.2 to 3.7 Å. All other parameters were kept the same. This run of HADDOCK resulted to similar docking models as the first run; models were now grouped in two clusters (table S3).

Microtubule isolation

Microtubules were prepared from an HCT116 triple-mutant cell line (ΔMATCAP ΔVASH1ΔVASH2) or fresh mouse brains. Cells were harvested with PBS-EDTA using a cell scraper and resuspended in 1:1 v/v isolation buffer (100 mM PIPES/KOH pH 6.9, 2 mM EGTA, 1 mM $MgCl_2$, 1 mM PMSF, complete ultra-protease inhibitor tablet (Fisher Scientific)). Brains were homogenized in isolation buffer (1 μl/mg) on ice. Samples were sonicated on ice and cleared by centrifugation (1 hour, 100000×*g*, 4°C). Paclitaxel (final concentration 20 μM) and GTP (final concentration 1 mM) were added to the supernatant and incubated at 37°C for 30 min. Polymerized microtubules were then pelleted over a cushion (60% v/v glycerol, 20 μM paclitaxel in isolation buffer) for 40 min at 100000×*g* at 37°C. The pellet was resuspended in warm isolation buffer (fig. S6A).

Cryo-EM grid preparation and data collection

Purified full-length, E281Q inactive MATCAP was thawed and kept on ice (fig. S6, B and C). To increase microtubule binding, MATCAP (5.5 mg ml^{-1}) was diluted 1:1 v/v with low salt buffer (100 mM PIPES/KOH, pH 6.9, 2 mM K-EGTA, 1 mM $MgCl_2$). 3.5 μL of the freshly prepared HCT116-derived microtubules were applied to a glow discharged (30 mA, 60 s, GloQube, Quorum) 300 mesh quantifoil holey carbon copper grid R1.2/1.3 (Quantifoil micro tools GmbH), which was blotted for 2 s, force 10 in a humidified (30°C, 100% humidification) Vitrobot chamber (ThermoFisher Scientific) Subsequently, 3.5 μL diluted MATCAP was applied to the grid and allowed to adhere to the microtubules for 10 s. After 6.5 s of blotting (Whatman, cat no. 47000-100) the grid was plunge-frozen in liquid ethane and transferred to liquid nitrogen until imaging. Grids were screened in JEM-F200 "F2" 200 kV (JEOL) with a K2 camera (Gatan). A dataset of 8400 micrographs was collected with EPU-2.10.0 on a 300 kV Titan Krios1 (ThermoFisher Scientific) with a K3 camera (Gatan) in super-resolution mode. We used a calibrated pixel size of 0.53 Å/pixel with a nominal magnification of 81000x. A total dose of 50 electrons per micrograph divided over 50 frames with a total exposure time of 2.14s was used. The defocus range was −0.6 and −2.1 μm.

Cryo-EM image processing and modeling

Data analysis and processing was done in cryoSPARC (*55*) in the Oncode and RHPC GPU facility at the NKI, unless mentioned otherwise. First, micrographs were preprocessed: Imported micrographs were corrected for gain, patch-motion (*56*), and CTF (*57*) with an F-crop of 0.5, resulting in a working pixel size of 1.06 Å/pixel. CTF-corrected micrographs were then used to pick particles on. First, five micrographs were used to manually pick particles to create picking templates. Using these templates, particles could then be reliably picked with optimized parameters using the cryoSPARC filament picker job. Particles were subsequently extracted with a box size of 512 by 512 pixels and F-cropped to 128 by 128 pixels. The 4x binned particle stack was iteratively classified in 2D to remove broken, contaminated and clearly undecorated microtubule particles. To sort the particles to different microtubules classes, we created initial microtubule models (11 to 16 protofilaments) using the helical refinement option with parameters as listed in Table S4. The particles were then sorted over the different microtubule types with a heterogeneous refinement job. The 14 protofilament containing microtubule particles showed the best signal-to-noise ratio and contained most particles. The particles of this class were selected, un-binned to an F-crop of 416x416, and used for a subsequent helical refinement job, creating a clean 14 protofilament microtubule model and allowing good alignment of the particles. The helical refinement job, however, is unable to align particles to the characteristic microtubule seam. Consequently, these maps did not differentiate between α and β monomers, and thus the density for MATCAP was blurred along the protofilament axis, preventing further analysis. To overcome this, particles were 14x symmetry expanded and used for local refinement with a mask spanning a 2 by 2 tubulin lattice (fig. S6D). This mask was created using Chimera (*58*) as follows: we first docked the crystal structure of a tubulin dimer to two protofilaments; then we placed one MATCAP catalytic domain per tubulin dimer in the (blurred) density; finally, the *molmap* command was used to create an asymmetric simulated map of four MATCAPs bound to four tubulin dimers belonging to two adjacent protofilaments. After local refinement with this big mask, the characteristic loop differentiating α and β tubulin was clearly visible (fig. S5C). At this point the crystal structure of MATCAP could be fitted in the map reliably, in a unique orientation. Then, a smaller mask was created, containing only one protofilament and the bound MATCAP. A final local refinement with this smaller mask resulted in the final map. No preferential orientation was observed. (fig. S6E) The map has a nominal resolution of 2.9 Å and a median resolution of 5.3 Å. (fig. S6F and Table S5). A model was obtained by rigid body fitting (without further refinement) MATCAP (PDB: 7Z5H) and tubulin (PDB: 7SJ7) into the map. The locally refined map and the model were deposited to the PDB and EMDB (PDB: 7Z6S, EMDB: EMD-14529). To ease visualization, the local resolution of the map was estimated (fig. S6G-J) (*59*) and locally filtered by using cryoSPARC. The HADDOCK cluster 2 model agreed well with the cryo-EM density and was therefore connected to the last modeled residue of tubulin for a more intuitive interpretation, using Coot (fig. S7A) (*49*). Buried surface areas between the contacting interfaces were calculated by using PDBePISA (*60*). Maps were visualized and figures were created by using ChimeraX (*43*).

In vitro peptide assay

Peptides incubated with MATCAP were analyzed as decribed previously (*24*). Briefly, 500 μM peptides were incubated with 500 nM MATCAP for 4 hours at 37°C. Reactions were frozen until analysis. Samples were passed through a Microcon-10 spin filter (Millipore), diluted with 2% formic acid and analyzed by LC-MS/MS on a Thermo Orbitrap Fusion hybrid mass spectrometer (Q-OT-qIT, Thermo Scientific) equipped with a Proxeon nLC 1000 system (Thermo Scientific, Bremen), using a 30min gradient. RAW files were processed using Proteome Discoverer (version 2.5.400, Thermo Fisher Scientific). MS2 spectra were searched against a custom database containing the mutagenized synthetic versions of tubulin-like C-terminal peptides, using SequestHT. No enzyme and miscleavages were allowed and data were filtered with Xcorr score >1. Determination of the extent of peptide cleavage by MATCAP –and subsequent assessment of VASH1 substrate specificity- was performed based on the number of peptide spectrum matches (PSM) for the intact and cleaved/detyrosinated version of each peptide.

Analysis of TUBA1A/B C-termini from mouse brain microtubules

Mouse brain tubulin pellets were heated for 5 min at 95°C in 1x S-Trap lysis buffer (50mM TEAB pH 8.5, 5% SDS), after which 30 μg protein amounts (as determined by BCA Protein Assay Kit, Thermo Fisher Scientific) were digested on S-Trap Micro spin columns according to the manufacturer's instructions (ProtiFi, NY, United States), using 1:15 (enzyme:protein) Lys-N (ImmunoPrecise Antibodies Europe BV, Utrecht, The Netherlands). Digests were analyzed by LC-MS/MS on the system described above, using a 210-min gradient. RAW files were analyzed by MaxQuant (version 2.0.1.0) (*61*) using standard settings. Spectra were searched against the reviewed Swissprot M. musculus database (2021_04, 17073 sequences) with

semi-specific LysN as cleavage specificity, allowing the identification of full-length and truncated versions of the tubulin C terminus. The amount of C-terminal detyrosination was calculated for each sample, based on the LFQ abundances of (truncated) terminal peptides.

In vitro detyrosination assays

The detyrosination activity on tubulin dimers was assessed by incubating 50 nM Hela α/β-tubulin dimers (Cytoskeleton) with 25 nM recombinant MATCAP protein in 50 mM Tris-HCl, pH 8, 10% glycerol, 1 mM DTT and 1 mM PMSF for 45 min at 37°C. MATCAP was inhibited with 25 μM EDTA. For testing MATCAP's activity on microtubules versus α/β-tubulin dimers, 3 mg/ml HeLa α/β-tubulin (Cytoskeleton) were polymerized into microtubules by the addition of 1 mM GTP, 10% glycerol and stepwise addition of paclitaxel (0.3 to 3 to 30 μM every 10 min). The reaction was incubated at 37°C for 60 min. Microtubules equivalent of 500 nM tubulin dimers and 10 nM MATCAP or 2nM MATCAP$^{137-471}$ protein were incubated in 50 mM Tris-HCl, pH 8, 10% glycerol, 1 mM DTT and 1 mM PMSF for the indicated times at 37°C. Detyrosination levels were quantified by immunoblot analysis. To estimate the intensity of each band, the sum of pixel values in a square block, larger than the band, were measured and corrected by the subtraction of a background value using Image Lab software (Bio-Rad). To account for differences in the efficacy of blotting between experiments, a linear scale was applied between equivalent datasets from different experiments. Scale factors were calculated by linear regression to minimize the least squared difference between the points of all datasets. For each dataset, the detyrosination activity was normalized by the measured intensity for α-tubulin. A linear model was fit to estimate the rates of hydrolysis for the two reactions.

Co-sedimentation assay

Microtubules were assembled by incubating porcine tubulin dimers (Cytoskeleton) with GTP (1 mM), glycerol (10%) and paclitaxel (30 μM) at 37°C for 30 min. MATCAP protein (0.5 μM) and in vitro assembled microtubules (corresponding to 1 μM tubulin dimers) were incubated at room temperature for 20 min and then pelleted (100000×*g*, 35°C, 40 min) over a paclitaxel-glycerol cushion. The supernatant and microtubule-containing pellet were then analyzed by immunoblotting.

Use, generation and maintenance of mouse strains

Mouse experiments were approved by the Animal Ethics Committee of the Netherlands Cancer Institute (AVD301002017840 authorized by the national agency Centrale Commissie Dierproeven) and implemented in accordance with institutional, national and European guidelines for Animal Care and Use. SVBP-deleted mice (57BL/6), as described before (*11*), were recovered by in vitro fertilization of FVB oozytes. MATCAP KO mice were generated on FVB background (Janvier, FVB/NRj) using two gRNAs (5′-CTGCATGTATTTGCGCACGG-3′, 5′-AGATGATTGGCTCGGGCATT-3′) to create a 1348 bp deletion, which destroys the catalytic HEIGHT motif. SVBP and MATCAP genomic loci were genotyped by PCR amplification using the following primers:

MATCAP 5′-GCATCATTGAGGCTGTCCTG-GAG-3′,

5′-CACCATCATCACAGCCTGGGAC-3′,

5′-GCAGCCTGTGAGAAGGATAACCA-3′

SVBP 5′-GATCCACCTGCCCGGAAA-3′,

5′-CAAACCATGGATCCACGAAA, and

5′-TTTCTTCCAGCACCCTCTCC-3′.

For genotyping of MATCAP locus an annealing temperature of 67°C and 45 s extension time and for the SVBP locus 50°C for 30 s, respectively. Amplicons were analyzed on a 1% agarose gel. For in vivo studies randomization and statistical methods to predetermine the sample size were not performed. All recorded measurements were included.

In vivo MRI scanning of mouse brains

Mice were injected intraperitoneally with 0.4 mmol/kg dose of 30 mM Manganese Chloride ($MnCl_2$) 24 hours before scanning them individually with ParaVision 6.0.1 software in a 7 Tesla BioSpec 70/20 USR MRI system with a ø23 mm ^{1}H transmit-receive mouse brain volume coil (RF RES 300 1H 023 M.BR QSN TR 2.4M), all from Bruker BioSpin. During the acquisition, mice were anaesthetized with 1-2% isoflurane in a mix of air and oxygen. Acquisition parameters are T1-weighted, 3D gradient echo sequence, TR = 31 ms, TE = 7.7 ms, flip angle = 37°, field-of-view = 20 by 15 by 17 mm, matrix size = 200 by 150 by 170, number of averages and repetitions = 1, total acquisition time = 20 min with respiratory trigger, isotropic resolution = 100 μm. For quantifications, DICOM files were loaded into 3D Slicer (*62*). Brain structures were manually outlined on every third (substructures) or tenth (total brain) slice. Then slices in-between were automatically filled using the segmentation editor tool, the selection was visually inspected and if needed manually refined. Measurements were made using the quantification tool in 3D Slicer. 3D reconstructions are shown as orthographic renderings. Measurements were done blinded. Statistical tests were performed using GraphPad Prism.

Counting of brain cells

The total number of brain cells per adult mouse brain was counted with the isotropic fractionator method (*63*). Briefly, intact nuclei were isolated from paraformaldehyde (PFA)–fixed adult brains by homogenization in a 40 mM sodium citrate, 1% Triton X-100 solution. Washes from rinsing the glass homogenizer were collected and centrifuged (15 min at 4000 xg) together with the homogenate. Pelleted nuclei were resuspended in PBS with 0.5 μg/ml DAPI. A fraction of the nuclei solution was mixed with 50 μl CountBright Absolute Counting Beads (Thermo Fisher) and technical duplicates for each sample were analyzed on a flow cytometer. The flow cytometer operator was blinded. Acquired measurements of cells and beads were used to calculate the cell concentration of each sample according to the manufacturer's manual.

Nest building test

Nest building behavior was assessed as previously described (*64*). Briefly, adult mice were moved to individual cages with one flat enrichment sheets (7 g) per cage. The next morning, nests were scored using the following scale: (i) nests with wall higher than mouse body height, (ii) flat nest, (iii) no clear nest but >50% shredded nest material, (iv) no nest but >50% shredded nest material, (v) no visible engagement with the nesting material at all. The experimenter scored the nests blinded.

Immunohistochemistry

Sections of formalin-fixed tissues were deparaffinized and rinsed three times with wash buffer (0.05% Tween20 in PBS). Antigen retrieval was performed for the deY-tubulin (Citric buffer from Scytek, CBB999, 20 min, 98°C) and cleaved caspase 3 (Tris/EDTA pH 9, 30 min, 96°C) staining. After inactivation of endogenous peroxidases with 3% H_2O_2 in Methanol, again rinsed three times and blocked in 4% bovine serum albumin (BSA) 5% normal goat serum in PBS in normal goat serum. Primary antibodies were applied overnight at 4°C. After three washes sections were incubated with Envision+ System-HRP labeled antibodies. After another three washes with wash buffer, sections were visualized with DAB+ (Dako, K3468, 1 ml substrate buffer + 20 μl Chromogen) for 3 min, rinsed with demiH_2O, counterstained with Haematoxylin, dehydrated and mounted with Entellan. Primary antibodies were rabbit anti-detyrosinated tubulin (Barisic lab) and cleaved caspase 3 (Cell signaling, #9661, RRID:AB_2341188). Apoptotic cells were quantified using QuPath (*65*).

For mouse brain stainings, embryonic brains dissected at E14.5 were fixed for 7 hours with 4% PFA in PBS. After three PBS washes brains were cryopreserved using a 30% sucrose solution, and then frozen in 7.5% gelatin plus 15% sucrose solution. Coronal cryosections were obtained at 12 μm thickness and post-fixed with 4% PFA for 10 min, washed with 1x PBS, then treated with 0.3% Triton X-100 for 5 min, and incubated in blocking solution

containing 5% FBS, 3% BSA, 0.1% Triton X-100 in 1× PBS, for 2 hours. Samples were incubated with primary antibodies diluted in blocking solution at 4°C overnight, as previously described (*66*). The primary antibodies used were: rabbit anti-phospho-Histone H3 (Merck-Millipore, 06-570, RRID:AB_310177), mouse anti-Tuj1 (Sigma, T8660, RRID:AB_477590) and rabbit anti-cleaved caspase 3 (R&D Systems, AF835, RRID:AB_2243952).

Next, after three washes with 0.1% Tween-20 in 1x PBS, sections were incubated with secondary antibodies (goat anti-rabbit Alexa Fluor 488, goat anti-mouse Alexa Fluor 568) diluted in blocking solution for 1 hour. Draq-5 (Biostatus) was used to stain DNA. Sections were mounted in Mowiol 4-88 (Calbiochem). Images were recorded on a confocal fluorescence microscopy Leica TCS SP5 with a Leica DMI6000B microscope.

REFERENCES AND NOTES

1. A. Roll-Mecak, The tubulin code in microtubule dynamics and information encoding. *Dev. Cell* **54**, 7–20 (2020). doi: 10.1016/j.devcel.2020.06.008; pmid: 32634400
2. C. Janke, M. M. Magiera, The tubulin code and its role in controlling microtubule properties and functions. *Nat. Rev. Mol. Cell Biol.* **21**, 307–326 (2020). doi: 10.1038/s41580-020-0214-3; pmid: 32107477
3. J. Nieuwenhuis, T. R. Brummelkamp, The tubulin detyrosination cycle: Function and enzymes. *Trends Cell Biol.* **29**, 80–92 (2019). doi: 10.1016/j.tcb.2018.08.003; pmid: 30213517
4. C. Sanyal *et al*., The detyrosination/re-tyrosination cycle of tubulin and its role and dysfunction in neurons and cardiomyocytes. *Semin. Cell Dev. Biol.*S1084-9521(21)00314-1 (2021). doi: 10.1016/j.semcdb.2021.12.006; pmid: 34924330
5. S. Liao *et al*., Molecular basis of vasohibins-mediated detyrosination and its impact on spindle function and mitosis. *Cell Res.* **29**, 533–547 (2019). doi: 10.1038/s41422-019-0187-y; pmid: 31171830
6. M. Barisic *et al*., Microtubule detyrosination guides chromosomes during mitosis. *Science* **348**, 799–803 (2015). doi: 10.1126/science.aaa5175; pmid: 25908662
7. L. T. Ferreira *et al*., α-Tubulin detyrosination impairs mitotic error correction by suppressing MCAK centromeric activity. *J. Cell Biol.* **219**, e201910064 (2020). doi: 10.1083/jcb.201910064; pmid: 32328631
8. T. Akera *et al*., Spindle asymmetry drives non-Mendelian chromosome segregation. *Science* **358**, 668–672 (2017). doi: 10.1126/science.aan0092; pmid: 29097549
9. Z. Iqbal *et al*., Loss of function of SVBP leads to autosomal recessive intellectual disability, microcephaly, ataxia, and hypotonia. *Genet. Med.* **21**, 1790–1796 (2019). doi: 10.1038/s41436-018-0415-8; pmid: 30607023
10. C. Aillaud *et al*., Vasohibins/SVBP are tubulin carboxypeptidases (TCPs) that regulate neuron differentiation. *Science* **358**, 1448–1453 (2017). doi: 10.1126/science.aao4165; pmid: 29146868
11. A. T. Pagnamenta *et al*., Defective tubulin detyrosination causes structural brain abnormalities with cognitive deficiency in humans and mice. *Hum. Mol. Genet.* **28**, 3391–3405 (2019). doi: 10.1093/hmg/ddz186; pmid: 31363758
12. J. P. Kerr *et al*., Detyrosinated microtubules modulate mechanotransduction in heart and skeletal muscle. *Nat. Commun.* **6**, 8526 (2015). doi: 10.1038/ncomms9526; pmid: 26446751
13. C. Y. Chen *et al*., Suppression of detyrosinated microtubules improves cardiomyocyte function in human heart failure. *Nat. Med.* **24**, 1225–1233 (2018). doi: 10.1038/s41591-018-0046-2; pmid: 29892068
14. X. Yu *et al*., MARK4 controls ischaemic heart failure through microtubule detyrosination. *Nature* **594**, 560–565 (2021). doi: 10.1038/s41586-021-03573-5; pmid: 34040253
15. P. Robison *et al*., Detyrosinated microtubules buckle and bear load in contracting cardiomyocytes. *Science* **352**, aaf0659 (2016). doi: 10.1126/science.aaf0659; pmid: 27102488
16. M. E. Pero *et al*., Pathogenic role of delta 2 tubulin in bortezomib-induced peripheral neuropathy. *Proc. Natl. Acad. Sci. U.S.A.* **118**, e2012685118 (2021). doi: 10.1073/pnas.2012685118; pmid: 33468672
17. J. Nieuwenhuis *et al*., Vasohibins encode tubulin detyrosinating activity. *Science* **358**, 1453–1456 (2017). doi: 10.1126/science.aao5676; pmid: 29146869
18. K. Ersfeld *et al*., Characterization of the tubulin-tyrosine ligase. *J. Cell Biol.* **120**, 725–732 (1993). doi: 10.1083/jcb.120.3.725; pmid: 8093886
19. N. Cerdà-Costa, F. X. Gomis-Rüth, Architecture and function of metallopeptidase catalytic domains. *Protein Sci.* **23**, 123–144 (2014). doi: 10.1002/pro.2400; pmid: 24596965
20. D. Ghilarov *et al*., The origins of specificity in the microcin-processing protease TldD/E. *Structure* **25**, 1549–1561.e5 (2017). doi: 10.1016/j.str.2017.08.006; pmid: 28943336
21. K. Fukasawa *et al*., Dipeptidyl peptidase III is a zinc metallo-exopeptidase. Molecular cloning and expression. *Biochem. J.* **329**, 275–282 (1998). doi: 10.1042/bj3290275; pmid: 9425109
22. J. Jumper *et al*., Highly accurate protein structure prediction with AlphaFold. *Nature* **596**, 583–589 (2021). doi: 10.1038/s41586-021-03819-2; pmid: 34265844
23. G. C. P. van Zundert *et al*., The HADDOCK2.2 web server: User-friendly integrative modeling of biomolecular complexes. *J. Mol. Biol.* **428**, 720–725 (2016). doi: 10.1016/j.jmb.2015.09.014; pmid: 26410586
24. A. Adamopoulos *et al*., Crystal structure of the tubulin tyrosine carboxypeptidase complex VASH1-SVBP. *Nat. Struct. Mol. Biol.* **26**, 567–570 (2019). doi: 10.1038/s41594-019-0254-6; pmid: 31270470
25. N. Wang *et al*., Structural basis of tubulin detyrosination by the vasohibin-SVBP enzyme complex. *Nat. Struct. Mol. Biol.* **26**, 571–582 (2019). doi: 10.1038/s41594-019-0241-y; pmid: 31235911
26. C. Zhou, L. Yan, W. H. Zhang, Z. Liu, Structural basis of tubulin detyrosination by VASH2/SVBP heterodimer. *Nat. Commun.* **10**, 3212 (2019). doi: 10.1038/s41467-019-11277-8; pmid: 31324789
27. F. Li, Y. Hu, S. Qi, X. Luo, H. Yu, Structural basis of tubulin detyrosination by vasohibins. *Nat. Struct. Mol. Biol.* **26**, 583–591 (2019). doi: 10.1038/s41594-019-0242-x; pmid: 31235910
28. X. Liu *et al*., Structural insights into tubulin detyrosination by vasohibins-SVBP complex. *Cell Discov.* **5**, 65 (2019). doi: 10.1038/s41421-019-0133-7; pmid: 31908845
29. H. S. Barra, C. A. Arce, C. E. Argarañа, Posttranslational tyrosination/detyrosination of tubulin. *Mol. Neurobiol.* **2**, 133–153 (1988). doi: 10.1007/BF02935343; pmid: 3077315
30. G. G. Deanin, S. F. Preston, R. K. Hanson, M. W. Gordon, On the mechanism of turnover of the carboxy-terminal tyrosine of the alpha chain of tubulin. *Eur. J. Biochem.* **109**, 207–216 (1980). doi: 10.1111/j.1432-1033.1980.tb04786.x; pmid: 7408878
31. N. Kumar, M. Flavin, Preferential action of a brain detyrosinolating carboxypeptidase on polymerized tubulin. *J. Biol. Chem.* **256**, 7678–7686 (1981). doi: 10.1016/S0021-9258(19)69014-9; pmid: 6114100
32. F. Li *et al*., Cryo-EM structure of VASH1-SVBP bound to microtubules. *eLife* **9**, e58157 (2020). doi: 10.7554/eLife.58157; pmid: 32773040
33. C. Erck *et al*., A vital role of tubulin-tyrosine-ligase for neuronal organization. *Proc. Natl. Acad. Sci. U.S.A.* **102**, 7853–7858 (2005). doi: 10.1073/pnas.0409626102; pmid: 15899979
34. J. E. Carette *et al*., Generation of iPSCs from cultured human malignant cells. *Blood* **115**, 4039–4042 (2010). doi: 10.1182/blood-2009-07-231845; pmid: 20233975
35. E. K. Brinkman, T. Chen, M. Amendola, B. van Steensel, Easy quantitative assessment of genome editing by sequence trace decomposition. *Nucleic Acids Res.* **42**, e168–e168 (2014). doi: 10.1093/nar/gku936; pmid: 25300484
36. M. Brockmann *et al*., Genetic wiring maps of single-cell protein states reveal an off-switch for GPCR signalling. *Nature* **546**, 307–311 (2017). doi: 10.1038/nature22376; pmid: 28562590
37. J. Schindelin *et al*., Fiji: An open-source platform for biological-image analysis. *Nat. Methods* **9**, 676–682 (2012). doi: 10.1038/nmeth.2019; pmid: 22743772
38. W. Stauffer, H. Sheng, H. N. Lim, EzColocalization: An ImageJ plugin for visualizing and measuring colocalization in cells and organisms. *Sci. Rep.* **8**, 15764 (2018). doi: 10.1038/s41598-018-33592-8; pmid: 30361629
39. W. T. M. Mooij, E. Mitsiki, A. Perrakis, *ProteinCCD*: Enabling the design of protein truncation constructs for expression and crystallization experiments. *Nucleic Acids Res.* **37**, W402-5 (2009). doi: 10.1093/nar/gkp256; pmid: 19395596
40. M. P. A. Luna-Vargas *et al*., Enabling high-throughput ligation-independent cloning and protein expression for the family of ubiquitin specific proteases. *J. Struct. Biol.* **175**, 113–119 (2011). doi: 10.1016/j.jsb.2011.03.017; pmid: 21453775
41. P. R. Evans, G. N. Murshudov, How good are my data and what is the resolution? *Acta Crystallogr. D Biol. Crystallogr.* **69**, 1204–1214 (2013). doi: 10.1107/S0907444913000061; pmid: 23793146
42. L. Potterton *et al*., CCP4i2: The new graphical user interface to the CCP4 program suite. *Acta Crystallogr. D Struct. Biol.* **74**, 68–84 (2018). doi: 10.1107/S2059798317016035; pmid: 29533233
43. E. F. Pettersen *et al*., UCSF ChimeraX: Structure visualization for researchers, educators, and developers. *Protein Sci.* **30**, 70–82 (2021). doi: 10.1002/pro.3943; pmid: 32881101
44. T. Pape, T. R. Schneider, HKL2MAP: A graphical user interface for macromolecular phasing with SHELX programs. *J. Appl. Cryst.* **37**, 843–844 (2004). doi: 10.1107/S0021889804018047
45. G. M. Sheldrick, Experimental phasing with SHELXC/D/E: Combining chain tracing with density modification. *Acta Crystallogr. D Biol. Crystallogr.* **66**, 479–485 (2010). doi: 10.1107/S0907444909038360; pmid: 20383001
46. N. S. Pannu *et al*., Recent advances in the CRANK software suite for experimental phasing. *Acta Crystallogr. D Biol. Crystallogr.* **67**, 331–337 (2011). doi: 10.1107/S0907444910052224; pmid: 21460451
47. K. Cowtan, Recent developments in classical density modification. *Acta Crystallogr. D Biol. Crystallogr.* **66**, 470–478 (2010). doi: 10.1107/S090744490903947X; pmid: 20383000
48. G. N. Murshudov *et al*., REFMAC5 for the refinement of macromolecular crystal structures. *Acta Crystallogr. D Biol. Crystallogr.* **67**, 355–367 (2011). doi: 10.1107/S0907444911001314; pmid: 21460454
49. P. Emsley, B. Lohkamp, W. G. Scott, K. Cowtan, Features and development of Coot. *Acta Crystallogr. D Biol. Crystallogr.* **66**, 486–501 (2010). doi: 10.1107/S0907444910007493; pmid: 20383002
50. R. P. Joosten, K. Joosten, S. X. Cohen, G. Vriend, A. Perrakis, Automatic rebuilding and optimization of crystallographic structures in the Protein Data Bank. *Bioinformatics* **27**, 3392–3398 (2011). doi: 10.1093/bioinformatics/btr590; pmid: 22034521
51. O. V. Sobolev *et al*., A global Ramachandran score identifies protein structures with unlikely stereochemistry. *Structure* **28**, 1249–1258.e2 (2020). doi: 10.1016/j.str.2020.08.005; pmid: 32857966
52. C. J. Williams *et al*., MolProbity: More and better reference data for improved all-atom structure validation. *Protein Sci.* **27**, 293–315 (2018). doi: 10.1002/pro.3330; pmid: 29067766
53. C. Dominguez, R. Boelens, A. M. J. J. Bonvin, HADDOCK: A protein-protein docking approach based on biochemical or biophysical information. *J. Am. Chem. Soc.* **125**, 1731–1737 (2003). doi: 10.1021/ja026939x; pmid: 12580598
54. G. A. Bezerra *et al*., Entropy-driven binding of opioid peptides induces a large domain motion in human dipeptidyl peptidase III. *Proc. Natl. Acad. Sci. U.S.A.* **109**, 6525–6530 (2012). doi: 10.1073/pnas.1118005109; pmid: 22493238
55. A. Punjani, J. L. Rubinstein, D. J. Fleet, M. A. Brubaker, cryoSPARC: Algorithms for rapid unsupervised cryo-EM structure determination. *Nat. Methods* **14**, 290–296 (2017). doi: 10.1038/nmeth.4169; pmid: 28165473
56. J. L. Rubinstein, M. A. Brubaker, Alignment of cryo-EM movies of individual particles by optimization of image translations. *J. Struct. Biol.* **192**, 188–195 (2015). doi: 10.1016/j.jsb.2015.08.007; pmid: 26296328
57. J. Zivanov, T. Nakane, S. H. W. Scheres, Estimation of high-order aberrations and anisotropic magnification from cryo-EM data sets in *RELION*-3.1. *IUCrJ* **7**, 253–267 (2020). doi: 10.1107/S2052252520000081; pmid: 32148853
58. E. F. Pettersen *et al*., UCSF Chimera—A visualization system for exploratory research and analysis. *J. Comput. Chem.* **25**, 1605–1612 (2004). doi: 10.1002/jcc.20084; pmid: 15264254
59. G. Cardone, J. B. Heymann, A. C. Steven, One number does not fit all: Mapping local variations in resolution in cryo-EM reconstructions. *J. Struct. Biol.* **184**, 226–236 (2013). doi: 10.1016/j.jsb.2013.08.002; pmid: 23954653
60. E. Krissinel, K. Henrick, Inference of macromolecular assemblies from crystalline state. *J. Mol. Biol.* **372**, 774–797 (2007). doi: 10.1016/j.jmb.2007.05.022; pmid: 17681537
61. J. Cox *et al*., Accurate proteome-wide label-free quantification by delayed normalization and maximal peptide ratio extraction, termed MaxLFQ. *Mol. Cell. Proteomics* **13**, 2513–2526 (2014). doi: 10.1074/mcp.M113.031591; pmid: 24942700

62. A. Fedorov *et al*., 3D Slicer as an image computing platform for the Quantitative Imaging Network. *Magn. Reson. Imaging* **30**, 1323–1341 (2012). doi: 10.1016/j.mri.2012.05.001; pmid: 22770690
63. N. A. Young *et al*., Use of flow cytometry for high-throughput cell population estimates in brain tissue. *Front. Neuroanat.* **6**, 27 (2012). doi: 10.3389/fnana.2012.00027; pmid: 22798947
64. R. M. Deacon, Assessing nest building in mice. *Nat. Protoc.* **1**, 1117–1119 (2006). doi: 10.1038/nprot.2006.170; pmid: 17406392
65. P. Bankhead *et al*., QuPath: Open source software for digital pathology image analysis. *Sci. Rep.* **7**, 16878 (2017). doi: 10.1038/s41598-017-17204-5; pmid: 29203879
66. M. E. Lalioti *et al*., GemC1 is a critical switch for neural stem cell generation in the postnatal brain. *Glia* **67**, 2360–2373 (2019). doi: 10.1002/glia.23690; pmid: 31328313

ACKNOWLEDGMENTS

We thank members of the Brummelkamp group for helpful discussions and critical reading of the manuscript and members of the Perrakis and Sixma group (in particular, A. Murachelli and S. Brueckner) for discussions about cryo-EM data processing. We also thank the NKI Bioimaging, Flow cytometry, Genomics Core, Protein, Animal, cryo-EM, Research High Performance Computing (RHPC), MRI scanning, and experimental animal pathology NKI facilities for technical support, and in particular X. Guo (cryo-EM) and N. de Wit (MRI). The cryo-EM work benefited from access to the Netherlands Centre for Electron Nanoscopy (NeCEN) at Leiden University, an Instruct-ERIC centre, with assistance from W. E. M. Noteborn; financial support was provided by the Netherlands Electron Microscopy Infrastructure (NEMI). We acknowledge the Paul Scherrer Institut, Villigen, Switzerland, for provision of synchrotron radiation beamtime for the x-ray work at beamline, PXIII; SFR Biosciences (UAR3444/CNRS, US8/Inserm, ENS de Lyon, UCBL) and the ANIRA-PBES facility for help with the generation of SVBP mice; and the Advanced Light Microscopy Facility of the Medical School at the University of Patras for imaging support. We thank C. Nikolaou for advice on statistics. **Funding:** This work was supported by NWO Vici grant 016.Vici.170.033 to T.R.B.; A.P. and T.R.B. are Oncode investigators (https://www.oncode.nl) and receive funding from NWO ENW (OCENW.M20.324). L.L. was supported by the Austrian Science Fund (FWF):[J 4448]. O.B.B. is supported by the NWO X-omics Initiative. M.-J.M. is supported by the Leducq Foundation (20CVD01) and ANR (20-CE16-0021). M.B. is supported by the Lundbeck Foundation (R215-2015-4081) and the Novo Nordisk Foundation (NNF19OC0058504). This work benefited from access to the NKI Protein Facility and to NeCEN, both Instruct-ERIC centres. **Author contributions:** L.L., J.B., A.P., and T.R.B. wrote the manuscript and visualized the data; A.A. and T.H. established protein purification and crystallized MATCAP; A.A. and A.P. determined and J.B. refined the crystal structure; J.B. perfomed the cryo-EM structure determination and analysis and computational modeling; K.K performed the experiment on embryonic proliferation under the supervision of S.T.; HADDOCK-related mutagenesis experiments were performed by M.M.; O.B.B. performed mass spectrometry and analysis; L.G.v.d.H. organized mouse experiments and genotyping; J.-Y.S. performed and interpreted brain stainings; M.-J.M provided the SVBP KO mouse line; M.B. shared the deY-tubulin antibody; J.N. performed the Y-tubulin screen; L.H. generated the MATCAP KO mice; and L.L. performed all other experiments. L.L., A.P., and T.R.B conceptualized and coordinated the research. **Competing interests:** T.R.B. is a cofounder and scientific advisor at Scenic Biotech. **Data and material availability:** Cell lines, MATCAP antibody, and MATCAP-deleted mice are available from T.R.B. under a materials transfer agreement with the Netherlands Cancer Institute. Structures and data are available from the corresponding databases: PDB, 7Z5G (human apo-MATCAP), 7Z5H (human Zn^{2+} MATCAP), and 7Z6S (MATCAP complex with a protofilament); EMDB, EMD-14529 (cryo-EM maps supporting the 7Z6S model); and screen data are available in the NCBI Sequence Read Archive (www.ncbi.nlm.nih.gov/sra, BioProject ID PRJNA809639) and on an interactive visualization platform (https://phenosaurus.nki.nl). **License information:** Copyright © 2022 the authors, some rights reserved; exclusive licensee American Association for the Advancement of Science. No claim to original US government works. https://www.science.org/about/science-licenses-journal-article-reuse.

SUPPLEMENTARY MATERIALS

science.org/doi/10.1126/science.abn6020
Figs. S1 to S8
Tables S1 to S5
Data Files S1 and S2

Submitted 7 December 2021; accepted 19 April 2022
10.1126/science.abn6020

Science
JOURNALS AAAS

Publish your research in the *Science* family of journals

The *Science* family of journals (*Science, Science Advances, Science Immunology, Science Robotics, Science Signaling*, and *Science Translational Medicine)* are among the most highly-regarded journals in the world for quality and selectivity. Our peer-reviewed journals are committed to publishing cutting-edge research, incisive scientific commentary, and insights on what's important to the scientific world at the highest standards.

Submit your research today!

Learn more at **Science.org/journals**

RESEARCH ARTICLE SUMMARY

TOPOLOGICAL MATTER

All topological bands of all nonmagnetic stoichiometric materials

Maia G. Vergniory*†, Benjamin J. Wieder*†, Luis Elcoro, Stuart S. P. Parkin, Claudia Felser, B. Andrei Bernevig, Nicolas Regnault*

INTRODUCTION: Since the theoretical proposals of the first topological insulators (TIs), solid-state realizations of TIs and topological semimetals (TSMs) have been discovered at a rapid pace. The recently introduced theories of topological quantum chemistry and symmetry-based indicators (SIs) have in particular facilitated the discovery of topological phases of matter and large-scale searches for materials with experimentally accessible topological properties at the Fermi energy (E_F). Away from E_F, energetically isolated bands and topological gaps are also useful in numerous experimental settings; they can be accessed via (electro)chemical doping, electrostatic gating, hydrostatic pressure, and nonequilibrium photoexcitation and are relevant to Floquet engineering and nonlinear optical experiments. We have completed a catalog of stable and fragile topology in all of the bands and band-gaps both at and away from E_F in the materials contained in the Inorganic Crystal Structure Database (ICSD). We have made our results publicly accessible through a substantial upgrade of the Topological Materials Database (https://topologicalquantumchemistry.com/).

RATIONALE: At the time of our study, the ICSD contained 193,426 entries, of which 96,196 characterized stoichiometric chemical compounds with processable (noncorrupt) CIF structure files. We performed first-principles calculations on all 96,196 processable ICSD entries, resulting in convergent electronic structures for 73,234 entries when taking into account the effects of spin-orbit coupling. For each convergent electronic structure calculation, we computed the topological class and stable and fragile SIs of all bands above the core shell up to an energetic cutoff set to a filling of roughly twice the number of valence electrons. The 73,234 convergent electronic structures were grouped into 38,298 unique materials by common chemical formulas and stable topology at E_F.

Our calculations represent the completion of the symmetry-indicated band topology of known nonmagnetic materials, and a doubling of the number of materials accessible in previous topological material catalogs. We reveal the existence of repeat-topological (RTopo) materials with stable topological insulating (TI) gaps at and just below E_F, and super-topological (STopo) materials in which every energetically isolated set of bands above the core shell is stable topological.

RESULTS: Our findings recontextualize several previous experimental investigations of topological materials. We find that the transition-metal chalcogenides Ta_2NiSe_5 in space group (SG) 15 ($C2/c$) and Ta_2NiSe_7 in SG 12 ($C2/m$)—previously highlighted for hosting exciton-insulator and charge density wave phases, respectively—are 3D TIs in their normal states. Additionally, we find that the higher-order TI rhombohedral bismuth in SG 166 ($R\bar{3}m$) and the indirect-gap TI Bi_2Mg_3 in SG 164 ($P\bar{3}m1$) are both RTopo and STopo materials. Previous angle-resolved photoemission spectroscopy (ARPES) investigations of Bi_2Mg_3 have demonstrated the presence of "surface resonance bands" below E_F; here, we identify these bands as RTopo Dirac-cone surface states. Our computations reveal that 52.65% of all studied materials are topological at E_F, roughly two-thirds of bands across all materials exhibit symmetry-indicated stable topology, and 87.99% of all materials contain at least one connected set of bands with symmetry-indicated stable or fragile topology.

CONCLUSION: Our findings motivate the formulation of a periodic table of chemical compounds based on the ubiquity of nontrivial electronic band topology in solid-state materials. The relative preponderance of RTopo and STopo materials in the ICSD, combined with our recognition that the surface resonance bands in Bi_2Mg_3 are RTopo surface states, suggests that many of the surface resonances detected in previous ARPES investigations are in fact topological surface states protected by spectral flow below E_F. Lastly, as there are known TI and TSM phases that cannot be detected by SIs, our results represent a lower bound on the percentage of materials in nature with topologically nontrivial electronic properties; future investigations may reveal that an even higher percentage of solid-state materials exhibit previously overlooked topological properties. ■

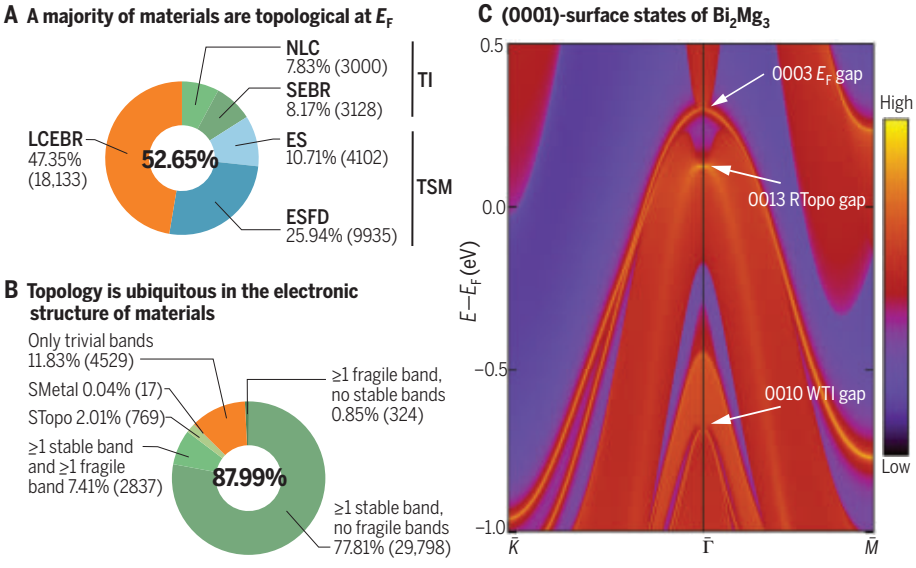

Topological materials statistics and repeat-topological surface states. (**A** and **B**) Percentage of known 3D materials that are topological at intrinsic electronic filling (52.65%) (A) and contain at least one topological band (87.99%) (B). (**C**) The (0001)-surface states of Bi_2Mg_3 obtained from surface Green's functions. Topological Dirac-cone surface states appear at $\bar{\Gamma}$ both slightly above the Fermi level (E_F gap) and in the next gap below E_F (RTopo gap), revealing the topological origin of the "surface resonance bands" observed in previous ARPES experiments.

The list of author affiliations is available in the full article online.
*Corresponding author. Email: regnault@princeton.edu (N.R.); maiagvergniory@dipc.org (M.G.V.); bwieder@mit.edu (B.J.W.)
†These authors contributed equally to this work.
Cite this article as M. G. Vergniory *et al.*, *Science* **376**, eabg9094 (2022). DOI: 10.1126/science.abg9094

READ THE FULL ARTICLE AT
https://doi.org/10.1126/science.abg9094

RESEARCH ARTICLE

TOPOLOGICAL MATTER

All topological bands of all nonmagnetic stoichiometric materials

Maia G. Vergniory[1,2,3]*†, Benjamin J. Wieder[4,5,6]*†, Luis Elcoro[7], Stuart S. P. Parkin[8], Claudia Felser[3], B. Andrei Bernevig[6], Nicolas Regnault[6,9]*

Topological quantum chemistry and symmetry-based indicators have facilitated large-scale searches for materials with topological properties at the Fermi energy (E_F). We report the implementation of a publicly accessible catalog of stable and fragile topology in all of the bands both at and away from E_F in the 96,196 processable entries in the Inorganic Crystal Structure Database. Our calculations, which represent the completion of the symmetry-indicated band topology of known nonmagnetic materials, have enabled the discovery of repeat-topological and supertopological materials, including rhombohedral bismuth and Bi_2Mg_3. We find that 52.65% of all materials are topological at E_F, roughly two-thirds of bands across all materials exhibit symmetry-indicated stable topology, and 87.99% of all materials contain at least one stable or fragile topological band.

The field of solid-state physics has over the past 15 years been advanced in large part by the discovery of nontrivial electronic band topology in nonmagnetic crystalline solids (*1*, *2*). Since the conceptual proposal and theoretical prediction of the first two-dimensional (2D) (*3*, *4*) and 3D (*5*) topological insulators (TIs), researchers have predicted solid-state realizations of topological phases of matter at a rapid pace. Notable examples include symmetry-protected topological semimetals (TSMs) (*6*–*10*) and topological crystalline insulators (TCIs) (*11*–*17*). Owing to negligible electron-electron interactions, many of the theoretical predictions of TI, TCI, and TSM phases in solid-state materials were quickly confirmed in spectroscopic and transport experiments (*18*–*27*).

Initially, solid-state TIs and TSMs were believed to be rare and esoteric phases of matter. However, over the past 4 years, the theories of topological quantum chemistry (TQC) (*28*, *29*) and symmetry-based indicators (SIs) (*16*, *17*, *30*–*36*) have facilitated high-throughput searches for magnetic (*37*) and nonmagnetic (*38*–*40*) topological materials, revealing solid-state TIs and TSMs to be ubiquitous in nature. For example, Vergniory *et al.* (*38*) reported high-throughput analyses of the symmetry-indicated stable band topology at the Fermi level (E_F) in ~26,000 stoichiometric, inorganic, "high-quality" crystal structures obtained from the Inorganic Crystal Structure Database (ICSD) (*41*). Of the ~26,000 ICSD entries, roughly ~7000 were found to be topological at E_F (*38*).

This result raises two questions. First, the complete ICSD contains 96,196 stoichiometric ICSD entries with processable (noncorrupt) structural data as defined in text S4 (*42*), raising the question of whether a high percentage of all known inorganic materials are topological at E_F. Second, energetically isolated groupings of bands may exhibit nontrivial topology, independent of the electronic filling. Hence, the distribution of topological bands away from E_F in real materials is also a major outstanding question in the study of quantum matter. In this work, we answer both questions by performing a complete study of symmetry-indicated band topology in all known, stoichiometric, inorganic crystalline solids without magnetic order. In contrast to the previous high-throughput topological materials searches in (*38*–*40*), our calculations included a complete diagnosis of symmetry-indicated band topology away from E_F. Using TQC and nonmagnetic SIs, we computed the symmetry-indicated, nonmagnetic band topology of all bands in all 96,196 stoichiometric ICSD entries with valid structure files from electronic fillings ranging from the core shell up to at least $2N_e$ above, where N_e is the number of valence electrons. Unlike in (*38*–*40*), the SIs used in this work include the SIs of stable band topology—which indicate familiar strong and weak TI and TCI phases—as well as the recently introduced SIs of fragile band topology (*43*–*46*)—which represent more exotic TCI phases with topological corner modes (*34*) and twisted-boundary edge states (*47*). Fragile topological phases have emerged as an area of intense interest after recent theoretical studies indicated that the superconducting and correlated-insulating states in magic-angle twisted bilayer graphene may originate from nearly flat fragile topological bands (*48*, *49*).

Through our calculations, we discovered previously unrecognized classes of topological materials, including enforced TSMs with energetically isolated fragile bands at E_F, repeat-topological (RTopo) materials with stable topological insulating gaps at and just below E_F, and supertopological (STopo) materials in which every energetically isolated set of bands above the core shell is stable topological. We have upgraded the Topological Materials Database (*50*)—a publicly available online catalog of topological materials—for accessing and intuitively searching the results of this study. In (*42*), we present detailed statistics for our computations, offer lists of idealized materials in each topological class, and highlight the features of the Topological Materials Database (*50*) implemented for this work, which include dynamical zoom options, density-of-states calculations, electronic-structure calculations in the absence of spin-orbit coupling (SOC), and advanced search options (see text S7 for a complete list of added features). We find that 52.65% of all materials are topological at E_F, and roughly two-thirds of bands across all materials exhibit the symmetry-indicated topology of 3D strong TIs, weak TIs, TCIs, and higher-order TIs. These phases are classified as topologically stable, as they are robust to the addition of trivial or fragile bands (although sensitive to the relaxation of time-reversal and crystal symmetries) (*1*–*5*, *11*–*17*, *29*, *30*). Most surprisingly, we find that 87.99% of all materials contain at least one stable or fragile topological band in their energy spectrum, even if away from E_F. Our discovery of ubiquitous electronic band topology in solid-state materials motivates the formulation of a new periodic table of chemical compounds in which electronic bands in materials are sorted by a combination of common topological features and chemical and structural properties.

Lastly, our characterization of electronic band topology away from E_F is immediately useful in numerous experimental settings, including angle-resolved photoemission spectroscopy (ARPES) experiments, which measure states at and below E_F, and pump-probe experiments, in which electrons can be excited to observe bands above E_F. As discussed below, our theoretical calculations provide robust explanations for previously puzzling ARPES data. Beyond photoemission experiments, states away from E_F may also be accessed

[1]Donostia International Physics Center, 20018 Donostia–San Sebastian, Spain. [2]IKERBASQUE, Basque Foundation for Science, Bilbao, Spain. [3]Max Planck Institute for Chemical Physics of Solids, 01187 Dresden, Germany. [4]Department of Physics, Massachusetts Institute of Technology, Cambridge, MA 02139, USA. [5]Department of Physics, Northeastern University, Boston, MA 02115, USA. [6]Department of Physics, Princeton University, Princeton, NJ 08544, USA. [7]Department of Condensed Matter Physics, University of the Basque Country UPV/EHU, 48080 Bilbao, Spain. [8]Max Planck Institute of Microstructure Physics, 06120 Halle, Germany. [9]Laboratoire de Physique de l'École Normale Supérieure, PSL University, CNRS, Sorbonne Université, Université Paris Diderot, Sorbonne Paris Cité, Paris, France.
***Corresponding author. Email: regnault@princeton.edu (N.R.); maiagvergniory@dipc.org (M.G.V.); bwieder@mit.edu (B.J.W.)**
†These authors contributed equally to this work.

via (electro)chemical doping, electrostatic gating, hydrostatic pressure, and nonequilibrium photoexcitation, and are relevant to Floquet engineering and nonlinear optical experiments (*51*). Additionally, even in topologically trivial insulating materials, exotic interaction effects may be accessed by doping or gating the Fermi level into an isolated topological band. For example, independent of the cumulative band topology at higher energies, if a superconducting state is induced from a partially occupied, isolated band, then the nontrivial stable or fragile topology of the isolated band has been shown to provide a lower bound on the superfluid weight (*52*, *53*).

Dataset generation

In this work, we applied TQC (*28*, *29*) and stable and fragile SIs (*16*, *17*, *30*–*37*, *43*–*46*) to diagnose the symmetry-indicated topology of all isolated bands above the core shell in the stoichiometric materials in the ICSD. To obtain the topological classification of each separated group of bands in the energy spectrum, we adopted the methods previously used in the high-throughput material searches in (*37*, *38*). Uniquely in this work, after computing the electronic structure using the intrinsic electronic filling $\nu = N_e$, we varied ν to compute the topological properties above and below E_F. Below, we summarize the numerical and topological details of our calculations (Fig. 1); further specific details are provided in texts S2 to S4.

We began by selecting one of the 96,196 processable entries in the ICSD with a stoichiometric chemical formula. We next converted the crystal structure listed in the ICSD into an input file for density functional theory (DFT) calculations, excluding cases in which the ICSD structure file was missing atoms listed in the chemical formula or reported atomic positions incompatible with the symmetries of the material space group (SG) (text S4). We then performed self-consistent, ab initio calculations of the electronic band structure and density of states with ν set to charge neutrality ($\nu = N_e$), filtering out cases in which the calculations did not converge or converged to a magnetic (meta)stable state.

Next, as detailed in text S3, we used the VASP2Trace (*54*) and Check Topological Mat (*55*) programs to determine the unitary symmetry eigenvalues of each of the Bloch-state multiplets at each of the maximal (high-symmetry) k vectors. For each degenerate multiplet of Bloch states, the combination of extracted symmetry eigenvalues establishes a correspondence to an irreducible small corepresentation (corep) of the little group at k (*56*). Then, choosing increasing integer values of the valence electronic filling ν from 0 to at least $2N_e$ (or up to the first filling $\nu > N_e$ at which the electronic band structure is not symmetric and convergent; see text S3A), we identified fillings at which all of the Bloch states in each maximal k vector are fully occupied, such that a gap is present in the energy spectrum at each maximal k vector (although not necessarily at the same energy, as states are taken to be separately filled up to ν at each k point). Lastly, at $\nu = N_e$, as well as at each ν at which there is a gap at all maximal k points, we extracted the symmetry data vector (*29*, *37*, *38*), defined as the multiplicities of the small coreps corresponding to the filled Bloch-eigenstate multiplets across each of the maximal k vectors.

Crucially, the symmetry data vector at each ν facilitates the topological classification of filled or energetically isolated groupings of bands. Specifically, in each SG, the elementary band coreps (EBRs) correspond to the independent, topologically trivial [i.e., "Wannierizable" (*57*)] bands (*28*, *58*). Hence, if a set of bands does not transform in an integer-valued linear combination of EBRs, then the bands exhibit nontrivial stable topology. As established in (*37*, *38*) and detailed in text S2, a symmetry data vector can be classified into one of five possible topological classes. First, if the symmetry data vector corresponds to a set of Bloch states in which a degenerate multiplet at a maximal k point is partially filled, then the system is an enforced semimetal with Fermi degeneracy (ESFD). As an example, 3D HgTe [ICSD 31845, SG 216 ($F\bar{4}3m$)] is an experimentally established, ESFD-classified TSM that realizes a 2D TI phase in few-layer quantum-well geometries (*4*). Next, if the symmetry data vector corresponds to a set of high-symmetry-point Bloch eigenstates that are implied by the compatibility relations to connect to other states outside of the symmetry data along a high-symmetry line or plane, then the system is an enforced semimetal (ES). A well-studied ES material is the archetypal higher-order-topological Dirac semimetal Cd_3As_2 [ICSD 107918, SG 137 ($P4_2/nmc$)] (*6*, *19*, *59*, *60*). Conversely, if the symmetry data vector satisfies the compatibility relations along all high-symmetry lines and planes, then the bands that transform in the symmetry data either correspond to a stable or fragile TI or TCI, correspond to a TSM phase, or are topologically trivial. In the case in which the symmetry data vector corresponds to a stable topological set of bands, the bands described by the symmetry data may be classified into two categories. If stable topological bands transform in an integer-valued linear combination of pieces of a disconnected EBR, then the bands are classified as a split EBR (SEBR) (*28*, *58*). Alternatively, if stable topological bands do not transform in an integer-valued linear combination of disconnected EBR pieces, then the bands are classified as "not equal to a linear combination" (NLC). The archetypal symmetry-indicated stable topological material is the experimentally established 3D TI Bi_2Se_3 [ICSD 617079, SG 166 ($R\bar{3}m$)] (*18*), which is classified as SEBR. Lastly, if the symmetry data of an isolated grouping of bands does correspond to an integer-valued linear combination of EBRs (LCEBR), then the symmetry eigenvalues of the occupied bands are compatible with either fragile or trivial topology [although the bands may also exhibit non–symmetry-indicated stable topology (*34*)].

In the above cases in which the symmetry data vector satisfies the compatibility relations (SEBR, NLC, and LCEBR), a finer topological classification can be obtained using stable and fragile topological SIs. First, in the presence of non-negligible SOC, nonmagnetic SEBR and NLC bands correspond to stable TIs and TCIs with anomalous surface Dirac cones and helical hinge states (*16*, *17*, *30*). Conversely, as

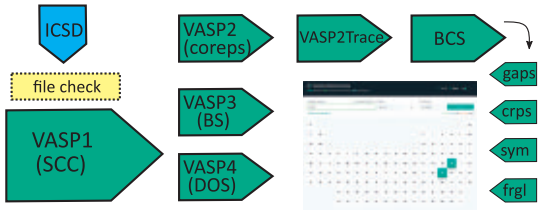

Fig. 1. Workflow schematic for generating the Topological Materials Database. For each entry in the Inorganic Crystal Structure Database (ICSD) (*41*), we first determine whether the entry is stoichiometric, contains coordinates for all of the atoms listed in the chemical formula, and lists atomic coordinates compatible with the crystallographic space group of the material. We then perform self-consistent DFT calculations, both with and without incorporating the effects of spin-orbit coupling (SOC). Irrespective of whether SOC is taken into account, each DFT calculation consists of four steps (labeled VASP1 to VASP4; see text S4 for details) in which we perform a self-consistent calculation (SCC) of the charge density, obtain the symmetry data [small corepresentation (corep) multiplicities] at all integer electronic fillings above the core shell, and compute the electronic band structure (BS) at E_F and the density of states (DOS). Lastly, using the VASP2Trace program (*54*) previously implemented for (*38*) and an updated version of the Check Topological Mat program on the Bilbao Crystallographic Server (*55*) implemented for this work, we compute for each DFT calculation the stable and fragile topological classifications of all isolated groupings of bands above the core shell as determined by the compatibility relations in topological quantum chemistry (*28*) (see texts S2 and S3 for details).

shown in (*29*, *31*, *34*, *36*) and detailed in text S6, in the absence of SOC and magnetism, bands with nontrivial stable SIs correspond to TSM (specifically SEBR-SM and NLC-SM) phases with bulk nodal degeneracies in the Brillouin zone (BZ) interior and topological surface Fermi arcs or flat band–like surface and intrinsic hinge states. Lastly, it was recently discovered that LCEBR bands with or without SOC may in some cases be further classified as fragile topological (*43*, *44*) through the fragile SIs elucidated in (*45*, *46*). For all possible classes of symmetry-indicated stable and fragile TI, TCI, and TSM phases in the presence of SOC, we provide a detailed enumeration of the most idealized material realizations across all stoichiometric materials in the ICSD (text S11). Although we find that there do not exist materials in which the entire valence manifold is fragile topological, we do find numerous examples of experimentally accessible materials with well-isolated fragile bands close to E_F (see text S11E).

We begin by summarizing the symmetry-indicated topological properties of the stoichiometric materials in the ICSD. First, we discuss statistical trends uncovered across the materials analyzed in this work, including the distribution of topological features at E_F and statistics for SOC-driven topological phase transitions, which are defined by comparing the stable topology at E_F for each ICSD entry in calculations performed with and without incorporating the effects of SOC. We then highlight material candidates in which our investigations have uncovered previously unrecognized topological features at experimentally accessible energies.

Material statistics

At the time of our investigations, the ICSD (*41*) contained 193,426 entries, of which 96,196 characterized stoichiometric chemical compounds with processable (noncorrupt) CIF structure files. We performed first-principles calculations on all 96,196 processable stoichiometric entries, resulting in convergent electronic structures for 73,234 entries in the presence of SOC, which we grouped into 38,298 unique materials by common chemical formulas and stable topology at E_F (see text S3A). In Fig. 2A,

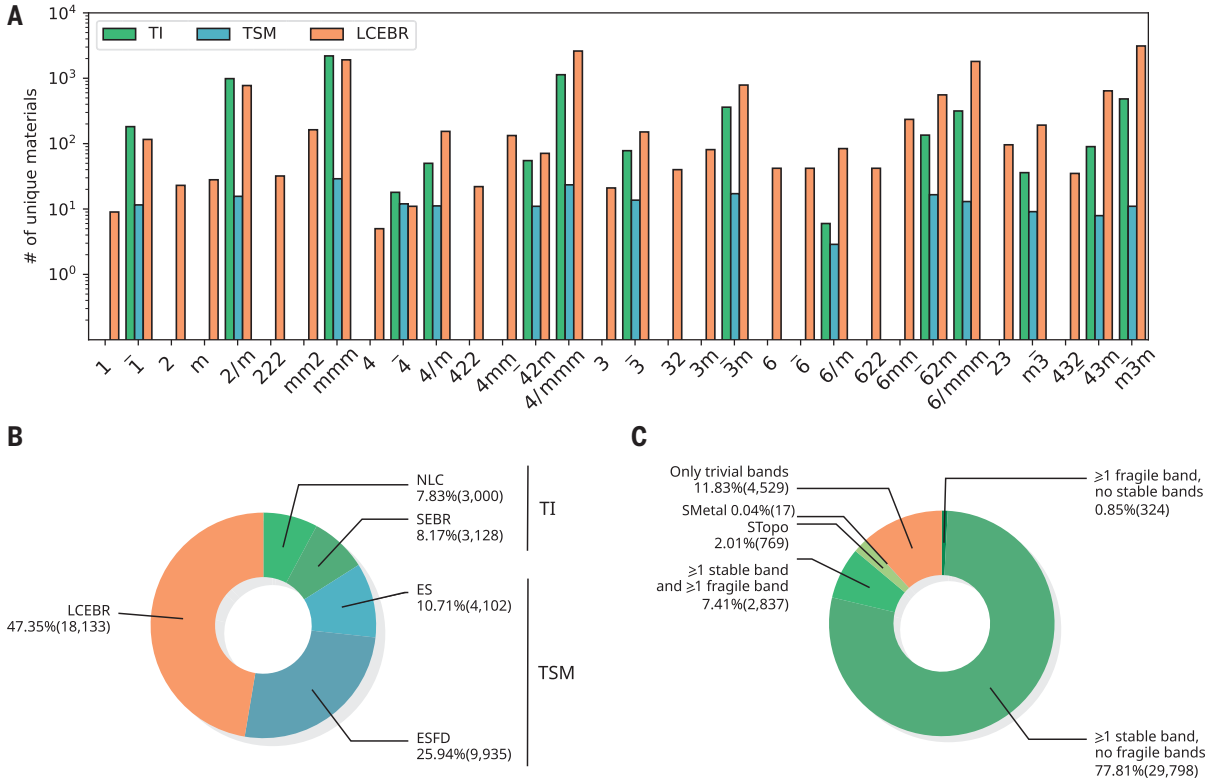

Fig. 2. Topology of the stoichiometric materials in the ICSD. (**A**) Distribution of the topology at E_F with SOC among the 38,298 stoichiometric unique materials in the ICSD as defined in text S4, subdivided by crystallographic point group (PG). For each of the 32 PGs of the 230 space groups (*56*), we list the number of symmetry-indicated stable topological (crystalline) insulators (NLC- or SEBR-classified TIs and TCIs), TSMs (ES or ESFD), or unique materials with trivial symmetry-indicated topology (LCEBR). (**B**) The distribution of the topology at E_F across all PGs and topological classes (*37*, *38*) (text S2). Of the unique materials at E_F, 16.00% are TIs or TCIs and 36.65% are TSMs, implying that a remarkable 52.65% of the stoichiometric materials in nature are topological at intrinsic filling. (**C**) Distribution of the symmetry-indicated band topology away from E_F across the stoichiometric unique materials in the ICSD. An overwhelming 87.99% of materials contain at least one symmetry-indicated stable or fragile topological band across the energy range of our first-principles calculations (see text S4 for calculation details), which is even more notable when considering that many materials (e.g., noncentrosymmetric crystals) have SGs without either stable or fragile SIs [see (*1*, *16*, *17*, *29*–*36*, *45*, *46*)]. Because previous works have demonstrated the existence of non–symmetry-indicated TI and TCI phases in materials with trivial stable SIs (*1*, *3*, *13*, *14*, *34*), then the percentage of materials in nature with topological bands at and away from E_F is necessarily even larger than 87.99%, suggesting an intriguing direction for future study. In addition to the repeat-topological and supertopological materials (Fig. 4 and text S9), we have also discovered the existence of supermetallic (SMetal) materials, in which all of the bands above the core shell are connected up to at least a filling of $2N_e$, where N_e is the number of valence electrons (texts S6 and S8). Although SMetal materials are relatively rare in the presence of SOC [17 unique materials; see (C)], there are 1138 unique SMetal materials without SOC, which is consistent with the general trend of increased band connectivity in materials when neglecting the effects of SOC (Table 1 and texts S6, S8, and S10). In text S8, we provide further detailed statistics for the symmetry-indicated band topology at and away from E_F across all of the stoichiometric materials in the ICSD.

we show the distribution of the topology at E_F for the unique materials within each of the 32 crystallographic point groups of the 230 nonmagnetic SGs, and in Fig. 2B, we show the total number of unique materials in each topological class. We find that at intrinsic filling, 6128 unique materials are symmetry-indicated stable TIs or TCIs, and 14,037 unique materials are TSMs. Our findings represent a doubling of the number of known topological materials from those identified in previous high-throughput calculations (*38*–*40*). Furthermore, we find that 52.65% of unique materials are symmetry-indicated stable TIs, TCIs, or TSMs at E_F, which also represents a doubling from previous estimates of the percentage of 3D topological materials in nature (*38*, *39*). This percentage is considerably higher than the percentage of topological stoichiometric 2D materials, which has previously been computed to lie within the range of a few to 20% (*61*, *62*).

In texts S5 and S8, we respectively provide detailed statistics for the computational resources expended for the calculations performed for this work, and for the topology at and away from E_F across the stoichiometric materials in the ICSD. In the presence of SOC, we find that an overwhelming 87.99% of unique materials contain at least one symmetry-indicated stable or fragile topological band (Fig. 2C). This percentage is all the more surprising, as we have included materials whose SGs have trivial stable SI groups [e.g., noncentrosymmetric crystals without high-fold rotoinversion symmetries (*16*, *17*, *29*)], such that all isolated bands in the SG are classified by SIs as trivial or fragile. Taking all 38,298 unique materials into consideration—including the materials in SGs with trivial stable SI groups (*16*, *17*, *29*)—we find that nearly two-thirds of all energetically isolated bands in nature exhibit symmetry-indicated stable topology. Hence, our investigations reveal that even away from E_F, the majority of electronic features in solid-state materials can only be robustly modeled by incorporating topological band theory.

Lastly, we have also computed detailed statistics for the relative topology of each stoichiometric ICSD entry with and without incorporating the effects of SOC. As discussed above and in text S10 and demonstrated in (*29*, *31*, *34*, *36*), all symmetry-indicated, nonmagnetic stable topological phases without SOC are TSMs. Hence, in the absence of SOC, there are ESFD- and ES-classified TSMs—in which the nodal degeneracies respectively lie at high-symmetry points (ESFD) and along high-symmetry lines and planes (ES)—as well as SEBR-SM– and NLC-SM–classified TSMs, in which the bands along all high-symmetry lines and planes satisfy the insulating compatibility relations (*28*, *58*) and the nodal degeneracies lie in the BZ interior. In Table 1, we show the number of unique materials in each topological class with and without SOC. Table 1 indicates that the majority of ES-, NLC-SM–, and SEBR-SM–classified TSMs without SOC become stable TIs and TCIs (NLC- and SEBR-classified) when SOC is introduced, whereas ESFD-classified TSMs without SOC overwhelmingly remain TSMs (ES- and ESFD-classified) when the effects of SOC are incorporated. In text S10, we provide complete statistics for the SOC-driven topological phase transitions at E_F in the ICSD; in text S11D, we identify representative materials for each class of SOC-driven TSM-insulator transition in Table 1.

Material candidates

We next highlight the materials in which our investigations have revealed or provided a different context for topological features within an experimentally accessible range from E_F; an extensive tabulation of the most idealized realizations in nature of all previously established classes of symmetry-indicated TI, TCI, and TSM phases in the presence of SOC is further provided in text S11. To begin, in Fig. 3, we present experimentally favorable material candidates with stable and fragile topology at E_F. First, in Fig. 3A, we show the electronic band structure of $MoGe_2$ [ICSD 76139, SG 139 ($I4/mmm$)]—a higher-order-topological, centrosymmetric TSM (*59*) in which the doubly degenerate valence and conduction bands that meet along ΓM_1 in fourfold Dirac points at E_F, along with the next-highest doubly degenerate valence bands, are as a set fragile topological (i.e., the two conduction bands and four valence bands closest to E_F in Fig. 3A as a set exhibit nontrivial fragile SIs). Next, in Fig. 3B, we highlight $HgBa_2CuO_4$ [ICSD 75720, SG 123 ($P4/mmm$)]—a well-studied high-temperature cuprate superconductor (*63*), which we find to be an ideal ESFD-classified metal with a doubly degenerate, half-filled band at E_F. Then, in Fig. 3, C and D, we respectively show the band structures of the transition metal chalcogenides (TMCs) $TaSe_2$ [ICSD 24313, SG 164 ($P\bar{3}m1$)] and TiS_2 [ICSD 72042, SG 227 ($Fd\bar{3}m$)]. Both $TaSe_2$ and TiS_2 host well-established 2D charge density wave phases (*64*–*66*); in this work, we discover that the valence bands extending to ~3 eV below E_F in 3D $TaSe_2$ are fragile topological, as are the conduction bands extending to ~1.5 eV above E_F in 3D TiS_2.

In Fig. 3, E and F, we respectively show the electronic band structures of the closely related TMCs Ta_2NiSe_5 [ICSD 61148, SG 15 ($C2/c$)] and Ta_2NiSe_7 [ICSD 61352, SG 12 ($C2/m$)], which show particular promise for experimental investigations owing to their relatively simple normal-state Fermi surfaces. Ta_2NiSe_5 and Ta_2NiSe_7 belong to a larger family of materials previously highlighted for hosting metal-insulator transitions and strongly correlated phases of matter. Previous investigations have demonstrated that the layered TMC Ta_2NiSe_5 hosts an exotic exciton-insulator phase (*67*, *68*). By comparing the parity (inversion) eigenvalues of Ta_2NiSe_5 with and without incorporating the effects of SOC (Fig. 4, A and B), we find that the narrow-gap semiconducting state of Ta_2NiSe_5 in fact realizes a 3D TI phase originating from weak, SOC-driven band inversion at the Γ point. Unlike Ta_2NiSe_5, Ta_2NiSe_7 (Fig. 3F) is instead a quasi-1D TMC and has been previously highlighted for exhibiting a charge density wave instability (*69*). Ta_2NiSe_7 is closely related to the ES-classified, structurally chiral, quasi-1D TMC Weyl semimetal Ta_2ISe_8

Table 1. SOC-driven topological phase transitions in the unique stoichiometric materials in the ICSD. We show the statistics for the band topology at E_F for the unique stoichiometric materials in the ICSD with and without incorporating the effects of SOC in first-principles calculations. Rows list the topological classification at E_F in the absence of SOC; columns list the topological classification at E_F in the presence of SOC. We find that nearly two-thirds of ES-classified unique materials without SOC become stable TIs and TCIs with SOC, whereas most ESFD TSMs without SOC remain semimetallic when SOC is incorporated. Conversely, more than 85% of NLC-SM– and SEBR-SM–classified TSMs without SOC [see (*31*, *34*, *36*) and text S6] become stable TIs and TCIs after incorporating SOC. Complete statistics for the SOC-driven topological phase transitions at E_F in the ICSD are provided in text S10, and representative materials for each class of TSM-insulator phase transition are provided in text S11D.

	NLC	SEBR	ES	ESFD	LCEBR
ES	2104 (35%)	1585 (26.4%)	944 (15.7%)	38 (0.6%)	1335 (22.2%)
ESFD	207 (1.5%)	1089 (7.8%)	2792 (19.9%)	9423 (67.3%)	486 (3.5%)
LCEBR	49 (0.3%)	78 (0.5%)	42 (0.3%)	24 (0.2%)	15,672 (98.8%)
NLC-SM	208 (82.9%)	24 (9.6%)	2 (0.8%)	–	17 (6.8%)
SEBR-SM	–	38 (86.4%)	5 (11.4%)	–	1 (2.3%)

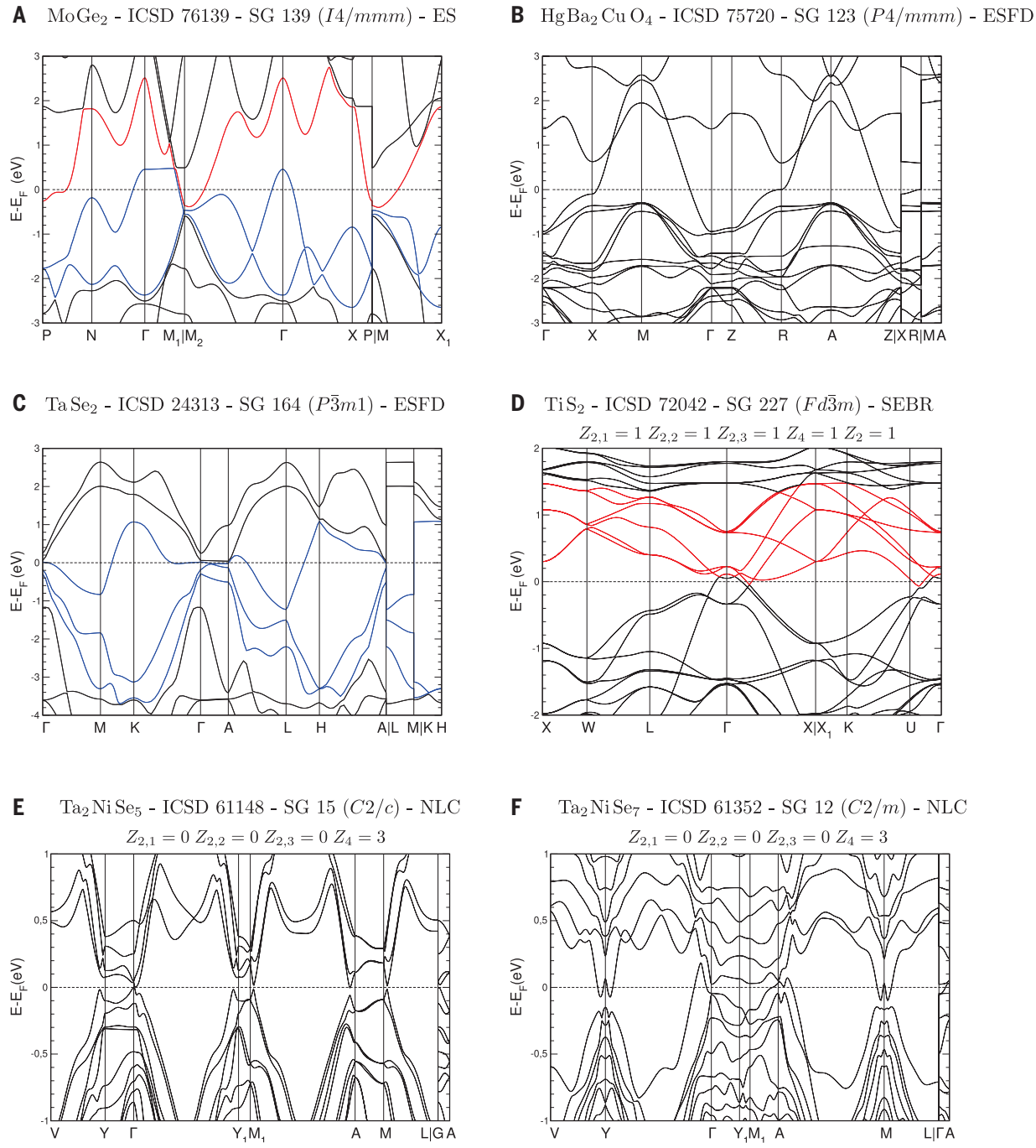

Fig. 3. Material candidates with topological features at E_F. We highlight materials with previously unidentified or recontextualized topological features at E_F. In all panels, bands with symmetry-indicated stable and trivial topology are plotted in black, symmetry-indicated fragile valence bands in blue, and symmetry-indicated fragile conduction bands in red. (**A**) $MoGe_2$ [ICSD 76139, SG 139 (*I*4/*mmm*)] is a higher-order-topological, centrosymmetric Dirac TSM (*59*) in which the doubly degenerate valence and conduction bands that meet along ΓM_1 in fourfold Dirac points at E_F, along with the next-highest doubly degenerate valence bands, are as a set fragile topological. (**B**) $HgBa_2CuO_4$ [ICSD 75720, SG 123 (*P*4/*mmm*)]—an established high-T_c superconductor (*63*)—is found to be an ideal ESFD-classified metal with a doubly degenerate, half-filled band at E_F. (**C** and **D**) In the transition-metal chalcogenides (TMCs) $TaSe_2$ [ICSD 24313, SG 164 ($P\bar{3}m1$)] and TiS_2 [ICSD 72042, SG 227 ($Fd\bar{3}m$)]—previously determined to host 2D charge density wave phases (*64*–*66*)—the highest valence and lowest conduction bands are respectively fragile topological. (**E**) Ta_2NiSe_5 [ICSD 61148, SG 15 (*C*2/*c*)] is a layered TMC that has been demonstrated to host an exciton-insulator phase (*67*, *68*); we find that the narrow-gap semiconducting state of Ta_2NiSe_5 is in fact a 3D TI. (**F**) Conversely, the closely related quasi-1D TMC Ta_2NiSe_7 [ICSD 61352, SG 12 (*C*2/*m*)]—which we find to also be a 3D TI—exhibits a charge density wave instability (*69*). In Fig. 4, we provide further analysis of the band ordering in Ta_2NiSe_5 and Ta_2NiSe_7.

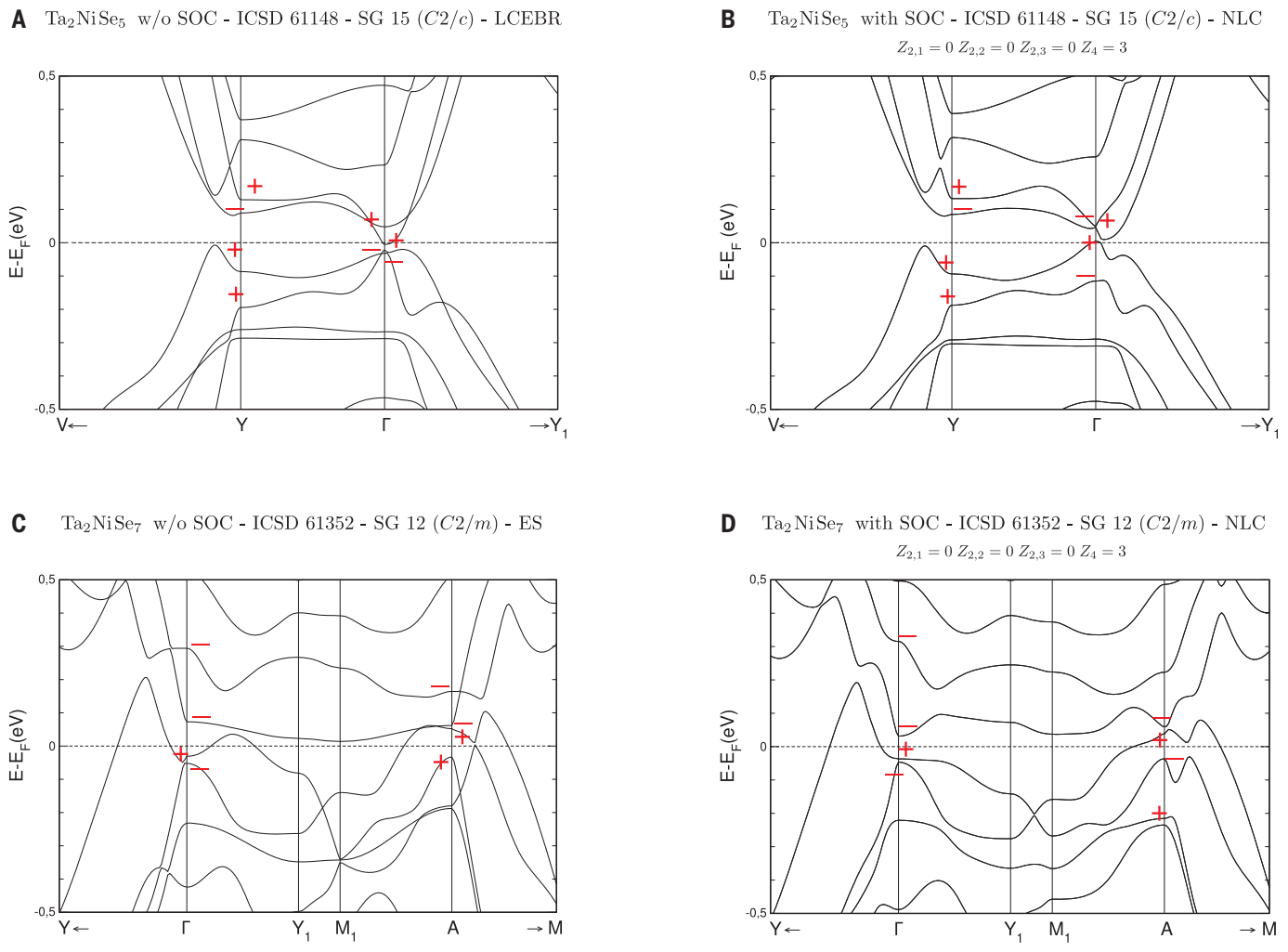

Fig. 4. Topological band-inversion transitions in Ta_2NiSe_5 and Ta_2NiSe_7. We analyze the band ordering of Ta_2NiSe_5 [ICSD 61148, SG 15 (*C2/c*)] and Ta_2NiSe_7 [ICSD 61352, SG 12 (*C2/m*)] with and without SOC. In all panels, the red + and − symbols respectively indicate Kramers pairs of states with positive and negative parity (inversion) eigenvalues. (**A** and **B**) The electronic band structure of Ta_2NiSe_5 respectively neglecting and incorporating the effects of SOC. Without SOC (A), Ta_2NiSe_5 exhibits trivial symmetry-indicated stable topology at E_F (i.e., Ta_2NiSe_5 is LCEBR-classified without SOC). When SOC is reintroduced in (B), it drives a band inversion at Γ, transitioning Ta_2NiSe_5 into a Z_4 = 3 3D TI phase. (**C** and **D**) The electronic band structure of Ta_2NiSe_7 respectively neglecting and incorporating the effects of SOC. Unlike in Ta_2NiSe_5 (A), the bands at Γ and *A* ($k_{x,y}$ = 0, k_z = 0, π, respectively) in Ta_2NiSe_7 (C) are already inverted by orbital coupling in the *xy*- (*ab*-) plane, taking the Ta_2NiSe_7 chains to be oriented along the *z*- (*c*-axis) direction (see ICSD 61352). Hence, without SOC, Ta_2NiSe_7 realizes an ES-classified nodal-line-semimetal phase with the same parity eigenvalues as a *z*-directed weak TI [($z_{2,1}$, $z_{2,2}$, $z_{2,3}$, z_4) = (0012) when subduced onto SG 2 ($P\bar{1}$) (text S6B) (*5*, *30*, *31*, *36*)]. When SOC is reintroduced, the nodal lines at E_F in Ta_2NiSe_7 become gapped, the band inversion at *A* is removed by SOC, and the bands at Γ remain inverted, overall driving Ta_2NiSe_7 into a Z_4 = 3 3D TI phase.

[ICSD 35190, SG 97 (*I*422); see text S11C], which was shown in recent experimental work to exhibit a topological (axionic) charge density wave that competes with a superconducting phase under applied pressure (*26*, *27*, *70*). In this work, we find that the room-temperature phase of Ta_2NiSe_7 is a 3D TI originating from a combination of anisotropic orbital coupling and SOC-driven band inversion. Specifically, we find that without SOC, Ta_2NiSe_7 is an ES-classified nodal-line semimetal with band inversions at $k_{x,y}$ = 0, k_z = 0, π (respectively the Γ and *A* points in Fig. 4C) driven by orbital coupling in the *xy*- (*ab*-) plane [taking the Ta_2NiSe_7 chains to be oriented along the *z*- (*c*-axis) direction; see ICSD 61352]. This can be seen by recognizing that Ta_2NiSe_7 without SOC (Fig. 3C) exhibits the same parity eigenvalues as a *z*-directed weak TI [($z_{2,1}$, $z_{2,2}$, $z_{2,3}$, z_4) = (0012) when subduced onto SG 2 ($P\bar{1}$); see text S6B and (*5*, *30*, *31*, *36*)]. When SOC is reintroduced, the nodal lines at E_F in Ta_2NiSe_7 become gapped, and the band inversion at *A* is removed, whereas the bands at Γ remain inverted (see Fig. 4D).

Finally, we performed a high-throughput search for topological bands away from E_F. Our calculations have revealed the existence of two additional classes of topological materials: RTopo materials with stable topological insulating gaps at and just below E_F (Fig. 5A and text S9A), and STopo materials in which every energetically isolated set of bands above the core shell exhibits symmetry-indicated stable topology (Fig. 5B and text S9B). From a physical perspective, STopo phases result from a combination of EBR splitting, band backfolding from unit cell enlargement, and favorable hopping parameters—hence, the identification of an STopo phase in a particular material can be sensitive to sample and calculation details. In text S9B, we highlight the example of the experimentally established higher-order TI rhombohedral bismuth [ICSD 64703, SG 166 ($R\bar{3}m$)] (*22*), for which some ICSD entries (e.g.,

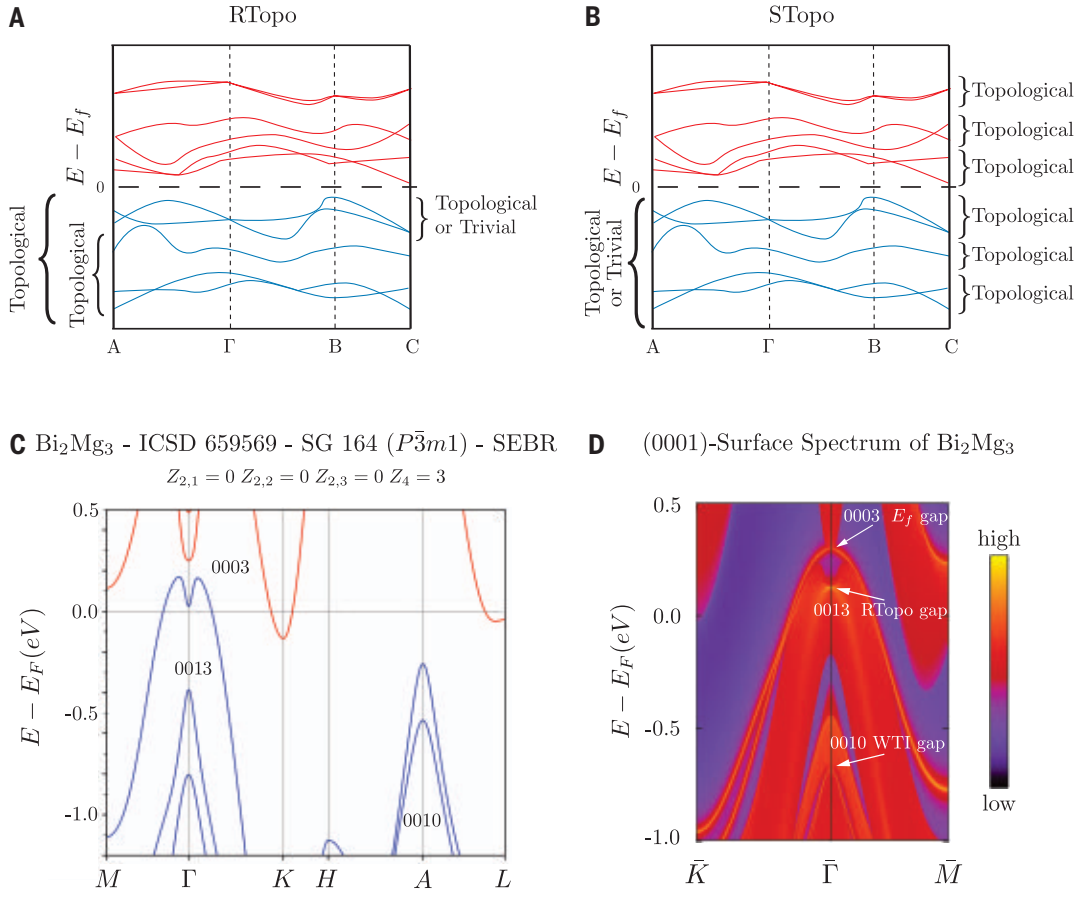

Fig. 5. Repeat-topology and supertopology in Bi_2Mg_3. (**A**) A schematic depiction of a repeat-topological (RTopo) band structure. In RTopo materials, the gap at the Fermi level, as well as the next gap below E_F as measured by band connectivity through TQC (text S2), exhibit cumulative symmetry-indicated stable topology (text S9A). By this definition—which is motivated by the experimental accessibility of topological gaps and boundary states below E_F—we note that it is possible for the isolated bands between E_F and the next-highest gap below E_F to be topologically trivial. (**B**) A schematic depiction of a supertopological (STopo) band structure. In STopo materials, every energetically isolated set of bands in the spectrum exhibits symmetry-indicated stable topology (although the system at E_F is still free to be a TSM or exhibit cumulative trivial topology; see text S9B). (**C**) Bulk band structure of Bi_2Mg_3 [ICSD 659569, SG 164 ($P\bar{3}m1$)], an experimentally established 3D TI (*72*) revealed by our investigations to additionally be RTopo and STopo. The numbers between the stable topological bands in (C) indicate the cumulative stable SIs of each bandgap in the order $Z_{2,1}$, $Z_{2,2}$, $Z_{2,3}$, Z_4 [see (*16*, *17*, *29*, *30*, *33*, *34*) and text S11 for the physical meaning of the stable SIs in SG 164 ($P\bar{3}m1$)]. (**D**) (0001)-surface states of Bi_2Mg_3 obtained from surface Green's functions (see text S9A for calculation details). We have labeled the surface states using the cumulative stable SIs of the projected bulk gaps (as determined by band connectivity; see table S2 for details). Previous ARPES investigations of Bi_2Mg_3 have revealed the existence of "surface resonance bands" below E_F at the (0001)-surface Γ point (*72*). We find that the surface resonance bands in Bi_2Mg_3 are in fact RTopo Dirac-cone surface states in the first gap below E_F (the "0013 RTopo gap"). The surface Green's function calculations exhibit additional twofold-Dirac cone surface states within the projected bulk gap ~0.8 eV below E_F (the "0010 WTI gap"). Although the earlier ARPES experiments also observed surface states in the projected 0010 gap in Bi_2Mg_3 (*72*), we emphasize that the surface states in the 0010 gap in (D) are either trivial or originate from non–symmetry-indicated stable topology, because the cumulative stable SIs (0010) characterize an (obstructed) weak TI phase that does not generically exhibit anomalous twofold-Dirac cones on *z*-normal [(0001)-] surfaces (see text S11A6).

ICSD 64703) are STopo, whereas others (e.g., ICSD 53797) are not. Crucially, Bi (ICSD 64703) and Bi (ICSD 53797) differ only by weak band inversion away from E_F, and both exhibit topologically nontrivial gaps at E_F and just below E_F. This provides a physical motivation for introducing a second topological class—RTopo—for materials like Bi (ICSD 64703). In idealized RTopo materials, there exist two sets of surface or hinge states within consecutive bulk gaps that both lie at energies accessible to ARPES probes without doping (~1.5 eV below E_F), a property that is crucially insensitive to band inversions at experimentally inaccessible energies far from E_F. The repeated topological surface and hinge states of RTopo materials are analogous to the Fermi-arc "quantum ladder" recently observed in the unconventional chiral semimetal alloy Rh_xNi_ySi (*71*) (see text S9A). Lastly, we emphasize that in principle, the STopo and RTopo classification of materials can be extended from stable topological states to fragile topology; however, we did not in this study encounter any ICSD entries with super- or repeat-fragile topology.

In Fig. 5, C and D, we show the bulk and surface states of the RTopo and STopo material Bi_2Mg_3 [ICSD 659569, SG 164 ($P\bar{3}m1$)]. Previous theoretical investigations and spectroscopic experiments have determined Bi_2Mg_3 to be a 3D TI with "surface resonance bands" below E_F at the (0001)-surface Γ point (*72*). We find that the surface resonance bands detected in (*72*) are in fact the RTopo Dirac-cone surface states of Bi_2Mg_3 in the first gap below E_F (the "0013 RTopo gap" in Fig. 5D). In texts S11B and 9C, respectively, we provide detailed tabulations of RTopo and STopo materials in the ICSD. Taken together, the large number of experimentally accessible materials in the ICSD with stable topological bands away from E_F (see text S8), as well as the relative preponderance of RTopo and STopo materials, suggest that many of the surface resonances detected in previous ARPES investigations may in fact be topological surface states protected by spectral flow below E_F.

Discussion

We have performed a complete calculation of symmetry-indicated stable and fragile band topology at and away from E_F across all known stoichiometric, solid-state, nonmagnetic materials. We have discovered that more than half of the materials in nature are stable TIs and TSMs at E_F, and nearly two-thirds of bands across all materials exhibit symmetry-indicated stable topology. Our investigations raise several questions. First, there

exist well-established classes of noncentrosymmetric TI and TCI phases that cannot be diagnosed through SIs. For example, depending on experimental or first-principles calculation details, WTe_2 [ICSD 14348, SG 31 ($Pmn2_1$)] can realize an LCEBR-classified TSM phase with tilted Weyl cones (*73*), or a non–symmetry-indicated twofold-rotation-anomaly TCI phase (*34*). Additionally, like stable topological phases with trivial SIs, there also exist non–symmetry-indicated fragile phases that evade the methods used in this work (*59*). It remains an important outstanding question whether computationally efficient methods beyond TQC and SIs can be formulated for the high-throughput discovery of non–symmetry-indicated topological materials. Several promising studies have recently introduced alternative, scalable methods for high-throughput topological materials identification (*74*, *75*), suggesting a future in which an even larger percentage of materials in nature are recognized as topologically nontrivial. Furthermore, while we have focused our efforts on nonmagnetic topological materials, recent studies have expanded the methods of TQC and SIs to magnetic systems (*29*, *35*), facilitating the high-throughput identification of more than 100 magnetic materials with nontrivial topology at E_F (*37*). Following the results of this work, future investigations may be directed toward identifying nontrivial electronic band topology away from E_F in magnetic materials, in particular targeting bands in which the topology and magnetism are coupled and experimentally tunable.

Lastly, we note that during the final stages of preparing this work, the 3D TMCs $Ta_2Pd_3Te_5$ and $Ta_2Ni_3Te_5$—which are closely related to the TMCs Ta_2NiSe_5 and Ta_2NiSe_7 discovered to be 3D TIs in this work—were theoretically predicted in (*76*) to be non–symmetry-indicated mirror TCIs. Experimental evidence of a 2D TI phase in $Ta_2Pd_3Te_5$ monolayers was also reported in (*77*).

Materials and methods

The first-principles calculations in this work were performed using the Vienna Ab-initio Simulation Package (VASP) (*78*–*80*). We treated the interaction between the ion cores and the valence electrons using the projector augmented-wave method (*81*), and we used the generalized gradient approximation with the Perdew-Burke-Ernzerhof parameterization for the exchange-correlation potential (*82*). For each material calculation, we used as input the structural parameters reported on the ICSD (*41*). For calculations incorporating the effects of SOC, we accounted for the effects of SOC using the second variation method (*83*). For the self-consistent calculations (SCC) of the charge density and the density of states, we used a grid of $11 \times 11 \times 11$ k points centered at the Γ point (k = 0). For the band structure calculations along high-symmetry lines and planes, we then used the input from the SCC. Each segment of the k path contained 20 k points. At each k point along each path segment, we specifically calculated the energies of at least $2N_e$ Bloch states, where N_e is the number of valence electrons in the primitive cell; we did not include bands originating from core-shell atomic orbitals. To identify the symmetry-indicated stable and fragile topological bands in each analyzed material, we then used the VASP2Trace (*54*, *84*) program and an implementation of the Check Topological Mat (*55*) program updated for this work (see text S3 for details). Lastly, to compute the (0001)-surface spectrum of Bi_2Mg_3 in Fig. 5D, we used WANNIER90 (*85*) to construct a Wannier-based tight-binding model from the s and p orbitals of Mg and the p orbitals of Bi, which we found to accurately reproduce the bulk electronic band structure of Bi_2Mg_3 (see text S9A for further calculation details).

REFERENCES AND NOTES

1. B. J. Wieder *et al*., Topological materials discovery from crystal symmetry. *Nat. Rev. Mater.* **7**, 196–216 (2022). doi: 10.1038/s41578-021-00380-2
2. M. Z. Hasan, C. L. Kane, Topological insulators. *Rev. Mod. Phys.* **82**, 3045–3067 (2010). doi: 10.1103/RevModPhys.82.3045
3. C. L. Kane, E. J. Mele, Z_2 topological order and the quantum spin Hall effect. *Phys. Rev. Lett.* **95**, 146802 (2005). doi: 10.1103/PhysRevLett.95.146802; pmid: 16241681
4. B. A. Bernevig, T. L. Hughes, S.-C. Zhang, Quantum spin Hall effect and topological phase transition in HgTe quantum wells. *Science* **314**, 1757–1761 (2006). doi: 10.1126/science.1133734; pmid: 17170299
5. L. Fu, C. L. Kane, E. J. Mele, Topological insulators in three dimensions. *Phys. Rev. Lett.* **98**, 106803 (2007). doi: 10.1103/PhysRevLett.98.106803; pmid: 17358555
6. Z. Wang, H. Weng, Q. Wu, X. Dai, Z. Fang, Three-dimensional Dirac semimetal and quantum transport in Cd_3As_2. *Phys. Rev. B* **88**, 125427 (2013). doi: 10.1103/PhysRevB.88.125427
7. B. J. Wieder, Y. Kim, A. M. Rappe, C. L. Kane, Double Dirac Semimetals in Three Dimensions. *Phys. Rev. Lett.* **116**, 186402 (2016). doi: 10.1103/PhysRevLett.116.186402; pmid: 27203335
8. B. Bradlyn *et al*., Beyond Dirac and Weyl fermions: Unconventional quasiparticles in conventional crystals. *Science* **353**, aaf5037 (2016). doi: 10.1126/science.aaf5037; pmid: 27445310
9. P. Tang, Q. Zhou, S.-C. Zhang, Multiple Types of Topological Fermions in Transition Metal Silicides. *Phys. Rev. Lett.* **119**, 206402 (2017). doi: 10.1103/PhysRevLett.119.206402; pmid: 29219362
10. N. P. Armitage, E. J. Mele, A. Vishwanath, Weyl and Dirac semimetals in three-dimensional solids. *Rev. Mod. Phys.* **90**, 015001 (2018). doi: 10.1103/RevModPhys.90.015001
11. L. Fu, Topological crystalline insulators. *Phys. Rev. Lett.* **106**, 106802 (2011). doi: 10.1103/PhysRevLett.106.106802; pmid: 21469822
12. T. H. Hsieh *et al*., Topological crystalline insulators in the SnTe material class. *Nat. Commun.* **3**, 982 (2012). doi: 10.1038/ncomms1969; pmid: 22864575
13. Z. Wang, A. Alexandradinata, R. J. Cava, B. A. Bernevig, Hourglass fermions. *Nature* **532**, 189–194 (2016). doi: 10.1038/nature17410; pmid: 27075096
14. B. J. Wieder *et al*., Wallpaper fermions and the nonsymmorphic Dirac insulator. *Science* **361**, 246–251 (2018). doi: 10.1126/science.aan2802; pmid: 30026220
15. W. A. Benalcazar, B. A. Bernevig, T. L. Hughes, Electric multipole moments, topological multipole moment pumping, and chiral hinge states in crystalline insulators. *Phys. Rev. B* **96**, 245115 (2017). doi: 10.1103/PhysRevB.96.245115
16. Z. Song, T. Zhang, Z. Fang, C. Fang, Quantitative mappings between symmetry and topology in solids. *Nat. Commun.* **9**, 3530 (2018). doi: 10.1038/s41467-018-06010-w; pmid: 30166539
17. E. Khalaf, H. C. Po, A. Vishwanath, H. Watanabe, Symmetry Indicators and Anomalous Surface States of Topological Crystalline Insulators. *Phys. Rev. X* **8**, 031070 (2018). doi: 10.1103/PhysRevX.8.031070
18. D. Hsieh *et al*., A tunable topological insulator in the spin helical Dirac transport regime. *Nature* **460**, 1101–1105 (2009). doi: 10.1038/nature08234; pmid: 19620959
19. S. Borisenko *et al*., Experimental realization of a three-dimensional Dirac semimetal. *Phys. Rev. Lett.* **113**, 027603 (2014). doi: 10.1103/PhysRevLett.113.027603; pmid: 25062235
20. S.-Y. Xu *et al*., Discovery of a Weyl fermion semimetal and topological Fermi arcs. *Science* **349**, 613–617 (2015). doi: 10.1126/science.aaa9297; pmid: 26184916
21. H. Weng, C. Fang, Z. Fang, B. A. Bernevig, X. Dai, Weyl Semimetal Phase in Noncentrosymmetric Transition-Metal Monophosphides. *Phys. Rev. X* **5**, 011029 (2015). doi: 10.1103/PhysRevX.5.011029
22. F. Schindler *et al*., Higher-order topology in bismuth. *Nat. Phys.* **14**, 918–924 (2018). doi: 10.1038/s41567-018-0224-7; pmid: 30349581
23. D. S. Sanchez *et al*., Topological chiral crystals with helicoid-arc quantum states. *Nature* **567**, 500–505 (2019). doi: 10.1038/s41586-019-1037-2; pmid: 30894753
24. Z. Rao *et al*., Observation of unconventional chiral fermions with long Fermi arcs in CoSi. *Nature* **567**, 496–499 (2019). doi: 10.1038/s41586-019-1031-8; pmid: 30894751
25. N. B. M. Schröter *et al*., Observation and control of maximal Chern numbers in a chiral topological semimetal. *Science* **369**, 179–183 (2020). doi: 10.1126/science.aaz3480; pmid: 32646998
26. W. Shi *et al*., A charge-density-wave topological semimetal. *Nat. Phys.* **17**, 381–387 (2021). doi: 10.1038/s41567-020-01104-z
27. J. Gooth *et al*., Axionic charge-density wave in the Weyl semimetal $(TaSe_4)_2I$. *Nature* **575**, 315–319 (2019). doi: 10.1038/s41586-019-1630-4; pmid: 31590178
28. B. Bradlyn *et al*., Topological quantum chemistry. *Nature* **547**, 298–305 (2017). doi: 10.1038/nature23268; pmid: 28726818
29. L. Elcoro *et al*., Magnetic topological quantum chemistry. *Nat. Commun.* **12**, 5965 (2021). doi: 10.1038/s41467-021-26241-8; pmid: 34645841
30. L. Fu, C. L. Kane, Topological insulators with inversion symmetry. *Phys. Rev. B* **76**, 045302 (2007). doi: 10.1103/PhysRevB.76.045302
31. Y. Kim, B. J. Wieder, C. L. Kane, A. M. Rappe, Dirac Line Nodes in Inversion-Symmetric Crystals. *Phys. Rev. Lett.* **115**, 036806 (2015). doi: 10.1103/PhysRevLett.115.036806; pmid: 26230819
32. J. Kruthoff, J. de Boer, J. van Wezel, C. L. Kane, R.-J. Slager, Topological Classification of Crystalline Insulators through Band Structure Combinatorics. *Phys. Rev. X* **7**, 041069 (2017). doi: 10.1103/PhysRevX.7.041069
33. H. C. Po, A. Vishwanath, H. Watanabe, Symmetry-based indicators of band topology in the 230 space groups. *Nat. Commun.* **8**, 50 (2017). doi: 10.1038/s41467-017-00133-2; pmid: 28667305
34. Z. Wang, B. J. Wieder, J. Li, B. Yan, B. A. Bernevig, Higher-Order Topology, Monopole Nodal Lines, and the Origin of Large Fermi Arcs in Transition Metal Dichalcogenides XTe_2 (X=Mo,W). *Phys. Rev. Lett.* **123**, 186401 (2019). doi: 10.1103/PhysRevLett.123.186401; pmid: 31763917
35. H. Watanabe, H. C. Po, A. Vishwanath, Structure and topology of band structures in the 1651 magnetic space groups. *Sci. Adv.* **4**, eaat8685 (2018). doi: 10.1126/sciadv.aat8685; pmid: 30083612
36. Z. Song, T. Zhang, C. Fang, Diagnosis for Nonmagnetic Topological Semimetals in the Absence of Spin-Orbital Coupling. *Phys. Rev. X* **8**, 031069 (2018). doi: 10.1103/PhysRevX.8.031069
37. Y. Xu *et al*., High-throughput calculations of magnetic topological materials. *Nature* **586**, 702–707 (2020). doi: 10.1038/s41586-020-2837-0; pmid: 33116291
38. M. G. Vergniory *et al*., A complete catalogue of high-quality topological materials. *Nature* **566**, 480–485 (2019). doi: 10.1038/s41586-019-0954-4; pmid: 30814710
39. T. Zhang *et al*., Catalogue of topological electronic materials. *Nature* **566**, 475–479 (2019). doi: 10.1038/s41586-019-0944-6; pmid: 30814713
40. F. Tang, H. C. Po, A. Vishwanath, X. Wan, Comprehensive search for topological materials using symmetry indicators. *Nature* **566**, 486–489 (2019). doi: 10.1038/s41586-019-0937-5; pmid: 30814709
41. G. Bergerhoff, R. Hundt, R. Sievers, I. D. Brown, The inorganic crystal structure data base. *J. Chem. Inf. Comput. Sci.* **23**, 66–69 (1983). doi: 10.1021/ci00038a003
42. See supplementary materials.

43. J. Cano *et al*., Topology of Disconnected Elementary Band Representations. *Phys. Rev. Lett.* **120**, 266401 (2018). doi: 10.1103/PhysRevLett.120.266401; pmid: 30004773
44. H. C. Po, H. Watanabe, A. Vishwanath, Fragile Topology and Wannier Obstructions. *Phys. Rev. Lett.* **121**, 126402 (2018). doi: 10.1103/PhysRevLett.121.126402; pmid: 30296141
45. Z.-D. Song, L. Elcoro, Y.-F. Xu, N. Regnault, B. A. Bernevig, Fragile Phases as Affine Monoids: Classification and Material Examples. *Phys. Rev. X* **10**, 031001 (2020). doi: 10.1103/PhysRevX.10.031001
46. Y. Hwang, J. Ahn, B.-J. Yang, Fragile topology protected by inversion symmetry: Diagnosis, bulk-boundary correspondence, and Wilson loop. *Phys. Rev. B* **100**, 205126 (2019). doi: 10.1103/PhysRevB.100.205126
47. Z.-D. Song, L. Elcoro, B. A. Bernevig, Twisted bulk-boundary correspondence of fragile topology. *Science* **367**, 794–797 (2020). doi: 10.1126/science.aaz7650
48. Z. Song *et al*., All Magic Angles in Twisted Bilayer Graphene are Topological. *Phys. Rev. Lett.* **123**, 036401 (2019). doi: 10.1103/PhysRevLett.123.036401; pmid: 31386469
49. H. C. Po, L. Zou, T. Senthil, A. Vishwanath, Faithful tight-binding models and fragile topology of magic-angle bilayer graphene. *Phys. Rev. B* **99**, 195455 (2019). doi: 10.1103/PhysRevB.99.195455
50. Topological Materials Database, www.topologicalquantumchemistry.com/.
51. D. N. Basov, R. D. Averitt, D. Hsieh, Towards properties on demand in quantum materials. *Nat. Mater.* **16**, 1077–1088 (2017). doi: 10.1038/nmat5017; pmid: 29066824
52. S. Peotta, P. Törmä, Superfluidity in topologically nontrivial flat bands. *Nat. Commun.* **6**, 8944 (2015). doi: 10.1038/ncomms9944; pmid: 26586543
53. F. Xie, Z. Song, B. Lian, B. A. Bernevig, Topology-Bounded Superfluid Weight in Twisted Bilayer Graphene. *Phys. Rev. Lett.* **124**, 167002 (2020). doi: 10.1103/PhysRevLett.124.167002; pmid: 32383962
54. VASP2Trace, https://github.com/zjwang11/irvsp.
55. Check Topological Mat, www.cryst.ehu.es/cryst/checktopologicalmat.
56. C. Bradley, A. Cracknell, *The Mathematical Theory of Symmetry in Solids: Representation Theory for Point Groups and Space Groups* (Clarendon, 1972).
57. A. A. Soluyanov, D. Vanderbilt, Wannier representation of Z_2 topological insulators. *Phys. Rev. B* **83**, 035108 (2011). doi: 10.1103/PhysRevB.83.035108
58. L. Elcoro *et al*., Double crystallographic groups and their representations on the Bilbao Crystallographic Server. *J. Appl. Crystallogr.* **50**, 1457–1477 (2017). doi: 10.1107/S1600576717011712
59. B. J. Wieder *et al*., Strong and fragile topological Dirac semimetals with higher-order Fermi arcs. *Nat. Commun.* **11**, 627 (2020). doi: 10.1038/s41467-020-14443-5; pmid: 32005893
60. C.-Z. Li *et al*., Reducing Electronic Transport Dimension to Topological Hinge States by Increasing Geometry Size of Dirac Semimetal Josephson Junctions. *Phys. Rev. Lett.* **124**, 156601 (2020). doi: 10.1103/PhysRevLett.124.156601; pmid: 32357024
61. A. Marrazzo, M. Gibertini, D. Campi, N. Mounet, N. Marzari, Relative Abundance of Z_2 Topological Order in Exfoliable Two-Dimensional Insulators. *Nano Lett.* **19**, 8431–8440 (2019). doi: 10.1021/acs.nanolett.9b02689; pmid: 31658415
62. D. Wang *et al*., Two-dimensional topological materials discovery by symmetry-indicator method. *Phys. Rev. B* **100**, 195108 (2019). doi: 10.1103/PhysRevB.100.195108
63. Y. Li *et al*., Unusual magnetic order in the pseudogap region of the superconductor $HgBa_2CuO_{4+\delta}$. *Nature* **455**, 372–375 (2008). doi: 10.1038/nature07251; pmid: 18800135
64. J. Zhou *et al*., A library of atomically thin metal chalcogenides. *Nature* **556**, 355–359 (2018). doi: 10.1038/s41586-018-0008-3; pmid: 29670263
65. Y. Chen *et al*., Strong correlations and orbital texture in single-layer 1T-$TaSe_2$. *Nat. Phys.* **16**, 218–224 (2020). doi: 10.1038/s41567-019-0744-9
66. K. Dolui, S. Sanvito, Dimensionality-driven phonon softening and incipient charge density wave instability in TiS_2. *Europhys. Lett.* **115**, 47001 (2016). doi: 10.1209/0295-5075/115/47001
67. Y. F. Lu *et al*., Zero-gap semiconductor to excitonic insulator transition in Ta_2NiSe_5. *Nat. Commun.* **8**, 14408 (2017). doi: 10.1038/ncomms14408; pmid: 28205553
68. G. Mazza *et al*., Nature of Symmetry Breaking at the Excitonic Insulator Transition: Ta_2NiSe_5. *Phys. Rev. Lett.* **124**, 197601 (2020). doi: 10.1103/PhysRevLett.124.197601; pmid: 32469559
69. R. M. Fleming, S. A. Sunshine, C. H. Chen, L. F. Schneemeyer, J. V. Waszczak, Defect-inhibited incommensurate distortion in Ta_2NiSe_7. *Phys. Rev. B* **42**, 4954–4959 (1990). doi: 10.1103/PhysRevB.42.4954; pmid: 9996055
70. Q.-G. Mu *et al*., Suppression of axionic charge density wave and onset of superconductivity in the chiral Weyl semimetal Ta_2Se_8I. *Phys. Rev. Mater.* **5**, 084201 (2021). doi: 10.1103/PhysRevMaterials.5.084201
71. T. A. Cochran *et al*., A Fermi Arc Quantum Ladder. arXiv 2004.11365 (2020).
72. T.-R. Chang *et al*., Realization of a Type-II Nodal-Line Semimetal in Mg_3Bi_2. *Adv. Sci.* **6**, 1800897 (2018). doi: 10.1002/advs.201800897; pmid: 30828518
73. A. A. Soluyanov *et al*., Type-II Weyl semimetals. *Nature* **527**, 495–498 (2015). doi: 10.1038/nature15768; pmid: 26607545
74. J. Gao *et al*., High-throughput screening for Weyl semimetals with S_4 symmetry. *Sci. Bull.* **66**, 667–675 (2021). doi: 10.1016/j.scib.2020.12.028
75. K. Choudhary, K. F. Garrity, N. J. Ghimire, N. Anand, F. Tavazza, High-throughput search for magnetic topological materials using spin-orbit spillage, machine learning, and experiments. *Phys. Rev. B* **103**, 155131 (2021). doi: 10.1103/PhysRevB.103.155131
76. Z. Guo *et al*., Quantum spin Hall effect in $Ta_2M_3Te_5$ (M = Pd, Ni). *Phys. Rev. B* **103**, 115145 (2021). doi: 10.1103/PhysRevB.103.115145
77. X. Wang *et al*., Observation of quantum spin Hall states in $Ta_2Pd_3Te_5$. arXiv 2012.07293 (2020).
78. G. Kresse, J. Furthmüller, Efficiency of ab-initio total energy calculations for metals and semiconductors using a plane-wave basis set. *Comput. Mater. Sci.* **6**, 15–50 (1996). doi: 10.1016/0927-0256(96)00008-0
79. G. Kresse, J. Furthmüller, Efficient iterative schemes for *ab initio* total-energy calculations using a plane-wave basis set. *Phys. Rev. B* **54**, 11169–11186 (1996). doi: 10.1103/PhysRevB.54.11169; pmid: 9984901
80. G. Kresse, J. Hafner, *Ab initio* molecular dynamics for open-shell transition metals. *Phys. Rev. B* **48**, 13115–13118 (1993). doi: 10.1103/PhysRevB.48.13115; pmid: 10007687
81. G. Kresse, D. Joubert, From ultrasoft pseudopotentials to the projector augmented-wave method. *Phys. Rev. B* **59**, 1758–1775 (1999). doi: 10.1103/PhysRevB.59.1758
82. J. P. Perdew, K. Burke, M. Ernzerhof, Generalized Gradient Approximation Made Simple. *Phys. Rev. Lett.* **77**, 3865–3868 (1996). doi: 10.1103/PhysRevLett.77.3865; pmid: 10062328
83. D. Hobbs, G. Kresse, J. Hafner, Fully unconstrained noncollinear magnetism within the projector augmented-wave method. *Phys. Rev. B* **62**, 11556–11570 (2000). doi: 10.1103/PhysRevB.62.11556
84. J. Gao, Q. Wu, C. Persson, Z. Wang, Irvsp: To obtain irreducible representations of electronic states in the VASP. *Comput. Phys. Commun.* **261**, 107760 (2021). doi: 10.1016/j.cpc.2020.107760
85. G. Pizzi *et al*., Wannier90 as a community code: New features and applications. *J. Phys. Condens. Matter* **32**, 165902 (2020). doi: 10.1088/1361-648X/ab51ff; pmid: 31658458
86. Data for "All Topological Bands of All Nonmagnetic Stoichiometric Materials"; https://doi.org/10.5281/zenodo.6123281.

ACKNOWLEDGMENTS

We are grateful to Z. Wang for collaboration on previous related works and for writing the VASP2Trace program (*54*, *84*) extensively used in this study (see text S3). We acknowledge helpful discussions with M. I. Aroyo, B. Bradlyn, J. Cano, L. Schoop, Z. Song, and Y. Xu. M.G.V. and N.R. additionally thank B. Y. Scarpin for enlightening discussions on VASP and CIF files. We acknowledge the computational resources Cobra/Draco in the Max Planck Computing and Data Facility (MPCDF) and Atlas in the Donostia International Physics Center (DIPC). **Funding:** This research was conducted using the resources of the National Energy Research Scientific Computing Center (NERSC), a US Department of Energy Office of Science User Facility operated under contract DE-AC02-05CH11231. This work was primarily supported by US Department of Energy grant DE-SC0016239 (B.J.W., B.A.B., and N.R.). Also supported by NSF EAGER grant DMR 1643312, Simons Investigator grant 404513, Office of Naval Research grant N00014-20-1-2303, NSF-MRSEC grant DMR-142051, the Packard Foundation, the Schmidt Fund for Innovative Research, BSF Israel US foundation grant 2018226, the Gordon and Betty Moore Foundation through grant GBMF8685 toward the Princeton theory program, and a Guggenheim Fellowship from the John Simon Guggenheim Memorial Foundation (B.J.W., B.A.B., and N.R.); the Government of the Basque Country (project IT1301-19) and the Spanish Ministry of Science and Innovation (PID2019-106644GB-I00) (L.E.); Spanish Ministerio de Ciencia e Innovacion grant PID2019-109905GB-C21 (M.G.V.); European Research Council advanced grant 742068 "TOP-MAT," Deutsche Forschungsgemeinschaft (DFG) through SFB 1143, and the Würzburg-Dresden Cluster of Excellence on Complexity and Topology in Quantum Matter-ct.qmat (EXC 2147, project 390858490) (C.F.); and DFG project 314790414 (S.S.P.P.). This work is part of a project that has received funding from the European Research Council (ERC) under the European Union's Horizon 2020 research and innovation programme (grant agreement 101020833). **Author contributions:** All authors contributed equally to the intellectual content of this work. N.R. and M.G.V. performed the high-throughput first-principles calculations with help from L.E., B.A.B., and B.J.W. The topological analysis of the material calculations was performed by B.J.W. and M.G.V. with help from L.E. and B.A.B. B.J.W., M.G.V., and N.R. proposed the existence of RTopo and STopo phases and identified material candidates. The representative topological materials listed in text S11 were manually selected by B.J.W. and M.G.V. with help from N.R., and the most experimentally relevant candidates were identified by C.F., S.S.P.P., M.G.V., and B.J.W. Upgrades to the Topological Materials Database (*50*) were implemented by N.R. The main text was written by M.G.V., B.J.W., B.A.B., and N.R. with help from all other authors. The supplementary material in (*42*) was written by B.J.W., M.G.V., and N.R. This study was conceived by B.A.B., M.G.V., and N.R. N.R. was responsible for the overall research direction. **Competing interests:** The authors declare that they have no competing interests. **Data and materials availability:** The data supporting the findings of this study are available within the paper and on the Topological Materials Database (*50*). The data to generate every figure and table within the paper in an open file format have been made publicly accessible on Zenodo (*86*). Additional information regarding the data generated for this study is available from the corresponding authors upon reasonable request. For this study, we used versions 5.4.1 and 5.4.4 of the Vienna Ab-initio Simulation Package (VASP) (*78*–*80*), a commercial first-principles software package available at www.vasp.at/. **License information:** Copyright © 2022 the authors, some rights reserved; exclusive licensee American Association for the Advancement of Science. No claim to original US government works. www.science.org/about/science-licenses-journal-article-reuse

SUPPLEMENTARY MATERIALS

science.org/doi/10.1126/science.abg9094
Supplementary Text
Figs. S1 to S103
Tables S1 to S33
References (*87*–*231*)

Submitted 3 February 2021; accepted 8 April 2022
10.1126/science.abg9094

Your Legacy to Science

AN ESTATE GIFT TO THE
AMERICAN ASSOCIATION FOR THE ADVANCEMENT OF SCIENCE

Since 1848, our founding year, the American Association for the Advancement of Science (AAAS) has been deeply committed to advancing science, engineering and innovation around the world for the benefit of all people.

By making AAAS a beneficiary of your will, trust, retirement plan or life insurance policy, you become a member of our 1848 Society, joining Thomas Edison, Alexander Graham Bell and the many distinguished individuals whose vision led to the creation of AAAS and our world-renowned journal, *Science*, so many years ago.

Unlike many of its peers, *Science* is not for-profit. Your estate gift would provide long-term financial stability and durable annual income that will support operations and competitive innovation for years to come. **This support is vital.**

"As a teacher and instructor, I bear responsibility for the younger generations. If you have extra resources, concentrate them on organizations, like AAAS, that are doing work for all."

—Prof. Elisabeth Ervin-Blankenheim, 1848 Society member

If you intend to include AAAS in your estate plans, provide this information to your lawyer or financial adviser:

Legal Name: American Association for the Advancement of Science
Federal Tax ID Number: 53-0196568
Address: 1200 New York Avenue, NW, Washington, DC 20005

If you would like more information on making an estate gift to AAAS, cut out and return the form below or send an email to philanthropy@aaas.org. Additional details are also available online at **www.aaas.org/1848Society**.

1848 SOCIETY
AAAS

cut here

Yes, I would like more information about joining the AAAS 1848 Society.

PLEASE CONTACT ME AT:

Name: _____

Address: _____

City: _____ State: _____ Zip code: _____ Country: _____

Email: _____ Phone: _____

RETURN THIS FORM TO:
AAAS Office of Philanthropy and Strategic Partnerships • 1200 New York Avenue, NW • Washington, DC 20005 USA

RESEARCH ARTICLE SUMMARY

NEURODEVELOPMENT

Oligodendrocyte precursors guide interneuron migration by unidirectional contact repulsion

Fanny Lepiemme, Julie Stoufflet, Míriam Javier-Torrent, Gabriel Mazzucchelli, Carla G. Silva*†, Laurent Nguyen*†

INTRODUCTION: The cerebral cortex is an evolutionarily advanced brain region made of cellular layers tangentially organized into areas that serve higher cognitive functions. During development, most cortical interneurons (hereafter called interneurons) are born in the ventral forebrain, where some progenitors concomitantly generate oligodendrocyte precursor cells (OPCs). OPCs differentiate into oligodendrocytes, the principal functions of which are to wrap axons with myelin to support the rapid saltatory conduction of action potentials and to provide metabolic support to neurons in the postnatal brain. Three distinct populations of OPCs have been identified in the forebrain. These cells are born as successive waves with a defined spatiotemporal pattern, and they all migrate from their birthplace to colonize the brain. The two initial waves are born in the ventral forebrain and named vOPCs. They migrate together with the interneurons toward the cortex, whereas the third OPC wave is generated locally around birth by some progenitors of the cortical wall. Despite their distinct origin, all OPC lineages converge at the transcriptional level, which may reflect their contribution to myelination.

RATIONALE: While migrating, some neural cells promote transient cellular interactions that confer upon them roles additional to those played once integrated into the cortical network. Accordingly, recent studies have reported that some first-wave vOPCs establish synaptic contacts with lineage-related interneurons during early postnatal periods. It is intriguing that a large fraction of the first-wave vOPCs do not contribute to synaptogenesis and are eliminated during the second postnatal week. Here, we assessed whether vOPCs play additional noncanonical functions during brain development by testing whether they cross-talk with interneurons to support their concomitant migration to the cerebral cortex.

RESULTS: We hypothesized that some early functions of vOPCs would rely on their spatiotemporal origin, further defining their field of possible interactions with neighboring cells. Despite being born in shared germinal regions of the ventral forebrain, vOPCs and interneurons occupy mutually exclusive territories while migrating. Live imaging of both cell populations in brain slices from mouse embryos showed that first-wave vOPCs and interneurons use distinct migration strategies to reach the cortex. Cortical interneurons navigate into organized streams within the parenchyma, whereas first-wave vOPCs prefer migration along blood vessels. The ordered migration of interneurons in cortical streams relies mostly on gradients of chemoattractant molecules such as Cxcl12, to which interneurons are responsive through their expression of the Cxcr4 receptor. This chemokine is also abundantly released by endothelial cells covering the complex and dense network of growing blood vessels that perfuse the ganglionic eminences and later the cortical wall. A long-standing question in the field of brain development is how cortical interneurons cope with different sources, and thus gradients of Cxcl12, to properly navigate within the cortex. Here, we show that first-wave vOPCs, which are also attracted by Cxcl12, migrate along blood vessels and promote unidirectional contact repulsion to repel migrating interneurons from blood vessels. This cellular mechanism, which is not shared by second-wave vOPCs, relies on the expression of the semaphorin 6a/6b by first-wave vOPCs that binds and activates the plexin A3 receptors expressed at the surface of interneurons. This atypical signaling triggers interneuron polarity reversal, preventing them from clustering around blood vessels and allowing them to follow the cortical Cxcl12 gradient (released by intermediate progenitors and meningeal cells) to reach and settle in their cortical layer in a timely manner. Moreover, a prolonged interaction of migrating interneurons with cells that release high levels of Cxcl12, such as endothelial cells, may not only bias their migration directionality but also reduce their motility through a sustained activation of Cxr4 receptors by Cxcl12, leading to their internalization.

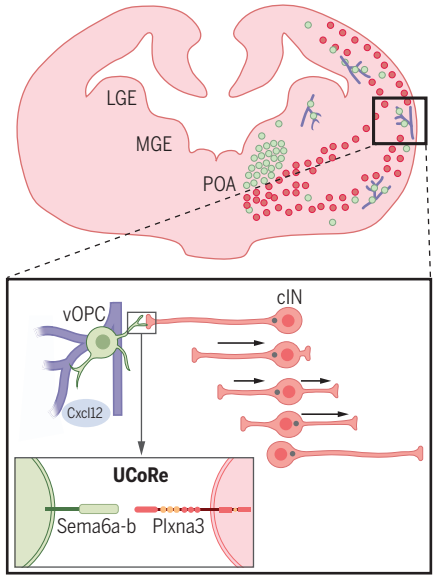

Unidirectional contact repulsion provides guidance to migrating interneurons. During embryogenesis, interneurons and first-wave vOPCs are attracted by the Cxcl12 released by blood vessels. By migrating along these structures, first-wave vOPCs prevent contact between interneurons and blood vessels through unidirectional contact repulsion. This mechanism provides guidance to migrating interneurons and relies on the interaction between Sema6a/6b ligands and Plxna3 receptors expressed by first-wave vOPCs and interneurons, respectively. LGE, lateral ganglionic eminence; MGE, medial ganglionic eminence; POA, preoptic area; UCoRe, unidirectional contact-repulsion event.

CONCLUSION: During brain development, vOPCs and interneurons are born in the ventral forebrain and migrate concomitantly along tangential routes to reach the cerebral cortex. Here, we show by coupling histological analysis of mouse genetic models with live imaging that, while being responsive to Cxcl12 gradients, both cell populations occupy mutually exclusive forebrain territories enriched in this chemokine. Live-imaging analyses demonstrated that first-wave, but not second-wave, vOPCs perform unidirectional contact repulsion on interneurons. This mechanism steers interneurons away from blood vessels that release Cxcl12, thereby allowing them to follow cortical gradients of this chemokine to later settle in their cortical layer. This mode of contact repulsion is specific to first-wave vOPC-interneuron pairs and distinct from self-repulsion. It relies on the activation of an atypical semaphorin-plexin signaling that induces directional change of interneurons upon their polarity reversal. Whether the specificity of this interaction relies on the degree of interneuron maturation and/or the signaling toolbox of vOPCs belonging in two distinct waves remains to be determined. ■

The list of author affiliations is available in the full article online.
*Corresponding author. Email: lnguyen@uliege.be (L.N.); c.s.gomesdasilva@umcutrecht.nl (C.G.S.)
Cite this article as F. Lepiemme *et al.*, *Science* 376, eabn6204 (2022). DOI: 10.1126/science.abn6204
†These authors contributed equally to this work.

READ THE FULL ARTICLE AT
https://doi.org/10.1126/science.abn6204

RESEARCH ARTICLE

NEURODEVELOPMENT

Oligodendrocyte precursors guide interneuron migration by unidirectional contact repulsion

Fanny Lepiemme[1], Julie Stoufflet[1], Míriam Javier-Torrent[1], Gabriel Mazzucchelli[2], Carla G. Silva[1]*†, Laurent Nguyen[1]*†

In the forebrain, ventrally derived oligodendrocyte precursor cells (vOPCs) travel tangentially toward the cortex together with cortical interneurons. Here, we tested in the mouse whether these populations interact during embryogenesis while migrating. By coupling histological analysis of genetic models with live imaging, we show that although they are both attracted by the chemokine Cxcl12, vOPCs and cortical interneurons occupy mutually exclusive forebrain territories enriched in this chemokine. Moreover, first-wave vOPC depletion selectively disrupts the migration and distribution of cortical interneurons. At the cellular level, we found that by promoting unidirectional contact repulsion, first-wave vOPCs steered the migration of cortical interneurons away from the blood vessels to which they were both attracted, thereby allowing interneurons to reach their proper cortical territories.

Oligodendrocytes differentiate from oligodendrocyte progenitor cells (OPCs) and populate the entire central nervous system. After birth, they progressively wrap axons to support rapid saltatory conduction of action potentials as well as to provide metabolic support to neurons through axomyelinic channels (*1*). Some OPCs convert into neural/glial antigen 2 (NG2)–expressing glia, which is the most proliferative pool of cells in the mature brain (*2*). These cells also form synapses with neurons (*3*–*5*). OPCs from different central nervous system regions are genetically distinct, and several intermediates coexist during development (*6*), but some further converge into similar transcriptional states after birth (*7*). In the forebrain, OPCs have multiple origins and are generated in successive "spatiotemporal waves" that populate the cortex from embryonic development onward (*8*). The two first OPC waves are ventrally derived OPCs (vOPCs) that are produced in the ventral forebrain and are followed by a perinatal wave born in the cerebral cortex, which gradually expands and outnumbers the others (*8*). Although the second and third OPC waves mainly contribute to axon myelination, the function of the first-wave vOPC cohort remains elusive. This cell population was first thought to be transient and eliminated at birth (*8*), but despite undergoing massive cell death, recent single-cell analyses showed its maintenance and persistence in some brain regions during adulthood (*7*). Most first-wave vOPCs share common embryonic origins with cortical interneurons (hereafter referred as interneurons). They are born from progenitors of the medial ganglionic eminence and the preoptic area, where genetic cross-inhibitory mechanisms control the balanced generation of interneurons and first-wave vOPCs. The expression of some Distal-less (Dlx) homeobox transcription factors drives interneuron fate by repressing the OPC gene Oligodendrocyte Transcription Factor 2 (*Olig2*) (*9*), whereas Oligodendrocyte Transcription Factor 1 (*Olig1*) expression promotes the specification of first-wave vOPCs and prevents the acquisition of an interneuron fate by repressing *Dlx1/2* expression (*10*). Some first-wave vOPCs from the preoptic area (Dbx1$^+$) or from the medial ganglionic eminence (Nkx2.1$^+$) cluster with their lineage-related interneurons in the cortex of newborn mice, where they form transient synapses before engaging into myelination of specific local circuits (*5*, *11*). During embryogenesis, vOPCs and interneurons migrate concomitantly into the cerebral cortex (*8*, *12*), a process during which these cells may interact and cooperate. We tested this hypothesis by performing live imaging on organotypic forebrain slices from transgenic mice to analyze the distribution and dynamic behavior of vOPCs and interneurons. We first showed that, despite coexisting in time and space, these cells occupy different territories and invade the cortex using distinct migration modes and paths. The elimination of first-wave vOPCs from the early forebrain results in changes of interneuron distribution and migration, supporting the existence of a functional cross-talk between these two cell types that starts at the onset of corticogenesis. At the cellular level, we found that first- but not second-wave vOPCs repel interneurons by a process that we named unidirectional contact repulsion. This atypical behavior contributes to the guidance of interneurons in streams, preventing them from clustering around blood vessels. vOPCs and interneurons are both attracted by the chemokine Cxcl12 released by blood vessels. However, vOPCs are the only ones to move along blood vessels, where they also divide (*13*). Here, we show that the forebrain depletion of some first-wave vOPCs results in interneuron clustering around blood vessels by locally increasing Cxcl12 availability. Altogether, our data demonstrate that by inducing unidirectional contact repulsion, first-wave vOPCs play a transient role in supporting interneuron migration in the developing brain. Unidirectional contact repulsion is thus a strategy allowing first-wave vOPCs and interneurons, which are both responsive to a common chemoattractant, to progress in a coordinated fashion on shared forebrain territories.

Results

Forebrain spatial segregation of interneurons and vOPCs

We analyzed the dynamic distribution pattern of first-wave vOPCs (platelet-derived growth factor receptor A, Pdgfrα$^+$) (*8*) and most interneurons (calbindin$^+$) that migrate in the early forebrain (*14*). At embryonic day 11.5 (E11.5), both cell types mostly distribute into nonoverlapping subpallial territories (Fig. 1, A to D). First-wave vOPCs populate the germinal zones of the medial ganglionic eminence/preoptic area, whereas interneurons are distributed throughout their subventricular and mantle zones (SVZ and MAZ, respectively) (Fig. 1, A and B). At E13.5, first-wave vOPCs accumulate in the SVZ and along the MAZ against a stream of migrating interneurons (Fig. 1, E to H). Calbindin$^+$ interneurons born in the medial ganglionic eminence organize into a deep migratory stream (DMS), and those derived from the preoptic area form a superficial migratory stream (SMS) (Fig. 1E) (*15*). Most first-wave vOPCs do not integrate these migratory streams, suggesting that during early embryonic periods, first-wave vOPCs and interneurons are spatially segregated in the subpallium. This was further confirmed by the analysis of maximum fluorescence intensities and relative number of cells expressing Pdgfrα or calbindin at E11.5 (Fig. 1, C and D) and at E13.5 (Fig. 1, G and H), supporting the spatial segregation of first-wave vOPC and interneuron populations in the ventral forebrain. We showed that vOPCs occupying the medial ganglionic eminence/preoptic area territory above the DMS mainly arise from Nkx2.1$^+$ (87.72 ± 5.04%) and Dbx1$^+$ (31.23 ± 2.05%) progenitors (Fig. 1, I to L). We next analyzed the distribution of first-wave vOPCs and interneurons in the cortical wall of E13.5 embryos and followed their migration in transgenic mice [Dlx5,6:Cre-GFP

[1]Laboratory of Molecular Regulation of Neurogenesis, GIGA-Stem Cells and GIGA-Neurosciences, Interdisciplinary Cluster for Applied Genoproteomics (GIGA-R), University of Liège, CHU Sart Tilman, 4000 Liège, Belgium. [2]Laboratory of Mass Spectrometry, MolSys Research Unit, Liege University, Liege, Belgium.
*Corresponding author. Email: lnguyen@uliege.be (L.N.); c.s.gomesdasilva@umcutrecht.nl (C.G.S.)
†These authors contributed equally to this work.

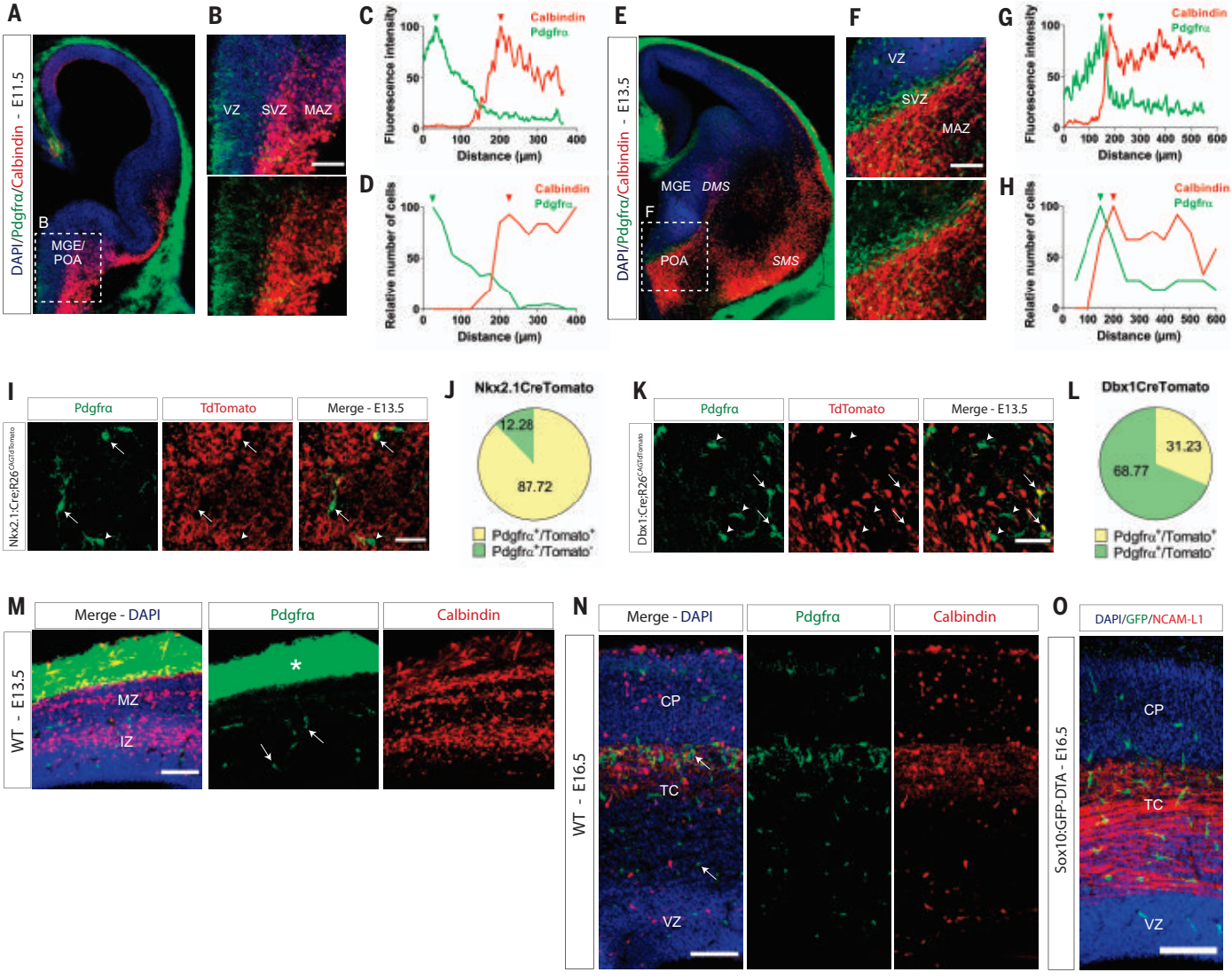

Fig. 1. vOPCs and interneurons occupy distinct territories. (**A** and **B**) Immunolabeling of first-wave vOPCs (Pdgfrα$^+$, green) and interneurons (calbindin$^+$, red) in a coronal brain slice of a wild-type (WT) E11.5 mouse embryo (cells never coexpressed both markers). First-wave vOPCs localize mostly in VZ and interneurons in SVZ and MAZ of medial ganglionic eminence/preoptic area. Nuclei were counterstained with 4′,6-diamidino-2-phenylindole (DAPI) (blue). (**C**) Fluorescence intensity distribution of Pdgfrα and calbindin immunolabelings within the magnified area represented in (B) from VZ to MAZ. Maximum fluorescence intensities (MFIs) are indicated by color-matching arrowheads. (**D**) Distribution of relative numbers of Pdgfrα$^+$ and calbindin$^+$ cells observed in (B). Maximum relative numbers are indicated by color-matching arrowheads. (**E**) Immunolabeling of first-wave vOPCs and interneurons in a coronal brain slice of a WT E13.5 mouse embryo. (**F**) Magnified regions of medial ganglionic eminence and preoptic area are squared in (E), where first-wave vOPCs localize across the VZ/SVZ with accumulation in the SVZ, and interneurons in the MAZ of the medial ganglionic eminence and preoptic area. Nuclei were counterstained with DAPI (blue). (**G**) Fluorescence intensity distribution of Pdgfrα and calbindin immunolabelings within the magnified area represented in (F). MFIs are indicated by color-matching arrowheads. (**H**) Distribution of relative numbers of Pdgfrα$^+$ and calbindin$^+$ cells observed in (F). Maximum relative numbers are indicated by color-matching arrowheads for Pdgfrα$^+$ (green) or calbindin$^+$ (red) cells. (**I**) Lineage tracing of Pdgfrα$^+$ first-wave vOPCs in Nkx2.1:Cre;R26^{CAGTdTomato} in a medial ganglionic eminence region above the DMS from E13.5 embryos. White arrows indicate Pdgfrα$^+$ first-wave vOPCs generated by Nkx2.1$^+$ progenitors and the white arrowhead indicates a Pdgfrα$^+$ first-wave vOPC of other origin. (**J**) Proportion of Pdgfrα$^+$ first-wave vOPCs originating from Nkx2.1$^+$ progenitors (yellow) or from other progenitors (green). (**K**) Lineage tracing of Pdgfrα$^+$ first-wave vOPCs in Dbx1:Cre;R26^{CAGTdTomato} in a medial ganglionic eminence region above DMS from E13.5 embryos. White arrows indicate Pdgfrα$^+$ first-wave vOPCs generated from Dbx1$^+$ progenitors, and white arrowheads indicate Pdgfrα$^+$ first-wave vOPCs of other origin. (**L**) Proportion of Pdgfrα$^+$ cells originating from Dbx1$^+$ progenitors (yellow) or from other progenitors (green). (**M**) Distribution of first-wave vOPCs (Pdgfrα$^+$, green) and interneurons (calbindin$^+$, red) in the cortex of a WT E13.5 embryo (25-μm *Z*-stack). Interneurons distribute within two migratory streams located in the MZ and IZ. White arrows indicate first-wave vOPCs that are distributed randomly. Nuclei were counterstained with DAPI (blue). The asterisk shows immunolabeling of meninges that are Pdgfrα$^+$. (**N**) Distribution of vOPCs (Pdgfrα$^+$, green) and interneurons (calbindin$^+$, red) in the cortical plate (CP) of an E16.5 WT embryo. Interneurons largely populate the CP, whereas vOPCs accumulate under the CP and above the VZ. Nuclei were counterstained with DAPI (blue). (**O**) Immunolabeling of a brain section of a E16.5 Sox10:GFP-DTA embryo showing the accumulation of vOPCs (Pdgfrα$^+$, green) on NCAM-L1$^+$ thalamocortical fibers (NCAM-L1, red). Nuclei were counterstained with DAPI (blue). Scale bars: (I) and (K), 50 μm; (B), (F), (M), (N), and (O), 100 μm. MGE, medial ganglionic eminence; POA, preoptic area; SMS, superficial migratory stream; TC, thalamocortical fibers.

for interneurons, and Sox10:loxGFP-STOPlox-DTA (further referred as Sox10:GFP-DTA) for vOPCs, which largely coexpress calbindin and Pdgfrα, respectively; fig. S1, A to C]. Although interneurons migrate within two main tangential streams located in the marginal zone (MZ) and the intermediate zone (IZ), vOPCs show erratic distribution within the cortical wall (Fig. 1M and movies S1 and S2). At the cellular level, both interneurons and vOPCs undergo saltatory migration, but vOPCs move at a slower speed as a result of a reduced nucleokinesis frequency and amplitude (fig. S1, D to F) combined with longer pausing time of their nucleus (fig. S1G). At E16.5, numerous interneurons undergo intracortical dispersion, whereas most vOPCs accumulate under the cortical plate, where NCAM-L1$^+$ thalamocortical fibers extend (Fig. 1, N and O).

Depletion of vOPCs alters forebrain interneuron distribution

We next wondered whether the spatial segregation of interneurons and first-wave vOPCs in the forebrain results from responsiveness to different cues or if it arises from their mutual interaction. To investigate these two possibilities, we crossed Pdgfrα-Cre^{ERT} and Sox10:GFP-DTA mice to generate embryos devoid of first-wave vOPCs (OPC-depleted embryos) upon successive (E11.5 and E12.5) intraperitoneal injections of tamoxifen in pregnant dams. The depletion of first-wave vOPCs was confirmed at E13.5 and E14.5 (Fig. 2A and fig. S2, A and B). This procedure did not induce bystander cell death, changes in ganglionic eminence progenitor proliferation, or changes in interneuron numbers (fig. S2, C to I). The forebrain of E14.5 OPC-depleted embryos showed enlarged DMS as a result of an increased dispersion of calbindin$^+$ interneurons (Fig. 2, B and C). Analysis of the dorsal forebrain of E13.5 and E16.5 embryos showed a reduced number of calbindin$^+$ interneurons into cortical streams upon first-wave vOPC depletion (Fig. 2, D to G). The acute loss of first-wave vOPCs did not prevent later-born second-wave vOPCs from invading the cortical wall of OPC-depleted embryos at E16.5 (fig. S2, J and K). We next crossed OPC-depleted mice with Dlx5,6:Cre-GFP mice to generate green fluorescent protein–positive (GFP$^+$) cortical interneuron (cIN)–OPC–depleted embryos and followed the migration of GFP$^+$ interneurons, which included most future cortical interneuron subtypes (Fig. 2A). The number of GFP$^+$ interneurons in E13.5 GFP$^+$cIN-OPC–depleted embryos was reduced in the cortical wall, suggesting that the loss of first-wave vOPCs affects

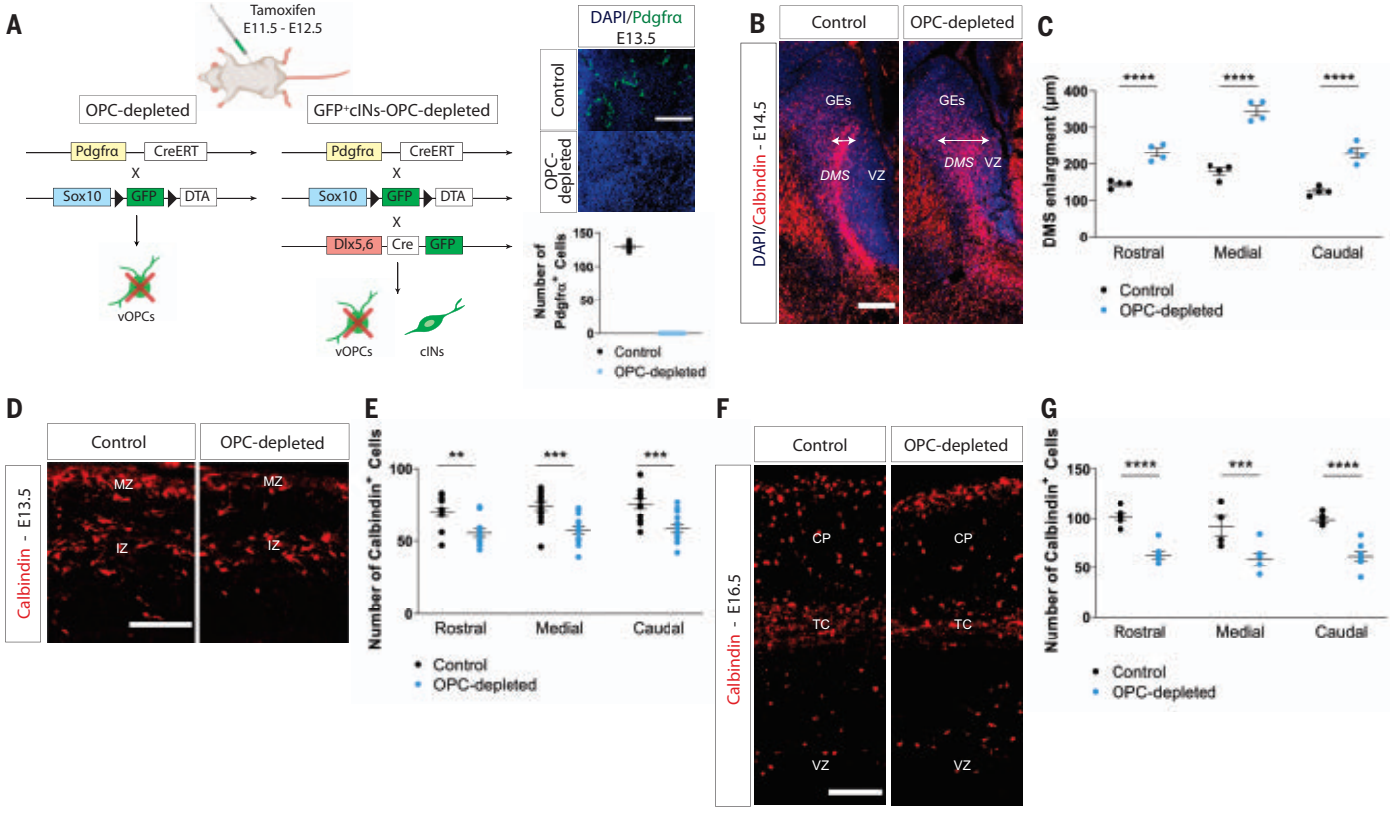

Fig. 2. Depletion of first-wave vOPCs alters interneuron distribution in the forebrain. (**A**) Mouse breeding strategies to deplete Pdgfrα$^+$:Sox10$^+$ first-wave vOPCs through conditional expression of DTA upon tamoxifen injection (OPC-depleted) and to visualize Dlx5,6-GFP$^+$ interneurons (GFP$^+$cIN-OPC–depleted). Immunolabeling of brain slices from E13.5 siblings Pdgfrα-Cre^{ERT} (Control) and Pdgfrα-Cre^{ERT};Sox10:GFP-DTA (OPC-depleted) embryos shows complete loss of first-wave vOPCs (green) in the medial ganglionic eminence/preoptic area after tamoxifen injection in OPC-depleted embryos. Right, immunolabeling and quantification (n = 13 embryos, 100% of depletion). Nuclei were counterstained with DAPI. (**B**) Immunolabeling of interneurons (red) in the subpallium of E14.5 control and OPC-depleted embryos. Migrating interneurons are organized into a DMS stream, which is enlarged in OPC-depleted embryo at three rostrocaudal levels. (**C**) Quantifications of DMS width in its upper part at three rostrocaudal levels, as illustrated in (B) (n = 4 embryos; ****P < 0.0001, two-way ANOVA). (**D**) Immunolabeling of interneurons (red) in the cortical wall of E13.5 control and OPC-depleted embryos. The number of migrating interneurons in the MZ and IZ streams is decreased upon first-wave vOPC depletion. (**E**) Quantification of the number of interneurons (red) in rostrocaudal regions of the cortex of E13.5 control and OPC-depleted embryos (n = 13 to 14 embryos; **P = 0.0024, ***P = 0.0004, ***P = 0.0003, respectively, two-way ANOVA). (**F**) Immunolabeling of interneurons (red) in the cortical wall of E16.5 control and OPC-depleted embryos. The number of interneurons (red) is decreased in the CP. (**G**) Quantification of the number of interneurons (red) in the rostrocaudal regions of the cortex of E16.5 control and OPC-depleted embryos (n = 6 to 7 embryos; ****P < 0.0001, ***P = 0.0007, ****P < 0.0001, two-way ANOVA). Scale bars: (A) and (D), 50 μm; (F), 100 μm; (B), 200 μm. GE, ganglionic eminence.

the migration of most interneurons (fig. S3, A and B). This was further supported by the ventral accumulation of a cohort of 5-ethynyl-2′-deoxyuridine (EdU)–positive interneurons born at E11.5 in the forebrain of E13.5 OPC-depleted embryos (fig. S3, C to E). Despite the progressive increase of vOPC numbers generated by the second wave in OPC-depleted cortex (where most first-wave vOPCs had been eliminated), the number of interneurons in the cortical wall remained decreased at E18.5, just before the death of embryos (fig. S3, H and I). This defect seems specific to interneurons because cortical distribution of microglia, which migrate concomitantly with both interneurons and vOPCs, remained unchanged at E13.5 (fig. S3, J and K). Moreover, depleting interneurons by expressing diphteria toxin subunit A (DTA) in Dlx5,6^{+} cells (Dlx5,6:Cre-GFP;R26:DTA) had no effect on the number or localization of vOPCs within the cortical parenchyma (fig. S3, L to N). These results contrast with those observed with OPCs generated dorsally around birth, the generation of which is impaired upon loss of interneurons (*16*). Altogether, these results suggest that first-wave vOPCs selectively influence the forebrain distribution and sorting of interneurons into the cortical wall.

vOPCs prevent interneuron–blood vessel interaction

During late development, vOPCs migrate in close association to blood vessels (*13*). We observed that during the early developmental stages, when the cortical wall is less vascularized, first-wave vOPCs migrate independently of blood vessels with similar dynamics, suggesting an intrinsic regulation of their migration (fig. S4, A to E). The percentage of vOPCs migrating on blood vessels increases as corticogenesis proceeds, following the spatiotemporal progression of cortical angiogenesis (*17*) (E13.5: 52.46 ± 4.45%; E16.5: 77.52 ± 7.86%; fig. S4, A and F). Our analysis may underestimate the blood vessel coverage by vOPCs because these cells extend thin processes between blood vessels while migrating, which are difficult to image by time-lapse recordings. Although interneurons do not preferentially migrate on blood vessels, they can be detected in their vicinity (*18*).

We tested whether the impaired forebrain distribution of interneurons upon depletion of first-wave vOPCs results from a change in their migratory behavior. We crossed OPC-depleted mice with Dlx5,6:Cre-GFP mice to generate GFP^{+}cIN-OPC–depleted embryos and follow the migration of GFP^{+} interneurons (Fig. 2A). Live imaging of organotypic brain slices from E13.5 embryos showed a reduction of cortical invasion by interneurons in GFP^{+}cIN-OPC–depleted embryos (Fig. 3, A and B, and movie S3). In brain slices from E13.5 GFP^{+}cIN-OPC–depleted embryos, interneurons were migrating more slowly (Fig. 3C) and closer to isolectinB4-labeled blood vessels in the cortical wall (Fig. 3D) and in the ventral forebrain (fig. S3, C to G). At E13.5, the migration parameters of interneurons in cortical parenchyma devoid of blood vessels were comparable between GFP^{+} cIN-OPC–depleted and control cortices (fig. S5, A to D), suggesting that changes in interneuron migration between genotypes result from a lack of blood vessel coverage by first-wave vOPCs. In the forebrain, blood vessels are an important source of Cxcl12 (*13*) (fig. S5, E and F), which attracts vOPCs that express the C-X-C chemokine receptor 4 (Cxcr4) upon activation of Wnt signaling (*13*). Although loss of Ng2^{+} OPCs results in an impaired blood vessel network before birth (*19*), the vasculature was not affected at E13.5 upon first-wave vOPC depletion in OPC-depleted embryos (fig. S5, G to S). This was further supported by a proteomic analysis of the cortical wall that did not indicate specific molecular changes associated with blood vessels (despite detected proteomic changes associated with the loss of first-wave vOPCs) (fig. S5, T and U). Moreover, we did not detect a change of Cxcl12 amount in cortical extracts from E13.5 OPC-depleted embryos compared with their controls (fig. S5V and table S4).

The ordered migration of interneurons in cortical streams relies mostly on gradients of chemoattractant molecules, including Cxcl12, to which interneurons are responsive through their expression of Cxcr4 (*18*, *20*–*22*). Therefore, we postulated that a loss of blood vessel coverage by first-wave vOPCs in E13.5 OPC-depleted embryos would free a local source of Cxcl12, resulting in attraction and rerouting of interneurons toward cortical blood vessels. To test this hypothesis, we incubated organotypic brain slices from E13.5 GFP^{+}cIN-OPC–depleted embryos with Cxcl12-blocking antibodies (Cxcl12 Ab) and measured the distance traveled by interneurons after contacting a blood vessel. We found that interneurons spent less time interacting with blood vessels and migrated farther away from these structures upon initial contact in GFP^{+}cIN-OPC–depleted brain slices incubated with Cxcl12 Ab (Fig. 3E and movie S4). These changes correlated with an increased average speed of interneurons (Fig. 3F). Incubation of control brain slices (GFP^{+}cIN-control) with Cxcl12 Ab did not modify the distance traveled by interneurons from blood vessels (Fig. 3E). The average speed was also similar between Cxcl12 treatment conditions (Fig. 3F). Altogether, these results suggest that the coverage of blood vessels by first-wave vOPCs prevents the Cxcl12-mediated interaction between interneurons and blood vessels. To further support this hypothesis, we induced first-wave vOPC detachment from the vasculature by blocking Wnt signaling with XAV939 in control brain slices (*13*). This pharmacological induction of first-wave vOPC detachment led to an accumulation of interneurons around blood vessels that were migrating more slowly (Fig. 3, G and H, and movie S5). Blood vessels also release Cxcl11 (*23*, *24*) that selectively binds to C-X-C chemokine receptor type 7 (Cxcr7), which acts as a Cxcl12 scavenger and maintains Cxcr4 activation by preventing its internalization (*25*–*27*). We thus blocked Cxcl11 with antibodies (Cxcl11 Ab) and found that it rescued interneuron migration in GFP^{+}cIN-OPC–depleted cortices, likely by preventing Cxcr4 internalization upon blood vessel–released Cxcl12 activation (Fig. 3, I and J). Furthermore, we found that first-wave vOPCs express higher levels of both Cxcr4 and Cxcr7 compared with interneurons (Fig. 3, K and L), which may help them to migrate more efficiently than interneurons along blood vessels.

vOPCs modulate interneuron migration by unidirectional contact repulsion

We found that first-wave vOPC depletion impairs the distribution and migration of concomitantly born interneurons in forebrain parenchyma, including along its blood vessels, suggesting the existence of a cross-talk between first-wave vOPCs and interneurons. Culturing medial ganglionic eminence explants from E13.5 Nkx2.1:Cre; R26^{CAGTdTomato} embryos [containing TdTomato^{+} (Tom^{+}) interneurons] with dissociated preoptic area isolated from E13.5 Sox10:GFP-DTA embryos (enriched in GFP^{+} first-wave vOPCs) in compartmented dishes did not change the migration of Tom^{+} interneurons around their medial ganglionic eminence core explants (Fig. 4, A to H). This suggests that factors released by first-wave vOPCs in culture do not influence interneuron migration. We next investigated whether contact between interneurons and first-wave vOPCs would influence their respective migration behavior. To test this, we cocultured medial ganglionic eminence and preoptic area explants (with or without first-wave vOPCs), which include isolectinB4-labeled cells (Fig. 4I and fig. S5W). After 48 hours of culture, we observed a reduction of preoptic area explant invasion by Tom^{+} interneurons when they included first-wave vOPCs (Fig. 4, J to L). This suggested that first-wave vOPCs prevent preoptic area invasion by interneurons. At the cellular level, live imaging showed that first-wave vOPC-interneuron contact is a multistep event during which first-wave vOPC extends one branch recognizing the interneuron leading process on its growth cone–like structure, followed by polarity reversal and migration of interneuron, without altering first-wave vOPC migration (Fig. 4M and movie S6). This unidirectional contact repulsion (UCoRe) ended on average 78.6 ± 6.11 min after the initial contact (Fig. 4N) and was highly specific, only occurring between first-wave vOPCs and interneurons (Fig. 4, O to R). Unidirectional contact

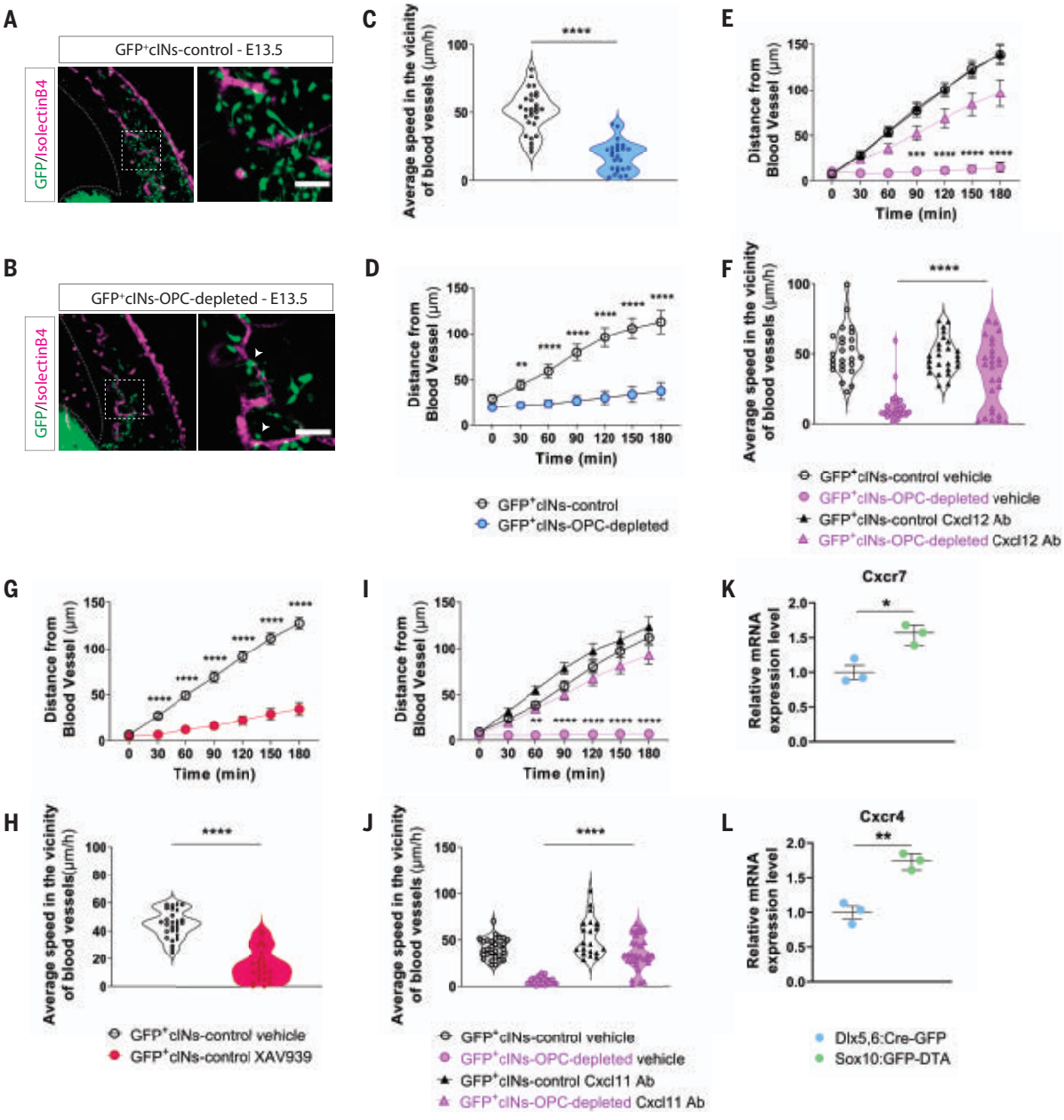

Fig. 3. First-wave vOPC depletion leads to changes in interneuron migration behavior. (**A** and **B**) Images showing the distribution of interneurons (green) around blood vessels (purple) on organotypic brain slices from E13.5 GFP$^+$cIN-control (A) and GFP$^+$cIN-OPC–depleted embryos (B). Right panels are magnified images of corresponding left panels. White arrowheads in (B) indicate interneurons located in the vicinity of blood vessels. (**C**) Distribution of average migration speed of interneurons moving along cortical blood vessels in E13.5 GFP$^+$cIN-control and GFP$^+$cIN-OPC–depleted brain slices (n = 25 to 28 cells; ****P < 0.0001, unpaired t test). (**D**) Histogram of the distance traveled by interneurons, starting from their closest position to blood vessels, in brain slices from E13.5 GFP$^+$cIN-control or GFP$^+$cIN-OPC–depleted embryos. Time 0 corresponds to initial contact of interneuron with a blood vessel (n = 23 cells; **P = 0.0048 after 30 min, ****P < 0.0001 after 60 to 180 min, two-way ANOVA). (**E**) Histogram of the distance traveled by interneurons, starting from their closest position to blood vessels, in brain slices from E13.5 GFP$^+$cIN-control or from GFP$^+$cIN-OPC–depleted embryos (n = 24 to 25 cells; ***P = 0.0006 after 90 min, ****P < 0.0001 after 120 to 180 min, two-way ANOVA). (**F**) Distribution of average migration speed of interneurons moving along cortical blood vessels on Cxcl12 Ab-treated or vehicle-treated organotypic brain slices from E13.5 GFP$^+$cIN-control and GFP$^+$cIN-OPC–depleted embryos (n = 25 to 26 cells; ****P < 0.0001, one-way ANOVA). (**G**) Histogram of the displacement of interneurons, starting from their closest position to blood vessels, on brain slices from E13.5 GFP$^+$cIN-control vehicle-treated and GFP$^+$cIN-control XAV939-treated embryos (n = 23 to 28 cells; ****P < 0.0001 after 30 to 180 min, two-way ANOVA). (**H**) Distribution of average migration speed of interneurons moving along cortical blood vessels on organotypic brain slices from E13.5 GFP$^+$cIN-control vehicle-treated or GFP$^+$cIN-control XAV939-treated embryos (n = 24 to 28 cells; ****P < 0.0001, unpaired t test). (**I**) Histogram of the distance traveled by interneurons, starting from their closest position to blood vessels, in brain slices from E13.5 GFP$^+$cIN-control or GFP$^+$cIN-OPC–depleted embryos (n = 30 cells; **P = 0.0069 after 60 min, ****P < 0.0001 after 90 to 180 min, two-way ANOVA). (**J**) Distribution of average migration speed of interneurons moving along cortical blood vessels on Cxcl11 Ab-treated or vehicle-treated organotypic brain slices from E13.5 GFP$^+$cIN-control or GFP$^+$cIN-OPC–depleted embryos (n = 30 cells; ****P < 0.0001, one-way ANOVA). (**K** and **L**) Dot plots of relative mRNA expression levels of *Cxcr7* and *Cxcr4* in first-wave vOPCs, compared with interneurons (n = 3 samples; *P = 0.014 and **P = 0.0029, respectively, unpaired t test). Scale bars: (A) and (B), 50 µm.

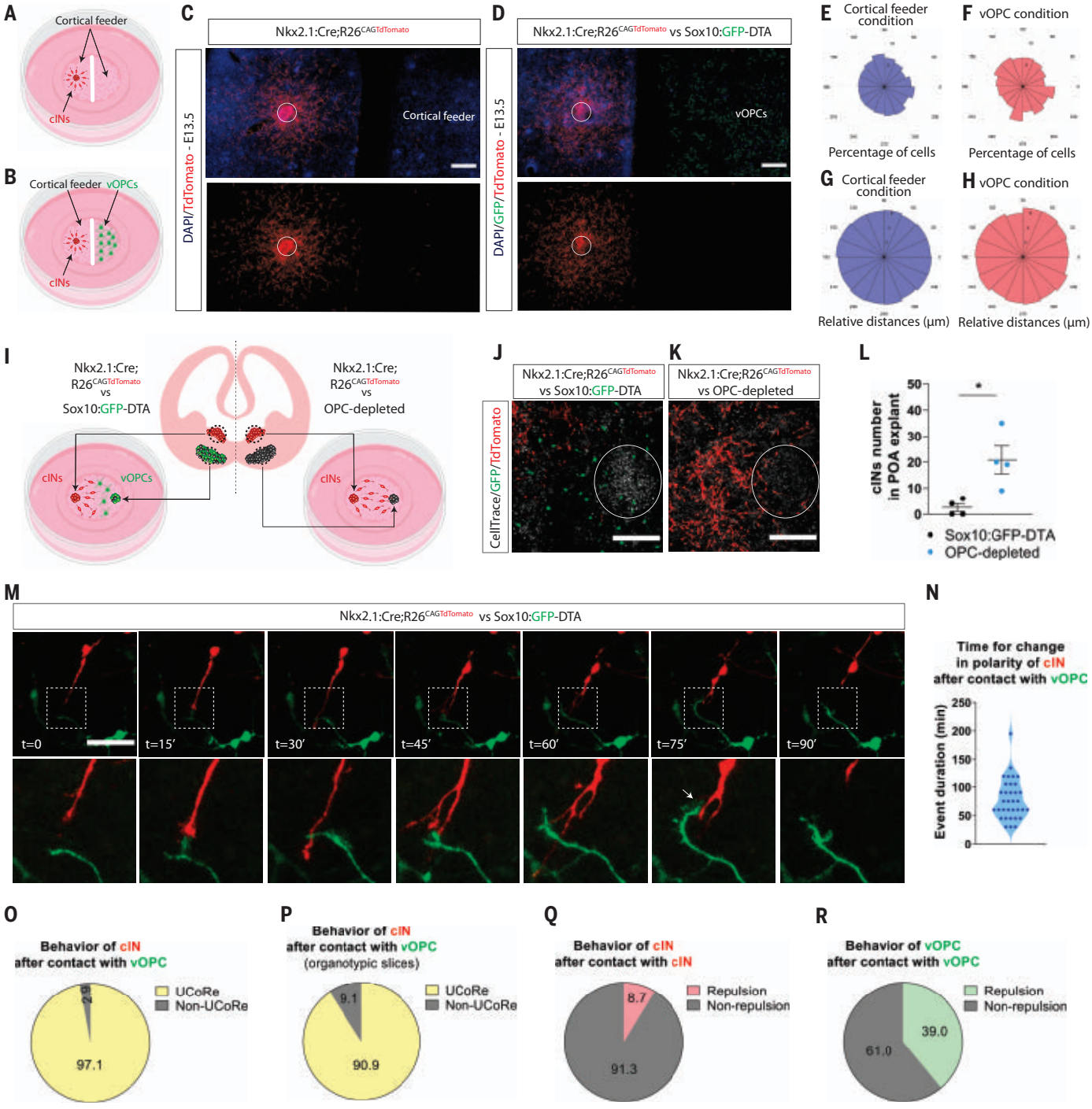

Fig. 4. Analysis of first-wave vOPC-interneuron interactions. (**A** and **B**) Experimental culture setup to test whether first-wave vOPC secretome influences interneuron migration. (**C** and **D**) Images showing cocultures of interneurons with or without first-wave vOPCs, as depicted in (A) and (B). (**E** to **H**) Phase histograms showing the cell percentage [(E) and (F)] or the distance traveled by interneurons [(G) and (H)] from the explant core in the culture as depicted in (A) and (B). (**I**) Experimental in vitro setup to assess the ability of interneurons (red) to invade the preoptic area that contains or does not contain first-wave vOPCs (green). (**J** and **K**) Representative images of medial ganglionic eminence–derived explants isolated from organotypic brain slices of E13.5 Nkx2.1:Cre;R26^{CAGTdTomato} embryos cocultured with preoptic area–derived explants obtained from organotypic brain slices of E13.5 Sox10:GFP-DTA (J) or OPC-depleted (K) embryos. (**L**) Absolute numbers of interneurons that invade preoptic area–derived explants from Sox10:GFP-DTA or OPC-depleted embryos (n = 4 explants; *P = 0.0286, Mann-Whitney test). (**M**) Time-lapse sequence showing the interaction (white arrow) between an interneuron (red) and a first-wave vOPC (green). (**N**) Violin plot of the timing of unidirectional contact repulsion (UCoRe) when interneurons contact first-wave vOPCs (78.60 ± 6.11 min; n = 34 interactions). (**O** and **P**) Pie charts reporting the frequency of UCoRe or non-UCoRe behaviors among interneuron-first-wave vOPC contacts in explant cultures [(O); n = 35 cells] or in situ in organotypic slices [(P); n = 11 cells]. (**Q** and **R**) Pie charts of the frequency of repulsive and neutral behaviors upon interneuron-interneuron [(Q); n = 46 cells] or first-wave vOPC-first-wave vOPC [(R); n = 41 cells] contacts. Scale bars: (J), (K), and (M), 200 µm; (C) and (D), 500 µm. UCoRe, unidirectional contact-repulsion event.

repulsion is a distinct mode of cell repulsion compared with the mutual ones occurring between pairs of first-wave vOPCs (39.0% of the recorded contacts) or interneurons (8.7% of the recorded contacts) that never experienced polarity reversal (Fig. 4, Q and R). This mode of cell repulsion likely occurs in vivo as it guides interneuron migration in cortical regions from organotypic slices in the vicinity of or at a distance from blood vessels through dynamic branching of first-wave vOPCs (Fig. 4P and movies S7 and S8).

We next performed coculture of E16.5 lateral ganglionic eminence explants containing second-wave vOPCs (Sox10:venus/GFP; green) with homochronic medial ganglionic eminence explants (Nkx2.1:Cre;$R26^{CAGTdTomato}$; red) containing interneurons or homochronic caudal ganglionic eminence explants (Dlx5,6:Cre-GFP; $R26^{CAGTdTomato}$; yellow) containing interneurons. In both cultures, second-wave vOPCs did not promote unidirectional contact repulsion to most medial ganglionic eminence– or caudal ganglionic eminence–derived interneurons (fig. S6, A to D).

Unidirectional contact repulsion relies on atypical semaphorin-plexin signaling

To identify the molecular mechanism underlying unidirectional contact repulsion, we performed enrichment analysis of a gene set obtained by RNA sequencing of GFP^+ interneurons purified by fluorescence-activated cell sorting (FACS) from E13.5 Dlx5,6:Cre-GPF embryos (*28*). We ran gene ontology (GO) analysis (*29*) to identify the GO term related to chemotaxis and refined the analysis by selecting genes coding for transmembrane receptors and membrane-bound signaling molecules (table S1). Among the 10 genes showing the highest enrichment in interneurons, we found several members of the Eph-ephrin and Plexin (Plxn)–Semaphorin (Sema) signaling families, two families of receptor ligands involved in contact-repulsion mechanisms (*30*, *31*) (fig. S7, A and B) that are also expressed in vOPCs (*7*). We next tested whether these signaling pathways underlie unidirectional contact repulsion in cocultures of preoptic area and medial ganglionic eminence explants containing GFP^+ first-wave vOPCs and Tom^+ interneurons, respectively. We showed that the pharmacological blockade of type a and b Eph receptor families with 200 μM of the competitive and reversible ligand lithocholic acid (*32*) did not affect unidirectional contact repulsion (Fig. 4O and fig. S7C). Therefore, we investigated whether Plxn-Sema signaling underlies unidirectional contact repulsion by knocking down simultaneously several Plxn members (Plxna1, a2, a3, b1, and b2) with expression of a small interfering RNA (siRNA) pool in interneurons. Unidirectional contact repulsion was largely impaired upon expression of the Plxn siRNA pool (90.90% of the first-wave vOPC-interneuron contacts) compared with its control (fig. S7, D and E). While testing the involvement of each individual Plxn in unidirectional contact repulsion, we found that only targeting Plxna3 in interneurons abolished unidirectional contact repulsion (15.40%; Fig. 5, A to D, and fig. S7, F to K). We observed that the knockdown of Plxnb2 induced growth cone retraction without unidirectional contact repulsion (fig. S7L). Analysis of bulk RNA sequencing from first-wave vOPCs (*7*) revealed expression of several Semas (table S2). To identify the Sema(s) expressed by first-wave vOPCs that would partner with Plxna3 in unidirectional contact repulsion, we excluded secreted Semas and focused our analysis on transmembrane class 5 and 6 Semas, which are known receptors for a-class Plxns (*33*). The analysis of GFP^+ first-wave vOPCs FACS-isolated from E13.5 Sox10:GFP-DTA embryos showed that messengers of all class 5 and 6 Semas are expressed by first-wave vOPCs (fig. S8A). We next tried to knock down these Semas in first-wave vOPCs by siRNAs or infection with short hairpin lentiviruses. Unfortunately, we were not able to transduce first-wave vOPCs. As an alternative, we used Neuro2A (N2A) cells, in which the endogenous expression of class 5 and 6 Semas is low (fig. S8, B to G). Accordingly, we detected unidirectional contact repulsion in a small fraction of E13.5 Tom^+ interneurons that were cocultured with N2A cells (Fig. 5, E and H). The frequency of unidirectional contact repulsion was increased after overexpression of Sema6a and Sema6b (Fig. 5, F, G, I, and J), but not of other class 5 and 6 Semas, in N2A cells (fig. S8, H to K). By knocking down Plxna3 in interneurons, we demonstrated that the increase in unidirectional contact-repulsion frequency triggered upon Sema6a or Sema6b overexpression in N2A cells required endogenous expression of Plxna3 by interneurons (Fig. 5, K and L). This further suggests that a transient interaction between interneuron Plxna3 and first-wave vOPC Sema6a/6b drives unidirectional contact repulsion. To further test this hypothesis, we used blocking antibodies that recognize both Sema6a and Sema6b (Sema6a/6b; fig. S8, L to N) in coculture of interneurons and first-wave vOPCs, which dose-dependently abolished unidirectional contact repulsion (Fig. 5, M and N, and fig. S8O). At the subcellular level, we detected some enrichment of Plxna3 and Sema6a/6b signal in growth cones of interneurons and first-wave vOPCs, respectively (Fig. 5, O and P). Such subcellular location suggests that these molecules are important players to drive growth cone collapse and lead process retraction during unidirectional contact repulsion. We further investigated polarity reversal in interneurons by electroporating centrin-GFP and memb-Cherry. We observed a sequence during which the growth cone of the leading process initiates retraction just before the regrowth of the new leading process at the opposite side, whereas the centrosome (centrin-GFP) initiates its migration later. Because the centrosome acts as microtubule organizing center (MTOC), our results suggest that microtubules are not initially involved in the growth of the new leading process after interacting with first-wave vOPCs or N2A cells overexpressing Sema6b (Fig. 5, Q and R, and movies S9 and S10). Altogether, our data demonstrate that unidirectional contact repulsion is driven by an interaction between Plxna3 and Sema6a/6b, further suggesting that first-wave vOPCs use a singular mechanism to signal to interneurons during development.

Discussion

Here, we provide a characterization of the migration pattern of first-wave vOPCs in the developing mouse brain. Despite being born in shared subpallial germinal regions, vOPCs and interneurons use distinct migration modes and occupy mutually exclusive forebrain territories while moving toward the cortex. Moreover, these cell types undergo saltatory migration characterized by different kinetics, and although vOPCs preferentially use blood vessels to move in the cortex, interneurons navigate in organized tangential streams. Among the important diffusible cues that guide neural migration in the cortex, the chemokine Cxcl12 attracts both interneurons and vOPCs. The Cxcl12 released by intermediate progenitors in the cortex marks a migratory stream that steers interneurons within the IZ or SVZ (*21*, *34*). This chemokine is also secreted by forebrain blood vessels and attracts vOPCs (*13*). Whereas genetic ablation of interneurons does not affect the cortical distribution of vOPCs, loss of first-wave vOPCs impairs interneuron migration in the cortical wall, further suggesting that interneurons require first-wave vOPCs to properly navigate within the cerebral cortex. We showed that first-wave vOPC ablation increases the local availability of Cxcl12 in the vicinity of blood vessels to which interneurons are then attracted, thereby altering their progression toward the cortex. Because both cell types are responsive to Cxcl12, we postulated that an active mechanism carried on by first-wave vOPCs prevents interneurons from migrating along blood vessels. Our live-imaging analysis indeed demonstrated that first- but not second-wave vOPCs perform unidirectional contact repulsion on interneurons, thus guiding them to prevent their interaction with blood vessels while contributing to their overall progression into the forebrain. This mode of contact repulsion with polarity reversal is specific to first-wave vOPC-interneuron pairs and distinct from self-repulsion, as previously described for OPCs themselves (*35*) and

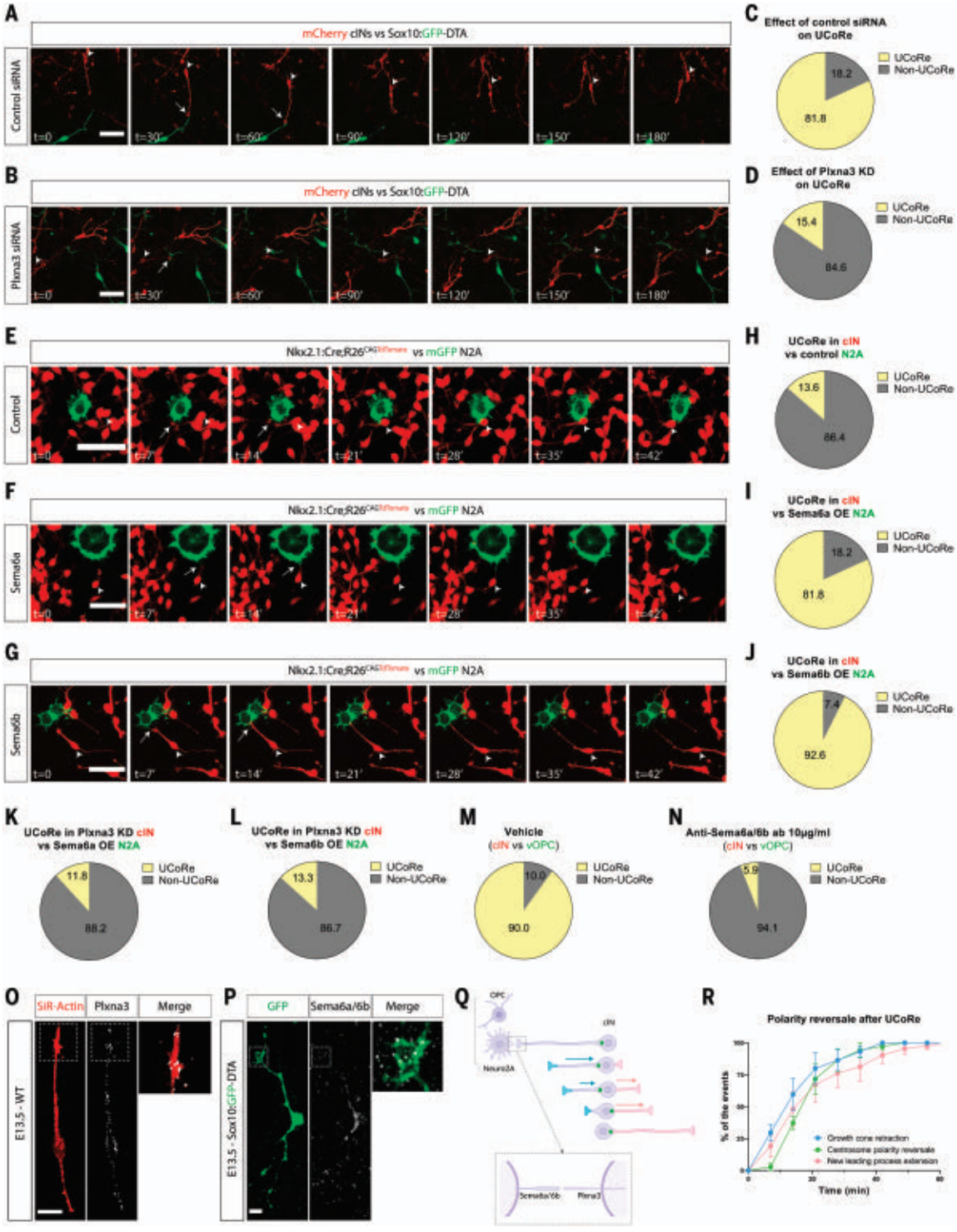

Fig. 5. Molecular mechanism underlying a UCoRe. (**A** and **B**) Time-lapse sequences illustrating the behavior of an interneuron (memb-Cherry, red) electroporated with control siRNA [(A); UCoRe) or Plxna3 siRNA (B; non-UCoRe), after contacting a first-wave vOPC (green). White arrows indicate contacts between interneuron and first-wave vOPC. Arrowheads track the soma of the interneuron of interest. (**C** and **D**) Pie charts reporting the fraction of interneurons undergoing UCoRe or non-UCoRe upon contacting first-wave vOPCs, as illustrated by (A) and (B) (n = 11 to 13 cells; $^{**}P$ = 0.0031, Fisher's exact test). (**E** to **G**) Time-lapse sequences illustrating the behavior of interneurons (TdTomato^{+}, red), after contacting N2A cells (green) overexpressing mGFP (control, E; non-UCoRe), Sema6a [(F); UCoRe] or Sema6b plasmids [(G); UCoRe]. White arrows indicate contact between an interneuron and a N2A cell. Arrowheads track the soma of the interneuron of interest. (**H** to **J**) Pie charts reporting the fraction of interneurons undergoing UCoRe or non-UCoRe upon contacting N2A cells, as illustrated by (E), (F), and (G) (n = 22 to 27 cells; $^{****}P < 0.0001$, Fisher's exact test). (**K** and **L**) Pie charts reporting the fraction of interneurons (memb-Cherry, red) undergoing UCoRe or non-UCoRe after electroporation with Plxna3 siRNA and upon contact with N2A cells overexpressing Sema6a (K) or Sema6b plasmids (L) (n = 15 to 17 cells; $^{****}P < 0.0001$, Fisher's exact test). (**M** and **N**) Pie charts reporting the fraction of interneurons (TdTomato^{+}, red) undergoing UCoRe or non-UCoRe upon contact with

first-wave vOPCs (green) while being incubated with vehicle (M) or 10 μg/ml of anti-Sema6b antibody (N) (n = 10 to 17 cells; ****P < 0.0001, Fisher's exact test). (**O**) Immunolabeling of an interneuron (SiR-Actin, red) and Plxna3 (white). Nuclei were counterstained with DAPI (blue). (**P**) Immunolabeling of a first-wave vOPC (GFP^+, green) and Sema6a/6b (white). Nuclei were counterstained with DAPI (blue). Merges are the corresponding squared regions. (**Q**) Scheme of UCoRe sequence when an interneuron contacts a first-wave vOPC or a N2A cell overexpressing Sema6a or Sema6b. Growth cone retraction is in blue, centrosome (or MTOC) in green, and the extending new leading process in red. (**R**) Graph showing the order and timing of UCoRe sequence. Scale bars: (O) and (P), 10 μm; (A), (B), (E), (F), and (G), 50 μm. KD, knockdown; OE, overexpression.

Cajal-Retzius cells (*36*, *37*). Unidirectional contact repulsion on interneurons involves a sequence of events that starts with the growth cone collapse of their leading process and its retraction, followed by the regrowth of a new leading process at the opposite side of the cell body. We observed that centrosome migration (which acts as a MTOC) from the base of the disassembling leading process to the base of the new one occurs after growth initiation of the new process. This suggests that growth initiation of the leading process is independent of nucleation and polymerization of microtubules from the MTOC. At the molecular level, we identified that an atypical interaction between Plxna3 and Sema6a/6b expressed by interneurons and first-wave vOPCs, respectively, triggers a signaling pathway promoting unidirectional contact repulsion. Our attempt to detect a physical interaction between these molecules by coimmunoprecipitation on extracts from cocultured N2A cells transfected with either Plxna3 or Sema6b was unsuccessful, likely because such interaction is short (<10 min, as reported in Fig. 5R). Moreover, the nature of the intracellular cascade activated in interneurons upon first-wave vOPC interaction remains to be clarified. The reduction of interneuron number in the cortex upon first-wave vOPC depletion is still observed just before birth, an age during which second-wave vOPCs are actively migrating. This suggests that second-wave vOPCs cannot rescue the migration of interneurons, which is further supported by the demonstration that second-wave vOPCs do not perform unidirectional contact repulsion to most homochronic interneurons. We observed that interneuron depletion does not have a significant impact on the generation, survival, and migration of first- and second-wave vOPCs. However, by releasing factors such as Sonic hedgehog and fraktaline, interneurons control the generation of dorsally born OPCs (*16*, *38*). This is another example suggesting that interneuron-OPC cross-talk varies spatially and temporally. Some first-wave vOPCs and interneurons establish specific interaction to form transient synapses at early postnatal stages and later engage in myelination of specific local circuits (*5*, *11*). However, most first-wave vOPCs die before postnatal day 10 (*11*). Therefore, by showing that first-wave vOPCs support the migration of interneurons in the developing cerebral cortex, our work identifies a noncanonical and transient role for first-wave vOPCs. Furthermore, whereas unidirectional contact repulsion occurs during development between pairs of interneurons and first-wave vOPCs, some pairs must express mutual recognition molecular codes after birth to promote longer-term interaction for the formation of transient synapses and later axon myelination.

Our results show that despite being less numerous, first-wave vOPCs support the migration of interneurons across cortical territories by using unidirectional contact repulsion. This mechanism allows both cell populations to adopt specific migration patterns in the cortex while also being attracted by Cxl12. Blood vessels are found throughout the cortical wall and are indeed an important source of Cxcl12 that, if not covered and consumed by first-wave vOPCs, may affect interneuron migration by interfering with the existing cortical IZ and MZ Cxcl12 gradients generated by intermediate progenitors and meningeal cells, respectively (*21*, *39*). Unidirectional contact repulsion contributes to the guidance of interneurons as the cortex matures and gets more perfused by blood vessels, which are a source of Cxcl12 release.

Methods summary

Genetic mouse models were used to visualize or deplete either vOPCs or interneurons. First-wave vOPC progenies were analyzed at E13.5 in Nkx2.1:Cre;$R26^{CAGTdTomato}$ and Dbx1:Cre;$R26^{CAGTdTomato}$ mouse models. Sox10:GFP-DTA and Dlx5,6:Cre-GFP E13.5 and E16.5 brains were processed into organotypic slices to track the migration of vOPCs and cortical interneurons, respectively. Brains from Sox10:GFP-DTA, Sox10:Venus, Nkx2.1:Cre;$R26^{CAGTdTomato}$, and Dlx5,6:Cre-GFP;$R26^{CAGTdTomato}$ mice were microdissected into explants and cultured to analyze unidirectional contact repulsion between vOPCs and interneurons. Sox10:GFP-DTA females were crossed with either Pdgfrα:Cre^{ERT} or Dlx5,6:CreGFP;Pdgfrα:Cre^{ERT} males to deplete first-wave vOPCs after intraperitoneal injections of tamoxifen at E11.5 and E12.5. A model of interneuron depletion was generated by breeding R26:DTA females with Dlx5,6:Cre-GFP males.

For all histological analyses, embryonic heads or brains were fixed in 4% paraformaldehyde overnight at 4°C and then cryopreserved in a 20% sucrose solution diluted in phosphate-buffered saline (PBS) overnight at 4°C. Brains were then frozen in optimal cutting temperature medium and kept at −80°C until cryostat cutting. Brain slices were permeabilized, blocked in PBS/0.3% Triton X-100/10% donkey serum, and then incubated overnight at 4°C with primary antibodies diluted in PBS/0.3% Triton X-100/1% donkey serum. After three rinses with PBS/0.3% Triton X-100/5% donkey serum, slices were incubated in the same solution containing secondary antibodies for 2 hours at room temperature. Images were obtained using an inverted confocal microscope (Nikon A1).

Organotypic slice cultures from embryonic brains were used to study the migration of vOPCs and cortical interneurons. Brains were processed into 300-μm coronal slices and harvested on a Millicell(Millipore) culture insert placed on glass-bottomed dishes. Dishes were filled with neurobasal medium supplemented in B27, N2, and glutamine. Slices were kept in a humidified incubator saturated with 5% CO_2 for a maximum of 8 hours before time-lapse recording. IsolectinB4 was added on top of organotypic slices to stain blood vessels. For every treatment (Cxcl11 Ab, Cxcl12 Ab, or XAV939), molecules were added on top of organotypic slices as well. Time-lapse acquisitions were obtained every 5 min for at least 5 hours using an inverted confocal microscope. Analyses of migration parameters were performed using the mTrackJ plugin in Fiji.

Study of vOPC-interneuron interaction was performed in a two-dimensional culture of primary vOPCs and interneurons. These cultures were generated by placing microdissected ganglionic eminence and preoptic area explants on top of a homochronic cortical feeder. Briefly, glass-bottomed dishes were coated with poly-ornithine and laminin. The feeder layer of cortical cells was prepared by mechanical dissociation of either E13.6 or E16.5 wild-type cortices in supplemented neurobasal medium. The dissociated cells were plated in coated glass-bottomed dishes and left to adhere for 2 hours at 37°C in a humidified incubator saturated with 5% CO_2. The next day, ganglionic eminence or preoptic area explants of ~300 μm were then plated on top of the cortical feeder layer. To knock down Plexins in interneurons at E13.5, ex vivo electroporation of medial ganglionic eminences was performed before microdissecting the explants. For analyses of contact repulsion between vOPCs and interneurons, time-lapse acquisitions were obtained every 5 min for at least 10 hours using an inverted confocal microscope.

REFERENCE AND NOTES

1. K. A. Nave, Myelination and the trophic support of long axons. *Nat. Rev. Neurosci.* **11**, 275–283 (2010). doi: 10.1038/nrn2797; pmid: 20216548

2. A. M. Ravanelli *et al*., Sequential specification of oligodendrocyte lineage cells by distinct levels of Hedgehog and Notch signaling. *Dev. Biol.* **444**, 93–106 (2018). doi: 10.1016/j.ydbio.2018.10.004; pmid: 30347186
3. D. E. Bergles, J. D. Roberts, P. Somogyi, C. E. Jahr, Glutamatergic synapses on oligodendrocyte precursor cells in the hippocampus. *Nature* **405**, 187–191 (2000). doi: 10.1038/35012083; pmid: 10821275
4. S. C. Lin, D. E. Bergles, Synaptic signaling between GABAergic interneurons and oligodendrocyte precursor cells in the hippocampus. *Nat. Neurosci.* **7**, 24–32 (2004). doi: 10.1038/nn1162; pmid: 14661022
5. D. Orduz *et al*., Interneurons and oligodendrocyte progenitors form a structured synaptic network in the developing neocortex. *eLife* **4**, e06953 (2015). doi: 10.7554/eLife.06953; pmid: 25902404
6. S. Marques *et al*., Oligodendrocyte heterogeneity in the mouse juvenile and adult central nervous system. *Science* **352**, 1326–1329 (2016). doi: 10.1126/science.aaf6463; pmid: 27284195
7. S. Marques *et al*., Transcriptional convergence of oligodendrocyte lineage progenitors during development. *Dev. Cell* **46**, 504–517.e7 (2018). doi: 10.1016/j.devcel.2018.07.005; pmid: 30078729
8. N. Kessaris *et al*., Competing waves of oligodendrocytes in the forebrain and postnatal elimination of an embryonic lineage. *Nat. Neurosci.* **9**, 173–179 (2006). doi: 10.1038/nn1620; pmid: 16388308
9. M. A. Petryniak, G. B. Potter, D. H. Rowitch, J. L. Rubenstein, Dlx1 and Dlx2 control neuronal versus oligodendroglial cell fate acquisition in the developing forebrain. *Neuron* **55**, 417–433 (2007). doi: 10.1016/j.neuron.2007.06.036; pmid: 17678855
10. J. C. Silbereis *et al*., Olig1 function is required to repress dlx1/2 and interneuron production in Mammalian brain. *Neuron* **81**, 574–587 (2014). doi: 10.1016/j.neuron.2013.11.024; pmid: 24507192
11. D. Orduz *et al*., Developmental cell death regulates lineage-related interneuron-oligodendroglia functional clusters and oligodendrocyte homeostasis. *Nat. Commun.* **10**, 4249 (2019). doi: 10.1038/s41467-019-11904-4; pmid: 31534164
12. S. A. Anderson, D. D. Eisenstat, L. Shi, J. L. Rubenstein, Interneuron migration from basal forebrain to neocortex: Dependence on Dlx genes. *Science* **278**, 474–476 (1997). doi: 10.1126/science.278.5337.474; pmid: 9334308
13. H. H. Tsai *et al*., Oligodendrocyte precursors migrate along vasculature in the developing nervous system. *Science* **351**, 379–384 (2016). doi: 10.1126/science.aad3839; pmid: 26798014
14. S. A. Anderson, O. Marín, C. Horn, K. Jennings, J. L. Rubenstein, Distinct cortical migrations from the medial and lateral ganglionic eminences. *Development* **128**, 353–363 (2001). doi: 10.1242/dev.128.3.353; pmid: 11152634
15. G. Zimmer *et al*., Bidirectional ephrinB3/EphA4 signaling mediates the segregation of medial ganglionic eminence- and preoptic area-derived interneurons in the deep and superficial migratory stream. *J. Neurosci.* **31**, 18364–18380 (2011). doi: 10.1523/JNEUROSCI.4690-11.2011; pmid: 22171039
16. A. Voronova *et al*., Migrating interneurons secrete fractalkine to promote oligodendrocyte formation in the developing mammalian brain. *Neuron* **94**, 500–516.e9 (2017). doi: 10.1016/j.neuron.2017.04.018; pmid: 28472653
17. C. Lange *et al*., Relief of hypoxia by angiogenesis promotes neural stem cell differentiation by targeting glycolysis. *EMBO J.* **35**, 924–941 (2016). doi: 10.15252/embj.201592372; pmid: 26856890
18. M. Barber *et al*., Vascular-derived Vegfa promotes cortical interneuron migration and proximity to the vasculature in the developing forebrain. *Cereb. Cortex* **28**, 2577–2593 (2018). doi: 10.1093/cercor/bhy082; pmid: 29901792
19. S. Minocha *et al*., NG2 glia are required for vessel network formation during embryonic development. *eLife* **4**, e09102 (2015). doi: 10.7554/eLife.09102; pmid: 26651999
20. N. Flames *et al*., Short- and long-range attraction of cortical GABAergic interneurons by neuregulin-1. *Neuron* **44**, 251–261 (2004). doi: 10.1016/j.neuron.2004.09.028; pmid: 15473965
21. M. C. Tiveron *et al*., Molecular interaction between projection neuron precursors and invading interneurons via stromal-derived factor 1 (CXCL12)/CXCR4 signaling in the cortical subventricular zone/intermediate zone. *J. Neurosci.* **26**, 13273–13278 (2006). doi: 10.1523/JNEUROSCI.4162-06.2006; pmid: 17182777
22. G. López-Bendito *et al*., Chemokine signaling controls intracortical migration and final distribution of GABAergic interneurons. *J. Neurosci.* **28**, 1613–1624 (2008). doi: 10.1523/JNEUROSCI.4651-07.2008; pmid: 18272682
23. L. Kurmann *et al*., Transcryptomic analysis of human brain-microvascular endothelial response to pericytes: Cell orientation defines barrier function. *Cells* **10**, 963 (2021). doi: 10.3390/cells10040963; pmid: 33924251
24. Y. Zhang *et al*., An RNA-sequencing transcriptome and splicing database of glia, neurons, and vascular cells of the cerebral cortex. *J. Neurosci.* **34**, 11929–11947 (2014). doi: 10.1523/JNEUROSCI.1860-14.2014; pmid: 25186741
25. P. Abe *et al*., CXCR7 prevents excessive CXCL12-mediated downregulation of CXCR4 in migrating cortical interneurons. *Development* **141**, 1857–1863 (2014). doi: 10.1242/dev.104224; pmid: 24718993
26. U. Naumann *et al*., CXCR7 functions as a scavenger for CXCL12 and CXCL11. *PLOS ONE* **5**, e9175 (2010). doi: 10.1371/journal.pone.0009175; pmid: 20161793
27. Y. Wang *et al*., CXCR4 and CXCR7 have distinct functions in regulating interneuron migration. *Neuron* **69**, 61–76 (2011). doi: 10.1016/j.neuron.2010.12.005; pmid: 21220099
28. C. G. Silva *et al*., Cell-intrinsic control of interneuron migration drives cortical morphogenesis. *Cell* **172**, 1063–1078.e19 (2018). doi: 10.1016/j.cell.2018.01.031; pmid: 29474907
29. H. Mi *et al*., PANTHER version 16: A revised family classification, tree-based classification tool, enhancer regions and extensive API. *Nucleic Acids Res.* **49** (D1), D394–D403 (2021). doi: 10.1093/nar/gkaa1106; pmid: 33290554
30. L. T. Alto, J. R. Terman, Semaphorins and their signaling mechanisms. *Methods Mol. Biol.* **1493**, 1–25 (2017). doi: 10.1007/978-1-4939-6448-2_1; pmid: 27787839
31. A. Kania, R. Klein, Mechanisms of ephrin-Eph signalling in development, physiology and disease. *Nat. Rev. Mol. Cell Biol.* **17**, 240–256 (2016). doi: 10.1038/nrm.2015.16; pmid: 26790531
32. C. Giorgio *et al*., Lithocholic acid is an Eph-ephrin ligand interfering with Eph-kinase activation. *PLOS ONE* **6**, e18128 (2011). doi: 10.1371/journal.pone.0018128; pmid: 21479221
33. R. J. Pasterkamp, Getting neural circuits into shape with semaphorins. *Nat. Rev. Neurosci.* **13**, 605–618 (2012). doi: 10.1038/nrn3302; pmid: 22895477
34. A. Sessa *et al*., Tbr2-positive intermediate (basal) neuronal progenitors safeguard cerebral cortex expansion by controlling amplification of pallial glutamatergic neurons and attraction of subpallial GABAergic interneurons. *Genes Dev.* **24**, 1816–1826 (2010). doi: 10.1101/gad.575410; pmid: 20713522
35. E. G. Hughes, S. H. Kang, M. Fukaya, D. E. Bergles, Oligodendrocyte progenitors balance growth with self-repulsion to achieve homeostasis in the adult brain. *Nat. Neurosci.* **16**, 668–676 (2013). doi: 10.1038/nn.3390; pmid: 23624515
36. M. Barber *et al*., Migration speed of Cajal-Retzius cells modulated by vesicular trafficking controls the size of higher-order cortical areas. *Curr. Biol.* **25**, 2466–2478 (2015). doi: 10.1016/j.cub.2015.08.028; pmid: 26387718
37. V. Villar-Cerviño *et al*., Contact repulsion controls the dispersion and final distribution of Cajal-Retzius cells. *Neuron* **77**, 457–471 (2013). doi: 10.1016/j.neuron.2012.11.023; pmid: 23395373
38. C. C. Winkler *et al*., The dorsal wave of neocortical oligodendrogenesis begins embryonically and requires multiple sources of Sonic Hedgehog. *J. Neurosci.* **38**, 5237–5250 (2018). doi: 10.1523/JNEUROSCI.3392-17.2018; pmid: 29739868
39. V. Borrell, O. Marín, Meninges control tangential migration of hem-derived Cajal-Retzius cells via CXCL12/CXCR4 signaling. *Nat. Neurosci.* **9**, 1284–1293 (2006). doi: 10.1038/nn1764; pmid: 16964252

ACKNOWLEDGMENTS

We thank E. Huillard (Sox10:GFP-DTA), H. Okano (Sox10:Venus), R. Franzen (Pdgfrα:Cre^{ERT}), and A. Pierani (Dbx1:Cre) for providing transgenic mouse lines; A. Püschel (Sema6a-Flag, Sema6c-Flag, Sema5a-Flag, Sema5b-Flag), L. Tamagnone (Sema6b-Myc, Sema6d-V5His), I. Caillé (centrin-GFP), and A. Chédotal (Sema6a) for providing plasmids; M. C. Angulo, A. Pierani, L. Tamagnone, and S. Cappello for providing feedback on the manuscript, as well as all the members of the Nguyen laboratory for their input; and S. Ormenese, A. Hego, C. Vanwinge, and R. Stephan from the GIGA-Cell Imaging and flow cytometry platforms and D. Baiwir from the GIGA-proteomics platform for technical support. All drawings were created with BioRender.com. **Funding:** This work was supported by the Fonds de la Recherche Scientifique (FRS) – Fonds National de la Recherche Scientifique (FNRS) (Synet; Excellence of Science grant no. 0019118F-RG36), the Fonds Leon Fredericq, the Fondation Médicale Reine Elisabeth, the Fondation Simone et Pierre Clerdent, the Belgian Science Policy (IAP-VII network P7/20), the ERANET Neuron (STEM-MCD and NeuroTalk), and the Win2Wal (ChipOmics; no. 2010126). F.L. is a Fonds pour la Formation à la Recherche dans l'Industrieet dans l'Agriculture (FRIA) doctoral fellow, M.J.-T. and J.S. are postdoctoral researchers, C.G.S. is an EOS postdoctoral fellow, and L.N. is research director at the FRS-FNRS. **Author contributions:** C.G.S. and L.N. conceptualized and supervised the study. F.L. designed, conceptualized, performed, and analyzed most experiments. J.S. designed, performed, and analyzed experiments to investigate the molecular mechanisms of unidirectional contact repulsion. M.J.-T. designed, performed, and analyzed molecular biology and biochemistry experiments. G.M. performed proteomic analysis. F.L., C.G.S., and L.N. wrote the manuscript with input from all authors. **Competing interests:** The authors declare no competing interests. **Data and materials availability:** All annotated data are available from the ProteomeXchange Consortium in the Proteomics Identification Database (PRIDE accession no. PXD031876). All other data are available in the main text or the supplementary materials. **License information:** Copyright © 2022 the authors, some rights reserved; exclusive licensee American Association for the Advancement of Science. No claim to original US government works. https://www.science.org/about/science-licenses-journal-article-reuse

SUPPLEMENTARY MATERIALS

science.org/doi/10.1126/science.abn6204
Materials and Methods
Figs. S1 to S8
Tables S1 to S4
References (*40*–*48*)
MDAR Reproducibility Checklist
Movies S1 to S10

Submitted 8 December 2021; accepted 5 April 2022
10.1126/science.abn6204

RESEARCH ARTICLES

CELL BIOLOGY

The deubiquitinase USP8 targets ESCRT-III to promote incomplete cell division

Juliette Mathieu*, Pascale Michel-Hissier, Virginie Boucherit, Jean-René Huynh*

In many vertebrate and invertebrate organisms, gametes develop within groups of interconnected cells called germline cysts formed by several rounds of incomplete divisions. We found that loss of the deubiquitinase USP8 gene in *Drosophila* can transform incomplete divisions of germline cells into complete divisions. Conversely, overexpression of USP8 in germline stem cells is sufficient for the reverse transformation from complete to incomplete cytokinesis. The ESCRT-III proteins CHMP2B and Shrub/CHMP4 are targets of USP8 deubiquitinating activity. In *Usp8* mutant sister cells, ectopic recruitment of ESCRT proteins at intercellular bridges causes cysts to break apart. A Shrub/CHMP4 variant that cannot be ubiquitinated does not localize at abscission bridges and cannot complete abscission. Our results uncover ubiquitination of ESCRT-III as a major switch between two types of cell division.

Clonal multicellularity arises by incomplete divisions of single-cell precursors and gives rise to groups of sister cells linked by cytoplasmic bridges. Such mechanisms underlie the formation of colonies of unicellular organisms and the emergence of multicellularity (*1*). It is also a conserved feature of germline cell development, where cysts of sister cells share the same cytoplasm (*2*). During *Drosophila* oogenesis, cells display complete or incomplete cytokinesis. Indeed, germline stem cells (GSCs) first divide completely to produce a single-cell precursor called a cystoblast (CB). Then, each CB goes through four rounds of incomplete division to generate germline cysts made of 16 sister cells, all linked by cytoplasmic bridges called ring canals (RCs) (*3*) (Fig. 1, A and B).

USP8 is necessary and sufficient to promote incomplete divisions

To identify genes involved in cyst formation, we expressed a collection of short hairpin RNAs (shRNAs) and screened for egg chambers with an abnormal number of nuclei. Two independent shRNA lines targeting the deubiquitinating enzyme USP8 (*4*) induced the formation of egg chambers made of eight, four, or two nuclei, instead of 16 (Fig. 1, C and E, and fig. S1, A and B). These egg chambers resulted from partial breaking of cysts due to ectopic cytokinetic abscission in the germarium. Indeed, the fusome, an endoplasmic reticulum (ER)–derived organelle, formed a midbody-like structure, a feature of complete abscission, which is not seen in wild-type (WT) cysts (Fig. 1, D and F, and fig. S1, B and C) (*5*, *6*). We demonstrated that they were complete abscissions by showing that photoactivatable molecules were not able to diffuse between sister cells, when the midbody structure was present (fig. S2, A and B, and movies S1 to S4). Furthermore, using live imaging, we observed the physical separation of the fusome in mutant cysts (fig. S2, C and D, and movies S5 and S6). Depletion of *Usp8* caused similar ectopic abscissions in male germ cells (fig. S1, D and E). Homozygous mutant cysts for a null allele of *Usp8* (*7*) [$Usp8^{KO}$ germline clone (GLC)] exhibited the same complete abscission phenotype, arguing for the specificity of these shRNAs (fig. S1, F to H). To rule out the possibility that complete abscissions of *Usp8*-depleted cysts were caused by dedifferentiation of cysts into GSCs (*8*, *9*), we verified that *Usp8*-depleted cysts still expressed the differentiation marker Bam (fig. S3, A and B). $Usp8^{KO}$ GLC also lacked Nanos expression at four-cell cysts (*10*), similarly to control differentiating cysts (fig. S3C). In addition, we found that mutant cysts could enter meiosis, although an oocyte was never maintained (fig. S3, D and E). Together, these observations indicated that *Usp8* is necessary to maintain incomplete cytokinesis in *Drosophila* germline cysts.

Conversely, we tested whether USP8 could be sufficient to inhibit cytokinesis in cells that normally complete abscission, such as GSCs. We overexpressed a wild-type form of USP8 in these stem cells and observed the formation of stabilized cytoplasmic bridges in stem cells ("stem cysts") (*11*) (Fig. 1H), which led to CBs made of two cells and egg chambers made of 32 rather than 16 cells (Fig. 1G and fig. S4A) (*6*, *11*, *12*). Incomplete cytokinesis in GSCs overexpressing USP8 was not caused by premature differentiation of GSCs, as these GSCs did not express the cyst-specific protein Bam (Fig. 1H). Similarly, we found that overexpressing USP8 in somatic follicle cells surrounding germline cells and in Schneider 2 (S2) cells also led to the formation of ectopic cysts (fig. S4, C to I). Taken together, these results demonstrated that USP8 is necessary and sufficient to promote incomplete divisions in germline and somatic cells.

USP8 deubiquitinates ESCRT-III proteins

Next, we tested whether USP8 deubiquitinase activity (DUB) was required for the regulation of abscission. We expressed a catalytically inactive form of USP8, called USP8-C572A (*7*, *13*, *14*), in $Usp8^{KO}$ cysts and found that, in contrast to wild-type USP8, it was unable to rescue germline cysts from breaking (Fig. 2, A and B, and fig. S5, A to C). Similarly, overexpression of USP8-C572A was not sufficient to arrest cytokinesis or induce the formation of stem cysts in GSCs, follicle cells, or S2 cells (fig. S4, A to I). Hence, USP8 DUB activity is required for the regulation of abscission.

We observed that USP8 localized at sites of cytokinesis in both males and females, that is, in midbodies of GSC/CB pairs, RCs of germline cysts, and follicle cell RCs (Fig. 2, C and D, and fig. S6, A to C). In the absence of *Usp8*, we noticed an accumulation of ubiquitinated proteins at ectopic midbodies (Fig. 2, E and F), in addition to cytoplasmic aggregates, as described in mammals (fig. S7, A to F). These data suggest that the relevant targets of USP8 could be localized at abscission sites.

The N-terminal microtubule interacting and transport (MIT) domain of human USP8 interacts with ESCRT-III proteins, which are thought to be the driving force of several membrane scission events, including abscission (*15*–*18*). We found that three *Drosophila* ESCRT-III proteins, CHMP1 (charged multivesicular body protein 1), CHMP2B (charged multivesicular body protein 2b), and Shrub (the unique *Drosophila* homolog of CHMP4), could immunoprecipitate USP8 (Fig. 3A and fig. S8A) (*19*–*21*). All three proteins were ubiquitinated in *Drosophila* cells (Fig. 3B and fig. S8B). Expressing a wild-type form of USP8 was sufficient to greatly reduce the amount of ubiquitinated CHMP2B and Shrub, but not of CHMP1 (Fig. 3B and fig. S8B). In contrast, the inactive USP8-C572A had no effect on the ubiquitination levels, although it could still bind all three ESCRT-III proteins (Fig. 3, A and B, and fig. S8, A and B). Conversely, knocking down *Usp8* in S2 cells led to increased levels of ubiquitinated Shrub and CHMP2B (fig. S8, C to E). We concluded that, unlike in intralumenal vesicle formation in yeast (*22*), USP8 is necessary and sufficient to deubiquitinate CHMP2B and Shrub.

USP8 regulates ESCRT-III accumulation at the intercellular bridge

We then investigated whether CHMP2B and Shrub could be relevant targets in vivo. Shrub,

Center for Interdisciplinary Research in Biology, Collège de France, PSL Research University, CNRS, Inserm, Paris, France.
*Corresponding author. Email: juliette.mathieu@college-de-france.fr (J.M.); jean-rene.huynh@college-de-france.fr (J.-R.H.)

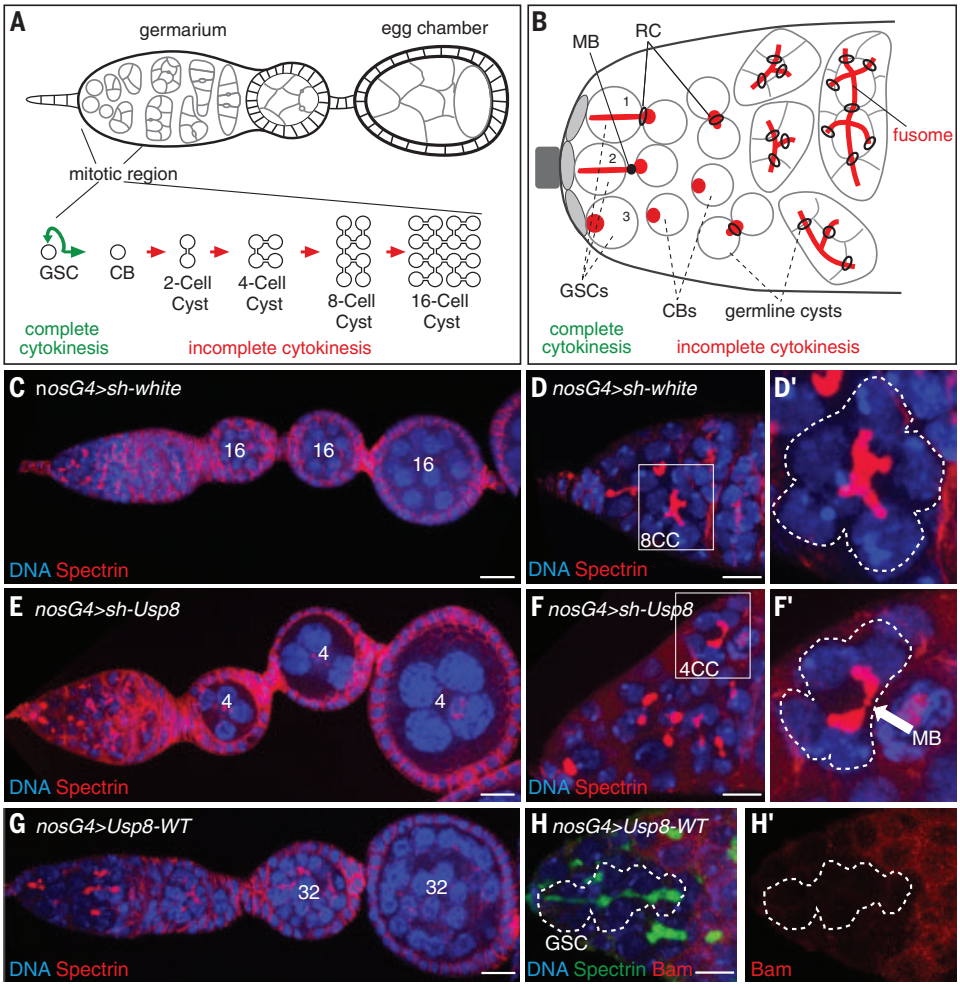

Fig. 1. USP8 is necessary and sufficient to block abscission in the germline lineage. (**A**) (Top) Female ovariole. (Bottom) Cell lineage of the germline stem cell (GSC). (**B**) Mitotic region of the germarium. At the end of mitosis, GSCs are connected to their daughter CBs through a ring canal (RC) (GSC #1) and later by a midbody (MB) (GSC #2). After complete cytokinesis, GSCs and CBs are fully separated (GSC #3). The fusome (red) links the GSC and the CB before abscission and also passes through all RCs of germline cysts. Cap cells, light gray; terminal filament cells, dark gray. (**C** to **H′**) Confocal images of fixed ovarioles [(C), (E), and (G)] and germaria [(D), (F), and (H)] of females expressing *shRNA-w*, *shRNA-Usp8*, or *Usp8-WT* under the control of *nos-GAL4* driver. [(D′) and (F′)] Close-up images of the cysts framed in (D) and (F). Dashed lines surround germline cysts [(D′) and (F′)] or a stem cyst that originates from the GSC [(H) and (H′)]. The white arrow indicates the ectopic MB of a breaking cyst. Scale bars: 20 μm [(C), (E), and (G)] and 10 μm [(D), (F), and (H)]. 4CC, four-cell cyst; 8CC, eight-cell cyst.

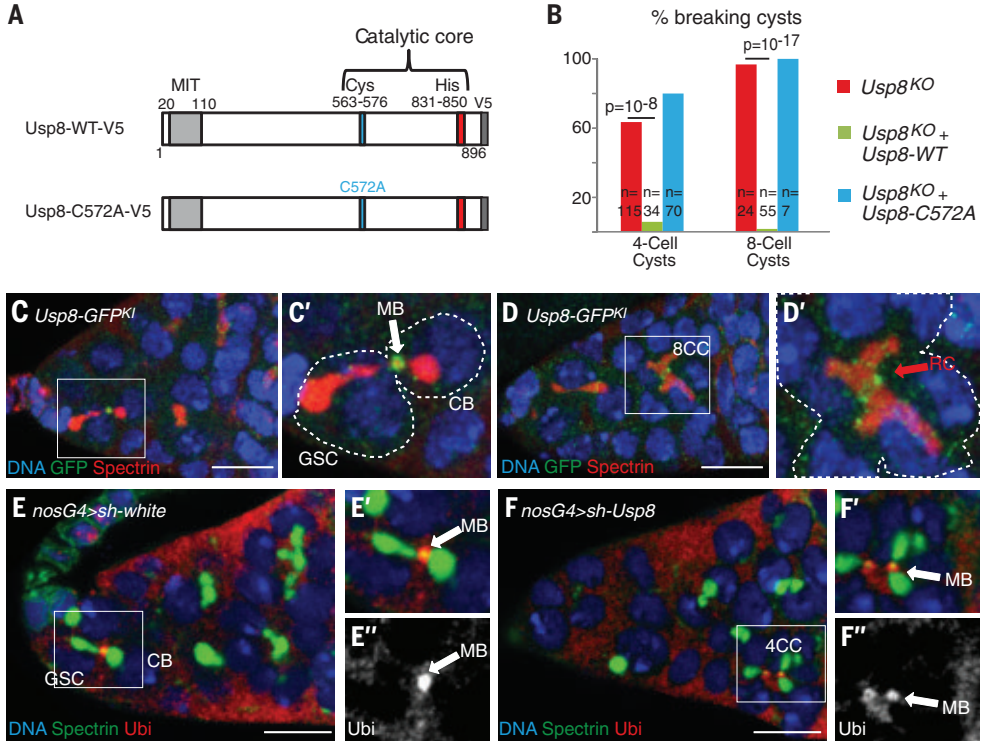

Fig. 2. The deubiquitinating activity of USP8 is essential for its function in germline cysts. (**A**) Scheme of the V5-tagged variants of USP8 proteins. (**B**) Fraction of four- and eight-cell cysts exhibiting a breaking phenotype. *P* values (p) are indicated and derived from Chi square tests. The *n* values indicate the number of cysts analyzed. (**C** and **D**) Confocal images of germaria expressing green fluorescent protein (GFP)–tagged USP8 from the endogenous locus. (**C′** and **D′**) Close-up of the cells framed in (C) and (D). Dashed lines surround a GSC and its daughter CB (C′) and a germline cyst (D′). The white arrow indicates the MB between the GSC and the CB in (C′), and the red arrow indicates the central RC in (D′). (**E** and **F**) Confocal images of germaria expressing *shRNA-w* (E) or *shRNA-Usp8* (F) under the control of *nos-GAL4* driver stained with α-ubiquitin (Ubi) and α-spectrin. (**E′** and **E″**) Close-up views of the GSC/CB pair framed in (E). (**F′** and **F″**) Close-up views of the breaking 4CC framed in (F). White arrows indicate the MB between the GSC and the CB in (E), and the MB of the breaking 4CC in (F). Scale bars: 10 μm.

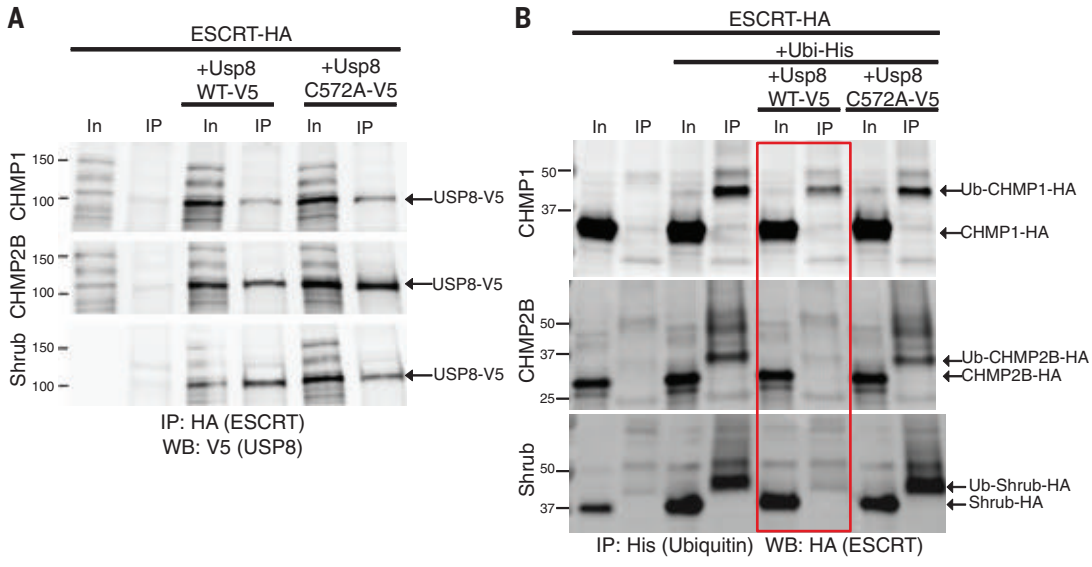

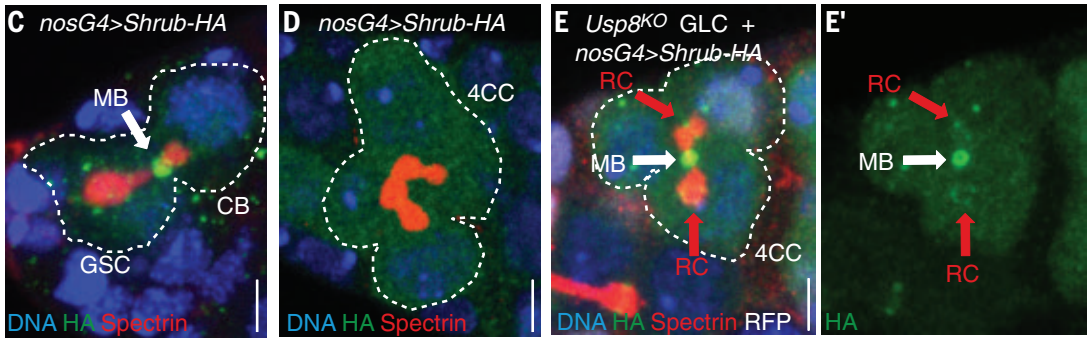

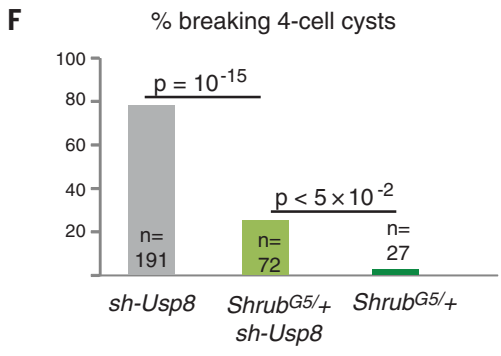

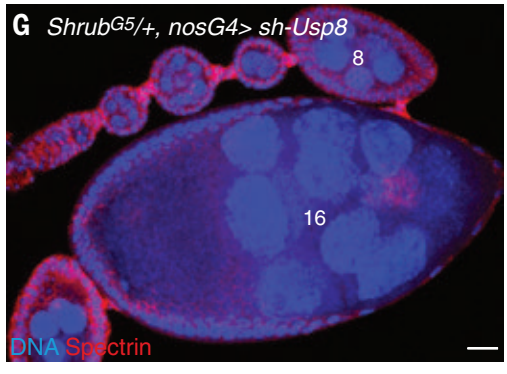

Fig. 3. USP8 regulates CHMP2B and Shrub ubiquitination levels and localization. (**A**) Immunoblots of input ("In," 1/20 of the IP) or immunoprecipitated ("IP") ESCRT-III proteins from S2 cells transfected with ESCRT-HA (hemagglutinin) and V5-tagged USP8 variants. Membranes were blotted with α-V5 antibody. (**B**) Immunoblots of input (1/20 of the IP) or IP ubiquitinated proteins from S2 cells transfected with ESCRT-HA, His-tagged ubiquitin, and V5-tagged USP8 variants. Membranes were blotted with α-HA antibody to reveal ubiquitinated ESCRT-III. USP8 transfection is sufficient to abolish CHMP2B and Shrub ubiquitination (red frame). (**C** and **D**) Confocal images of fixed germaria of females expressing *Shrub-HA* under the control of *nos-Gal4*. A GSC/CB pair (C) and a 4CC (D) are surrounded by dashed lines. The white arrow in (C) indicates the MB between the GSC and the CB. Shrub-HA is not detected at the 4CC RC. Scale bars: 5 μm. (**E**) Confocal images of a fixed germarium of a female expressing *Shrub-HA* under the control of *nos-Gal4* with *Usp8*^{KO} GLC [red fluorescent protein (RFP)–negative cells]. The white arrow indicates the ectopic MB of the breaking 4CC, the red arrows indicate ectopic Shrub-HA at the RCs of the mutant 4CC. Scale bar: 5 μm. (**F**) Fraction of 4CCs exhibiting a breaking phenotype. *P* values (p) are derived from Chi Square tests. The *n* values indicate the number of cysts analyzed. (**G**) Confocal images of a fixed ovariole of a female expressing *shRNA-Usp8* in a *shrb*^{G5}/+ background. The number of nuclei of some ovarioles are indicated. Scale bar: 20 μm.

CHMP2B, and CHMP1 localized at the RC and midbody of GSC/CB pairs (*6*) but were absent at cyst RCs (Fig. 3, C and D, and figs. S9, A, B, D, F, G, I, and J, and S10, A and C). However, in male and female cysts lacking *Usp8*, Shrub, CHMP2B, and CHMP1 all localized at ectopic midbodies and cyst RCs (Fig. 3E and figs. S9, C, E, H, and K, and S10, B and D). To test whether the ectopic localization of ESCRT-III was responsible for ectopic abscissions seen in the absence of USP8, we reduced Shrub or CHMP2B levels in *Usp8*-depleted cysts. In these contexts, we counted fewer four-cell cysts in the process of breaking apart than in cysts depleted of USP8 alone (Fig. 3F and fig. S11, A to C). In addition, we found that older egg chambers contained more nuclei than did *sh-Usp8* mutant egg chambers (fig. S11, D and E). We also observed complete rescue with egg chambers made of 16 cells and a posterior oocyte, which was not seen with *sh-Usp8* alone (Fig. 3J). Altogether, we conclude that deubiquitination of Shrub and CHMP2B by USP8 is required to block their localization at RCs and subsequent abscissions, allowing the formation of 16-cell germline cysts.

Ubiquitination of Shrub is essential to promote abscission in the GSCs

Next, we assessed the relevance of ESCRT protein ubiquitination during complete abscission by testing the ability of a nonubiquitinable variant of Shrub (Shrub-KR) (fig. S12A) to replace endogenous Shrub in GSCs. When we removed both copies of *Shrub* from GSCs, we found that Shrub-KR only poorly compensated

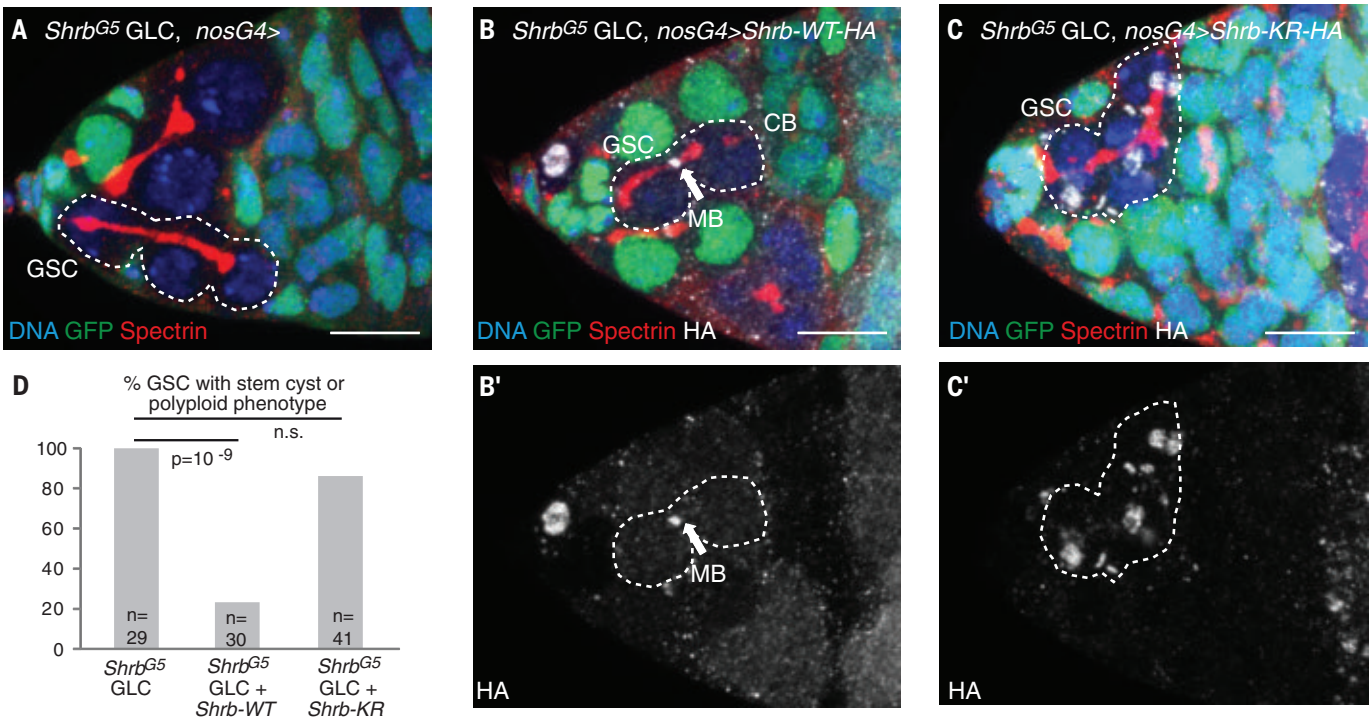

Fig. 4. Ubiquitination of Shrub is essential to promote abscission in the GSCs. (**A** to **C**) Confocal images of fixed germaria with *shrb*^{G5} GLC (GFP negative) expressing *Shrb-WT-HA* (B), *Shrb-KR-HA* (C), or no transgene (A). Dashed lines surround a GSC/CB pair (B) or stem cysts [(A) and (C)]. White arrow indicates the MB positive for Shrb-WT-HA. Scale bars: 10 μm. (**D**) Fraction of GSCs exhibiting a stem-cyst or polyploid phenotype. *P* values (p) are derived from Chi Square tests. ns, not significant (*P* = 0.01). The *n* values indicate the number of GSCs analyzed.

for the absence of Shrub, whereas Shrub-WT rescued *Shrub* mutant germline clones (Fig. 4, A to D, and fig. S12, A and B). In these nonrescued GSCs, Shrub-KR only formed cytoplasmic aggregates and did not localize at RCs (Fig. 4C). Shrub-KR and Shrub-WT were equally able to fully rescue stem-cyst phenotypes when only one copy of *Shrub* was removed in *Shrub*^{G5}/+ females (fig. S12C). Like Shrub-WT, Shrub-KR localized at RCs and midbodies of *Shrub*^{G5}/+ heterozygous GSC/CB pairs (fig. S12, D and E). Furthermore, we could precipitate Shrub-KR and Shrub-WT in *Drosophila* cells, indicating that both proteins could interact physically (fig. S12F). These results showed that Shrub-KR was still functional and able to localize properly when one copy of endogenous Shrub remained in GSCs. Finally, knocking down *Usp8* in *Shrub*^{G5}/+ heterozygous females rescued abscission arrest and the formation of stem cysts, indicating that ubiquitination could also regulate ESCRT-III in GSCs (fig. S12, G to I). Overall, our results show that in both GSCs and germline cysts, USP8 deubiquitinates ESCRT-III proteins to inhibit their localization at intercellular bridges.

A model for the differential accumulation of ESCRT-III at intercellular bridges in GSCs and germline cysts.

Whereas ESCRT proteins are barely detectable in germline cysts, they accumulate at GSC midbodies, despite the expression of USP8 in both cell types (Figs. 2, C and D, and 3, C and D, and fig. S9). This apparent contradiction could be explained by a major difference in cell cycle length between GSCs and germline cysts. GSCs cycle in 24 hours and take ~15 hours to complete abscission (*23*, *24*). In contrast, cysts go through four rounds of mitosis in 24 hours, that is, 6 hours for each cycle. In GSCs, we measured a progressive accumulation of ESCRT-III proteins at the GSC-CB intercellular bridge during the 15 hours after mitosis, whereas ESCRT-III remained barely detectable in cyst cells (Fig. 5A). In contrast, in the absence of *Usp8*, CHMP2B also accumulated progressively in cyst cells with ectopic abscission (Fig. 5A). We noted that the levels of USP8 varied along the cell cycle, peaking during mitosis (Fig. 5B). These observations suggest that in GSCs, ESCRT proteins have time to accumulate to complete abscission before the next mitosis, whereas in cysts, shorter cell cycles and the presence of peak levels of USP8 prevent ESCRT accumulation and stabilize incomplete divisions. In this model, the combination of different cell cycle lengths and USP8 accumulation during mitosis is sufficient to explain the switch from complete to incomplete cytokinesis (Fig. 5E). To test this model experimentally, we reasoned that lengthening the postmitotic phase of germline cysts could be sufficient for ESCRT protein accumulation and completion of cell divisions. We used flies in which the differentiation of germline cysts could be synchronized by the expression of the *bam* gene following a heat shock (HS) (*9*, *25*). At 18 hours after HS, the majority of four-cell cysts in these flies were devoid of ESCRT proteins as in wild-type cysts (Fig. 5, C and D, left, and fig. S13, A, B, D, and E). When we dissected flies 28 hours after HS, most four-cell cysts exhibited CHMP2B-GFP at the RCs (Fig. 5D, middle, and fig. S13, D and E), some of which were even breaking apart, as in *Usp8* mutant cysts (fig. S13F). At 38 hours after HS, we observed an increase in both the amount of CHMP2B-GFP at the RCs and the number of four-cell cysts breaking apart (Fig. 5D, right, and fig. S13, E and F). These results show that when germline cysts were blocked at the four-cell stage for at least 10 hours (from 18 to 28 hours) or 20 hours (from 18 to 38 hours), they accumulated ESCRT proteins at ring canals and completed abscission. These results showed that lengthening the postmitotic phase of four-cell cysts is sufficient for ESCRT proteins to accumulate at ring canals and induce ectopic abscission in germline cysts, as in a *Usp8* mutant (Fig. 5E).

Collectively, our data demonstrate that ubiquitination of ESCRT-III is critical to regulate the switch between complete and incomplete divisions. We propose a model in which USP8 deubiquitinates the ESCRT-III proteins Shrub and CHMP2B, which prevents complete

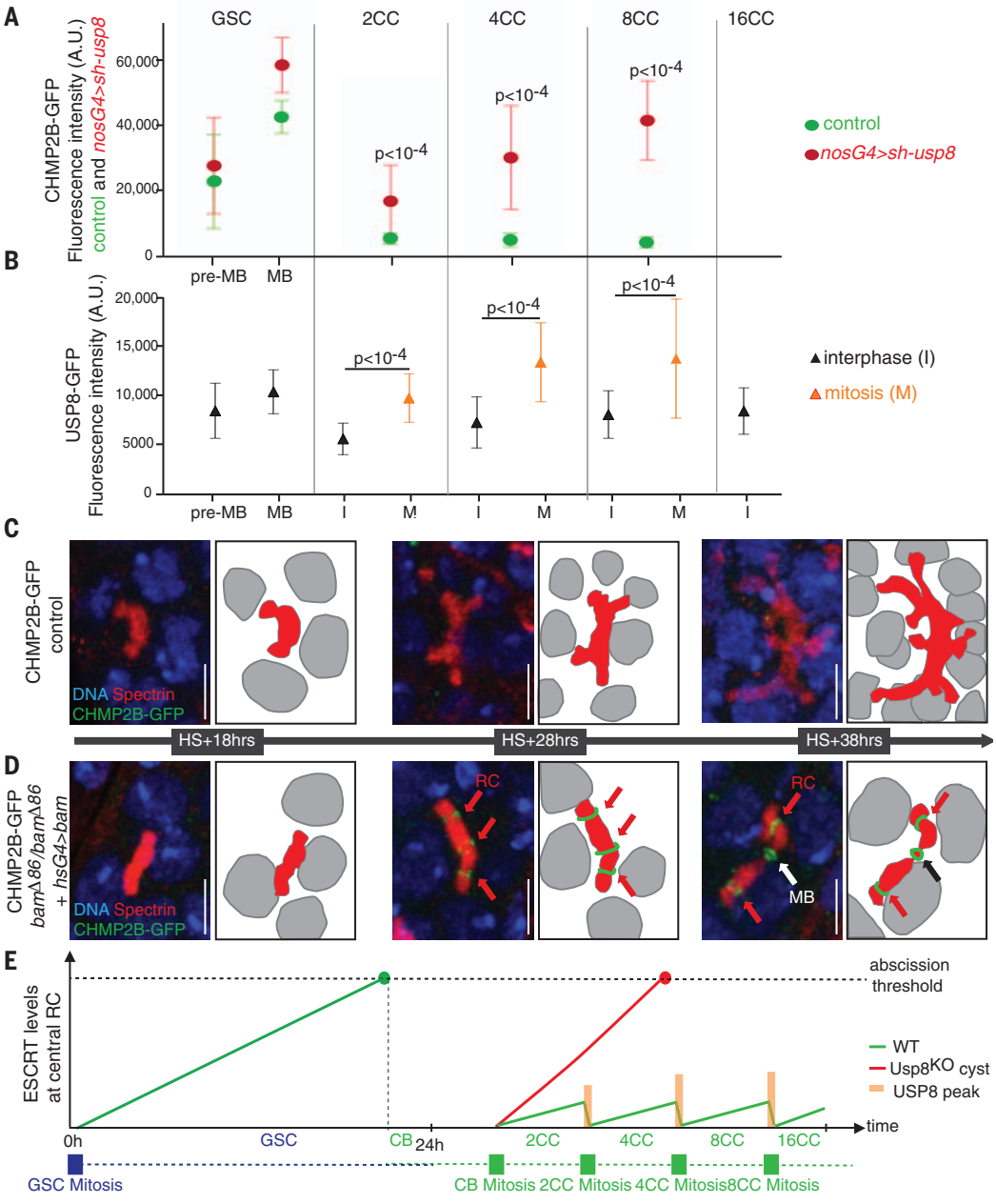

Fig. 5. Differential accumulation of ESCRT-III at intercellular bridges in GSCs and germline cysts. (**A**) Fluorescence intensity [arbitrary units (A.U.)] of CHMP2B-GFP at the RC (pre-MB) or the MB of GSC and at the central RC of cysts (2CC, 4CC, and 8CC) in control (green) or *sh-Usp8* (red)–expressing flies. *P* values (p) between control and shRNA-expressing flies are derived from Mann-Whitney tests. (**B**) Fluorescence intensity (A.U.) of USP8-GFP at the RC (pre-MB) or the MB of GSC and at the central RC of cysts (2CC, 4CC, 8CC, and 16CC) in $Usp8^{KI}$ flies in interphase (black) or mitosis (orange). *P* values (p) between interphase and mitosis are derived from Mann-Whitney tests. (**C** and **D**) Confocal images and schemes of fusomes (stained for α-spectrin, red) in germaria of WT females expressing *CHMP2B-GFP* (C) or of $bam^{\Delta 86}$ females expressing *CHMP2B-GFP* and *HS*-bam (D). Time after heat shock is indicated on the dark arrow between (C) and (D). In (D), 4CCs are observed at 18 hours after HS (left). CHMP2B-GFP is then observed at the RCs (red arrow) of a 4CC (28 hours, middle), and the central RC of a 4CC breaks into a MB (white arrow) at 38 hours after HS (right). Scale bars: 5 μm. (**E**) Schematic model of ESCRT levels over time in the germarium. The GSC has a 24-hour cell cycle. Abscission between the newly formed GSC and its daughter CB occurs late in the cell cycle, before the next mitosis, and thus the GSC/CB pair never experiences a USP8 peak. During this long period, the GSC/CB RC therefore accumulates ESCRT, reaching a high level allowing abscission. The CB becomes a 16CC in 24 hours; therefore each cycle lasts only 6 hours, leaving much less time to accumulate ESCRT at RC at each cycle. In addition, USP8 levels at the RC in the cyst peak at each mitosis (orange bars) and remove (or block the dynamic recruitment of) ESCRTs at the RCs. We propose that short cell cycle duration combined with USP8 peaks in mitosis are responsible for both the low levels of ESCRT at cyst RCs and the absence of abscission. When USP8 is absent (red), ESCRT levels increase at each cyst cycle, allowing abscission.

abscission and allows sister cells to remain linked by stabilized cytoplasmic bridges. Both GSCs and germline cysts express *Usp8* and several ESCRT-III proteins, despite different outcomes for abscission. Complete and incomplete abscission are thus not inherently different in nature. We propose that it is mainly the duration of abscission, regulated by the cell cycle, that differs in the two cases (Fig. 5E).

A major question arising from our work is the evolutionary relationship between complete and incomplete division, and whether USP8 played a role in the emergence of one from the other. We observed the most drastic consequences of *Usp8* loss in germline cysts, not in stem cells, indicating that the main function of USP8 is to promote incomplete division and that it seems dispensable for complete cytokinesis. Besides germ cells, unicellular organisms such as the choanoflagellates can also form colonies of sister cells by incomplete divisions. These colonies, considered a first step toward multicellularity, are linked by cytoplasmic bridges that resemble metazoan ring canals (*1*). Given that ESCRT-III function in abscission is conserved from archaebacteria to vertebrates (*26*), it will be interesting to investigate whether ubiquitination of ESCRT-III plays a role in the emergence of these incomplete divisions.

REFERENCES AND NOTES

1. S. R. Fairclough, M. J. Dayel, N. King, *Curr. Biol.* **20**, R875–R876 (2010).
2. M. E. Pepling, M. de Cuevas, A. C. Spradling, *Trends Cell Biol.* **9**, 257–262 (1999).
3. J. R. Huynh, D. St Johnston, *Curr. Biol.* **14**, R438–R449 (2004).

4. N. Loncle, M. Agromayor, J. Martin-Serrano, D. W. Williams, *Sci. Rep.* **5**, 8461 (2015).
5. J. Mathieu, J. R. Huynh, *Methods Cell Biol.* **137**, 105–118 (2017).
6. N. R. Matias, J. Mathieu, J. R. Huynh, *PLOS Genet.* **11**, e1004653 (2015).
7. A. Mukai *et al.*, *EMBO J.* **29**, 2114–2125 (2010).
8. D. McKearin, B. Ohlstein, *Development* **121**, 2937–2947 (1995).
9. T. Kai, A. Spradling, *Nature* **428**, 564–569 (2004).
10. L. Gilboa, R. Lehmann, *Curr. Biol.* **14**, 981–986 (2004).
11. J. Mathieu *et al.*, *Dev. Cell* **26**, 250–265 (2013).
12. A. H. Eikenes *et al.*, *PLOS Genet.* **11**, e1004904 (2015).
13. E. Mizuno *et al.*, *Mol. Biol. Cell* **16**, 5163–5174 (2005).
14. W. Luo *et al.*, *Genes Dev.* **26**, 2536–2549 (2012).
15. P. E. Row *et al.*, *J. Biol. Chem.* **282**, 30929–30937 (2007).
16. J. Guizetti *et al.*, *Science* **331**, 1616–1620 (2011).
17. J. Schöneberg, I. H. Lee, J. H. Iwasa, J. H. Hurley, *Nat. Rev. Mol. Cell Biol.* **18**, 5–17 (2017).
18. B. Mierzwa, D. W. Gerlich, *Dev. Cell* **31**, 525–538 (2014).
19. E. Nikko, B. André, *Traffic* **8**, 566–581 (2007).
20. N. Johnson, M. West, G. Odorizzi, *Mol. Biol. Cell* **28**, 661–672 (2017).
21. X. Crespo-Yáñez *et al.*, *PLOS Genet.* **14**, e1007456 (2018).
22. D. Buysse, A. K. Pfitzner, M. West, A. Roux, G. Odorizzi, *J. Cell Sci.* **133**, jcs241455 (2020).
23. G. Villa-Fombuena, M. Lobo-Pecellín, M. Marín-Menguiano, P. Rojas-Ríos, A. González-Reyes, *Development* **148**, dev199716 (2021).
24. L. X. Morris, A. C. Spradling, *Development* **138**, 2207–2215 (2011).
25. B. Ohlstein, D. McKearin, *Development* **124**, 3651–3662 (1997).
26. G. Tarrason Risa *et al.*, *Science* **369**, eaaz2532 (2020).

ACKNOWLEDGMENTS

We thank M. O. Fauvarque, S. Goto, F. K. Teixeira, M. Furthauer, P. Thérond, K. Haglund, the Bloomington Stock center, and the Developmental Studies Hybridoma Bank for reagents used in this study. We thank A. Echard for discussions and suggestions and the Huynh lab, M. H. Verlhac, D. St Johnston, and E. Montembault for helpful comments on the manuscript. We are grateful to the Orion Imaging Facility (Collège de France) and BDD Curie Imaging facility. **Funding:** The J.-R.H. lab is supported by CNRS, INSERM, Collège de France, La Fondation pour la Recherche Médicale (FRM) (Equipes FRM DEQ20160334884), Agence Nationale de la Recherche (ANR) (ANR-15-CE13-0001-01, AbsCyStem), and the Bettencourt Schueller Foundation. **Author contributions:** J.M. and J.-R.H. designed the project, analyzed the data, and wrote the manuscript. J.M., P.M.-H., and V.B. produced reagents and performed experiments. **Competing interests:** The authors declare no competing or financial interests. **Data and materials availability:** All materials are available upon request. **License information:** Copyright © 2022 the authors, some rights reserved; exclusive licensee American Association for the Advancement of Science. No claim to original US government works. https://www.science.org/about/science-licenses-journal-article-reuse.

SUPPLEMENTARY MATERIALS

science.org/doi/10.1126/science.abg2653
Materials and Methods
Supplementary Text
Figs. S1 to S13
List of Genotypes
References (*27*–*40*)
MDAR Reproducibility Checklist
Movies S1 to S6

Submitted 22 December 2020; accepted 12 April 2022
10.1126/science.abg2653

MOLECULAR EVOLUTION

Epistatic drift causes gradual decay of predictability in protein evolution

Yeonwoo Park[1], Brian P. H. Metzger[2], Joseph W. Thornton[1,2,3]*

Epistatic interactions can make the outcomes of evolution unpredictable, but no comprehensive data are available on the extent and temporal dynamics of changes in the effects of mutations as protein sequences evolve. Here, we use phylogenetic deep mutational scanning to measure the functional effect of every possible amino acid mutation in a series of ancestral and extant steroid receptor DNA binding domains. Across 700 million years of evolution, epistatic interactions caused the effects of most mutations to become decorrelated from their initial effects and their windows of evolutionary accessibility to open and close transiently. Most effects changed gradually and without bias at rates that were largely constant across time, indicating a neutral process caused by many weak epistatic interactions. Our findings show that protein sequences drift inexorably into contingency and unpredictability, but that the process is statistically predictable, given sufficient phylogenetic and experimental data.

A mutation's evolutionary fate depends on its phenotypic effects. If the effects are stable over time, knowledge of them in the present can help predict the future course of evolution and explain the causes of evolutionary change in the past. Epistatic interactions, however, may cause a mutation's effects to change over time and its evolutionary accessibility to become contingent on the particular sequence changes that preceded it during history (*1*, *2*).

Despite a recent tide of information about epistatic interactions within proteins, we lack a comprehensive understanding of changes in the effects of mutations (the set of all potential amino acid changes) caused by interactions with substitutions (the subset of mutations that fix during evolution). What fraction of mutations change in their effects over evolutionary time, and how drastically? Do they change gradually or episodically and at what rate? What are the consequences for evolutionary outcomes? Deep mutational scanning (DMS) experiments have detected epistasis among mutations within present-day proteins (*3*–*9*), but these studies do not address interactions with historical substitutions or reveal changes in the effects of mutations over evolutionary time. Some mutations have different effects when introduced into various present-day proteins, implying epistatic interactions with the substitutions that occurred as these proteins diverged from each other (*10*–*14*); without polarizing and calibrating these differences with respect to time, however, it is not possible to illuminate the rate, direction, or regularity of the process by which the effects of mutations changed during evolution. Ancestral protein reconstruction studies have shown that the effects of particular mutations changed during particular phylogenetic intervals (*15*–*22*), but these works have examined only the beginning and end of an interval and therefore cannot reveal the temporal dynamics of epistasis.

Here, we address this knowledge gap by using DMS to comprehensively assess the effect of introducing every possible amino acid mutation into a series of reconstructed ancestral and extant proteins along a densely sampled phylogenetic trajectory. We used as a model the DNA binding domain (DBD) of steroid hormone receptors, a family of essential transcription factors in bilaterian animals that mediate the actions of sex and adrenal steroids by binding to specific DNA sequences and regulating the expression of target genes (*23*–*25*). This approach allowed us to measure changes in the functional effect of every possible amino acid mutation during a series of defined intervals across 700 million years of DBD evolution. To analyze these data, we developed a quantitative framework that treats each mutation's effect as a trait that evolves probabilistically on a phylogeny, which we used to characterize the temporal dynamics, evolutionary consequences, and underlying genetic architecture of epistatic interactions.

Results

Phylogenetic DMS

We first inferred the phylogeny of steroid and related receptors (Fig. 1A and fig. S1) and reconstructed the maximum a posteriori protein sequences of seven ancestral DBDs along two lineages—one leading to the human glucocorticoid receptor (GR) and the other to the steroid receptor of the annelid *Capitella teleta*, which are among the most diverged of all functionally characterized extant DBDs. The reconstructed ancetral proteins include the ancient progenitor protein whose duplication and divergence gave rise to the first steroid

[1]Committee on Genetics, Genomics, and Systems Biology, University of Chicago, Chicago, IL, USA. [2]Department of Ecology and Evolution, University of Chicago, Chicago, IL, USA. [3]Department of Human Genetics, University of Chicago, Chicago, IL, USA.
*Corresponding author. Email: joet1@uchicago.edu

receptor (AncNR3), the ancestor of all extant steroid receptors (AncSR, which existed in the ancestor of all bilaterians), and five descendants of AncSR (Fig. 1B and fig. S2). These nine DBDs are separated by eight phylogenetic intervals, each comprising 3 to 42% sequence divergence. We constructed a yeast strain that carries a green fluorescent protein (GFP) reporter driven by a DNA response element for these DBDs and confirmed that all reconstructed ancestral DBDs bind to it, as expected based on prior studies (*25*). GFP fluorescence in this strain correlates well with binding affinity, which was previously measured using fluorescence anisotropy (fig. S4D).

For each of the seven ancestral and two extant DBDs, we generated a library of variants that contains all 19 possible amino acid mutations at all 76 sites (fig. S3). We used a bulk assay of fluorescence-activated cell sorting coupled with deep sequencing to quantify the GFP fluorescence of each variant with very high repeatability [Pearson's correlation coefficient squared (r^2) = 0.99 across three replicates; Fig. 1C and figs. S4 and S5]. We calculated the effect of a mutation as the difference in the mean $\log_{10}$-GFP fluorescence (ΔF) between variants that differ by a single amino acid; we applied this approach to all mutations from the wild-type amino acid in any of the nine DBDs to all other 19 amino acids.

Differences in the effect of a mutation between successive nodes on the phylogeny ($\Delta\Delta F$) indicate that the mutation interacts with historical substitutions that occurred during that interval (Fig. 1D). We normalized the effects of the mutations to remove global background-dependence caused by different wild-type activity levels (fig. S6). After this correction, differences in a mutation's effect among the nine DBDs are attributable to specific epistatic interactions with intervening substitutions on the phylogeny.

Pervasive random changes in the effects of mutations

To analyze the evolutionary dynamics of epistasis over time, we adapted a classic quantitative framework for modeling trait evolution on phylogenies (*26*, *27*), including the extent, direction, and rate of evolutionary change of the trait; the underlying genetic architecture; and the relative roles of selection and genetic drift. Our approach treats the phenotypic effect of each mutation as a trait that changes probabilistically across phylogenetic intervals, allowing us to ask these questions about epistatic change during historical DBD evolution.

Sixty percent of all mutations display significantly different effects among the nine backgrounds, and 22% differ in the direction of their effects [false discovery rate (FDR) ≤ 0.1; Fig. 2A]. Most of the mutations that show no evidence of epistasis destroy protein function regardless of genetic background (ΔF always at the lower bound of measurement, −1.3). Only 5% of mutations have a nondestructive effect that did not vary significantly across the phylogeny.

Epistatic changes occurred during all eight phylogenetic intervals (Fig. 2B and fig. S7A). Even in the shortest interval, during which there were only two sequence substitutions, the effects of more than 200 mutations changed significantly. During the other intervals, even more mutations changed in effect. On average, each substitution is associated with significant changes in the effects of about 60 mutations, about 2% of the total set of possible mutations (fig. S7B).

These epistatic changes were unbiased over time. Changes in the effects of mutations ($\Delta\Delta F$) are distributed almost symmetrically around 0 (mean = −0.01; Fig. 2C). The fraction of mutations that reduce activity was nearly constant among the nine intervals, as was the fraction of mutations that destroy activity (Fig. 2D). No individual mutations had effects that changed with a significant bias in either direction over time (fig. S7C). These data indicate that directional selection did not drive long-term epistatic changes in the effects of mutations, and mutational robustness did not change systematically over time. Further, the variance

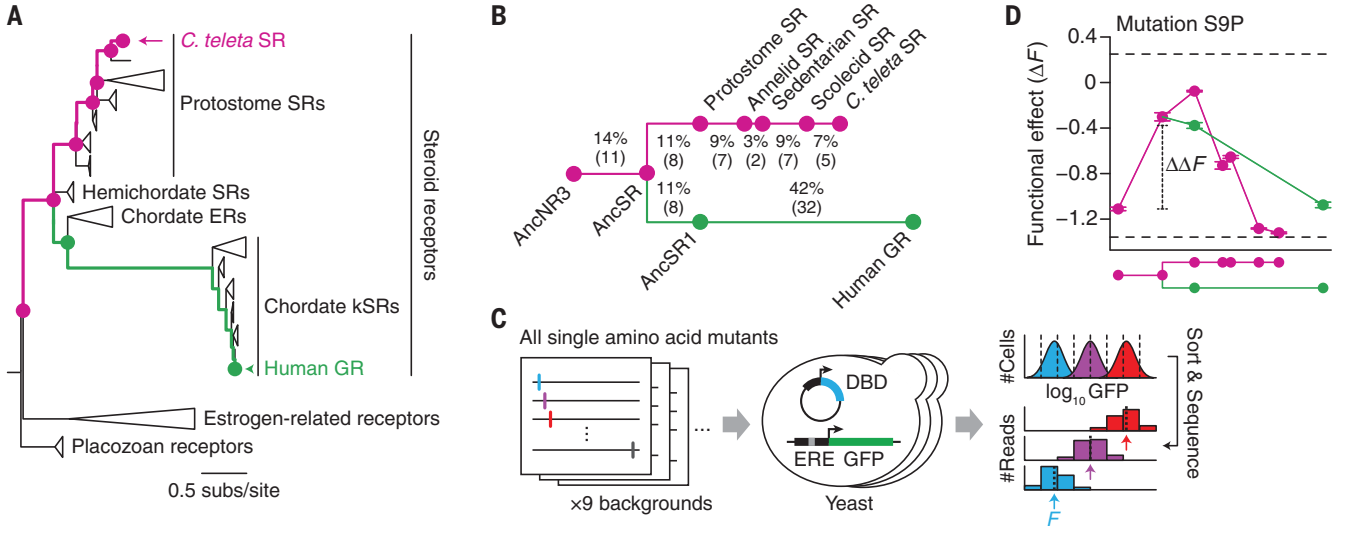

Fig. 1. Phylogenetic DMS. (**A**) Phylogeny of the DBD of steroid and related receptors. Circles represent DBDs characterized here by DMS. The complete phylogeny is shown in fig. S1. ERs, estrogen receptors; kSRs, ketosteroid receptors, including GR; SRs, steroid receptors; subs/site, substitutions per site. (**B**) Phylogenetic relations among the nine characterized DBDs. Colors distinguish trajectories to *C. teleta* SR and human GR. Sequence divergence (percent) and number of sequence differences (in parentheses) in each interval are shown. (**C**) Sort-seq assay for DBD activity. For each DBD, a library containing all possible single-amino-acid mutations was generated using microarray-based synthesis and cassette assembly (fig. S3) and cloned into yeast carrying a GFP reporter (left and middle). The activity of each mutant was measured by sorting the library of cells into fluorescence bins, inferring the distribution of each mutant among bins by sequencing, and calculating the mean $\log_{10}$-GFP fluorescence (*F*). Hypothetical distributions for three variants with high, medium, and low *F* are shown (right). ERE, estrogen response element. (**D**) Tracing epistatic change across the phylogeny using example mutation S9P. The effect on each DBD's activity (points) was quantified as the change in mean $\log_{10}$-GFP fluorescence (ΔF). The *x* axis shows each DBD in order on the phylogeny, positioned by sequence divergence and colored by trajectory. $\Delta\Delta F$ represents the change in the mutation's effect between a pair of DBDs, which is caused by epistatic interactions with intervening substitutions. Error bars represent SEM (*n* = 3). Dashed lines indicate upper and lower measurement bounds.

of the distribution of $\Delta\Delta F$ in each interval increased linearly with sequence divergence, rather than plateauing (Fig. 2, E and F); this result suggests that stabilizing selection did not maintain the effects of mutations at intermediate values within defined limits.

The effects of most mutations drifted gradually

To test whether epistatic change was gradual or episodic, we fit probabilistic models of trait evolution to the trajectory of changes in the effect of each mutation. Brownian motion represents a simple model of gradual evolution at a constant rate without directional bias: Changes in the trait value among phylogenetic intervals are normally distributed when normalized for the length of the interval, with a mean change of zero and constant variance per unit sequence divergence (which represents the rate of evolution). In the alternative model of episodic evolution, the normalized variance is a free parameter for each interval, which allows the rate to differ among intervals (Fig. 3A). We fit both models to the eight $\Delta\Delta F$ values of each mutation and used a likelihood-ratio test to compare the fit of the two models.

We found that the Brownian motion model was the best-fit model for 92% of mutations that changed epistatically (Fig. 3, B and C), irrespective of whether the effects of the mutations changed rapidly or slowly (Fig. 3D). For the 8% of mutations best fit by the episodic model, effects were nearly constant in most intervals, with substantial changes during one or a few intervals. The functional effects of most mutations therefore evolved as a random variable that changes gradually along the phylogeny at a characteristic rate and without bias. We call this process epistatic drift.

Phylogenetic cross-validation confirmed that the effects of most mutations evolved at a steady rate across the phylogeny (Fig. 3E). For each mutation, we predicted the epistatic change expected in each of the eight intervals given the rate of epistatic change estimated from the seven other intervals; we then compared these predictions with experimental observations, pooling mutations with similar estimated rates (Fig. 3F). Predicted and observed epistatic changes were strongly correlated (Spearman's $\rho \geq 0.94$ for every interval; Fig. 3G), indicating that the mutations' relative rates of epistatic change did not strongly vary along the phylogeny. The absolute rate of total epistatic change, however, was systematically faster than predicted in some intervals and slower in others: The mean rate of epistatic change for all mutations in each interval ranges from 0.7 to 1.4 of the average across the phylogeny (Fig. 3H). Epistatic change in the effect of each mutation therefore varies stochastically across intervals (consistent with Brownian motion), but this variation is correlated among mutations; as a result, the total amount of epistatic change across all mutations is systematically greater in some intervals than in others. This pattern is likely to arise because the total epistatic change depends on the particular substitutions that fixed during an interval, and some substitutions are more epistatic than others because they interact more strongly or with a larger number of mutations. The mean rate of epistatic change was not systematically different during intervals that followed gene duplications.

These observations have two major implications for evolution and the genetic architecture of epistatic interactions (Fig. 3I). First, epistatic

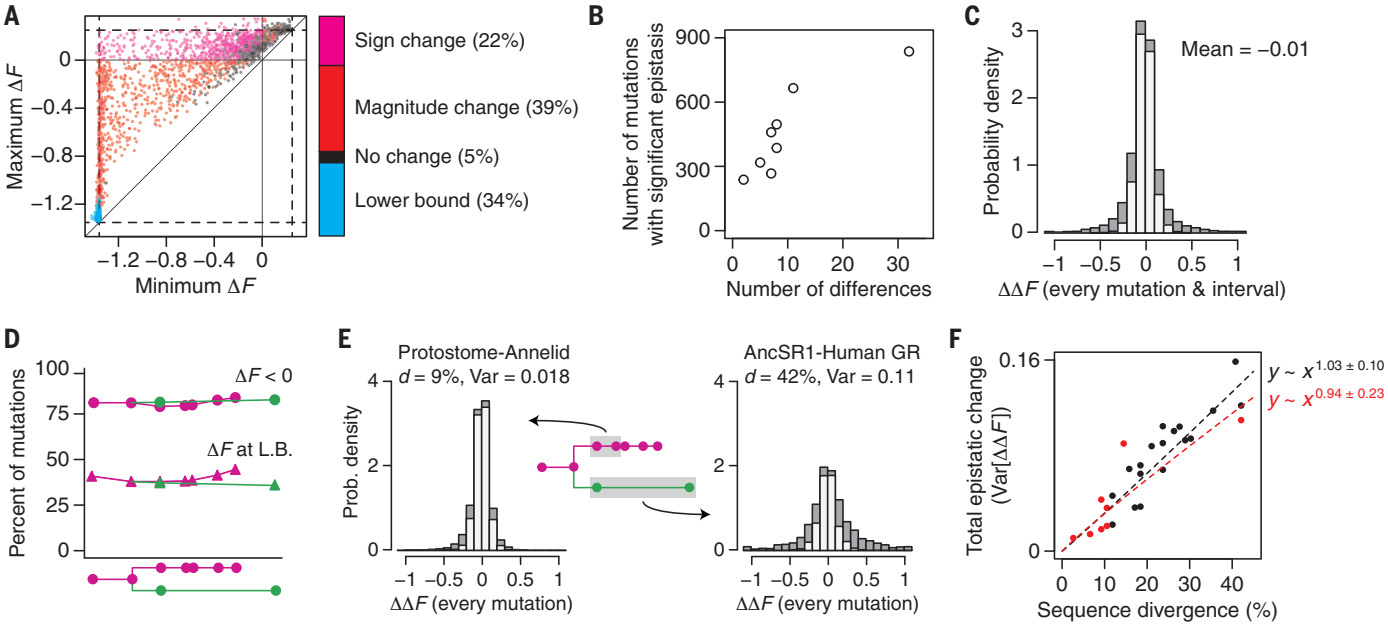

Fig. 2. Pervasive random changes in the effects of mutations. (**A**) Maximum and minimum effect of each mutation (points) across the nine DBDs, colored according to the stacked column on the right, which shows the proportion of mutations in four categories: magenta, significant effect of DBD background on ΔF and the sign of ΔF different between the maximum and minimum; red, significant effect of background but no sign difference; black, no significant effect of background and ΔF within measurement limits; and cyan, ΔF at the lower bound of measurement in all nine DBDs. Significance was evaluated by Welch's analysis of variance, Benjamini-Hochberg FDR ≤ 0.1. Dashed lines indicate measurement bounds. (**B**) Number of mutations in each phylogenetic interval that changed significantly in ΔF (heteroscedastic t test between parent and child node, FDR ≤ 0.1) plotted against the number of amino acids that diverged in the interval. (**C**) Distribution of epistatic change in the effect of every mutation during every phylogenetic interval ($\Delta\Delta F$). Dark gray indicates a $\Delta\Delta F$ significantly different from zero. Mutations that were always at the lower bound of measurement were excluded. (**D**) Fraction of mutations in each DBD with a ΔF less than zero (circles) or a ΔF at the lower bound (L.B.) of measurement (triangles). (**E**) Distribution of $\Delta\Delta F$ of all mutations for the protostome-annelid interval (left) or the AncSR1-human GR interval (right). The variance of the distribution (Var) quantifies the total epistatic change in the effects of all mutations during an interval. d, sequence divergence. (**F**) Total epistatic change as a function of sequence divergence across the phylogeny. Red dots represent each of the eight independent phylogenetic intervals between characterized DBDs; black dots represent all composite intervals. Dashed lines indicate the best-fit power function for all (black) or the eight independent (red) intervals.

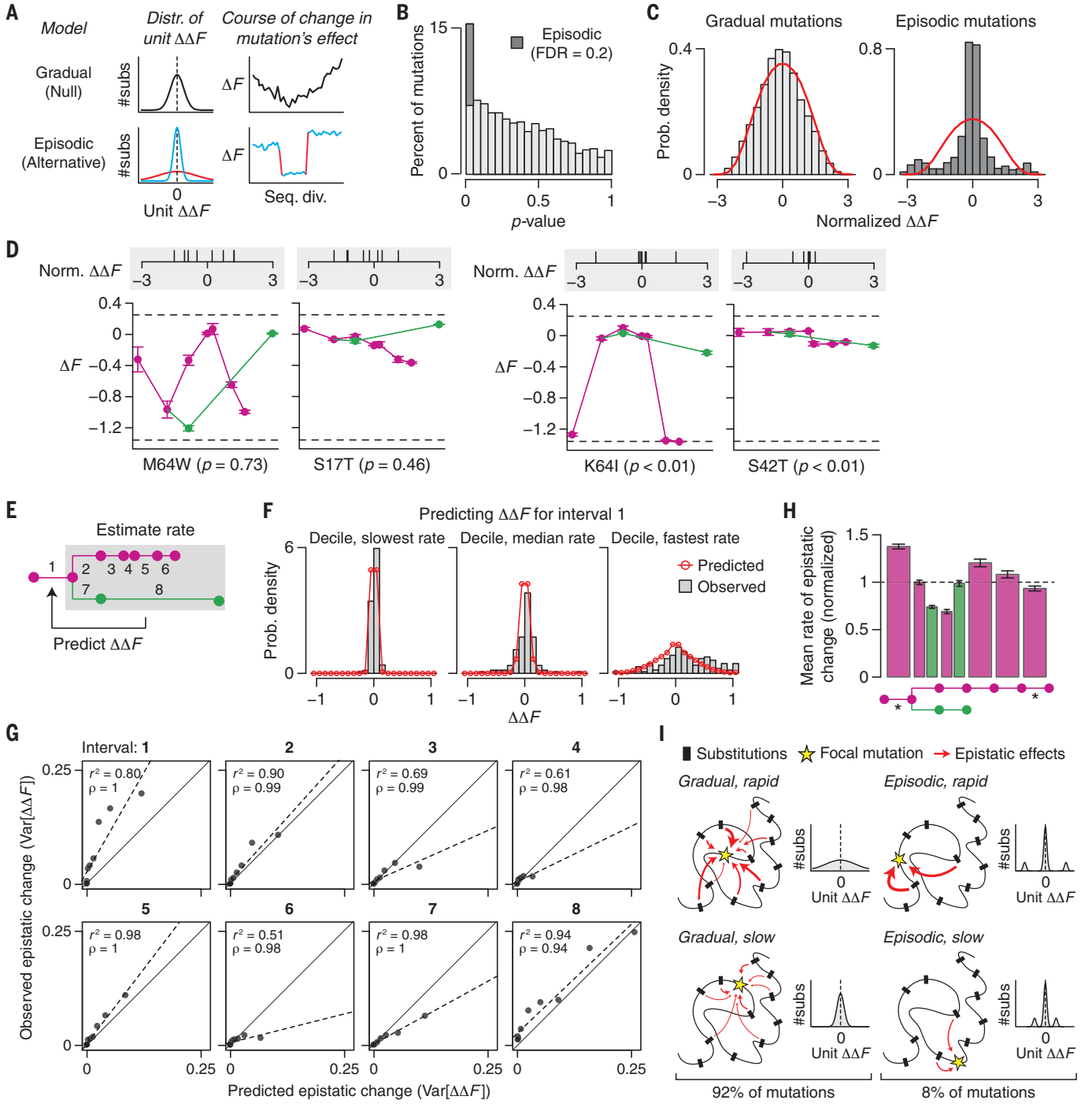

Fig. 3. Effects of most mutations changed gradually at characteristic rates. (**A**) Models of the tempo of epistatic change. In the null model, the amount of change in a mutation's effect per substitution in an interval (unit $\Delta\Delta F$) is randomly drawn from a normal distribution centered at 0; the variance is the same among intervals, so the mutation's effect changes gradually at a constant expected rate as substitutions accrue. In the alternative model, the variance may differ among phylogenetic intervals (cyan versus red), leading to episodic changes in a mutation's effect. Seq. div., sequence divergence. (**B**) Distribution of the *p* value of the likelihood-ratio test comparing gradual and episodic models for each mutation. Darker gray indicates mutations for which the gradual model is rejected (FDR ≤ 0.2). Mutations that were always at the lower bound of measurement were excluded from this analysis. (**C**) Distribution of the normalized amount of epistatic change in each interval, for all mutations better fit by the gradual model (left) or the episodic model (right). Normalized $\Delta\Delta F$ is the $\Delta\Delta F$ of a mutation in an interval divided by $\sigma d^{1/2}$, where σ is the mutation's average rate of epistatic change and d is the length of the interval. Gray columns are observed data; the red line shows the distribution expected under the null model. (**D**) Trajectory of changes in the effect of two sets of example mutations that are better fit by the gradual model (left) or the episodic model (right); in each category, one evolves rapidly and the other slowly. Each mutation's *p* value in the likelihood-ratio test is shown. The gray box shows normalized $\Delta\Delta F$ across each of the eight intervals. Dashed lines indicate measurement bounds. (**E**) Phylogenetic cross-validation. In the example shown, $\Delta\Delta F$ in interval 1 is

predicted from the average rate of epistatic change measured across intervals 2 to 8 (gray box). (**F**) Distribution of observed $\Delta\Delta F$ during interval 1 (gray columns) and predicted by cross validation (red line). Mutations were grouped into deciles by their rate of epistatic change across intervals 2 to 8; predictions are shown for deciles with the slowest, median, or fastest rates. (**G**) The relative rates of epistatic change for mutations are consistent across phylogenetic intervals. Points represent deciles of mutations grouped by the predicted rate of epistatic change; observed epistatic change is plotted against that predicted by cross-validation. The dashed line indicates the linear regression. (**H**) Among-interval differences in average rate of epistatic change. Each column shows the mean rate of epistatic change of all mutations in one phylogenetic interval, normalized so that the mean across all intervals equals one. Error bars represent the estimated standard deviation obtained by bootstrap-resampling of mutations. Asterisks indicate the intervals immediately following gene duplication. (**I**) Inferring the architecture of epistatic interactions between substitutions (subs; black boxes) and a focal mutation (star) from phylogenetic DMS. Gradual changes in the mutation's effect during evolution arise if many substitutions act as epistatic modifiers (arrows, with thickness showing the strength of interaction), yielding a normal distribution of $\Delta\Delta F$ per substitution (left). Episodic changes arise from interactions with only a few substitutions, yielding a distribution heavy at zero and the tails (right). In either case, strong versus weak interactions cause rapid (top) versus slow (bottom) epistatic change. The fraction of all mutations in each category in our experiments is shown.

interactions within the DBD are dense: The effects of most mutations changed gradually because of weak interactions with many substitutions, and each substitution typically modified the effects of many mutations (Fig. 2B). If most epistatic changes were triggered by rare, large-effect modifiers, the distribution of $\Delta\Delta F$ would be enriched near zero and at extreme values, a pattern that we observed for only a small fraction of mutations. Most historical contingency is therefore the cumulative result of many small-effect epistatic modifications. Against this background of gradual epistatic drift, a few mutations occasionally undergo substantial changes in their effects.

Second, some mutations are more epistatically sensitive than others, with effects that diverged more rapidly as substitutions accumulated. Conversely, some substitutions are more epistatic than others, changing the effects of more target mutations or causing changes of greater magnitude. As a result, there are systematic differences among intervals in the average rate of epistatic change across all mutations.

Mutations vary in memory length and the time scale of contingency

Because the effect of each mutation drifts at random at a steady rate, there should be a characteristic time period after which the mutation's effect can no longer be reliably predicted from its known effect at some other time. We call this period the mutation's memory length, the measure of which is the memory half-life—the amount of sequence divergence over which the correlation of a mutation's effect with its initial effect is reduced by half. To estimate memory half-life, we partitioned mutations into deciles by their rate of epistatic change and calculated for each decile how correlated the effects of mutations are between each pair of DBDs (Fig. 4, A to D). We modeled the correlation coefficient as an exponentially decaying function of sequence divergence. We then used this relationship to estimate the memory half-life of each mutation from its rate of epistatic change.

Reflecting the wide variation in the rate of epistatic change among mutations, memory half-lives range from just 3% sequence divergence to virtually infinite (Fig. 4E). Mutations with the shortest half-lives therefore forget the effects they had in the past after just a few sequence substitutions at other sites. At any moment, their effect and likely fate depend primarily on the substitutions that occurred most recently during their history.

Relative to the time scale of DBD evolution, about one-fourth of all mutations have short memories (half-life < 50% sequence divergence); in this group, the effects in present-day human GR are almost completely independent of their initial effects in AncSR (r^2 = 0.10; Fig. 4F). Twenty percent of mutations have medium memory (half-life 50 to 200%), with present-day effects that can be partially predicted from their initial effects (r^2 = 0.68). The remaining 54% of mutations have long memories (>200% divergence) and interacted negligibly with historical substitutions, retaining their initial effects throughout DBD evolution (r^2 = 0.98).

Contingency of historical sequence evolution

We next focused on the subset of mutations that became substitutions during historical DBD evolution. We first assessed the functional effects of the 79 substitutions that occurred during the phylogenetic intervals that we experimentally characterized (Fig. 5, A and B). When measured in the ancestral background in which they historically occurred, substitutions that reduce activity by a ΔF less than −0.2 were nearly absent; of the few exceptions, most fixed during intervals immediately after gene duplication (fig. S8A). This represents a 29-fold depletion compared with the set of all mutations, most of which have a ΔF less than −0.2. These results imply that the DBD evolved primarily under purifying selection against mutations that strongly reduce activity, and they establish a ΔF of −0.2 as a boundary that roughly defines the evolutionary accessibility of mutations under purifying selection.

Epistasis shaped the fate of most historical substitutions, which occurred during limited windows when they were transiently accessible. Of all substitutions that fixed between AncSR and any extant steroid receptor on our phylogeny, 43% have short or medium memories (Fig. 5C). Among the short-memory substitutions, most were inaccessible in AncSR ($\Delta F_{\mathrm{AncSR}} < -0.2$), implying that they became accessible in one or more descendant proteins because of permissive epistatic substitutions, which render otherwise deleterious mutations neutral or advantageous. The remaining short-memory substitutions were accessible in AncSR ($\Delta F_{\mathrm{AncSR}} \geq -0.2$), but almost all of these became subsequently inaccessible because of restrictive substitutions, which render previously neutral or advantageous mutations deleterious (fig. S8B). By contrast, 95% of long-memory substitutions were accessible in AncSR and remained so across the entire phylogeny (fig. S8B). Medium-memory substitutions displayed an intermediate pattern. The evolutionary fate of long-memory substitutions could therefore have been reliably predicted from their initial effects, but the accessibility of substitutions with short or medium memory depended on other substitutions that occurred during history.

Epistasis also shaped the fate of the many mutations that did not become substitutions. Of all short-memory mutations that were accessible in AncSR, 90% became inaccessible in one or more descendant proteins, indicating that evolutionary paths to them were closed by restrictive substitutions (Fig. 5D). Conversely, 55% of the short-memory mutations that were inaccessible in AncSR subsequently became accessible because of permissive substitutions. Overall, two-thirds of short-memory mutations and one-third of medium-memory mutations changed in accessibility among the DBDs we tested; each category of mutations was accessible in an average of 2.4 and 4.9 of the 9 DBDs, respectively (Fig. 5E).

These data indicate that epistatic interactions with the particular set of substitutions that occurred along the phylogeny contingently determined the evolutionary fate not only of the mutations that fixed historically because of permissive substitutions but also of those that did not have the opportunity to fix because of restrictive substitutions. Studying only the sequence changes that occurred during evolution therefore underestimates the role of historical contingency: Doing so cannot detect the many evolutionary roads that were closed off contingently but which could have been taken if

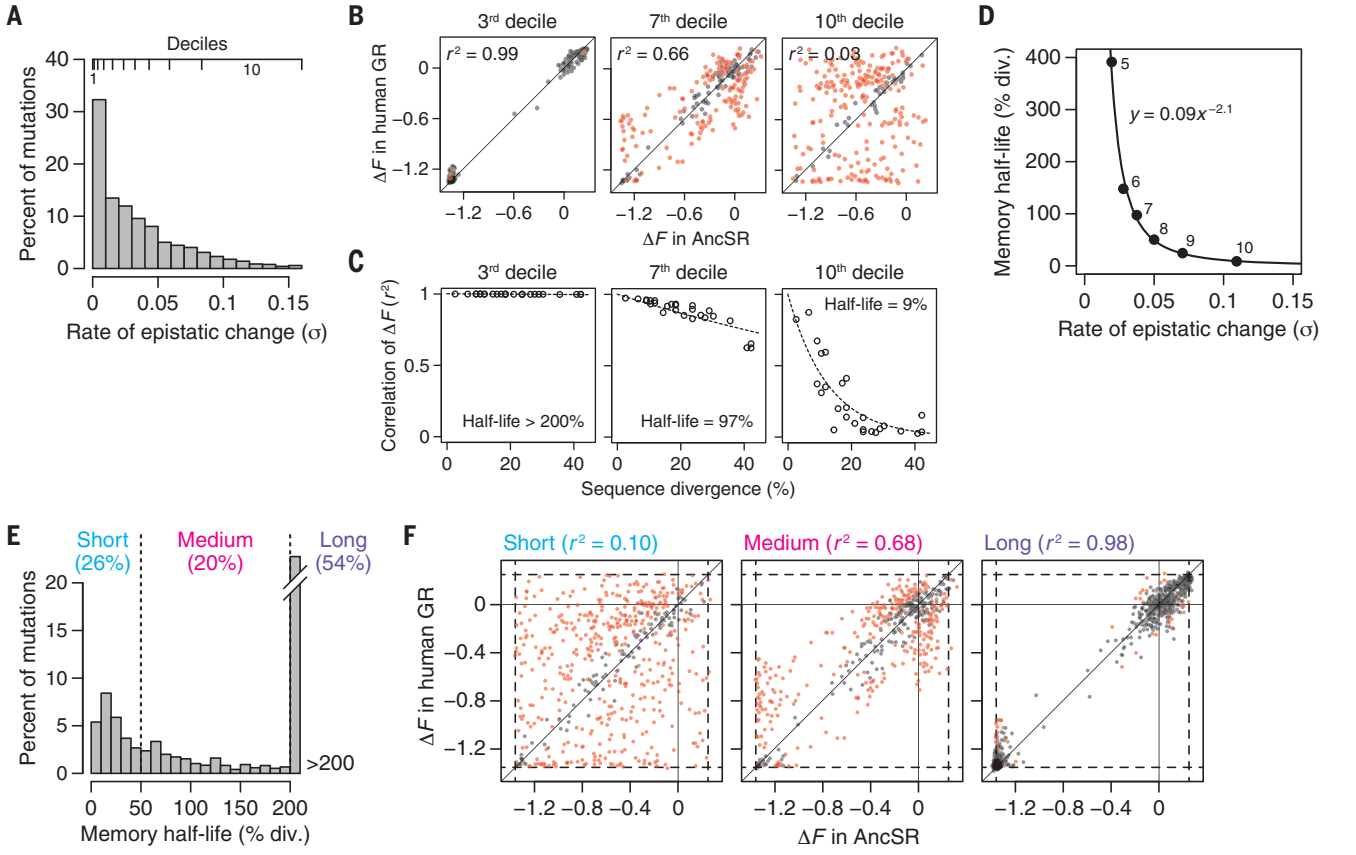

Fig. 4. Memory length of mutations and the time scale of historical contingency. (**A** to **D**) Measuring the memory length of mutations. In (A), mutations were grouped into deciles by their rate of epistatic change (σ, expected standard deviation of $\Delta\Delta F$ per 1% sequence divergence). In (B), the effects of mutations in each decile were compared between every pair of DBDs; shown are comparisons between AncSR and human GR (42% divergence). In (C), the r^2 for each DBD pair was plotted against the sequence divergence of that pair. The dotted line represents the best-fit exponential decay curve; memory half-life is the sequence divergence at which r^2 is equal to 0.5. The relationship between the rate of epistatic change and memory half-life inferred by fitting a power function to the mean rate of epistatic change and memory half-life of the deciles is shown in (D). This relationship was used to calculate the memory half-life of each mutation from its rate of epistatic change. (**E**) Distribution of memory half-life among mutations. Mutations were classified into short-, medium-, and long-memory categories using cutoffs of 50 and 200% divergence. (**F**) Comparing the effects of mutations between AncSR and human GR (42% divergence) for each memory category. Red dots are mutations with significant difference in ΔF (heteroscedastic *t* test, FDR ≤ 0.1); black dots are those with no significant difference.

the trajectory of sequence changes at interacting sites had unfolded differently.

Causes of variation in memory length

Finally, we sought to identify the factors that determine a mutation's memory length. Some variation in memory length is attributable to the sequence site at which a mutation occurs: The median memory half-life of mutations to any of the 19 mutant states at the same site varies among sites from 11 to >200% divergence (Fig. 6A). But this variation is not associated with any obvious structural or functional properties: The median memory half-life of a site is poorly correlated with relative solvent accessibility, rate of substitution, rate of substitution at physically adjacent sites, distance to the DNA-binding residues, and distance to the dimerization interface ($r^2 < 0.1$ for every factor; fig. S9). Further, memory length varies extensively within each site, with 59 of 76 sites in the DBD containing both short- and long-memory mutations. As a consequence, predicting a mutation's memory half-life by the median of all mutations at that site achieves an r^2 of only 0.25 (Fig. 6B).

Another possibility is that certain types of mutations (to and from the same pair of states) might be consistently associated with memory length, irrespective of the sites at which they occur. Predicting the memory length of individual mutations from the median memory length of all mutations of the same type at any site achieved an r^2 of only 0.13 (Fig. 6C). Explaining memory length variation therefore requires analysis of each particular mutation at each site in the protein.

To estimate a mutation's memory length, experiments are necessary in multiple genetic backgrounds across a phylogenetic trajectory. But how many backgrounds are necessary? When the rate of epistatic change of mutations is estimated from two backgrounds that were randomly chosen from the nine we assayed, the correlation (r^2) with the rate measured using all nine backgrounds is, on average, equal to 0.40, and the rate of epistatic change is systematically underestimated (Fig. 6, D and E). The correlation improves as more backgrounds are sampled and reaches 0.8 when estimates are based on five backgrounds. A moderate number of experiments is therefore sufficient to provide a rough estimate of a mutation's rate of epistatic change and hence its memory length.

Robustness to uncertainty in ancestral sequence reconstruction

Our conclusions are robust to uncertainties in the reconstruction of ancestral sequences. The ancestral DBDs were generally inferred with high confidence and contained zero to 10 sites at which more than one amino acid state is plausible. For each ancestral DBD with more than one ambiguous site, we generated an "Alt-All" reconstruction, which contains the alternative plausible amino acid at all ambiguously

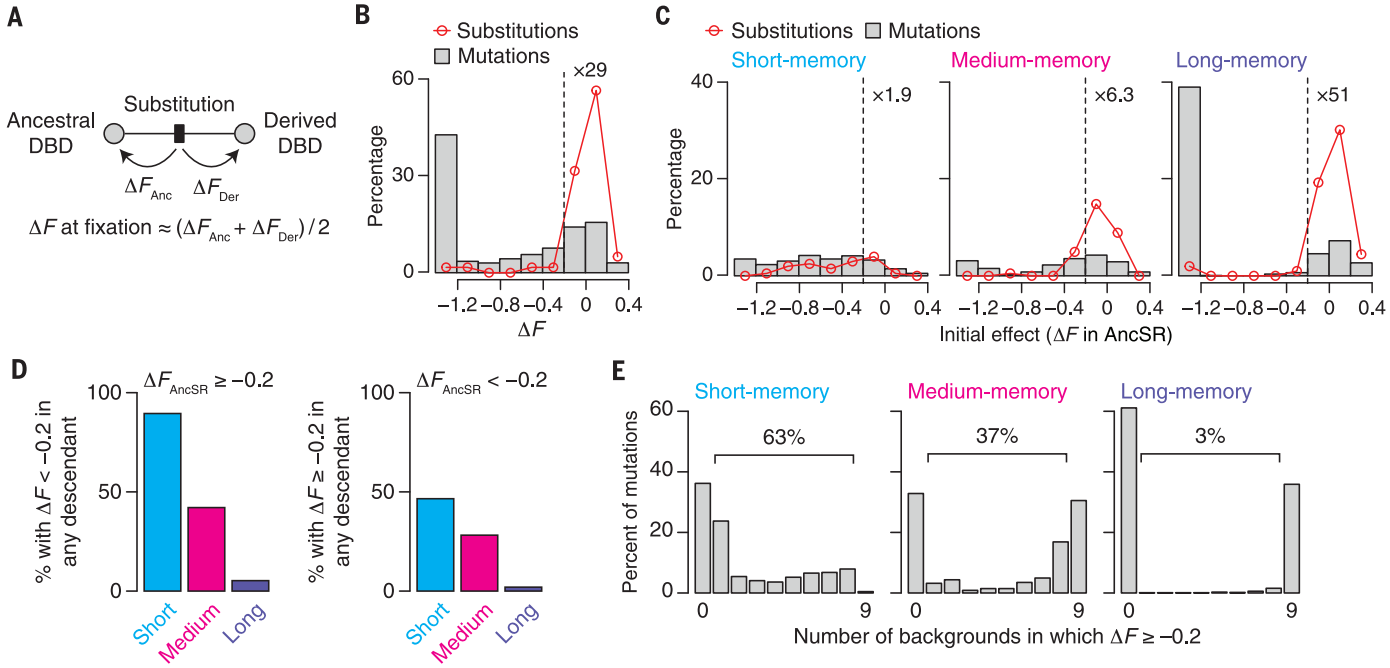

Fig. 5. Impact on sequence evolution of memory length and initial functional effect. (**A**) The effect of a substitution at the time it fixed during history was calculated as the mean of ΔFs measured by DMS in the nearest ancestral and descendant nodes. (**B**) Comparing the effects of the 79 substitutions that occurred along the phylogenetic trajectories we characterized to the effects of all possible mutations. Substitutions are 29-fold enriched for a ΔF greater than or equal to −0.2 compared with mutations, providing an estimate of the threshold of accessibility during DBD evolution (dashed line). (**C**) Distribution of the initial effect (ΔF on AncSR) of 275 substitutions that fixed between AncSR and any extant DBD in our phylogeny. Distributions are shown by memory half-life category. Enrichment of substitutions with a ΔF greater than or equal to −0.2 (dashed line) relative to mutations is shown. (**D**) The proportion of initially accessible mutations ($\Delta F_{AncSR} \geq -0.2$) that become inaccessible in at least one descendant DBD is shown on the left. The proportion of initially inaccessible mutations that become accessible in at least one descendant DBD is shown on the right. (**E**) Distribution of the number of characterized DBDs in which each mutation is accessible ($\Delta F \geq -0.2$), classified by memory-length category. The percentage of mutations that were accessible in some, but not all, DBDs is shown.

reconstructed sites (*28*); this sequence represents the least likely of all plausible reconstructions and allows a conservative estimate of robustness to sequence uncertainty. We then constructed a complete DMS library of each Alt-All protein and repeated all of our experiments and analyses. Although the effects of some mutations differ between the Alt-All and maximum-posterior-probability reconstructions, all conclusions concerning the temporal dynamics of epistasis were unchanged (fig. S10).

Discussion

Prior experimental studies have identified cases in which the functional effects of a few mutations changed substantially during particular intervals of evolutionary history (*12*, *15*–*18*, *29*, *30*). Our observations show that such rare, large-effect epistatic modifications occur against a background of pervasive gradual drift in the effects of most mutations (*11*, *20*, *31*–*36*). Most epistatic changes were of small magnitude when they occurred, but across an evolutionary trajectory of moderate length (<50% sequence divergence), they were sufficient to completely or partially decorrelate the effects of most mutations from their initial effects and substantially alter the set of available opportunities for future sequence change. The fold and function of all proteins depend on interactions among many residues, so we expect that epistatic drift will be a widespread feature of protein evolution. The temporal dynamics and distribution of memory lengths may depend on each protein's structure, function, and the selective regime under which it evolved.

Our findings establish strong limits on the ability to predict future evolution and interpret evolutionary history, but they also provide a quantitative framework for understanding those limits. Classical evolutionary theories assume that the constraints imposed by purifying selection do not change as sequences diverge, so the effects and evolutionary fate of mutations can be predicted or retroactively inferred based on their effects measured in the present. Our results show that this assumption of constancy and independence is wrong for about half of DBD mutations, which have short or medium memories. Because epistatic modification occurs at a mostly constant rate for each mutation, however, an estimate of memory length from experimental data across phylogenetic time can quantify the extent to which any mutation's effect can be predicted at any point in time, either future or past. Further, although point projections of the effects of short- and medium-memory mutations across long time scales are unreliable, a probability distribution of those effects can be generated if we know any mutation's memory length and its effect at some other time. Ancestral protein reconstruction can replace predictions with experimental knowledge, but only for proteins in the past.

A probabilistic description of contingency and uncertainty using memory length does not require detailed knowledge of the particular genetic interactions that cause epistatic change. If we had microscopic knowledge of all the interactions that modify each mutation's effect and a dense phylogenetic reconstruction of past trajectories of sequence change, we could reliably predict the effect of every possible mutation in any past historical background. But even complete knowledge like this would not be sufficient to predict future evolutionary trajectories: the accessibility of each future mutation depends on the chain of epistatic substitutions that occur before it, many of which will occur by chance. We can use experimental and

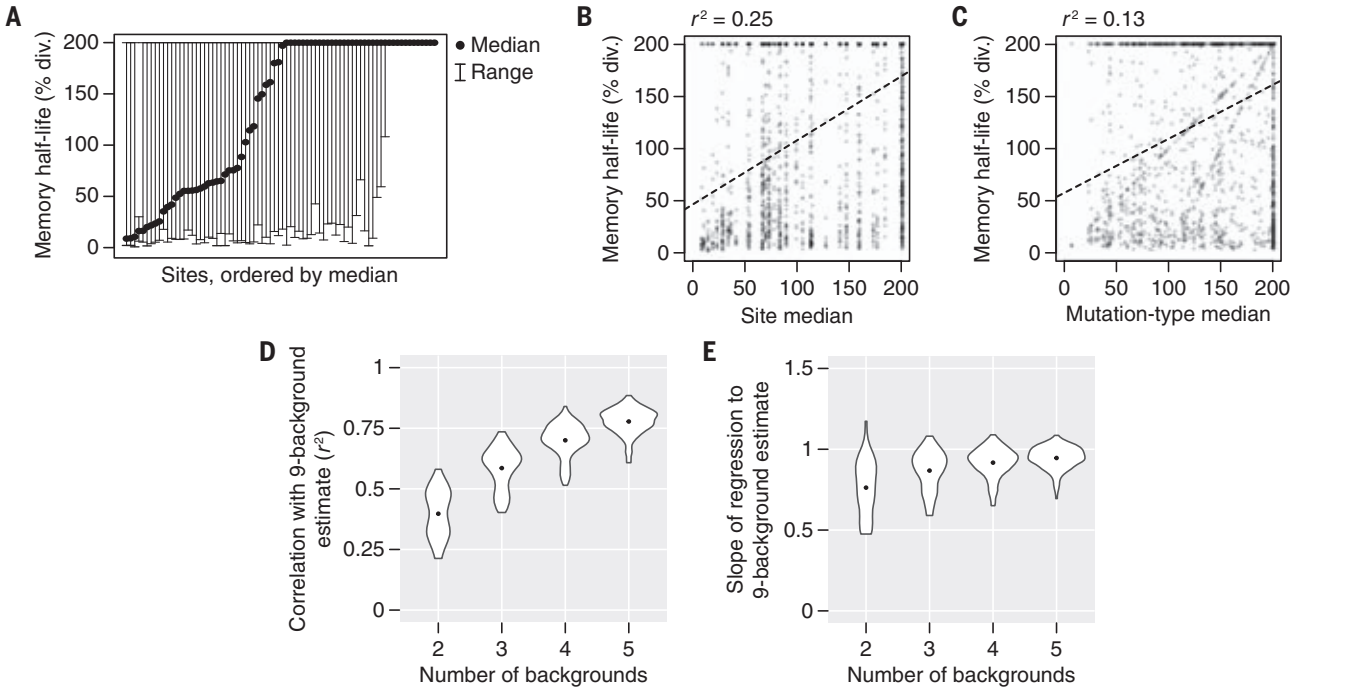

Fig. 6. Variation of memory half-life of mutations among and within sites. (**A**) Distribution of memory half-life among sites. Each line shows the range of memory half-life of all mutations at one site in the DBD sequence. (**B** and **C**) Predicting the memory half-life of a mutation (points) by the median memory half-life of all possible mutations at the same site (B) or by the median of mutations of the same type (between the same wild-type and mutant amino acid) at all sites (C). Dashed lines indicate the linear regression. (**D** and **E**) Effect of the number of DBDs characterized by DMS on estimates of rate of epistatic change. The rate of epistatic change of every mutation was estimated using a subset of the nine DMS experiments; the relationship between the estimated rate from each subset to that estimated from all nine experiments was analyzed by linear regression. The graphs show the distribution of correlation coefficient (D) and best-fit regression slope (E) across every possible subset of a given size.

phylogenetic data to tame evolutionary uncertainty by recognizing and quantifying it, but the future will always surprise.

REFERENCES AND NOTES

1. T. N. Starr, J. W. Thornton, *Protein Sci.* **25**, 1204–1218 (2016).
2. Z. D. Blount, R. E. Lenski, J. B. Losos, *Science* **362**, eaam5979 (2018).
3. D. Melamed, D. L. Young, C. E. Gamble, C. R. Miller, S. Fields, *RNA* **19**, 1537–1551 (2013).
4. C. A. Olson, N. C. Wu, R. Sun, *Curr. Biol.* **24**, 2643–2651 (2014).
5. A. I. Podgornaia, M. T. Laub, *Science* **347**, 673–677 (2015).
6. K. S. Sarkisyan *et al.*, *Nature* **533**, 397–401 (2016).
7. N. C. Wu, L. Dai, C. A. Olson, J. O. Lloyd-Smith, R. Sun, *eLife* **5**, e16965 (2016).
8. G. Diss, B. Lehner, *eLife* **7**, e32472 (2018).
9. V. O. Pokusaeva *et al.*, *PLOS Genet.* **15**, e1008079 (2019).
10. A. S. Kondrashov, S. Sunyaev, F. A. Kondrashov, *Proc. Natl. Acad. Sci. U.S.A.* **99**, 14878–14883 (2002).
11. M. Lunzer, G. B. Golding, A. M. Dean, *PLOS Genet.* **6**, e1001162 (2010).
12. C. Natarajan *et al.*, *Science* **340**, 1324–1327 (2013).
13. M. B. Doud, O. Ashenberg, J. D. Bloom, *Mol. Biol. Evol.* **32**, 2944–2960 (2015).
14. H. K. Haddox, A. S. Dingens, S. K. Hilton, J. Overbaugh, J. D. Bloom, *eLife* **7**, e34420 (2018).
15. E. A. Ortlund, J. T. Bridgham, M. R. Redinbo, J. W. Thornton, *Science* **317**, 1544–1548 (2007).
16. J. T. Bridgham, E. A. Ortlund, J. W. Thornton, *Nature* **461**, 515–519 (2009).
17. J. D. Bloom, L. I. Gong, D. Baltimore, *Science* **328**, 1272–1275 (2010).
18. L. I. Gong, M. A. Suchard, J. D. Bloom, *eLife* **2**, e00631 (2013).
19. C. Natarajan *et al.*, *Science* **354**, 336–339 (2016).
20. T. N. Starr, J. M. Flynn, P. Mishra, D. N. A. Bolon, J. W. Thornton, *Proc. Natl. Acad. Sci. U.S.A.* **115**, 4453–4458 (2018).
21. M. Karageorgi *et al.*, *Nature* **574**, 409–412 (2019).
22. V. C. Xie, J. Pu, B. P. H. Metzger, J. W. Thornton, B. C. Dickinson, *eLife* **10**, e67336 (2021).
23. G. K. Whitfield, P. W. Jurutka, C. A. Haussler, M. R. Haussler, *J. Cell. Biochem.* **33**, 110–122 (1999).
24. C. Helsen *et al.*, *Mol. Cell. Endocrinol.* **348**, 411–417 (2012).
25. A. N. McKeown *et al.*, *Cell* **159**, 58–68 (2014).
26. P. H. Harvey, M. D. Pagel, *The Comparative Method in Evolutionary Biology* (Oxford Series in Ecology and Evolution, Oxford Univ. Press, 1991).
27. L. J. Harmon, *Phylogenetic Comparative Methods: Learning From Trees* (CreateSpace, 2018).
28. G. N. Eick, J. T. Bridgham, D. P. Anderson, M. J. Harms, J. W. Thornton, *Mol. Biol. Evol.* **34**, 247–261 (2017).
29. Z. D. Blount, C. Z. Borland, R. E. Lenski, *Proc. Natl. Acad. Sci. U.S.A.* **105**, 7899–7906 (2008).
30. M. J. Harms, J. W. Thornton, *Nature* **512**, 203–207 (2014).
31. I. S. Povolotskaya, F. A. Kondrashov, *Nature* **465**, 922–926 (2010).
32. M. S. Breen, C. Kemena, P. K. Vlasov, C. Notredame, F. A. Kondrashov, *Nature* **490**, 535–538 (2012).
33. D. D. Pollock, G. Thiltgen, R. A. Goldstein, *Proc. Natl. Acad. Sci. U.S.A.* **109**, E1352–E1359 (2012).
34. P. Shah, D. M. McCandlish, J. B. Plotkin, *Proc. Natl. Acad. Sci. U.S.A.* **112**, E3226–E3235 (2015).
35. Z. R. Sailer, M. J. Harms, *Proc. Natl. Acad. Sci. U.S.A.* **114**, 11938–11943 (2017).
36. A. J. Morrison, D. R. Wonderlick, M. J. Harms, *Genetics* **219**, iyab105 (2021).

ACKNOWLEDGMENTS

We thank the members of the Thornton laboratory for discussion and comments, R. Ranganathan and R. Kanan for assistance with Illumina sequencing, the University of Chicago Cytometry and Antibody Technology Facility (RRID: SCR_017760) for assistance with fluorescence-activated cell sorting, and the University of Chicago Research Computing Center for high-performance computing. **Funding:** This work was funded by National Institutes of Health (NIH) grants R01GM131128 (J.W.T.), R01GM121931 (J.W.T.), R01GM139007 (J.W.T.), and F32GM122251 (B.P.H.M.); and a Samsung Scholarship (Y.P.). **Author contributions:** Conceptualization: Y.P., B.P.H.M., J.W.T.; Experiments: Y.P.; Data analysis: Y.P.; Development of methodology: Y.P., J.W.T., B.P.H.M.; Writing – original draft: Y.P., J.W.T.; Writing – review and editing: Y.P., J.W.T., B.P.H.M.; Funding acquisition: J.W.T. **Competing interests:** The authors declare that they have no competing interests. **Data and materials availability:** All data and scripts are available in the main text or the supplementary materials. A duplicate is also available on GitHub (https://github.com/JoeThorntonLab). **License information:** Copyright © 2022 the authors, some rights reserved; exclusive licensee American Association for the Advancement of Science. No claim to original US government works. https://www.science.org/about/science-licenses-journal-article-reuse

SUPPLEMENTARY MATERIALS

science.org/doi/10.1126/science.abn6895
Materials and Methods
Figs. S1 to S10
Tables S1 and S2
References (*37*–*54*)
MDAR Reproducibility Checklist
Data S1

Submitted 14 December 2021; accepted 11 April 2022
10.1126/science.abn6895

STRUCTURAL BIOLOGY

Structures of *Tetrahymena*'s respiratory chain reveal the diversity of eukaryotic core metabolism

Long Zhou[1]†, María Maldonado[2]†, Abhilash Padavannil[2], Fei Guo[3], James A. Letts[2]*

Respiration is a core biological energy–converting process whose last steps are carried out by a chain of multisubunit complexes in the inner mitochondrial membrane. To probe the functional and structural diversity of eukaryotic respiration, we examined the respiratory chain of the ciliate *Tetrahymena thermophila* (Tt). Using cryo–electron microscopy on a mixed sample, we solved structures of a supercomplex between Tt complex I (Tt-CI) and Tt-$CIII_2$ (Tt-SC I+III_2) and a structure of Tt-CIV_2. Tt-SC I+III_2 (~2.3 megadaltons) is a curved assembly with structural and functional symmetry breaking. Tt-CIV_2 is a ~2.7-megadalton dimer with more than 50 subunits per protomer, including mitochondrial carriers and a $TIM8_3$-$TIM13_3$–like domain. Our structural and functional study of the *T. thermophila* respiratory chain reveals divergence in key components of eukaryotic respiration, thereby expanding our understanding of core metabolism.

Cellular respiration is an essential metabolic process that provides chemical energy, in the form of adenosine triphosphate (ATP), to all free-living eukaryotes. The final energy-converting steps of cellular respiration are carried out by the mitochondrial oxidative phosphorylation electron transport chain (mETC), which transfers electrons from reduced metabolites such as NADH (reduced nicotinamide adenine dinucleotide) or succinate to the final electron acceptor, O_2. The mETC, located in the inner mitochondrial membrane (IMM), is composed of four protein complexes: NADH-ubiquinone (Q) oxidoreductase (complex I, CI), succinate dehydrogenase (complex II, CII), dimeric ubiquinol (QH_2)–cytochrome c (cyt c) oxidoreductase (complex III_2, $CIII_2$), and cytochrome c oxidase (complex IV, CIV). By coupling the energetically favorable electron transfer reactions to H^+ pumping across the IMM, the mETC complexes CI, $CIII_2$, and CIV establish a proton motive force that is used by the ATP synthase complex (complex V, CV) to synthesize ATP (*1*). In all eukaryotes investigated, the mETC complexes are found both individually and as parts of higher-order supercomplexes (SCs) of defined stoichiometry (*2*), including SC I+III_2, SC I+III_2+IV, and SC III_2+$IV_{(2)}$ (*3*). CIV and CV are also commonly found as dimers (CIV_2 and CV_2) (*4*, *5*) or, in the case of CV, higher-order arrays (*6*–*9*).

Although the catalytic mechanisms of the individual mETC complexes are likely conserved across species, some structural differences have been observed between model organisms. Each mETC complex can be split into core subunits, which are essential for catalysis and are conserved from the bacterial homologs, and accessory subunits, which are important for the assembly and activity of the complexes but are not universally conserved (*10*, *11*). CI is composed of 14 core subunits, arranged into two "arms" of an "L"-shape, universally conserved in the model eukaryotes with known structures, covering the Opisthokont [fungi (*12*) and metazoan (*13*)] and Archaeplastida [red/green algae and plants (*14*–*16*)] clades. However, each structure of CI has a variable set of 31 to 37 accessory subunits, some of which are shared across all known examples of eukaryotic CI and some of which are only found in a specific branch of the eukaryotic tree of life (table S1) (*17*). For the other H^+-pumping complexes of the mETC ($CIII_2$ and CIV), much less compositional variability has been observed between the characterized examples from opisthokonts (*4*, *18*, *19*) and archaeplastidans (*20*) (tables S2 and S3). Although the biochemical and structural characterization of eukaryotic CI, $CIII_2$, and CIV has been limited to model organisms of the Opisthokonta and Archaeplastida clades, mitochondrial CV has been structurally characterized from a broader array of eukaryotes, including not only opisthokonts (*5*, *21*) and archaeplastidans (*22*), but also kinetoplastids (*23*) and euglenids (*24*) (euglenozoans), as well as ciliates (*9*) and apicomplexans (*8*) (alveolates). These structures have revealed a broad diversity in subunit composition and higher-order organization of CV, correlated with differences in the organisms' IMM morphology (*7*, *8*, *23*, *25*). The diversity in CV and the IMM morphology across eukaryotic clades suggests that the limited diversity seen in CI, $CIII_2$, and CIV may be attributed to the limited model eukaryotes in which they have been biochemically and structurally investigated.

Early functional characterization of the model ciliate *Tetrahymena thermophila* led to the conclusion that its mETC lacked CIV and contained a distinct terminal oxidase instead (*26*). However, the identification of *T. thermophila* homologs of CIV core subunits COX1 and COX2 (but not COX3) in the mitochondrial genome (*27*) and the discovery that *T. thermophila* possesses an acidic rather than a basic cyt c (*28*) indicated that although *T. thermophila* does possess a CIV homolog, the complex has functionally diverged. Similarly, some but not all of the core subunits of CI and $CIII_2$ were identified in the *T. thermophila* mitochondrial genome (*27*) and proteome (*29*). This is in line with proteomic studies of $CIII_2$ and CIV composition in alveolates *Toxoplasma gondii* and *Plasmodium falciparum*, which show a substantial compositional divergence of these respiratory complexes relative to organisms with known structures (*30*, *31*). Furthermore, unlike the disc-shaped cristae of opisthokonts and archaeplastidans, the cristae of the ciliates and other alveolates are tubular (*7*). Given these functional, sequence, compositional, and morphological differences from previously studied organisms, *T. thermophila* is an ideal system to examine the diversity, evolution, and conserved aspects of mETC complexes.

The *T. thermophila* mETC requires a divergent cyt c

To examine the functional consequences of the acidic versus basic charge flip of *T. thermophila*'s cyt c (Tt–cyt c), we characterized isolated mitochondrial membranes from *T. thermophila*, mammals (*Sus scrofa*, pig), and plants (*Vigna radiata*, mung bean) using both mammalian cyt c purified from horse heart (*Equus ferus*, equine, Eq–cyt c) and heterologously expressed Tt–cyt c (fig. S1, A to E) (*32*). Spectroscopic activity assays for SC I+III_2 showed NADH–cyt c oxidoreduction using Eq–cyt c for all three species (fig. S1, F to J). However, CIV activity assays showed that whereas mammalian and plant mitochondrial membranes readily oxidize reduced Eq–cyt c, no cyt c oxidation could be detected from *T. thermophila* mitochondrial membranes (Fig. 1A). Conversely, using the recombinant Tt–cyt c, only the *T. thermophila* mitochondrial membranes showed cyanide-sensitive cyt c oxidation activity (Fig. 1A). These data establish that *T. thermophila* possesses a CIV that has functionally diverged from those of opisthokonts and archaeplastidans (fig. S1, K to M).

High-resolution structures of the respiratory chain from a single mixed sample

To better understand the functional divergence of the *T. thermophila* mETC complexes, we extracted them from mitochondrial membranes using digitonin, stabilized them in amphipathic polymer A8-35, and enriched them using sucrose gradient ultracentrifugation and size exclusion chromatography (fig. S2). We then obtained the structures of Tt-CI, Tt-$CIII_2$,

[1]Department of Biophysics and Department of Critical Care Medicine of Sir Run Run Shaw Hospital, Zhejiang University School of Medicine, Hangzhou 310058, China. [2]Department of Molecular and Cellular Biology, University of California, Davis, CA 95616, USA. [3]BIOEM Facility, University of California, Davis, CA 95616, USA.
*Corresponding author. Email: jaletts@ucdavis.edu
†These authors contributed equally to this work.

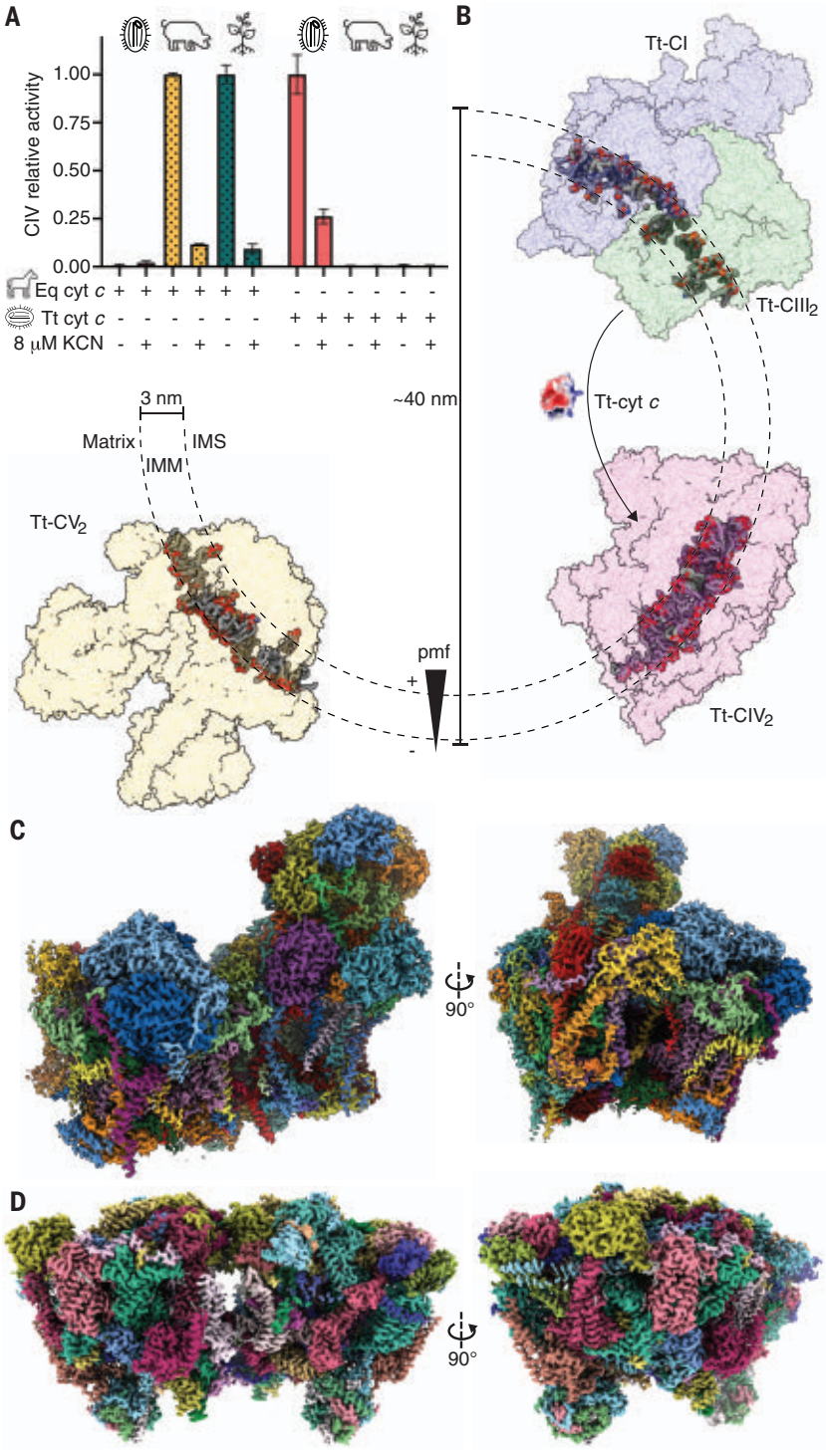

Fig. 1. Functional and structural divergence of *T. thermophila*'s electron transport chain. (**A**) Relative CIV activity of isolated mitochondrial membranes from *T. thermophila* (ciliate symbol, red), *S. scrofa* (pig symbol, yellow), and *V. radiata* (plant symbol, green) using cyt c from horse (Eq, horse symbol, dotted) or *T. thermophila* (Tt, ciliate symbol, solid) in the presence or absence of 8 μM potassium cyanide (KCN). Data are averages ± SEM (n = 4). (**B**) Representation of *T. thermophila*'s mitochondrial electron transport chain on a tubular crista, with the width of the membrane determined by the observed phospholipids and hydrophobic regions of the complexes. Complexes are shown in surface (blue, Tt-CI; green, Tt-$CIII_2$; pink, Tt-CIV_2; yellow, Tt-CV_2); PDB 6YNY (*9*). Lipids are shown as spheres, colored by heteroatom. Cyt c homology model is shown in surface, colored by electrostatic potential. The arrow shows approximate binding sites for cyt c on Tt-$CIII_2$ and Tt-CIV_2. IMM, inner mitochondrial membrane; IMS, intermembrane space; pmf, proton motive force. (**C**) Cryo-EM map of Tt-SC I+III_2 colored by individual subunits. (**D**) Cryo-EM map of Tt-CIV_2 colored by individual subunits.

and Tt-CIV_2 from a single mixed sample by single-particle cryo–electron microscopy (cryo-EM) (Fig. 1, B to D, figs. S3 to S6, and tables S4 to S7). Our dataset also allowed us to obtain a high-resolution reconstruction of Tt-CV_2 (fig. S5 and supplementary text), whose structure has been previously characterized (*9*). Thus, the current study reconstructed an entire metabolic pathway (NADH to ATP) involving 277 proteins in three multi-MDa complexes from a single sample (Fig. 1B).

Tt-CI and Tt-$CIII_2$ form a supercomplex (Tt-SC I+III_2) (Fig. 1C and movie S1) while Tt-CIV forms a dimer (Tt-CIV_2) (Fig. 1D and movie S2), resolved to nominal resolutions of 2.6 Å and 3.0 Å, respectively (figs. S3 to S6). The subunit composition of the complexes was determined from the cryo-EM density maps (*33*) and confirmed by mass spectrometry analysis (tables S5 to S7). Using this approach, we were able to structurally identify 70 proteins previously annotated as putative or uncharacterized in the sequence databases. Tt-SC I+III_2 is composed of 91 protein subunits and has an overall mass of ~2.3 MDa (Fig. 1C and tables S5 and S6), ~900 kDa larger than the mammalian SC I+III_2 (67 subunits, 1.4 MDa) (*34*). The position and relative orientation of CI and $CIII_2$ in Tt-SC I+III_2 are analogous to the conserved orientation of other eukaryotes (fig. S7A) (*2*), suggesting either a common SC ancestor or convergent evolution across Opisthokonta, Archaeplastida, and Alveolata. In contrast to mammalian, yeast, and plant CIV with 10 to 14 subunits (table S3) (*4*, *20*, *35*), Tt-CIV_2 has an overall mass of ~2.7 MDa with more than 52 subunits per protomer (Fig. 1D and tables S3 and S7).

Unlike the planar architecture of previously described supercomplexes (fig. S7B) (*34*), Tt-SC I+III_2 and Tt-CIV_2 are curved assemblies (Fig. 1B), as demonstrated by the orientation of individual complexes (fig. S7, B to D) and the modeled lipids (Fig. 1B). When Tt-SC I+III_2, Tt-CIV_2, and Tt-CV_2 structures were fit into a circular membrane corresponding to the known diameter of the tubular ciliate cristae (~40 nm) (*7*), the modeled lipids (Fig. 1B) and hydrophobic regions of the proteins (fig. S7, B to D) matched the predicted curvature of a ~3-nm bilayer. The mETC complexes thus contribute to the tubular morphology of the ciliate cristae via specific structural features that are not conserved in opisthokonts or archaeplastidans.

Tt-CI has a fragmented core and 51 accessory subunits

Unlike all previous structurally characterized CIs, three core membrane subunits of Tt-CI responsible for Q binding and H^+ pumping (ND1, ND2, and ND5) are each split into two subunits, making a total of 17 core subunits across both CI arms (Fig. 2A). Comparison of

the structures of these split subunits with the core subunits of other CIs indicates that subunits ND1A and ND1B, ND2A (formerly YMF65) and ND2B (formerly ND2), and ND5A and ND5B (formerly YMF57) come together to form structural elements equivalent to ND1, ND2, and ND5, respectively (fig. S8A and supplementary text) (*27*). Our structure also confirmed the previous speculative assignments of YMF62 and YMF58 as core subunits ND6 and ND4L, respectively (table S5) (*27*). Notwithstanding these differences, the relative locations of the flavin mononucleotide (FMN) cofactor and eight iron-sulfur clusters of the peripheral arm are highly conserved (fig. S8B). In addition, the hydrophilic axis along the center of the membrane is maintained, although it now involves residues of the additional subunits ND1B and ND2B (Fig. 2B). Furthermore, the positions of key Q reduction site loops (NDUS7, NDUS2 β1-β2, ND1A TMH5-6, ND3 TMH1-2, ND6 TMH3-4) are well resolved (Fig. 2C) and consistent with positions of the equivalent loops in the mammalian "closed" state structure (fig. S9) (*13*).

Among the 51 accessory subunits present in Tt-CI (Fig. 2D), 26 have homologs in all other known eukaryotic CIs, five subunits have homologs outside of the alveolates, and 20 are newly identified here as CI subunits (fig. S10, tables S1 and S5, and supplementary text). The conservation of subunits across Opisthokonta, Archaeplastida, and Alveolata defines a minimal set of 31 accessory subunits present in CI of the last eukaryotic common ancestor (LECA) (fig. S10 and table S1). As seen in the archaeplastidan structures (*14*–*16*), Tt-CI contains a γ-carbonic anhydrase (γCA) domain composed of three γCA subunits (Fig. 2E). Unlike vascular plants (*14*, *16*) but like the nonphotosynthetic alga *Polytomella* (*15*), none of the Tt-γCA subunits (NDUCA1 to 3) retain their catalytic Zn^{2+}-coordinating residues (fig. S11, A and B). The ferredoxin bridge domain connecting the peripheral and membrane arms in plant and algal CI (*15*) is also present in Tt-CI (Fig. 2F). In addition to the *T. thermophila* homologs of the ferredoxin-like subunit (NDUFX), the acyl carrier protein subunit (NDUAB1-α), and accessory subunit NDUA6, the bridge in Tt-CI is further stabilized by a J-domain subunit (coined NDUJ1) and the extended C terminus of NDUCA3 (Fig. 2F). Whereas the plant and algal CI-FDX has lost its ability to coordinate an iron-sulfur cofactor (*15*), we observe clear density for a 2Fe2S cluster in *T. thermophila*'s NDUFX (figs. S7E and S11, C and D), indicating that it may be a functional redox cofactor.

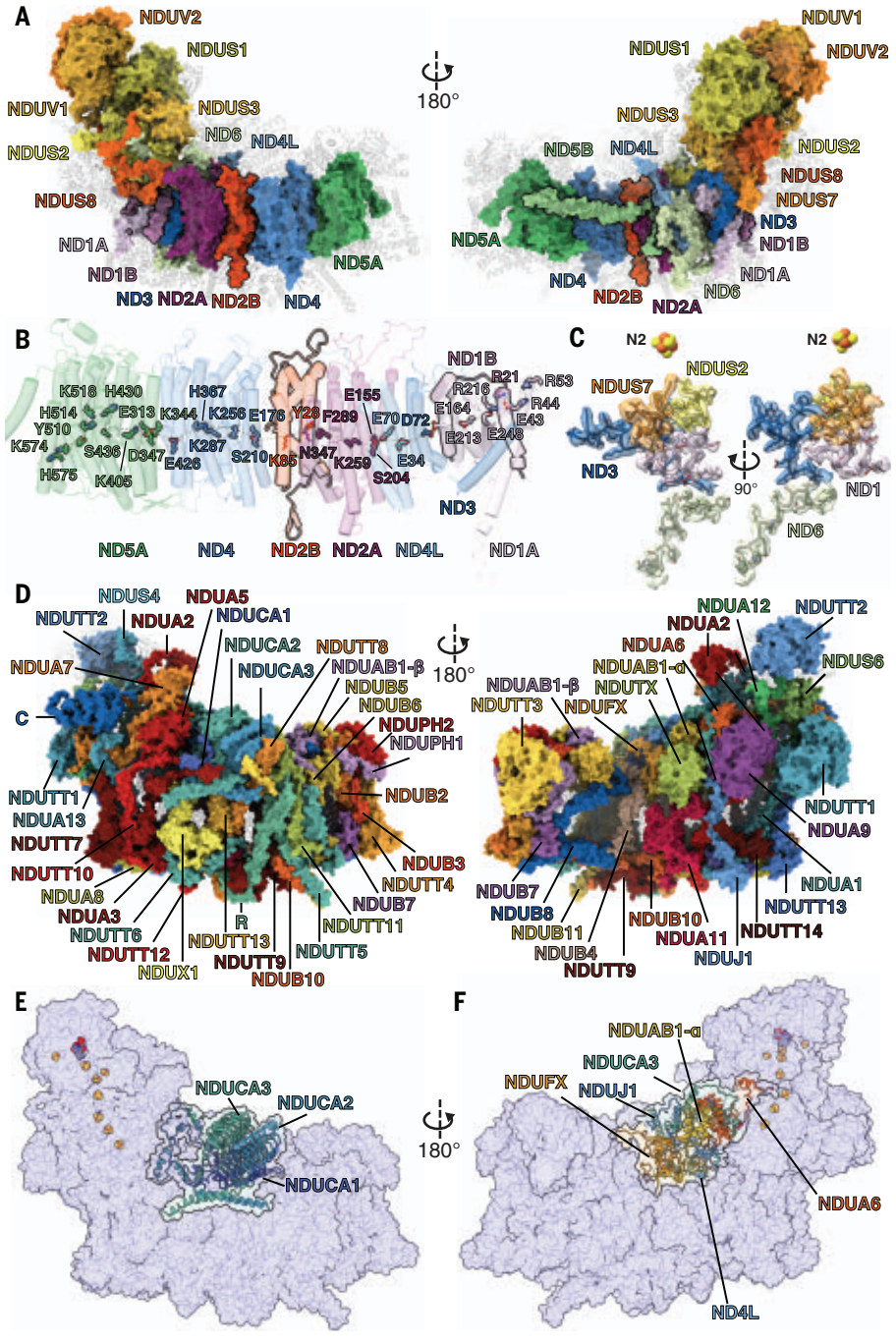

Fig. 2. Structural and functional features of Tt-CI. (**A**) Tt-CI's 17 core subunits in colored surfaces; accessory subunits are shown as gray cartoons. Core subunits ND1B, ND2B, and ND5B are highlighted with black borders. (**B**) Hydrophilic axis along the membrane arm of Tt-CI. Core subunits that form the membrane arm are shown as cylinders, colored as in (A). Core subunits ND1B and ND2B are highlighted with black borders. Conserved charged residues along the hydrophilic axis as sticks, colored by subunit. (**C**) Q-site loops are shown as cartoons embedded in the density, colored by subunit. Terminal iron-sulfur cluster N2 is shown as spheres, residues as sticks. (**D**) The 51 accessory subunits are shown in colored surfaces, core subunits as gray transparent cartoons. (**E**) Tt-CI's three γ-carbonic anhydrase subunits are shown as colored cartoons on the Tt-CI surface (blue). (**F**) Tt-CI's ferredoxin bridge shown as colored cartoons on the Tt-CI surface (blue).

Tt-CI lacks an A/D transition and has crowded Q-site loops

Structural analyses of yeast and mammalian CI have revealed that the complex adopts distinct "open" and "closed" conformational states characterized by a global change in the angle between the two arms, as well as order-to-disorder rearrangements of the Q-reduction site loops (e.g., the ND3 TMH1-2 loop, Fig. 3A) and an α-helix to π-bulge conversion in ND6 TMH3 (fig. S9) (*13*, *34*, *36*, *37*). These conformational changes have been proposed to be part of CI's coupling mechanism between Q reduction and H^+ pumping (*13*, *38*). However, yeast and mammalian CIs are also capable of

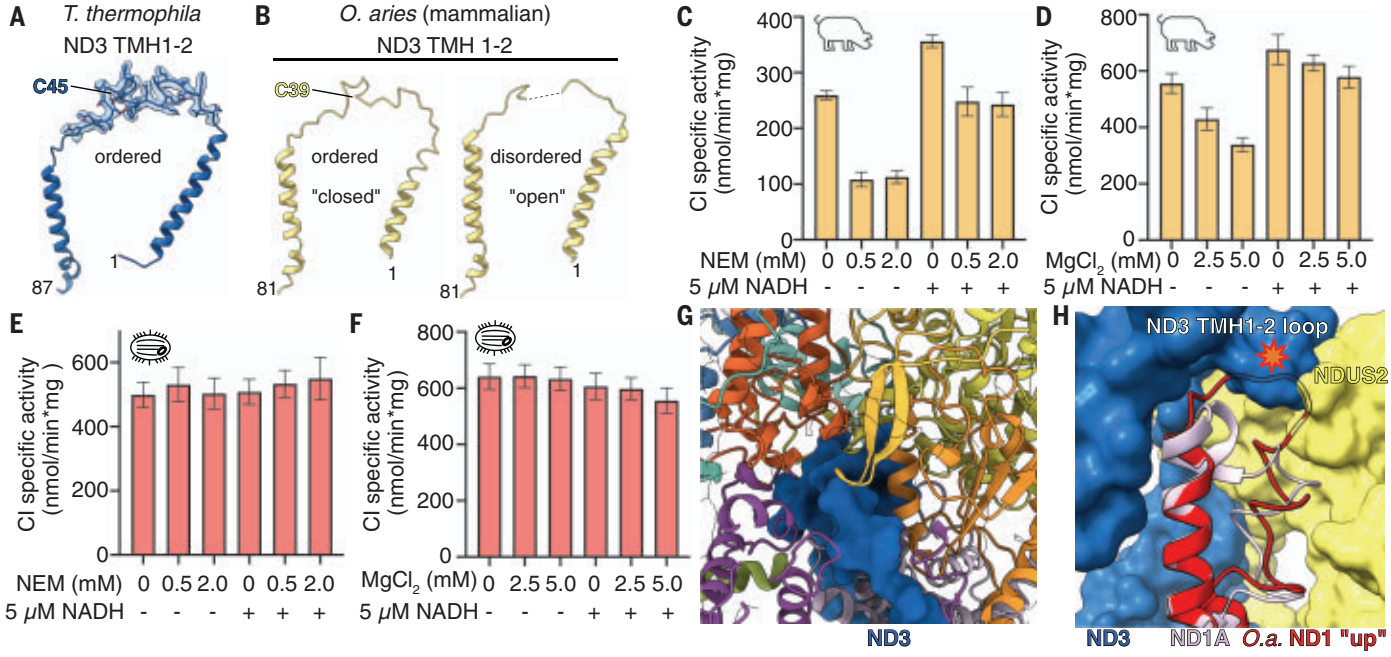

Fig. 3. Structural and functional comparison of complex I's active-to-deactive (A/D) transition. (**A** and **B**) Comparison of complex I's ND3 TMH1-2 loop in *T. thermophila* (A) and *O. aries* (B) in the ordered ("closed," PDB 6ZKO) and disordered ("open," PDB 6ZKS) conformations. (**C** to **F**) Functional characterization of A/D in isolated mitochondrial membranes of *S. scrofa* [(C) and (D)] and *T. thermophila* [(E) and (F)] by spectroscopic measurement of NADH dehydrogenase activity at 340 nm in the presence of the indicated concentrations of *N*-ethylmaleimide (NEM) [(C) and (E)] or $MgCl_2$ [(D) and (F)] with preincubation with 5 μM NADH or water. Data are averages ± SEM; n = 3 or 4. (**G**) Crowding around Tt-CI's ND3 TMH1-2 loop. ND3 is shown in blue surface. Secondary structure elements of various accessory subunits that pack against the ND3 loop are shown as colored cartoons. Accessory subunits are colored as in Fig. 2. (**H**) Superposition of *T. thermophila* ND1 (light purple cartoon) with *O. aries* ND1 in NADH-bound, open-state CI ("up" conformation, red cartoon, PDB 6ZKH). *O. aries* ND1 up conformation would clash with ND3 TMH1-3 loop (blue surface) and NDUS2 (yellow surface). The clash is marked with a red star.

undergoing an "active-to-deactive" (A/D) transition, whereby CI enters an off-pathway deactive (D) state that is incapable of catalytic turnover (*39*). Therefore, it has been controversial whether the structural rearrangements of the open and closed states (fig. S9) are central to CI turnover or represent A and D states (*13*, *40*). The A/D transition is not a universal feature of CI, as several bacterial and invertebrate CIs lack a D state (*39*). Structural characterization of a CI lacking the A/D transition would address this controversy: If these structural rearrangements were required for CI's catalytic mechanism, they should be possible even in CIs that lack an A/D transition.

Upon entering the D state—for example, by incubating the mitochondrial membranes at 37°C in the absence of substrate—a conserved cysteine residue in CI's ND3 TMH1-2 loop (Cys^{45} of ND3 in *T. thermophila*; Fig. 3, A and B) becomes accessible to modification by *N*-ethylmaleimide (NEM) (*41*). NEM modification of this cysteine traps CI in the D state and reduces overall activity (fig. S12). The detrimental effect of NEM on mammalian CI activity can be prevented by pre-activating the complex with a small amount of NADH substrate (Fig. 3C). This outcome can be understood structurally: When mammalian CI is in the "closed" state, the ND3 TMH1-2 loop is ordered and the cysteine residue (Cys^{39} of ND3 in *O. aries*) is buried in the structure, whereas when CI is in the "open" state, the ND3 TMH1-2 is disordered and the cysteine is accessible to NEM (Fig. 3B). A similar effect can be seen with the addition of Mg^{2+}, which is known to inhibit the A/D transition in mammals and yeast (Fig. 3D) (*39*). When treated identically to the mammalian sample to induce entry into the D state (i.e., incubation without substrate at 37°C for 10 to 20 min), the CI activity of *T. thermophila*'s mitochondrial membranes was insensitive to NEM or Mg^{2+} (Fig. 3, E and F). These data indicate that, like bacteria and invertebrates (*39*), Tt-CI does not possess an A/D transition. Furthermore, in Tt-CI, the presence of additional *T. thermophila*–specific subunits (NDUJ1, NDUTX, and NDUCA3) and of extensions in NDUA6 and NDUA9 leads to crowding of the region surrounding the ND3 TMH1-2 loop (Fig. 3G). As a result of this crowding, any conformational changes of the ND3 TMH1-2 loop during the catalytic cycle would require rearrangements of the surrounding structure. For example, the observed position of Tt-CI's ND3 TMH1-2 loop conflicts with the "up" position of the ND1 TMH5-6 loop seen in the *O. aries* complex I bound to NADH (Fig. 3H) (*12*). Thus, if the "up" position of the loop is a conserved on-pathway state, the ND3 TMH1-2 loop and the surrounding subunits must undergo large (>5 Å) displacements during turnover. Disulfide crosslinking of the ND3 TMH1-2 loop has been shown to uncouple Q reduction and H^+ pumping in yeast CI (*Y. lipolytica*) (*42*), indicating that conformational flexibility in this region is essential for redox-driven H^+ pumping. Given the crowded environment of this loop in Tt-CI, explicit disordering of this loop during turnover is unlikely. Thus, Tt-CI is an important model system in which to study these coordinated conformational changes during the CI catalytic cycle.

Although the angle between Tt-CI's membrane and the peripheral arm is more similar to that in some "open" states (fig. S9, E to H), given Tt-CI's well-ordered Q-reduction site loops (Fig. 2C) and the lack of a π-bulge in ND6 TMH3 (fig. S9D), our structure corresponds most closely with the "closed" state of mammalian and yeast CIs. This confirms that the "closed" state is an active state of the enzyme (*12*, *37*, *38*). Unlike the CI structures from opisthokonts and archaeplastidans (*12*, *13*, *15*, *34*), resting Tt-CI does not contain structural classes with distinct angles between the membrane

and peripheral arms (i.e., open and closed states). Given the multiple additional subunits that bridge the two arms of Tt-CI (Fig. 2, E and F), large conformational changes between the peripheral and membrane arms are unlikely. Therefore, we can conclude that both the ND6 TMH3 π-bulge and the open state of CI with disordered Q-site loops are features of the D state of the enzyme and are not related to the conserved coupling mechanism.

Tt-SC I+III$_2$ breaks the symmetry of Tt-CIII$_2$

Although the overall arrangement of Tt-SC I+III$_2$ is like that of the mammalian supercomplex (fig. S7A) (*34*), the interactions between Tt-CI and Tt-CIII$_2$ are more extensive. Whereas mammals show one interaction site in the matrix and one in the IMM involving six subunits (*3*), Tt-SC I+III$_2$ possesses three matrix bridges (sites 1 to 3), IMM interactions (site 4), and an IMS bridge (site 5; Fig. 4A) involving 10 Tt-CIII$_2$ subunits and 11 Tt-CI subunits (fig. S13 and supplementary text). Two of *T. thermophila*'s matrix sites—the "thioredoxin/J bridge" and the "toe bridge"—are formed by Tt-CI subunits not seen in other organisms (Fig. 4, B and C). The additional bridges in the matrix wedge between Tt-CI and Tt-CIII$_2$ and push their matrix domains apart. Concomitantly, novel interactions in the IMS, including a shared Zn^{2+} coordination between NDUA11 and UQCRH (fig. S13I), pull the complexes together. Overall, these interactions splay Tt-SC I+III$_2$ in line with the IMM curvature (Fig. 1B and fig. S7B). Furthermore, ordered lipids bridge the Tt-CI and Tt-CIII$_2$ interface at the matrix and IMS leaflets of the membrane (Fig. 4, D and E).

Although divergent in sequence, each Tt-CIII protomer is composed of the 10 known CIII subunits seen in other eukaryotic species (Fig. 4, F and G) and two unidentified short chains (figs. S14 and S15 and supplementary text). CIII$_2$ is a symmetric dimer, but the structures of mammalian supercomplexes provided initial indications that CIII$_2$ may be symmetry-broken in higher-order assemblies (*34*, *43*, *44*). The structure of Tt-CIII$_2$ displays extensive structural and functional symmetry breaking caused by its interaction with Tt-CI, including differential flexibility or occupancy of several subunits (Fig. 4H). The UQCRFS1 head domain adjacent to the CI Q reduction site is highly flexible and therefore lacks clear cryo-EM density, whereas the head domain proximal to the "toe bridge" (Fig. 4B) is restricted by its proximity to Tt-CI's NDUB8, leading to clear density (Fig. 4, H and I). Given that the swinging motion of the UQCRFS1 head domain is essential for CIII$_2$'s electron transfer from QH_2 to cyt c_1 (*45*), we conclude that the UQCRFS1 proximal to the toe bridge is likely not functional. Thus, only the Tt-CIII protomer adjacent to the source of QH_2 on CI is capable of QH_2 oxidation. The symmetry breaking of Tt-CIII$_2$ is further demonstrated by the widening of the distance between the two catalytic b_L hemes (Fig. 4, J and K). In bacteria, yeast, plants, and mammals, the CIII$_2$ dimer arranges the b_L hemes within direct electron-transfer distance (~11 Å) (*20*, *46*); a similar distance is also conserved in the distantly related cytochrome b_6f complex of the photosynthetic ETC (Fig. 4J) (*47*). Direct electron transfer between the b_L hemes is known to occur and is thought to play a role in the catalytic mechanism of CIII$_2$ (*48*). In contrast, in *T. thermophila* the supercomplex interactions (Fig. 4A) and the membrane curvature (Fig. 1B) widen the distance and change the relative tilt between the two Tt-CIII protomers, resulting in an increased gap between the b_L hemes, placing them beyond rapid electron-transfer distance (Fig. 4J).

The symmetry breaking of the Rieske head domains and the increased distance between the b_L hemes would result in the inability of the Tt-CIII COB subunit distal to the Tt-CI Q site to accept electrons, leading to the functional specialization of the two Q cavities (Fig. 4L). In a symmetric CIII$_2$, each Q binding cavity contains a QH_2-oxidizing site (Q_P) near the IMS and a Q-reducing site (Q_N) near the matrix, each provided by the opposite COB protomer (*34*). Direct electron transfer across protomers means that there are four possible electron pathways between the Q_P and Q_N sites during the Q cycle (*49*). The symmetry breaking of the Rieske head domains and increased b_L-heme distance in the Tt-SC I+III$_2$ structure remove three possible pathways. The only possible electron transfer path is from the Q_P site of the Q cavity adjacent to Tt-CI's Q tunnel (the source of QH_2) to the Q_N site of the same COB subunit in the opposite Q cavity (Fig. 4L). This leads to the specialization of the Q cavities in the Q cycle: The one adjacent to the source of QH_2 would be responsible for QH_2 oxidation, and the other one for Q reduction (Fig. 4L). Although this functional symmetry breaking has been previously proposed for mammalian SC I+III$_2$ (*3*, *34*), the unprecedented asymmetry in Tt-SC I+III$_2$ reveals how the CIII$_2$ electron transfer pathways are limited within the supercomplex, validating previous predictions and confirming a key physiological function of supercomplex formation. Furthermore, the large number of contacts between Tt-CI and Tt-CIII$_2$, the adaptation of the supercomplex to the high membrane curvature, and the lack of biochemical detection of individual Tt-CI on BN-PAGE gels (fig. S2E) all suggest that Tt-SC I+III$_2$ is the minimal organization of Tt-CI (i.e., no free Tt-CI is present in *T. thermophila* mitochondrial membranes). Although obligatory supercomplexes have been seen between CIII$_2$ and CIV in actinobacteria (*50*), none have been previously observed in eukaryotes.

Tt-CIV$_2$ is a 2.7-MDa dimer with a deep, charge-swapped cytochrome c crater

Tt-CIV$_2$ is unlike any cytochrome c oxidase of known structure (fig. S16A). With its 2.7-MDa size (1.35 MDa per protomer), it surpasses CI as the largest complex of the mETC (Fig. 1D). Its subunits include the three universally conserved core catalytic subunits, six accessory subunits found in other eukaryotes, and 44 accessory subunits not seen in other CIV structures (fig. S17, table S3, and supplementary text). Although the transmembrane domains and catalytic cofactors are conserved (fig. S18), all three Tt-CIV core subunits (COX1 to 3) contain large extensions and insertions (Fig. 5A). The sequence and structural divergence of COX3 (formerly YMF68) is such that previous identification by homology was not possible (*27*). In the IMS, the core subunits' extensions form the cyt c binding "crater" (Fig. 5B) together with several accessory subunits (fig. S19A). Analogous to Tt–cyt c (fig. S1, A and B), the Tt-CIV crater shows a flipped surface electrostatic potential relative to bacteria, opisthokonts, and plants (Fig. 5, B to D, and supplementary text). This "swapped" charge property between Tt-CIV$_2$ and Tt–cyt c (fig. S20) explains why electron transfer cannot happen between mammalian cyt c and Tt-CIV$_2$ but can happen between mammalian cyt c and plant CIV (Fig. 1A).

The proton conductance pathways ("K-, D-, and H-channels") (*51*) that provide the chemical and pumped protons to CIV also show differences in *T. thermophila*. Although a critical proton acceptor in the D-channel is conserved (Glu^{393} of COX1), a key threonine of the K-channel important for turnover in bacterial, archaeplastidan, and opisthokont CIV (Thr^{316} in yeast) (*52*) is replaced by a nonprotonatable alanine in Tt-COX1 (Ala^{466}) (fig. S19B). Thus, the Tt-CIV$_2$ K-channel either follows a different path or is not operational. Similarly, a key proton acceptor (Asp^{51} of COX1 in bovine CIV) (*53*) and a conserved cation (*18*) are missing in Tt-CIV$_2$'s H-channel (fig. S19B), suggesting a function as a dielectric regulator rather than as a proton channel in Tt-CIV$_2$ (*51*). Other key residues for O_2 access to the binuclear center and electron transfer from cyt c are conserved (fig. S19, C and D, and supplementary text).

Tt-CIV$_2$ incorporates mitochondrial carriers and a small TIM-like hexamer

Most of Tt-CIV's 44 accessory subunits remained uncharacterized or putative in the *T. thermophila* genome (fig. S17E) (*29*), with only 13 showing recognizable folds (fig. S17C). These subunits include three mitochondrial carriers (COXMC1 to 3; Fig. 5E), a hexameric

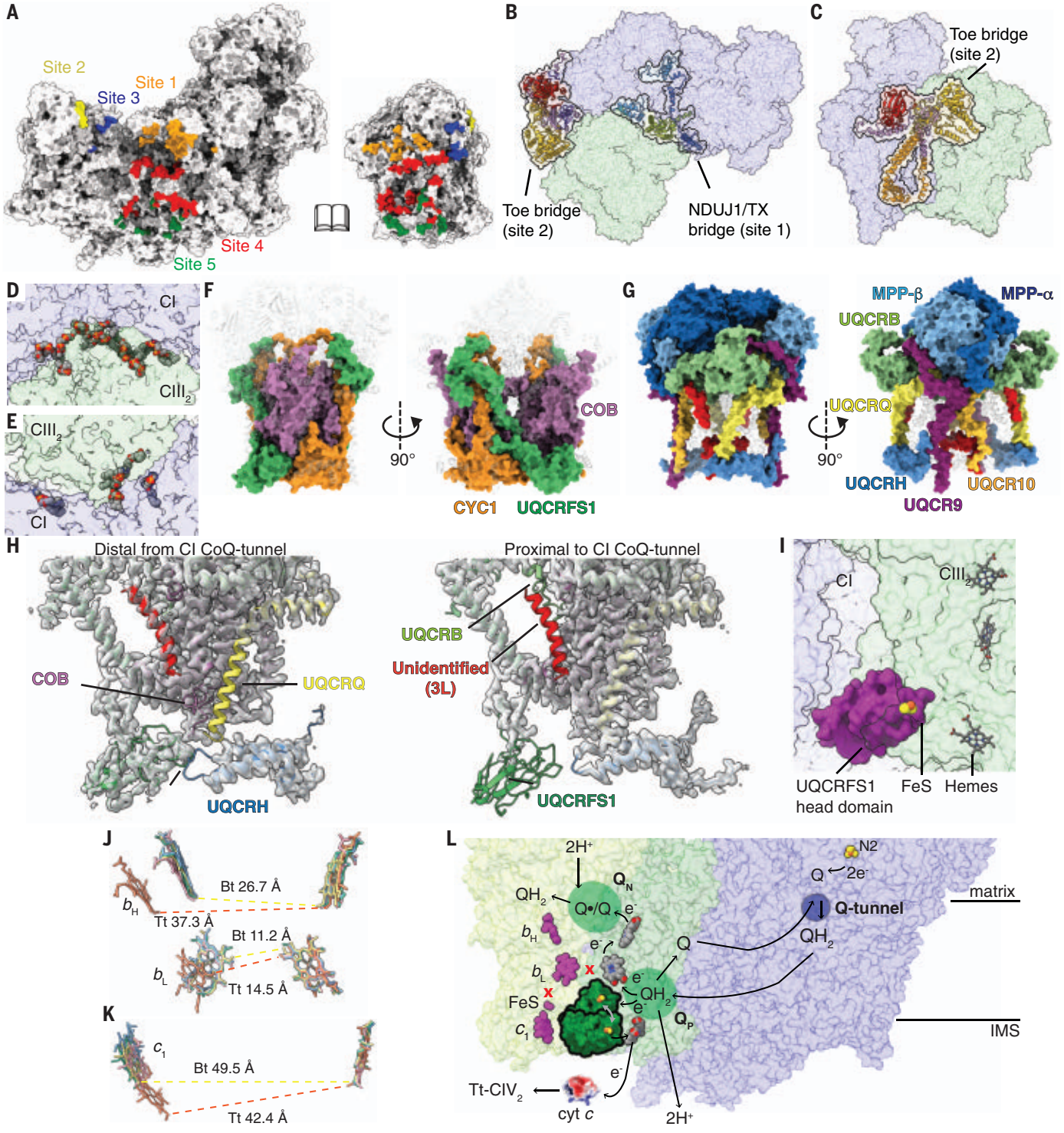

Fig. 4. Tt-SC I+III$_2$ interactions and Tt-CIII$_2$ symmetry breaking. (**A**) Contact sites between Tt-CI and Tt-CIII$_2$ in Tt-SC I+III$_2$, color-coded and shown in open-book configuration (orange, site 1; yellow, site 2; blue, site 3; red, site 4; green, site 5). (**B** and **C**) *T. thermophila*–specific Tt-SC I+III$_2$ matrix bridges (NDUJ1/TX bridge and toe bridge) in the context of Tt-SC I+III$_2$, viewed from the matrix (B) or from the plane of the membrane (C). Key subunits are shown as colored cartoons and highlighted in black outline. (**D** and **E**) Modeled lipids (spheres) at the interface between Tt-CI (blue surface) and Tt-CIII$_2$ (green surface). Lipids at the matrix (D) or IMS (E) leaflet of the membrane are viewed from the matrix or IMS, respectively. (**F** and **G**) Structure of Tt-CIII$_2$, with core (F) or accessory (G) subunits shown in surface and the rest of the complex as transparent cartoon. Unidentified chains (polyalanine model) are in red. (**H**) Broken symmetry in the Tt-CIII$_2$ dimer. For clarity, maps were carved around the asymmetric subunits. For each protomer, density is shown in transparent gray, models as cartoons. The subunit labels indicate differences in each protomer. (**I**) UQCRFS1 head domain (magenta surface) constrained at the interface between Tt-CI and Tt-CIII$_2$. Iron-sulfur (FeS) and heme cofactors (sticks) are shown. (**J** and **K**) Comparison of b-hemes (J) and c-hemes (K) in respiratory CIII$_2$ and photosynthetic b$_6$f complex dimers across cyanobacteria [PDB 1VF5 *Mastigocladus laminosus* b$_6$f complex (*63*)] in gray, bacteria [PDB

2YIU *P. denitrificans* (*64*)] in pink, yeast [PDB 6HU9 *S. cerevisiae* (*18*)] in blue, plants [PDB 7JRG *V. radiata* (*20*)] in green, mammals [PDB 1BGY *B. taurus* (*46*)] in yellow, and *T. thermophila* (orange). Hemes were superposed by one Tt-COB subunit in the dimer. Distances between hemes were calculated edge-to-edge of the macrocyclic conjugated system. For clarity, only distances for *T. thermophila* and *B. taurus* are shown. (**L**) Schematic of the symmetry-broken Q cycle and Q cavity specialization of Tt-CIII$_2$. Tt-CIII protomers are shown in dark green surface (proximal to Tt-CI Q tunnel, blue oval) or light green surface (distal to Tt-CI Q tunnel). The functional Q_N and Q_P sites are indicated with dark green ovals, corresponding to the dark green protomer. The functional UQCRFS1 head domain that is capable of a flexible swinging motion (double-headed gray arrow) is shown in dark green surface, with its FeS cluster as spheres. Both b_L and c_1 positions of the head domain are shown. Tt-CIII$_2$'s functional hemes are shown as heteroatom-colored spheres. nonfunctional hemes as magenta spheres. Red crosses indicate inability of electron transfer. Tt-CI's N2 FeS cluster is shown as spheres. Homology model of Tt–cyt c is shown in surface colored by electrostatic potential. Approximate position of inner mitochondrial membrane is marked with black lines. b_H, heme b_H; b_L, heme b_L; c_1, heme c_1; e^-, electron; H^+, proton; Q, oxidized quinone; QH_2, reduced quinone (quinol); Q•, semiquinone.

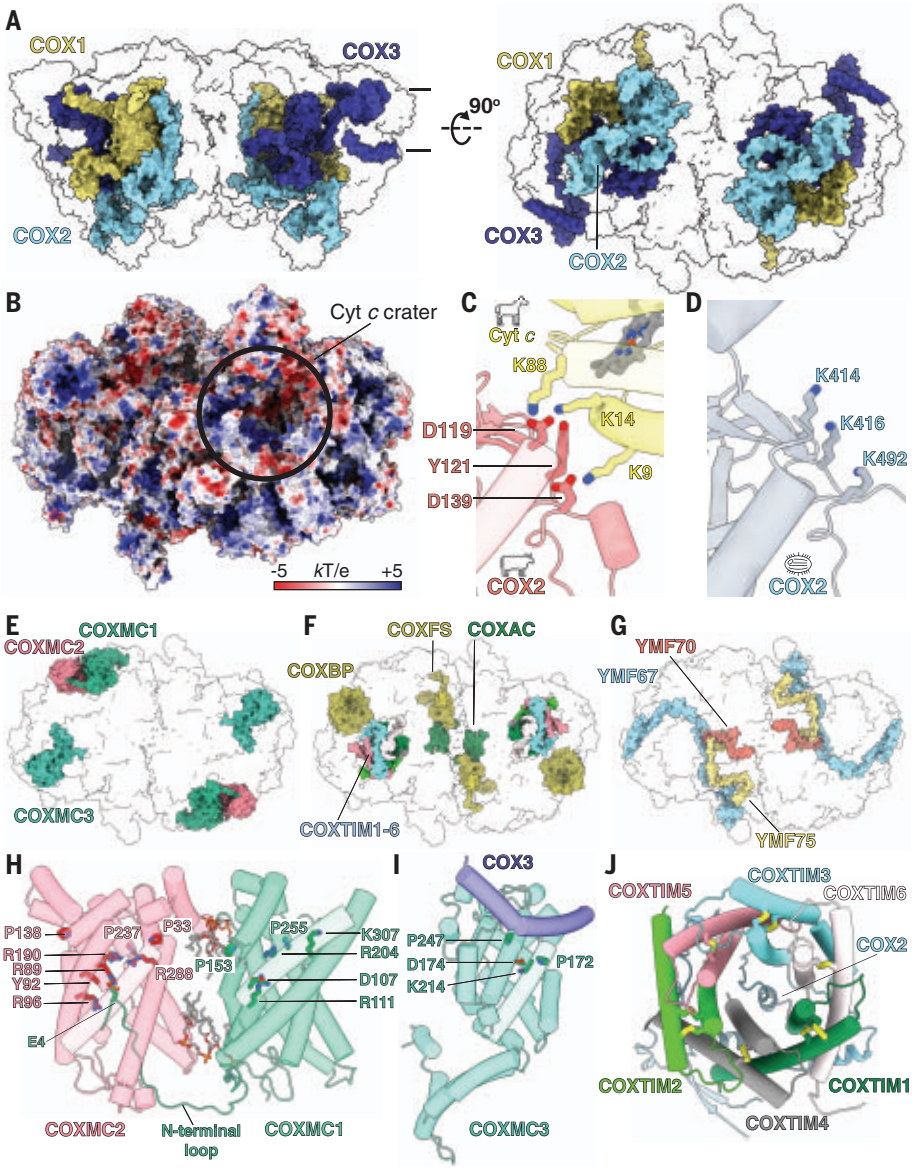

Fig. 5. Structural features of Tt-CIV$_2$. (**A**) Structure of Tt-CIV$_2$, with core subunits in surface over silhouette of entire complex, viewed from the membrane (left) or IMS (right). (**B**) Surface electrostatic potential of Tt-CIV$_2$. Cyt c crater is marked with a black circle. (**C** and **D**) Charge reversal in CIV–cyt c binding between mammals and *T. thermophila*. CIVs were aligned by COX2. Key residues are shown as sticks. (C) Binding of bovine COX2 (red cylinder, cow symbol) to equine cyt c (yellow cylinder, horse symbol) (PDB 5IY5) (*74*). (D) *T. thermophila* COX2 (gray cylinder). (**E** to **G**) Notable Tt-CIV$_2$ accessory subunits viewed from the IMS. (E) Mitochondrial carrier subunits COXMC1 to COXMC3. (F) Other subunits with annotated folds. (G) Mitochondrially encoded subunits YMF67, YMF70, and YMF75. (**H**) Side view of COXMC1-COXMC2 dimer (pink and green cylinders) with interfacial lipids (sticks). Key substrate-contacting residues, as well as conserved prolines of PX[D/E]XX[R/K] motif on odd-numbered helices, are shown as sticks. (**I**) Side view of COXMC3 (cyan cylinders) and the constraining amphipathic helix of COX3. (**J**) TIM8$_3$-TIM13$_3$–like heterohexamer domain with disulfide bonds in yellow. The Tt-specific loop of COX2 wraps around five of the COXTIM subunits and inserts itself into the central cavity of the hexamer. Amino acid abbreviations: D, Asp; E, Glu; K, Lys; P, Pro; R, Arg; Y, Tyr.

TIM8$_3$-TIM13$_3$ chaperone-like domain (COXTIM1 to 6) in the IMS, a β-propeller domain protein (COXBP), an acyl carrier protein (COXAC), and a [2Fe2S]-MitoNEET–like domain protein (COXFS; Fig. 5F) with two FeS cofactors in the matrix (fig. S21 and supplementary text). Tt-CIV$_2$ also contains three mitochondrially encoded subunits (YMF67, YMF70, and YMF75) that do not have homologs in any other known CIV structures (Fig. 5G), including the ancestral α-proteobacterial CIV (*54*), indicating that the ciliate mitochondrial genome has gained new genes. Additionally, there are several posttranslational modifications in accessory subunits visible in the cryo-EM maps (fig. S18 and supplementary text).

Mitochondrial carriers, or solute carrier family 25 (SLC25), are essential proteins that carry solutes into and out of the mitochondrial matrix (*55*). Although direct interaction between carriers and respiratory complexes has been

proposed (*56*), this has remained controversial. The structure of Tt-CIV_2 revealed a mitochondrial carrier dimer (COXMC1-COXMC2) adjacent to COX1 (Fig. 5, E and H) and a monomeric mitochondrial carrier (COXMC3) adjacent to COX3 (Fig. 5, E and I, and supplementary text).

Although both COXMC1 and COXMC2 are annotated as 2-oxoglutarate carriers (SLC25A11), key dicarboxylate-contacting residues (*57*) are fully conserved only for COXMC2 (Fig. 5H). The COXMC1-COXMC2 dimer is attached to the rest of Tt-CIV_2 via interactions with COX1's N-terminal helical extension as well as with subunit COX7C (fig. S21A). COXMC1's interactions with COX7C and COXTT22 block accessibility from the IMS (fig. S21A), making it unlikely that COXMC1 functions as a transporter. Instead, COXMC1 may have been coopted by Tt-CIV_2 as a structural or regulatory subunit. The COXMC1 N-terminal loop (residues 1 to 8 of COXMC2) inserts deeply into the COXMC2 central cavity (Fig. 5H). Glu^4 of COXMC1 is in close proximity to several of COXMC2's dicarboxylate-binding residues (Fig. 5H). Given the similar chemical structures of oxaloacetate and glutamate, Glu^4 of COXMC1 may act as a substrate analog, placing COXMC2 in an inhibited state.

The monomeric mitochondrial carrier subunit COXMC3 has long amphipathic α-helical extensions on both termini (Fig. 5I). These extensions interact with core subunit COX3 via bridging lipids in the IMS (fig. S21B). The N-terminal helix of COX3 also interacts with COXMC3 in the matrix (Fig. 5I). These interactions, as well as the broken symmetry of the carrier's TMHs (*55*) (Fig. 5I), make COXMC3 unlikely to function as a solute carrier. Rather, given its interactions on either side of the membrane and its peripheral location (fig. S21C), it is likely that COXMC3 has been coopted to help bend *T. thermophila*'s cristae.

Tt-CIV_2 also contains a hexameric α-propeller domain composed of small TIM8-like subunits next to the cyt c crater (Fig. 5, F and J). Soluble $TIM9_3$-$TIM10_3$ (*58*) or $TIM8_3$-$TIM13_3$ (*59*) hexamers function as IMS chaperones during mitochondrial protein import (fig. S22). Moreover, a $TIM9_3$-$TIM10_2$-TIM12 hexamer forms part of the TIM22 complex (*60*) that inserts mitochondrial carriers into the IMM (fig. S22). In contrast to canonical soluble TIM hexamers, the Tt-CIV_2 TIM assembly is a heterohexamer of six distinct subunits (COXTIM1 to 6) (Fig. 5J). The TIM hexamer is anchored to Tt-CIV_2 via interaction with a Tt-specific loop of COX2. As seen in structures of TIM hexamers binding to substrate peptides (*61*), this Tt-COX2 loop embeds itself in the interhelical clefts of the COXTIM subunits (Fig. 5J). Additionally, a short Tt-COX2 helix inserts itself into the central channel of the Tt-TIM hexamer, parallel to the hexamer's pseudo-symmetry axis (Fig. 5J). Human TIM8a has been implicated in CIV maturation through interactions with COX6B and assembly factors COX17 and COX19, which deliver essential copper atoms to COX2 (*62*). In *T. thermophila*, a group of subunits, including homologs of COX6B and COX17, are found adjacent to the TIM hexamer of Tt-CIV_2 (fig. S19A). These subunits may be a part of Tt-CIV's maturation pathway and that stay bound to the final complex, which suggests that one pathway to subunit addition into mETC complexes may be via the permanent incorporation of assembly factors.

Conclusions

The structures of Tt-SC $I+III_2$ and Tt-CV_2 reveal the diversity present in eukaryotic core metabolism. Collecting cryo-EM data on a partially purified sample allowed for the simultaneous structure determination of an entire metabolic pathway. This work demonstrates that ciliate mETC complexes have diverged from those of opisthokonts and archaeplastidans, including incorporating additional accessory subunits, flipping surface charges, splitting core subunits, and enhancing intercomplex interactions to produce highly curved and symmetry-broken assemblies. Furthermore, functional differences in the *T. thermophila* mETC complexes, such as the lack of a deactive state in Tt-CI, allow for the disambiguation of previous observations and will contribute to a more complete understanding of the conserved mechanisms of these essential complexes.

REFERENCES AND NOTES

1. P. Mitchell, *J. Bioenerg.* **3**, 5–24 (1972).
2. K. M. Davies, T. B. Blum, W. Kühlbrandt, *Proc. Natl. Acad. Sci. U.S.A.* **115**, 3024–3029 (2018).
3. J. A. Letts, L. A. Sazanov, *Nat. Struct. Mol. Biol.* **24**, 800–808 (2017).
4. K. Shinzawa-Itoh *et al*., *BBA Adv.* **1**, 100009 (2021).
5. T. E. Spikes, M. G. Montgomery, J. E. Walker, *Proc. Natl. Acad. Sci. U.S.A.* **117**, 23519–23526 (2020).
6. K. M. Davies, C. Anselmi, I. Wittig, J. D. Faraldo-Gómez, W. Kühlbrandt, *Proc. Natl. Acad. Sci. U.S.A.* **109**, 13602–13607 (2012).
7. A. W. Mühleip *et al*., *Proc. Natl. Acad. Sci. U.S.A.* **113**, 8442–8447 (2016).
8. A. Mühleip *et al*., *Nat. Commun.* **12**, 120 (2021).
9. R. K. Flygaard, A. Mühleip, V. Tobiasson, A. Amunts, *Nat. Commun.* **11**, 5342 (2020).
10. D. A. Stroud *et al*., *Nature* **538**, 123–126 (2016).
11. A. Padavannil, M. G. Ayala-Hernandez, E. A. Castellanos-Silva, J. A. Letts, *Front. Mol. Biosci.* **8**, 798353 (2022).
12. K. Parey *et al*., *Sci. Adv.* **5**, eaax9484 (2019).
13. D. Kampjut, L. A. Sazanov, *Science* **370**, eabc4209 (2020).
14. M. Maldonado, A. Padavannil, L. Zhou, F. Guo, J. A. Letts, *eLife* **9**, e56664 (2020).
15. N. Klusch, J. Senkler, Ö. Yildiz, W. Kühlbrandt, H.-P. Braun, *Plant Cell* **33**, 2072 (2021).
16. H. Soufari, C. Parrot, L. Kuhn, F. Waltz, Y. Hashem, *Nat. Commun.* **11**, 5195 (2020).
17. D. M. Elurbe, M. A. Huynen, *Biochim. Biophys. Acta* **1857**, 971–979 (2016).
18. A. M. Hartley *et al*., *Nat. Struct. Mol. Biol.* **26**, 78–83 (2019).
19. D. Xia *et al*., *Science* **277**, 60–66 (1997).
20. M. Maldonado, F. Guo, J. A. Letts, *eLife* **10**, e62047 (2021).
21. A. P. Srivastava *et al*., *Science* **360**, eaas9699 (2018).
22. M. Allegretti *et al*., *Nature* **521**, 237–240 (2015).
23. O. Gahura *et al*., bioRxiv 463820 (2021).
24. A. Mühleip, S. E. McComas, A. Amunts, *eLife* **8**, e51179 (2019).
25. T. B. Blum, A. Hahn, T. Meier, K. M. Davies, W. Kühlbrandt, *Proc. Natl. Acad. Sci. U.S.A.* **116**, 4250–4255 (2019).
26. H. J. Eichel, *J. Biol. Chem.* **222**, 121–136 (1956).
27. C. F. Brunk, L. C. Lee, A. B. Tran, J. Li, *Nucleic Acids Res.* **31**, 1673–1682 (2003).
28. L. Kilpatrick, M. Erecińska, *Biochim. Biophys. Acta* **462**, 515–530 (1977).
29. D. G. S. Smith *et al*., *J. Mol. Biol.* **374**, 837–863 (2007).
30. A. E. Maclean *et al*., *PLOS Pathog.* **17**, e1009301 (2021).
31. F. Evers *et al*., *Nat. Commun.* **12**, 3820 (2021).
32. Y. Y. Londer, *Methods Mol. Biol.* **705**, 123–150 (2011).
33. C.-M. Ho *et al*., *Nat. Methods* **17**, 79–85 (2020).
34. J. A. Letts, K. Fiedorczuk, G. Degliesposti, M. Skehel, L. A. Sazanov, *Mol. Cell* **75**, 1131–1146.e6 (2019).
35. S. Zong *et al*., *Cell Res.* **28**, 1026–1034 (2018).
36. A. A. Agip *et al*., *Nat. Struct. Mol. Biol.* **25**, 548–556 (2018).
37. K. Parey *et al*., *eLife* **7**, e39213 (2018).
38. K. Parey *et al*., *Sci. Adv.***7**, eabj3221 (2021).
39. E. Maklashina, A. B. Kotlyar, G. Cecchini, *Biochim. Biophys. Acta* **1606**, 95–103 (2003).
40. J. N. Blaza, K. R. Vinothkumar, J. Hirst, *Structure* **26**, 312–319. e3 (2018).
41. E. V. Gavrikova, A. D. Vinogradov, *FEBS Lett.* **455**, 36–40 (1999).
42. A. Cabrera-Orefice *et al*., *Nat. Commun.* **9**, 4500 (2018).
43. J. S. Sousa, D. J. Mills, J. Vonck, W. Kühlbrandt, *eLife* **5**, e21290 (2016).
44. I. Vercellino, L. A. Sazanov, *Nature* **598**, 364–367 (2021).
45. D. Xia *et al*., *Biochim. Biophys. Acta* **1827**, 1278–1294 (2013).
46. S. Iwata *et al*., *Science* **281**, 64–71 (1998).
47. L. A. Malone *et al*., *Nature* **575**, 535–539 (2019).
48. M. Świerczek *et al*., *Science* **329**, 451–454 (2010).
49. W. A. Cramer, S. S. Hasan, E. Yamashita, *Biochim. Biophys. Acta Bioenerg.* **1807**, 788–802 (2011).
50. P. Brzezinski, A. Moe, P. Ädelroth, *Chem. Rev.* **121**, 9644–9673 (2021).
51. P. R. Rich, A. Maréchal, *J. R. Soc. Interface* **10**, 20130183 (2013).
52. A. Maréchal *et al*., *Proc. Natl. Acad. Sci. U.S.A.* **117**, 9349–9355 (2020).
53. S. Yoshikawa, K. Muramoto, K. Shinzawa-Itoh, *Biochim. Biophys. Acta* **1807**, 1279–1286 (2011).
54. J. Koepke *et al*., *Biochim. Biophys. Acta Bioenerg.* **1787**, 635–645 (2009).
55. J. J. Ruprecht, E. R. S. Kunji, *Annu. Rev. Biochem.* **90**, 535–558 (2021).
56. Y.-W. Lu *et al*., *Mol. Biol. Cell* **28**, 1489–1506 (2017).
57. M. Monné, D. V. Miniero, V. Iacobazzi, F. Bisaccia, G. Fiermonte, *J. Bioenerg. Biomembr.* **45**, 1–13 (2013).
58. C. T. Webb, M. A. Gorman, M. Lazarou, M. T. Ryan, J. M. Gulbis, *Mol. Cell* **21**, 123–133 (2006).
59. M. J. Baker *et al*., *Mol. Biol. Cell* **20**, 769–779 (2009).
60. N. Wiedemann, N. Pfanner, *Annu. Rev. Biochem.* **86**, 685–714 (2017).
61. K. Weinhäupl *et al*., *Cell* **175**, 1365–1379.e25 (2018).
62. A. Ghosh *et al*., *Hum. Mol. Genet.* **25**, 660–671 (2016).
63. G. Kurisu, H. Zhang, J. L. Smith, W. A. Cramer, *Science* **302**, 1009–1014 (2003).
64. T. Kleinschroth *et al*., *Biochim. Biophys. Acta Bioenerg.* **1807**, 1606–1615 (2011).

ACKNOWLEDGMENTS

Dataset 1 was collected at the UC Davis BioEM Core facility. Dataset 2 was collected at the UCSF W. M. Keck Foundation Advanced Microscopy Laboratory, accessed through the Bay Area CryoEM Consortium BACEM, with the assistance of D. Bulkley and Z. Yu. We thank the UC Davis Proteomics Core for technical assistance, F. Han for assistance with modeling Tt-CIV_2, and R. Murguia and K. Abe for assistance with Tt–cyt c preparations. **Funding:** Supported by National Institute of General Medical Sciences award R35GM137929. The

content is solely the responsibility of the authors and does not necessarily represent the official views of the National Institutes of Health. Also supported by a ZJU100 Young Professor award from Zhejiang University School of Medicine (L.Z.). **Author contributions:** conceptualization: J.A.L.; methodology: L.Z., M.M., F.G., J.A.L.; investigation: L.Z., M.M., A.P., F.G., J.A.L.; visualization: L.Z., M.M., A.P., J.A.L.; funding acquisition: L.Z., J.A.L.; project administration: J.A.L.; supervision: J.A.L.; writing–original draft: L.Z., M.M., J.A.L.; writing–review and editing: L.Z., M.M., A.P., J.A.L. **Competing interests:** The authors declare that they have no competing interests. **Data and materials availability:** Single-particle cryogenic electron micrograph movies and motion-corrected micrographs for datasets 1 and 2 are available on the Electron Microscopy Public Image Archive, accession codes EMPIAR-10882 and EMPIAR-10919. The maps and models for Tt-SC I+III$_2$ and Tt-CIV2 are available on the Electron Microscopy Database (EMDB) and the Protein Data Bank (PDB) with accession codes Tt-SC I+III$_2$ EMDB-25882, PDB-7TGH; Tt-CIV$_2$ EMDB-32325, PDB-7W5Z. The maps for Tt-CV$_2$ are available on the EMDB with accession codes EMDB-32631 and EMDB-32632. **License information:** Copyright © 2022 the authors, some rights reserved; exclusive licensee American Association for the Advancement of Science. No claim to original US government works. www.science.org/about/science-licenses-journal-article-reuse

SUPPLEMENTARY MATERIALS

science.org/doi/10.1126/science.abn7747
Materials and Methods
Supplementary Text
Figs. S1 to S22
Tables S1 to S7
References (*65*–*102*)
Movies S1 and S2

Submitted 19 December 2021; accepted 21 March 2022
Published online 31 March 2022
10.1126/science.abn7747

FOREST ECOLOGY

The biodiversity and ecosystem service contributions and trade-offs of forest restoration approaches

Fangyuan Hua[1,2]*, L. Adrian Bruijnzeel[3,4]*, Paula Meli[5,6], Philip A. Martin[2,7], Jun Zhang[4,8], Shinichi Nakagawa[9], Xinran Miao[1], Weiyi Wang[1], Christopher McEvoy[2], Jorge Luis Peña-Arancibia[10], Pedro H. S. Brancalion[5], Pete Smith[11], David P. Edwards[12], Andrew Balmford[2]

Forest restoration is being scaled up globally to deliver critical ecosystem services and biodiversity benefits; however, there is a lack of rigorous comparison of cobenefit delivery across different restoration approaches. Through global synthesis, we used 25,950 matched data pairs from 264 studies in 53 countries to assess how delivery of climate, soil, water, and wood production services, in addition to biodiversity, compares across a range of tree plantations and native forests. Benefits of aboveground carbon storage, water provisioning, and especially soil erosion control and biodiversity are better delivered by native forests, with compositionally simpler, younger plantations in drier regions performing particularly poorly. However, plantations exhibit an advantage in wood production. These results underscore important trade-offs among environmental and production goals that policy-makers must navigate in meeting forest restoration commitments.

As the UN Decade on Ecosystem Restoration gets underway (*1*), forest restoration on degraded and deforested land is being scaled up globally, with far-reaching environmental and social implications (*2*–*4*). The Bonn Challenge, for example, has pledged to restore 350 million hectares of land by 2030 (*5*), and many other initiatives are similarly ambitious (*6*, *7*). Large-scale programs to restore forests are frequently motivated by a desire to recover ecosystem services such as carbon storage (*8*), soil erosion control (*9*), water provisioning (*10*), and wood production (*11*). Based on an implicit assumption that these services can be effectively delivered by forests regardless of their composition, many of these programs gravitate toward reforesting with compositionally simple tree plantations rather than restoring native forests (*7*, *10*, *12*). However, this premise has yet to be tested rigorously with paired data that limit potential confounding factors (*13*) (supplementary text). This omission is critically important for reasons beyond the target ecosystem services per se, because a focus on tree plantations has limited (*14*)—and at times negative (*9*)—effects on native biodiversity and consequently risks severely limiting the conservation potential of large-scale forest restoration, in turn hampering progress toward global commitments to halt and reverse biodiversity loss (*15*–*17*) and ecosystem degradation (*1*).

We present a global synthesis of paired data from the world's main forest biomes to assess the merits of forest restoration approaches, in particular reforesting with tree plantations versus restoring native forests, on deforested land that would have been naturally forested in recent history (see materials and methods) (*18*). We compare the performance of a range of compositionally simple tree plantations spanning a wide spectrum of management regimes ("tree plantations" hereafter) (*18*) with the performance of native forests (including restored and preexisting native forests) in delivering the key ecosystem services of carbon storage, soil erosion control, water provisioning, and wood production, as well as in supporting biodiversity. We further assess how variation in the relative performance of tree plantations versus native forests may be explained by plantation features and biophysical conditions. Our study aims to enable forest restoration to achieve cobenefits in addressing today's multiple environmental challenges (*4*), including the dual climate and biodiversity crises (*8*, *17*). By simultaneously considering the performance of forests in carbon, soil, water, and biodiversity (i.e., environmental outcomes) in addition to performance in wood production, our study also provides a critical assessment of the trade-offs likely to confront forest restoration decision makers.

For each environmental outcome, we identified the most informative metric with a reasonable amount of empirical data: aboveground biomass [megagrams per hectare (Mg ha^{-1})], amount of eroded soil [kilograms per square meter per year (kg m^{-2} y^{-1})], catchment- or plot-scale water yield (percent of rainfall), and species-specific abundance [individuals per hectare compiled for each species in a given ecological community; see (*18*) for rationale of metric choices]. After searching peer-reviewed and gray literature and corresponding with authors, we compiled pairs of data that involved a tree plantation (classified into three types) and a matching native forest (classified into four types; Fig. 1A) from the same study system (*18*). For wood production, we compiled pairs of empirical data on wood yield [cubic meters per hectare (m^3 ha^{-1})] or profit [US dollars per hectare (USD ha^{-1})] that involved a tree plantation and a matching restored native forest (Fig. 1A) over equal time horizons (*18*); we excluded native forests not resulting from restoration because the sustainability of their wood harvest could rarely be confirmed. Given the paucity of paired wood production data, we relaxed the matching requirement to also compile annualized yield data just from restored native forests [(cubic

[1]Institute of Ecology and Key Laboratory for Earth Surface Processes of the Ministry of Education, College of Urban and Environmental Sciences, Peking University, Beijing 100871, P.R. China. [2]Conservation Science Group, Department of Zoology, University of Cambridge, Cambridge CB2 3EJ, UK. [3]Department of Geography, King's College London, Bush House, London WC2B 4BG, UK. [4]Institute of International Rivers and Eco-Security, Yunnan University, Kunming 650091, Yunnan, P.R. China. [5]Department of Forest Sciences, Luiz de Queiroz College of Agriculture, University of São Paulo, Piracicaba, SP, 13.418-900, Brazil. [6]Departmento de Ciencias Forestales, Universidad de La Frontera, Av. Francisco Salazar 01145, Temuco, Chile. [7]Basque Centre for Climate Change (BC3), Edificio sede no 1, planta 1, Parque científico UPV/EHU, Barrio Sarriena s/n, 48940 Leioa, Bizkaia, Spain. [8]Environmental Modelling, Sensing & Analysis, TNO, 1755 LE Petten, Netherlands. [9]Evolution & Ecology Research Centre and School of Biological, Earth and Environmental Sciences, University of New South Wales, Sydney, NSW 2052, Australia. [10]CSIRO Land and Water, Canberra, ACT 2601, Australia. [11]Institute of Biological & Environmental Sciences, University of Aberdeen, Aberdeen AB24 3UU, UK. [12]Ecology and Evolutionary Biology, School of Biosciences, University of Sheffield, Sheffield S10 2TN, UK.
***Corresponding author. Email: fhua@pku.edu.cn (F.H.); sampurno.bruijnzeel@kcl.ac.uk (L.A.B.)**

meters per hectare per year ($m^3\ ha^{-1}\ y^{-1}$)] (*18*), which we compared with known annualized yields of some of the world's main monoculture plantations (*19*).

We assessed the rigor of matching for each data pair and weighed it accordingly in subsequent analyses (*18*). We calculated a log response ratio (RR) [ln(tree plantation over native forest)] from each data pair to represent the relative performance of tree plantations versus native forests; we reversed the RR signs for eroded soil to represent soil erosion control. In total, our searches (*18*) (fig. S1 and tables S1 to S3) yielded 25,535 RRs for species-specific abundance on 13 species groups from 405 plantation-native forest pairs, 146 RRs for aboveground biomass, 82 RRs for eroded soil, 167 RRs for water yield, and 20 RRs for wood production, from 264 studies in 53 countries (Fig. 1 and table S4). In addition, we collated 223 records on the standing wood volume of restored native forests with known age from 10 studies in six countries (fig. S2 and table S4).

We first asked how well tree plantations performed in environmental outcomes relative to reference native forests not resulting from restoration, namely old growth forests and "generic" native forests (i.e., other non-restored native forests not reported as old growth). Not having undergone deforestation, these native forests represent reference environmental conditions (*20*) toward which forest restoration can aspire (Fig. 2A) (*18*). Consistent with prevailing understanding (*14*, *21*), tree plantations supported on average 29.3% lower species-specific abundance than did reference native forests [95% confidence interval (CI): 22.0 to 35.9%; Fig. 2B, upper panel, and table S5; for differences among species groups, see fig. S3]. This biodiversity contrast was echoed across the other three environmental metrics, with tree plantations delivering 32.8% lower aboveground biomass (95% CI: 16.5 to 45.9%), 60.6% lower soil erosion control (16.2 to 81.4%), and 13.4% lower water yield (4.1 to 21.9%; Fig. 2B, upper panel; table S5). These patterns were mainly driven by the poor performance of monoculture plantations, which exhibited the greatest contrasts with reference native forests (Fig. 2B, upper panel, and table S5). Prolonged age (≥40 years) or abandonment appeared to somewhat improve the environmental performance of plantations (*18*), with water yield shortfall no longer significant (mean: 6.7%; 95% CI: −23.4 to 29.4%; Fig. 2B, lower panel; table S5). However, differences for the other metrics persisted, albeit less marked: 14.6% (2.3 to 25.3%) for species-specific abundance and 24.0% (6.2 to 38.5%) for aboveground biomass; there were too few data to assess soil erosion control (Fig. 2B, lower panel, fig. S3, and table S5).

We next asked how well tree plantations performed relative to restored native forests of similar age (i.e., ≤10 years of age difference), represented by secondary forests resulting from natural regeneration, as well as actively restored native forests resulting from the planting of a diverse native tree mix (typically ≥50 species; Fig. 1A, fig. S4, and Fig. 2A, lower panel) (*18*). With regards to environmental performance, tree plantations performed significantly more poorly than restored native forests of similar age in species-specific abundance (32.3% poorer; 95% CI: 15.7 to 45.7%; there were insufficient data to contrast between species groups; fig. S3) and marginally so for soil erosion control (80.2% poorer; −57.9 to 97.5%), but not aboveground biomass (4.1% greater; −23.1 to 40.9% and spanning zero; Fig. 2C, upper panel, and table S5; data paucity precluded analysis for water yield). The similarity in aboveground biomass appeared to be due to the strong performance of abandoned plantations, which seemed to outperform both monocultures and mixed plantations (Fig. 2C, upper panel; although data paucity precluded formal analysis on this).

For wood production, the limited paired data showed that tree plantations had a clear advantage over restored native forests, with 222.7% (105.8 to 406.0%) higher wood volume

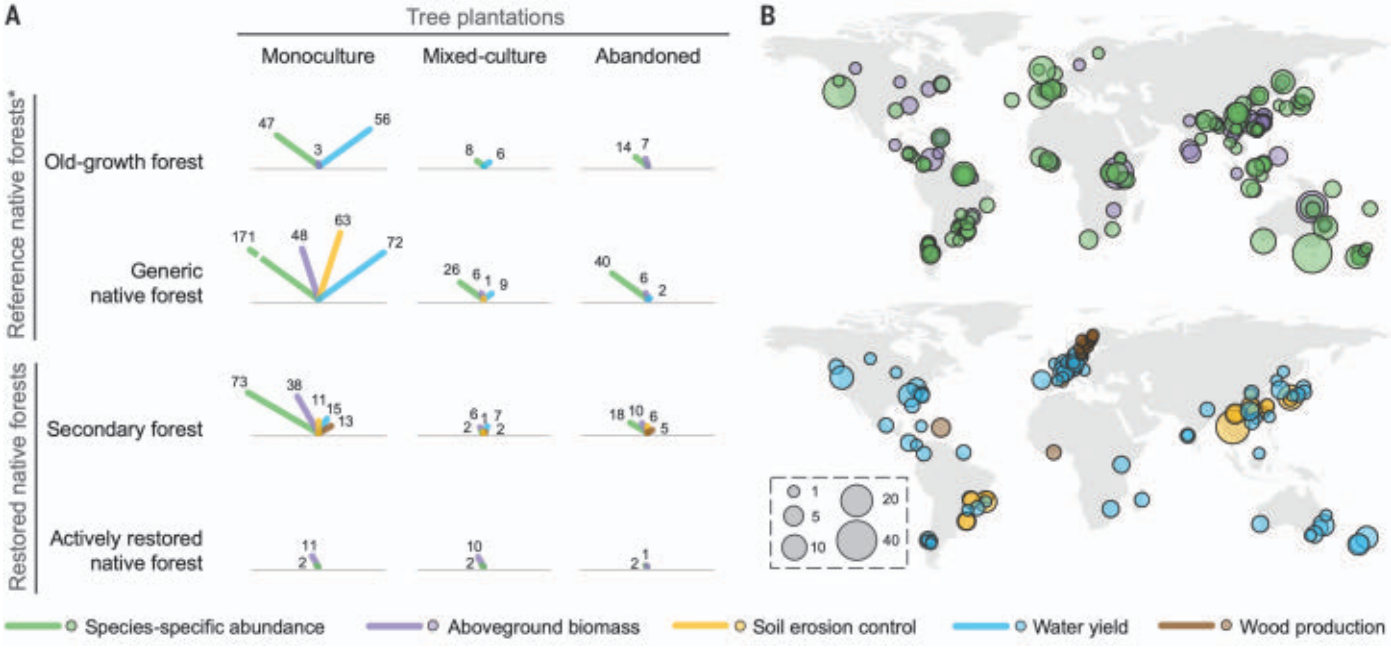

Fig. 1. Database overview. (**A**) The amount of paired data compiled into our database for different combinations of plantations and native forests. For species-specific abundance, the amount of data is represented by the number of plantation-native forest pairs that supplied species-level RRs for entire ecological communities; for all other metrics, it is represented by the number of RRs. (**B**) Geographical distribution of RRs of different metrics, displayed in two maps for better visualization: species-specific abundance and aboveground biomass (upper panel) and soil erosion control, water yield, and wood production (lower panel). Bubble size in maps is proportional to the cube root of the amount of data for a given geographical location. * indicates that we did not compile paired wood production data for the comparison between tree plantations and reference native forests.

at comparable age (Fig. 2C, lower panel, and table S5; data paucity precluded analysis of profits from wood production). This advantage was apparent for both intensively managed and abandoned plantations, and regardless of whether wood volume included all woody species or only merchantable species (fig. S5). The same conclusion was reached by use of supplementary nonpaired data on annualized wood yields of restored native forests and various prominent monocultures: average annual volume increments for restored native forests were 61.3% (Welch two-sample t test: $t_{28.8} = -6.40$, $P < 0.0001$) and 86.9% ($t_{26.4} = -9.76$, $P < 0.0001$) lower than the lower and upper bounds of the monocultures, respectively (Fig. 2D).

For all the above meta-analyses we found high levels of heterogeneity (*18*) with I^2—the metric for heterogeneity—generally ≥80% (table S5). Findings were robust to publication bias (supplementary text; fig. S6) and various sensitivity analyses related to weighting schemes and model structure (*18*) (table S5). They also showed that across the environmental metrics examined, tree plantations performed particularly poorly for soil erosion control (Fig. 2, right-hand panels). Because data for different metrics were obtained for different regions (Fig. 2, left-hand panels), the difference among environmental outcomes might reflect inherent biophysical differences among ecosystems. To address this potential

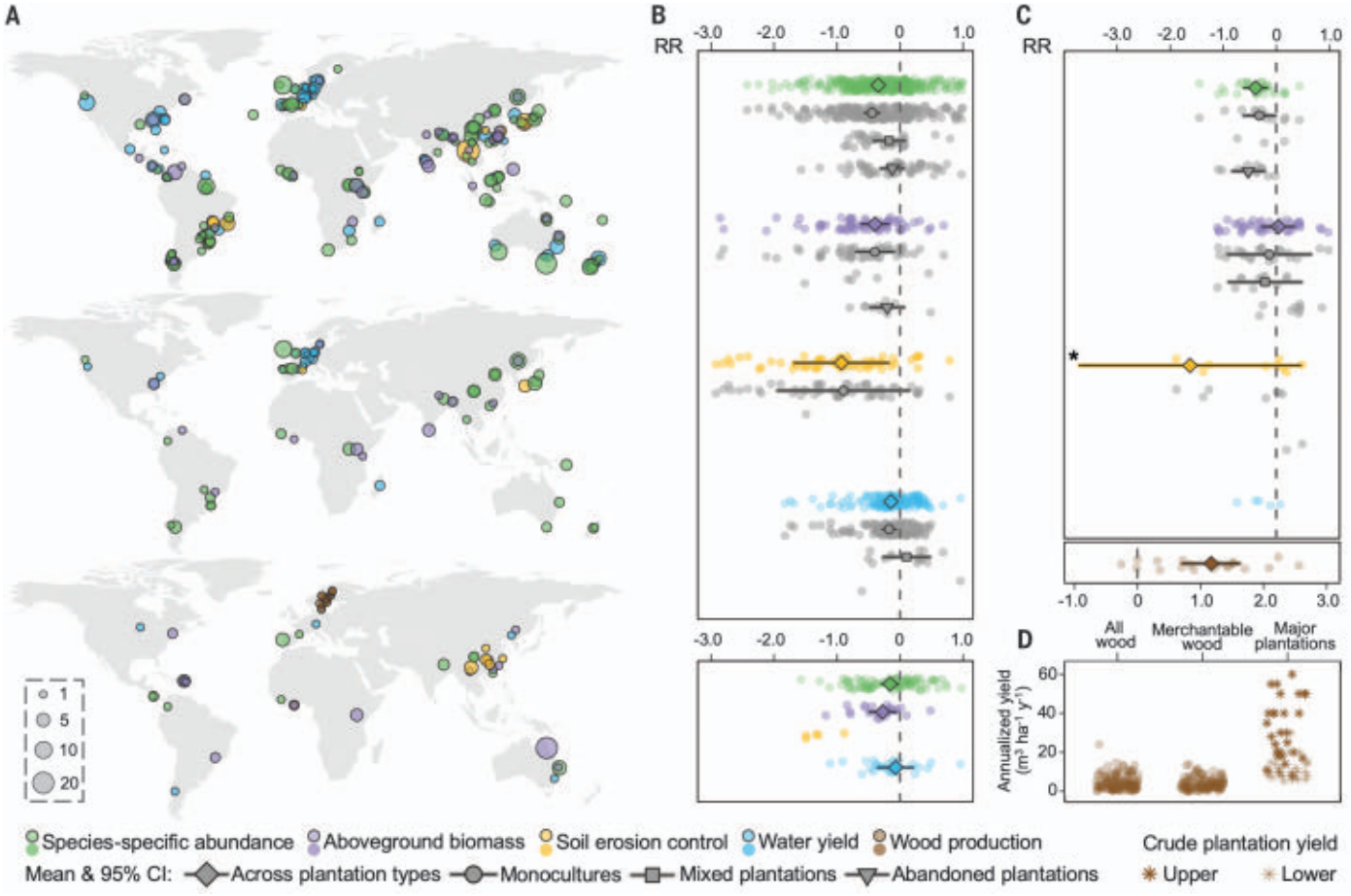

Fig. 2. Relative performance of tree plantations versus native forests across the metrics assessed. (**A**) Maps displaying the distribution and amount of data analyzed, for three types of comparisons: plantations versus reference native forests (upper panel), old (≥40 years of age) or abandoned plantations versus reference native forests (middle panel), and plantations versus restored native forests of similar age (i.e., ≤10 years of age difference; lower panel). As with Fig. 1, bubble size is proportional to the cube root of the amount of data for a given geographical location. (**B**) Relative performance of plantations versus reference native forests (upper panel) and of old or abandoned plantations versus reference native forests (lower panel), in environmental metrics. Scattered dots in color represent RRs from primary studies across all types of plantations, and diamonds and associated error bars represent the mean and 95% confidence intervals (CI), respectively, of RR values obtained from meta-analyses in which the numbers of RRs are ≥10 (in the case of species-specific abundance, in which the numbers of plantation-native forest pairs are ≥10). For the comparison between plantations and reference native forests (upper panel), we also analyzed RRs separately for different types of plantations for which the numbers of RRs are ≥10. For these analyses, we display their RR values from primary studies in gray, distinguishing among plantation types with different symbols for their meta-analysis–derived means and 95% CI. (**C**) Relative performance of plantations versus restored native forests of similar age in environmental (upper panel) and production (lower panel) metrics, with symbol use following that of (B). (**D**) Annualized wood volume increment of restored native forests compared with the lower and upper bounds of the annual wood increment of the world's major monoculture plantations. In our display, we differentiate between records on all woody plants and those on only merchantable species for restored native forests, and between the lower and upper bounds for plantations. In panels (B) and (C), scattered dots for species-specific abundance data represent the average RR within the ecological community concerned in each plantation-native forest pair, and a small number of RR values are not displayed because they fell outside the display range, including five highly negative RRs for soil erosion control indicated by * in (C).

geographical confounding effect, we next focused on a subset of our database in which data for different metrics could be geographically matched to a given ecosystem type, the biophysical conditions of which were largely coherent. Overlaying our data onto the Holdridge Life Zones map (*22*, *23*), we identified "data bundles" for each forest biome where RRs were available for ≥2 metrics. In total, we identified 11 such data bundles for the comparison between tree plantations and reference native forests (Fig. 3A) and seven for the comparison between tree plantations and restored native forests of similar age (Fig. 3B). The patterns of how RRs for soil erosion control compared with other environmental metrics within each data bundle corroborated our earlier findings: Relative to reference native forests, plantation shortfalls were almost always greatest for soil erosion control and least for water yield (Fig. 3).

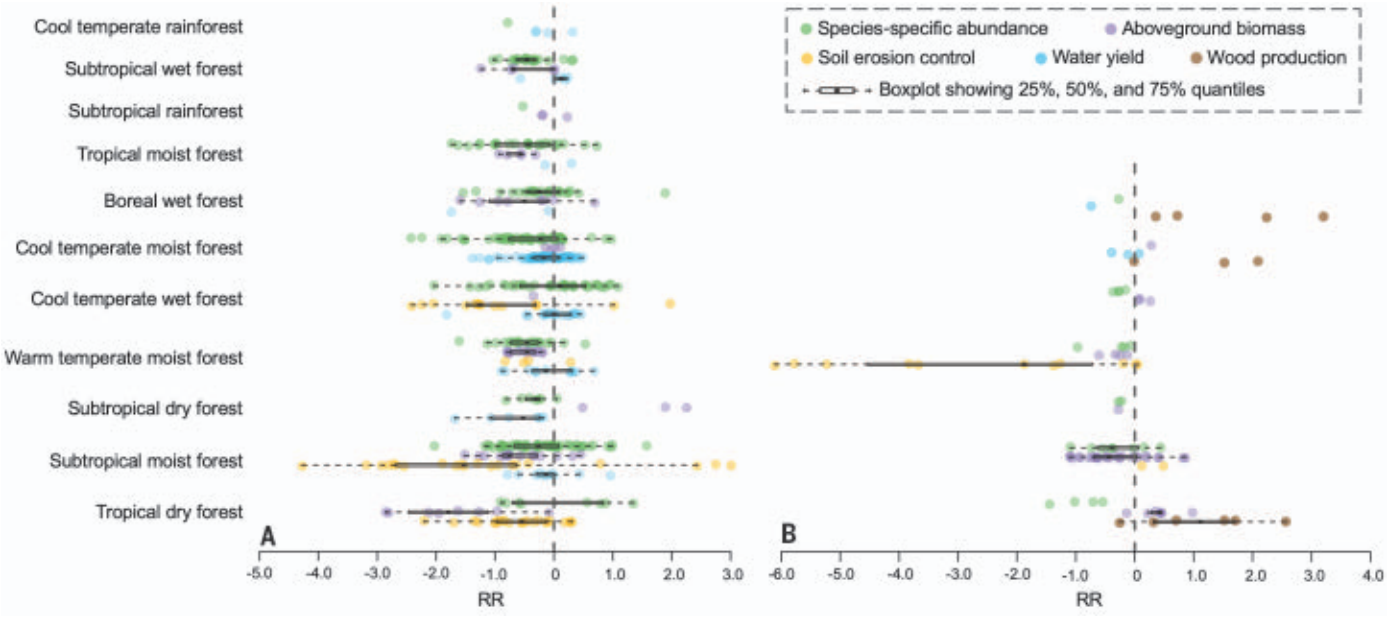

Fig. 3. Relative performance of plantations versus native forests compared among the metrics assessed, based on geographically matched data bundles for individual forest biomes. (**A**) Plantations versus reference native forests. (**B**) Plantations versus restored native forests of similar age (i.e., ≤10 years of age difference). RR values (in the case of species-specific abundance, the average RR within the ecological community concerned in each plantation-native forest pair) are represented by scattered dots, and their quartiles by boxplots where the numbers of RRs are ≥5. For the comparison between plantations and restored native forests of similar age, data bundles were not available for the four forest biomes on the top.

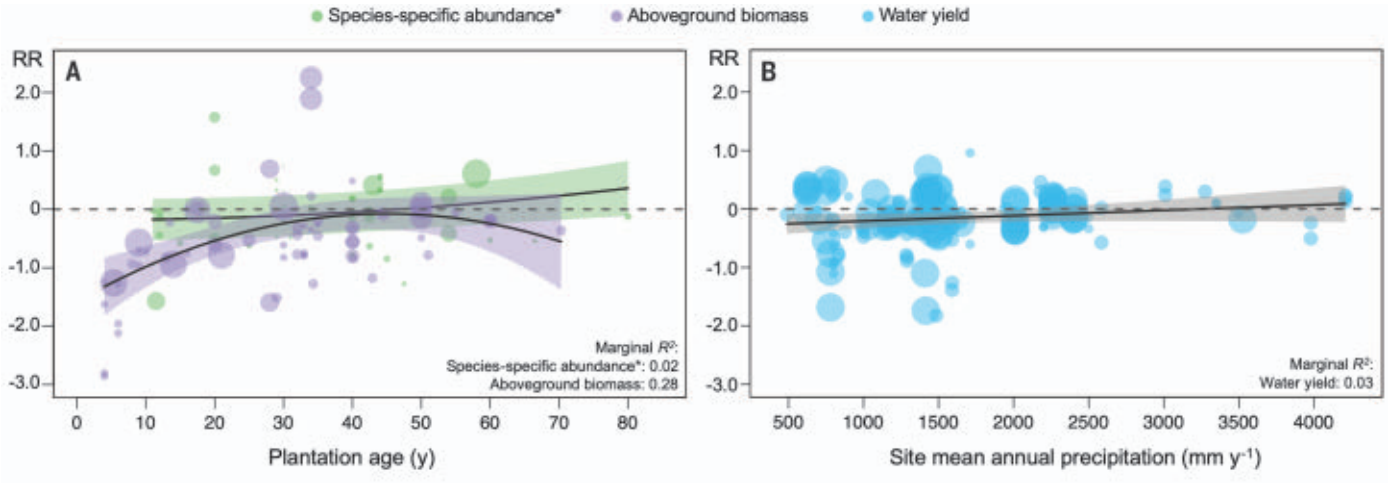

Fig. 4. Factors explaining the relative performance of plantations versus reference native forests. Best models selected based on AICc scores identified the following factors as explaining RRs: (**A**) plantation age for aboveground biomass and for species-specific abundance (* indicates the latter concerning the comparison between abandoned plantations and reference native forests only) and (**B**) MAP for water yield. Scattered dots represent RR values from primary studies (in the case of species-specific abundance, average RR within the ecological community concerned in each plantation-native forest pair), with dot size proportional to the weight of each RR in the meta-regressions, standardized within each metric to the RR with the greatest weight. Fitted curves (black lines) and 95% confidence bands and 95% confidence bands [colored bands in (A) and a gray band in (B)] were generated from meta-regressions.

We also asked what factors might underlie the variation in environmental performance of tree plantations relative to native forests. For the comparisons of plantations versus reference native forests and plantations versus restored native forests of similar age, respectively, we assessed the relationship between RRs and a set of variables representing plantation features and site biophysical conditions [note that analyses of wood production were dropped because of data paucity (*18*)]. We considered plantation type, plantation age (except for the comparison involving restored native forests of similar age), and mean annual temperature (MAT), measured in degrees Celsius (*18*). The rationale for considering MAT was that by supporting higher plant diversity (*24*), warmer climates may show greater contrasts between plantations and native forests in terms of vegetation complexity, and in turn, in delivery of ecosystem services related to carbon, soil, and water (*25*). We also considered mean annual precipitation (MAP), in millimeters per year, for soil erosion because of its likely influence on protective ground cover, as well as MAP and the seasonality of native forests (evergreen or deciduous) for water yield because of their likely influence on the hydrological behaviors of forest ecosystems (*18*, *26*, *27*).

The most parsimonious models selected through small-sample corrected Akaike Information Criterion (AIC) scores (*18*) (table S6) showed that increasing plantation age improved plantation performance relative to that of reference native forests in species-specific abundance and aboveground biomass (table S7), although such improvement was limited (Fig. 4A): particularly for aboveground biomass even old (≥40 years) plantations performed less well than reference native forests. Combined with the environmental shortfalls of old or abandoned plantations (Fig. 2B, lower panel), this finding suggests that old plantations no longer intended for productive use (*28*) would deliver environmental benefits more effectively if they were restored to native forest or native forest-like conditions. The fact that such areas are common in our database (Figs. 1A and 2A) indicates the sizeable environmental gains that such "forgotten lands" offer, underscoring the need to assess their global distribution and restoration potential (*29*).

We also found that increasing MAP (range covered by our data: 490 to 4210 mm y^{-1}) predicted more positive RRs for water yield when comparing tree plantations with reference native forests (Fig. 4B; table S7), indicating greater plantation shortfalls in water provisioning in drier climates. Clearly, water-oriented forest restoration initiatives should reexamine the practice of establishing large areas of tree plantations in the world's drier regions (*30*). We did not find evidence of other variables explaining variation in RR values or for any variable explaining plantation performance relative to restored native forests of similar age (fig. S7 and table S6). These findings were again robust to various sensitivity analyses related to weighting schemes and model structure (*18*) (tables S6 and S7), with the exception of one sensitivity analysis on soil erosion control (table S6), which showed ameliorated plantation shortfalls relative to reference native forests in warmer or wetter climates (fig. S7 and table S7).

Our findings have implications for forest restoration as it is scaled up globally (*7*) and provide a knowledge base for exploring how outcomes can be best delivered by alternative restoration approaches. We found that restoring native forests typically delivers greater—and certainly no less—environmental benefits than establishing tree plantations in terms of biodiversity conservation and such key ecosystem services as aboveground carbon storage, soil erosion control, and water provisioning. However, delivering these outcomes will typically result in trade-offs with wood production because of the yield advantage of plantations over restored native forests (*31*–*33*), as measured in wood volume (distinct from aboveground carbon storage, which in addition to wood volume also factors in wood density).

These findings provide evidence that if the goal of forest restoration is to recover environmental services on the land being restored and if wood production is not a primary concern, native forest restoration should be prioritized through use of site-appropriate measures including unassisted and assisted natural regeneration and active planting of diverse native species (*34*–*36*). Beyond biodiversity, the stakes are especially high for soil erosion control given its far poorer delivery by tree plantations relative to native forests. Our synthesis refutes the implicit assumptions of ecosystem service-oriented forest restoration initiatives such as China's Grain-for-Green Program, which covers >34 million hectares (*37*, *38*), and a large collection of projects targeting carbon storage (*39*), soil conservation (*40*), and water provisioning (*41*) that have focused mostly on establishing (monoculture) tree plantations.

However, where the goals of forest restoration include wood production, decision makers must navigate the trade-off between environmental and production outcomes (*42*). Beyond weighing competing goals and adopting restoration approaches accordingly (*43*), larger-scale land-use planning must be invoked to also consider the "leakage" of forgone production to land parcels elsewhere; such leakage could alter—and even reverse—the overall environmental gains of forest restoration (*44*). Ensuring environmental gains while meeting production goals under forest restoration hinges on understanding their trade-offs for a range of restored forest covers, making the acquisition of such information an urgent research priority.

Interpretation of our results and associated policy recommendations raises three additional issues. First, although the environmental metrics assessed were our best choices given data availability (*18*), they each characterize one aspect of a focal outcome. For example, beyond aboveground biomass, an assessment of forest carbon storage must also consider carbon stored belowground (*45*) as well as in long-lived wood products. Second, because our data came from established tree covers, they represent achievable outcomes of successful forest restoration (*13*). In reality, restoration approaches and outcomes are often constrained by factors such as funding limitations, recurrent disturbances, livelihood needs, and regeneration stochasticity, among others (*46*, *47*). Third, although we used paired data and accounted for the rigor of site matching in our analyses (*18*), we cannot rule out the potential influence of preexisting site differences incurred by land-use history (*13*) and species turnover across space (betadiversity) (*48*), both of which are often difficult to ascertain.

By presenting a global comparison between tree plantations and native forests that simultaneously assesses their impacts related to biodiversity, climate, soil, water, and wood production based on rigorously paired data, our study provides insights into the alignment among these environmental goals and the trade-offs between environmental and production goals under forest restoration. Previous research on the cobenefits of forest restoration has focused on "where to restore" (*29*, *49*); by addressing "how to restore," our study will help to improve the realism of future spatial prioritization efforts. Finally, other forest restoration outcomes such as food and nutrition security will be important in some contexts (*50*). Future research should address how these outcomes may fare under different restoration approaches, as well as their cobenefit opportunities and unavoidable trade-offs with other environmental and production goals.

REFERENCES AND NOTES

1. UN Environment Programme, FAO, UN Decade on Ecosystem Restoration, www.decadeonrestoration.org.
2. R. Chazdon, P. Brancalion, *Science* **365**, 24–25 (2019).
3. COP26, Glasgow Leaders' Declaration on Forests and Land Use (2021); https://ukcop26.org/glasgow-leaders-declaration-on-forests-and-land-use/.
4. D. P. Edwards *et al.*, *Curr. Biol.* **31**, R1326–R1341 (2021).
5. R. Dave *et al.*, "Second Bonn Challenge progress report" (IUCN, 2019).
6. World Economic Forum, 1 Trillion Trees campaign, www.1t.org.
7. S. Lewis, C. E. Wheeler, E. T. A. Mitchard, A. Koch, *Nature* **568**, 25–28 (2019).
8. B. W. Griscom *et al.*, *Proc. Natl. Acad. Sci. U.S.A.* **114**, 11645–11650 (2017).
9. F. Hua *et al.*, *Nat. Commun.* **7**, 12717 (2016).

10. E. Romijn *et al*., *Forests* **10**, 1–17 (2019).
11. P. Besseau, S. Graham, T. Christophersen, Restoring forests and landscapes: the key to a sustainable future (Global Partnership on Forest and Landscape Restoration, 2018); https://www.forestlandscaperestoration.org/wp-content/uploads/2021/03/gpflr_final-27aug.pdf.
12. G. Wang, J. L. Innes, J. Lei, S. Dai, S. W. Wu, *Science* **318**, 1556–1557 (2007).
13. J. L. Reid, M. E. Fagan, R. A. Zahawi, Positive site selection bias in meta-analyses comparing natural regeneration to active forest restoration. *Sci. Adv.* **4**, eaas9143 (2018).
14. E. G. Brockerhoff, H. Jactel, J. A. Parrotta, C. P. Quine, J. Sayer, *Biodivers. Conserv.* **17**, 925–951 (2008).
15. IPBES, "Global assessment report on biodiversity and ecosystem services: Summary for policymakers", S. Díaz *et al*., Eds. (IPBES, 2019);
16. D. Leclère *et al*., *Nature* **585**, 551–556 (2020).
17. E. Dinerstein *et al.*, A Global Deal for Nature: Guiding principles, milestones, and targets. *Sci. Adv.* **5**, eaaw2869 (2019).
18. Materials and methods are available as supplementary materials.
19. FAO, "Mean annual volume increment of selected industrial forest plantation species" D. J. Mead, Ed. Forest Plantations Thematic Papers, Working Paper FP/1(FAO, 2001).
20. G. D. Gann *et al.*, International principles and standards for the practice of ecological restoration. Second edition. *Restor. Ecol.* **27**, S1–S46 (2019).
21. L. Gibson *et al*., *Nature* **478**, 378–381 (2011).
22. R. Leemans, Global Holdridge Life Zone Classifications. Digital Raster Data on a 0.5-degree Geographic (lat/long) 360x720 grid, Global Ecosystems Database Version 1.0: Disc A (1989); https://www.ngdc.noaa.gov/ecosys/cdroms/AVHRR97_d2/document/ncillary/lhold/aareadme.htm.
23. L. R. Holdridge, *Life Zone Ecology* (Tropical Science Center, 1967); www.worldcat.org/title/life-zone-ecology/oclc/625212.
24. J. G. Pausas, M. P. Austin, *J. Veg. Sci.* **12**, 153–166 (2001).
25. J. S. Lefcheck *et al*., *Nat. Commun.* **6**, 6936 (2015).
26. J. M. Bosch, J. D. Hewlett, *J. Hydrol.* **55**, 3–23 (1982).
27. J. M. Roberts, "Plants and water in forests and woodlands" in *Eco-Hydrology: Plants and Water in Terrestrial and Aquatic Environments*, A. J. Baird, R. L. Wilby, Eds. (Routledge, 1999) pp. 181–236.
28. H. C. A. Brown, F. A. Berninger, M. Larjavaara, M. Appiah, *For. Ecol. Manage.* **472**, 118236 (2020).
29. P. H. S. Brancalion *et al.*, Global restoration opportunities in tropical rainforest landscapes. *Sci. Adv.* **5**, eaav3223 (2019).
30. X. Feng *et al*., *Nat. Clim. Chang.* **6**, 1019–1022 (2016).
31. A. Paquette, C. Messier, *Front. Ecol. Environ.* **8**, 27–34 (2010).
32. F. Cubbage *et al*., *New For.* **33**, 237–255 (2007).
33. A. E. Lugo, *Ecol. Monogr.* **62**, 1–41 (1992).
34. R. L. Chazdon, M. Uriarte, *Biotropica* **48**, 709–715 (2016).
35. J. Kanowski, C. P. Catterall, *Ecol. Manage. Restor.* **11**, 119–126 (2010).
36. R. L. Chazdon *et al.*, The intervention continuum in restoration ecology: Rethinking the active–passive dichotomy. *Restor. Ecol.* (2021).
37. C. O. Delang, Z. Yuan, *China's Grain for Green Program* (Springer, 2015).
38. NFGA (National Forestry and Grassland Administration), "Twenty years of China's Grain-for-Green Program (1999–2019)" (2020) http://www.forestry.gov.cn/html/main/main_195/20200630085813736477881/file/20200630090428999877621.pdf.
39. S. A. Berkessy, B. A. Wintle, *Conserv. Biol.* **22**, 510–513 (2008).
40. C. E. Oyarzun, *Mt. Res. Dev.* **15**, 331–338 (1995).
41. E. Vadell, S. De-Miguel, J. Pemán, *Land Use Policy* **55**, 37–48 (2016).
42. J. Naime, F. Mora, M. Sánchez-Martínez, F. Arreola, P. Balvanera, *For. Ecol. Manage.* **473**, 118294 (2020).
43. P. H. S. Brancalion *et al*., *J. Appl. Ecol.* **57**, 55–66 (2020).
44. M. G. Betts *et al*., *Biol. Rev. Camb. Philos. Soc.* **96**, 1301–1317 (2021).
45. C. Liao, Y. Luo, C. Fang, B. Li, *PLOS ONE* **5**, e10867 (2010).
46. R. A. Zahawi, J. L. Reid, K. D. Holl, *Restor. Ecol.* **22**, 284–287 (2014).
47. E. A. Coleman *et al*., *Nat. Sustain.* **4**, 997–1004 (2021).
48. J. B. Socolar, J. J. Gilroy, W. E. Kunin, D. P. Edwards, *Trends Ecol. Evol.* **31**, 67–80 (2016).
49. B. B. N. Strassburg *et al*., *Nature* **586**, 724–729 (2020).
50. F. P. L. Melo *et al*., *Nat. Sustain.* **4**, 85–92 (2021).
51. F. Hua *et al.*, The ecosystem service and biodiversity contributions and trade-offs of contrasting forest restoration approaches, Version v_Feb16_2022, Zenodo (2022).

ACKNOWLEDGMENTS

The authors thank the many experts listed in table S3 for insights on data availability about soil erosion and particularly for providing data and related insights pertaining to water provisioning. The authors further thank D. A. Coomes, M. G. Betts, and G. Shackleton for helpful discussions, J. Dwyer for providing R code assistance on meta-regression plotting, N. Labrière for sharing potential data on soil erosion, and J. K. Vanclay for insights on timber production, as well as R. Heilmayr, M. Larjavaara, R. Pillay, D. S. Wilcove, and two anonymous reviewers for constructive comments that improved the quality of earlier versions of the manuscript. **Funding:** This work was supported by Royal Society Newton International Fellowship NF160839 and National Natural Science Foundation of China Grants 32122057 and 31988102 (to F.H.), as well as and São Paulo Research Foundation Postdoctoral Grant 2016/00052-9 (to P.M.). **Author contributions:** Conceptualization: F.H., D.P.E., and A.B. Methodology: F.H., L.A.B., S.N., P.M., D.P.E., and A.B. Investigation: F.H., L.A.B., P.M., P.A.M., J.Z., S.N., X.M., W.W., C.M., and J.L.P.A. Visualization: F.H. Funding acquisition: F.H. and A.B. Project administration: F.H. Supervision: F.H., L.A.B., D.P.E., and A.B. Writing – original draft: F.H., L.A.B., S.N., D.P.E., and A.B. Writing – review and editing: all coauthors. **Competing interests:** The authors declare that they have no competing interests. **Data and materials availability:** All data and code have been uploaded to a public repository, and can be accessed at (*51*). **License information:** Copyright © 2022 the authors, some rights reserved; exclusive licensee American Association for the Advancement of Science. No claim to original US government works. https://www.sciencemag.org/about/science-licenses-journal-article-reuse.

SUPPLEMENTARY MATERIALS

science.org/doi/10.1126/science.abl4649
Materials and Methods
Supplementary Text
Figs. S1 to S11
Tables S1 to S7
References (*52*–*536*)
MDAR Reproducibility Checklist

Submitted 16 July 2021; accepted 22 February 2022
Published online 17 March 2022
10.1126/science.abl4649

KINETOCHORE

Structure of the human inner kinetochore bound to a centromeric CENP-A nucleosome

Stanislau Yatskevich†, Kyle W. Muir†, Dom Bellini, Ziguo Zhang, Jing Yang, Thomas Tischer, Masa Predin, Tom Dendooven, Stephen H. McLaughlin, David Barford*

Kinetochores assemble onto specialized centromeric CENP-A (centromere protein A) nucleosomes (CENP-A^{Nuc}) to mediate attachments between chromosomes and the mitotic spindle. We describe cryo–electron microscopy structures of the human inner kinetochore constitutive centromere associated network (CCAN) complex bound to CENP-A^{Nuc} reconstituted onto α-satellite DNA. CCAN forms edge-on contacts with CENP-A^{Nuc}, and a linker DNA segment of the α-satellite repeat emerges from the fully wrapped end of the nucleosome to thread through the central CENP-LN channel that tightly grips the DNA. The CENP-TWSX histone-fold module further augments DNA binding and partially wraps the linker DNA in a manner reminiscent of canonical nucleosomes. Our study suggests that the topological entrapment of the linker DNA by CCAN provides a robust mechanism by which kinetochores withstand both pushing and pulling forces exerted by the mitotic spindle.

The centromere is a specialized genetic locus that interacts with the mitotic spindle to facilitate chromosome segregation. Centromeres of humans and other primates are made of multiple copies of the conserved ~171–base pair (bp) α-satellite repeat that contains the histone H3 variant centromere protein A (CENP-A) (*1*, *2*). Kinetochores assemble specifically onto centromeres to form large macromolecular machines that directly mediate chromosome segregation (*3*). A critical function of the kinetochore is to generate a load-bearing attachment between chromosomes and the spindle apparatus. How this function is achieved at the molecular level is unclear.

Throughout the cell cycle, CENP-A nucleosomes specify the constitutive association of the 16-subunit inner kinetochore constitutive centromere associated network (CCAN) complex with centromeric chromatin, whereas the 10-subunit KMN network of the outer kinetochore assembles onto CCAN during mitosis to couple CCAN to microtubules for spindle-mediated chromosome movement. Two human CCAN proteins, CENP-C and CENP-N, directly interact with CENP-A^{Nuc} (*4*, *5*). CENP-C interacts with the C terminus of CENP-A and histones H2A and H2B (*6*), whereas CENP-N binds the L1 loop and adjacent DNA gyre of CENP-A^{Nuc} (*7*–*11*). The 17-bp B-box motif that interacts with CENP-B is the only DNA sequence within the α-satellite repeat that is specifically recognized by a centromere-associated protein.

In budding yeast, a single kinetochore complex associates with a point centromere accommodating a sole CENP-A nucleosome. By contrast, the regional kinetochores of humans and other metazoans are generated from multiple copies of the CCAN and KMN network complexes to form large disk-like structures. In this work, we determined the cryo–electron

MRC Laboratory of Molecular Biology, Cambridge CB2 0QH, UK.
***Corresponding author. Email: dbarford@mrc-lmb.cam.ac.uk**
†These authors contributed equally to this work.

microscopy (cryo-EM) reconstruction of a CCAN–CENP-A^{Nuc} complex using a native 171-bp α-satellite repeat DNA, representing the repeating modular unit of a human inner kinetochore.

CCAN is assembled from a network of interdependent modules

Human CCAN comprises four modules—CENP-LN, CENP-HIKM, CENP-OPQUR, and CENP-TWSX—that are additionally linked by the largely disordered CENP-C through its interactions with CENP-LN and CENP-HIKM (*7*, *12*, *13*). We expressed and purified CCAN subcomplexes and used the N-terminal half of CENP-C (CENP-C^{N}) that contains all known CCAN

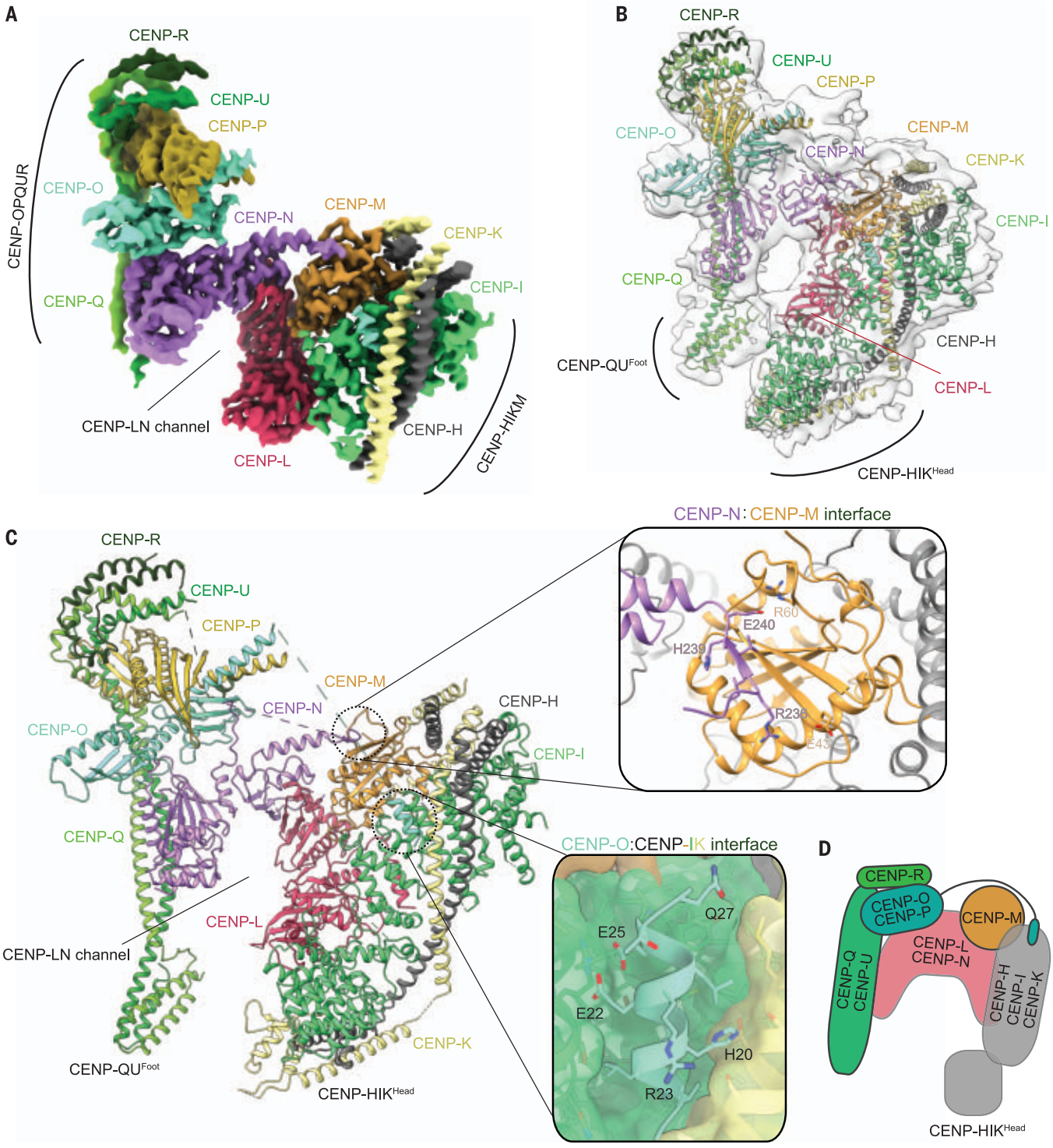

Fig. 1. CCAN is assembled from a network of interdependent modules. (**A** and **B**) Cryo-EM density map (A) and molecular architecture (B) of the apo-CCAN$^{\Delta CT}$ fitted into the cryo-EM map with resolved CENP-QU^{Foot} and CENP-HIK^{Head}. (**C**) Atomic model of the apo-CCAN$^{\Delta CT}$ with details of the CENP-N–CENP-M interface as well as CENP-O binding to the CENP-IK pocket shown as insets. (**D**) Cartoon schematic of the CCAN$^{\Delta CT}$ modules. Single-letter abbreviations for the amino acid residues are as follows: A, Ala; C, Cys; D, Asp; E, Glu; F, Phe; G, Gly; H, His; I, Ile; K, Lys; L, Leu; M, Met; N, Asn; P, Pro; Q, Gln; R, Arg; S, Ser; T, Thr; V, Val; W, Trp; and Y, Tyr.

binding sites and the central domain essential for centromere localization (*14*, *15*) (fig. S1A). Phosphoproteomic analysis indicated an interphase phosphorylation state of CCAN, as judged by the absence of cyclin-dependent kinase 1 (CDK1)–phosphorylation sites on CENP-T (*3*). Initially, we focused on the 11-subunit CCAN core complex (CENP-OPQUR-LN-HIKM), which could assemble without CENP-C^{N} (termed CCAN$^{\Delta CT}$) (fig. S1B). We determined the cryo-EM structure of CCAN$^{\Delta CT}$ at 3.2-Å resolution (Fig. 1; fig. S2, A to D; and table S1). The cross-linked structure was identical to a non–cross-linked reconstruction obtained at lower resolution (fig. S2E). We also

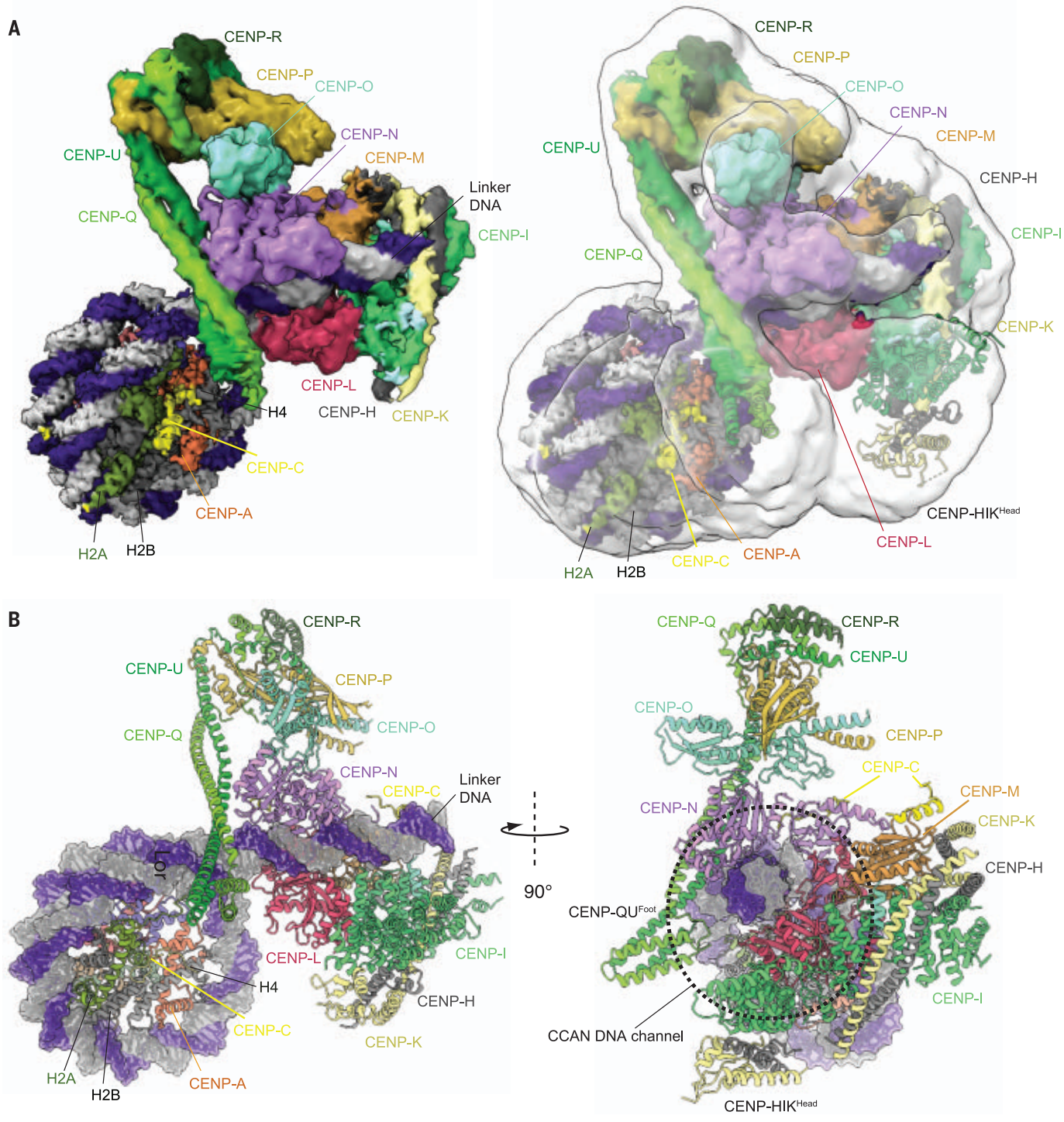

Fig. 2. Structure of the CCAN$^{\Delta T}$–CENP-A^{Nuc} complex. (**A**) (Right) Consensus CCAN$^{\Delta T}$–CENP-A^{Nuc} cryo-EM map (transparent white) overlaid onto the composite CCAN$^{\Delta T}$–CENP-A^{Nuc} cryo-EM density map based on individual cryo-EM maps for the CENP-A^{Nuc}–CENP-C^{N} and CCAN$^{\Delta T}$-DNA reconstructions. (Left) Composite map alone. (**B**) Two orthogonal views of the CCAN$^{\Delta T}$–CENP-A^{Nuc} complex depicted in cartoon representation for protein and space filling for DNA. CENP-A^{Nuc} has a diameter of 11 nm.

determined crystal structures of the CENP-OPQUR and CENP-HIK^{Head} modules (fig. S2F and table S2).

The architecture of CCAN$^{\Delta CT}$ resembles budding yeast CCAN (*Sc*CCAN) (*16*, *17*) with CENP-OPQUR and CENP-HIKM lobes assembled on either flank of a central CENP-LN module (Fig. 1). The arc-like CENP-LN module is the structural keystone of CCAN$^{\Delta CT}$ and generates a deep channel that is extended on one side by the N-terminal coiled-coil of CENP-QU. The RWD domains of CENP-O and CENP-P, with the C-terminal regions of CENP-QU and CENP-R, organize into a cap domain above CENP-N. In human CCAN$^{\Delta CT}$, CENP-R partially

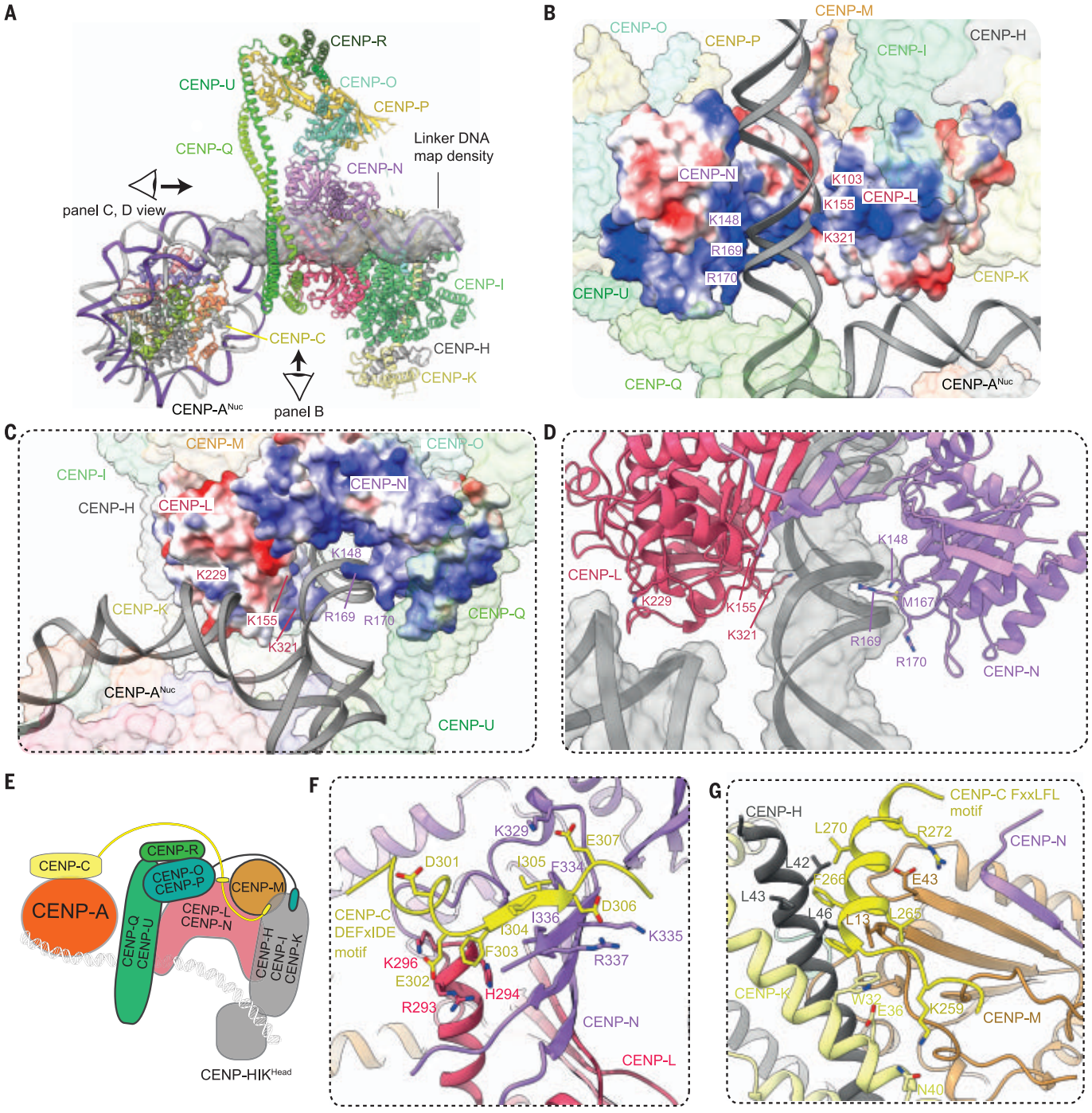

Fig. 3. The extranucleosomal linker DNA is gripped by the CENP-LN channel. (**A**) Cartoon representation of CCAN$^{\Delta T}$–CENP-A^{Nuc} with cryo-EM density shown for extranucleosomal linker DNA (from the CCAN$^{\Delta T}$-DNA cryo-EM density map). (**B**) The CENP-LN module features a positively charged channel that complements the DNA duplex. Electrostatic surface charge is shown for CENP-LN. (**C** and **D**) Details of the CENP-LN channel–DNA interaction. R169 of CENP-N inserts into the DNA minor groove. CENP-LN surface charge is shown in (C). (**E**) Cartoon schematic of the CCAN$^{\Delta T}$ modules showing DNA path. (**F** and **G**) CENP-C binds to two sites on CCAN. The DEFxIDE motif binds to CENP-LN (F), whereas the FxxLFL motif binds to CENP-HIKM (G).

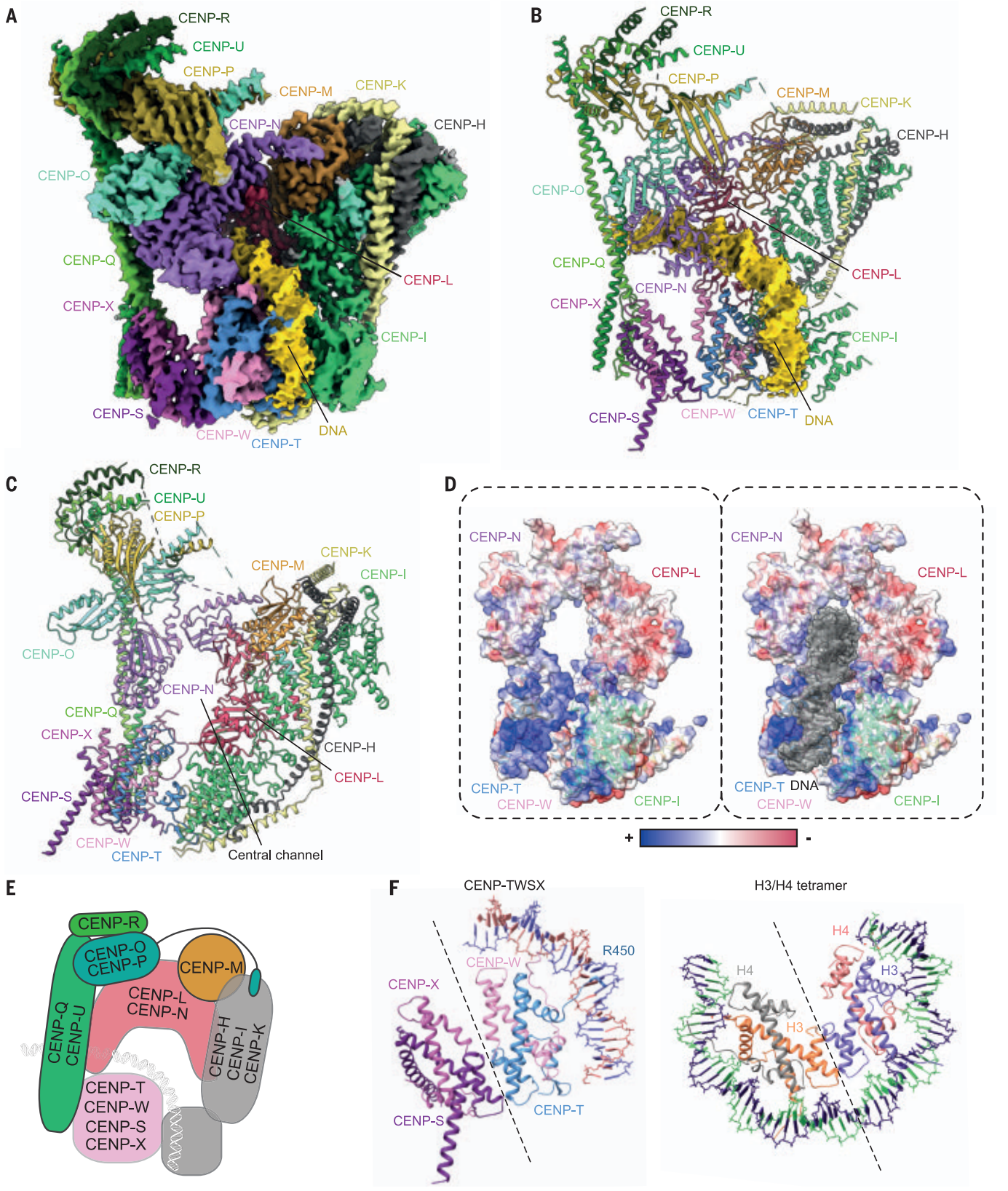

Fig. 4. Architecture of the full CCAN$^{\Delta C}$-DNA complex. (**A** and **B**) Cryo-EM density map (A) and molecular model (B) of the CCAN$^{\Delta C}$-DNA complex with DNA map density shown in yellow. (**C**) CCAN assembles an enclosed chamber that topologically entraps linker DNA. (**D**) Electrostatic representation of the DNA binding chamber formed by CENP-LN, CENP-TW, and CENP-HIK^{Head} modules shows a positively charged chamber that tightly grips DNA. (**E**) Cartoon schematic of CCAN showing DNA path through the CENP-LN, CENP-HIKM, and CENP-TWSX modules. (**F**) The CENP-TWSX module resembles the canonical H3-H4 nucleosome tetramer and partially wraps DNA.

substitutes for yeast Nkp1 and Nkp2. CENP-M, which is also specific to vertebrate CCAN, adopts a pseudo–guanosine triphosphatase (GTPase) fold and forms a stable complex with CENP-HIK (*18*). CENP-M makes extensive contacts with the HEAT domain of CENP-I and the N-terminal helical bundle of CENP-H and CENP-K and, in the context of CCAN, with CENP-L (Fig. 1). CENP-M has a small deletion that removes the switch I region and an adjacent β strand (*18*). A conserved β strand of CENP-N occupies this position to augment the central β sheet of CENP-M (Fig. 1C). An N-terminal α helix of CENP-O, connected through a flexible linker to CENP-OPQUR, interacts with a conserved pocket formed by CENP-I and CENP-K (Fig. 1C). Disrupting this interaction by deleting the N-terminal 35 residues of CENP-O destabilizes $CCAN^{\Delta CT}$ assembly, as does mutating residues on CENP-N that bind CENP-M (fig. S3, A and B). Further supporting the human CCAN architecture described here is its consistency with the interdependent localization of CCAN subunits to centromeres (*12*, *13*, *18*, *19*).

Two peripheral and conformationally flexible regions of CCAN are poorly resolved in the cryo-EM reconstruction: the $CENP\text{-}HIK^{Head}$ and N-terminal region of CENP-QU ($CENP\text{-}QU^{Foot}$) (Fig. 1). Focused three-dimensional (3D) classification of $CENP\text{-}HIK^{Head}$ identified multiple poses, two of which readily accommodate the $CENP\text{-}HIK^{Head}$ crystal structure (figs. S2F and S3C).

Reconstitution of CCAN–$CENP\text{-}A^{Nuc}$ onto a 171-bp α-satellite repeat

To assemble a complete $CCAN^{\Delta T}$–α-satellite nucleosome complex, we reconstituted $CCAN^{\Delta T}$ complexes with $CENP\text{-}C^{N}$ and $CENP\text{-}A^{Nuc}$ using 171-bp α-satellite repeat DNA ($CENP\text{-}A^{Nuc}$–171). The α-satellite DNA matches an α-satellite repeat from human chromosome 2 and shares 93% sequence identity with at least 14 other human centromeres (*20*) (fig. S4A). We used two separate 171-bp α-satellite sequences that differed in register by 22 bp (referred to as AS1 and AS2) (fig. S4A). To define the exact nucleosome positioning of the AS2 sequence, we determined a cryo-EM structure of a $CENP\text{-}A^{Nuc}$–$CENP\text{-}C^{N}$ complex at 2.4-Å resolution (fig. S4, B to D, and table S1). The dyad axis of the nucleosome is equivalent to nucleosome core particles (NCPs) containing X chromosome α-satellite DNA, with which it shares 71% sequence identity (*10*, *21*) (fig. S4A). This also matches nucleosome positions defined by in vivo chromatin immunoprecipitation (ChIP) micrococcal nuclease sequencing (MNase-seq) analyses of human centromeric chromatin (*21*, *22*). Relative to histone H3 nucleosomes ($H3^{Nuc}$), $CENP\text{-}A^{Nuc}$ exhibits continuous conformational flexibility of its terminal DNA segments as shown by a 3D variability analysis. The DNA ends fluctuate between fully wrapped at both ends to being unwrapped by ~22 bp at one end, with most particles in intermediate states (fig. S4E and movie S1). Unwrapped and flexible terminal DNA segments are seen in yeast and vertebrate $CENP\text{-}A^{Nuc}$ structures (*17*, *23*), and this correlates with a 110- to 120-bp nuclease-resistant DNA core (*17*, *23*). These in vitro studies are also in concordance with $CENP\text{-}A^{Nuc}$ protecting 110 to 150 bp of α-satellite DNA based on in vivo ChIP–MNase-seq studies of natural human centromeres and neocentromeres as well as observations that $CENP\text{-}A^{Nuc}$ is a canonical octameric nucleosome in cells (*21*, *24*, *25*). A structure of $CENP\text{-}A^{Nuc}$ reconstituted with AS1 (from the $CCAN^{\Delta T}$–$CENP\text{-}A^{Nuc}$–AS1 cryo-EM dataset) was positioned identically to $CENP\text{-}A^{Nuc}$–AS2, except that the 3′ unwrapped end is absent because of the 22-bp 5′ register

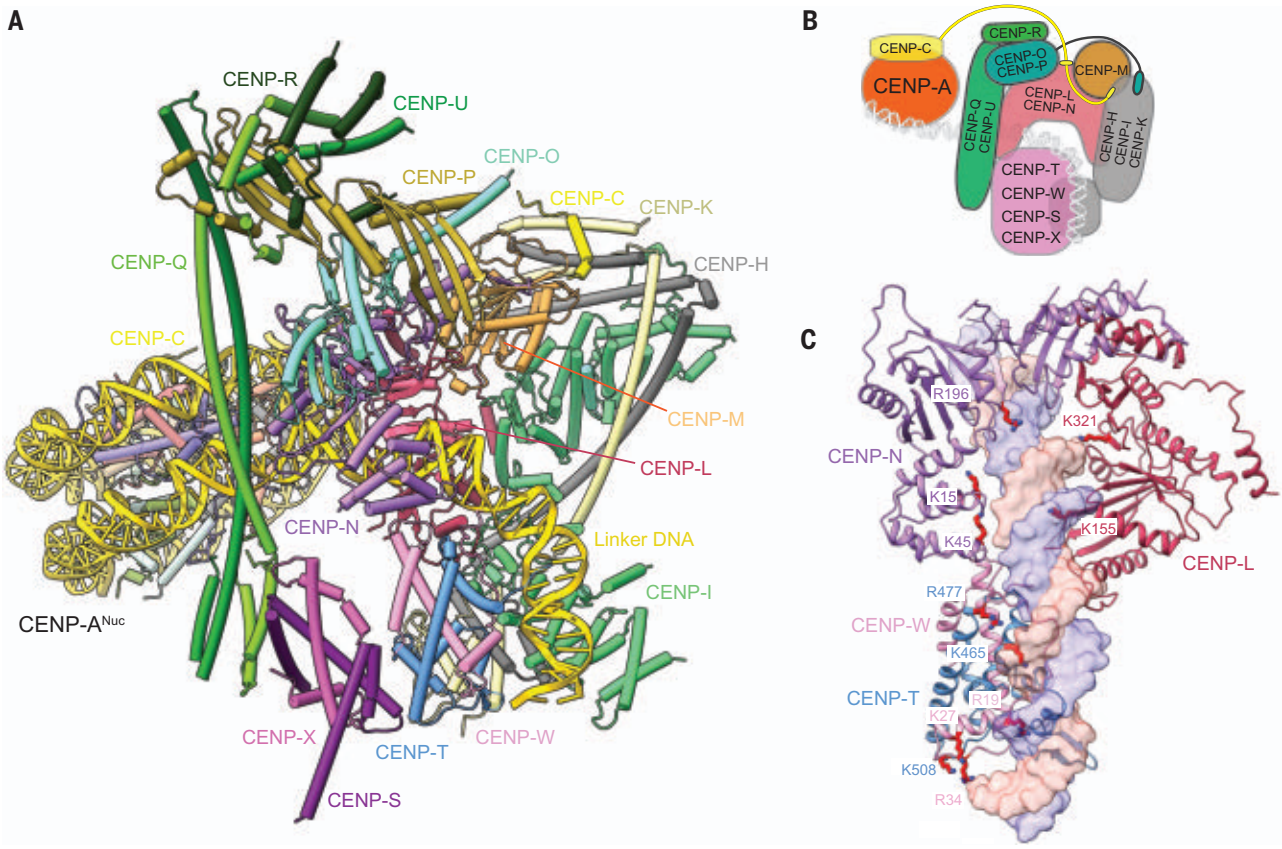

Fig. 5. Structure of the complete CCAN–$CENP\text{-}A^{Nuc}$ inner kinetochore module. (**A**) Atomic model of the CCAN–$CENP\text{-}A^{Nuc}$ complex. (**B**) Cartoon schematic of the CCAN–$CENP\text{-}A^{Nuc}$ complex. (**C**) Mutations of CENP-N and CENP-TW previously shown to impair centromere function contribute to the DNA binding channel of the CCAN (*4*, *7*–*9*, *19*, *29*). Residues implicated in DNA binding by CENP-L—and mutated in the current study—are also shown.

shift relative to AS2 (fig. S4A). In addition to resolving the CENP-A^{Nuc}, we were able to build the CENP-C central domain interacting with the C terminus of CENP-A, and histones H2A and H2B, a structural feature of CENP-A^{Nuc} recognition conserved from yeast to humans (*6*, *10*, *11*, *17*).

The positively charged CCAN channel grips linker α-satellite DNA of CENP-A^{Nuc}

We then determined cryo-EM structures of CCAN$^{\Delta T}$–CENP-A^{Nuc} complexes using both the AS1 and AS2 DNA (figs. S5 and S6). These two structures were identical except for their DNA boundaries (figs. S4A and S6B). Because the AS1 sequence produced a more stable complex, as judged by size exclusion chromatography (SEC), a larger cryo-EM dataset was collected with this DNA (table S1).

Cryo-EM micrographs of the CCAN$^{\Delta T}$–CENP-A^{Nuc} datasets and 2D-class averages showed particles corresponding to three species: (i) CENP-A^{Nuc}–CENP-C^{N}, (ii) CCAN$^{\Delta T}$ bound to free DNA, and (iii) CCAN$^{\Delta T}$ bound to CENP-A^{Nuc} (fig. S5, A to C). The observation of one CCAN$^{\Delta T}$ associated with CENP-A^{Nuc} is in agreement with an assessment of the oligomeric state of CCAN$^{\Delta T}$–CENP-A^{Nuc} in solution, which indicates a single CCAN$^{\Delta T}$ assembled onto CENP-A^{Nuc} (fig. S5D).

In the CCAN$^{\Delta T}$-DNA complex, determined at 4.5-Å resolution, EM density is visible for a linear ~24-bp DNA duplex threading through the CENP-LN channel (Fig. 2A, Fig. 3A, and fig. S5E). The CCAN$^{\Delta T}$–CENP-A^{Nuc} complexes exhibited conformational heterogeneity, limiting the resolution of a consensus cryo-EM reconstruction to 8.9 Å (Fig. 2A and figs. S5 and S6). Focused 3D classification and refinement of the CCAN$^{\Delta T}$-DNA component alone produced a 7.3-Å-resolution reconstruction with a protein and DNA structure identical to that of the CCAN$^{\Delta T}$-DNA complex (fig. S5, C and E). We therefore generated a composite CCAN$^{\Delta T}$–CENP-A^{Nuc} structure from the higher-resolution CENP-A^{Nuc}–CENP-C^{N} and CCAN$^{\Delta T}$-DNA reconstructions (Fig. 2A). In the CCAN$^{\Delta T}$–CENP-A^{Nuc} complex, the CENP-A^{Nuc} DNA is wrapped similarly to the free CENP-A^{Nuc}–CENP-C^{N} (fig. S6).

A notable feature of the CCAN$^{\Delta T}$–CENP-A^{Nuc} complex is that CCAN$^{\Delta T}$ forms few direct contacts with CENP-A^{Nuc}, but instead its primary contact with CENP-A^{Nuc} is through the extended extranucleosomal linker DNA. CENP-A^{Nuc} forms a small end-on contact, mediated through its DNA gyre, with the back-face of CCAN$^{\Delta T}$ (Fig. 3, B and C). This positions the extranucleosomal DNA to thread through the CENP-LN channel. Clearly resolved cryo-EM density for the DNA phosphate backbone shows it tightly gripped by conserved basic residues of the CENP-LN channel (fig. S5E). These create a dense, continuous, and positively charged surface complementing the shape and charge of the 24-bp linker DNA duplex (Fig. 2 and Fig. 3). Interactions of the side chains of CENP-N residues K148, M167, and R169 with the DNA minor groove contribute to defining a fixed DNA register (Fig. 3, C and D). In the DNA-bound state, the CENP-LN channel contracts, tightening its grip on the DNA duplex (fig. S5F), and the channel is extended by the apposition of CENP-HIK^{Head} in the raised conformation (Fig. 3, A and E).

CENP-C interaction sites on CENP-LN and CENP-HIKM modules

CENP-C is required for the centromere localization of CENP-LN, CENP-T, CENP-O, and the CENP-HIKM module (*5*, *7*, *12*, *13*, *18*). The CCAN-interacting region of CENP-C maps to the PEST sequence (CENP-C^{PEST}), a 200-residue intrinsically disordered region N-terminal of the CENP-C central domain that features two highly conserved short linear sequence motifs (*7*, *13*, *14*). Cryo-EM maps of the CCAN$^{\Delta T}$-DNA and CCAN$^{\Delta T}$–CENP-A^{Nuc} complexes indicated two volumes of unassigned map density not present in apo-CCAN$^{\Delta CT}$ and CCAN$^{\Delta C}$-DNA complexes (discussed below), associated with the CENP-HIKM and CENP-LN modules (fig. S6D), previously shown to interact with CENP-C (*7*, *12*–*14*). To guide the interpretation of these densities, we used AlphaFold2 (*26*) to predict potential models of how CENP-C^{PEST} would interact individually with CENP-LN, and CENP-HIKM. The first run predicted that the conserved DEFxIDE motif (residues 301 to 307) (*7*, *12*–*14*) of CENP-C^{PEST} would form an edge β strand with the CENP-N β sheet (Fig. 3F). This position corresponded well to additional cryo-EM density associated with CENP-N (fig. S6D). Phe and Ile residues of the DEFxIDE motif dock into a hydrophobic pocket at the CENP-LN interface, whereas the flanking acidic residues form electrostatic interactions with conserved Arg and Lys residues of CENP-N and CENP-L. In support of this model, a prior study mutating the EFxID residues of the CENP-C DEFxIDE motif abolished its interaction with CENP-LN in vitro and disrupted CENP-N recruitment to centromeres in vivo without perturbing CENP-C localization (*7*). For CENP-HIKM, AlphaFold2 also predicted that the CENP-C^{PEST} FxxLFL motif (residues 262 to 267) (*13*) would bind as an α helix to a hydrophobic site at the combined CENP-H–CENP-K–CENP-M interface (Fig. 3G). This prediction was validated by cryo-EM density at this location (fig. S6D) and is consistent with a previous study that found that mutating the LFL residues of this motif disrupts CENP-C interactions with CENP-HIKM in vitro and in vivo (*13*). Both the LN and HIKM interaction sites are located on the back-face of CCAN, facing CENP-A^{Nuc}, which suggests a mechanism for how CENP-C tethers kinetochores to CENP-A^{Nuc} (*5*) (Fig. 3E).

α-satellite linker DNA is a crucial determinant of stable CCAN association with CENP-A^{Nuc}

Our CCAN$^{\Delta T}$–CENP-A^{Nuc} structure suggests that the interaction of the extranucleosomal DNA duplex with the CENP-LN channel is a major determinant of CCAN assembly onto a centromeric α-satellite–CENP-A^{Nuc}. To test this, we performed reconstitutions assessing the role of the extranucleosomal DNA, CENP-C^{N}, basic residues lining the CENP-LN channel, CENP-HIK^{Head}, and CENP-QU^{Foot}. We first tested the requirement of the extranucleosomal DNA. Using SEC, we found that CENP-A^{Nuc} wrapped with 147 bp of α-satellite DNA (*10*) did not form stable complexes with CCAN$^{\Delta T}$ without CENP-C^{N}, whereas a 171-bp α-satellite that included the extranucleosomal DNA formed stable complexes with CCAN$^{\Delta T}$ independently of CENP-C^{N} (fig. S7, A and B). Interactions with CENP-A^{Nuc} reconstituted with a 171-bp α-satellite were equally stable in the presence or absence of the B-box, consistent with sequence-independent interactions with the DNA phosphate backbone (fig. S7C).

Having established a requirement for linker DNA in the assembly of CCAN$^{\Delta CT}$–CENP-A^{Nuc} complexes, we next assessed how modifications to the CENP-LN channel affected CCAN$^{\Delta T}$ interactions with CENP-A^{Nuc}. In the absence of CENP-C^{N}, mutating three positive patches of CENP-L (CENP-Lcm), which interact with linker DNA and the nucleosome gyre (Fig. 3, B to D, and fig. S5F), abolished binding of CCAN$^{\Delta CT}$ to CENP-A^{Nuc}–171 without perturbing CCAN assembly (fig. S7D). Identical results were obtained by deleting either CENP-HIK^{Head} or CENP-QU^{Foot} (fig. S8, A and B). These deletions also moderately reduced CCAN binding to isolated DNA (fig. S8C). To assess the validity of the CCAN–CENP-A^{Nuc} model in a cellular context, we tested the effect of the CENP-Lcm mutant that disrupted CCAN$^{\Delta CT}$ binding to CENP-A^{Nuc}–171 in vitro on centromere localization of CENP-L in vivo. In HEK293 cells, localization of the CENP-Lcm mutant to kinetochores was substantially impaired compared with wild-type CENP-L (fig. S8D).

In previous structures of the CENP-N N-terminal domain (CENP-N^{NT}) associated with CENP-A^{Nuc} (*7*, *8*, *10*), CENP-N^{NT} interacts with the L1 loop of CENP-A (CENP-A$^{L1\ loop}$) and adjacent DNA gyre at SHL2-3. In agreement with these structures, we found that mutating CENP-A$^{L1\ loop}$ disrupts the interaction of the isolated CENP-LN dimer with CENP-A^{Nuc} wrapped with 171-bp α-satellite DNA (fig. S9A). By contrast, our structure of CCAN–CENP-A^{Nuc}–171 does not involve an interaction of CENP-N^{NT} with CENP-A$^{L1\ loop}$, and, consistent

with this, mutating CENP-A$^{L1\ loop}$ did not disrupt interactions of CENP-A^{Nuc}–171 with CCAN$^{\Delta CT}$, as assessed by both pull-down assays and during reconstitution on SEC (fig. S9, A and B). These results, as well as previous structural information (*7*–*10*), suggest that the mode of interaction between CENP-LN and CENP-A^{Nuc} is different when CENP-LN is part of the full CCAN complex compared with CENP-LN alone. To further test this hypothesis, we performed competition assays where we added CENP-N^{NT}, which binds specifically to CENP-A$^{L1\ loop}$, at a fourfold excess over the CCAN–CENP-A^{Nuc} complex (fig. S9C). The CCAN–CENP-A^{Nuc} complex readily accommodated the additional CENP-N^{NT} without evident diminution of CCAN binding, and this additional CENP-N^{NT} incorporation was dependent on CENP-A$^{L1\ loop}$. This suggests that in a fully assembled CCAN–CENP-A^{Nuc} complex, CENP-A$^{L1\ loop}$ is not occupied and is therefore available for CENP-N^{NT} binding (fig. S9D), consistent with our cryo-EM reconstruction. Modeling a CENP-N^{NT}–based interaction of CCAN with CENP-A$^{L1\ loop}$ shows that CENP-A^{Nuc} would clash extensively with the CENP-L, CENP-HIK, and CENP-OPQUR modules (as well as the CENP-TWSX module, as discussed below) (fig. S9E). In both models, CENP-N^{NT} forms the same interactions with the DNA backbone, although at SHL7-8 for CENP-N^{NT} in CCAN (fig. S9F). Thus, previously described mutants at the CENP-N^{NT}–DNA interface that disrupt CENP-N–centromere localization in vivo (*4*, *7*, *8*) are consistent with, but do not distinguish between, both modes of CENP-N–CENP-A^{Nuc} interaction.

Overall, the interaction of free CENP-LN with CENP-A^{Nuc} is dependent on CENP-A$^{L1\ loop}$ but is independent of the linker DNA, whereas CCAN interactions with CENP-A^{Nuc} are dependent on the linker DNA but independent of CENP-A$^{L1\ loop}$. These results are consistent with different modes of interaction between CENP-LN and CENP-A^{Nuc} when CENP-LN is incorporated into CCAN. This agrees with a previous observation that the L1 loop is not required for the in vitro assembly of a functional kinetochore (*27*).

CENP-C confers selectivity of assembled CCAN for CENP-A mononucleosomes

The only direct interaction between CCAN$^{\Delta T}$ and the CENP-A histone in our structure is mediated by CENP-C^{N}. To validate this finding, we produced human H3 nucleosomes reconstituted either with a 147-bp 601 sequence or a 601 sequence extended at the 5′ end by 30 bp (177 bp) (fig. S4A). As expected, CCAN$^{\Delta T}$ failed to bind H3^{Nuc} reconstituted with the minimal 147-bp 601 sequence, whereas CCAN$^{\Delta T}$ bound CENP-A^{Nuc} with the same DNA only in the presence of CENP-C^{N}, similar to 147-bp α-satellite DNA (figs. S7A and S10A). Consistent with our structure, binding was observed with the extended 177-bp sequence for both H3^{Nuc}-177 and CENP-A^{Nuc}–177 (fig. S10B). The binding of CCAN$^{\Delta CT}$ to CENP-A^{Nuc}–177 but not to H3^{Nuc}-177, was enhanced four- to fivefold by CENP-C^{N}, consistent with selective recognition of CENP-A^{Nuc} by CENP-C (fig. S10C).

CENP-TWSX binds and partially wraps linker DNA

The CCAN$^{\Delta T}$–CENP-A^{Nuc} structure was reconstituted without the CENP-TWSX module because of our initial difficulties incorporating CENP-TWSX into CCAN. Removing all affinity tags from CENP-WSX enabled CENP-TWSX incorporation into CCAN (fig. S10D), and, as judged by SEC, this 16-subunit holocomplex interacts with the 171-bp α-satellite–CENP-A^{Nuc} similarly to CCAN$^{\Delta T}$ (fig. S10D), consistent with CENP-A, CENP-C, and CENP-T making up a single 20-subunit inner kinetochore complex (*28*). The full CCAN complex also requires extranucleosomal linker DNA to bind CENP-A^{Nuc} without CENP-C, which suggests that CENP-TWSX does not change the fundamental mechanism of CCAN assembly onto CENP-A^{Nuc} (fig. S10E). Electrophoretic mobility shift assay experiments revealed that CENP-TWSX increases the affinity of CCAN$^{\Delta CT}$ for both CENP-A^{Nuc} and H3^{Nuc} nucleosomes containing 177-bp 601 DNA by approximately threefold, which suggests that it does not confer additional selectivity for CENP-A^{Nuc} over canonical H3^{Nuc} (fig. S10, C and F).

To understand how CENP-TWSX contributes to CCAN recognition of DNA and CENP-A^{Nuc}, we determined a cryo-EM structure of CCAN$^{\Delta C}$ with a 53-bp DNA linker segment (fig. S4A). We obtained a well-resolved cryo-EM map at 2.8-Å resolution with all regions of CCAN and the DNA clearly defined (Fig. 4, A and B; fig. S11; table S1; and movie S2).

The four histone-fold domains of CENP-TWSX resemble the histone H3-H4 tetramer and are similar to crystal structures of isolated chicken CENP-TWSX (*19*). CENP-TWSX forms multiple interactions with neighboring CCAN subunits and DNA (Fig. 4, B and C). Contacts with a slightly repositioned CENP-HIK^{Head} are mediated by both CENP-T and the extended N terminus of CENP-W. CENP-W also directly contacts the CENP-N pyrin domain. A CENP-TWSX–mediated linkage of CENP-HIK^{Head} to CENP-N and CENP-QU^{Foot} creates an enclosed chamber that topologically entraps the extranucleosomal DNA (Fig. 4, A to D). The chamber comprises CENP-LN, CENP-HIK, and CENP-TW modules and is augmented and rigidified by all other CCAN subunits (Fig. 4E). As in the CCAN$^{\Delta T}$-DNA complex, the DNA duplex inserts into the deep CENP-LN channel; however, CENP-TWSX and the repositioned CENP-HIK^{Head} induce a marked curvature of the DNA. Notably, the DNA starts to wrap around the CENP-TW histone-fold domains as it emerges from the CENP-LN channel in a manner comparable to how a canonical H3-H4 tetramer wraps DNA (Fig. 4F). This DNA binding is augmented by CENP-HIK^{Head}. Consequently, the DNA duplex engages a 50-Å-long positively charged groove at the interface of CENP-I^{Head} and CENP-TW (Fig. 4D). Similar to nucleosomes, the N terminus of the CENP-T (HFD) inserts into the minor groove of the extranucleosomal DNA positioning the highly conserved R450 to contact the DNA backbone (Fig. 4F). The CENP-LN channel and CENP-TW–CENP-I^{Head} groove perfectly complement the DNA duplex, with the DNA phosphate backbone forming a continuous interface with CCAN, burying ~976 Å^2 of DNA surface area.

To complete our structural analysis, we determined cryo-EM structures of CCAN in complex with CENP-A^{Nuc} reconstituted with 171-bp α-satellite DNA (Fig. 5, A and B, and fig. S11, C to E). CCAN assembles onto CENP-A^{Nuc} similarly to CCAN$^{\Delta T}$. The nucleosome associates with the back-face of CCAN, and the extranucleosomal DNA threads through the CENP-LN channel. The linker DNA of the α-satellite repeat is gently curved and interacts with CENP-TW–CENP-I^{Head} reminiscent of the CCAN$^{\Delta C}$-DNA complex. We note that the AS2 α-satellite DNA of 171 bp in length is ~15 bp too short to wrap all the way around the CENP-TWSX module.

CENP-TW contributes to DNA binding through conserved basic residues that were previously implicated in mediating DNA binding in vitro and, for CENP-W, are required for mitotic progression and its recruitment to kinetochores in vivo. These functions of CENP-TW—and the ability of CENP-TWSX to supercoil DNA—led to proposals that CENP-TWSX is a DNA binding nucleosome-like particle, consistent with the curvature of the DNA in our structure (*19*, *29*). These residues of CENP-TW, together with basic residues of CENP-N, whose mutation disrupts CENP-N association with CENP-A^{Nuc} in vitro, and centromere localization in vivo (*4*, *7*–*9*) form a continuous spine lining the conserved CCAN-DNA interface (Fig. 5C).

Many vertebrate cell lines are viable and exhibit normal chromosome segregation without the CENP-OPQUR module (*12*, *30*), which contrasts with our finding that deletion of the CENP-QU$^{\Delta Foot}$ abrogates CCAN$^{\Delta CT}$ binding to CENP-A^{Nuc} (fig. S8, B and C). A likely explanation for this is the absence of the CENP-TWSX module in CCAN$^{\Delta CT}$, which contributes to DNA binding (Fig. 4 and Fig. 5, A and B). Consistent with this, we found that in the presence of CENP-TWSX, removing the entire

CENP-OPQUR module ($CCAN^{\Delta CO}$) caused only a small decrease in the affinity for both DNA and CENP-A^{Nuc} (fig. S12, A and B). Additionally, $CCAN^{\Delta CO}$ readily formed a complex with CENP-A^{Nuc} (fig. S12C). These in vitro results support the idea that CENP-OPQUR contributes relatively little to the attachment of vertebrate kinetochores to chromatin.

Discussion

The absence of both mitotic phosphorylation and the outer kinetochore suggests that the structure we describe likely reflects an interphase kinetochore. A cryo-EM structure of human apo-CCAN (*31*) agrees with our CCAN reconstructions, and the proposed model of DNA engagement by the CENP-LN channel is shown from our CCAN–CENP-A^{Nuc} complex to represent extranucleosomal linker DNA. Defining the structure of the holo-kinetochore at mitosis remains an outstanding challenge, and it will be important to further validate the cryo-EM structures in cells.

The notably similar features of DNA duplex recognition by the basic CENP-LN channel of *Hs*CCAN and *Sc*CCAN (*17*) suggests a common evolutionary origin of centromere-kinetochore assembly. In humans, however, the DNA duplex engaged by CCAN is the α-satellite linker DNA rather than the unwrapped CENP-A^{Nuc} DNA of budding yeast. CCAN engages ~40 bp of extranucleosomal DNA, which could be facilitated either by the unwrapping of ~16 bp of the upstream CENP-A^{Nuc}—consistent with our structures showing DNA unwrapping in CENP-A^{Nuc}—and/or by the sparse occupancy of CENP-A^{Nuc} on centromeric DNA (*32*). Such organization is also consistent with evidence that CENP-C and CENP-T bridge adjacent nucleosomes (*28*). The topological entrapment of linker DNA provides a molecular explanation for how the inner kinetochore can withstand strong pushing and pulling forces applied by the mitotic spindle, a central function of this large macromolecular assembly. Our work also confirms CENP-C as a key determinant of CCAN specificity for CENP-A^{Nuc}, providing a molecular explanation for how this essential CCAN component directly links the inner kinetochore to centromeric chromatin.

Our finding that CCAN can bind to either canonical or CENP-A nucleosomes bearing adequate linker DNA could provide an explanation for how the inner kinetochore maintains attachments at centromeres where $H3^{Nuc}$ vastly exceeds CENP-A^{Nuc} across the entire centromeric α-satellite repeats (*33*). Furthermore, it could explain why synthetic depletion of CENP-A once CCAN is assembled onto centromeres nevertheless permits mitotic centromere function in human cells (*34*). Salt extraction of CENP-A does not reduce CENP-N and CENP-C levels in centromeric chromatin (*35*), which suggests that once CCAN is assembled at centromeres in a CENP-A–dependent process (*36*, *37*), CENP-A is dispensable for localization. Lastly, assembly of CCAN onto linker DNA provides a possible explanation for how some organisms that lack CENP-A, yet still depend on CCAN for chromosome segregation, might function (*38*).

An emerging question from this study is how human CCAN localizes specifically to the centromere given its modest preference for CENP-A^{Nuc} mononucleosomes compared with $H3^{Nuc}$ (*33*). One explanation is that the CENP-LN module is selectively recruited to the centromere, through recognition of CENP-$A^{L1\ loop}$, during early stages of the cell cycle and is then displaced to form a fully assembled CCAN, thus confining kinetochore assembly to a specific chromatin locus. CENP-LN levels at the centromere decline upon mitotic entry (*10*, *39*), which supports this sequential and specific localization mechanism. CDK-mediated CENP-C phosphorylation (*11*, *40*) and/or chromatin compaction (*39*) might regulate this process. CENP-B recognizes the B-box motifs of the α-satellite repeat and interacts with CENP-C, which provides another possible mechanism for specific CCAN recruitment (*41*). Different degrees of wrapping of CENP-A^{Nuc} in centromeric arrays compared with $H3^{Nuc}$ might also provide selectivity for CCAN assembly, as could the H1 histone that would block access of CCAN to the linker DNA at $H3^{Nuc}$. Our structure permits a model for the arrangement of CCAN within the centromeric arrays of regional kinetochores (fig. S12D). This study also highlights the common mechanisms of topological entrapment used by biological systems responsible for accurately mediating chromosome segregation, such as the cohesin complex that—likewise resisting vast forces exerted by the spindle—maintains cohesion between sister chromatids.

REFERENCES AND NOTES

1. W. C. Earnshaw, N. Rothfield, *Chromosoma* **91**, 313–321 (1985).
2. G. A. Logsdon *et al*., *Nature* **593**, 101–107 (2021).
3. A. P. Navarro, I. M. Cheeseman, *Semin. Cell Dev. Biol.* **117**, 62–74 (2021).
4. C. W. Carroll, M. C. Silva, K. M. Godek, L. E. Jansen, A. F. Straight, *Nat. Cell Biol.* **11**, 896–902 (2009).
5. C. W. Carroll, K. J. Milks, A. F. Straight, *J. Cell Biol.* **189**, 1143–1155 (2010).
6. H. Kato *et al*., *Science* **340**, 1110–1113 (2013).
7. S. Pentakota *et al*., *eLife* **6**, e33442 (2017).
8. S. Chittori *et al*., *Science* **359**, 339–343 (2018).
9. T. Tian *et al*., *Cell Res.* **28**, 374–378 (2018).
10. P. K. Allu *et al*., *Curr. Biol.* **29**, 2625–2639.e5 (2019).
11. M. Ariyoshi *et al*., *EMBO J.* **40**, e105671 (2021).
12. K. L. McKinley *et al*., *Mol. Cell* **60**, 886–898 (2015).
13. K. Klare *et al*., *J. Cell Biol.* **210**, 11–22 (2015).
14. L. Y. Guo *et al*., *Nat. Commun.* **8**, 15775 (2017).
15. M. E. Pesenti *et al*., *Mol. Cell* **71**, 923–939.e10 (2018).
16. S. M. Hinshaw, S. C. Harrison, *eLife* **8**, e44239 (2019).
17. K. Yan *et al*., *Nature* **574**, 278–282 (2019).
18. F. Basilico *et al*., *eLife* **3**, e02978 (2014).
19. T. Nishino *et al*., *Cell* **148**, 487–501 (2012).
20. Y. Tanaka *et al*., *J. Biol. Chem.* **280**, 41609–41618 (2005).
21. D. Hasson *et al*., *Nat. Struct. Mol. Biol.* **20**, 687–695 (2013).
22. J. G. Henikoff, J. Thakur, S. Kasinathan, S. Henikoff, *Sci. Adv.* **1**, e1400234 (2015).
23. H. Tachiwana *et al*., *Nature* **476**, 232–235 (2011).
24. Y. Nechemia-Arbely *et al*., *J. Cell Biol.* **216**, 607–621 (2017).
25. A. Padeganeh *et al*., *Curr. Biol.* **23**, 764–769 (2013).
26. J. Jumper *et al*., *Nature* **596**, 583–589 (2021).
27. A. Guse, C. W. Carroll, B. Moree, C. J. Fuller, A. F. Straight, *Nature* **477**, 354–358 (2011).
28. J. Thakur, S. Henikoff, *Genome Res.* **26**, 1178–1187 (2016).
29. T. Hori *et al*., *Cell* **135**, 1039–1052 (2008).
30. M. Okada *et al*., *Nat. Cell Biol.* **8**, 446–457 (2006).
31. M. E. Pesenti *et al*., bioRxiv 2022.01.06.475204 [Preprint] (2022).
32. S. Hoffmann *et al*., *EMBO J.* **39**, e105505 (2020).
33. D. L. Bodor *et al*., *eLife* **3**, e02137 (2014).
34. S. Hoffmann *et al*., *Cell Rep.* **17**, 2394–2404 (2016).
35. S. Cao, K. Zhou, Z. Zhang, K. Luger, A. F. Straight, *Mol. Biol. Cell* **29**, 751–762 (2018).
36. D. Fachinetti *et al*., *Nat. Cell Biol.* **15**, 1056–1066 (2013).
37. B. E. Black *et al*., *Nature* **430**, 578–582 (2004).
38. N. Cortes-Silva *et al*., *Curr. Biol.* **30**, 561–572.e10 (2020).
39. J. Fang *et al*., *Genes Dev.* **29**, 1058–1073 (2015).
40. R. Watanabe *et al*., *J. Cell Biol.* **218**, 4042–4062 (2019).
41. D. Fachinetti *et al*., *Dev. Cell* **33**, 314–327 (2015).

ACKNOWLEDGMENTS

We are grateful to the LMB and eBIC EM facilities and to Diamond Light Source for help with the EM and x-ray data collection, to J. Grimmett and T. Darling for computing, to A. Burt for assistance with 3D variability analysis, to H. Kramer and F. Begum for mass spectrometry analysis, and to J. Shi for help with insect cell expression. **Funding:** This study was supported by UKRI/Medical Research Council MC_UP_1201/6 (to D.Ba.), Cancer Research UK C576/A14109 (to D.Ba.), and a Boehringer Ingleheim Fonds Fellowship (to S.Y.). **Author contributions:** D.Ba., K.W.M., and S.Y. designed the study and experiments. K.W.M. and S.Y. cloned constructs except for the H3 nucleosome, which was cloned by Z.Z. Z.Z. produced and purified all DNA substrates. S.Y. and K.W.M. purified all proteins with help from J.Y., Z.Z., and M.P. S.Y. and K.W.M. performed all biochemical experiments, prepared EM grids, collected and processed the cryo-EM data, and built atomic models together with D.Ba. T.D. helped with cryo-EM data processing. T.T. performed all in vivo experiments. D.Be. crystallized $OPQUR^{Foot}$, collected crystallography data, and assisted with crystallography data processing. S.H.M. performed SEC–multiangle light scattering (MALS) experiments. D.Ba., K.W.M., and S.Y. wrote the manuscript with input from all authors. **Competing interests:** The authors declare that they have no competing interests. **Data and materials availability:** Protein Data Bank and cryo-EM maps have been deposited with the Research Collaboratory for Structural Bioinformatics (RCSB) and the Electron Microscopy Data Bank (EMDB), respectively. Accession numbers are listed in tables S1 and S2.

License information: Copyright © 2022 the authors, some rights reserved; exclusive licensee American Association for the Advancement of Science. No claim to original US government works. https://www.science.org/about/science-licenses-journal-article-reuse

SUPPLEMENTARY MATERIALS

science.org/doi/10.1126/science.abn3810
Materials and Methods
Figs. S1 to S12
Tables S1 and S2
References (*42*–*62*)
MDAR Reproducibility Checklist
Movies S1 and S2

Submitted 3 December 2021; accepted 1 April 2022
Published online 14 April 2022
10.1126/science.abn3810

REPORTS

FOSSIL RECORD

Global record of "ghost" nannofossils reveals plankton resilience to high CO_2 and warming

Sam M. Slater[1]*, Paul Bown[2], Richard J. Twitchett[3], Silvia Danise[4], Vivi Vajda[1]

Predictions of how marine calcifying organisms will respond to climate change rely heavily on the fossil record of nannoplankton. Declines in calcium carbonate ($CaCO_3$) and nannofossil abundance through several past global warming events have been interpreted as biocalcification crises caused by ocean acidification and related factors. We present a global record of imprint—or "ghost"—nannofossils that contradicts this view, revealing exquisitely preserved nannoplankton throughout an inferred Jurassic biocalcification crisis. Imprints from two further Cretaceous warming events confirm that the fossil records of these intervals have been strongly distorted by $CaCO_3$ dissolution. Although the rapidity of present-day climate change exceeds the temporal resolution of most fossil records, complicating direct comparison with past warming events, our findings demonstrate that nannoplankton were more resilient to past events than traditional fossil evidence suggests.

As CO_2 levels in the atmosphere rise, resultant ocean acidification (OA) and declining seawater carbonate ion concentrations will likely make it more difficult for marine organisms to form their calcium carbonate ($CaCO_3$) skeletons or shells (*1*, *2*). Coccolithophores, a group of unicellular phytoplanktonic algae (also known as nannoplankton), are the most productive marine calcifiers (*3*), but predicting their response to future environmental change has proven challenging. Experiments testing the effects of high CO_2 and temperatures on living coccolithophores and their calcitic exoskeletons have shown apparently contradictory results within and between species (*4*–*8*). However, interpretations of geological and fossil-based evidence have evoked globally catastrophic responses in nannoplankton during past intervals of high temperature and CO_2. Specifically, prominent studies have observed substantial declines in $CaCO_3$ and nannoplankton abundance through past global warming events—especially throughout the Mesozoic oceanic anoxic events (OAEs)—and have interpreted these signals as biocalcification crises, whereby OA, and related environmental change, directly compromised biogenic $CaCO_3$ production (reviewed in data S1 to S3). Conversely, others have argued that these declines in $CaCO_3$ are caused by dissolution of carbonate at the seafloor during these warming events and that independent evidence for nannoplankton responses to OA must be better understood and demonstrated before biocalcification crises are invoked (*9*, *10*). Given that the biocalcification crisis paradigm continues to be widely applied to past warming episodes (data S1 to S3) and that this model predicts potentially disastrous changes to future marine biodiversity and carbon cycle function, we tested this hypothesis using a novel methodology.

We examined the biocalcification crisis associated with the Toarcian OAE [T-OAE; ~183 million years ago (Ma)] in the Early Jurassic—considered as one of the most severe such events of the past 200 million years. The T-OAE was a geologically rapid global warming event caused by volcanism in the Southern Hemisphere (*11*) and is characterized by a range of environmental, geological, and ecological changes, including high CO_2, OA, oceanic anoxia, the deposition of organic-rich sediments, a major negative carbon isotope excursion, and widespread extinction [(*12*) and references therein]. Previous interpretations of the biocalcification crisis are primarily based on declining $CaCO_3$ in the sedimentary rock record and decreased nannoplankton species abundances and sizes (data S1), but this evidence is dependent on conventional nannofossil analyses, whereby data are derived from calcite "body" fossils. Here we report on an overlooked form of preservation—namely, imprint (or "ghost") nannofossils—which provides critical information that may be lost from the more routinely studied body fossil record.

Toarcian rock samples from the UK, Germany, Japan, and New Zealand (fig. S1) were processed for organic matter analysis. Scanning electron microscopy (SEM) of organic particles revealed nannoplankton imprints preserved on the surfaces of marine organic-walled plankton (dinoflagellate cysts, prasinophytes, and acritarchs), amorphous organic matter (AOM), and spores and pollen from land plants (Fig. 1). Imprints are also visible with the use of transmitted light, fluorescence, and confocal microscopy (fig. S2), but fine details are evident when SEM is used, with specimens displaying diagnostic coccolith rims, radial and imbricating sutures, and fragile axial and radiating central structures (figs. S3 to S12). Preservation is often pristine, and digital inversion of imprint images provides "virtual casts" that assist in visualization and identification of the original nannofossils (Fig. 1). Imprints were found as single or multiple specimens of the same or different species and cover a range of forms, including small coccoliths (<3 μm; fig. S3I), larger nannoplankton (figs. S3, J to O, and S8, A to D), and collapsed coccolithophore exoskeletons (coccospheres) (figs. S5, A and B, and S8F). Nannoplankton imprints on organic matter have only occasionally been reported from the fossil record (*13*–*15*), presumably because of their cryptic mode of preservation and minute size. Some studies have interpreted imprints as the negative molds of coccoliths that were dissolved during acid digestion of rock samples in the laboratory (*14*). However, we recorded imprints on unprocessed rock surfaces (fig. S6) and in samples devoid of $CaCO_3$, indicating that these fossils occur naturally.

Reduced nannoplankton abundances during the T-OAE have been reported from multiple locations (data S1), but this signal is most extreme in the Cleveland Basin, Yorkshire (UK), where a nannoplankton disappearance event has been observed (*16*). Samples from Yorkshire, which we studied using traditional nannoplankton body fossil methods, were either barren or yielded rare or very rare nannofossils (figs. S13 and S14). These observations essentially replicate previous findings of reduced species abundances or absences throughout the T-OAE (*16*) and seemingly support the biocalcification crisis paradigm. However, imprints from the same samples challenge this view, revealing abundant and rich nannoplankton communities throughout the T-OAE interval, refuting the disappearance event hypothesis. Imprints are not just confined to the Cleveland Basin but have been discovered in a wide range of depositional settings in globally distributed lower Toarcian strata (e.g., Germany, Japan, and New Zealand; Figs. 1 and 2). These results indicate that observed decreases in $CaCO_3$ and nannofossil abundance through the T-OAE are due to $CaCO_3$ dissolution after burial rather than representing a primary crisis of the living nannoplankton. The imprint fossils from Japan and New Zealand (Fig. 1) are the oldest coccoliths recorded from these countries, demonstrating that this approach is widely applicable and can expand nannofossil records, even in rocks where body fossils are absent and

[1]Department of Palaeobiology, Swedish Museum of Natural History, SE-104 05 Stockholm, Sweden. [2]Department of Earth Sciences, University College London, London WC1E 6BT, UK. [3]Department of Earth Sciences, The Natural History Museum, London SW7 5BD, UK. [4]Dipartimento di Scienze della Terra, Università degli Studi di Firenze, Via La Pira 4, 50121 Firenze, Italy.
*Corresponding author. Email: sam.slater@nrm.se

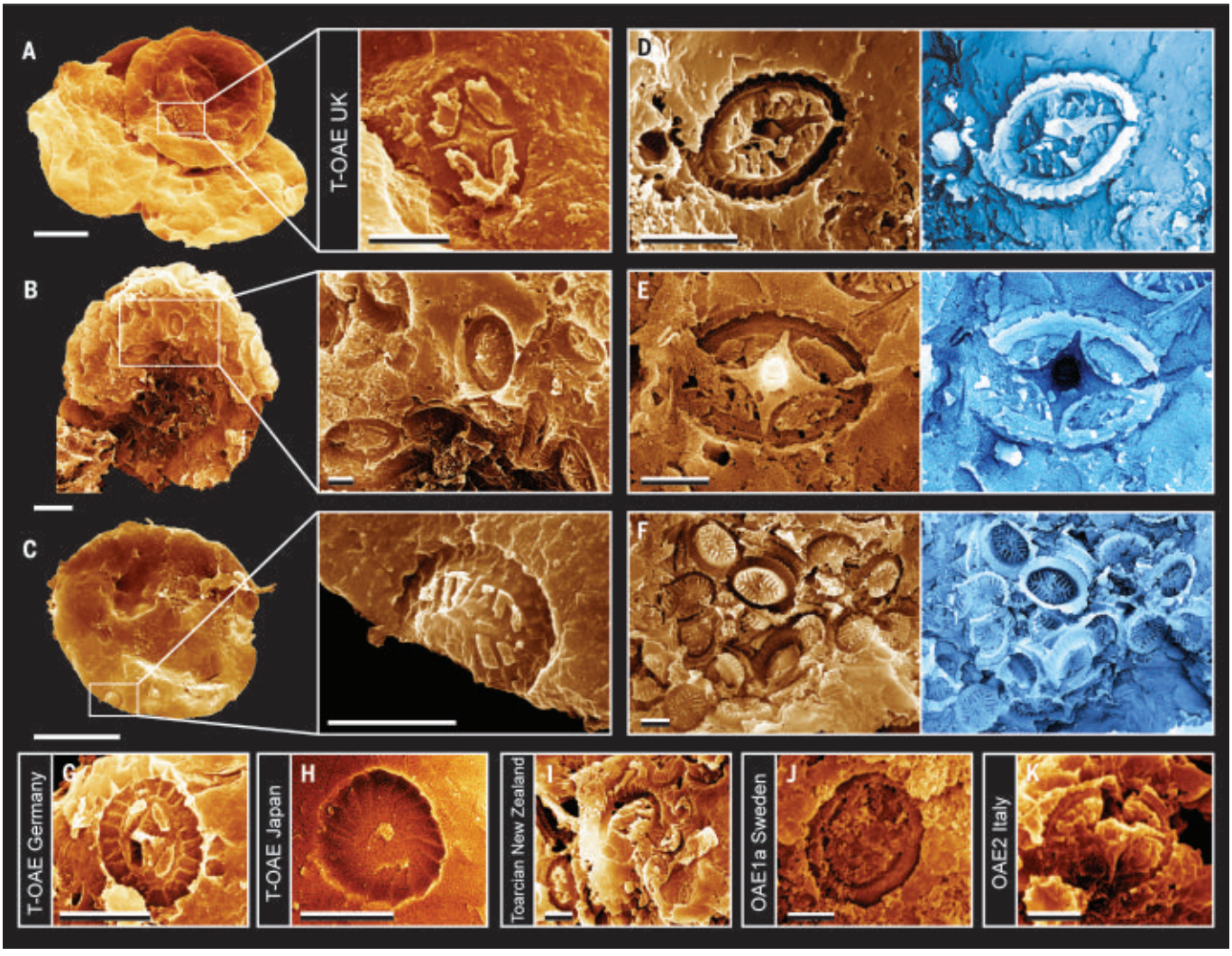

Fig. 1. Ghost nannofossils imprinted on organic matter. (**A**) *Staurolithites* sp. imprint on *Classopollis* sp. (pollen) [NHMUK PM FM 2355 (2)]. (**B**) *Crepidolithus impontus* imprints on *Cerebropollenites macroverrucosus* (pollen) [NHMUK PM FM 2355 (2)]. (**C**) *Bussonius prinsii* imprint on prasinophyte alga [NHMUK PM FM 2355 (2)]. (**D** to **K**) Imprints on AOM. (D) *B. prinsii* [NHMUK PM FM 2355 (2)]. (E) *Axopodorhabdus atavus* [NHMUK PM FM 2377 (1)]. (F) *Calyculus serrai* coccosphere [NHMUK PM FM 2377 (1)]. (G) *Axopodorhabdus* sp. [S043981]. (H) *Lotharingius hauffii* [S043957]. (I) *Calyculus* sp., *Staurolithites* sp., and others [S043993]. (J) *Manivitella pemmatoidea* [S043946]. (K) *Stoverius achylosus* [S043941]. Blue images are inverted virtual casts. Scale bars in overview images in (A) to (C) are 10 μm; all other scale bars are 2 μm.

have been subjected to thermal alteration [e.g., Japanese material studied here; see also (*17*)].

We further extended our study to test for imprints through two Cretaceous OAEs—the early Aptian OAE1a (~120 Ma) and the Cenomanian-Turonian OAE2 (~94 Ma)—for which there are also claims of biocalcification crises (reviewed in data S2 and S3). The Cretaceous OAEs are also associated with distinct episodes of volcanism and are characterized by comparable suites of environmental, geological, and ecological changes [(*12*) and references therein]. We found imprint fossils through both Cretaceous OAEs (Figs. 1 and 2 and figs. S11 and S12), demonstrating that ghost nannofossil preservation is not limited to the T-OAE and that observed decreases in $CaCO_3$ and nannoplankton abundances during OAE1a and OAE2 (data S2 and S3) are probably linked to the secondary removal of $CaCO_3$ from the rock record. Imprints from the OAE2 Contessa section, Italy, are particularly important because these were recorded during an inferred nannoplankton biocalcification "blackout," corresponding to the Bonarelli Level (a ~1-m-thick black shale virtually devoid of $CaCO_3$), which abruptly interrupts a limestone succession rich in body fossils (fig. S14 and data S3). Our results overturn the blackout hypothesis and indicate that the original $CaCO_3$ has been lost through post-burial dissolution, leaving a misleading signal of declining carbonate production during OAE2.

The recurrence of imprints in OAE-related sediments demonstrates that these organic-rich intervals are especially prone to this type of nannofossil preservation—indeed, the OAE intervals record the richest imprint assemblages (Fig. 2). Abundances of imprints and AOM are generally positively correlated (fig. S15), which suggests that plentiful organic matter was an important requirement, providing the necessary "plastic" substrate for imprinting. This also explains the subsequent dissolution of $CaCO_3$, because high amounts of organic matter can lead to acidic pore waters during diagenesis (*18*). The formation of imprints also required overburden pressure before the loss of body fossils, indicating that dissolution took place after burial, and the absence of compressed imprints reveals that this occurred after lithification.

Nannofossil abundances in sedimentary rocks are the product of a range of factors,

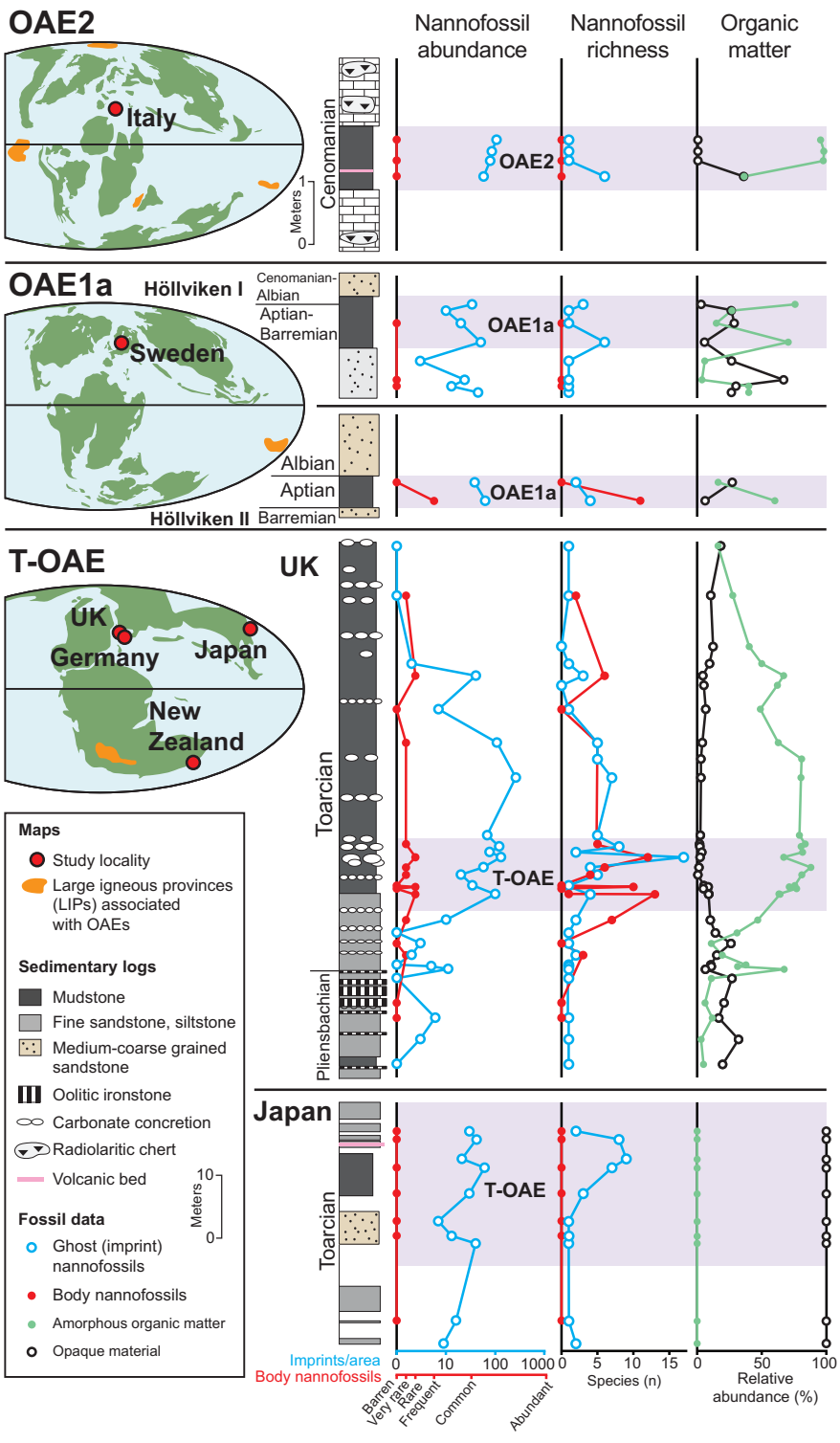

Fig. 2. Ghost nannofossil, body nannofossil, and organic matter records through the T-OAE (Japan and UK), OAE1a (Sweden), and OAE2 (Italy). Imprints/area denotes the number of imprints recorded across a standard area of organic matter. Body nannofossil abundance categories: Abundant, >10% of particles; Common, >1 to 10%; Frequent, 0.1 to 1%; Rare, <0.1%; Very Rare, <20 specimens in total; Barren, no body nannofossils. See materials and methods for further details, including richness and organic matter data collection methods. Note the different vertical scale for OAE2. Figure S14 is an extended version of this figure that includes data from Germany and New Zealand. For raw data, see data S4.

including those that affect original populations (temperature, nutrients, water chemistry), export pathways (grazing, ballasting), secondary abundances (exported plankton versus siliciclastic dilution), and preservation (diagenesis). None of these factors necessarily disrupts calcification in the living nannoplankton, and therefore preserved abundance changes alone do not provide evidence of biocalcification crises. On the contrary, our observations show that $CaCO_3$ and nannoplankton body fossil abundances can be severely modified or eradicated after deposition, indicating that these records are unreliable proxies for OA or pelagic carbonate production. Independent geochemical proxy evidence for OA at the T-OAE remains contentious (*19*, *20*). Given the uncertainty about rates of carbon injection that drove this and other OAEs, these rates may well have been too slow to have induced prolonged or high-magnitude surface water OA (*10*, *21*). However, regardless of the severity or duration of OA during the T-OAE—or other proposed causes of a nannoplankton crisis, such as changes in temperature, salinity, nutrients, or anoxia (data S1)—our records challenge the concept of a crisis. More generally, these findings call for the reexamination of other inferred biocalcification crises, and ghost nannofossils represent a tool with which to test such claims.

Our imprint record shows that nannoplankton communities were more resilient to environmental changes during the T-OAE—including high CO_2 and warming, evident from independent proxies [(*12*) and references therein]—than traditional nannofossil and $CaCO_3$ records suggest. However, several previously observed species-specific changes, such as declines in *Schizosphaerella punctulata* and nannoconids during the T-OAE and OAE1a, respectively, may still represent primary responses of nannoplankton to environmental change (data S1 and S2). At the community level, however, the imprint record shows that nannoplankton flourished during the T-OAE, and their resilience is supported by observations of increased speciation rates and an absence of elevated extinctions across the T-OAE and OAE1a (data S1 and S2).

The abundance of prasinophyte algae in many T-OAE intervals has been interpreted as a rise to dominance at the expense of nannoplankton (*16*), but the close association of imprints and prasinophyte fossils observed here demonstrates that both groups coexisted or occurred in close succession (Fig. 1C). Near-monospecific assemblages of prasinophytes during the T-OAE likely represent persistent algal blooms (*22*); similarly, the monospecific concentrations of nannofossil imprints (Fig. 1F and figs. S3B and S7A) are pellets or aggregates that provide snapshots of high-dominance communities. Rather than being considered casualties of the T-OAE, our findings indicate

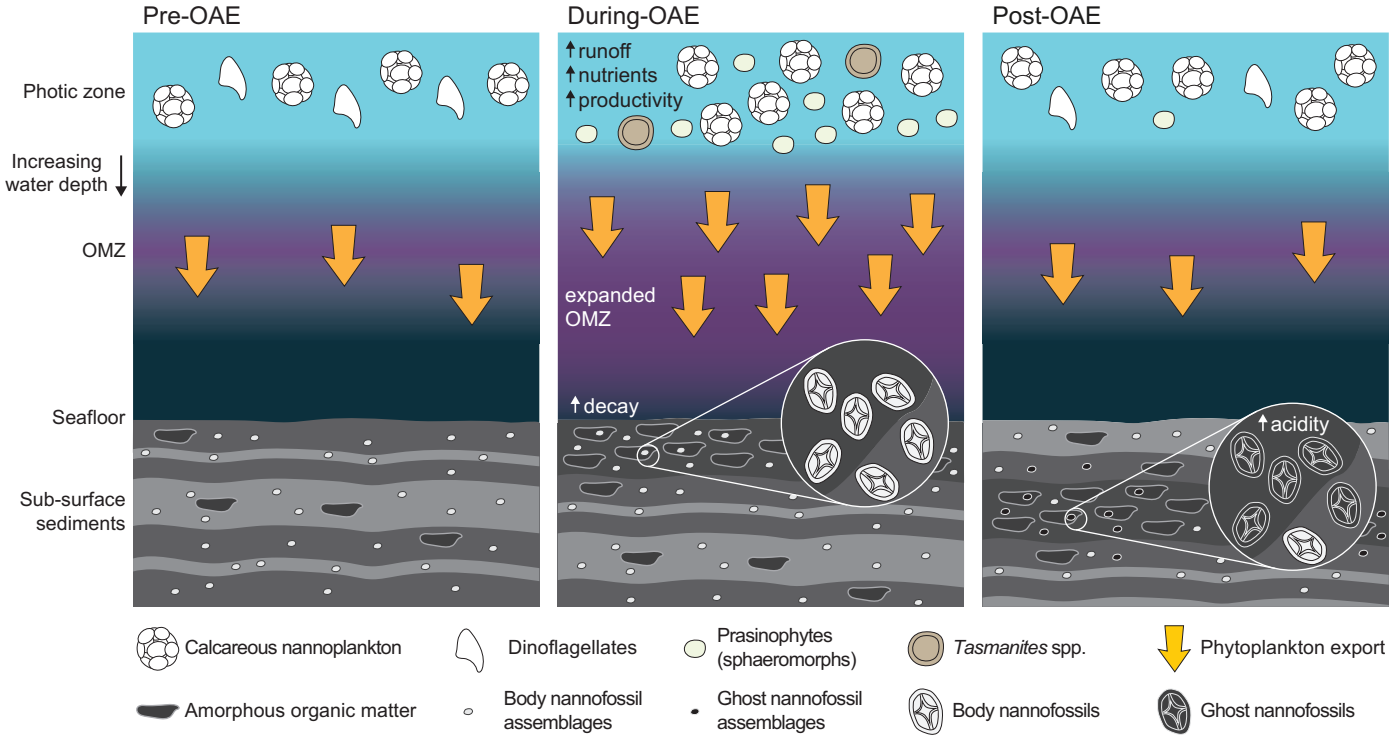

Fig. 3. Schematic summary of the major changes in phytoplankton groups through the T-OAE, showing changes in phytoplankton export and the formation of nannofossil imprints. Note that the oxygen minimum zone (OMZ) expands during the OAE and that, after the OAE, the acidic pore waters within subsurface sediments lead to the dissolution of nannoplankton body fossils and the formation of imprints.

that nannoplankton continued to draw down CO_2 and sequester carbon in seafloor sediments, which in the long-term likely expedited the termination of the event. However, high production, blooms, and potential toxicity (*23*) suggest that in the short term nannoplankton, like prasinophytes, fueled anoxia through eutrophication and increased accumulation of organic matter at the seafloor, enhanced by coccolith ballasting (*24*) (Fig. 3).

Our records of ghost nannofossils, discovered through unconventional methods, indicate no evidence of biocalcification crises during the studied Mesozoic OAEs, at least for plankton that form calcite, the more stable $CaCO_3$ polymorph compared to aragonite. Instead, these findings show how diagenesis can completely reshape the geological archive and highlight that a literal reading of the fossil record can mislead interpretations. Given that atmospheric CO_2 concentrations are currently rising at previously unseen rates, the use of individual OAEs as past analogs of current change may be premature because carbon-input rates—and therefore the duration and intensity of surface water OA—remain uncertain for these events (*10*, *21*). Nevertheless, our imprint record demonstrates the resilience of nannoplankton communities during multiple past global warming events and shows that plankton proliferation can accelerate the development of OAEs. Our findings also indicate that the conditions that prevailed during OAEs may become more prevalent (*25*, *26*), with plankton blooms and hypoxic dead zones becoming widespread across globally warming oceans.

REFERENCES AND NOTES

1. J. C. Orr *et al.*, *Nature* **437**, 681–686 (2005).
2. S. C. Doney, D. S. Busch, S. R. Cooley, K. J. Kroeker, *Annu. Rev. Environ. Resour.* **45**, 83–112 (2020).
3. B. Rost, U. Riebesell, in *Coccolithophores: Molecular Processes to Global Impact*, H. R. Thierstein, J. R. Young, Eds. (Springer, 2004), pp. 99–125.
4. U. Riebesell *et al.*, *Nature* **407**, 364–367 (2000).
5. M. D. Iglesias-Rodriguez *et al.*, *Science* **320**, 336–340 (2008).
6. L. Schlüter *et al.*, *Nat. Clim. Chang.* **4**, 1024–1030 (2014).
7. J. Meyer, U. Riebesell, *Biogeosciences* **12**, 1671–1682 (2015).
8. L. T. Bach, U. Riebesell, M. A. Gutowska, L. Federwisch, K. G. Schulz, *Prog. Oceanogr.* **135**, 125–138 (2015).
9. S. J. Gibbs, S. A. Robinson, P. R. Bown, T. Dunkley Jones, J. Henderiks, *Science* **332**, 175 (2011).
10. B. Hönisch *et al.*, *Science* **335**, 1058–1063 (2012).
11. J. Pálfy, P. L. Smith, *Geology* **28**, 747–750 (2000).
12. H. C. Jenkyns, *Geochem. Geophys. Geosyst.* **11**, Q03004 (2010).
13. C. Downie, *Q. J. Geol. Soc. Lond.* **112**, 413–434 (1956).
14. D. J. Batten, *J. Micropalaeontol.* **4**, 111–116 (1985).
15. M.-C. Janin, *Abh. Geol. B.-A.* **59**, 121–141 (1987).
16. R. B. Bucefalo Palliani, E. Mattioli, J. B. Riding, *Mar. Micropaleontol.* **46**, 223–245 (2002).
17. D. B. Kemp, V. Baranyi, K. Izumi, R. D. Burgess, *Palaeogeogr. Palaeoclimatol. Palaeoecol.* **530**, 90–102 (2019).
18. C. D. Curtis, *J. Geol. Soc. London* **137**, 189–194 (1980).
19. T. Müller *et al.*, *Geology* **48**, 1184–1188 (2020).
20. Q. Li *et al.*, *Chem. Geol.* **574**, 120228 (2021).
21. B. D. A. Naafs *et al.*, *Nat. Geosci.* **9**, 135–139 (2016).
22. S. M. Slater, R. J. Twitchett, S. Danise, V. Vajda, *Nat. Geosci.* **12**, 462–467 (2019).
23. A. Houdan *et al.*, *J. Plankton Res.* **26**, 875–883 (2004).
24. G. Fischer, G. Karakaş, *Biogeosciences* **6**, 85–102 (2009).
25. S. Rivero-Calle, A. Gnanadesikan, C. E. Del Castillo, W. M. Balch, S. D. Guikema, *Science* **350**, 1533–1537 (2015).
26. R. J. Diaz, R. Rosenberg, *Science* **321**, 926–929 (2008).

ACKNOWLEDGMENTS

We thank W. Foster, D. Murphy, M.-E. Clémence, H. Campbell, I. Raine, S. Monechi, K. Tanabe, and Y. Takeda for their help with fieldwork. **Funding:** This work was supported by Wenner-Gren Foundation grant UPD2018-0114 (S.M.S. and V.V.); Swedish Research Council grants VR 2019-04524 (S.M.S.), and VR 2019-4061 (V.V.); Carl Tryggers Foundation grant 19:380 (V.V.); Knut and Alice Wallenberg Foundation grant KAW 2020.0145 (V.V.); Natural Environment Research Council grant NE/I005641/1 (R.J.T.); Lund University Carbon Cycle Centre (V.V.); Bolin Centre for Climate Research (S.M.S.); and The Great Britain Sasakawa Foundation 4390 (S.D.). **Author contributions:** Conceptualization: S.M.S., P.B., R.J.T., S.D., and V.V.; Methodology: S.M.S., P.B., R.J.T., S.D., and V.V.; Investigation: S.M.S., P.B., R.J.T., S.D., and V.V.; Visualization: S.M.S.; Funding acquisition: S.M.S., R.J.T., V.V., and S.D.; Project administration: S.M.S.; Supervision: P.B., R.J.T., and V.V.; Writing – original draft: S.M.S.; Writing – review and editing: S.M.S., P.B., R.J.T., S.D., and V.V. **Competing interests:** The authors declare that they have no competing interests. **Data and materials availability:** This Report is based on material housed and curated by the Department of Palaeobiology, Swedish Museum of Natural History, Stockholm; The Natural History Museum (NHMUK), London; and the Department of Earth Sciences, University College London (see data S5 for details). All data are available in the main text or the supplementary materials. **License information:** Copyright © 2022 the authors, some rights reserved; exclusive licensee American Association for the Advancement of Science. No claim to original US government works. https://www.science.org/about/science-licenses-journal-article-reuse

SUPPLEMENTARY MATERIALS

science.org/doi/10.1126/science.abm7330
Materials and Methods
Figs. S1 to S15
References (*27*–*74*)
Data S1 to S5

Submitted 7 October 2021; accepted 10 March 2022
10.1126/science.abm7330

PLANT SCIENCE

Recognition of pathogen-derived sphingolipids in *Arabidopsis*

H. Kato[1]*, K. Nemoto[2], M. Shimizu[2], A. Abe[2], S. Asai[3], N. Ishihama[3], S. Matsuoka[4], T. Daimon[1], M. Ojika[5], K. Kawakita[5], K. Onai[1], K. Shirasu[3,6], M. Yoshida[4,7], M. Ishiura[8], D. Takemoto[5], Y. Takano[1], R. Terauchi[1,2]*

In plants, many invading microbial pathogens are recognized by cell-surface pattern recognition receptors, which induce defense responses. Here, we show that the ceramide *Phytophthora infestans*–ceramide D (Pi-Cer D) from the plant pathogenic oomycete *P. infestans* triggers defense responses in *Arabidopsis*. Pi-Cer D is cleaved by an *Arabidopsis* apoplastic ceramidase, NEUTRAL CERAMIDASE 2 (NCER2), and the resulting 9-methyl–branched sphingoid base is recognized by a plasma membrane lectin receptor–like kinase, RESISTANT TO DFPM-INHIBITION OF ABSCISIC ACID SIGNALING 2 (RDA2). 9-Methyl–branched sphingoid base is specific to microbes and induces plant immune responses by physically interacting with RDA2. Loss of *RDA2* or *NCER2* function compromised *Arabidopsis* resistance against an oomycete pathogen. Thus, we elucidated the recognition mechanisms of pathogen-derived lipid molecules in plants.

Plants defend themselves against a multitude of microbial pathogens by sensing pathogen invasion through cell-surface pattern recognition receptors (PRRs) that recognize microbe- or pathogen-associated molecular patterns (MAMPs, PAMPs) or damage-associated molecular patterns (DAMPs) of host-derived molecules that result from damage caused by pathogen attack. This recognition then activates immune signaling (*1*–*3*). The *Arabidopsis* genome contains genes encoding ~580 PRRs, including ~410 receptor-like kinases (RLKs) and ~170 receptor-like proteins (RLPs) that lack the kinase domain (*4*). However, molecular interactions between MAMPs or PAMPs and PRRs have only been demonstrated in a limited number of cases, with the majority involving peptides, proteins, and carbohydrates. Lipids derived from microbes are also recognized by plant PRRs. The *Arabidopsis* PRR LIPOOLIGOSACCHARIDE-SPECIFIC REDUCED ELICITATION recognizes medium-chain 3-hydroxy fatty acids of bacterial pathogens (*5*), but whether other PRRs recognize pathogen lipids remains unknown.

Ceramides belong to a class of sphingolipids consisting of a sphingoid base and a fatty acid and are present at high concentrations in eukaryotic cell membranes. Ceramide and its metabolites are also involved in intracellular signal transduction in animal cells and plants (*6*, *7*). *Phytophthora infestans*, an oomycete pathogen, is the causal agent of the potato late blight that devastated potato crops and caused famine in the 19th century. It is still a threat to potato production worldwide. A

[1]Graduate School of Agriculture, Kyoto University, Kyoto 606-8502, Japan. [2]Iwate Biotechnology Research Center, Kitakami 024-0003, Japan. [3]RIKEN Center for Sustainable Resource Science, Yokohama 230-0045, Japan. [4]RIKEN Center for Sustainable Resource Science, Wako 351-0198, Japan. [5]Graduate School of Bioagricultural Sciences, Nagoya University, Nagoya 464-8601, Japan. [6]Graduate School of Science, The University of Tokyo, Tokyo 113-8654, Japan. [7]Graduate School of Agricultural and Life Sciences, The University of Tokyo, Tokyo 113-8657, Japan. [8]Graduate School of Science, Nagoya University, Nagoya 464-8601, Japan.
***Corresponding author. Email: terauchi.ryohei.3z@kyoto-u.ac.jp (R.T.); kato.hiroaki.6a@kyoto-u.ac.jp (H.K.)**

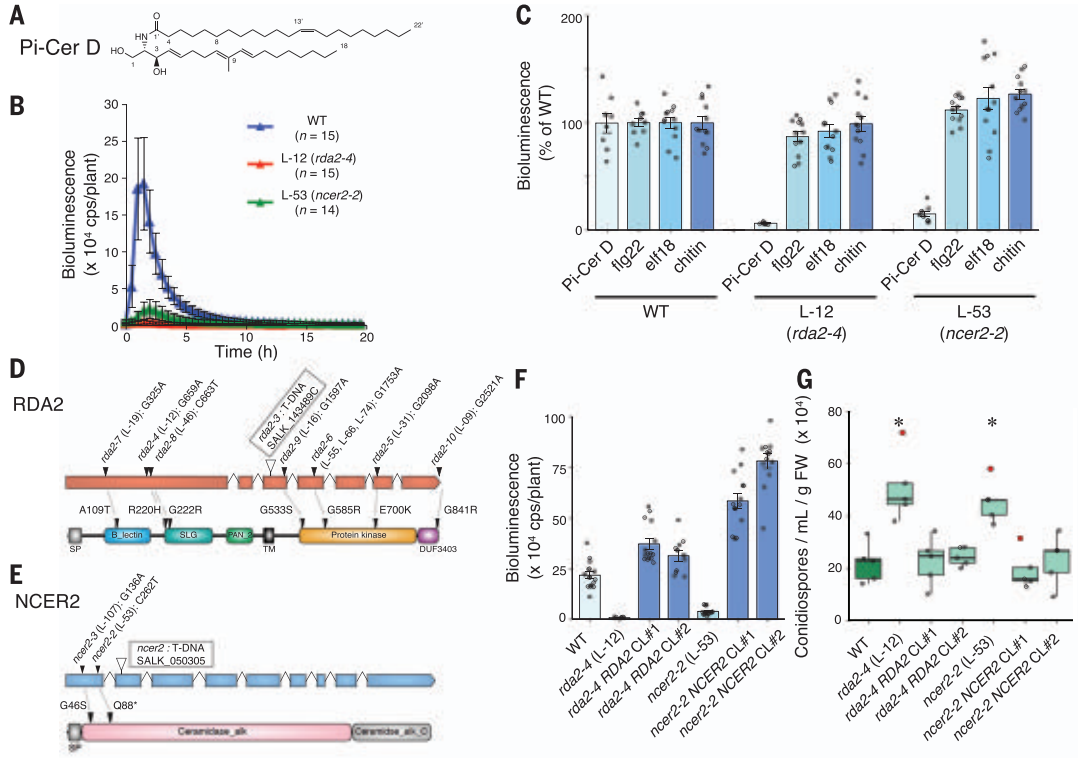

Fig. 1. *Arabidopsis RDA2* and *NCER2* are required for recognition of Pi-Cer D and resistance against *H. arabidopsidis*. (**A**) Chemical structure of Pi-Cer D. (**B**) Bioluminescence response of *Arabidopsis* p*WRKY33-LUC* reporter (WT, wild type), *rda2-4*, and *ncer2-2* after Pi-Cer D (0.17 μM) treatment (means ± SD). For additional data, see fig. S3. (**C**) Bioluminescence of WT and mutant seedlings after treatment with Pi-Cer D, flg22, elf18, or chitin. Relative peak bioluminescence values are shown as a percentage of the WT (means ± SE). For additional data, see fig. S4. (**D** and **E**) Gene and protein structures of RDA2 (D) and NCER2 (E). Gene structure (top), showing exons in boxes and introns as lines between the boxes. Protein structure (bottom), showing the different domains. The positions of the mutations in different alleles (closed triangle) and T-DNA insertion sites (opened triangle) are indicated. B-lectin, an extracellular D-mannose–binding lectin domain; SLG, S-locus glycoprotein family domain. (**F**) Complementation of *rda2* and *ncer2* mutants with wild-type alleles. Bioluminescence (means ± SE) of WT, *rda2-4*, *ncer2-2*, and complemented lines after Pi-Cer D (0.17 μM) treatment is shown. For additional data, see fig. S7. (**G**) Growth of *H. arabidopsidis* Waco9 on *Arabidopsis* WT, *rda2-4*, *ncer2-2*, and complementation lines. Conidiospores were harvested and counted 5 days after inoculation ($n = 5$). *$p < 0.05$ in two-tailed t tests comparing the corresponding values from WT. Experiments were performed three times with similar results.

ceramide-related compound, *P. infestans* ceramide D (Pi-Cer D, Fig. 1A), induces immune responses in potato plants (*8*). Pi-Cer D also induces defense responses in *Arabidopsis* (*8*); therefore, we aimed to identify the *Arabidopsis* components involved in the perception of Pi-Cer D. For this, we used Lumi-Map, a platform consisting of a luciferase (LUC)–based mutant screen and gene identification (fig. S1) (*9*). Because the *ArabidopsisWRKY33* gene is induced by PAMPs, including flg22, a peptide derived from bacterial flagellin, and is required for resistance against pathogens (*10*, *11*), we tested whether Pi-Cer D induced the expression of a *LUC* transgene driven by the *WRKY33* promoter (p*WRKY33-LUC*) in *Arabidopsis*, which resulted in a transient induction of bioluminescence (fig. S2). We then screened 10,000 M_2 seedlings generated by ethyl methanesulfonate mutagenesis of the p*WRKY33-LUC* reporter line (W33-1B) for mutants that showed a reduction in bioluminescence after Pi-Cer D treatment [named low (L) mutants]. We isolated nine mutants insensitive to Pi-Cer D (L-09, L-12, L-16, L-19, L-31, L-46, L-55, L-66, and L-74) and two mutants with a low response to Pi-Cer D (L-53 and L-107) (Fig. 1B, fig. S3, and table S1). These mutants showed normal bioluminescence responses to other PAMPs, such as flg22, elf18 (derived from bacterial elongation factor Tu), and chitin, a component of fungal cell walls, indicating that they carried lesions affecting the signaling pathway that is required for the specific response to Pi-Cer D (Fig. 1C and fig. S4).

To identify the gene(s) altered in these mutants, we performed MutMap analysis (*12*). All nine Pi-Cer D–insensitive mutants showed single-nucleotide polymorphism (SNP)–index peaks on chromosome 1 and contained SNPs within the gene *At1g11330* encoding a lectin receptor-like kinase RESISTANT TO DFPM-INHIBITION OF ABSCISIC ACID SIGNALING 2 (RDA2) (Fig. 1D, fig. S5, and table S2), a mutant of which (*rda2*) is insensitive to a small synthetic molecule, [5-(3,4-dichlorophenyl)furan-2-yl]-piperidine-1-ylmethanethione (DFPM), and incapable of mounting DFPM-mediated immune signaling and inhibition of abscisic acid signaling (*13*). RDA2 belongs to the S-locus receptor kinase (SRK)–like kinase family, and its homologs are found in potato (fig. S6). Thus, we tentatively named the nine Pi-Cer D–insensitive mutants *rda2-4* through *rda2-10*. The two Pi-Cer D low-response mutants showed SNP-index peaks on chromosome 2 and carried mutations in the gene *At2g38010*, which encodes neutral ceramidase 2 (NCER2; Fig. 1E, fig. S5, and table S2) (*14*). Potato has a homolog of *NCER2* (fig. S6). We then tentatively named the L-53 and L-107 mutants *ncer2-2* and *ncer2-3*, respectively. Complementation of the *rda2* and *ncer2* mutant lines by the respective wild-type alleles restored bioluminescence induction after Pi-Cer D treatment, confirming that *RDA2* and *NCER2* are the responsible genes for the given phenotypes (Fig. 1F and fig. S7). Furthermore, transfer DNA (T-DNA) insertion mutant lines for *RDA2* and *NCER2* showed either no or reduced induction of *WRKY33* gene expression after Pi-Cer D treatment (figs. S8 and S9). Collectively, these results indicate that *RDA2* and *NCER2* are required for Pi-Cer D recognition in *Arabidopsis*. We then asked whether *RDA2* and *NCER2* contribute to *Arabidopsis* immunity against the oomycete pathogen *Hyaloperonospora arabidopsidis*, which also produces Pi-Cer D (fig. S10) as *P. infestans*, a nonpathogen of *Arabidopsis*. Both *rda2* and *ncer2* mutants showed increased susceptibility to *H. arabidopsidis* and complementation by the respective wild-type alleles restored resistance (Fig. 1G), indicating that *RDA2* and *NCER2* are required for resistance to this pathogen (fig. S11).

We hypothesized that (i) Pi-Cer D is cleaved by NCER2 into a mature ligand product in the apoplastic space, and (ii) the ligand is recognized via plasma membrane–localized RDA2. To test the first hypothesis, we investigated whether the *ncer2* mutant phenotype was rescued by the product generated by NCER2 ceramidase treatment of Pi-Cer D. The lipid fraction containing Pi-Cer D and NCER2 produced in *Nicotiana benthamiana*, as well as that

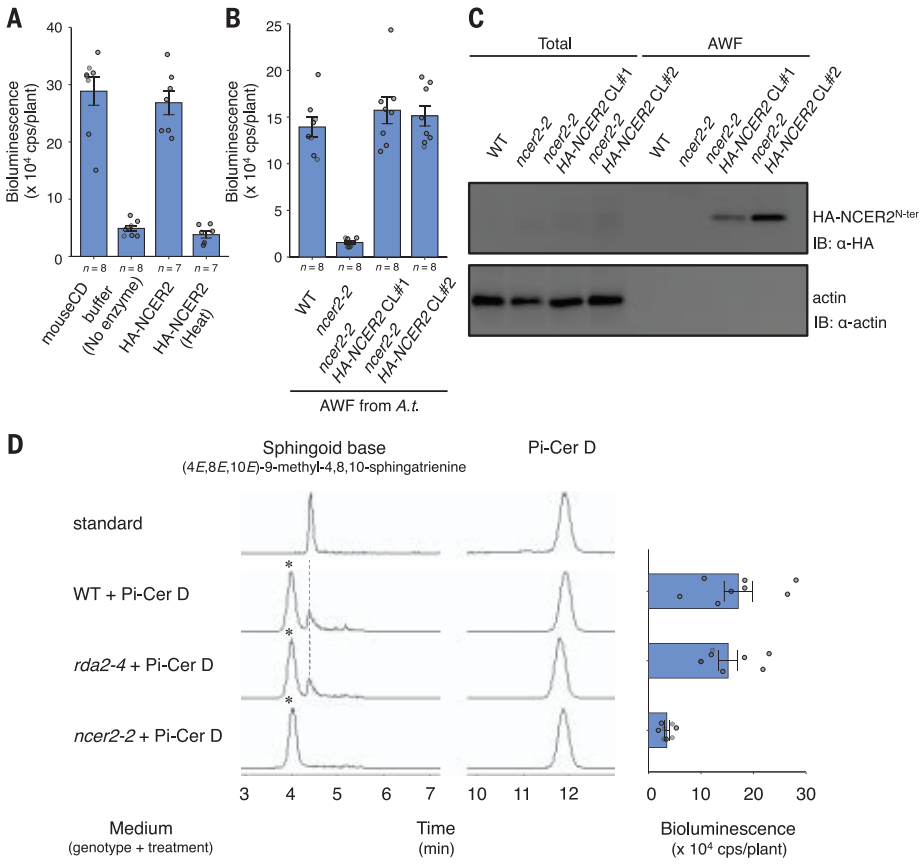

Fig. 2. NCER2 cleaves Pi-Cer D to produce a sphingoid base in the apoplast. (**A**) Pi-Cer D is cleaved by the *Arabidopsis* ceramidase NCER2. HA-NCER2 was expressed and purified from *N. benthamiana*. The lipid fraction containing metabolites derived from Pi-Cer D incubated with HA-NCER2 was recovered and applied to *ncer2-2*, and their bioluminescence was measured. Heat-inactivated HA-NCER2 and mouse ceramidase (mouse CD) were used as controls. Peak bioluminescence is shown (means ± SE). For additional data, see fig. S12. (**B**) Pi-Cer D–cleavage activity of *Arabidopsis* (*A.t.*) apoplast wash fluid (AWF). AWFs were isolated from the p*WRKY33-LUC* reporter line (WT), *ncer2-2,* and *ncer2-2 HA-NCER2* lines. Peak bioluminescence is shown (means ± SE). For additional data, see fig. S13. (**C**) Immunoblot (IB) analysis of total protein and AWF. Actin-specific antibody was used to detect cytosolic protein. (**D**) Detection of sphingoid base in the growth medium of plant treated with Pi-Cer D. (Left) Spectra obtained by liquid chromatography–mass spectrometry of sphingoid base recovered from growth media. (4*E*,8*E*,10*E*)-9-methyl-4,8,10-sphingatrienine and Pi-Cer D were used as a standard. Values shown are relative ones normalized to the highest peaks. Background peaks are denoted by an asterisk. (Right) p*WRKY33-LUC* bioluminescence induction activity of the recovered lipid to *ncer2-2*. Peak bioluminescence values are shown (means ± SE). Additional data are available in fig. S18. Experiments were performed two [(A) and (D)] or three times [(B) and (C)].

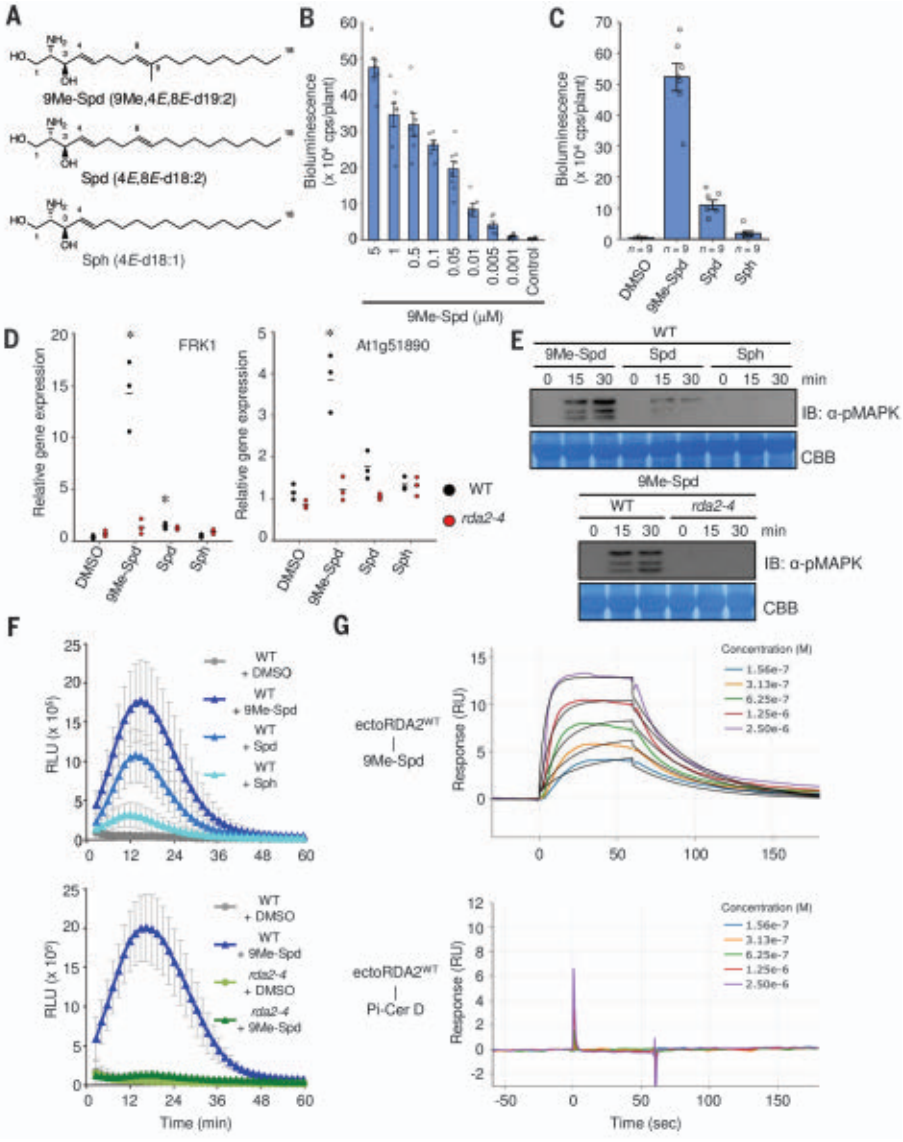

Fig. 3. RDA2 recognizes 9-methyl sphingoid base and induces defense responses. (**A**) Structures of (4*E*,8*E*)-9-methyl-4,8-sphingadienine (9Me-Spd), (4*E*,8*E*)-4,8-sphingadienine (Spd), and sphingosine (Sph). (**B** and **C**) Peak bioluminescence values for *Arabidopsis* p*WRKY33-LUC* reporter seedlings (WT) treated with (B) different concentrations of 9Me-Spd or (C) 0.5 μM sphingoid bases (means ± SE). For additional data, see figs. S19 and S21. (**D**) Expression of defense genes in *Arabidopsis* seedlings 3 hours after elicitation with sphingoid bases (0.5 μM) relative to WT (DMSO, dimethyl sulfoxide). Individual data (symbols) and means (bars) are shown (n = 3); *p < 0.01 (two-tailed t-test). (**E**) Mitogen-activated protein kinase (MAPK) activation after treatment with sphingoid bases (0.5 μM). (**F**) ROS accumulation in *Arabidopsis* leaves. (Top) Leaf disks from WT treated with 30 μM sphingoid bases (n = 12). (Bottom) Leaf disks from WT and *rda2-4* treated with 30 μM 9Me-Spd (n = 10). Relative light units (RLU) are shown (means ± SD). (**G**) SPR binding kinetics analysis of the wild-type ectoRDA2 with 9Me-Spd (top) or Pi-Cer D (bottom). RU, resonance unit. For additional data, see figs. S25 to S27. Experiments were performed two [(B), (D), (F), and (G)] or three times [(C) and (E)] with similar results.

containing Pi-Cer D and a mouse ceramidase, induced p*WRKY33-LUC* bioluminescence in the *ncer2-2* mutant (L-53) (Fig. 2A, fig. S12, and table S3). We observed no bioluminescence when heat-inactivated NCER2 was used. These results indicate that Pi-Cer D was cleaved by *NCER2*-encoded ceramidase, and the resulting compound was recognized by RDA2. We detected the hemagglutinin (HA)–NCER2 protein and Pi-Cer D-cleavage activity in the apoplast wash fluid (AWF) of *ncer2-2 HA-NCER2* complementation lines (Fig. 2, B and C, and fig. S13). Mass spectrometry analysis of compounds in the lipid fraction prepared from a mixture of Pi-Cer D and ceramidase detected a sphingoid base, (4*E*,8*E*,10*E*)-9-methyl-4,8,10-sphingatrienine (9Me,4*E*,8*E*,10*E*-d19:3, hereafter 9Me-Spt), which might be the ligand for RDA2 (fig. S14 to S17). We detected 9Me-Spt in the growth medium of the wild-type plant and the *rda2* mutant, but not in that of *ncer2* mutant of *Arabidopsis* plants treated with Pi-Cer D (Fig. 2D and fig. S18). Detection of 9Me-Spt in the medium correlated with its ability to induce *WRKY33* expression, suggesting that apoplastic NCER2 cleaves Pi-Cer D to 9Me-Spt, which is recognized by RDA2.

9Me-Spt contains a branching methyl group at the ninth carbon position. This 9-methyl–branching structure is present in sphingoid bases of oomycete, fungi, and marine invertebrates but has not been reported in plants and mammals (*15*–*17*). We thus hypothesized that the 9-methyl–branching structure of the sphingoid base plays a role in distinguishing between "self" and "nonself" in plants. Therefore, we investigated the ability of various sphingoid bases to induce a defense response. Because 9Me-Spt was difficult to obtain, we used (4*E*,8*E*)-9-methyl-4,8-sphingadienine (9Me,4*E*,8*E*-d19:2, hereafter 9Me-Spd) to evaluate the 9-methyl structure (Fig. 3A and fig. S19). The *rda2* mutants were almost completely insensitive to 9Me-Spd, indicating that 9Me-Spd is specifically recognized by RDA2 (fig. S19). Among the sphingoid bases that we tested, 9Me-Spd showed the strongest RDA2-dependent elicitor activity (Fig. 3, B and C, and figs. S19 and S20). In addition, (4*E*,8*E*)-4,8-sphingadienine (4*E*,8*E*-d18:2, Spd) and sphingosine (4*E*-d18:1, Sph), neither of which contain 9-methyl branching, also showed elicitor activity, although this was significantly weaker than that of 9Me-Spd (Fig. 3C and figs. S20 and S21). To identify the structural correlates of RDA2-dependent sensing of the sphingoid base, we tested sphingosine derivatives with different lengths of long-chain bases. Among these derivatives, Sph (4*E*-d18:1) induced the highest bioluminescence in the p*WRKY33-LUC* reporter line, followed by 4*E*-d16:1, 4*E*-d14:1, and 4*E*-d12:1 (fig. S22). This indicates that efficient sensing by RDA2 requires a long-chain base structure that includes 18 carbon atoms. We also tested phytosphingosine (4-hydroxysphinganine, 4-t18:0, PHS) and found that it did not elicit bioluminescence in the p*WRKY33-LUC* reporter line. This indicates that the 4*E* double-bond structure in Sph is crucial for its sensing by RDA2 (fig. S23).

To further investigate the downstream events following RDA2-mediated sensing, we tested the ability of 9Me-Spd and its derivatives to activate *Arabidopsis* immune responses. The 9Me-Spd activated RDA2-dependent bioluminescence induction, transcript accumulation of defense-related genes (*FRK1*, *At1g51890*), phosphorylation of mitogen-activated protein

kinases, and the production of reactive oxygen species (ROS) more strongly than did Spd and Sph (Fig. 3, C to F, and fig. S24). To investigate the physical interaction between RDA2 and sphingoid bases, we performed a thermal shift assay and a surface plasmon resonance (SPR) assay using the extracellular domain of RDA2 (ectoRDA2) produced in silkworm (fig. S25). In both assays, the wild-type ectoRDA2 bound 9Me-Spd, Spd, and Sph at a similar strength (dissociation constant K_d of 0.31 μM for 9Me-Spd, 0.43 μM for Spd, and 0.49 μM for Sph), whereas the mutant ectoRDA2 did not (Fig. 3G, figs. S26 and S27, and tables S4 and S5). Pi-Cer D was not bound by ectoRDA2. A protein-lipid overlay (PLO) assay using a purified RDA2 protein showed similar results (fig. S28). By contrast, PLO with a membrane fraction containing HA-tagged RDA2 showed higher interaction signals between 9Me-Spd and RDA2 than that of Sph and RDA2 (figs. S29 and S30), suggesting the possible presence of another component that determines the recognition specificity of sphingoid bases by RDA2. Collectively, these results suggest that RDA2 is the receptor for sphingoid bases, including 9-methyl sphingoid base, which is derived from Pi-Cer D.

Sphingolipids such as ceramide are components of eukaryotic membranes (*16*–*18*). Our findings revealed that a plant apoplastic ceramidase cleaves an oomycete-derived ceramide, and the resulting sphingoid base is recognized by a lectin receptor-like kinase (fig. S31). The 9-methyl–branching structure of sphingoid bases is prevalent in oomycetes and fungi, and plants perceive the abundance of nonself sphingolipid to mount defense. *RDA2* is required for immune signaling and inhibition of abscisic acid signaling by a small synthetic molecule, DFPM, as identified by a chemical genetic screen (*13*). We hypothesize that DFPM or its metabolized product functions as a mimic of sphingoid base, but further study is required to clarify this. Our study provides a basis on which to engineer RDA2 to detect various pathogen-specific lipids and to enable plants to mount a stronger defense against devastating crop pathogens such as *P. infestans*.

REFERENCES AND NOTES

1. F. Boutrot, C. Zipfel, *Annu. Rev. Phytopathol.* **55**, 257–286 (2017).
2. S. Ranf, *Curr. Opin. Plant Biol.* **38**, 68–77 (2017).
3. D. H. Lee, H. S. Lee, Y. Belkhadir, *Curr. Opin. Plant Biol.* **62**, 102044 (2021).
4. D. Tang, G. Wang, J. M. Zhou, *Plant Cell* **29**, 618–637 (2017).
5. A. Kutschera *et al.*, *Science* **364**, 178–181 (2019).
6. Y. A. Hannun, L. M. Obeid, *Nat. Rev. Mol. Cell Biol.* **19**, 175–191 (2018).
7. R. Berkey, D. Bendigeri, S. Xiao, *Front. Plant Sci.* **3**, 68 (2012).
8. M. S. Monjil *et al.*, *bioRxiv* 2021.10.22.465218 (2021).
9. H. Kato *et al.*, *Mol. Plant Microbe Interact.* **33**, 1366–1380 (2020).
10. Z. Zheng, S. A. Qamar, Z. Chen, T. Mengiste, *Plant J.* **48**, 592–605 (2006).
11. C. Denoux *et al.*, *Mol. Plant* **1**, 423–445 (2008).
12. A. Abe *et al.*, *Nat. Biotechnol.* **30**, 174–178 (2012).
13. J. Park *et al.*, *Plant J.* **98**, 492–510 (2019).
14. A. Zienkiewicz *et al.*, *New Phytol.* **226**, 170–188 (2020).
15. K. Umemura *et al.*, *Phytopathology* **94**, 813–818 (2004).
16. P. Sperling, E. Heinz, *Biochim. Biophys. Acta* **1632**, 1–15 (2003).
17. S. T. Pruett *et al.*, *J. Lipid Res.* **49**, 1621–1639 (2008).
18. H. Imai, Y. Morimoto, K. Tamura, *J. Plant Physiol.* **157**, 453–456 (2000).

ACKNOWLEDGMENTS

We thank H. Utsushi, E. Kanzaki, K. Ito, E. Sato (IBRC), T. Sakai, and Y. Inoue (Kyoto University) for technical support. We also thank Y. Kadota (RIKEN CSRS) for the seed of 35S-GFP-LTI6b; M. Sato and H. Bando (Hokkaido University) for providing the BmNPV bacmid system; and the National Bio-Resource Project (NBRP) of the MEXT for the silkworm strain d17. Computational analysis was partially performed on the NIG supercomputer at the ROIS National Institute of Genetics. **Funding:** Japan Society for the Promotion of Science (JSPS) KAKENHI grant 20K15528 (H.K.), JSPS KAKENHI grant 20H02995 (S.A.), JSPS KAKENHI grant 17H03963 (K.K.), JSPS KAKENHI grant 17H06172 (K.S.), JSPS KAKENHI grant 18H05503 (M.Y.), JSPS KAKENHI grant 19H05640 (M.Y.), JSPS KAKENHI grant 20H02985 (D.T.), JSPS KAKENHI grant 21H05032 (Y.T.), JSPS KAKENHI grant 21K19112 (Y.T.), JSPS KAKENHI grant 15H05779 (R.T.), and JSPS KAKENHI grant 20H05681 (R.T.). **Author contributions:** Conceptualization: H.K., D.T., Y.T., K.S., R.T.; Methodology: H.K., M.S., A.A., K.O., M.I., R.T.; Investigation: H.K., K.N., S.A., N.I., T.D., M.O., S.M., M.Y.; Visualization: H.K., M.S., A.A.; Funding acquisition: H.K., S.A., K.K., K.S., M.Y., D.T., Y.T., R.T.; Project administration: H.K., D.T., Y.T., R.T.; Supervision: D.T., K.K., K.S., Y.T., R.T.; Writing – original draft: H.K.; Writing – review & editing: H.K., D.T., Y.T., K.S., R.T. **Competing interests:** The authors declare no conflicts of interest. **Data and materials availability:** All data are available in the main text or supplementary materials.

License information: Copyright © 2022 the authors, some rights reserved; exclusive licensee American Association for the Advancement of Science. No claim to original US government works. https://www.science.org/about/science-licenses-journal-article-reuse.

SUPPLEMENTARY MATERIALS

science.org/doi/10.1126/science.abn0650
Materials and Methods
Figs. S1 to S31
Tables S1 to S9
References (*19*–*30*)
MDAR Reproducibility Checklist

Submitted 1 November 2021; accepted 11 April 2022
10.1126/science.abn0650

SUPERCONDUCTIVITY

Enhanced charge density wave coherence in a light-quenched, high-temperature superconductor

S. Wandel[1], F. Boschini[2,3,4], E. H. da Silva Neto[5,6,7], L. Shen[1,8], M. X. Na[2,3], S. Zohar[1], Y. Wang[1]†, S. B. Welch[1], M. H. Seaberg[1], J. D. Koralek[1], G. L. Dakovski[1], W. Hettel[1], M.-F. Lin[1], S. P. Moeller[1], W. F. Schlotter[1], A. H. Reid[1], M. P. Minitti[1], T. Boyle[5,6,7], F. He[9], R. Sutarto[9], R. Liang[2,3], D. Bonn[2,3], W. Hardy[2,3], R. A. Kaindl[10,11], D. G. Hawthorn[12], J.-S. Lee[13], A. F. Kemper[14], A. Damascelli[2,3], C. Giannetti[15], J. J. Turner[1,8], G. Coslovich[1]*

Superconductivity and charge density waves (CDWs) are competitive, yet coexisting, orders in cuprate superconductors. To understand their microscopic interdependence, a probe capable of discerning their interaction on its natural length and time scale is necessary. We use ultrafast resonant soft x-ray scattering to track the transient evolution of CDW correlations in $YBa_2Cu_3O_{6+x}$ after the quench of superconductivity by an infrared laser pulse. We observe a nonthermal response of the CDW order characterized by a near doubling of the correlation length within ≈1 picosecond of the superconducting quench. Our results are consistent with a model in which the interaction between superconductivity and CDWs manifests inhomogeneously through disruption of spatial coherence, with superconductivity playing the dominant role in stabilizing CDW topological defects, such as discommensurations.

Unconventional superconductivity often emerges in proximity to other low-energy broken-symmetry states, including antiferromagnetism, spin order, and charge density waves (CDWs). These orders exist on similar energy scales and often become "intertwined" (*1*, *2*), manifesting a complex interplay arising from strong correlations. The presence of CDW order—a periodic modulation of the electronic density—is ubiquitous in cuprates (*3*–*14*) and has been detected by x-ray scattering (*7*–*11*, *13*–*15*), scanning tunneling spectroscopy (STS) (*4*–*6*, *10*, *12*, *16*), and nuclear magnetic resonance (NMR) (*17*, *18*). The periodicity of such CDWs is generally incommensurate; however, STS and NMR experiments have revealed locally commensurate CDW patterns (*4*, *5*, *12*, *17*, *18*). CDW order can coexist with superconductivity below the superconducting critical temperature (T_c), and its temperature dependence suggests a tendency to compete with superconductivity (*8*, *10*). In $YBa_2Cu_3O_{6+x}$ (YBCO), high magnetic fields suppress superconductivity and lead to the enhancement of CDW ordering (*15*, *17*, *19*). More recently, CDW enhancement has been achieved by means of applying uniaxial pressure (*20*), yet dynamical information about the interaction between order parameters has not been accessed so far.

An emerging approach to studying intertwined orders is to measure their response to ultrafast photoexcitation in the time domain. Ultrafast laser pulses enable selective quenching of orders, thereby inducing an enhancement of the competing orders (*21*–*24*).

The use of free-electron lasers enables ultrafast x-ray scattering experiments in charge-ordered systems. However, such studies have thus far centered on the photoinduced melting dynamics of charge order (*25*–*29*). In this work, we focus instead on unveiling the interaction between superconductivity and CDWs in the time domain. We do so by performing time-resolved resonant soft x-ray scattering on YBCO, tracking the CDW response to a laser-driven ultrafast quench of superconductivity.

To probe electronic modulations connected to the CDW, we used an incident photon energy of 931.5 eV, resonant with the Cu L_3-edge, and scanned the momentum transfer around wave vector $\boldsymbol{Q}_{CDW}$ = (0.31, 0, 1.45) (Fig. 1A). The sample was photoexcited by 100-fs infrared laser pulses, which were variably delayed in time with respect to the 100-fs x-ray pulses. The doping of the sample (x = 0.67) was selected to be at the apex of the CDW dome (Fig. 1B) in order to maximize the competition with superconductivity. The experiment was performed in the superconducting phase (<20 K) and, for comparison, at T_c (65 K), where the CDW scattering intensity is maximal [Fig. 1A and (*8*)]. It has been shown that 800-nm laser pulses strongly perturb superconductivity in cuprates, inducing a nonthermal phase transition within a few hundreds of femtoseconds (*23*, *30*–*33*). Here, we kept the fluence of the pump pulses near the minimum needed to quench the superconducting phase (*32*), which is 0.05 mJ/cm^2, such that parasitic local heating is minimized.

The photoinduced response of the CDW state in the time domain is tracked by probing the peak intensity integrated around $\boldsymbol{Q}_{CDW}$ at varying time delays with respect to the pump pulse. At T_c, the pump induces a prompt resolution-limited decrease of the CDW peak intensity (Fig. 1C), followed by a ≈3-ps recovery. This dynamic behavior is similar to the well-known photoinduced melting in other charge-ordered systems (*25*–*28*, *34*, *35*). However, below T_c (at 20 K) the pump yields the opposite effect, inducing an enhancement of the CDW peak signal with notably different dynamics (Fig. 1E). Whereas at 65 K a relatively high pump fluence (0.16 mJ/cm^2) is necessary to observe the prompt CDW melting with good signal-to-noise ratio, at 20 K, a low pump fluence (0.05 mJ/cm^2) produces a large enhancement of the CDW signal, with a rise time of 1.5 ps and a considerably longer decay time (7 ps). This peculiar response, appearing only below T_c, is clearly linked to the presence of the superconducting condensate. We reiterate that the low-fluence pump allows for the transient quenching of superconductivity while minimizing heating effects and

[1]Linac Coherent Light Source, SLAC National Accelerator Laboratory, Menlo Park, CA 94025, USA. [2]Department of Physics and Astronomy, University of British Columbia, Vancouver, BC V6T 1Z1, Canada. [3]Quantum Matter Institute, University of British Columbia, Vancouver, BC V6T 1Z4, Canada. [4]Centre Énergie Matériaux Télécommunications, Institut National de la Recherche Scientifique, Varennes, QC J3X 1S2, Canada. [5]Department of Physics, Yale University, New Haven, CT 06520, USA. [6]Energy Sciences Institute, Yale University, New Haven, CT 06516, USA. [7]Department of Physics, University of California, Davis, CA 95616, USA. [8]Stanford Institute for Materials and Energy Sciences, SLAC National Accelerator Laboratory and Stanford University, Menlo Park, CA 94025, USA. [9]Canadian Light Source, Saskatoon, SK S7N 2V3, Canada. [10]Department of Physics, Arizona State University, Tempe, AZ 85287, USA. [11]Materials Sciences Division, Lawrence Berkeley National Laboratory, Berkeley, CA 94720, USA. [12]Department of Physics and Astronomy, University of Waterloo, Waterloo, ON N2L 3G1, Canada. [13]Stanford Synchrotron Radiation Lightsource, SLAC National Accelerator Laboratory, Menlo Park, CA 94025, USA. [14]Department of Physics, North Carolina State University, Raleigh, NC 27695, USA. [15]Department of Mathematics and Physics, Università Cattolica del Sacro Cuore, Brescia, BS I-25121, Italy.
***Corresponding author. Email: gcoslovich@slac.stanford.edu**
†Present address: Department of Physics, University of California Berkeley, Berkeley, CA 94720, USA.

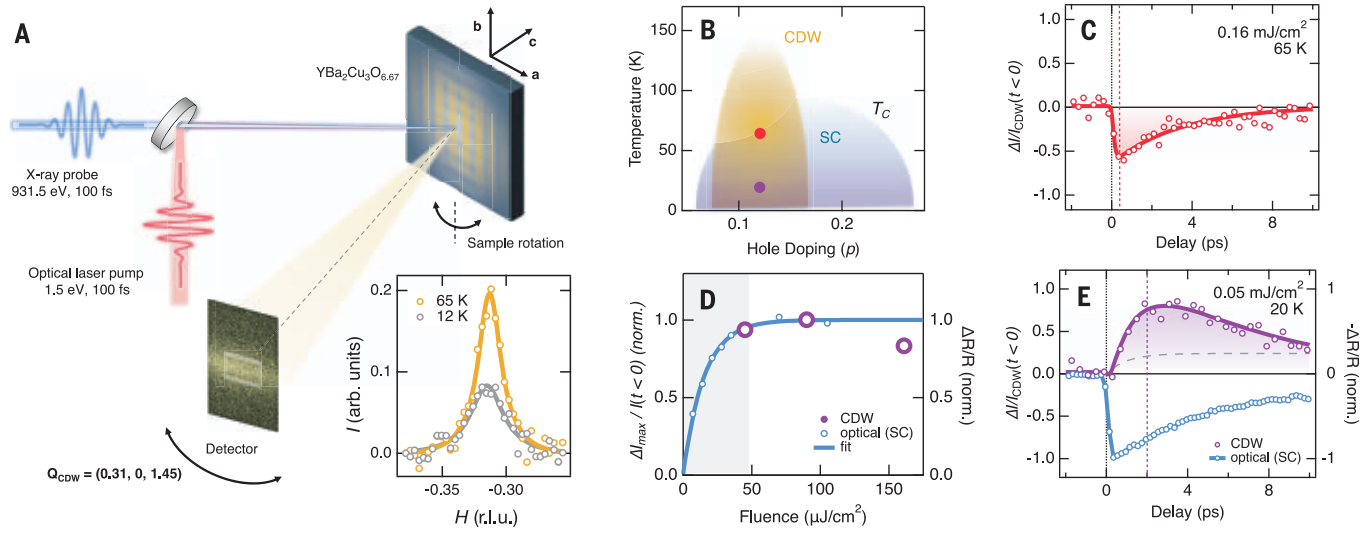

Fig. 1. Experimental conditions and time-domain results. (**A**) Diagram of the experiment. Optical laser pulses perturb the sample, and x-rays pulses probe the CDW peak. The momentum space is explored by rocking the sample. Both a two-dimensional area detector and a point detector (gray rectangle) were used to collect the scattered light. Two representative H scans, $\boldsymbol{Q}$ = (H, 0, 1.45), are shown in the inset, after subtraction of the fluorescence background, at temperatures of 12 and 65 K (*36*). (**B**) Schematic phase diagram of $YBa_2Cu_3O_{6+x}$ showing the two temperatures of interest, within (20 K) and just above (65 K) the superconducting (SC) dome for x equal to 0.67 (hole doping p = 0.12). (**C**) CDW signal at 65 K as a function of the delay time, t, between the pump and probe pulses, with a laser pump fluence of 0.16 mJ/cm^2. The solid line is a fit to exponential relaxation dynamics. (**D**) Fluence dependence of the normalized maximum transient optical reflectivity, $\Delta R/R$ (blue circles), and x-ray scattering photoinduced enhancement (purple circles) at 20 K (*36*). The blue line is a fit with an exponential function that represents saturation of the superconducting response. The gray area highlights fluences below the saturation point. (**E**) Optical (blue circles) and x-ray scattering (purple circles) signals measuring the superconducting and CDW dynamics, respectively, at 20 K with a laser pumping fluence of 0.05 mJ/cm^2. The solid purple line indicates a fit of the x-ray scattering dynamics, where the largest component is a positive enhancement of the CDW signal (*36*). The gray dashed line represents the estimate of quasi-thermal heating effects (*36*). To match the fluence value, the optical data are obtained by averaging the two closest curves from the full fluence-dependence characterization (fig. S4). In (C) and (E), the black vertical dotted lines mark time zero, and the vertical dashed lines mark the delays considered in Fig. 2, at which photoinduced variations are maximal.

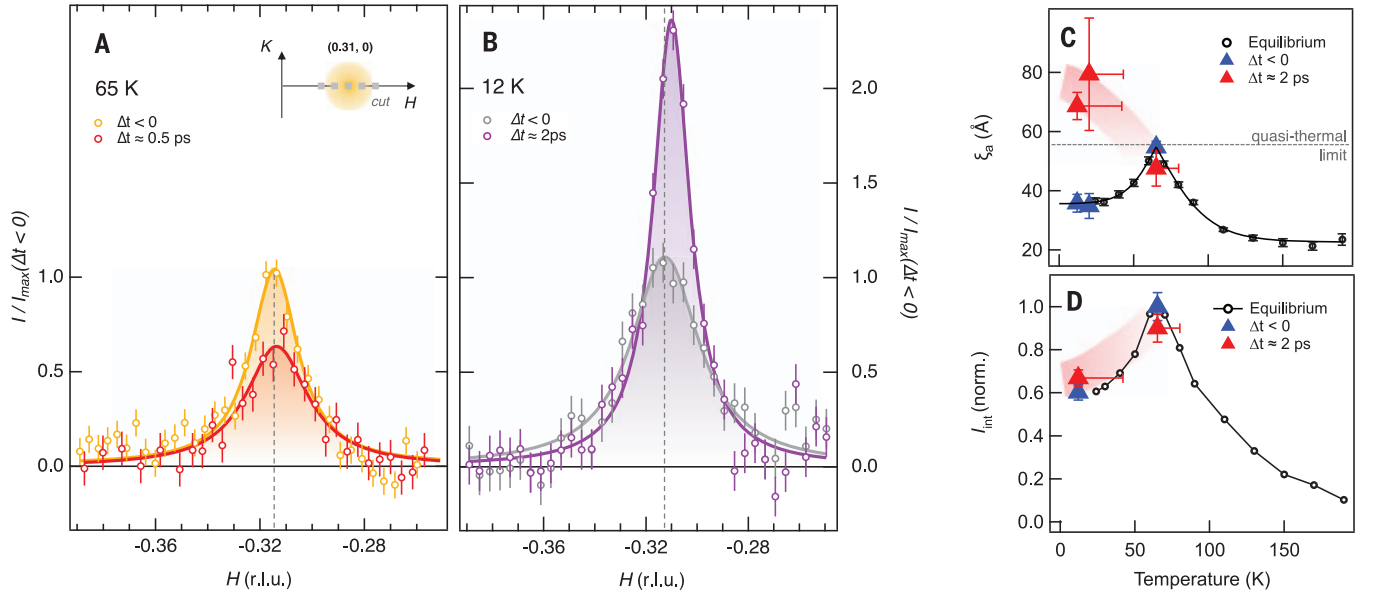

Fig. 2. X-ray scattering profiles of the CDW peak before and after photoexcitation. (**A** and **B**) *H*-scan plots of the CDW scattering signal, after background subtraction, in equilibrium [yellow symbols in (A) and gray symbols in (B)] and after photoexcitation [red symbols in (A) and purple symbols in (B)] at 65 K (A) and 12 K (B). The pump fluence was 0.05 mJ/cm^2. Vertical dashed lines mark the wave vector of the peak at negative delays. Similar results to (B) were obtained using a different detector and at a temperature of 20 K (fig. S2) (*36*). The inset in (A) shows the cut of the CDW peak in the (*H*, *K*) reciprocal plane. Error bars are 1 SD. (**C** and **D**) Correlation length ξ_a along the *a* axis (C) and normalized integrated intensity I_{int} (D) as a function of temperature measured at equilibrium (black circles) and under photoexcitation at negative delays (blue triangles) and around a ≈2-ps delay time (red triangles). For the data at 65 K, the 2-ps values were extrapolated from 0.5 ps, assuming the decay dynamics reported in Fig. 1C. The red shading highlights the temperature trend after photoexcitation. Error bars are evaluated as 1 SD for the fit coefficient. The error bars on the temperature value of the pumped data reflect possible heating effects (*36*).

keeping the temperature below T_c. The maximum rise of the lattice temperature is estimated to be about 20 K, and the dashed line in Fig. 1E displays the estimated heat-induced changes in reflectivity (*36*). In addition, the CDW enhancement signal saturates at this fluence (Fig. 1D), and for higher fluences (>0.1 mJ/cm^2), the CDW response switches to a fast melting and a slow enhancement, with a fluence-dependent cross-over time (fig. S3) (*36*). Notably, this enables full optical control over the CDW phase, switching between enhancement and suppression by tuning the laser power.

To better understand these results and draw a direct comparison with the dynamics of the superconducting order, we performed complementary transient optical reflectivity measurements at 800 nm. At this wavelength, we expect to observe the well-known spectral weight transfer from the low-energy superconducting gap to interband transitions (*23*). The transient optical reflectivity signal is dominated by the superconducting response, as confirmed by its temperature and fluence dependence (fig. S4) and by comparison to transient mid-infrared spectroscopy resonant to the superconducting gap on an analogous sample (fig. S5) (*36*, *37*). The optical reflectivity dynamics show typical features that result from the quench of the superconducting state—the signal saturates at a critical fluence, φ_c (*23*, *30*–*32*) (Fig. 1D), above which a flat-top–shaped dynamics develops (fig. S4) (*33*, *36*). When we normalize the transient reflectivity by its saturated value, we note that at the fluence of 0.05 mJ/cm^2, superconductivity is almost completely quenched (>90%) in the probing volume. Superconductivity recovers on a similar time scale as the CDWs (Fig. 1E); however, their early dynamics are clearly distinct and cannot be described by a thermodynamic variable, such as an effective temperature. After subtracting a small residual melting signal, we note that the CDW enhancement happens on a time scale of ≈1 ps, reaching a maximum around ≈2 ps (*36*), whereas the quench of the superconductivity is complete within 300 fs. Thus, within the first ≈2 ps after photoexcitation, we observe the nonthermal dynamical reaction of CDWs to the quench of superconductivity.

To obtain a snapshot of the CDW spatial correlations after photoexcitation, we scanned the *H* direction, $\boldsymbol{Q}$ = (*H*, 0, 1.45), in reciprocal space (Fig. 2) at the delay times where photoinduced variations are maximal (~0.5 ps at T_c and ~2 ps below T_c). At 65 K, the CDW peak signal suppression is given by a decrease of integrated intensity (16%), as well as a decrease of correlation length (25%). This response is comparable, for example, to the ultrafast CDW melting in tritellurides (*38*), with the variation in correlation length commonly attributed to the formation of topological defects (*25*, *38*). When the system is cooled to well below T_c (12 K; Fig. 2B), the *H* scan reveals a considerable CDW peak enhancement of ≈120% after photoexcitation. The CDW peak intensity increase is mostly caused by the dramatic peak narrowing, indicating a ≈90% increase of the correlation length, from 36 ± 3 Å to 69 ± 5 Å, that is, almost a doubling in size of coherent CDW domains. Concurrently, the integrated intensity increases, but by a smaller amount, between 10 and 20%. We also note a ≈0.003–reciprocal lattice units (r.l.u.) momentum shift at 12 K. This shift is not present in the melting case (65 K), suggesting that it is not related to heating or to CDW sliding effects that are directly induced by light (*35*).

The nature of the nonthermal CDW state becomes evident when comparing the correlation length along the *a* axis (ξ_a) and the integrated intensity (I_{int}) obtained after photoexcitation with a conventional equilibrium synchrotron-based temperature-dependence study (Fig. 2, C and D). The values of I_{int} and ξ_a at 65 and 12 K that are obtained at the free-electron laser before photoexcitation (blue triangles) are in line with the equilibrium characterization (black open circles).

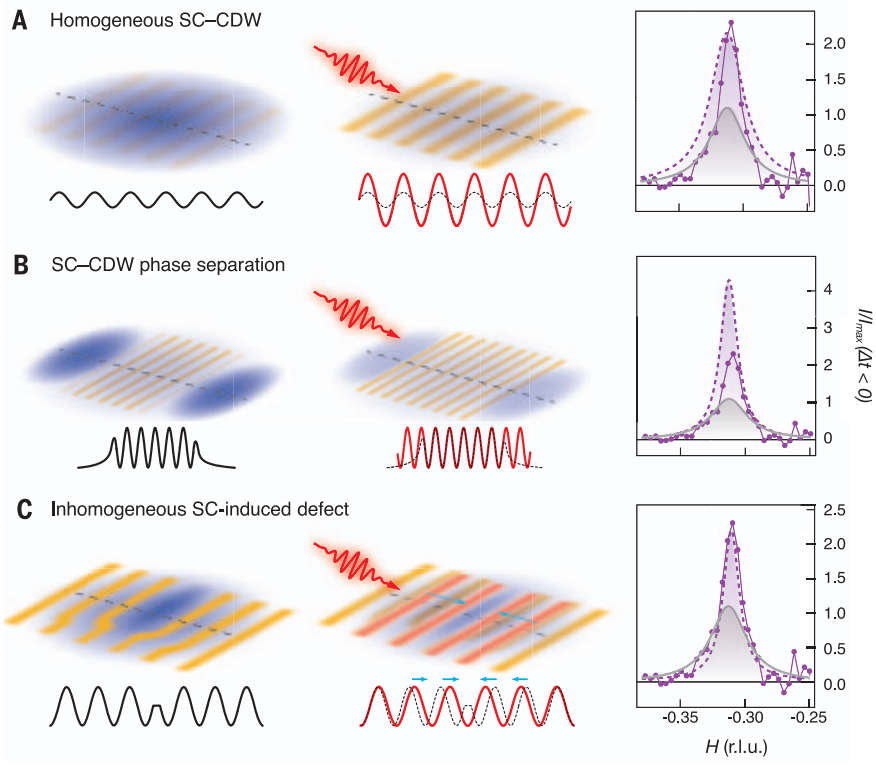

Fig. 3. Scenarios for superconductivity and CDW interactions. (**A** to **C**) Models of the spatial arrangements of CDW and superconductivity (SC) regions before and after photoexcitations. The first column represents the ground state in each case, and the second column represents the state after the quench of the superconducting state by a laser pulse. The third column shows the simulated scattering profile for each of these cases for the equilibrium (gray solid lines) and photoexcited (purple dashed lines) cases (*36*). The profiles are compared to the experimental data from Fig. 2B (purple solid lines and symbols). The three scenarios considered are coexisting homogeneous superconductivity and CDW orders (A), mesoscale (>1 nm) phase separation between superconductivity and CDW domains (B), and a superconductivity-induced topological defect within the CDW domain (*36*) (C). The data are well reproduced in the case shown in (C). Note that in (C), the superconducting state is inhomogeneous and developing more strongly around the defects but still permeates the whole sample volume.

However, the dynamical CDW data (red triangles) clearly do not follow the equilibrium temperature dependence; hence, they cannot be described by an effective temperature scenario. The increase in ξ_a is well beyond what can be achieved at equilibrium, whereas the increase in I_{int} remains small compared with the temperature-dependent swing. These data clearly corroborate that the nonthermal state created by the 800-nm laser pulse has no equilibrium counterpart.

The ability to measure both CDWs and superconductivity on the same sample under similar excitation conditions provides unparalleled insight into the dynamics of intertwined orders. Next, we discuss three possible scenarios for the superconductivity-CDW interaction. First, we consider the case of homogeneous and coexisting orders, which we interpret within the framework of time-dependent Ginzburg-Landau (TDGL) theory, as discussed in other systems (*22*, *39*). TDGL theory predicts that for homogeneous and competitive orders, the CDW order parameter amplitude will increase on a picosecond time scale, driven by the quench of superconductivity (*36*). This scenario is depicted in Fig. 3A, and the corresponding CDW scattering peak shows a notable increase in the integrated intensity [compare with (*24*, *36*)]. This is in stark disagreement with our data, where the signal is dominated by a change in correlation length instead. We thus conclude that a simple competition model, assuming homogeneous and coexisting orders, is incompatible with our results.

A second scenario is that of phase-separated, strongly competitive orders. In this case we consider well-separated CDW and superconducting domains [see, e.g., (*11*)], with an average spacing between neighboring CDW domains that is larger than the CDW periodicity (>1 nm). In this scenario, depicted in Fig. 3B, ξ_a coincides with the size of the CDW domains, which expand in response to the suppression of neighboring superconducting domains. This inflation leads to an increase in I_{int}, thanks to the expanding CDW filling factor, where $I_{int} \propto \xi_a^2$. Such scaling is incompatible with our data, ruling out domain expansion as the root cause of the notable correlation length increase that we observe within ≈2 ps after photoexcitation. Even in the case of a unidirectional expansion of domains, where the filling factor scales linearly with ξ_a, hence, $I_{int} \propto \xi_a$, this scenario remains incompatible with the data [see Fig. 3B and (*36*)].

To explain our observations, we describe a third hypothesis, illustrated in Fig. 3C. Before photoexcitation, the spatial coherence of the CDW domain is disrupted by a superconductivity-induced defect, stabilized by an interstitial superconducting region within the domain. Similar situations have been discussed theoretically (*40*–*42*) in the context of CDW dislocations primarily caused by quenched disorder, with superconductivity forming opportunistically around them. However, in our experiment, the light quench of the superconducting condensate directly causes a reaction of the CDW within ≈1 ps. Extrinsic CDW defects, that is, those pinned to disorder, typically relax on much longer time scales of hundreds of picoseconds (*43*) or longer (*44*), with light-driven dynamics of oxygen ordering taking place on time scales on the order of minutes (*45*). Furthermore, the depinning process is thermally activated (*42*, *44*, *46*), which is clearly incompatible with our observation of faster defect removal dynamics at 20 K (≈1 ps) as compared to 65 K (>3 ps). We thus conclude that our data are consistent with the hypothesis that superconductivity plays the lead role in shaping the inhomogeneous CDW landscape by creating intrinsic defects, which rapidly disappear as superconductivity is quenched. To further corroborate this point, we note that vacancies caused by quenched disorder primarily affect I_{int}, as reported in (*47*) and confirmed by our simulations (*36*).

For comparison, we note that high magnetic field and uniaxial pressure experiments can explore the effects of quasi-static suppression of superconductivity. These works report an increase in the integrated intensity in addition to the increase in correlation length (*15*, *19*, *20*). We interpret this difference in terms of the slower time scale of those external stimuli (>10^{-6} s), which in turn affect both extrinsic and intrinsic defects. Instead, our experiment, by using ultrafast light excitation, can isolate the dynamics of the rapidly reacting intrinsic defects, which are primarily caused by superconductivity and not pinned to disorder.

In terms of the microscopic character of these superconductivity-induced defects, we reiterate that nontopological point-like defects in the CDW pattern, such as vacancies, can be

excluded because their photoinduced removal should primarily affect I_{int} (*36*), in disagreement with the data. We thus consider the case of topological defects, such as CDW dislocations and discommensuration lines (sketched in Fig. 3C), whose presence is well known in cuprates (*12*, *16*, *18*) and which can affect CDW coherence beyond small local perturbations. We find that the removal of discommensuration lines after the photoquench of superconductivity captures the salient aspects of the data (Fig. 3C), where ξ_a nearly doubles without a increase in I_{int} (*36*). The sudden photoquench of superconductivity leads to the annihilation of this topological defect, thus reestablishing phase coherence. Within this model, the ≈0.003-r.l.u. momentum shift reported in Fig. 2B can be explained in terms of a ≈1% increase in periodicity after defect annihilation and subsequent expansion of the CDW pattern within the domain.

The presence of periodic discommensuration lines could reconcile the experimental observation of an incommensurate CDW wave vector (*6*–*11*, *13*–*16*) with reports of local commensurate order, as detected in Bi2212 (*4*, *5*, *12*) and YBCO (*17*, *18*). Importantly, our data are consistent with an active role of superconductivity in the formation and stabilization of discommensurations, which is suggestive of a strong coupling between such defects and superconductivity, as recently discussed with respect to transition-metal dichalcogenides (*48*). Within this scenario, we expect superconductivity to be enhanced along the discommensuration lines, as depicted in Fig. 3C, forming a corresponding spatially modulated state, in line with the observation of pair density waves in Bi-based superconductors (*49*, *50*). Although we cannot determine the periodicity of these defects at the moment, we estimate an average spacing of at least ≈3 to 4 nm between discommensurations (*36*).

Importantly, in our experiment, superconductivity appears to disrupt the spatial coherence within a CDW domain. This differs markedly from a phase-separated state for strongly competitive orders and corroborates the intertwining between superconductivity and CDWs. In this context, we also note that an ultrafast sliding of CDWs is required to restore a common phase pattern across the CDW domain within ≈1 ps. The time scale of this CDW motion is compatible with the relaxation dynamics of periodic lattice distortions (*34*), with an estimated speed of $\approx 3 \times 10^5$ cm/s, which is comparable to the speed of sound in YBCO (*51*).

By using an ultrafast probe of the CDW order parameter after the optical quench of superconductivity, we observe the dynamical interaction between superconductivity and CDWs. The results suggest that superconductivity disrupts the CDW spatial coherence within CDW domains by stabilizing topological defects, such as discommensurations. Although further studies are needed to unequivocally identify the microscopic nature of these defects, this approach establishes opportunities to study competing orders that are complementary to current steady-state methods, such as high fields and uniaxial pressure experiments. By observing the early state after the quench of one of the order parameters, our strategy allows the sensitive detection of spatial patterns that are intrinsically related to the interaction between intertwined orders.

REFERENCES AND NOTES

1. J. C. S. Davis, D. H. Lee, *Proc. Natl. Acad. Sci. U.S.A.* **110**, 17623–17630 (2013).
2. E. Fradkin, S. A. Kivelson, J. M. Tranquada, *Rev. Mod. Phys.* **87**, 457–482 (2015).
3. J. M. Tranquada, B. J. Sternlieb, J. D. Axe, Y. Nakamura, S. Uchida, *Nature* **375**, 561–563 (1995).
4. J. E. Hoffman *et al*., *Science* **295**, 466–469 (2002).
5. C. Howald, H. Eisaki, N. Kaneko, A. Kapitulnik, *Proc. Natl. Acad. Sci. U.S.A.* **100**, 9705–9709 (2003).
6. M. Vershinin *et al*., *Science* **303**, 1995–1998 (2004).
7. P. Abbamonte *et al*., *Nat. Phys.* **1**, 155–158 (2005).
8. G. Ghiringhelli *et al*., *Science* **337**, 821–825 (2012).
9. W. Tabis *et al*., *Nat. Commun.* **5**, 5875 (2014).
10. E. H. da Silva Neto *et al*., *Science* **343**, 393–396 (2014).
11. G. Campi *et al*., *Nature* **525**, 359–362 (2015).
12. A. Mesaros *et al*., *Proc. Natl. Acad. Sci. U.S.A.* **113**, 12661–12666 (2016).
13. R. Comin, A. Damascelli, *Annu. Rev. Condens. Matter Phys.* **7**, 369–405 (2016).
14. R. Arpaia *et al*., *Science* **365**, 906–910 (2019).
15. J. Chang *et al*., *Nat. Phys.* **8**, 871–876 (2012).
16. A. Mesaros *et al*., *Science* **333**, 426–430 (2011).
17. T. Wu *et al*., *Nature* **477**, 191–194 (2011).
18. I. Vinograd *et al*., *Nat. Commun.* **12**, 3274 (2021).
19. S. Gerber *et al*., *Science* **350**, 949–952 (2015).
20. H. H. Kim *et al*., *Science* **362**, 1040–1044 (2018).
21. D. Fausti *et al*., *Science* **331**, 189–191 (2011).
22. G. Coslovich *et al*., *Phys. Rev. Lett.* **110**, 107003 (2013).
23. C. Giannetti *et al*., *Adv. Phys.* **65**, 58–238 (2016).
24. A. Kogar *et al*., *Nat. Phys.* **16**, 159–163 (2020).
25. W. S. Lee *et al*., *Nat. Commun.* **3**, 838 (2012).
26. R. I. Tobey *et al*., *Phys. Rev. B* **86**, 064425 (2012).
27. P. Beaud *et al*., *Nat. Mater.* **13**, 923–927 (2014).
28. M. Mitrano *et al*., *Sci. Adv.* **5**, eaax3346 (2019).
29. H. Jang *et al*., *Rev. Sci. Instrum.* **91**, 083904 (2020).
30. P. Kusar *et al*., *Phys. Rev. Lett.* **101**, 227001 (2008).
31. G. Coslovich *et al*., *Phys. Rev. B* **83**, 064519 (2011).
32. L. Stojchevska *et al*., *Phys. Rev. B* **84**, 180507 (2011).
33. Y. Toda *et al*., *Phys. Rev. B* **84**, 174516 (2011).
34. G. Coslovich *et al*., *Sci. Adv.* **3**, e1600735 (2017).
35. M. Mitrano *et al*., *Phys. Rev. B* **100**, 205125 (2019).
36. See supplementary materials.
37. R. A. Kaindl *et al*., *Science* **287**, 470–473 (2000).
38. A. Zong *et al*., *Nat. Phys.* **15**, 27–31 (2019).
39. Y. F. Kung *et al*., *Phys. Rev. B* **88**, 125114 (2013).
40. Y. Yu, S. A. Kivelson, *Phys. Rev. B* **99**, 144513 (2019).
41. A. Moor, A. F. Volkov, K. B. Efetov, *Phys. Rev. B* **90**, 224512 (2014).
42. C. Chan, *Phys. Rev. B* **93**, 184514 (2016).
43. T. Mertelj *et al*., *Phys. Rev. Lett.* **110**, 156401 (2013).
44. N. P. Ong, D. D. Duggan, C. B. Kalem, T. W. Jing, P. A. Lee, in *Charge Density Waves in Solids*, G. Hutiray, J. Sólyom, Eds. (Springer, 1985), pp. 387–395.
45. A. Bruchhausen *et al*., *Phys. Rev. B* **69**, 224508 (2004).
46. N. P. Ong, Z. Z. Wang, in *Nonlinearity in Condensed Matter*, A. R. Bishop, D. K. Campbell, P. Kumar, S. E. Trullinger, Eds. (Springer, 1987), pp. 350–360.
47. A. J. Achkar *et al*., *Phys. Rev. Lett.* **113**, 107002 (2014).
48. C. Chen, L. Su, A. H. Castro Neto, V. M. Pereira, *Phys. Rev. B* **99**, 121108 (2019).
49. S. D. Edkins *et al*., *Science* **364**, 976–980 (2019).
50. M. H. Hamidian *et al*., *Nature* **532**, 343–347 (2016).
51. M. Saint-Paul *et al*., . *Solid State Commun.* **69**, 1161–1163 (1989).
52. S. Wandel *et al*., Dataset for "Enhanced charge density wave coherence in a light-quenched high temperature superconductor". Zenodo (2022); https://doi.org/10.5281/zenodo.6020036.

ACKNOWLEDGMENTS

We thank S. Kivelson, M. Trigo, M. Mitrano, M. Zonno, S. Dufresne, and V. Esposito for useful discussions. **Funding:** This work, and the use of the Linac Coherent Light Source (LCLS), SLAC National Accelerator Laboratory, is supported by the US Department of Energy (DOE), Office of Science, Office of Basic Energy Sciences (BES) under contract no. DE-AC02-76SF00515. The SXR instrument is funded by a consortium whose membership includes the LCLS, Stanford University through the Stanford Institute for Materials Energy Sciences (SIMES), Lawrence Berkeley National Laboratory (LBNL), University of Hamburg through the BMBF priority program FSP 301, and the Center for Free Electron Laser Science (CFEL). Part of the research described in this paper was performed at the Canadian Light Source, a national research facility of the University of Saskatchewan, which is supported by the Canada Foundation for Innovation (CFI), the Natural Sciences and Engineering Research Council of Canada (NSERC), the National Research Council (NRC), the Canadian Institutes of Health Research (CIHR), the Government of Saskatchewan, and the University of Saskatchewan. Use of the Stanford Synchrotron Radiation Lightsource (SSRL), SLAC National Accelerator Laboratory, is supported by the DOE BES under contract no. DE-AC02-76SF00515. This research was undertaken thanks in part to funding from the Max Planck-UBC-UTokyo Centre for Quantum Materials and the Canada First Research Excellence Fund, Quantum Materials and Future Technologies Program. This project is funded in part by the Killam, Alfred P. Sloan, and NSERC's Steacie Memorial Fellowships (A.D.); the Alexander von Humboldt Fellowship (A.D.); the Canada Research Chairs Program (A.D.); NSERC, Canada Foundation for Innovation (CFI); British Columbia Knowledge Development Fund (BCKDF); and CIFAR Quantum Materials Program. E.H.d.S.N. acknowledges prior support from the Max Planck-UBC postdoctoral fellowship and current support from the Alfred P. Sloan Fellowship in Physics and the National Science Foundation under grant nos. 1845994 and 2034345. This work was partially supported by University of California, Davis, start-up funds. J.J.T. acknowledges support from the DOE BES, Materials Sciences and Engineering Division, under contract no. DE-AC02-76SF0051, through the Early Career Research Program. R.A.K. was supported by the DOE BES Materials Sciences and Engineering Division under contract no. DE-AC02-05-CH11231. A.F.K. was supported by National Science Foundation grant DMR-1752713. **Author contributions:** G.C., J.J.T., C.G., F.B., and E.H.d.S.N. conceived and designed the experiments; G.C., F.B., E.H.d.S.N., J.J.T., S.W., J.D.K., G.L.D., A.H.R., M.P.M., S.P.M., W.F.S., M.-F.L., and T.B. performed the ultrafast resonant soft x-ray scattering measurements; S.W., L.S., G.C., M.X.N., S.Z., Y.W., S.B.W., and M.H.S. analyzed the ultrafast resonant soft x-ray scattering data; F.B., E.H.d.S.N., F.H., R.S., J.-S.L., D.G.H., and G.C. performed synchrotron-based soft x-ray scattering measurements; G.C., S.W., and W.He. performed the transient optical reflectivity measurements; G.C. carried out the theoretical simulations with the assistance of A.F.K. and F.B.; R.L., D.B., and W.Ha. grew and prepared the YBCO single crystals; and G.C. wrote the manuscript with input from S.W., F.B., J.J.T., E.H.d.S.N., A.F.K., R.A.K., A.D., and contributions from all co-authors. **Competing interests:** The authors declare no competing interests. **Data and materials availability:** All experimental data shown in the main text and in the supplementary materials, as well as the simulation codes, are accessible at the Zenodo repository (*52*). **License information:** Copyright © 2022 the authors, some rights reserved; exclusive licensee American Association for the Advancement of Science. No claim to original US government works. https://www.science.org/about/science-licenses-journal-article-reuse.

SUPPLEMENTARY MATERIALS

science.org/doi/10.1126/science.abd7213
Materials and Methods
Figs. S1 to S8
References (*53*–*58*)

Submitted 9 July 2020; resubmitted 22 October 2021
Accepted 9 April 2022
10.1126/science.abd7213

FORESTRY

Multispecies forest plantations outyield monocultures across a broad range of conditions

Yuhao Feng[1], Bernhard Schmid[1,2], Michel Loreau[3], David I. Forrester[4,5], Songlin Fei[6], Jianxiao Zhu[7], Zhiyao Tang[1], Jiangling Zhu[1], Pubin Hong[1], Chengjun Ji[1], Yue Shi[8], Haojie Su[1], Xinyu Xiong[1], Jian Xiao[1], Shaopeng Wang[1]*, Jingyun Fang[1,9]*

Multispecies tree planting has long been applied in forestry and landscape restoration in the hope of providing better timber production and ecosystem services; however, a systematic assessment of its effectiveness is lacking. We compiled a global dataset of matched single-species and multispecies plantations to evaluate the impact of multispecies planting on stand growth. Average tree height, diameter at breast height, and aboveground biomass were 5.4, 6.8, and 25.5% higher, respectively, in multispecies stands compared with single-species stands. These positive effects were mainly the result of interspecific complementarity and were modulated by differences in leaf morphology and leaf life span, stand age, planting density, and temperature. Our results have implications for designing afforestation and reforestation strategies and bridging experimental studies of biodiversity–ecosystem functioning relationships with real-world practices.

Forest plantations are an important means of restoring degraded land, supplying ecosystem services, and mitigating climate change (*1*–*4*). In recent years, several global initiatives, such as the Bonn Challenge (*5*), the New York Declaration on Forests (*6*), and the United Nations (UN) Decade on Ecosystem Restoration (*7*), have been launched to restore degraded ecosystems and provide nature-based solutions to mitigate climate change by increasing global forest cover in the coming decades. In the context of these global initiatives, there is an urgent need to understand the factors that promote the functions and services of forest plantations to ensure effective strategic planning of afforestation and reforestation practices.

In the hope of maximizing the benefits of plantations, early foresters explored various forest plantation strategies (*8*, *9*). One strategy was to plant several tree species with different traits, such as legume and nonlegume species or conifer and broad-leaved trees—i.e., multispecies plantations (*9*, *10*). Ecological theory and experiments predict that multiple species growing together will create more biomass, called the biodiversity–ecosystem functioning (BEF) relationship (*11*, *12*). Biodiversity can increase biomass production because of either niche differentiation among species (complementarity effects) or an increased likelihood that highly productive species are present (selection effects) (*12*). Field experiments in both grasslands (*12*, *13*) and forests (*14*–*16*) have revealed that complementarity effects generally contribute more than selection effects to the observed positive BEF relationships and that these effects change with traits of species, time, planting density, and environmental conditions. The positive effect of biodiversity on ecosystem productivity has also been documented by global and regional observational studies (*17*, *18*). The long history of multispecies plantation practices (*10*, *19*, *20*) and the growing experimental research on tree diversity effects [e.g., the global network of tree diversity experiments, TreeDivNet (*16*, *21*)] provide an opportunity for a systematic assessment of the effects of species mixing in forest plantations and the mechanisms that underpin them. Here, we hypothesize that, as in BEF experiments with random species selection, multispecies plantations established by foresters can also increase tree growth and biomass production through complementarity effects and that these effects are modulated by biotic and abiotic factors.

To test our hypotheses, we assembled a global dataset (Global MixTrees) of single-species (monocultures) and multispecies stands (mixtures or mixed stands) matched by age and planting density at 255 sites from 273 publications (*22*) (figs. S1 and S2). The dataset contains 243 tree species with diverse functional traits, wide ranges of stand age and

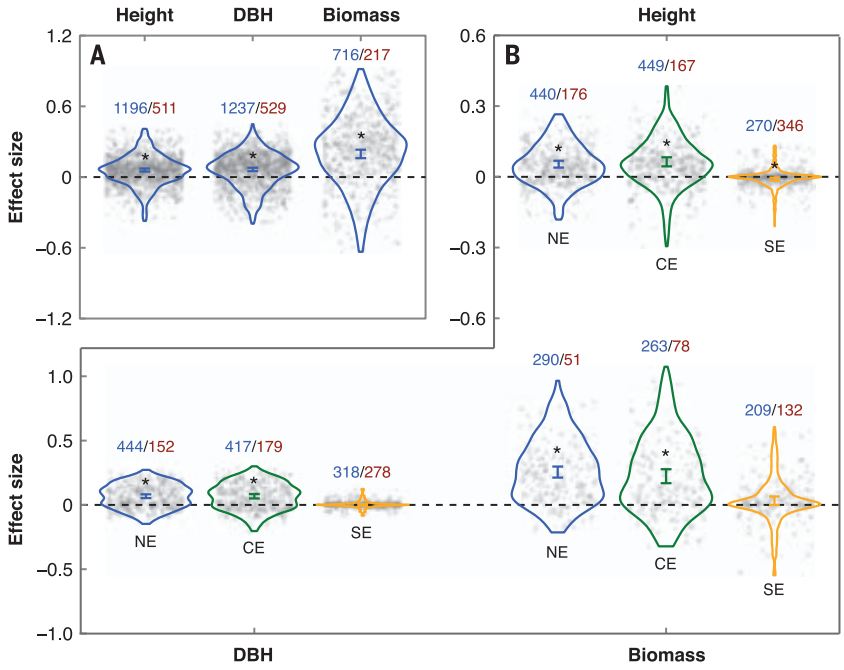

Fig. 1. Effect sizes of species mixing on height, DBH, and aboveground biomass. (**A**) Effect sizes at the species level. (**B**) Effect sizes at the whole-stand level. In (B), net effect (NE), complementarity effect (CE), and selection effect (SE) are shown in blue, green, and yellow colors, respectively. Gray bubbles show the original sample effect size, and the two numbers above each subset graph indicate the number of samples with effect sizes greater than (blue) or smaller than (red) zero. The colored bars represent the 95% confidence intervals of mean effect size across samples. *$P < 0.05$.

[1]Institute of Ecology, College of Urban and Environmental Sciences, and Key Laboratory for Earth Surface Processes of the Ministry of Education, Peking University, Beijing 100871, China. [2]Department of Geography, Remote Sensing Laboratories, University of Zürich, 8057 Zürich, Switzerland. [3]Theoretical and Experimental Ecology Station, CNRS, 09200 Moulis, France. [4]Swiss Federal Institute of Forest, Snow and Landscape Research WSL, 8903 Birmensdorf, Switzerland. [5]CSIRO Land and Water, Canberra, ACT 2601, Australia. [6]Department of Forestry and Natural Resources, Purdue University, West Lafayette, IN 47907, USA. [7]College of Pastoral Agriculture Science and Technology, Lanzhou University, Lanzhou, Gansu 730000, China. [8]State Key Laboratory of Vegetation and Environmental Change, Institute of Botany, Chinese Academy of Sciences, Beijing 100093, China. [9]College of Ecology and Environmental Sciences, Yunnan University, Chenggong, Kunming 650500, China.
*Corresponding author. Email: jyfang@urban.pku.edu.cn (J.F.); shaopeng.wang@pku.edu.cn (S.W.)

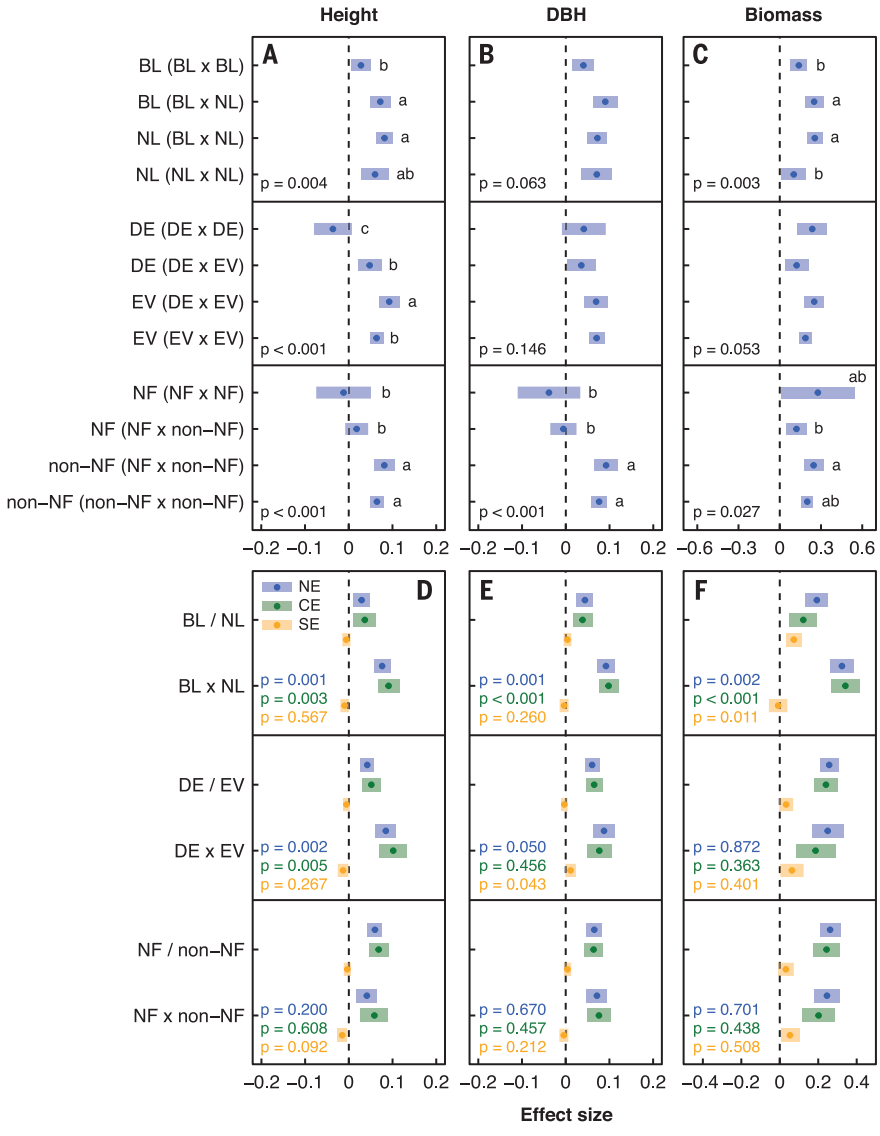

Fig. 2. Impacts of functional trait composition on the effect sizes of species mixing. (**A** to **C**) Impacts at the species level. (**D** to **F**) Impacts at the whole-stand level. (A and D) Tree height. (B and E) DBH. (C and F) Aboveground biomass. Functional traits are divided into three categories: leaf morphology [broad-leaved (BL) versus needle-leaved (NL)], leaf life span [deciduous (DE) versus evergreen (EV)], and nitrogen acquisition strategy [nitrogen-fixing (NF) versus non–nitrogen-fixing (non-NF)]. In (A) to (C), "BL (BL × NL)" denotes the effect size for the BL species in the mixed stands consisting of BL and NL species; in (D) to (F), "BL / NL" denotes the mixed stands consisting of only BL or only NL species, and "BL × NL" denotes the mixed stands consisting of both BL and NL species. Other notations are similarly defined. Colored dots and shaded bars represent the mean effect sizes and their 95% confidence intervals, respectively. *P* values are derived from likelihood ratio tests (*22*). In (A) to (C), different letters denote significant differences in the mean effect size between groups. In (D) to (F), NE, CE, and SE are shown in blue, green, and yellow colors, respectively.

planting density, and spanning a broad climatic gradient. It includes information on three major stand-level growth variables: mean tree height (in meters), mean diameter at breast height (DBH) (in centimeters), and aboveground biomass (in metric tons per hectare) (data S1 and S2). We defined a sample as a set of matched monocultures and mixed stands from the same site and with the same stand age, planting density, and mixing ratio (i.e., percentage of each species at planting) (figs. S3 and S4). Each sample typically had three to six replicates, which we used to characterize spatial environmental heterogeneity and estimate the variation of species mixing effects within the site. In total, our dataset consisted of 5959 samples, including 2323 samples for mean height, 2362 samples for mean DBH, and 1274 samples for aboveground biomass. Most samples had mixed stands consisting of two species (5439 samples), and the remaining had 3 to 16 species (520 samples) (fig. S5). We conducted our analyses at both the species (i.e., the single target species) and community (i.e., the whole stand) levels. For species-level analyses, 4406 samples were used to compare the growth of a target species in mixed stands with its growth in monocultures (fig. S3); for whole-stand–level analyses, the remaining 1553 samples were used to compare the growth of the whole mixed stands with that of the corresponding monocultures (fig. S4).

Using this dataset, we examined the effects of species mixing on three growth variables (tree height, DBH, and aboveground biomass) and explored how biotic (i.e., functional traits, stand age, and planting density) and abiotic (i.e., temperature and precipitation) factors influenced the effects of species mixing. For each growth variable, we quantified the effect size of species mixing at the species level using the logarithmic ratio of the growth variable in mixed stands versus monocultures of the target species [eqs. S7 and S8 (*22*, *23*)] and at the whole-stand level using the relative difference between the growth variable in mixed stands and the average of this variable in the monocultures of the component species [eqs. S9 and S10 (*22*)]. At the whole-stand level, we further partitioned the effect size of species mixing (also called net effect) additively into complementarity and selection effect to disentangle whether the mixing effect was caused by niche differentiation or the presence of specific species (*13*). Then, we pooled all effect sizes across samples to derive an overall effect size of species mixing at both species and whole-stand levels, as well as for complementarity and selection effects (*23*). For all analyses, we conducted tests of robustness using samples with two-species mixed stands and found that all results were qualitatively similar (figs. S6 to S9). We also tested whether effect sizes increased with species richness beyond two species.

Our analyses showed that, at the species level, the mean values of the three growth variables were all larger in multispecies stands than in monocultures (Fig. 1A). The mean effect sizes for height, DBH, and biomass were 0.060 (95% confidence interval, 0.047 to 0.073), 0.065 (0.050 to 0.079), and 0.196 (0.160 to 0.232), respectively, corresponding to a relative increase of 6.2% (4.8 to 7.6%), 6.7% (5.1 to 8.2%), and 21.7% (17.3 to 26.1%), respectively. Positive effect sizes for these variables occurred in 70.1, 70.0, and 76.7% of all samples, respectively (Fig. 1A and fig. S10, A to C). The effect sizes of these growth variables tended to increase with species richness (fig. S11, A to C).

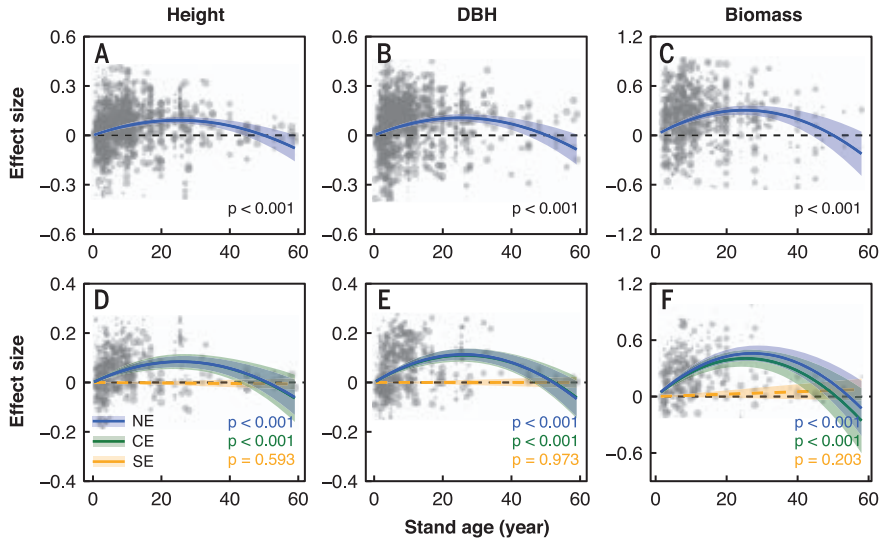

Fig. 3. Changes in the mixing effects with stand age. (**A** to **C**) Changes at the species level. (**D** to **F**) Changes at the whole-stand level. (A and D) Tree height. (B and E) DBH. (C and F) Aboveground biomass. Both linear and quadratic mixed-effects models were fit, and the optimal fits are shown according to the likelihood ratio tests (*22*). Shaded areas are 95% confidence intervals of fitted curves, with dashed lines indicating $P > 0.05$. Bubble sizes are proportional to the weights of samples. In (D) to (F), NE, CE, and SE are shown in blue, green, and yellow colors, respectively.

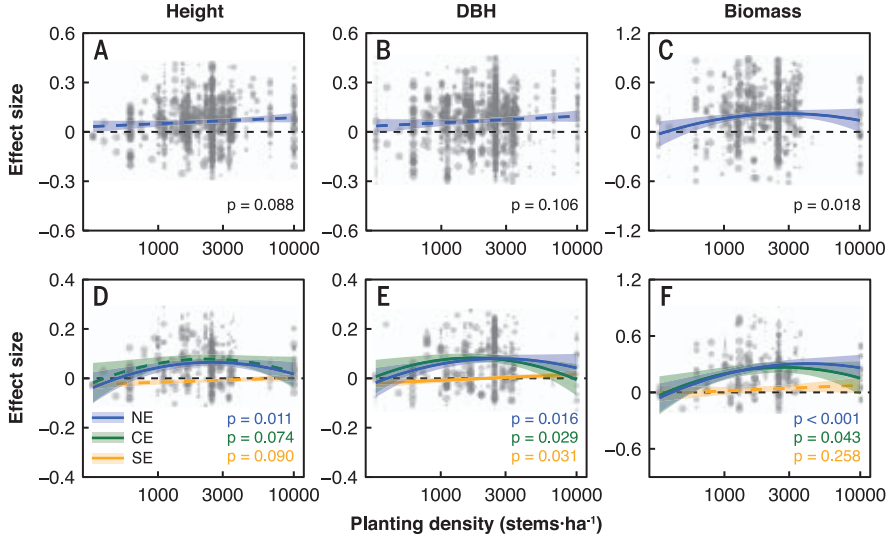

Fig. 4. Changes in the mixing effects with tree density. (**A** to **C**) Changes at the species level. (**D** to **F**) Changes at the whole-stand level. (A and D) Tree height. (B and E) DBH. (C and F) Aboveground biomass. The upper limit of planting density is set to 10,000 stems ha^{-1}, and the density values are log_{10}-transformed before statistical analyses to avoid bias as a result of high leverage of a few sites with very high densities. In (D) to (F), NE, CE, and SE are shown in blue, green, and yellow colors, respectively. For other explanations, see the caption of Fig. 3.

At the whole-stand level, the three growth variables were also higher in multispecies stands than in monocultures (Fig. 1B), with an increase of 5.4% (3.9 to 6.8%) in height, 6.8% (5.3 to 8.2%) in DBH, and 25.5% (21.2 to 29.8%) in biomass. Positive net effects of these variables occurred in 71.4, 74.5, and 85.0% of all samples, respectively (Fig. 1B and fig. S10, D to F). These positive net effects were mainly the result of complementarity rather than selection effects (which were close to zero or even negative) (Fig. 1B and fig. S10, G to L). These small selection effects can be understood by the fact that foresters deliberately use highly productive tree species (*24*) and thus exclude low-performing species that probably represent most of the species in BEF experiments with random species selection (*14*) (if component species have equal performance in monoculture, then selection effects are zero by definition). As at the species level, the net and complementarity effects of the growth variables increased with species richness beyond two species (fig. S11, D to F), which supports the conclusions of previous experimental and observational studies (*14*, *17*, *18*).

To disentangle the mechanisms underpinning the positive effects of species mixing, we investigated how combinations of tree species with different functional traits influenced tree size or biomass in multispecies plantations. We focused our analysis on three groupings of species according to functional traits: leaf morphology (i.e., broad-leaved versus needle-leaved species), leaf life span (i.e., deciduous versus evergreen species), and nitrogen acquisition strategy (i.e., nitrogen-fixing versus non–nitrogen-fixing species). For each of these three groupings, multispecies plantations with opposite functional traits may produce higher complementarity effects through niche partitioning: Broad-leaved and needle-leaved species can partition space in the canopy (*25*), deciduous and evergreen species can partition seasonal time (*26*), and non–nitrogen-fixing species and nitrogen-fixing species can partition the source of nitrogen nutrition (*27*).

At the species level, target species tended to benefit more in one or more growth variables when growing with species in the opposite functional trait categories compared with those growing with species with similar traits (fig. S12). Both broad- and needle-leaved species grew taller and produced more biomass when growing with species of the other functional group than when growing with species of the same functional group (Fig. 2, A and C). Deciduous and evergreen species also grew taller when growing with species of the other compared with species of the same functional group (Fig. 2A). However, nitrogen-fixing and non–nitrogen-fixing species performed similarly when growing with species of the other or with species of the same functional group (Fig. 2, A to C). Analyses at the whole-stand level corroborated these species-level results. Multispecies stands containing both broad- and needle-leaved species had larger net and

complementarity effects on all three growth variables than multispecies stands containing only broad-leaved or only needle-leaved species (Fig. 2, D to F, and fig. S13). Multispecies stands containing both deciduous and evergreen species had larger net and complementarity effects on height and DBH than multispecies stands containing only deciduous or only evergreen species (Fig. 2, D and E). However, multispecies stands containing both nitrogen-fixing and non–nitrogen-fixing species performed similarly to multispecies stands containing only nitrogen-fixing or only non–nitrogen-fixing species (Fig. 2, D to F). Overall, our results suggest that functional differences in leaf morphology and leaf life span—but notably not in nitrogen acquisition strategy—underpin stronger complementarity effects in mixed stands (*15*, *28*).

Next, we examined whether stand characteristics (stand age and planting density) modified the effects of species mixing. At both the species and whole-stand levels, the effect sizes of species mixing on height, DBH, and biomass all showed unimodal relationships when plotted against stand age, which peaked at ~25 years (Fig. 3). These unimodal patterns were mainly driven by time-dependent complementarity effects, which first increased and then decreased with stand age (Fig. 3, D to F). Previous BEF experiments have revealed increasing complementarity and biodiversity effects with experimental duration but were limited to a relatively short time span [e.g., <15 years (*14*, *29*)]. Our results corroborate findings from these short-term experiments, but they also suggest that as stands develop further, complementarity effects may subsequently decrease, possibly as a result of enhanced interspecific competition for light or soil resources (*30*).

Along a gradient of tree planting density, the species-level effect sizes for height and DBH showed increasing trends (Fig. 4, A and B), but that for biomass showed a unimodal pattern, peaking at a density of ~2860 stems ha^{-1} (Fig. 4C). At the whole-stand level, the effect sizes for all three growth variables showed similar unimodal patterns along a gradient of tree density, peaking at ~2500, 2700, and 4100 stems ha^{-1}, respectively (Fig. 4, D to F). These results support previous findings that the effect of species mixing increases with planting density within low-density ranges [e.g., <2000 stems ha^{-1} (*31*)] but that negative effects can emerge at high densities (*32*). In other words, the benefits of multispecies plantations may be reduced at both very low densities, where individuals are far apart and thus do not interact, and very high densities, where intense competition may inhibit the operation of complementarity (*30*).

Climate (temperature and precipitation) may be a factor that influences the effects of species mixing (*20*). At both the species and whole-stand levels, the effect sizes for the three growth variables all showed increasing trends along a gradient of mean annual temperature [fig. S14; see (*22*) for climatic data]. This increase was largely the result of interspecific complementarity, whereas selection effects were negligible at the whole-stand level. This suggests that warmer climates could benefit tree growth in multispecies stands more than in monocultures, which may be because of longer growing seasons that promote complementarity in time (*33*). Compared with temperature, mean annual precipitation did not significantly influence the mixing effect sizes (fig. S15), probably because forest plantations mainly occurred in humid areas where precipitation may not be a limiting factor (*34*).

Our study demonstrates substantial benefits of multispecies plantations, which corroborates and generalizes findings from forest BEF experiments (*14*, *16*, *21*) and helps to show their implications for real-world forestry applications. Our analyses offer predictions that go beyond the conclusions of short-term BEF experiments with random species selection and call for more long-term experiments with deliberate species selection to reveal the time dependency of biodiversity effects. Our findings also have direct implications for forest management and afforestation and reforestation practices. Foresters often prefer monoculture plantations because of their lower planting and management costs, targeted special uses of trees (e.g., kind and amount of timber production and economic value) (*35*), and the difficulty in identifying the site characteristics that will give the best result for a given multispecies plantation (*30*, *35*). However, a growing body of research is revealing the benefits of multispecies plantations in terms of productivity (this study), stability (*16*, *36*), community structure (*15*), and biodiversity (*4*). Therefore, we advocate a multifunctional cost-benefit analysis framework to identify planting strategies that optimize the benefits of forest plantations for restoration, conservation, and climate change mitigation.

REFERENCES AND NOTES

1. J. G. Canadell, M. R. Raupach, *Science* **320**, 1456–1457 (2008).
2. J.-F. Bastin *et al*., *Science* **365**, 76–79 (2019).
3. S. C. Cook-Patton, D. Shoch, P. W. Ellis, *Nat. Clim. Chang.* **11**, 366–368 (2021).
4. F. Hua *et al*., *Science* eabl4649 (2022).
5. International Union for Conservation of Nature (IUCN), "The Bonn Challenge" (2020); https://www.bonnchallenge.org.
6. United Nations Development Programme, "New York Declaration on Forests" (2022); https://www.climateandforests-undp.org/new-york-declaration-forests.
7. United Nations Environment Programme, "UN Decade on Ecosystem Restoration" (2021); https://www.decadeonrestoration.org.
8. D. M. Smith, *The Practice of Silviculture* (Wiley, 1986).
9. J. D. Nichols, M. Bristow, J. K. Vanclay, *For. Ecol. Manage.* **233**, 383–390 (2006).
10. K. B. Hulvey *et al*., *Nat. Clim. Chang.* **3**, 869–874 (2013).
11. M. Loreau *et al*., *Science* **294**, 804–808 (2001).
12. D. Tilman, F. Isbell, J. M. Cowles, *Annu. Rev. Ecol. Evol. Syst.* **45**, 471–493 (2014).
13. M. Loreau, A. Hector, *Nature* **412**, 72–76 (2001).
14. Y. Huang *et al*., *Science* **362**, 80–83 (2018).
15. L. J. Williams, A. Paquette, J. Cavender-Bares, C. Messier, P. B. Reich, *Nat. Ecol. Evol.* **1**, 0063 (2017).
16. J. J. Grossman *et al*., *Environ. Exp. Bot.* **152**, 68–89 (2018).
17. J. Liang *et al*., *Science* **354**, aaf8957 (2016).
18. S. Fei *et al*., *Nat. Commun.* **9**, 5436 (2018).
19. D. Piotto, *For. Ecol. Manage.* **255**, 781–786 (2008).
20. H. Jactel *et al*., *Biol. Lett.* **14**, 20170747 (2018).
21. A. Paquette *et al*., *Nat. Ecol. Evol.* **2**, 763–766 (2018).
22. Materials and methods are available as supplementary materials.
23. L. V. Hedges, J. Gurevitch, P. S. Curtis, *Ecology* **80**, 1150–1156 (1999).
24. P. Savill, *The Silviculture of Trees Used in British Forestry* (CABI, 2019).
25. H. Ishii, S. Asano, *Ecol. Res.* **25**, 715–722 (2010).
26. H. Lu, G. M. J. Mohren, J. den Ouden, V. Goudiaby, F. J. Sterck, *For. Ecol. Manage.* **376**, 321–332 (2016).
27. D. I. Forrester, J. Bauhus, A. L. Cowie, P. A. Mitchell, J. Brockwell, *For. Sci.* **53**, 426–434 (2007).
28. Y. Zhang, H. Chen, P. B. Reich, *J. Ecol.* **100**, 742–749 (2012).
29. F. J. Bongers *et al*., *Nat. Ecol. Evol.* **5**, 1594–1603 (2021).
30. D. I. Forrester, *For. Ecol. Manage.* **312**, 282–292 (2014).
31. M. M. Amoroso, E. C. Turnblom, *Can. J. For. Res.* **36**, 1484–1496 (2006).
32. S. B. Boyden, P. B. Reich, K. J. Puettmann, T. R. Baker, *J. Ecol.* **97**, 277–288 (2009).
33. J. Oehri, B. Schmid, G. Schaepman-Strub, P. A. Niklaus, *Proc. Natl. Acad. Sci. U.S.A.* **114**, 10160–10165 (2017).
34. J. Fang *et al*., *Proc. Natl. Acad. Sci. U.S.A.* **111**, 9527–9532 (2014).
35. J. Bauhus *et al*., in *Mixed-Species Forests: Ecology and Management*, H. Pretzsch, D. I. Forrester, J. Bauhus, Eds. (Springer, 2017), pp. 433–501.
36. F. Schnabel *et al*., *Sci. Adv.* **7**, eabk1643 (2021).
37. Y. Feng *et al*., Data from: Multispecies forest plantations outyield monocultures across a broad range of conditions, version 1.0.0, Zenodo (2022); https://doi.org/10.5281/zenodo.6520748.

ACKNOWLEDGMENTS

The authors thank three anonymous reviewers for their constructive comments, which improved the quality of earlier versions of the manuscript. **Funding:** This study was funded by National Natural Science Foundation of China 31988102 (to J.F.) and 32122053 (to S.W.), Basic Research Program of Yunnan Province grant 202101BC070000 (to J.F.), and TULIP Laboratory of Excellence grant ANR-10-LABX-41 (to M.L.). **Author contributions:** Conceptualization: J.F.; Methodology: Y.F., Jianx.Z., Jiang.Z., X.X., J.X., and Z.T.; Investigation: Y.F., S.W., B.S., P.H., H.S., C.J., and Y.S.; Visualization: Y.F. and H.S.; Funding acquisition: J.F., S.W., and M.L.; Project administration: J.F. and Jiang.Z.; Supervision: J.F.; Writing – original draft: Y.F., S.W., and J.F.; Writing – review and editing: S.W., J.F., Y.F., B.S., D.I.F., M.L., S.F., and all other other authors. **Competing interests:** The authors declare that they have no competing interests. **Data and materials availability:** The data used in this study (i.e., the Global MixTrees dataset) are uploaded as online content (data S1 and S2). All code can be accessed at Zenodo (*37*).

License information: Copyright © 2022 the authors, some rights reserved; exclusive licensee American Association for the Advancement of Science. No claim to original US government works. https://www.science.org/about/science-licenses-journal-article-reuse.

SUPPLEMENTARY MATERIALS

science.org/doi/10.1126/science.abm6363
Materials and Methods
Figs. S1 to S16
Tables S1 to S11
References (*38*–*54*)
MDAR Reproducibility Checklist
Data S1 and S2

Submitted 24 October 2021; accepted 25 April 2022
10.1126/science.abm6363

BIOCATALYSIS

Directed evolution of nonheme iron enzymes to access abiological radical-relay C(sp^3)–H azidation

Jinyan Rui[1]†, Qun Zhao[1]†, Anthony J. Huls[1]†, Jordi Soler[2], Jared C. Paris[3], Zhenhong Chen[1], Viktor Reshetnikov[1], Yunfang Yang[4], Yisong Guo[3]*, Marc Garcia-Borràs[2]*, Xiongyi Huang[1]*

We report the reprogramming of nonheme iron enzymes to catalyze an abiological C(sp^3)–H azidation reaction through iron-catalyzed radical relay. This biocatalytic transformation uses amidyl radicals as hydrogen atom abstractors and Fe(III)–N_3 intermediates as radical trapping agents. We established a high-throughput screening platform based on click chemistry for rapid evolution of the catalytic performance of identified enzymes. The final optimized variants deliver a range of azidation products with up to 10,600 total turnovers and 93% enantiomeric excess. Given the prevalence of radical relay reactions in organic synthesis and the diversity of nonheme iron enzymes, we envision that this discovery will stimulate future development of metalloenzyme catalysts for synthetically useful transformations unexplored by natural evolution.

Introducing abiological chemical transformations to natural proteins represents a powerful approach to advance enzymatic catalysis to reaction territories unexplored by natural evolution (*1*). This strategy enables enzyme reprogramming to achieve challenging synthetic reactions regio- and enantioselectively while maintaining genetic tunability (*2*, *3*). Representative examples include taming heme and nonheme metalloenzymes to mediate carbene- and nitrene-transfer reactions (*4*), reprogramming flavoenzymes for photoredox catalysis (*5*, *6*), and reconfiguring carbonic anhydrase to perform metal-hydride chemistry (*7*). Despite this progress, most reactions in organic synthesis have no known biological counterparts, and the mechanisms that empower these transformations were not developed by nature during the course of natural evolution (*1*). To unleash the full potential of enzymes for modern chemical synthesis, it is pivotal to introduce fundamental reaction modes in synthetic chemistry to the catalytic repertoire of biology.

We consider a mechanism-driven approach to expand the scope of biocatalysis. We envisioned that natural metalloenzymes that share mechanistic elements with synthetic metal-catalyzed reactions would exhibit promiscuous activity toward these reactions, from which new catalytic functions can be evolved. Guided by this design principle, we envisaged that nonheme iron enzymes could be reprogrammed to perform radical-relay C–H functionalization—an important class of unnatural reactions widely used in organic synthesis (*8*–*11*). The defining feature of a metal-catalyzed radical relay is the use of a reactive radical (X•) to activate a C(sp^3)–H bond through hydrogen atom transfer (HAT) and the interception of the resulting carbon-centered radical by a redox-

[1]Department of Chemistry, Johns Hopkins University, Baltimore, MD 21218, USA. [2]Institut de Química Computacional i Catàlisi (IQCC) and Departament de Química, Universitat de Girona, Campus Montilivi, Girona E-17071 Catalonia, Spain. [3]Department of Chemistry, Carnegie Mellon University, Pittsburgh, PA 15213, USA. [4]College of Chemical Enginering, Zhejiang University of Technology, Hangzhou, Zhejiang 310014, China.
*Corresponding author. Email: xiongyi@jhu.edu (X.H.); marc.garcia@udg.edu (M.G.B.); ysguo@andrew.cmu.edu (Y.G.)
†These authors contributed equally to this work.

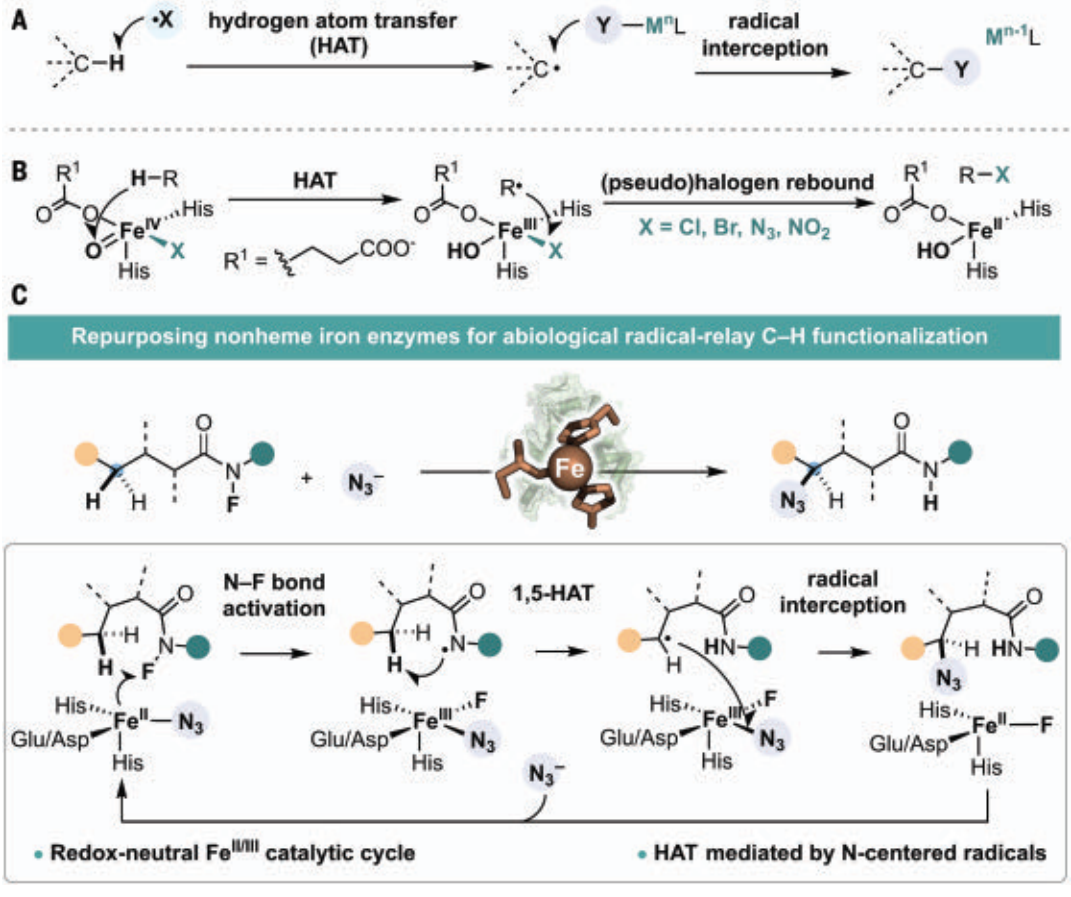

Fig. 1. Conceptualization of enzymatic C–H functionalization via metal-catalyzed radical relay. (**A**) Radical-relay C–H functionalization involves an initial hydrogen atom transfer (HAT) mediated by a heteroatom-centered radical (X•) followed by trapping of the carbon-centered radical with a redox-active metal complex. (**B**) Mechanism employed by natural nonheme iron enzymes for C(sp^3)–H halogenation/azidation. (**C**) Integration of radical relay chemistry into nonheme iron enzymes enables unnatural C–H functionalization reactions.

active metal complex (Fig. 1A). This process mechanistically resembles the C(sp^3)–H halogenation reactions catalyzed by nonheme iron halogenases, in which an iron(IV)-oxo complex is used to activate substrates by means of HAT and an iron(III)halide/azide intermediate intercepts substrate radicals to form carbon–halogen/azide bonds (Fig. 1B) (*12*–*16*). Enlightened by this mechanistic similarity, we proposed that a nonheme iron enzyme could mediate a radical relay process through an initial substrate activation at a Fe(II) center to generate a reactive amidyl radical for HAT and subsequent transfer of a Fe(III)-bound ligand to the carbon-centered radical (Fig. 1C). This new biocatalytic reaction proceeds through a redox neutral pathway involving an Fe^{II}/Fe^{III} redox couple, which offers a complementary approach to the native $Fe^{II/IV}$ catalytic cycle of nonheme iron enzymes for C–H functionalization.

As proof-of-concept, we employed this enzymatic radical-relay strategy to develop new biocatalysts to perform a nonnatural C(sp^3)–H azidation reaction. Current synthetic approaches for this reaction are limited in turnovers, not enantioselective, and require an acidic azide source (scheme S4) (*17*). We presumed that these challenges could be met by leveraging the genetic tunability and high catalytic efficiency of nonheme iron enzymes. We began our investigation by testing a panel of nine functionally diverse nonheme iron enzymes with an *N*-fluoroamide substrate **1NF** under whole-cell conditions. A (4-hydroxyphenyl)pyruvate dioxygenase from *Streptomyces avermitilis* (*Sav* HppD) provided the desired azidation product with 250 total turnovers (TTN), an enantiomeric ratio (e.r.) of 63:37, and a chemoselectivity of 9:1 for azidation over fluorination product (tables S1 and S2). Only a trace amount of the azidation product was obtained in a reaction lacking *Sav* HppD entry 10, table S1. Moreover, mutating the two iron-coordinating histidines to alanines abolished the enzyme activity while retaining the fold of wild-type (WT) *Sav* HppD (entry 11, table S1, and fig. S1), supporting the proposal that this enzymatic azidation occurs at the 2-His-1-carboxylate iron center. The unazidated amide product was also detected in trace amounts but was likely formed through an unidentified nonenzymatic process as the double alanine mutant afforded this product in a yield comparable to that of the WT enzyme (tables S1 and S2).

We set out to improve the performance of *Sav* HppD through directed evolution. We performed computational modeling on the WT enzyme with both azide and **1NF** substrate bound and chose fifteen residues for optimization (figs. S10, S11, S13, and S14). These residues primarily reside in three regions: the C-terminal, α helix, and β barrel of the C-terminal domain, as well as in loops surrounding the active site (Fig. 2A). We have also established a high-throughput screening (HTS) platform based on copper-catalyzed azide-alkyne cycloaddition (CuAAC) (*18*) and achieved reliable quantification of enzymatic azidation products with a coefficient of variation of 9% and a detection limit of 4 μM (scheme S1 and fig. S2). With this HTS platform, we evaluated more than 5000 clones generated through error-prone polymerase chain reaction (PCR) or site-saturation mutagenesis (Fig. 2, B and C). A sextuple mutant *Sav* HppD V189A F216A P243A N245Q Q255A L367I (denoted as *Sav* HppD Az1) furnished the product with 1340 TTN and 87:13 e.r. In this evolution campaign, we could not identify an enzyme variant with an e.r. higher than 87:13. This result indicates that mutations that were beneficial for improving activity might not necessarily lead to an increase in enantioselectivity, which might be due to the differences in substrate positioning and geometric requirements for the rate-determining

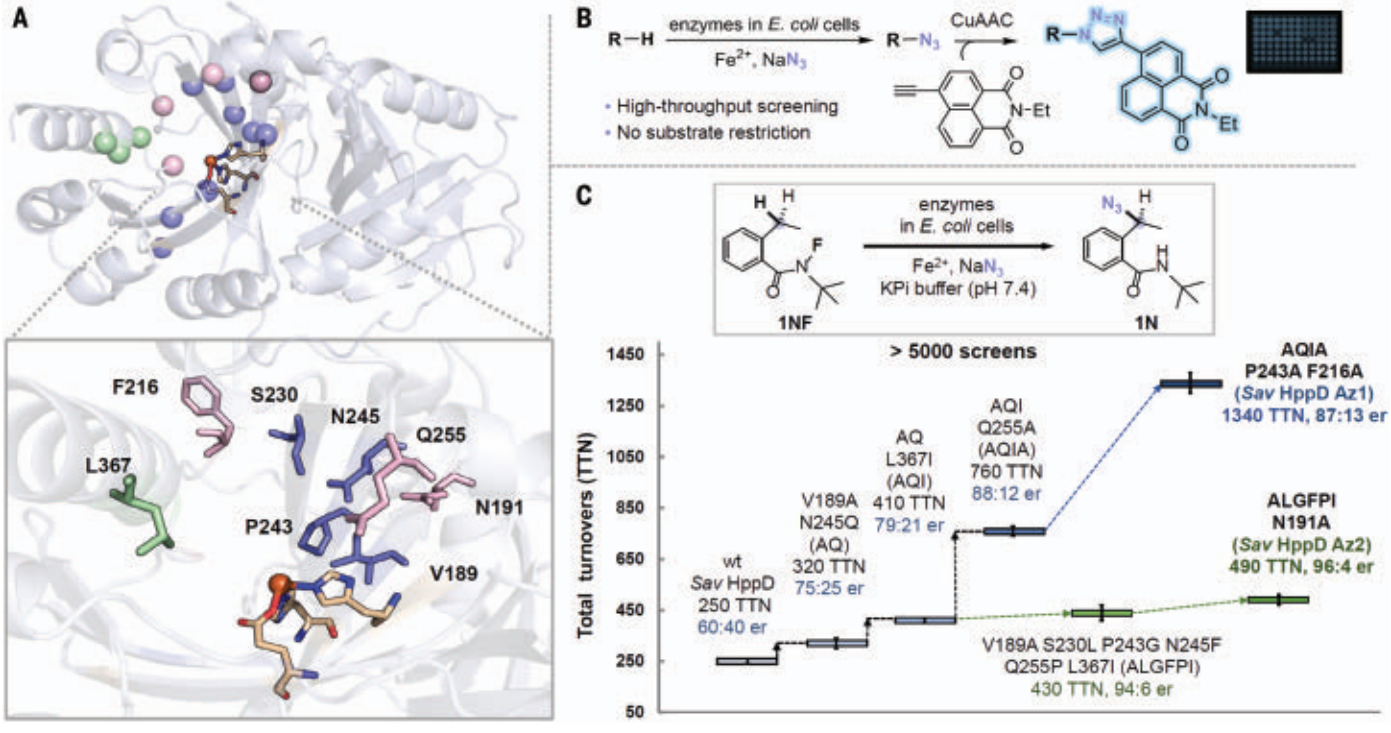

Fig. 2. Directed evolution of nonheme iron enzymes for radical–relay C–H azidation. (**A**) Protein residues selected for mutagenesis. Pink: loop residues surrounding the active site (N191, F216, Q255, and F359); green: residues on the C-terminal α helix (K361, L367, and N363); blue: residues on the β barrel of the C-terminal domain (V189, S230, P243, N245, Q269, Q334, F336, and R353) (PDB: 1T47). (**B**) A high-throughput screening platform for detection of enzymatic azidation products. (**C**) Representative variants identified during the directed evolution of *Sav* HppD. Experiments were performed at the analytical scale by using suspensions of *Escherichia coli* (*E. coli*) cells expressing *Sav* HppD variants (OD_{600} = 10), 10 mM substrate **1NF**, 25 mM NaN_3, 2.5 mM Fe^{2+} in KPi buffer (pH 7.4) at room temperature under anaerobic conditions for 24 hours (table S2).

N–F activation step and the enantio-determining azide rebound step as revealed by molecular dynamics (MD) simulation (fig. S18). In this regard, we reevaluated some of the libraries with chiral HPLC and performed additional rounds of evolution aided by computational modelling (for details see figs. S13 and S14). We found a septuple mutant *Sav* HppD V189A N191A S230L P243G N245F Q255P L367I (denoted as *Sav* HppD Az2) that showed an enantioselectivity of 96:4 e.r. and 490 TTN. Kinetic analyses with purified enzymes showed that the Az1 variant exhibited a 4.1-fold increase in k_{cat} and a 1.7-fold increase in K_M over the WT enzyme [29.4 min^{-1} (Az1) versus 7.20 min^{-1}

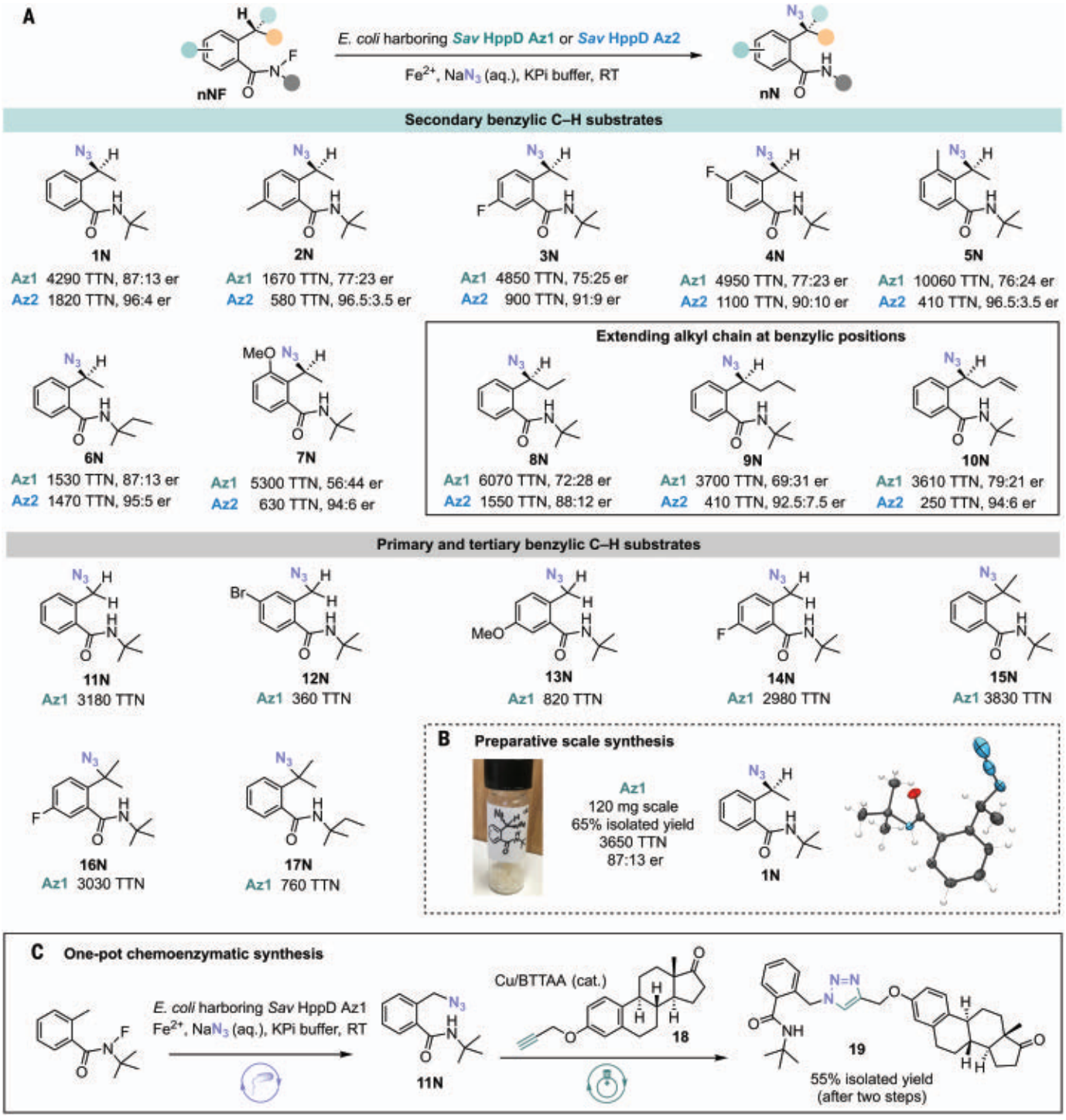

Fig. 3. Substrate scope and synthetic applications of enzymatic C–H azidation via iron-catalyzed radical relay. (**A**) Substrate scope of *Sav* HppD Az1 and *Sav* HppD Az2. Experiments were performed at the analytical scale by using suspensions of *E. coli* expressing *Sav* HppD variants in the KPi buffer (pH 7.4) at room temperature under anaerobic conditions for 24 hours (for detailed conditions see table S3). The absolute configuration of enzymatically synthesized azidation product **1** was determined to be *S* through x-ray crystallography. The absolute configurations of all other azidation products were inferred by analogy. (**B**) Preparative scale synthesis and absolute configuration determination. (**C**) One-pot chemoenzymatic synthesis by in situ derivatization of enzymatic azidation products through CuAAC (for detailed conditions see section IX of the supplementary materials).

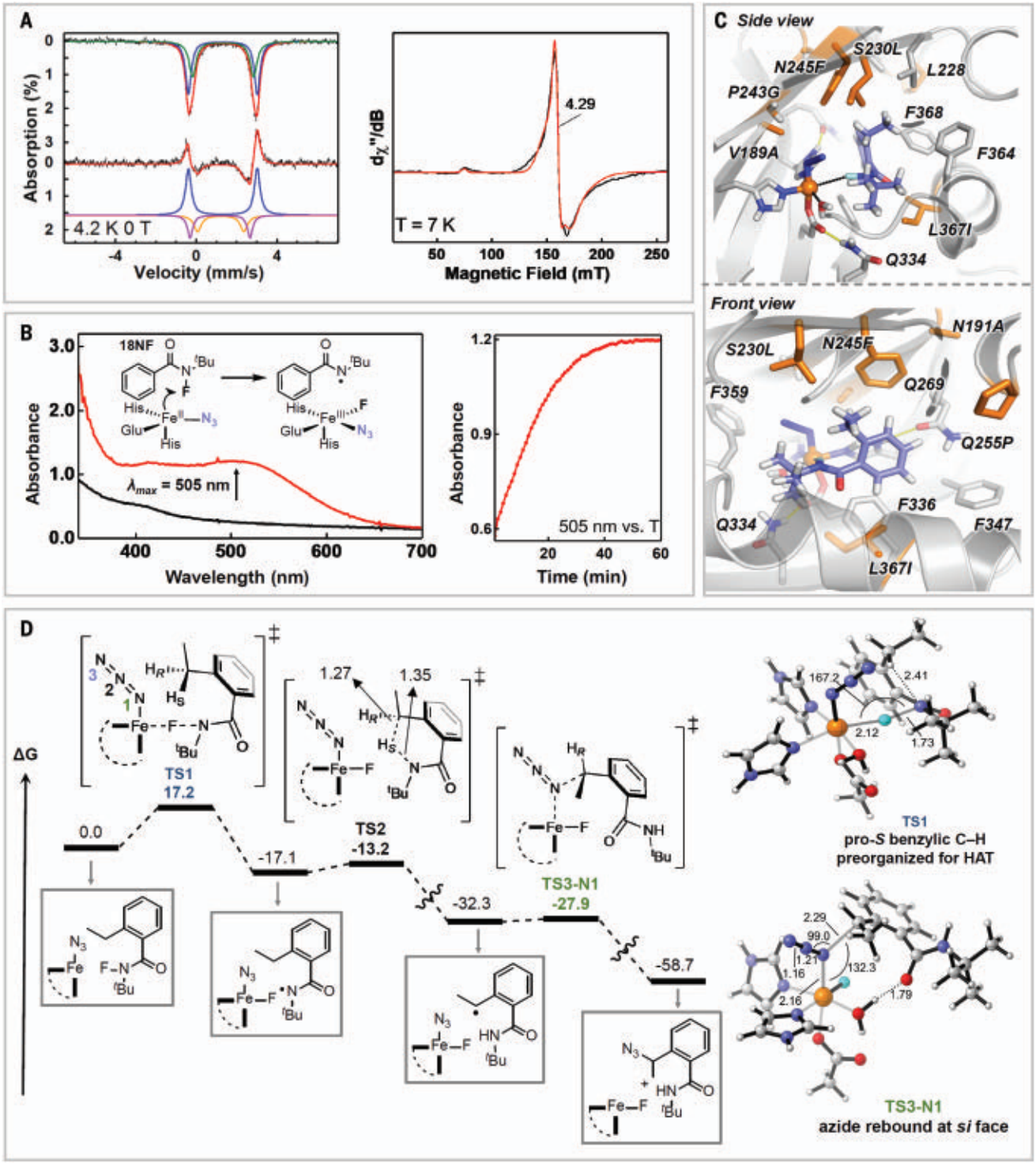

Fig. 4. Spectroscopic and computational studies of the enzymatic radical-relay C–H azidation. (**A**) (Left) Mössbauer spectrum of the *Sav* HppD Az1•Fe(II) complex (top, black) and the spectroscopic changes upon azide addition (bottom, black). The upward and downward absorption peaks represent the spectral components that disappeared or appeared, respectively, after the addition of azide. The colored solid lines represent spectral simulations (see supplementary materials for detailed discussion). (Right) EPR spectrum of *Sav* HppD Az1•Fe(II)•N_3 complex after incubation with **18NF** for 60 min (black) and the spectral simulation (red). (**B**) (Left) Optical absorption spectra of *Sav* HppD Az1•Fe(II)•N_3 complex with **18NF** (black) and after incubation with **18NF** for 60 min (red). The inset shows the reaction scheme. (Right) The time-dependent change in the 505 nm feature. (**C**) Active site arrangement of the Az2 variant with **1NF** substrate bound in a near-attack conformation for N–F activation characterized from MD simulations (see supplementary materials for details; fig. S15). (**D**) Reaction mechanism obtained from DFT calculations employing a truncated active-site model built from MD simulations (see fig. S18 for details) (energies in kcal/mol, distances in Å, and angles in degrees).

(wild type) for k_{cat} and 790 μM (Az1) versus 470 μM (wild type) for K_M], whereas the more enantioselective Az2 variant displayed a 9-fold decrease in k_{cat} (3.39 min^{-1}) and a 6.6-fold decrease in K_M (120 μM). Overall, both variants showed ~2-fold improvement in catalytic efficiency (k_{cat}/K_M) compared with that of the WT enzyme (fig. S3).

With these two final variants in hand, we optimized reaction conditions (table S3) and assayed a range of *N*-fluoroamide substrates to explore the scope and limitation of this reaction (Fig. 3A). *Sav* HppD Az1 generally exhibited higher activity but lower enantioselectivity than *Sav* HppD Az2. The enzymatic reaction tolerated a range of aromatic substitution patterns with total turnovers up to 10,060 and enantiomeric ratio up to 96.5:3.5 (product **5N**). Substrates with an extended alkyl chain at the benzylic position were well tolerated, providing products with moderate-to-good TTNs and enantioselectivity (products **8N** to **10N**). The amide nitrogen substituent also affected enzyme performance as evidenced by a decrease in activity when a larger *N-tert*-amyl group is substituted for the *N-tert*-butyl group (**1N** and **6N**, **15N** and **17N**). We also tried to extend the scope of *N*-radical precursors and replace azide with another halide or pseudohalide anion (scheme S2 and table S4). However, these efforts have not been successful as starting materials were recovered in most cases. As suggested by Mössbauer studies, the inability of our method to incorporate other anionic ligands might be due to much weaker binding of these anions to the Fe(II) center of the enzymes. In a larger-scale reaction, *Sav* HppD Az1 furnished **1N** in 65% isolated yield at a 120-mg scale with undiminished enantioselectivity (Fig. 3B). We also obtained single crystals of **1N** and assigned their absolute configuration as *S* by x-ray crystallography. We also produced primary organic azide **11N** at a preparative scale and subsequently converted it into the estrone derivative **18** through a CuAAC reaction (Fig. 3C). This chemoenzymatic two-step synthesis yielded the triazole product **19** in 55% isolated yield, demonstrating the potential of our platform to produce highly functionalized molecules when used in tandem with biocompatible reactions.

We conducted several mechanistic studies to investigate the catalytic cycle proposed in Fig. 1C. Addition of N_3^- to the *Sav* HppD Az1•Fe(II) complex induced the formation of two quadrupole doublets in the Mössbauer spectrum with isomer shifts (δ) of 1.20 and 1.17 mm/s and quadrupole splittings (ΔE_Q) of 2.29 and 2.97 mm/s, respectively. The observation of two quadrupole doublets may reflect different azide binding configurations to the Fe(II) center (Fig. 4A and figs. S5, S8, and S10; see section X of the supplementary materials for further discussion). We then carried out electron paramagnetic resonance (EPR) measurements on a nitric oxide (NO)-bound *Sav* HppD Az1•Fe(II) complex, which has a prominent g ~ 4 EPR resonance that can be used to monitor the interactions between the substrate and the nonheme iron center (*19*). Adding azide to the *Sav* HppD Az1•Fe(II)•NO complex increased the rhombicity (E/D) of the g ~ 4 signal from 0.014 to ~0.017, and further addition of **1NF** continued the increase in the signal rhombicity (E/D = 0.023). These observations suggest that both N_3 and **1NF** interact with the Fe(II) center of *Sav* HppD Az1 (Fig. 4A, fig. S7, and table S6). To demonstrate that an Fe(III)-N_3 species is involved in the reaction, we incubated *Sav* HppD Az1•Fe(II)•N_3 with an *N*-fluoroamide **18NF** that lacked the reactive benzylic C–H bonds. Slow accumulation of a red species was observed by optical absorption centered at 505 nm (Fig. 4B), which likely originated from the Fe(III)-N_3 ligand-to-metal charge transfer band (*20*–*22*). The EPR signal of this red species was located at g ~ 4.3, further confirming that the iron oxidation state of the formed species is in high spin ($S = 5/2$) Fe(III) (see section X of the supplementary materials). We also observed the formation of a minor stable organic radical centered at g = 2 (scheme S6). Although further studies are needed to characterize this radical species, we speculated that it may be a secondary radical formed through quenching of the initial amidyl radical, as this g = 2 signal was not observed when incubating *Sav* HppD Az1•Fe(II)•N_3 with the model *N*-fluoroamide substrate **1NF** (scheme S6).

We also performed computational modelling to understand the molecular basis of this reaction. Focusing on enantioselective variant *Sav* HppD Az2, MD simulations showed that V189A and P243G generated more space to accommodate iron-bound azide in the active site (Fig. 4C and figs. S8 to S12). In WT *Sav* HppD, N191, N245, and S230 participated in a hydrogen bonding network with Q269 for native substrate positioning (*23*). Introduction of the mutations N191A, S230L, and P243G disrupted this network. These mutations, together with N245F and L367I, created a hydrophobic environment to accommodate *N*-fluoroamide substrate **1NF** for N–F activation and position the ethyl group of the substrate closer to the iron-bound azide in a restricted and preorganized conformation for the subsequent reaction steps (Fig. 4C and fig. S18). Model DFT calculations (Fig. 4D) indicated that the initial N–F activation step ($\Delta G^{\ddagger}$(TS3-N1) = 17.2 kcal·mol^{-1}) was rate limiting and was followed by a fast 1,5-HAT ($\Delta G^{\ddagger}$(TS2) = 3.9 kcal·mol^{-1}) to the N-centered radical. This mechanistic scheme was similar to that reported in an iron-catalyzed fluoroamide-directed fluorination (*24*) and was consistent with the absence of a kinetic isotope effect through measuring independent initial rates for reactions with **1NF** and **1NF**-d_2 (fig. S4). The major conformation of substrate **1NF** in Az2 preorganized the pro-*S* benzylic C–H bond for HAT, with the benzylic carbon projected in proximity to the iron-bound azide (Figs. 4C and fig. S18). Therefore, after 1,5-HAT the resulting C-radical was well positioned for azide recombination in a stereo-retentive manner with low energy barriers ($\Delta G^{\ddagger}$(TS3-N1) = 4.4 kcal·mol^{-1}). Notably, although fluorine transfer had an intrinsically low activation barrier ($\Delta G^{\ddagger}$ = 5.0 kcal·mol^{-1}, fig. S18), steric constraints imposed within the active site likely prevented the substrate repositioning to enable fluorine recombination. Such control of radical rebound through substrate positioning has also been observed in native reactions catalyzed by nonheme iron halogenases, in which the proximity of substrate radicals toward the iron-bound chloride facilitated C–Cl bond formation over C–OH bond formation (*25*, *26*).

The biocatalytic system reported here performs C(sp^3)–H functionalization reactions through a metal-catalyzed radical-relay mechanism, thus expanding the scope of nonheme iron enzyme catalysis. We envision that the merger of various radical generation processes in synthetic chemistry and the capability of metalloenzymes for radical trapping will provide a powerful and general strategy to advance the frontier of radical biocatalysis.

REFERENCES AND NOTES

1. F. H. Arnold, *Angew. Chem. Int. Ed.* **57**, 4143–4148 (2018).
2. U. T. Bornscheuer, *Philos. Trans. R. Soc. A* **376**, 20170063 (2018).
3. K. Chen, F. H. Arnold, *Nat. Catal.* **3**, 203–213 (2020).
4. O. F. Brandenberg, R. Fasan, F. H. Arnold, *Curr. Opin. Biotechnol.* **47**, 102–111 (2017).
5. K. F. Biegasiewicz *et al*., *Science* **364**, 1166–1169 (2019).
6. X. Huang *et al*., *Nature* **584**, 69–74 (2020).
7. P. Ji, J. Park, Y. Gu, D. S. Clark, J. F. Hartwig, *Nat. Chem.* **13**, 312–318 (2021).
8. L. M. Stateman, K. M. Nakafuku, D. A. Nagib, *Synthesis* **50**, 1569–1586 (2018).
9. C. Zhang, Z.-L. Li, Q.-S. Gu, X.-Y. Liu, *Nat. Commun.* **12**, 475 (2021).
10. F. Wang, P. Chen, G. Liu, *Acc. Chem. Res.* **51**, 2036–2046 (2018).
11. B. J. Groendyke, D. I. AbuSalim, S. P. Cook, *J. Am. Chem. Soc.* **138**, 12771–12774 (2016).
12. C. Crowe *et al*., *Chem. Soc. Rev.* **50**, 9443–9481 (2021).
13. M. L. Matthews *et al*., *Nat. Chem. Biol.* **10**, 209–215 (2014).
14. M. E. Neugebauer *et al*., *Nat. Chem. Biol.* **15**, 1009–1016 (2019).
15. C. Y. Kim *et al*., *Nat. Commun.* **11**, 1867 (2020).
16. X. Huang, J. T. Groves, *J. Biol. Inorg* **22**, 185–207 (2017).
17. P. Sivaguru, Y. Ning, X. Bi, *Chem. Rev.* **121**, 4253–4307 (2021).
18. M. Meldal, C. W. Tornøe, *Chem. Rev.* **108**, 2952–3015 (2008).
19. A. M. Orville *et al*., *Biochemistry* **31**, 4602–4612 (1992).
20. C. Bull, J. A. Fee, *J. Am. Chem. Soc.* **107**, 3295–3304 (1985).
21. K. Meyer, E. Bill, B. Mienert, T. Weyhermüller, K. Wieghardt, *J. Am. Chem. Soc.* **121**, 4859–4876 (1999).
22. C. A. Grapperhaus, B. Mienert, E. Bill, T. Weyhermüller, K. Wieghardt, *Inorg. Chem.* **39**, 5306–5317 (2000).
23. J. M. Brownlee, K. Johnson-Winters, D. H. T. Harrison, G. R. Moran, *Biochemistry* **43**, 6370–6377 (2004).
24. E. N. Pinter, J. E. Bingham, D. I. AbuSalim, S. P. Cook, *Chem. Sci.* **11**, 1102–1106 (2020).
25. M. L. Matthews *et al*., *Proc. Natl. Acad. Sci. U.S.A.* **106**, 17723–17728 (2009).
26. L. C. Blasiak, C. L. Drennan, *Acc. Chem. Res.* **42**, 147–155 (2009).

ACKNOWLEDGMENTS

We thank M. Greenberg for helpful discussion and comments on the manuscript. We thank M.A. Siegler and the JHU X-ray Crystallography Facility for analytical support. We also thank K. Tripp and the JHU Center for Molecular Biophysics (CMB) for assistance in performing the CD experiments. **Funding:** Financial support was provided by the Johns Hopkins University, the David and

Lucile Packard Foundation, and National Institute for General Medical Sciences R00GM129419 (to X.H.). Y.G. is thankful for financial support from the National Science Foundation, CHE1654060. This work was also supported by the Generalitat de Catalunya AGAUR Beatriu de Pinós H2020 MSCA-Cofund 2018-BP-00204 project (to M.G.B.), the Spanish MICINN (Ministerio de Ciencia e Innovación) PID2019-111300GA-I00 project (to M.G.B.) and the Ramón y Cajal program via the RYC2020-028628-I fellowship (to M.G.B.), and the Spanish MIU (Ministerio de Universidades) predoctoral fellowship FPU18/02380 (to J.S.). **Author contributions:** X.H. conceived and directed the project. X.H., J.R., and Q.Z. designed the experiments. J.R. performed the screening of the initial enzyme activity. X.H. and A.J.H. developed the high-throughput screening platform. J.R., Q.Z., and A.J.H. performed the directed evolution and results analyses. J.R., Q.Z., V.R., and Z.C. performed the substrate scope study. J.C.P. carried out the spectroscopic studies with Y.G. providing guidance. M.G.B. conceived and directed the computational modelling studies. J.S. and M.G.B. performed the MD simulations. J.S., Y.Y., and M.G.B. performed the DFT calculations. X.H. and J.R. wrote the manuscript with input from all other authors, M.G.B. wrote the computational sections. **Competing Interests:** A provisional patent application covering enantioselective biocatalytic C–N_3 bond formation has been under preparation and will be filed through the Johns Hopkins University with J.R., Q.Z., X.H., A.J.H., and Z.C. as inventors. Authors J.S., J.C.P., V.R., Y.Y., Y.G., and M.G.B. declare no competing financial interests. **Data and materials availability:** All data needed to evaluate the conclusions in this study are present in the main paper or in the supplementary materials. The crystal structure of **1N** is available from the Cambridge Crystallographic Data Centre under reference number CCDC 2163783. **License information:** Copyright © 2022 the authors, some rights reserved; exclusive licensee American Association for the Advancement of Science. No claim to original US government works. https://www.sciencemag.org/about/science-licenses-journal-article-reuse

SUPPLEMENTARY MATERIALS

science.org/doi/10.1126/science.abj2830
Materials and Methods
Figs. S1 to S20
Schemes S1 to S6
Tables S1 to S9
References (*27*–*61*)

Submitted 2 May 2021; resubmitted 14 January 2022
Accepted 14 April 2022
10.1126/science.abj2830

GEOPHYSICS

Optical interferometry–based array of seafloor environmental sensors using a transoceanic submarine cable

G. Marra[1]*, D. M. Fairweather[2], V. Kamalov[3], P. Gaynor[1], M. Cantono[3], S. Mulholland[1], B. Baptie[4], J. C. Castellanos[3], G. Vagenas[1], J.-O. Gaudron[1], J. Kronjäger[1], I. R. Hill[1], M. Schioppo[1], I. Barbeito Edreira[1], K. A. Burrows[1], C. Clivati[5], D. Calonico[5], A. Curtis[2]

Optical fiber–based sensing technology can drastically improve Earth observations by enabling the use of existing submarine communication cables as seafloor sensors. Previous interferometric and polarization-based techniques demonstrated environmental sensing over cable lengths up to 10,500 kilometers. However, measurements were limited to the integrated changes over the entire length of the cable. We demonstrate the detection of earthquakes and ocean signals on individual spans between repeaters of a 5860-kilometer-long transatlantic cable rather than the whole cable. By applying this technique to the existing undersea communication cables, which have a repeater-to-repeater span length of 45 to 90 kilometers, the largely unmonitored ocean floor could be instrumented with thousands of permanent real-time environmental sensors without changes to the underwater infrastructure.

Despite substantial expansion of sensing capabilities, seas and oceans remain mostly unmonitored, limiting our understanding of Earth's structure and its dynamic behavior. However, research on techniques exploiting the sensitivity of optical fiber to environmental perturbations over the past few years has shown that the existing network of submarine cables could potentially be used as seafloor sensors. While backscattering-based techniques, such as distributed acoustic sensing (DAS), provide high sensitivity and spatial resolution, such approaches are currently limited to coastal areas up to 100 km from the shore owing to signal attenuation (*1*–*4*). Previously, we showed that optical interferometric techniques, which detect optical phase changes, provide a solution for monitoring over much longer distances than the working range of DAS, but at the expense of a lower spatial resolution (*5*). More recently, Zhan *et al*. demonstrated that polarization of light can also be used for environmental sensing over submarine cables up to 10,500 km in length (*6*). However, in both techniques, the measured quantity is the cumulative phase or polarization change over the entire length of the optical fiber cable. Although the detection of earthquakes and ocean waves was successfully demonstrated, measuring the integrated perturbations over the entire cable length has two major limitations. First, the measurement noise floor is set by the background environmental noise integrated over the entire cable length. This limits the detection of smaller-sized earthquakes and other environmental signals of interest. Second, because the cable acts as a single sensor, signals from multiple cables are required to triangulate the location of sources, such as earthquake epicenters (*5*).

Our work overcomes the first limitation and substantially improves on the second by using an optical technique that enables the measurement of environmentally induced optical phase changes over individual sections of the submarine cable rather than its entire length. In doing so, we demonstrate the detection of earthquakes, microseisms, and ocean currents spatially resolved at several locations along the cable. We show that the substantially higher sensitivity achieved by this interferometry-based technique enables the detection of signals that could not be observed when measuring the cumulative optical perturbation across the entire cable. Lastly, we show that, by performing spanwise measurements, a single cable is sufficient to identify the epicentral region of a teleseismic earthquake.

The cable sections correspond to one or more spans between the repeaters used for the amplification of the optical signal along the cable. The technique we used allows for the environmentally induced optical perturbations in each cable section to be measured independently, effectively converting a submarine cable into an array of fiber-based sensors. The number of sensors can be as high as the number of repeater-to-repeater cable spans. For an intercontinental link, such as the one we used, the number of spans can exceed 100. The technique we present has the potential to transform our Earth-monitoring capabilities, as the currently greatly undersampled seafloor could be instrumented with thousands of interferometry-based sensors without modifying the existing submarine telecommunication infrastructure. Crucially, although in our work we used a research-grade ultrastable laser, we show that more compact and lower cost narrow-linewidth telecommunications lasers could also be used with limited or no loss of sensitivity. This feature makes our technique highly scalable toward potential conversion of the existing subsea cable infrastructure into a global network of environmental sensors.

We achieved an array of sensing elements by exploiting the architecture of repeaters in modern submarine cables. These repeaters often include a high-loss loop back (HLLB) path that enables a small fraction of the transmitted light to be returned to the transmitting end via the second fiber of the fiber pair (Fig. 1). On many

[1]National Physical Laboratory (NPL), Teddington, UK. [2]School of GeoSciences, University of Edinburgh, Edinburgh, UK. [3]Google LLC, Mountain View, CA, USA. [4]British Geological Survey, Edinburgh, UK. [5]Istituto Nazionale di Ricerca Metrologica (INRIM), Turin, Italy.
*Corresponding author. Email: giuseppe.marra@npl.co.uk

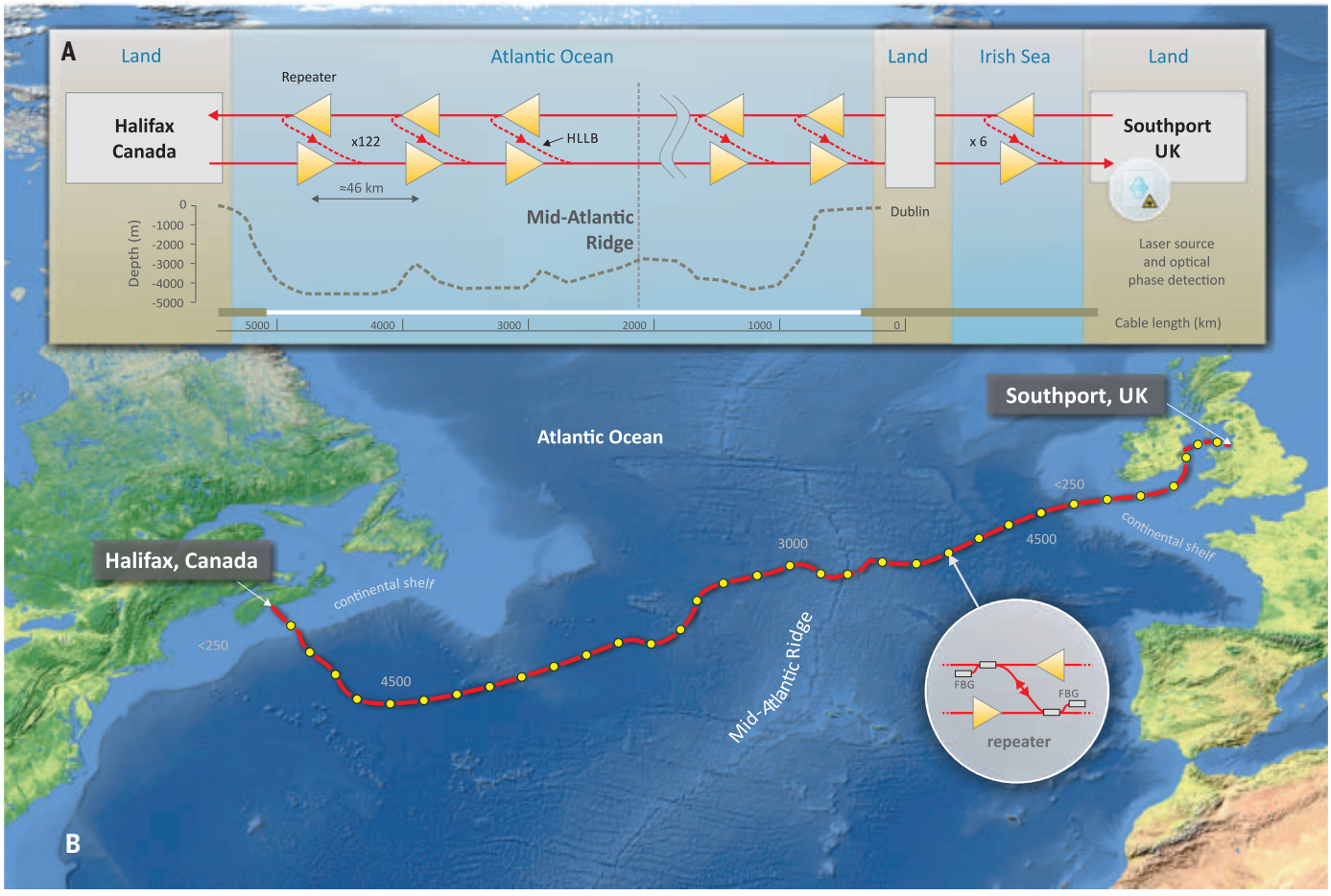

Fig. 1. Map and details of the UK-Canada submarine link. (**A**) Illustration of the high-loss loop back (HLLB) architecture and cable bathymetry. (**B**) Map of the UK-Canada submarine cable. The actual number of repeaters (128) was reduced in the figure for illustration purposes. Each repeater has a pair of fiber Bragg grating (FBG) reflectors.

cables, the return path is implemented by using fiber Bragg gratings (FBGs), acting as narrow-band reflectors (fig. S1A). These return paths are used by the cable operator to periodically check the health of the optical amplifiers (*7*). These checks are typically performed on a schedule or if there is a malfunction, leaving these channels unused most of the time. By injecting infrared light from an ultrastable laser source and performing high-precision interferometric measurements of the signal returned by the HLLBs, we extracted the round-trip (loop-back) accumulated optical phase changes in the fiber between the transmitter end of the cable and the chosen repeaters. To localize the perturbations to cable sections between two or multiple repeaters, we computed the difference between loop-back signals. As the wavelength of the FBG reflectors is the same for all HLLBs, we used an optical technique called optical frequency domain reflectometry (*8*), whereby the frequency of the light source is swept such that the loop-back signal from each repeater can be separated in the frequency domain. This technique is used in some Rayleigh scattering–based fiber sensing applications (*9*). However, in our test, we did not use the scattered light from the fiber inhomogeneities but rather the signal returned by the FBG-based reflector in the HLLBs. This resulted in a returned signal that was orders of magnitude higher in amplitude than from back-scattering. The frequency-swept laser light was injected into the forward path of the submarine cable. The light returned at the transmitter, which consisted of the overlap of the returned light from each repeater, was combined on a photodetector with the output of the swept laser. Here, a series of radio frequency signals was obtained, where each frequency identifies a different repeater with frequency proportional to the round-trip time (fig. S2). Each loop-back beat note was spectrally filtered and its phase, relative to that of the local laser source, was measured with a phase meter.

We tested this technique on a 5860-km-long intercontinental submarine optical fiber link between the UK and Canada. The link consists of two cables: a 248-km-long cable from Southport, UK, to Dublin, Ireland, and a 5612-km-long cable from Dublin to Halifax, Canada. A total of 128 optical repeaters are installed on the link, and the average span between them is 46 km. Our experimental setup allowed us to simultaneously measure loop-back signals from up to 12 repeaters at a time, which could be selected. The hardware upgrades required to extend the monitoring capability to the full number of spans between repeaters are shown in fig. S3. Because of temperature-induced polarization changes in the cable, the signal-to-noise ratio (SNR) of some of the available loop-back signals could temporarily become insufficient for the frequency counter to perform a correct measurement. In our tests, on average, seven to nine loop-back signals exhibited sufficient SNR. Moreover, the SNR of the returned signal degraded because of the accumulation of amplified spontaneous emission noise of the optical amplifiers for repeaters increasingly

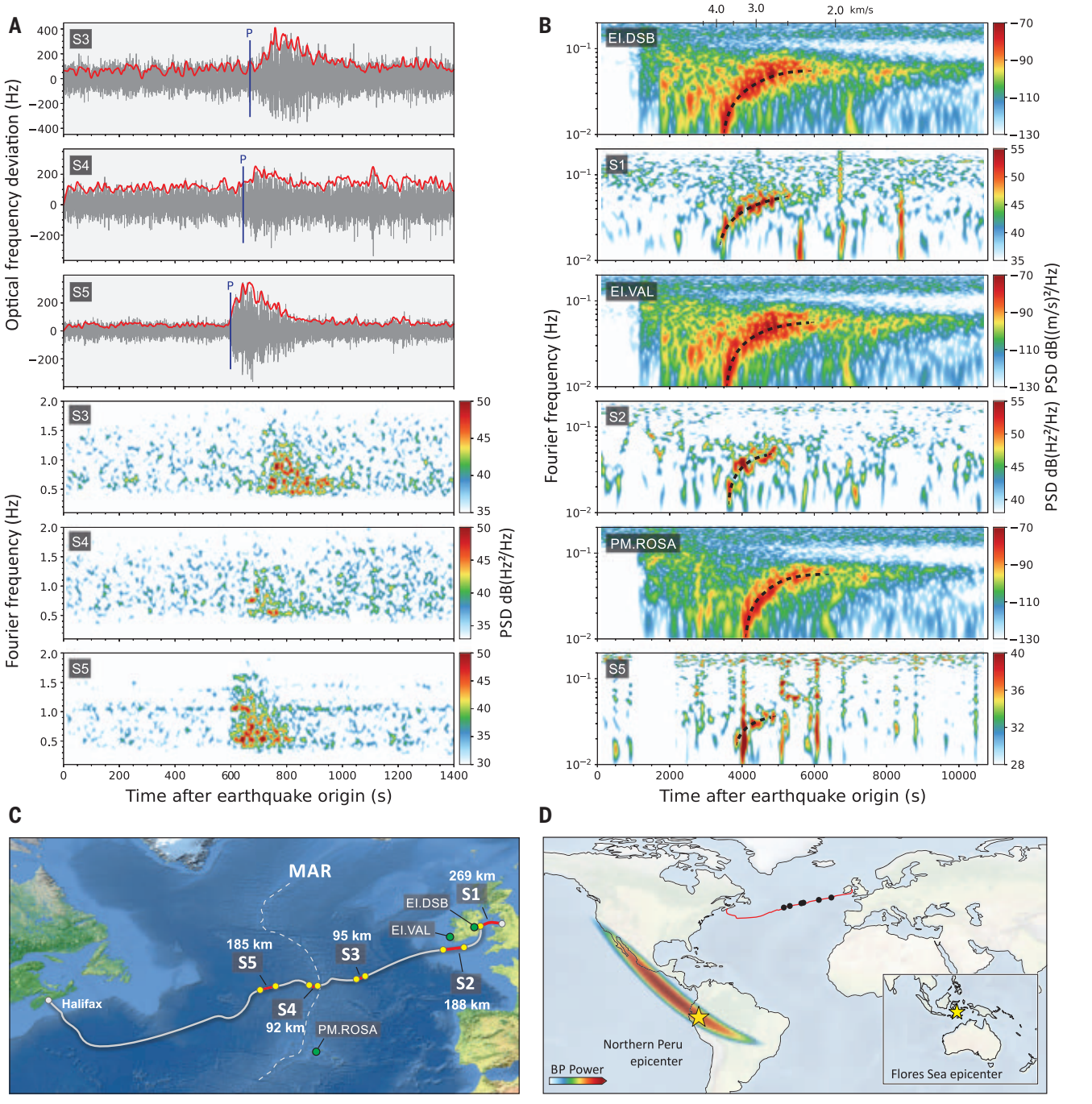

Fig. 2. Earthquake detections on submarine cable spans. (**A**) Time series and spectrograms of the optical frequency deviation induced by the Northern Peru earthquake detection. Vertical blue lines show the theoretical P wave arrival time. (**B**) Spectrograms of the Flores Sea earthquake detected by the cable sections and compared with their nearest seismic stations on land. The dashed black lines on the spectrograms track the surface wave group velocity dispersion. As a reference, we show the group velocity scale for station EI.DSB (Dublin, Ireland, Irish National Seismic Network). EI.VAL, Valentia, Ireland, Irish National Seismic Network; PM.ROSA, Rosais, Azores, Portugal, Portuguese National Seismic Network. (**C**) Map of the cable sections used for data displayed in (A) and (B) and location of the seismometers considered in (B). (**D**) Geographical area for the epicenter location for the Northern Peru earthquake, obtained by back-projection. The heatmap represents the probability of the epicenter location, with warm colors representing a higher probability. The stars indicate the event epicenters, as reported by the Global Centroid Moment Tensor earthquake catalog (*19*, *20*), and the black dots show the locations of the six cable sections used for the back-projection (*10*).

distant from the transmitting end. In our tests, we obtained signals with sufficient SNR from repeaters at a cable distance up to 3100 km. As this is more than half of the cable length, monitoring of all the submarine cable spans could be achieved by also measuring from the Canadian end. Both the polarization-induced degradation of the signal and the range of usable loop-back signals can be, respectively, eliminated and extended with further upgrades (*10*). We also successfully tested our technique while data traffic was present on other channels available in the fiber pair. This demonstrates the compatibility of our technique with standard optical communication technology,

which is a crucial prerequisite for its wide application over the submarine telecommunication network.

We show the detection of two earthquakes on multiple submarine cable spans, the Northern Peru moment magnitude (M_w) 7.5 earthquake (28 November 2021) and the Flores Sea M_w 7.3 earthquake (14 December 2021), respectively (Fig. 2, A and B). We detected the Northern Peru earthquake on six of the nine sections of the cable being tested. We plotted a spectrogram and time series of the signals detected by three of these sections (Fig. 2A). The signals and location of the additional six spans are shown in fig. S4. The spectrograms display the temporal evolution of the power spectral density (PSD) of the frequency fluctuations of the optical signal, induced by environmental perturbations, over the cable section that is being measured. For all the data shown in this work, we choose to display the optical frequency deviation rather than phase deviation, as we experimentally find that this allows us to better visualize notable features in the detected signals. Several factors can contribute to the amplitude of the observed waveform, including the

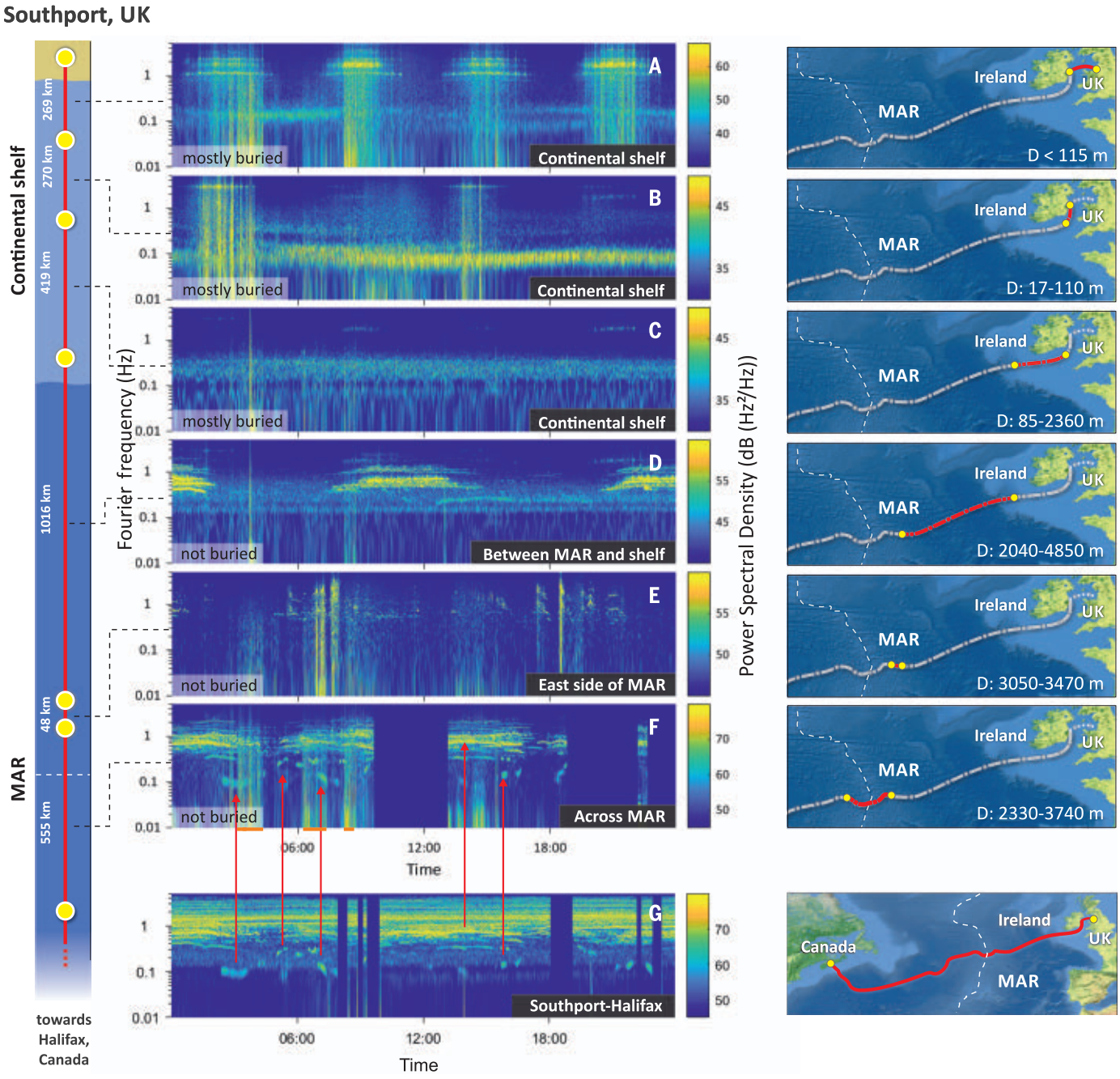

Fig. 3. Environmental noise detected by different sections of the trans-Atlantic cable. (**A** to **F**) Environmental noise detected on continental shelf, deep ocean, and Mid-Atlantic Ridge sections of the cable. (**G**) Environmental noise detected on the full link. Data with insufficient SNR was removed. The range of the color bar of each spectrogram is adjusted to best visualize the detected signals. The impulsive noise in the spectrograms corresponding to the time marked by the short horizontal orange lines at the bottom of (F) is due to glitches caused by temporary issue with the laser locking setup and not to environmental noise on the seafloor. D, depth.

earthquake fault geometry, the three-dimensional heterogeneity of the seismic structure between the fault and cable, the coupling of the cable to the external environment, and the length of the fiber. Further tests on a larger number of spans and events will allow better characterization of the weight of each contribution. From the time lag between envelopes of the detected teleseismic P waves (Fig. 2A) and using a simple back-projection (BP) approach (*10*), we were able to resolve the epicentral location of the seismic event (Fig. 2D).

The Flores Sea earthquake was detected on five of the nine cable sections being tested (fig. S7). The spectrogram of the optical frequency deviations (Fig. 2B) induced by the seismic wave on the S1, S2, and S5 cable sections (Fig. 2C) is shown in comparison with the closest available seismic station on land. Although the P wave arrival is not visible on the span data, the surface wave dispersion is clearly resolved and shows very good agreement with that measured by land seismometers. In addition to the measurements on separate sections of the cable, we also measured the optical frequency changes on the entire UK-Canada cable on a separate channel of the same fiber pair. We performed this measurement by connecting the fiber pair together at the Halifax end, such that we obtained a return signal in Southport after a 11,720-km-long round trip. We stress that in this arrangement the signal does not go through the HLLBs but forward-propagates for the entire length of the cable, as in our previous work (*5*). Whereas the surface wave of the Flores Sea earthquake was also visible in the full-cable measurement (fig. S7), the Northern Peru earthquake was not detected (fig. S4). This is because the detected surface waves from the Flores Sea signal had components between 0.01 and 0.1 Hz, which we measured to be a relatively low noise frequency range on the seafloor, whereas the detected body waves from the Northern Peru signal had components in the 0.1 to 5 Hz range, which is considerably noisier. The detection of the Northern Peru earthquake therefore demonstrates the substantially better detection threshold achieved with spanwise measurements, as the background environmental noise on the other parts of the cable does not contribute to the measurement noise floor.

We show the spectrogram of the environmental noise measured by different sections of the intercontinental submarine cable from the cable landing station (CLS) in Southport to the Mid-Atlantic Ridge (MAR) on 21 October 2021 (Fig. 3). On the first 269-km cable section, which crosses the Irish Sea floor, we observed narrow-band components in the 1 to 5 Hz range that repeated approximately every 6 hours (Fig. 3A). This periodic pattern is synchronous with tidal currents in the Irish Sea, and their amplitude correlates well with the neap/spring cycle, as shown by a longer dataset in Fig. 4A. We speculate that the observed signals arise from "strumming" of exposed cable sections or pressure changes

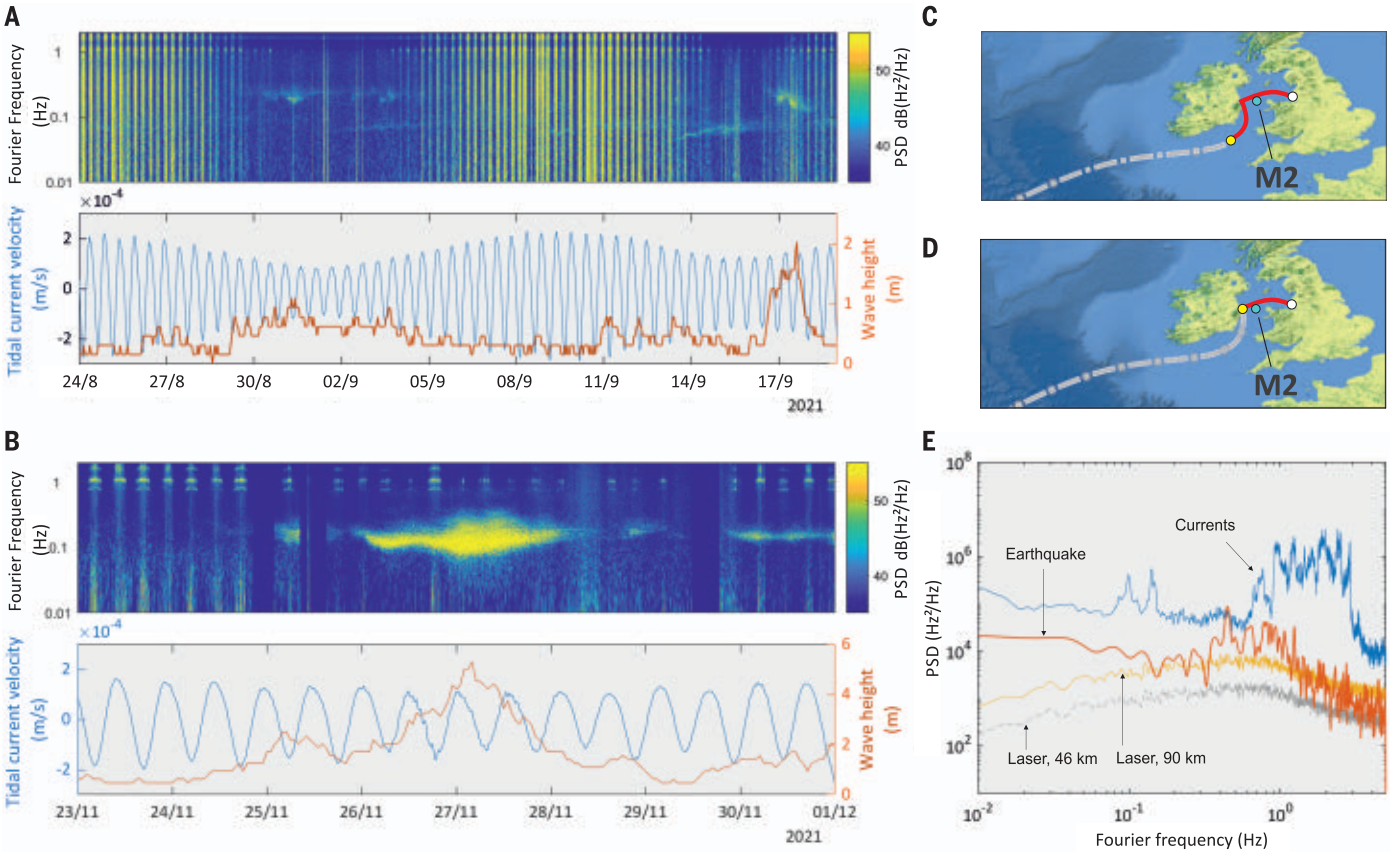

Fig. 4. Correlation of detected signals on cable spans with wave height and tidal currents. (**A**) Spectrogram of the frequency changes detected on the span shown in (C) compared with wave height measured at the M2 buoy in the Irish Sea and tidal current velocity measured by the Dublin Port tide gauge, showing a high degree of correlation. (**B**) Storm detected on the span shown in (D) in late November 2021 and correlation with water levels and tidal current velocity measured in the Irish Sea. (**C** and **D**) Maps of the cable sections used and M2 buoy. (**E**) Comparison between the power spectral density of environmental signals (earthquake and currents) and the calculated measurement noise floor that would be obtained if an off-the-shelf telecommunication narrow-linewidth laser, instead of research-grade laser, were used on a 46-km and 90-km span (*10*).

induced by the tidal currents. We also observed these periodic signals on the second section close to the southeastern coast of Ireland (Fig. 3B), although they were less pronounced, and a strong microseismic component in the 0.07 to 0.15 Hz range. The latter feature was likely caused by the coupling of ocean wave energy to the shallow seafloor.

On the cable section that extends from the Irish coast to the end of the continental shelf, where the bathymetry is consistently flat, we observed a drop in the environmental noise level of up to 30 dB (Fig. 3C and fig. S8). On the fourth section (Fig. 3D), extending from the end of the continental shelf to the MAR area, we detected excess noise between 0.5 and 1.5 Hz, this time with a 12-hour repeating pattern, which we attribute to tidal currents in the MAR area. We also observed a large increase in the detected noise as the cable approaches and crosses the MAR (Fig. 3, E and F). We attribute this to the interaction of ocean currents with the changing MAR bathymetry. Around this area, sea mounts rise from 3740 to 2330 m water depth, with the cable possibly being suspended between irregularities of the seafloor and thus more subject to current-induced movement. By comparing Fig. 3F and Fig. 3G, we can identify several features on the spectrogram of the integrated round-trip signal over the entire Halifax-Southport cable (Fig. 3G) on that of the cable section across the MAR (Fig. 3F), indicating that this area is a large contributor to the overall measured noise. We also observed a high level of correlation of the periodic signals observed on the shallow water sections of the cable with the tidal current velocity (Fig. 4A). We also found a high level of correlation between the signals in the 0.1 to 0.5 Hz range and the wave height measured at the M2 buoy in the Irish Sea (Fig. 4A). We identified Hurricane Larry to be the likely source of the dispersive microseism in the 0.05 to 0.1 Hz frequency range between 13 and 17 September (*10*). We show an 8-day-long dataset in late November 2021 (Fig. 4B), on the cable section shown in Fig. 4D. During this time, an extratropical cyclone moved southward across the UK, and a resulting strong microseismic component was observed on the Southport-Dublin section of the cable. This correlates very well with the increase of average wave height measured at the M2 buoy.

Crucially, in contrast to previous optical interferometric tests, which required a research-grade ultrastable laser (*5*), the technique we have demonstrated here greatly relaxes the requirements on the laser source. Because the optical perturbations are measured over sections of the cable rather than the whole length, the requirement for the laser coherence length is scaled accordingly (*10*). For the submarine cable used in these tests, the coherence length requirement is reduced by approximately a factor of 129, equating to the number of ~46-km-long spans between repeaters and to the CLSs. Although in our experiment we still used a research-grade stabilized laser developed at NPL, we show that commercially available narrow-linewidth lasers could be used instead to detect most of the signals we have presented. An example is in the PSD of the M_w 7.5 Peru earthquake (Fig. 4E) detected on the 95-km-long S3 span of Fig. 2C. For comparison, the contribution of the laser instability of a narrow-linewidth telecommunication laser to the measurement noise floor over the same span length is displayed. We also show the PSD of the current-induced noise measured over the 92-km-long S4 span west of MAR, which is up to 30 dB above the expected laser contribution to the noise floor.

By enabling the use of commercially available telecommunication lasers, our technique could easily be scaled up and applied to a large number of cables in the existing submarine network. By converting submarine cables into arrays of environmental sensors, a large network of hundreds or thousands of permanent and real-time seafloor sensors could be implemented without modification of the existing subsea infrastructure. This has the potential to transform our understanding of both shallow and deep processes inside Earth. The ability to record seismic phases in the middle of ocean basins could enable the imaging of previously obscured structures such as mid-ocean ridges and oceanic fault zones, advancing our understanding of the processes that underlie the generation of oceanic crust (*11*) and the mechanisms by which oceanic plates are hydrated (*12*).

The cable sensitivity to water currents could be explored to improve our understanding of deepwater flows (thermohaline circulation), including the proposed slowing down of ocean currents due to rising global temperatures (*13*, *14*). Furthermore, the joint detection of deepwater currents and seafloor pressure changes caused by the passing of ocean waves implies strong potential for tsunami sensing (*15*, *16*). Lastly, while more research is needed to characterize long-term measurement drifts (*10*), the sensitivity of the optical cables to temperature could be explored for climate change research (*17*, *18*).

REFERENCES AND NOTES

1. E. F. Williams *et al*., *Nat. Commun.* **10**, 5778 (2019).
2. N. J. Lindsey, T. C. Dawe, J. B. Ajo-Franklin, *Science* **366**, 1103–1107 (2019).
3. Z. J. Spica *et al*., *Geophys. Res. Lett.* **47**, e2020GL088360 (2020).
4. E. F. Williams *et al*., *Lead. Edge* **40**, 576–583 (2021).
5. G. Marra *et al*., *Science* **361**, 486–490 (2018).
6. Z. Zhan *et al*., *Science* **371**, 931–936 (2021).
7. N. S. Bergano *et al*., in *Undersea Fiber Communication Systems*, J. Chesnoy, Ed. (Academic Press, ed. 2, 2016), pp. 427–430.
8. W. Eickhoff, R. Ulrich, *Appl. Phys. Lett.* **39**, 693–695 (1981).
9. Z. Ding *et al*., *Sensors* **18**, 1072 (2018).
10. Materials and methods are available as supplementary materials.
11. R. C. Searle, A. V. Bralee, *Geochem. Geophys. Geosyst.* **8**, Q05015 (2007).
12. C. M. Eakin, C. A. Rychert, N. Harmon, *J. Geophys. Res. Solid Earth* **123**, 1736–1751 (2018).
13. J. R. Toggweiler, R. M. Key, in *Encyclopedia of Ocean Sciences*, J. H. Steele, Ed. (Academic Press, 2001), pp. 2941–2947.
14. J. M. Gregory, R. Tailleux, *Clim. Dyn.* **37**, 893–914 (2011).
15. A. B. Rabinovich, M. C. Eblé, *Pure Appl. Geophys.* **172**, 3281–3312 (2015).
16. R. E. Thomson *et al*., *Geophys. Res. Lett.* **38**, L11701 (2011).
17. W. Wu, Z. Zhan, S. Peng, S. Ni, J. Callies, *Science* **369**, 1510–1515 (2020).
18. C. S. Meinen, R. C. Perez, S. Dong, A. R. Piola, E. Campos, *Geophys. Res. Lett.* **47**, (2020).
19. A. M. Dziewonski, T.-A. Chou, J. H. Woodhouse, *J. Geophys. Res.* **86**, 2825–2852 (1981).
20. G. Ekström, M. Nettles, A. M. Dziewonski, *Phys. Earth Planet. Inter.* **200–201**, 1–9 (2012).
21. G. Marra *et al*., Interferometric array data for UK-Canada seafloor cable v1.0 Zenodo (2022); https://doi.org/10.5281/zenodo.6405431.

ACKNOWLEDGMENTS

We thank J. Tunesi and R. M. Godun (NPL) for careful reading of the manuscript and S. Robinson for useful discussions. We thank the NPL IT team for help setting up the NPL-Southport remote access capabilities. We thank EXA Infrastructure for providing access to the submarine cable. We thank U. Hölzle, B. Koley, and V. Vusirikala (Google LLC) for support and discussions, and D. Lloyd, M. Cox, T. Dickenson, M. Wildman, L. Taylor, and A. Walsh (EXA Infrastructure) and T. Aydin (Google LLC) for support on setting up the experiments on the UK-Canada cable. **Funding:** NPL: This work was supported by an ISCF Metrology Fellowship grant and as part of the National Measurement System Programme provided by the UK government's Department for Business, Energy and Industrial Strategy (BEIS), and by an Award from the National Physical Laboratory's Directors' Science and Engineering Fund. University of Edinburgh: This work was supported by the Engineering and Physical Sciences Research Council Doctoral Training Project EP/T517884/1. British Geological Survey: This work was funded by the Natural Environment Research Council (NERC). INRIM: This project received funding from the European Union's Horizon 2020 research and innovation programme under grant 951886 (CLONETS-DS). **Author contributions:** G.M., V.K., M.C., and D.C. planned and designed the work. G.M., S.M., and P.G. designed the experimental setup. P.G., S.M., G.V., J.-O.G., I.B.E., M.S., I.R.H., and G.M. built the experimental setup. G.M., P.G., and J.-O.G. conducted the experiments. G.M., J.K., C.C., and D.C. provided frequency metrology expertise. G.M., D.M.F., B.B., and J.C.C. prepared the initial draft, and all authors critically reviewed and approved the manuscript. D.M.F., A.C., B.B., J.C.C., G.M., V.K., M.C., and K.A.B. analyzed the data. **Competing interests:** A UK priority patent application has been filed in relation to this work. **Data and materials availability:** All data are available at Zenodo (*21*).

License information: Copyright © 2022 the authors, some rights reserved; exclusive licensee American Association for the Advancement of Science. No claim to original US government works. https://www.science.org/about/science-licenses-journal-article-reuse.

This research was funded in whole or in part by the UK Engineering and Physical Sciences Research Council under grant EP/T517884/1. The authors will make the Author Accepted Manuscript (AAM) version available under a CC BY public copyright license.

SUPPLEMENTARY MATERIALS

science.org/doi/10.1126/science.abo1939
Materials and Methods
Supplementary Text
Figs. S1 to S13
References (*22*–*31*)

Submitted 26 January 2022; accepted 11 April 2022
10.1126/science.abo1939

IMMUNOLOGY

Universal antigen encoding of T cell activation from high-dimensional cytokine dynamics

Sooraj R. Achar[1]†, François X. P. Bourassa[2]†, Thomas J. Rademaker[2]†, Angela Lee[1], Taisuke Kondo[3], Emanuel Salazar-Cavazos[1], John S. Davies[4], Naomi Taylor[3], Paul François[2]*, Grégoire Altan-Bonnet[1]*

Systems immunology lacks a framework with which to derive theoretical understanding from high-dimensional datasets. We combined a robotic platform with machine learning to experimentally measure and theoretically model CD8$^+$ T cell activation. High-dimensional cytokine dynamics could be compressed onto a low-dimensional latent space in an antigen-specific manner (so-called "antigen encoding"). We used antigen encoding to model and reconstruct patterns of T cell immune activation. The model delineated six classes of antigens eliciting distinct T cell responses. We generalized antigen encoding to multiple immune settings, including drug perturbations and activation of chimeric antigen receptor T cells. Such universal antigen encoding for T cell activation may enable further modeling of immune responses and their rational manipulation to optimize immunotherapies.

The design of immunotherapeutic tools may be enhanced by quantitative approaches tackling multidimensional immune responses (*1*). Although high-dimensional snapshots of immune cells are routinely acquired (*2*–*4*), they are often ill suited to elucidate the time-dependent processes of immune responses. For instance, expression of the Programmed Cell Death–1 (PD-1) protein correlates with either T cell activation or exhaustion depending on the timing and context (*4*). Such complexity stems from the multivariate responses triggered by multiple ligands (antigens) engaging a monogenic T cell receptor (TCR) (Fig. 1A). Downstream responses drive distinct patterns of activation dynamics encoding different stimuli using feed-forward processing (*5*, *6*).

We set out to robotically generate high-precision, multidimensional kinetic data of T cell activation, and applied supervised machine-learning approaches (*7*) to learn a dynamic encoding of information (*8*, *9*). We focused on modeling the responses of T cells to antigens on target cells. Current understanding of T cell responses defines three functional classes of antigen, non-agonists, weak agonists, and strong agonists, on the basis of their impact on thymic selection: death by neglect, positive selection, and negative selection, respectively (*10*). This observation led to the concept of antigen quality, which has proven useful in predicting successful eradication of viruses or tumors but has been difficult to predict

[1]Immunodynamics Group, Laboratory of Integrative Cancer Immunology, Center for Cancer Research, National Cancer Institute, Bethesda, MD, USA. [2]Department of Physics, McGill University, Montréal, Québec, Canada. [3]Pediatric Oncology Branch, Center for Cancer Research, National Cancer Institute, Bethesda, MD, USA. [4]Genitourinary Malignancies Branch, Center for Cancer Research, National Cancer Institute, Bethesda, MD, USA.
***Corresponding author. Email: paul.francois2@mcgill.ca (P.F.); gregoire.altan-bonnet@nih.gov (G.A.-B.)**
†These authors contributed equally to this work and are listed in alphabetical order.

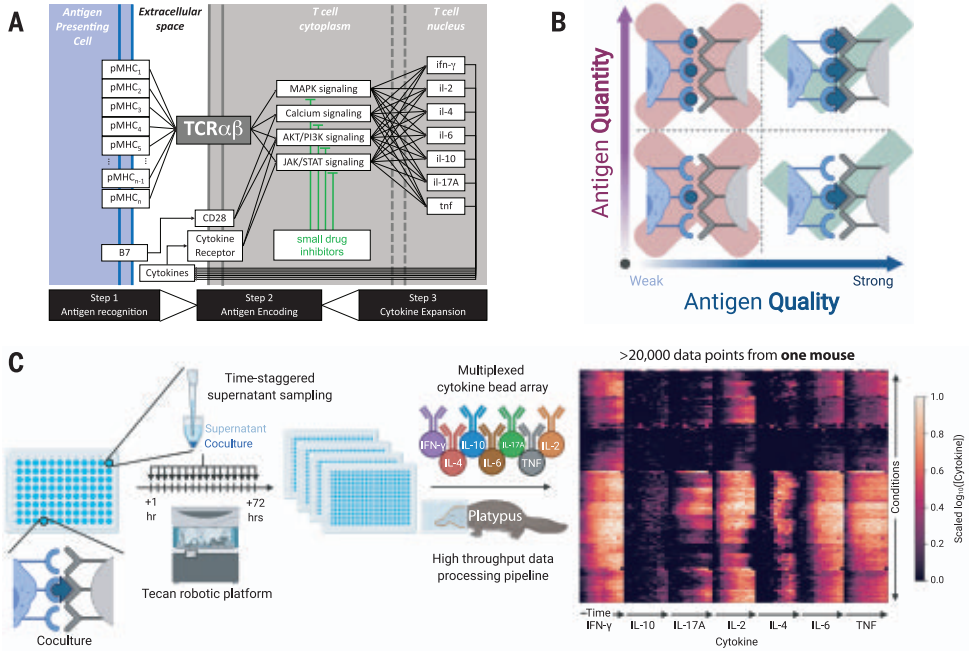

Fig. 1. Robotic platform to quantify the dynamics of antigen-driven activation of T cells. (**A**) The TCRαβ signaling machinery of T cells engages a repertoire of peptide–major histocompatibility complex (pMHC) ligands (antigens), triggers a signal transduction cascade, and activates a functional response (e.g., cytokine secretion). MAPK, mitogen-activated protein kinase; PI3K, phosphatidylinositol 3-kinase; JAK, Janus kinase; STAT, signal transducer and activator of transcription; IFN-γ, interferon-γ; IL, interleukin; TNF, tumor necrosis factor. (**B**) T cells must deconvolve quality and quantity to accurately discriminate between antigens. (**C**) Robotic platform to multiplex immunological settings and dynamic measurements (e.g., cytokines). This platform generates large datasets quantifying the inflammatory outputs generated by T cell activation ex vivo. We used a custom-designed pipeline to compile high-throughput bulk cytokine, surface marker, and single-cell data (see the supplementary materials, section 2.1). (**D**) Single readouts (here IL-2 and IFN-γ) of OT-1 T cell activation at varied time points for different antigenic peptides [SIIVFEKL(V4), SIITFEKL(T4), SIIQFEKL(Q4), and SIINFEKL(N4)] (left) failed to deconvolve antigen quality and quantity no matter the time point (center). This resulted in partial overlap between the amount of secreted cytokines depending on antigen quality and complete confusion depending on antigen quantity (right). (**E**) Mutual information between antigen quality and secreted cytokines combined versus individually.

from antigen sequences (*11*). Estimating antigen quality usually involves measuring the antigen levels triggering 50% of the maximal immune response (EC_{50}) (*10*–*12*). However, antigen quality should be defined as an absolute property because higher quantities of weak antigens do not functionally match low quantities of strong antigens (Fig. 1B) (*13*).

We measured the kinetics of multiple cytokines during T cell activation by different quantities and qualities of antigen (i.e., different peptide sequences). We built a robotic cell culture platform combined with a high-throughput data-processing pipeline (*14*) to multiplex automatic measurements of cytokine concentrations and single-cell activation markers over multiple time points (Fig. 1C and fig. S1). We tested different antigens (SIINFEKL peptide and its variants) recognized by the mouse ovalbumin-specific (OT-1) TCR on $CD8^+$ T cells (*10*, *12*) and found diverse yet overlapping patterns of cellular activation and cytokine secretion (Fig. 1D and figs. S2 and S3). Using mutual information (*15*–*19*), we quantified how well the cytokine dynamics at individual time points correlated to antigen quality independently of quantity and found that over time, these dynamics carried substantially higher information than individual cytokines at a given time point (Fig. 1E and supplementary materials, section 6).

To help explain immune activation, we analyzed and classified these complex dynamics with machine learning. Using the cumulative integral of the log-transformed concentrations of cytokines over time (fig. S6B and movie S1), we trained a neural network that performed supervised classification of cytokine dynamics according to antigen sequences irrespective of antigen quantity (Fig. 2, A and B, and fig. S8). We used a learning architecture with a two-node bottleneck for classification to match our estimate of the dimensionality of our datasets (fig. S6C). This projected the data onto a latent space where, after training, the five-dimensional (5D) cytokine time courses were compressed into 2D trajectories (Fig. 2C). The 2D trajectories separated well according to antigen sequences and were independent of antigen quantity over three orders of magnitude (Fig. 2, A and C). We refer to such well-separated projections in latent space as "antigen encoding" to emphasize how T cell responses are classifiable according to antigen quality (as determined by antigen sequences). This encoding reliably distinguished antigens even at high doses, when other markers typically saturate (Fig. 1D and fig. S11C).

We tested whether 2D antigen encoding preserved the information of the high-dimensional kinetics of the system. We built a nonlinear decoder to reconstruct the entire 5D cytokine dynamics (Fig. 2, D to F, and supplementary materials, section 5) from the 2D latent space, demonstrating that essentially no information was lost. To further test our decoder, we used two antigens that were not included in the initial model training. We compressed the 5D cytokine dynamics spurred by these antigens through our trained network and used the 2D latent space trajectories as inputs to reconstruct the 5D raw data (Fig. 2, E and F). In this way, we could map high-dimensional cytokine data onto our low-dimensional latent space.

We turned to mathematical modeling to derive more biological insight about antigen encoding. We fitted the cytokine trajectories in the latent space with four-parameter ballistic

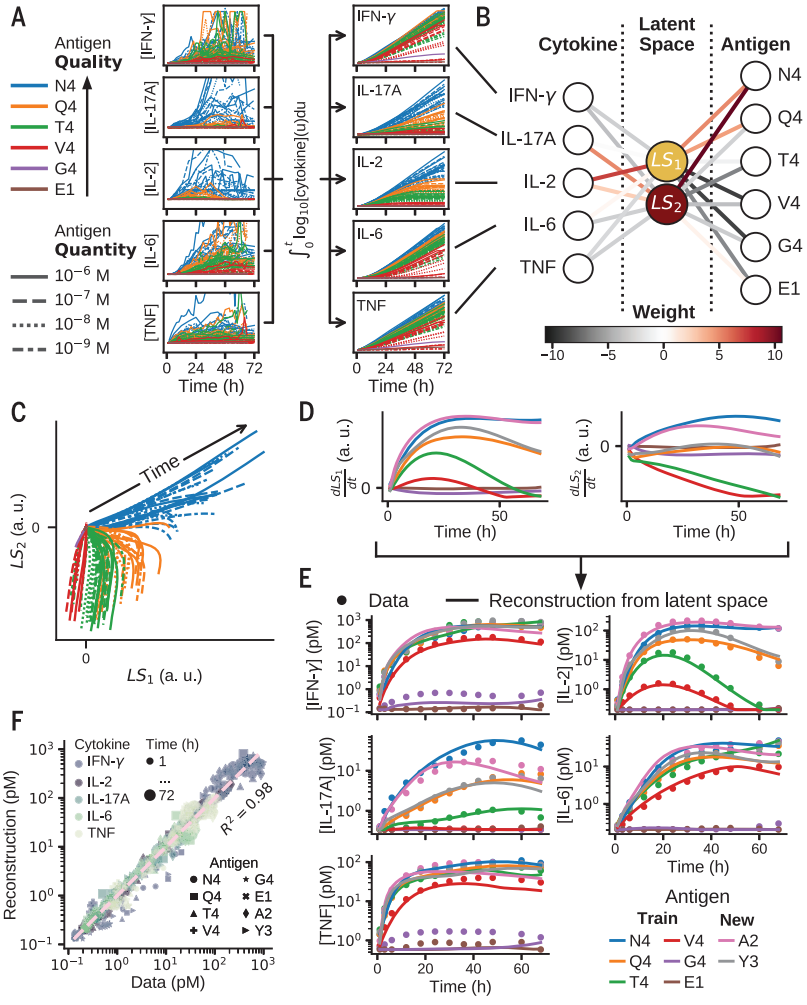

Fig. 2. Antigen encoding from a neural network that compresses the dynamics of T cell activation according to quality independently of quantity. (**A** and **B**) Dynamics of five cytokines for different quality and quantity of OT-1 antigens (left) are preprocessed (A) and classified (B) according to antigen sequences through a trained three-layer neural net with a 2D bottleneck (LS_1,LS_2). (**C**) Time courses of compressed cytokine dynamics in the latent space stratify T cell activation according to antigen sequence (quality) independently of antigen quantity (see movie S1 for data animation). Color and style for each line is the same as in (A). (**D**) Examples of latent space trajectories for different antigen qualities. (**E** and **F**) Nonlinear reconstruction of cytokine time series from latent space trajectories yielded an accurate fit with experimental data (fig. S19) (E), demonstrating completeness of antigen encoding [four peptide antigens are introduced here: EIINFEKL(E1), SIIGFEKL(G4), SIYNFEKL(Y3), and SAINFEKL(A2)] (F).

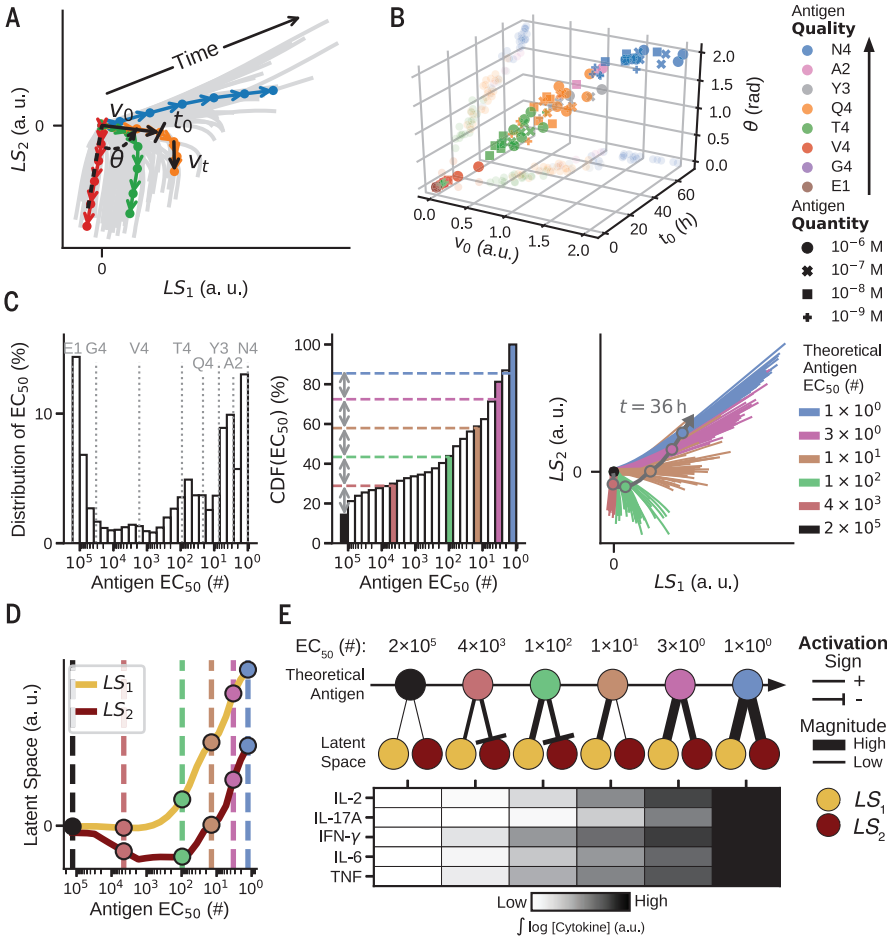

Fig. 3. Quantifying the classes of T cell activation using antigen encoding in latent space. (**A**) Cytokine trajectories in latent space can be fitted with a four-parameter ballistic model. (**B**) Although one parameter (v_t) is constant, the three others (v_0, θ, and t_0) are strongly correlated. a. u., arbitrary units. (**C**) Distribution of EC_{50} (left) that maximizes the mutual information extracted from model parameters (We estimate a channel capacity of ≈2.6 bits; supplementary materials, section 6). By evenly sampling the cumulative distribution function (CDF, center), we found $2^{2.6} \approx 6$ classes of antigen with nonoverlapping latent space trajectories (right). The arrow connects the 36-hour coordinates of trajectories of increasing antigen EC_{50}. (**D**) Latent space coordinates (LS_1,LS_2) at 36 hours as a function of antigen quality as defined by EC_{50}. (**E**) Sketch of the biochemical mechanisms governing antigen discrimination as suggested from the latent space coordinates in (D). Each class of antigen activates positive and negative signals differentially and yields varied patterns of cytokine secretion computed from the decoder (Fig. 2E) and trajectories in (C).

equations comprising an initial activation characterized by an initial speed v_0, followed by a decay (supplementary materials, section 4; Fig. 3A; and movie S1). We discovered strong correlations between the fitted parameters (Fig. 3B) and the EC_{50} measure of antigen quality (fig. S14B). This demonstrated that one parameter (e.g., v_0) was sufficient to describe each trajectory, thus defining antigen quality through a continuum of dynamics in the latent space. Ultimately, we obtained a generative model of cytokine dynamics by combining our nonlinear decoder (Fig. 2, D and E) with our one-parameter model (figs. S21 and S22).

Such parametrization of antigen encoding allowed us to apply information theory (*15*–*19*) to estimate the number of antigen classes that T cells can distinguish. We measured the variability of cytokine kinetics across many replicates and used our continuous model to estimate a theoretical limit of 2.6 bits of information transduced by the TCR pathway (figs. S23 to S26 and supplementary materials, sections 4 and 6). This defined $2^{2.6} \approx 6$ classes of antigens associated with distinct EC_{50} and cytokine dynamics evenly distributed in the latent space (Fig. 3C). Therefore, learning to classify patterns of TCR activation associated with discrete antigen sequences allowed us to build a continuous model of antigenicity subdivisible in at least six nonoverlapping classes compared with the previously described three canonical discrete classes.

The latent space also captured key modalities in terms of biological regulation. The latent space coordinates $(LS_1,LS_2)_{t=36hr}$ varied as a function of antigen quality (EC_{50}) (Fig. 3, C to E). Whereas LS_1 increased monotonically, LS_2 had an inverted bell-shaped dependency. The "decoding" weights in the second layer of the neural network lined up with these dependencies, as expected for antigen classification (fig. S27). Thus, the latent space can be interpreted as a competition between monotonic and non-monotonic pathways, consistent with the adaptive kinetic proofreading (AKPR) model that accounts for T cell antigen discrimination (*13*) and with information optimization in genetic networks (*20*).

We tested antigen encoding in diverse immune settings. We first plotted the parameter v_0 (Fig. 3A) as a function of EC_{50} for both our training and test sets and recovered a log-linear correlation above a minimum threshold (Fig. 4A). Our model of cytokine dynamics yielded a measure of antigen quality, v_0, as faithful as an EC_{50} derived from a functional dose response. We further confirmed the predictive power of v_0 on the following additional immunological settings: (i) two states of differentiation of OT-1 T cells (naïve or pre-activated effector; fig. S28); (ii) different antigen-presenting cells (splenocytes, bone marrow–derived macrophages, and dendritic cells) pulsed with peptides (fig. S29); (iii) different mouse TCR-transgenic T cells (Fig. 4B and fig. S12); (iv) human T cells expressing a TCR transgene (Fig. 4C and fig. S30); and (v) different tumors constitutively expressing antigens (Fig. 4D and fig. S31). Although the latent space may rotate (angle θ; Fig. 3A) according to immune contexts, e.g., when varying the number of T cells (Fig. 4E and fig. S32), in all settings, the structure of the latent space was preserved and v_0 accurately ranked antigens according to their quality. Overall, our model generalized well to infer antigen quality from unseen patterns of immune activation.

We tested whether molecular perturbations (small drug inhibitors, cytokines or antibody blocking) could generate new cytokine dynamics. For most perturbations, the strong correlation between parameters of antigen encoding remained intact, and antigen hierarchy was preserved, albeit with a downshift in apparent antigen quality. However, two types of perturbation (activation of innate signaling and inhibition of cytokine signaling) maximally broke this parameter correlation and generated distinct dynamic patterns, i.e., new classes of T cell activation with potentially new functions (Fig. 4F and fig. S33).

We also investigated T cells genetically engineered to express a chimeric antigen receptor (CAR) against ligands expressed on B cell leukemia (CD19), as used in patients

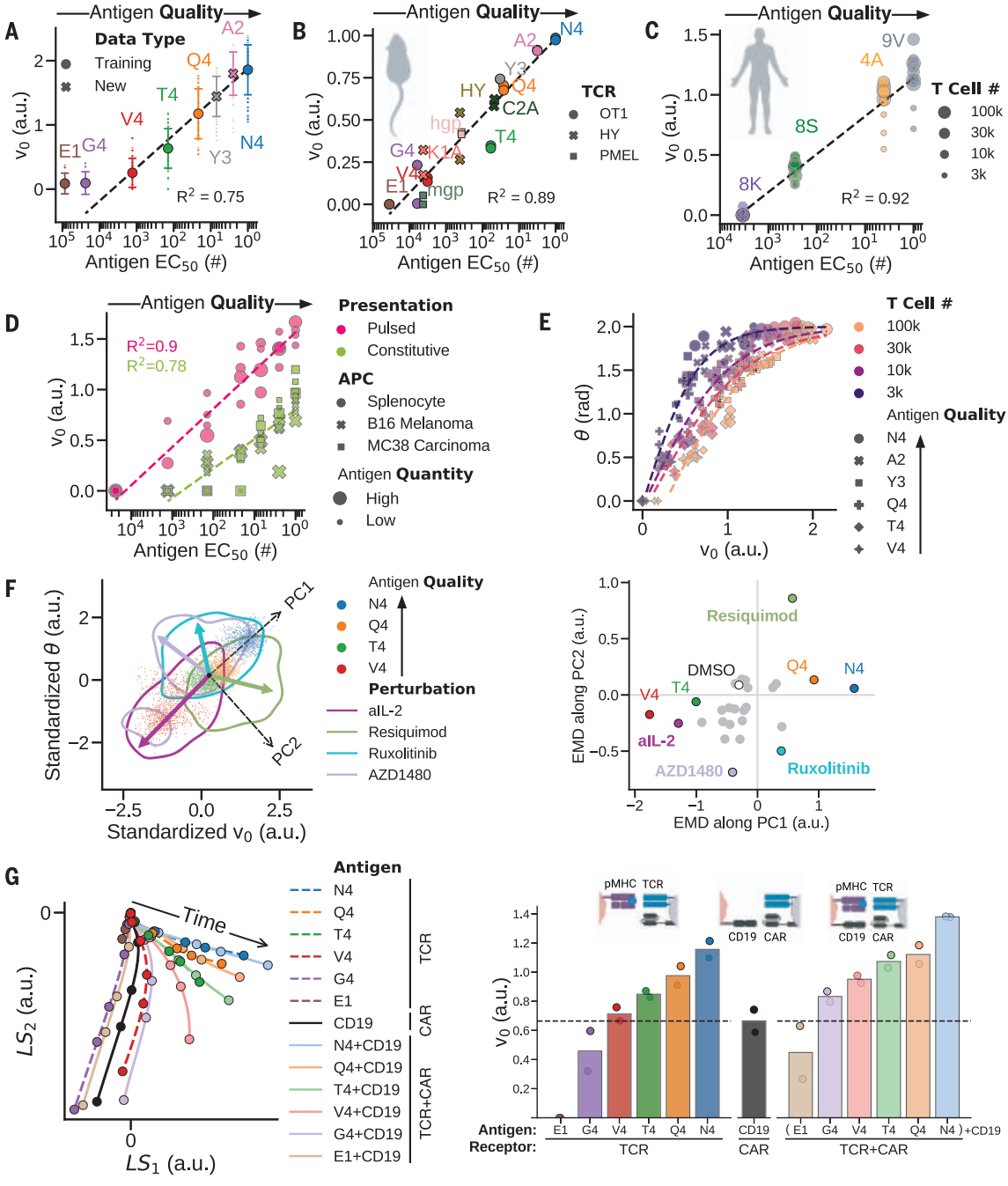

Fig. 4. Antigen encoding to explore diverse immunological settings. (**A**) Testing the ballistic model of the latent space on all OT-1 antigens yielded measurements of v_0 that correlated with their rank (as defined by the EC_{50} of a functional dose response; fig. S12). (**B** to **D**) Antigen encoding learned from naïve OT-1 T cells yields accurate v_0 ranking with different mouse TCR-transgenic T cells (B), with human TCR-transgenic T cells (C), and with OT-1 T cells responding to tumors constitutively expressing antigens (D). (**E**) Antigen encoding captures dependency on T cell numbers in (v_0,θ) space. (**F**) Left: antigen encoding (v_0,θ) of T cell activation under various molecular perturbations. Right: Earth mover's distance (EMD) for individual antigens. PC1 captures the variation in antigen quality (EMD2 = 0). Although most molecular perturbations simply downgraded the apparent antigenicity (EMD1 < 0, EMD2 ≈ 0), JAK inhibitors (AZD1480 and ruxolitinib) severely affected T cell activation (EMD2 < 0) and the TLR7/8 agonist resiquimod boosted it (EMD2 > 0). (**G**) Antigen encoding of anti-CD19 CAR-T cells (left) revealed a pattern of weak activation and antagonism for cytokine responses (right).

with relapsed lymphoma (*21*). The dynamics of cytokines released and consumed by CAR-T cells were similar to the trajectories derived from natural T cells (Fig. 4G, left). CAR-T cells responding to CD19 yielded cytokine dynamics similar to the OT-1 TCR responding to weak agonists such as V4 (Fig. 4G, right), so signaling through CAR may only suboptimally activate T cells. We therefore tested the response of CAR-OT-1 T cells to a mixture of CAR and TCR ligands. Our latent space parametrization then revealed highly nonlinear, hierarchical effects: Weak OT-1 ligands (E1) antagonized CD19, whereas stronger OT-1 ligands dominated the response to CD19. This is consistent with

the AKPR mechanism for T cell signaling with differential effects on positive and negative feedbacks (Fig. 3E) (*13*). Complex antagonism and synergism by weak TCR ligands highlight the importance of fine-tuning CAR-T cells for immunotherapeutic optimization.

Our approach yielded large, multiplexed kinetic measurements and a quantitative model of universal antigen encoding during T cell activation. Whereas classical approaches have qualitatively defined three discrete antigen categories, we rigorously derived a continuous parametrization of antigen quality. We applied information theory to quantify and interpret the phenotypic diversity of T cell activation beyond functional assays taken at a single time point. The universality of the model should prove useful for quantifying and fine-tuning the strength of antigens for immunotherapies and vaccine development (*11*). Thus, robotic platforms combined with machine learning and mathematical modeling provide quantitative tools with which to study high-dimensional biological dynamics and may help to optimize therapeutic strategies.

REFERENCES AND NOTES

1. S. Farkona, E. P. Diamandis, I. M. Blasutig, *BMC Med.* **14**, 73 (2016).
2. P. Gueguen *et al*., *Sci. Immunol.* **6**, eabd5778 (2021).
3. S. Krishna *et al*., *Science* **370**, 1328–1334 (2020).
4. M. Singer *et al*., *Cell* **166**, 1500–1511.e9 (2016).
5. S. S. Shen-Orr, R. Milo, S. Mangan, U. Alon, *Nat. Genet.* **31**, 64–68 (2002).
6. N. Tishby, F. C. Pereira, W. Bialek, The information bottleneck method. arXiv:physics/0004057 [physics.data-an] (2000).
7. B. C. Daniels, I. Nemenman, *Nat. Commun.* **6**, 8133 (2015).
8. M. Behar, D. Barken, S. L. Werner, A. Hoffmann, *Cell* **155**, 448–461 (2013).
9. N. Nandagopal *et al*., *Cell* **172**, 869–880.e19 (2018).
10. M. A. Daniels *et al*., *Nature* **444**, 724–729 (2006).
11. M. Łuksza *et al*., *Nature* **551**, 517–520 (2017).
12. D. Zehn, S. Y. Lee, M. J. Bevan, *Nature* **458**, 211–214 (2009).
13. P. François, G. Altan-Bonnet, *J. Stat. Phys.* **162**, 1130–1152 (2016).
14. S. Achar, G. Altan-Bonnet, "plateypus" (2021); https://doi.org/10.5281/zenodo.5759171.
15. R. S. Ganti *et al*., *Proc. Natl. Acad. Sci. U.S.A.* **117**, 26020–26030 (2020).
16. Y. Tang *et al*., *Nat. Commun.* **12**, 1272 (2021).
17. R. Cheong, A. Rhee, C. J. Wang, I. Nemenman, A. Levchenko, *Science* **334**, 354–358 (2011).
18. J. Selimkhanov *et al*., *Science* **346**, 1370–1373 (2014).
19. A. A. Granados *et al*., *Proc. Natl. Acad. Sci. U.S.A.* **115**, 6088–6093 (2018).
20. M. Bauer, M. D. Petkova, T. Gregor, E. F. Wieschaus, W. Bialek, Trading bits in the readout from a genetic network. arXiv:2012.15817 [q-bio.MN] (2020).
21. W. A. Lim, C. H. June, *Cell* **168**, 724–740 (2017).
22. Latent space and parameterization processing pipeline data for: S. R. Achar *et al*., Universal antigen encoding of T cell activation from high dimensional cytokine dynamics, Zenodo (2022); https://doi.org/10.5281/zenodo.5759168.
23. Theoretical analysis data for: S. R. Achar *et al*., Universal antigen encoding of T cell activation from high dimensional cytokine dynamics, Zenodo (2022); https://doi.org/10.5281/zenodo.5759148.
24. L. McInnes, J. Healy, J. Melville, UMAP: uniform manifold approximation and projection for dimension reduction. arXiv:1802.03426 [stat.ML] (2020)
25. S. V. Stassen *et al*., *Bioinformatics* **36**, 2778–2786 (2020).
26. U. Sahin, Ö. Türeci, *Science* **359**, 1355–1360 (2018).
27. R. Dash *et al*., *Adv. Appl. Bioinform. Chem.* **10**, 11–28 (2017).
28. J. C. Castle *et al*., *Cancer Res.* **72**, 1081–1091 (2012).
29. C. Liu *et al*., *Cell* **184**, 1836–1857.e22 (2021).
30. P. Dierckx, *J. Comput. Appl. Math.* **1**, 165–184 (1975).
31. P. Virtanen *et al*., *Nat. Methods* **17**, 261–272 (2020).
32. S. Dasgupta, C. F. Stevens, S. Navlakha, *Science* **358**, 793–796 (2017).
33. A. A. Alemi, I. Fischer, J. V. Dillon, K. Murphy, Deep variational information bottleneck. arXiv:1612.00410 [cs.LG] (2019).
34. R. Iten, T. Metger, H. Wilming, L. Del Rio, R. Renner, *Phys. Rev. Lett.* **124**, 010508 (2020).
35. F. Rosenblatt, *Psychol. Rev.* **65**, 386–408 (1958).
36. F. Pedregosa *et al*., *J. Mach. Learn. Res.* **12**, 2825–2830 (2011).
37. R. N. Germain, I. Stefanová, *Annu. Rev. Immunol.* **17**, 467–522 (1999).
38. H. H. Mattingly, M. K. Transtrum, M. C. Abbott, B. B. Machta, *Proc. Natl. Acad. Sci. U.S.A.* **115**, 1760–1765 (2018).
39. G. Voisinne *et al*., *Cell Rep.* **11**, 1208–1219 (2015).
40. C. M. Bender, S. A. Orszag, *Advanced Mathematical Methods for Scientists and Engineers I: Asymptotic Methods and Perturbation Theory* (Springer, 1999).
41. J. Theiler, *J. Opt. Soc. Am. A Opt. Image Sci. Vis.* **7**, 1055 (1990).
42. A. Kraskov, H. Stögbauer, P. Grassberger, *Phys. Rev. E Stat. Nonlin. Soft Matter Phys.* **69**, 066138 (2004).
43. B. C. Ross, *PLOS ONE* **9**, e87357 (2014).
44. K. Borgwardt, V. S. Vishwanathan, H.-P. Kriegel, in *Pacific Symposium on Biocomputing 2006: Maui, Hawaii, 3–7 January 2006* (World Scientific, 2006).
45. R. Blahut, *IEEE Trans. Inf. Theory* **18**, 460–473 (1972).
46. M. Razo-Mejia *et al*., *Phys. Rev. E* **102**, 022404 (2020).
47. W. H. Press, S. A. Teukolsky, W. T. Vetterling, B. P. Flannery, *Numerical Recipes in C: The Art of Scientific Computing* (Cambridge Univ. Press, ed. 2, 1992).
48. I. Olkin, *Linear Algebra Appl.* **67**, 201–205 (1985).
49. F. N. Fritsch, R. E. Carlson, *SIAM J. Numer. Anal.* **17**, 238–246 (1980).
50. M. Saito, M. Matsumoto, in *Monte Carlo and Quasi-Monte Carlo Methods 2008*, P. L' Ecuyer, A. B. Owen, Eds. (Springer, 2009), pp. 589–602.
51. L. Devroye, *Non-Uniform Random Variate Generation* (Springer, 1986).
52. F. Grabowski, P. Czyż, M. Kochańczyk, T. Lipniacki, *J. R. Soc. Interface* **16**, 20180792 (2019).

ACKNOWLEDGMENTS

We thank N. Altan-Bonnet, P. Mehta, S. Michnick, G. Trinchieri, and M. Vergassola for detailed comments and suggestions on our manuscript and members of the R. Bosselut, A. Singer, and S. A. Rosenberg laboratories at the National Cancer Institute's Center for Cancer Research (CCR-NCI) for reagents and mice. **Funding:** This work was partially supported by the intramural research program of the NCI (S.R.A., A.L., E.S.-C., T.K., N.T., and G.A.-B.); a NCI Flex Synergy Award to N.T and G.A.-B.; Simons Investigator in Mathematical Modelling of Living Systems, and NSERC Discovery grant awards to P.F.; Fonds de recherche du Québec – Nature et technologies awards to T.J.R. and F.X.P.B.; and a CREATE Complex Dynamics award to F.X.P.B. **Author contribution:** S.R.A., A.L., E.S.-C., and G.A.-B. performed the experimental measurements. F.X.P.B., T.J.R., and P.F. developed the model. S.R.A., F.X.P.B., T.J.R., P.F., and G.A.-B. analyzed the data and wrote the manuscript. T.K., J.S.D., and N.T. contributed key reagents. **Competing interests:** The authors declare no competing interests. **Data and material availability:** Data and processing code have been deposited in Zenodo: Latent space and parameterization processing pipeline codes are available at (*22*) and theoretical analyses codes are available at (*23*). Reagents and mice are available from G.A.-B. upon request. **License information:**

Copyright © 2022 the authors, some rights reserved; exclusive licensee American Association for the Advancement of Science. No claim to original US government works. https://www.science.org/about/science-licenses-journal-article-reuse

SUPPLEMENTARY MATERIALS

science.org/doi/10.1126/science.abl5311
Materials and Methods
Supplementary Text
Figs. S1 to S36
Tables S1 to S4
References (*24*–*52*)
Movie S1
MDAR Reproducibility Checklist

Submitted 20 July 2021; accepted 18 March 2022
10.1126/science.abl5311

MEDICAL SCHOOL
UNIVERSITY OF MINNESOTA
Driven to Discover℠

FOUNDING DIRECTOR

Center for Inflammation Science Medical School/Integrative Biology and Physiology

The Department of Integrative Biology and Physiology and the University of Minnesota Medical School is seeking an outstanding, tenured faculty member as Director of the Center for Inflammation Science.

We seek exceptional faculty candidates with established research programs in the study of inflammation in health and disease, from an integrative molecular to systems physiology perspective. Areas of particular interest include sterile inflammation and innate and adaptive immunology as related to the cardiovascular system, muscle, metabolism, diabetes, obesity, stress and related fields. The Director will lead the Center and articulate the vision, mission and integration of the center within the exceptional academic medical center framework. The Director will be given substantial resources to recruit additional tenure-track faculty members to further grow and strengthen the network of faculty studying inflammation in health and disease, including leading the development of NIH programmatic and center grant initiatives.

The director will be conferred as the Bacaner Endowed Chair in Physiology. Substantial resources, with state-of-the-art research space, is committed to this effort. Successful candidates will have an established and innovative research program that embraces biological complexity and physiology from molecular building blocks to the living organism and human disease. Applicants must have a strong record of research accomplishments, as documented by publications in leading peer-reviewed journals along with an outstanding record of extramural funding. Minimum requirements are a PhD, MD or MD/PhD with tenure at an academic research institution.

The Department is an integral component of outstanding Institutes/Centers including the Center for Immunology, Lillehei Heart Institute, Institute for Diabetes, Obesity and Metabolism, Institute for the Biology of Aging and Metabolism, Masonic Cancer Center, and Medical Discovery teams, with exceptional on-site research core facilities including the Physiology Core, University Imaging Center, Mouse Genetics Laboratory, and many others. There are also several active and relevant training grant (T32) programs that offer pre- and post-doctoral support for training students and fellows in several areas, including obesity/diabetes, aging, muscle biology and cardiology. Additional information about the department can be found at **https://med.umn.edu/physiology**.

To apply, please upload a letter of interest, curriculum vitae, statement of programmatic and research goals in response to job opening ID347727 at **http://www1.umn.edu/ohr/employment**. Please also arrange to have three (3) letters of recommendation sent to **jotto@umn.edu** or Search Committee, Department of Integrative Biology and Physiology, Medical School, 6-125 Jackson Hall, 321 Church Street SE, Minneapolis, MN 55455. Review of applications will begin May 1, 2022 and continue until the position is filled.

The University of Minnesota provides equal access to and opportunity in its programs, facilities, and employment without regard to race, color, creed, religion, national origin, gender, age, marital status, disability, public assistance status, veteran status, sexual orientation, gender identity, or gender expression.

ScienceCareers online @sciencecareers.org

By **Senka Holzer**

Don't panic

I was interviewing for the Ph.D. program of my dreams when my potential adviser invited me to look at a sample under the microscope. I meant to grab the eyepiece, but my maneuver went spectacularly wrong when my finger got caught between the two middle buttons of his shirt. My hasty attempt to remove it only made things worse, as the shirt popped open all the way down and even his undershirt pulled out of the waist of his pants. Even now, 15 years later, just writing about it is incredibly embarrassing. But my ability to not panic in that moment landed me the position, and became one of my greatest life lessons.

It was the second phase of the selection process for an international Ph.D. program. Coming from the war-torn country of ex-Yugoslavia, I had passion for research but zero experience. The 2-day interview got off to a rocky start when another professor—the one I most wanted to work with—was so impressed by my competitor's presentation he gave her a high-five. I went to the bathroom to cry, then reminded myself there was more than one spot to be filled, washed my face, and headed to the networking dinner. There, my future adviser found me. "It's brave of you to apply with such a track record," he said. "Don't miss visiting my lab tomorrow." I wasn't sure whether to be flattered or insulted, but I knew I needed to impress him to have a chance at the program.

The next day, things seemed to go from bad to worse. The shuttle that was supposed to take me to the lab never showed up. I desperately hailed a taxi, but was stymied by a language barrier until I thought to show the driver the hospital's logo on my paperwork. After he dropped me off, I had to find my way through a block of 40 hospital buildings. When I finally entered the room full of my competitors, with large sweat circles under my armpits and my face like a swollen tomato, the professor seemed amused. That's when he invited me to the microscope and I "undressed him," as the story was retold by those who witnessed the scene.

The rest of the group was frozen with embarrassment, but I managed to keep my composure. Compared with what I had seen growing up—bombings, widespread corruption, catastrophic inflation—this seemed like a relatively minor disruption. I took charge of the situation. "I'm so sorry," I said, then turned to the science. "There is a nonuniformly stained part of the cell. Which organelle is it?"

"When confronted with challenges, I have managed to keep a cool head and stay positive."

Years later, I asked my adviser why he selected me for the position, even though my track record was weak and I had made a total fool of myself. "Oh, that's simple," he replied. "I was looking for a dedicated troubleshooter who won't freak out at the time of crisis. And this is *exactly* what you demonstrated during the interview." At that moment, I realized that maybe the apparent setbacks during the interview happened not *to* me but *for* me, because otherwise I would have had no chance to stand out.

Looking back, I see my whole life as a series of such experiences. I was denied Ph.D. funding in my home country as its institutions crumbled. My adviser relocated to another country in the middle of my Ph.D. My application for a prestigious grant was rejected when I was already stretched thin maintaining my career after my second child was born. But when confronted with challenges, I have managed to keep a cool head and stay positive—an approach that has helped me find my way through, all the way to the tenure-track position I recently secured.

My intensely difficult early experiences amid political and economic turmoil helped me develop resilience in the heat of crisis. Bad things happen, and not everything has a silver lining. But I've learned to accept what I can't control and take charge of what I can. I certainly don't have it all figured out. But I know that, whatever I am going through, and however undeserved and devastating it feels, it helps tremendously to ask myself a single question: What if this is happening not *to* me, but *for* me? ■

Senka Holzer is a group leader at the Medical University of Graz.
Send your career story to SciCareerEditor@aaas.org.

ILLUSTRATION: ROBERT NEUBECKER

What's Your Next Career Move?

From networking to mentoring to evaluating your skills, find answers to your career questions on *Science* Careers

To view the complete collection, visit
ScienceCareers.org/booklets

Science Careers
FROM THE JOURNAL SCIENCE AAAS

CALL FOR PAPERS

SPJ
SCIENCE PARTNER JOURNALS

之江实验室
ZHEJIANG LAB

spj.sciencemag.org/icomputing

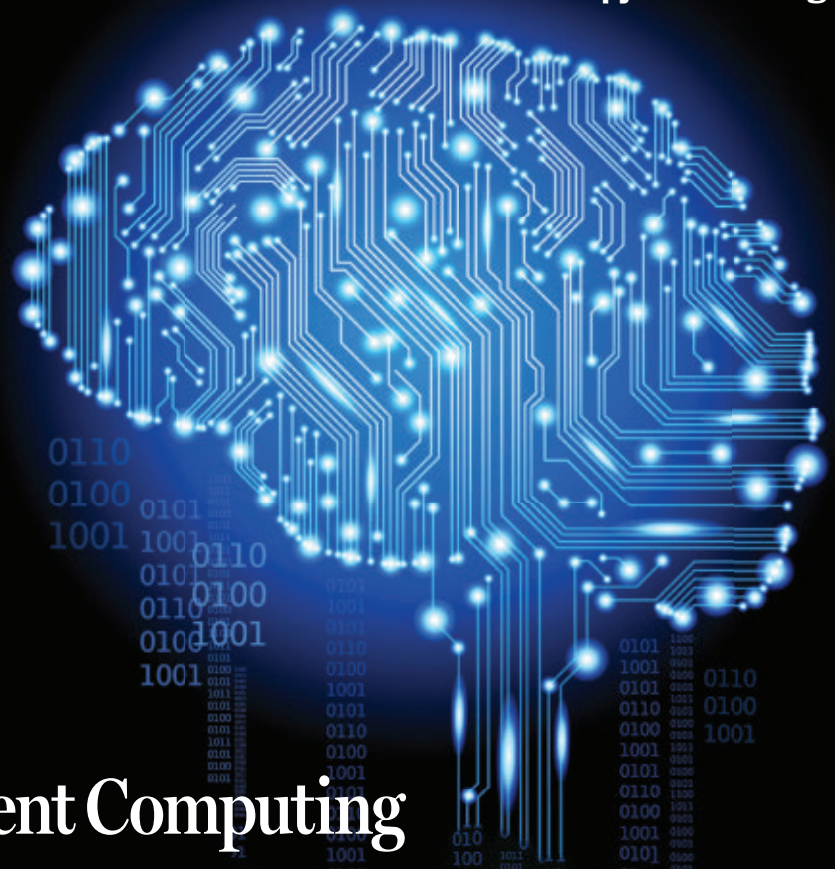

Intelligent Computing

Intelligent Computing is an Open Access journal published in affiliation with **Zhejiang Lab** and distributed by the **American Association for the Advancement of Science (AAAS)**. The journal aims to build a platform that promotes open communication and cooperation for global science and technology professionals in the field. *Intelligent Computing* presents the latest research outcomes and technological breakthroughs to boost the development of intelligent computing science and technology.

Submit your research to *Intelligent Computing* today!
Learn more at: **spj.sciencemag.org/icomputing**

The Science Partner Journals (SPJ) program was established by the American Association for the Advancement of Science (AAAS), the nonprofit publisher of the *Science* family of journals. The SPJ program features high-quality, online-only, open access publications produced in collaboration with international research institutions, foundations, funders and societies. Through these collaborations, AAAS expands its efforts to communicate science broadly and for the benefit of all people by providing top-tier international research organizations with the technology, visibility and publishing expertise that AAAS is uniquely positioned to offer as the world's largest general science membership society.

@SPJournals @SPJournals

OPEN ACCESS

ARTICLE PROCESSING CHARGES WAIVED THROUGH 2024